IAEA
International Atomic Energy Agency

IAEA TECDOC SERIES

No. 2085

# Experiences and Lessons Learned in Managing Severely Damaged Spent Fuel and Corium

Final Report of a Coordinated Research Project

# EXPERIENCES AND LESSONS LEARNED IN MANAGING SEVERELY DAMAGED SPENT FUEL AND CORIUM

The following States are Members of the International Atomic Energy Agency:

AFGHANISTAN
ALBANIA
ALGERIA
ANGOLA
ANTIGUA AND BARBUDA
ARGENTINA
ARMENIA
AUSTRALIA
AUSTRIA
AZERBAIJAN
BAHAMAS
BAHRAIN
BANGLADESH
BARBADOS
BELARUS
BELGIUM
BELIZE
BENIN
BOLIVIA, PLURINATIONAL STATE OF
BOSNIA AND HERZEGOVINA
BOTSWANA
BRAZIL
BRUNEI DARUSSALAM
BULGARIA
BURKINA FASO
BURUNDI
CABO VERDE
CAMBODIA
CAMEROON
CANADA
CENTRAL AFRICAN REPUBLIC
CHAD
CHILE
CHINA
COLOMBIA
COMOROS
CONGO
COOK ISLANDS
COSTA RICA
CÔTE D'IVOIRE
CROATIA
CUBA
CYPRUS
CZECH REPUBLIC
DEMOCRATIC REPUBLIC OF THE CONGO
DENMARK
DJIBOUTI
DOMINICA
DOMINICAN REPUBLIC
ECUADOR
EGYPT
EL SALVADOR
ERITREA
ESTONIA
ESWATINI
ETHIOPIA
FIJI
FINLAND
FRANCE
GABON
GAMBIA, THE
GEORGIA
GERMANY
GHANA
GREECE
GRENADA
GUATEMALA
GUINEA
GUYANA
HAITI
HOLY SEE
HONDURAS
HUNGARY
ICELAND
INDIA
INDONESIA
IRAN, ISLAMIC REPUBLIC OF
IRAQ
IRELAND
ISRAEL
ITALY
JAMAICA
JAPAN
JORDAN
KAZAKHSTAN
KENYA
KOREA, REPUBLIC OF
KUWAIT
KYRGYZSTAN
LAO PEOPLE'S DEMOCRATIC REPUBLIC
LATVIA
LEBANON
LESOTHO
LIBERIA
LIBYA
LIECHTENSTEIN
LITHUANIA
LUXEMBOURG
MADAGASCAR
MALAWI
MALAYSIA
MALI
MALTA
MARSHALL ISLANDS
MAURITANIA
MAURITIUS
MEXICO
MONACO
MONGOLIA
MONTENEGRO
MOROCCO
MOZAMBIQUE
MYANMAR
NAMIBIA
NEPAL
NETHERLANDS, KINGDOM OF THE
NEW ZEALAND
NICARAGUA
NIGER
NIGERIA
NORTH MACEDONIA
NORWAY
OMAN
PAKISTAN
PALAU
PANAMA
PAPUA NEW GUINEA
PARAGUAY
PERU
PHILIPPINES
POLAND
PORTUGAL
QATAR
REPUBLIC OF MOLDOVA
ROMANIA
RUSSIAN FEDERATION
RWANDA
SAINT KITTS AND NEVIS
SAINT LUCIA
SAINT VINCENT AND THE GRENADINES
SAMOA
SAN MARINO
SAUDI ARABIA
SENEGAL
SERBIA
SEYCHELLES
SIERRA LEONE
SINGAPORE
SLOVAKIA
SLOVENIA
SOMALIA
SOUTH AFRICA
SPAIN
SRI LANKA
SUDAN
SWEDEN
SWITZERLAND
SYRIAN ARAB REPUBLIC
TAJIKISTAN
THAILAND
TOGO
TONGA
TRINIDAD AND TOBAGO
TUNISIA
TÜRKİYE
TURKMENISTAN
UGANDA
UKRAINE
UNITED ARAB EMIRATES
UNITED KINGDOM OF GREAT BRITAIN AND NORTHERN IRELAND
UNITED REPUBLIC OF TANZANIA
UNITED STATES OF AMERICA
URUGUAY
UZBEKISTAN
VANUATU
VENEZUELA, BOLIVARIAN REPUBLIC OF
VIET NAM
YEMEN
ZAMBIA
ZIMBABWE

The Agency's Statute was approved on 23 October 1956 by the Conference on the Statute of the IAEA held at United Nations Headquarters, New York; it entered into force on 29 July 1957. The Headquarters of the Agency are situated in Vienna. Its principal objective is "to accelerate and enlarge the contribution of atomic energy to peace, health and prosperity throughout the world''.

IAEA-TECDOC-2085

# EXPERIENCES AND LESSONS LEARNED IN MANAGING SEVERELY DAMAGED SPENT FUEL AND CORIUM

## FINAL REPORT OF A COORDINATED RESEARCH PROJECT

INTERNATIONAL ATOMIC ENERGY AGENCY
VIENNA, 2025

## COPYRIGHT NOTICE



For further information on this publication, please contact:

Nuclear Fuel Cycle and Materials Section
International Atomic Energy Agency
Vienna International Centre
PO Box 100
1400 Vienna, Austria
Email: Official.Mail@iaea.org


Printed by the IAEA in Austria
April 2025
https://doi.org/10.61092/iaea.0tio-a4o3

**IAEA Library Cataloguing in Publication Data**

Names: International Atomic Energy Agency.
Title: Experiences and lessons learned in managing severely damaged spent fuel and corium / International Atomic Energy Agency.
Description: Vienna : International Atomic Energy Agency, 2025. | Series: IAEA TECDOC series, ISSN 1011-4289 ; no. 2085 | Includes bibliographical references.
Identifiers: IAEAL 25-01742 | ISBN 978-92-0-105925-3 (paperback : alk. paper) | ISBN 978-92-0-105825-6 (pdf)
Subjects: LCSH: Nuclear reactor accidents. | Nuclear power plants — Accidents. | Nuclear reactors — Safety measures. | Spent reactor fuels — Management.

## FOREWORD

Between 1979 and 2011, three severe nuclear power plant accidents resulted in melted reactor cores at the Three Mile Island nuclear power plant, the Chornobyl nuclear power plant and the Fukushima Daiichi nuclear power plant. To avoid future accidents, the IAEA has undertaken reviews of these accidents with experts from the international community to learn from them and to act upon the lessons identified. As each of these accidents had a different root cause, each review identified new lessons and in each case led to the implementation of preventative recommendations by Member States.

In response to the Fukushima Daiichi accident, the IAEA Action Plan on Nuclear Safety was developed and agreed by IAEA Member States in September 2011. The initial lessons identified and the actions taken by Member States through the IAEA are outlined in the Fukushima Daiichi Accident report by the Director General and its five technical volumes, released in 2015.

Two of the actions set out in the Action Plan were aimed at facilitating the use of available information and expertise and sharing results of research and development. To partly address these actions, the IAEA established a coordinated research project on the management of severely damaged spent fuel and corium. The intention of the project was to focus on the options for managing fuel debris and corium, and to address the long term behaviour of these materials in different storage environments. This publication presents the final report of the coordinated research project, pulling together experience gained in participating Member States on aspects such as characterizing, recovering and packaging fuel debris and corium, as well as ongoing research on the behaviour of fuel debris and corium in different storage environments, which can be used to inform future fuel debris and corium recovery and conditioning steps.

The IAEA is grateful to the project participants and to the experts who contributed to the drafting of this publication, in particular D. Hambley and A. Callaghan (United Kingdom), T. Washiya (Japan), B. Burakov (Russian Federation), P. Pöml (EC/JRC), L. Szöke (Hungary), and P. Winston (United States of America). The IAEA officers responsible for this publication were P. Standring and A. González-Espartero of the Division of Nuclear Fuel Cycle and Waste Technology.

*EDITORIAL NOTE*

*This publication has been prepared from the original material as submitted by the contributors and has not been edited by the editorial staff of the IAEA. The views expressed remain the responsibility of the contributors and do not necessarily represent the views of the IAEA or its Member States.*

*Guidance and recommendations provided here in relation to identified good practices represent expert opinion but are not made on the basis of a consensus of all Member States.*

*Neither the IAEA nor its Member States assume any responsibility for consequences which may arise from the use of this publication. This publication does not address questions of responsibility, legal or otherwise, for acts or omissions on the part of any person.*

*The use of particular designations of countries or territories does not imply any judgement by the publisher, the IAEA, as to the legal status of such countries or territories, of their authorities and institutions or of the delimitation of their boundaries.*

*The mention of names of specific companies or products (whether or not indicated as registered) does not imply any intention to infringe proprietary rights, nor should it be construed as an endorsement or recommendation on the part of the IAEA.*

*The authors are responsible for having obtained the necessary permission for the IAEA to reproduce, translate or use material from sources already protected by copyrights.*

*The IAEA has no responsibility for the persistence or accuracy of URLs for external or third party Internet web sites referred to in this publication and does not guarantee that any content on such web sites is, or will remain, accurate or appropriate.*

**CONTENTS**

# 1. INTRODUCTION

## 1.1. BACKGROUND

When a reactor is automatically shut down in response to an external or internal event, the residual heat must be removed. Residual heat is the sum of the heat originating from radioactive decay, shut down fission, the heat stored in reactor related structures and in heat transport media. If this residual heat cannot be managed by the various built–in defence mechanisms and operator procedures, then a loss of cooling accident (LOCA) will occur.

A LOCA involves the progressive heat up of the reactor core and in turn the fuel in-core and the materials surrounding the core. In terms of in-core Zircaloy clad fuel, as the temperature increases the fuel will undergo thermal creep leading to clad rupture and release of volatile fission products/filler gas. What happens next depends on the peak temperature and atmosphere inside the core. If steam is present and the fuel temperature is >1200 °C Zircaloy will readily react to produce hydrogen, which needs to be managed to prevent a deflagration or detonation. If oxygen or nitrogen are present, the peak temperature might escalate because of rapid cladding oxidation and/or nitriding. Since these processes are strongly exothermal, they can result in a self-sustained zirconium fire, leading to structural degradation of the fuel assembly and release of fission products. As the loss of cooling progresses semi and low volatile fission products will be released, uranium will have undergone transitions to higher oxidation states and finally the non-volatile fission products will be released when the fuel melts. At this stage the fuel/cladding might interact with core and structural materials forming corium. A continuation of the processes might lead to the core primary containment being breached and the corium passing through the containment barrier into secondary containment, where it can interact with concrete to form melted corium–concrete interaction (MCCI) products.

Between 1979 and 2011 there have been three severe nuclear power plant (NPP) accidents resulting in melted reactor cores at Three Mile Island (TMI, USA), Chornobyl (ChNPP, Ukraine), and Fukushima Daiichi (1F[1], Japan). In addition, there has been a loss of cooling accident at PAKs NPP Unit 2 (Hungary) associated with the cleaning of irradiated fuel in a tank in a service pit connected to the at-reactor (AR) pool. The accidents at TMI and PAKs have both been remediated to the point that the material is either in monitored safe storage or is packaged pending reprocessing.

Chornobyl Unit 4, which was destroyed during the accident, was eventually stabilized in 2016 with the installation of new safe containment. Dismantling of the old sarcophagus that covers the reactor and recovery of the debris is pending. After stabilization of the unit focus has turned to transferring the fuel from Units 1–3 into dry storage (intermediate spent fuel storage No.2 (ISF–2)) and the building of a liquid radioactive waste treatment plant (LRTP), to treat highly active liquid held on site. The first cask of loaded fuel was transferred to ISF–2 in 2020 and LRTP obtained a licence to operate in 2021.

The decommissioning of the Fukushima Daiichi NPP (1F) is a major challenge as three of the first–generation reactors suffered meltdown. The fourth reactor was shut down when the accident occurred and was unaffected, but the building suffered serious damage due to a hydrogen explosion initiated in Unit 3. Progress on the decommissioning of 1F is routinely reported to the IAEA by the Government of Japan. As of February 2023, fuel removal from Unit 4 to the common storage pool had been completed (2014); fuel removal from Unit 3 AR pool had been completed (2021); preparations are underway at Unit 2 to collect fuel debris from the pressure containment vessel (PCV)

[1] Fukushima Daiichi (number one) is referred to as 1F throughout this text.

using a robotic arm and other remotely operated devices, and in Unit 1, internal investigations of the PCV have been undertaken to establish the location of the debris.

The process of remediating these accidents and associated damaged fuel/fuel debris management provides valuable learning. The CRP on the management of severely damaged spent fuel and corium (referred to as CORIUM CRP) was set up in 2015 in response to actions raised in the Nuclear Safety Action Plan (2012) and provided a mechanism for bringing together interested parties, sharing information, experiences in this area.

This publication reports the experiences, and research and development of the participating Member States in the efforts associated with the characterization, recovery and management of fuel containing materials (fuel assemblies (FAs), fuel debris, corium and MCCI). The report also contains valuable information into the evolution of corium and fuel debris in storage.

Three coordinated research meetings were held during the CORIUM CRP: the first in February 2017 in Vienna, Austria; the second in November 2018 in Tomioka, Japan and the third in August—September 2022 in Vienna, Austria.

## 1.2. OBJECTIVES

The overall objective of the CRP was to expand the existing knowledge base and identify optimal approaches for managing corium and severely damaged spent fuel.

Specific research objectives were developed to assess the following:

- Techniques for the in–situ monitoring of severely damaged spent fuel;
- Characterization of severely damaged spent fuel;
- Computer modelling applied to all physical and chemical phenomena for all stages from retrieval through to disposal;
- Tools and techniques for the sampling and handling of severely damaged spent fuel;
- Long term behaviour of severely damaged spent fuel and packaged material (for example radiolysis, chemical and physical properties);
- Techniques for packaging materials/fuel debris;
- Tools and techniques for materials accountancy;
- Tools and techniques for conditioning severely damaged spent fuel for interim storage, processing (including reprocessing, separation, vitrification) or disposal;
- Drying of fuel debris/materials;
- Behaviour of severely damaged spent fuel during the transfer from one stage to the next stage (to support safety case development);
- Source term release during interim storage, transfer to next stage and disposal.

## 1.3. SCOPE

This publication describes severe power reactor accidents where the reactor core has been subject to a loss of cooling and has resulted in the formation of corium and products from (MCCI). It also provides learning on the characterization of corium and MCCI products, and the management of severely/ damaged spent fuel from NPPs/prototype NPPs and fuel debris.

Throughout this document the terminology ‘severely damaged spent fuel’ will be used. Severely damaged spent fuel includes material from post irradiation examination (PIE); fuel damaged during normal fuel handling operations; fuel damaged because of loss of cooling; corium; MCCI products.

## 1.4. STRUCTURE

The publication brings together a combination of existing information and up to date development/research in severely damaged spent fuel, provided by the participating institutes.

The publication is divided into Sections which enable easy access to the material of particular interest. For completeness, background information on the three severe power reactor accidents with an emphasis on the materials involved is provided. Other Sections provide information on:

(a) Characterization of corium/MCCI;
(b) Severely damaged, failed and degraded fuel;
(c) Computer modelling related to accident progression;
(d) Inspection technologies;
(e) Packaging, transport and disposal;
(f) Materials accountancy/safeguards considerations;
(g) Knowledge management.

## 2. REVIEW OF POWER REACTOR ACCIDENTS IN PARTICIPATING COUNTRIES RESULTING IN SEVERELY DAMAGED SPENT FUEL AND CORIUM

As a mechanism of providing context to the later Sections on characterization and the management of severely damaged spent fuel, an overview of severe power reactor accidents in participating Member States is provided. In this review emphasis is given to the materials involved in the accident as this forms the basis of the resulting fuel containing debris.

### 2.1. THREE MILE ISLAND (UNITED STATES OF AMERICA)

The debris at TMI, Unit 2 (TMI–2), located in Dauphin County, Pennsylvania, USA resulted from a meltdown accident that is well documented. An aerial view of the facility is shown in Fig. 1. The process of system recovery and core removal was done forensically, with the purpose of understanding the effects of the loss of coolant, the dynamics of the melting process and the release of fission products. As the recovery progressed, international laboratories participated in the characterization and analysis of the debris to understand the sequence of events that occurred in the core.

The accident recovery and debris management process following the initial post meltdown stabilization included core status, melted core characterization, and design phases for core removal, packaging, and transportation. Following interim wet storage, a dry storage system design was identified and adapted for use with the debris and its unique canister designs.


*FIG. 1. Aerial view of TMI NPP (courtesy of Idaho National Laboratory (INL)).*

#### 2.1.1. Reactor description

TMI-2 was a Babcock and Wilcox (B&W) Pressurized Water Reactor (PWR) rated at 890 MW(e) (2770 MW(th)) output with two steam generator loops and a core composed of 177 FAs. The FA design used a 15 × 15 rod array containing 208 (3.9 m long) fuel rods with an active fuel length of 3.7 m, 16 Zircaloy control rod guide tubes, and one Zircaloy centre position instrument tube with eight Inconel 814 spacer grids to maintain rod positioning, and upper and lower end fittings of type

304L stainless steel, as shown in Fig. 2. The fuel was composed of 9.36 mm outside diameter (OD) uranium dioxide ($UO_2$) pellets with enrichment ranging up to 2.98 wt%. Seventy–two of the assemblies contained Zircaloy rods with 1% boron carbide ($B_4C$) burnable poison, interspersed within 94% alumina ($Al_2O_3$) pellets amounting to a total of 626 kg. The total $UO_2$ fuel mass was 94 029 kg, with an average $^{235}U$ enrichment of 2.265 wt%. The Zircaloy–4 cladding mass was 23 177 kg, with zirconium being 97.9 wt% of the alloy [1].

Sixty–one control rod assemblies, using 304L stainless steel clad rods that contained 3403 mm of silver–indium–cadmium alloy provided shut down control in the core. At the time of the meltdown, the control rods were fully inserted. The fuel burnup at that point was 3175 MWd/tU. In a PWR design, the control rods are positioned in the core through the reactor pressure vessel upper head.

Eight stainless steel clad axial power shaping rods, containing 914 mm sections of silver–indium–cadmium, were included in the core.

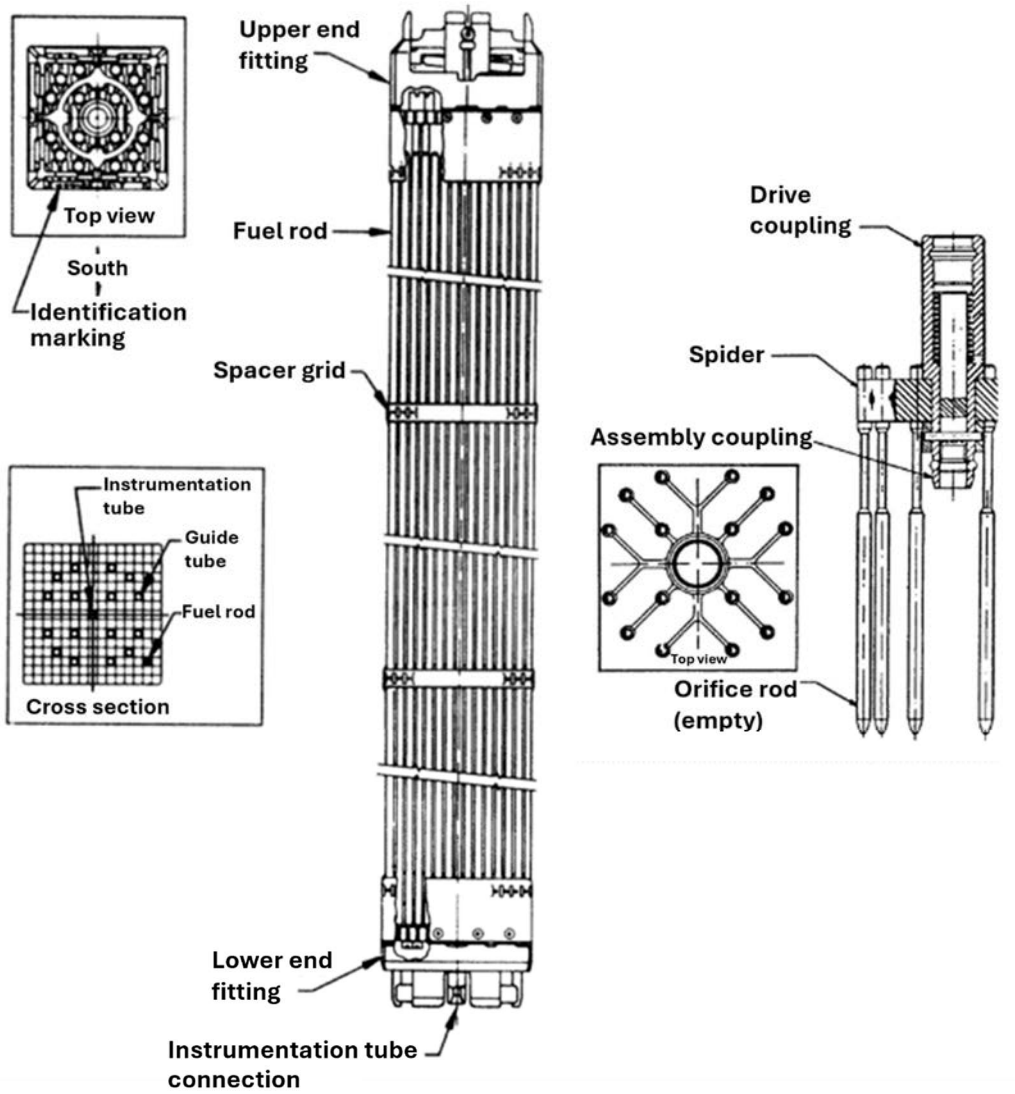


*FIG. 2. General configuration of 15×15 fuel assembly, left; control rod assembly right (reproduced from Ref [1] with permission courtesy of INL).*

The general reactor pressure vessel configuration, taken from a B&W training aid is shown as Fig. 3.

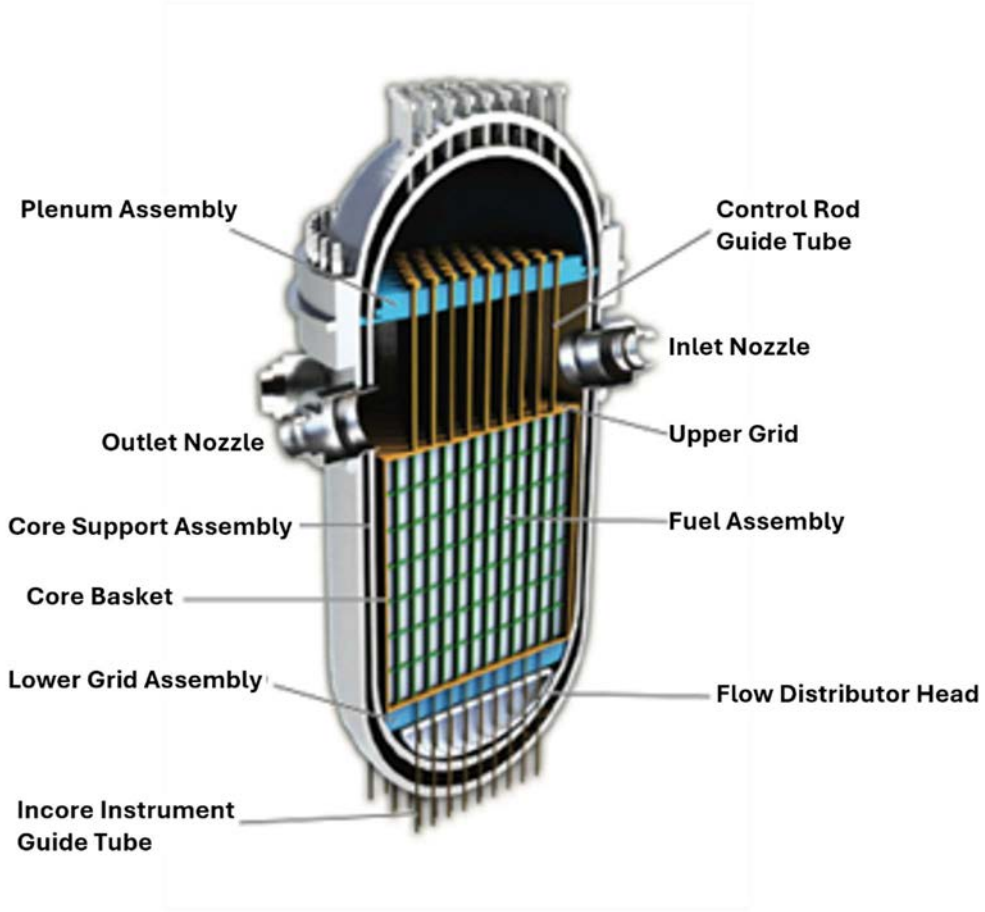


*FIG. 3. General PWR reactor pressure vessel configuration (courtesy of INL).*

The pressure vessel was constructed of American Society for Testing and Materials (ASTM) A533 Grade B low alloy steel made as a forged cylindrical shell with a welded hemispherical bottom head. The inner surfaces were lined with austenitic 300 series stainless steel to prevent corrosion due to contact with primary coolant. The vessel inner diameter was 434 cm with a wall thickness of 21.44 to 21.74 cm, with an inner liner thickness of 0.48 cm [2]. The nominal height of the complete vessel is 13.4 m. Instrument penetrations welded into the bottom head of the vessel were made of Inconel 600 [3].

PWR designs have pressurized primary cooling loop that circulates water through the core to remove fission energy, which is transferred via heat exchangers to water in the secondary loop(s) from which steam is generated, flowing to drive turbine generator sets to produce electrical power. Primary cooling water contains boron to provide supplemental reactivity control. Feedwater in the secondary is demineralized with ion exchange resins to minimize any dissolved chemical constituents that could cause problems in the steam system. The TMI–2 design used two steam generator loops as heat exchangers. Steam condensed following passage through the turbines was returned to the system by condensate pumps. The primary cooling loop was operated at 15.5 MPa at 561 K as controlled in a pressurizer vessel to maintain the primary core cooling water in the liquid phase. The pressurizer was maintained partially full of steam and partially of water to allow for expansion of the primary coolant due to core temperature heat up. If the system exceeded design pressure, the pressurizer had a set of relief valves that discharged to an overflow tank. System operability depended on having water in the secondary steam generator loops to remove the heat generated by fission. A schematic of the plant is shown as Fig. 4.

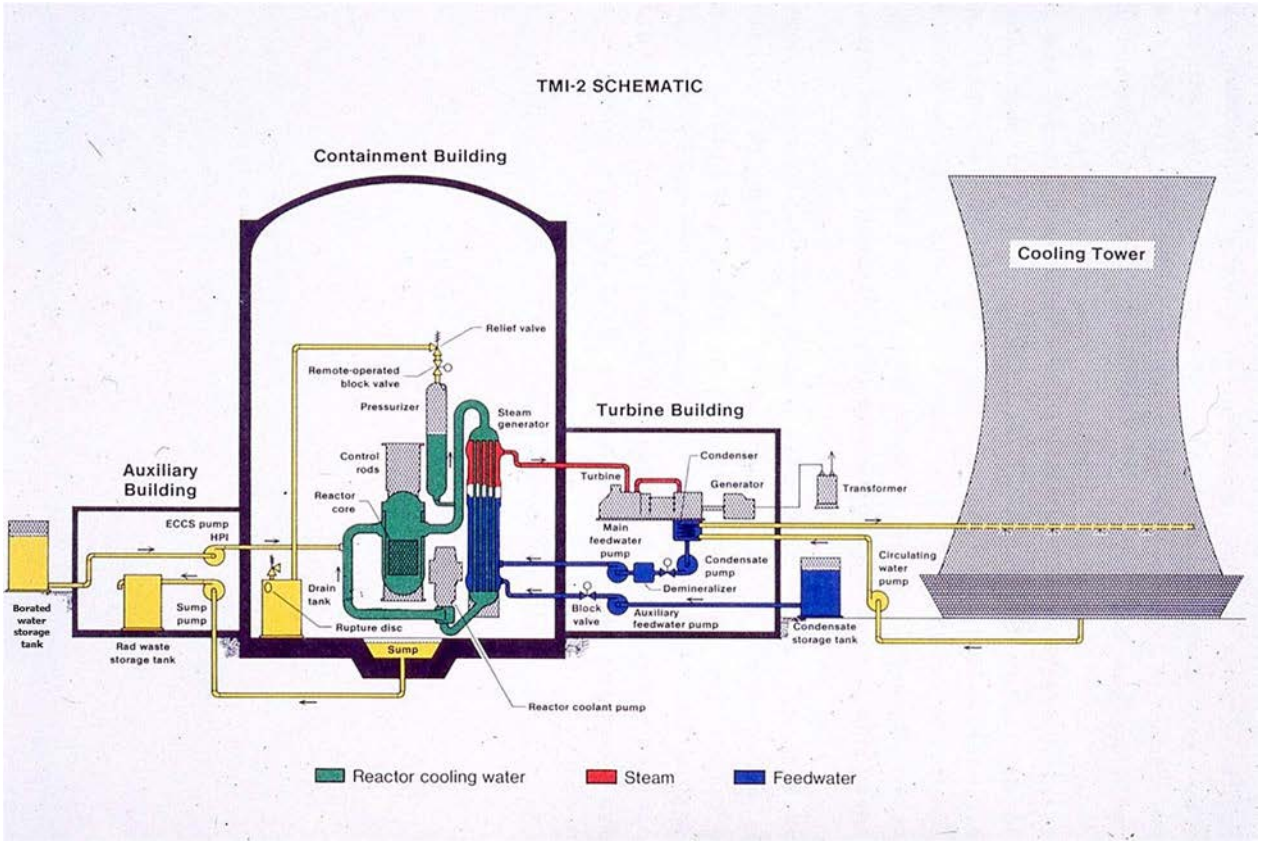


*FIG. 4. Simplified TMI–2 reactor process (courtesy of INL).*

### 2.1.2. Accident description

At 4.00 a.m. local time on 28 Mar. 1979, TMI–2 condensate pumps supplying feedwater to the secondary loop shut down while the reactor was operating at 97% nominal power with four reactor primary cooling pumps running. The reactor had operated since 7 March without interruption. The loss of feedwater would normally have been compensated for by the auxiliary feedwater system, however the supply to the auxiliary feedwater pumps was valved out following a maintenance test on the feedwater ion exchange system. Lacking feedwater to remove heat from the primary system, the primary coolant increased in temperature and volume, increasing the system pressure to the extent that the electrically actuated pilot operated relief valve (PORV) on the pressurizer vessel opened within four seconds of the loss of feedwater. After nine seconds, the reactor shut down system inserted control rods to terminate criticality. System pressure decreased as a result of the valve opening and the core shut down. The PORV should have closed due to the reduced pressure. A design flaw in the valve caused it to remain open, and a control system flaw gave operators the indication that the valve had closed. In accordance with procedures, the operators turned on the high pressure water injection system to maintain water level in the primary loop. Because the PORV was open, the pressurizer was not able to maintain the core in the liquid phase, allowing steam to form in the core, causing an increase in water level in the pressurizer. The indication of increased water level in the pressurizer caused the operators to shut off the high pressure water injection system to supposedly maintain the operational vapour space in the pressurizer to allow system control. The pressure in the system decreased and the water level increased. Due to the production of steam in the primary loop, the primary cooling pumps began to cavitate due to the vapour–liquid composition of the coolant. The operating pumps were shut down approximately one hundred minutes after the initial feedwater shut down. Lacking the forced circulation of the primary pumps, the coolant boiled off to the point that

the fuel assemblies in the core became uncovered, allowing the temperature to rise further. A significant increase in containment building radiation levels occurred at 142 minutes. From the thermocouple data, by 150 minutes, the core temperature rose to the point at which the Zircaloy cladding began to fail, with zirconium metal reacting with the steam, releasing fission products into the primary coolant water. The steam zirconium reaction is highly exothermic, generating hydrogen and increasing the core temperature further, causing cladding and fuel to melt and be drained to the lower core, solidifying at the vapour–liquid interface. Despite the high temperature and high hydrogen concentration in the system, there was limited oxygen available because it was being consumed in the zirconium metal to zirconium oxide reaction, resulting in a condition with no potential for explosion or deflagration. During this period of time, water and steam were being discharged to the drain tank through the PORV to the extent that the tank rupture disk failed, allowing release of the contaminated coolant to the reactor building sump.

Approximately two and a half hours after the incident started, operators were able to determine that the pressurizer relief valve was stuck open and closed the block valve downstream of the PORV. Once the relief block valve was closed, operators started a primary coolant pump briefly to try to cool the core and stabilize the system. The influx of water is believed to have caused the upper sections of the relatively intact remaining fuel to shatter and fall onto the top of the melted material in the centre of the vessel. Neither introduction of water from the cooling pump or the emergency injection system resulted in raising the core water level to the point that the core was again covered by 210 minutes. In another 15 minutes, the core temperature had risen to the melt temperature of the uranium–zirconium oxide mixture that formed the bulk of the melt, causing a portion of the melt to flow through a hole in the side baffle plates, draining through the upper and lower core support assemblies, solidifying on the bottom head of the reactor vessel. The presence of cooling water prevented the reactor pressure vessel wall from reaching the melting temperature of the steel, although some damage was later noted on the in–core instrumentation nozzles.

At this point it was no longer possible to make water circulate using the primary cooling pumps, so the core was cooled via the relief system using a once through water injection to remove the heat load. The system was stabilized after about 16 hours and core steam generation ceased. Hydrogen from the zirconium–steam reaction had been released into the air filled reactor containment building via the tank overflow to the sump, ultimately reaching a concentration >4 vol·%, which it is assumed was ignited by some electrical switchgear, resulting in a deflagration that produced a pressure surge of 0.19 MPa, significantly less than the containment building design pressure.

The water that had been discharged from the drain tank into the containment building sump was highly contaminated from the fission products being released from the melting core. As a consequence, manned entry into the building did not take place until Jul. 1980. Cleanup of the water progressed for several years. Boric acid was added to the water as a criticality prevention measure.

The first video inspection of the core was not accomplished until 1982, followed by ultrasonic mapping of the core void in 1983. Probing of the melt determined that loose material was present on the upper surface. Samples of the loose material acquired in 1984 gave the first indications of the character of the melt. Ultrasonic mapping of the upper debris surface and core bores through the depth of the melt to the lower core support structure, at ten points, were performed in 1986.

As a result of the accident, approximately 62 t of the core assemblies melted, and an estimated 22 t of core material flowed from the central core region and solidified on the lower vessel head. The upper plenum was largely intact, and analysis of the control rod lead screws indicated that the temperature above the central core region reached 1250 K while the perimeter only reached 700 K,

with the damage zones approximately 1.2 m in diameter and confined to the areas below the upper spacer grid [4].

Core damage was defined in terms of four zones: (a) a 9.3 $m^3$ void 1.5 to 2 m deep in centre of the upper core; (b) a 0.6 to 1 m deep layer of loose fragmented debris that reached 2200 K; (c) 32.7 t of solidified metal and ceramic mixture, formerly molten core, primarily composed of uranium and zirconium oxide with metallic silver and iron inclusions; (d) partial and full length FAs around the periphery of the melt. The central melt was surrounded by a crust, with the 10 cm layer below the melt composed of zirconium, iron and silver metal, and the 1 to 3 cm upper crust containing iron and silver with indium and nickel.

The core support assembly was damaged in the east quadrant, where baffle plates partially melted, allowing molten material to flow into the lower core support assembly and contact the wall of the reactor pressure vessel.

Low volatility fission products, $^{144}Ce$, $^{154}Eu$, and $^{155}Eu$, and medium volatile fission products, $^{90}Sr$, $^{125}Sb$, and $^{106}Ru$, were detected in melt samples while $^{85}Kr$, $^{137}Cs$ and $^{129}I$ were largely released from the fuel. Approximately 3.5% of the medium volatility species were transported beyond the reactor vessel, with only 0.1% reaching the reactor coolant bleed tanks in the auxiliary building. Isotopes $^{125}Sb$ and $^{106}Ru$ were found to have been selectively deposited in the metallic region below the core at concentrations 6 to 20 times that found in the fuel. Isotopes $^{85}Kr$, $^{137}Cs$ and $^{129}I$ were transported by the cooling system and distributed throughout the reactor building basement. Approximately 20% of the $^{137}Cs$ and $^{129}I$ was retained in the fuel debris, while 85% of the $^{85}Kr$ was released to the containment building atmosphere.

A consortium including General Public Utilities (GPU), Electric Power Research Institute (EPRI), the United States Nuclear Regulatory Commission (US NRC), and the United States Department of Energy (US DOE), collectively known as GEND, was responsible for determining the recovery process and directing the research into the cause and effects of the accident. A series of GEND reports containing predictions and documenting design choices was produced [5].

Over a period of seven years, the reactor building was decontaminated, the water treated, the reactor vessel head was removed, the core was recovered with the reactor vessel full of water, the recovered core debris placed in canisters and shipped from Pennsylvania to INL for wet storage. In 1995 a decision was taken to move the debris from wet to dry storage. This decision was based on the economics of actively maintaining controlled conditions and assuring that no contaminated water could leak to the environment in a wet pool system versus passive operation of an above ground dry storage system. The transfer of the debris to dry storage began in 1999 and was completed by 2001. The stored debris has been maintained in vented dry storage canisters at Idaho Nuclear Technology and Engineering Center (INTEC) CPP–2774 facility of INL under license from US NRC since its transfer.

Management of the debris was done according to primary concerns that included prevention of criticality during material recovery and packaging, avoiding potential chemical reactions including pyrophoricity and hydrogen ignition, preventing personnel radiological exposure beyond regulatory limits and prevention of environmental radiological release.

Recent review of the accident root cause highlights the lack of analysis of LOCA scenarios with a small discharge cross section (such as that resulting from the stuck PORV) and the fact that the PORV was not identified as a safety significant component. Because the safety analysis report (SAR) did not include a small break LOCA scenario, operators had no training on the correct response to this

type of incident. Given that PORVs had failed to close at other facilities on at least eight other occasions, having that information available to the operators could have allowed them to identify the problem in time to prevent further core overheating. It is also noted that the type of PORV used in this design was prone to having closure problems after discharging two phase steam–water flow. The valve is shown in Fig. 5.

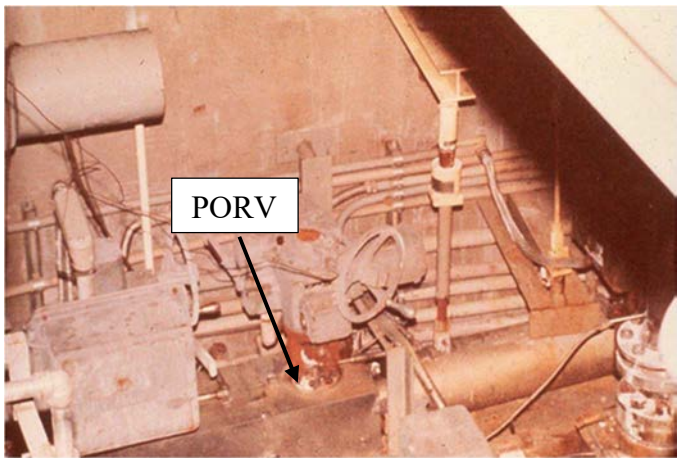


*FIG. 5. Pilot operated relief valve (courtesy of INL).*

It should be noted that a multitude of documents have been generated regarding virtually all aspects of the TMI–2 recovery [5] and various scientific papers have been published in Nuclear Technology [6–9]. Many of the documents and figures used in this report originate from these sources. Pennsylvania State University and University of Tennessee also maintain document archives on TMI–2.

A timeline of TMI Unit 2 cleanup is shown in Fig. 6.

## 2.2. CHORNOBYL (UKRAINE)

The accident at Unit 4 of ChNPP resulted in reactor destruction and spread of radioactive contamination to several bordering and western European countries. ChNPP near Pripyat, Ukraine, comprises four reactors of the *Reaktor Bol'shoi Moshchnosti Kanal'nii* (RBMK) 1000 type. The RBMK–1000 is a graphite moderated high power channel type boiling water reactor (BWR), with a design capacity of 3200 MW(th), 1000 MW(e). The channel design uses separate tubes for each FA. Each tube has a dedicated feedwater input pipe and steam discharge that allow isolation of each FA by closing the inlet and outlet valves. This arrangement allows fast fuel reloading without the need to shut down the reactor and permits blocking or reloading of selected channels. The design also allows a relatively simple scalability with a possibility to provide different power outputs. However, the presence of large number of water pipes and other systems complicates operations. It is reported that Unit 4 had 1661 fuel channels and 211 channels for several types of control rods [10], including 187 five meter rods inserted from above the reactor and 24 shorter three and half meter rods inserted from beneath.

The very large core size might, in certain regimes, allow the reactor to behave as several quasi–independent cores. The channel design of the RBMK reactor, where individual fuel assemblies are contained in separate channels, precludes the need for a dedicated containment building or large pressure containment vessel. The most severe foreseen accident was a rupture of the main water pipe and to mitigate consequences from such an event several dedicated concrete compartments, and two bubbler pools were constructed.

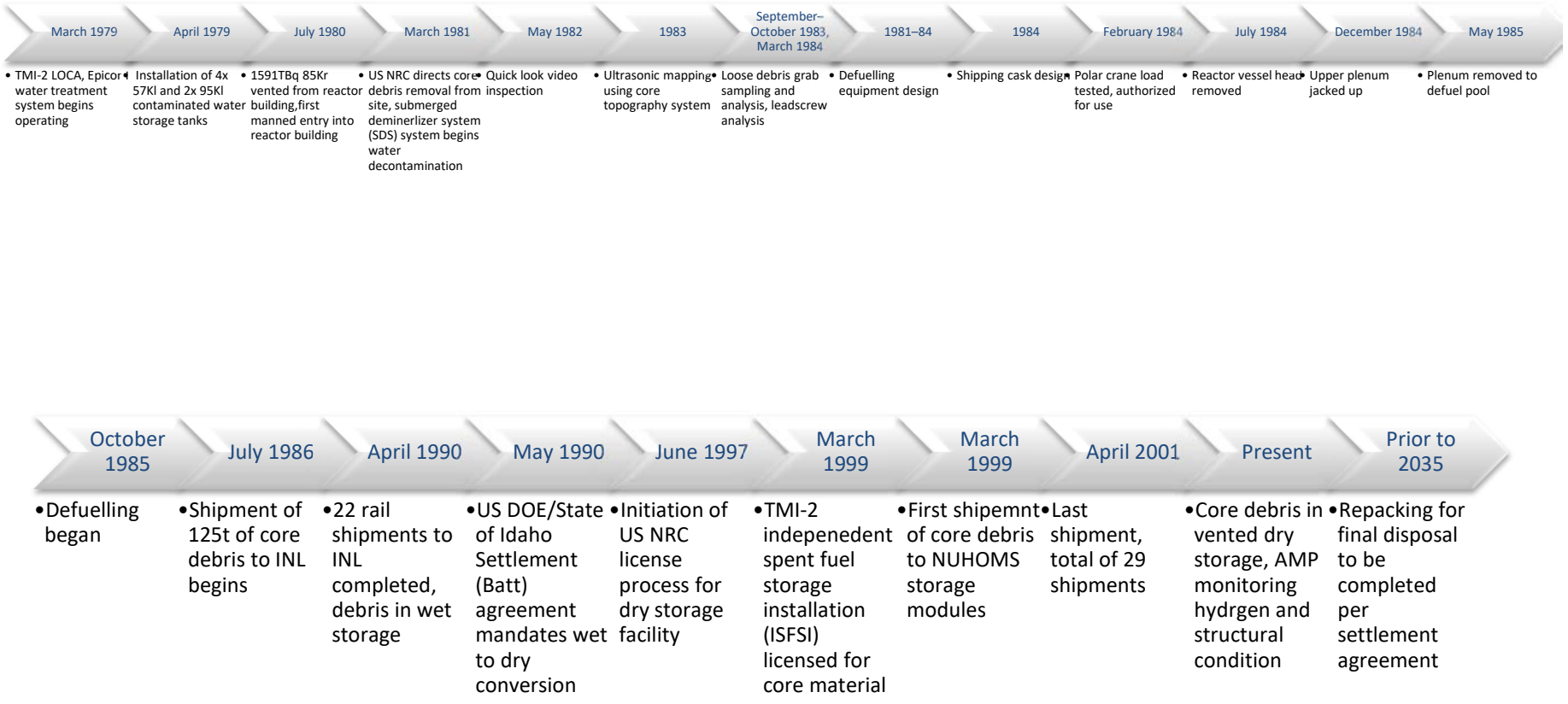


*FIG. 6. Three Mile Island Unit 2 cleanup timeline.*

ChNPP, planned to comprise six power units, commenced operations in 1977. By 1986 four units were in operation, Unit 4 was connected to the grid in Dec. 1983. Following the accident at Unit 4 in 1986 the remaining units were kept in service but were gradually shut down from 1991 with Unit 3 eventually shut down in 2000.

### 2.2.1. Reactor description

Although many publications that provide a detailed description of the design of a RBMK–1000 reactor are available [11—17], the evolution of its design and the associated changes in fuel composition and construction materials have led to some inconsistencies in the reporting. An inventory of the various materials used in Unit 4 is difficult to find, however these materials are described quite comprehensively in the reactor technical report [18]. The key features of the design and the materials that were available to react at the time of the accident to form the resultant melt are summarized below.

The main reactor vessel located 19–27 m above ground [16] consisted of three hollow steel cylinders (Fig. 7), hermetically sealed and welded to each other, made of Russian grade 10KHSND[2] structural steel. The central steel cylinder with a thickness of 16 mm, diameter of 14.5 m and height of 9.05 m weighed 70 t. The reactor cover plate, made from 40 mm thick steel [14], 17 m in diameter and 3 m in height, was filled with 1005 t of serpentinite[3] based material [11, 12, 15, 19], used to provide neutron shielding [20]. The total weight of steel used in the cover plate is stated as 450 t [15] and weight of the whole cover plate was estimated at ~3600 t [21]. The reactor base plate, 14.5 m in diameter and 2 m in height, had 40 mm thick stiffeners sectioning its interior into 1000 × 1000 × 2000 mm blocks. The stiffeners and pipes held the cover and base plates together. The internal space of the base plate was filled with ~425–490 t [22—23] of serpentine based material [11—12] in nitrogen atmosphere [11]. Total weight of steel is quoted between 280 and 933 t [16, 21].

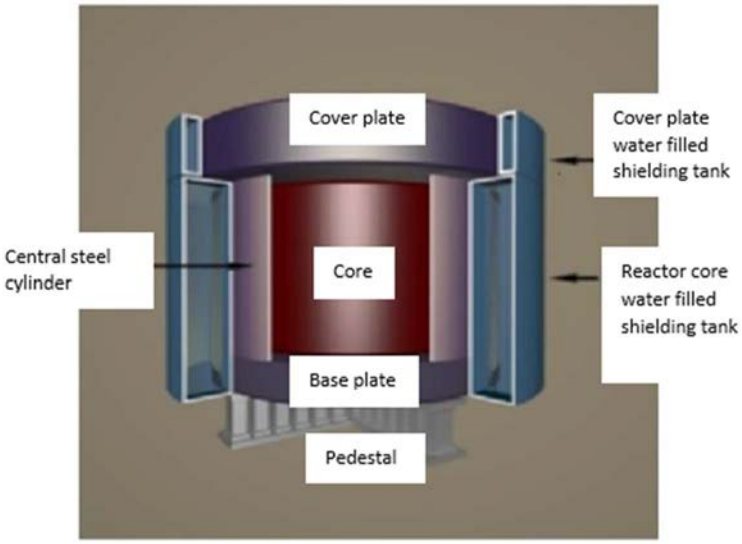


*FIG. 7. Simplified representation of RBMK reactor (courtesy of B.E. Burakov, Ioffe Physical-Technical Institute of the Russian Academy of Sciences (Ioffe Institute)).*

[2] Specification - C up to 0.12; Si 0.8–1.1; Ni 0.5–0.8; S up to 0.035; P up to 0.035; Cr 0.6–0.9; Cu 0.4–0.; Mn 0.5–0.8 (wt%) [22].

[3] Serpentinite is a highly hydrated type of naturally occurring magnesium silicate rock that has nominal chemical form of $Mg_3Si_2O_5(OH)_4$.

The biological shield was composed of two cylindrical, double walled, hollow, hermetically sealed 10KHSND steel tanks filled with water. The central shielding tank, 30 mm [21] thick, with internal and external diameters of 16.6 m and 19 m respectively and height of 11 m, weighed 592 t [15]. The tank surrounding the reactor cover plate, with internal and external diameters of 17.8 m and 19 m respectively and height of 3.2 m, weighed 236 t [16]. The space between the tanks and the outer concrete wall was filled with sand [11—12].

The internal reactor and all three cylinders were supported on a cross like shaped steel pedestal, 5.3 m in height, made from 10KHSND steel plated in aluminium (0.15−0.25 mm thick) and painted with an organic silicate varnish [14]. During the accident parts of the pedestal were displaced into room No.305/2 below the reactor base.

The reactor core consisted of graphite blocks (moderator and reflector (outer core)), fuel channels and two independent cooling loops (each cooling half the reactor). The graphite blocks of GR-280 type sized 250 × 250 $mm^2$ of varying height (200—600 mm) [11—12] were made up into 2488 columns to form a cylinder 14 m in diameter and 8 m in heigh. In addition, there were ring and bush graphite fittings (GRP2-125 graphite). The total weight of graphite ranged from 1700 to 1810 t + 105 t (graphite rings) [11, 12, 16, 19, 21]. The fuel channels were made from Zr + 2.5% Nb [11] tubes 88 mm in diameter and 4 mm thick [11—12]. Channel connections to the water–steam supply system were made of Russian type 08X18H10T[4] stainless steel [11—12]. The space between the external surface of the channels and the graphite blocks were secured by graphite rings. The coolant entered the reactor core from below as water, subcooled to below the boiling temperature, and began to boil at some point along the flow path. The reactor internal atmosphere consisted of a mixture of $N_2$ and He. Internal pressure was around 1.5 kPa and an $N_2$ gas overpressure of 0.2–1.2 kPa was maintained between the central reactor cylinder and the shielding tank to prevent leakage. The absolute pressure was ranged from 1.7–2.7 kPa of $N_2$ [11], or 2.0—2.5 kPa of $N_2$ [15]. The normal operating inlet temperature was 543 K and outlet temperature was 557 K.

Fuel assemblies (Fig. 8) comprised of two fuel elements [11—13] positioned on a central structural tube ~10 m in length [12, 15]. Each fuel element consisted of 18 fuel pins ~3.64 m long [12—14]. Fuel pins surrounding the central tube formed 2 rings of 6 and 12 pins, respectively [11—14]. The structural tube was made from Zr + 2.5% Nb, was 15 mm in diameter and 1.25 mm thick [11—12]. Fuel pins (Fig. 8) consisted of fuel pellets ($UO_2$) loaded into Zr + 1 wt.% Nb tubes [11]. The cladding tube was 3611 mm long with an external diameter of ~14 mm [15]. Each FA had three spacing grids [14] made of (unspecified) stainless steel. The amount of uranium in one FA was between 57.35 to 65.32 kg of $UO_2$ [15]. The total weight of one FA was 185 kg [12—13]. At the time of the accident the reactor was loaded with 1659 FAs [16], estimated to be between 187.63 to 192.94 tU [14]. There was also 129 spent FAs [21], 16–17 t of irradiated $UO_2$ in the AR pool and 48 fresh FAs [21], about 6 t of unirradiated $UO_2$.

Control rods were made from aluminium alloy CAB-1 or, in later designs, from various types of steel. The rods were filled with sintered boron carbide (close to $B_4C$) with a density of 1.6–1.9 g/$cm^3$ [12].

Table 1 summarizes the materials that were available to react at the time of the accident to form the resultant melt based on the abovementioned information and data given in Ref. [25], where materials directly involved in ‘lava’ formation were included.

[4] Specification C up to 0.08; Si up to 0.8; Mn up to 2.0; Cr 17.0–19.0; Ni 9.0–11.0, Fe balance [23].

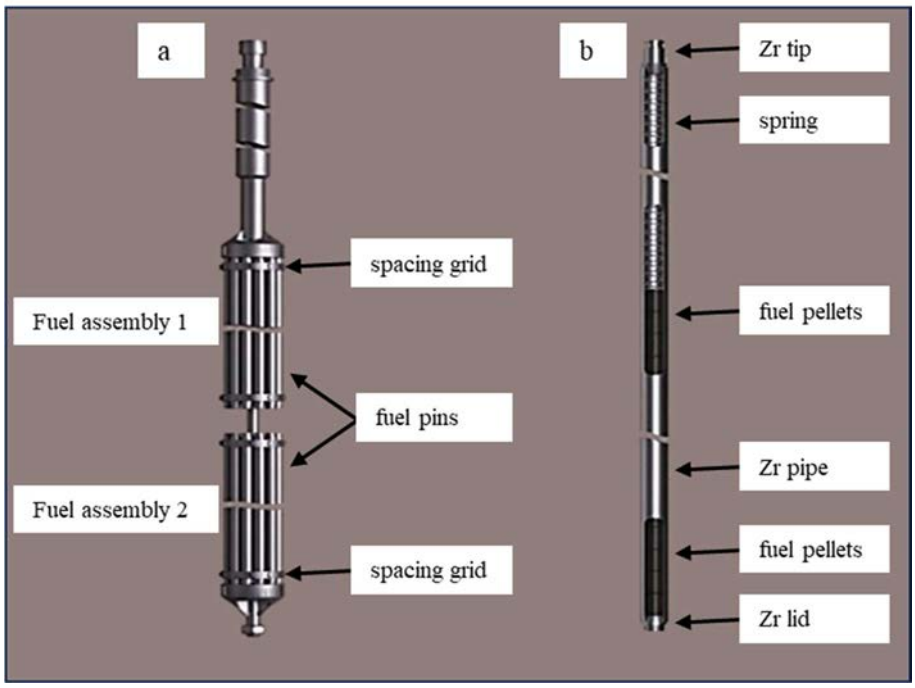


*FIG. 8. Fuel assembly (a) and fuel pin (b) of RBMK–1000. Images had been simplified and adapted from Ref. [15] (courtesy of B.E. Burakov, Ioffe Institute).*

TABLE 1. SUMMARY OF MATERIALS AVAILABLE TO REACT AND ESTIMATE OF MATERIALS IN MELT

| Material | Estimated quantities of materials available to react (t) | Estimated quantities of materials in melt [25] |
|---|---|---|
| Graphite | >1700 | >1700 |
| Steel Russian grade 10KHSND | 100s | up to 175 |
| Steel Russian grade 10XH1M | 125 | — |
| Steel Russian grade 08X18H10T | >50 | — |
| Steel from top and bottom plates | — | 90 |
| Cast iron balls (filled with serpentine) | — | — |
| Fuel ($UO_2$) | 216–224 | 90 or 120 |
| Zirconium | — | 45 |
| Stainless steel spacer grids (FAs) | — | — |
| Zr–2.5%Nb | 125 | 103 |
| Zr–1%Nb | >59 (fuel cladding/endcaps) | 74 |
| Zr–0.7% Mo:0.7%Cu | >0.35 (fuel pin internal springs) | |
| Sand | unknown | 30 |
| Concrete (various compositions) | — | 130 |
| Serpentinite | >1560 | 103 (+ contribution from concrete) |
| Gases (He, $N_2$, air) | — | — |
| Water/steam | — | — |

### 2.2.2. Accident description

The severe nuclear accident at Unit 4 ChNPP happened on 26 Apr. 1986 [16]. Information about the accident and the resulting fuel containing materials and hot particles are presented in numerous publications, although sometimes with conflicting conclusions (for example [12, 16, 17, 21, 25–56]).

In the hours before the accident the behaviour of the reactor was rather complex; progressive Xe poisoning, almost all control rods were retracted (only 6 were in the core despite an allowed absolute

minimum of 15), and the hydraulics were also far from stable. In many documents, the activation of an emergency button AZ–5 (26 Apr.1986 at 1:23:40 a.m. local time) is considered as a starting point of the active phase of the accident, although it is likely that local degradation of the core components had started several minutes before the explosion. The generally accepted view classifies the accident at Chornobyl as a reactivity induced accident (RIA) due to the poor neutron absorber rod design and non-optimal channel grids. Insertion of absorber rods with a long graphite plug in the end part into the core in combination with an abnormal neutron field led to local runaway increases in thermal and neutron power and, ultimately, a prompt neutron flash with corresponding extreme power excursion [15, 26–28, 42]. Direct proof of the supercriticality is scarce, however, the ratio of Xe isotopes ($^{133m}Xe/^{133}Xe$ [57]) serves as an unambiguous evidence. Unusually high $^{133}I/^{131}I$ ratio in the airmass over Helsinki, Finland a few days after the accident [58] also favours the criticality event. The RIA scenario, perhaps with some variations, explains the most important features of the accident progression in the active phase.

Actions by the operators to regulate the coolant flow complicated the situation by making it possible for steam to form in the lower part of the core (under normal operations the steam should be formed in the upper part of the core) [13]. Consequently, some fuel channels might have overheated, replicating similar accidents at RBMK reactors [13]. Although the extent of the damage at Unit 4 is virtually impossible to quantify, it can be inferred from the reactor log that the instability might have lasted up to 15 minutes. Recent studies of corium–steel interaction products [60], imply corium formation by reaction of the fuel with Zircaloy from guide tubes and/or fuel channels with Ni–Cr steel, situated at the very bottom of the core.

Logged data [15] as well as independent numerical models (e.g., [26—28]) show that in the active phase of the accident the increase in fuel temperature took approx. 3–5 s and was followed by (1−2 s lag) an increase in neutron power and reactivity. The supercriticality event was largely caused by prompt neutrons and lack of reactivity moderation by generated steam. Subsequently the reactor was destroyed in a massive steam explosion. Notable, at quoted timescales steam—zirconium reaction was most likely insignificant as suggested by investigation of ChNPP hot particles and RIA experiments. If the steam—zirconium reaction had occurred to a noticeable extent, abundant zirconia particles would have been found. Extensive research by V.G. Khlopin Radium Institute (KRI) of soil samples collected within 0.5 to 12 km along the axis of western plume [32–34] has not resulted in any particles of $ZrO_2$ being found. Neither have detailed studies of Chornobyl lava [32, 35–38]. Therefore, there is no evidence in support of a steam—zirconium reaction occurring.

One of the important features of a RBMK reactor is the large size of the core, which might lead to very heterogeneous distribution of neutron flux and temperature both during operation and under accident conditions. Independent models indicate that core averaged temperatures reached ~2000–2300 K [26, 27], but in energy stressed regions the excursions were much larger and localized fuel melting is anticipated. It is difficult to evaluate the highest temperature achieved in a local part of the reactor, but a study of high temperature phases of solid solutions $ZrO_2$—$UO_2$ in hot particles extracted from soils samples confirms at least 2673–2873 K [32–34, 39, 41, 45, 46], even higher values reaching 4500 K were obtained using models of Cs loss from dispersed fuel [61, 62]. Very different approaches give similar values for the most affected volume: neutronic calculations [27] suggest 40–200 fuel rods (only the lower part of the fuel rod is considered); estimates by $^{133m}Xe/^{133}Xe$ ratio [57] propose that affected fraction of the core was 0.01–0.1%. Neutron flash duration can be inferred from the grain size of dispersed fuel in hot particles and is estimated as 0.1–1 s. [54]. The latter estimate is based on the dimensions of the dispersed fuel grains when compared with the results from small–scale RIA experiments. Such a comparison does not necessarily give reliable results since the details of fuel destruction due to the interaction with steam/water are unknown.

The core was destroyed, leaving the reactor shaft (space inside internal wall of reactor shielding tank) largely empty except for rubble from falling construction material and pieces of the core. Ambiguity still exists on the amount of fuel dispersed as dust and expelled from the shaft; a generally accepted estimate is ~4–6% of the initial inventory [15, 16, 31]. The rest is either present as mechanically ruptured fuel fragments scattered on the roof of the NPP and subsequently thrown into space under the cascade wall of the later built sarcophagus. According to observations immediately after the accident, ejected macroscopic fragments of the core such as chunks of graphite reached a temperature of at least 1273 K [63]. Initially it was assumed that a part of the destroyed core remained located in the shaft; however, direct investigation using video cameras through inspection holes and entry in 1991 have shown that the shaft is largely empty and only a small number of FAs remain.

A fraction of the fuel was ejected and dispersed as hot particles of various types: fuel, cladding, material interaction products, and so–called condensation particles. They usually consist of atmospheric dust/aerosols, which either have trapped accident derived radionuclides on pre-existing nuclei or very small suspended radioactive cluster which served as a nucleus for larger particles.

The dynamics of radionuclide release during the first 10 days following the explosion were unusual and showed clear bimodal character (Fig. 9): gradually decreasing emission of radionuclides during first 4 days (26–30 Apr.) was followed by a plateau for two days (30 Apr.–1 May). Unexpectedly, there was a rise in the emission for 4 days (1–5 May) which suddenly terminated on 6 May (e.g., [16, 30]). The sudden drop after the 10$^{th}$ day is usually interpreted as a rapid spread of Chornobyl lava into parts of the destroyed reactor building and resulting cooling. While the general pattern is not disputed, detailed examination shows that a significant part of the reported data on dynamics of $^{137}$Cs and other radionuclides over several weeks and months are subject to sampling bias [64, 65].

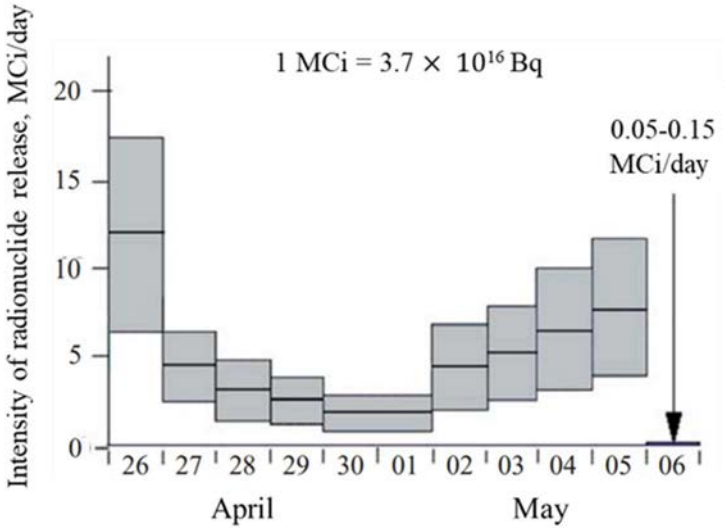


*FIG. 9. Fallout of radionuclides during the first 10 days after the explosion at 4th Unit of ChNPP (reproduced from Ref. [30] with permission courtesy of Kurchatov Institute).*

Visual investigation of the reactor shaft/interior started in 1988, using a periscope inserted into holes bored through the reactor shielding [21]. Despite some damage of the shielding in its lower part, the survey confirmed the presence of water inside the tank, the disappearance of the southeastern part of the base plate and movement of the plate by 3.85 m down into room No. 305/2. The most important discovery of 1988 related to the absence of the reactor core and the reactor shaft was almost empty [21]. In 1991, scientists from the Kurchatov Institute made an entry to the reactor shaft and did not see any evidence of high temperature processes having occurred at the top surface of the main part of

the base plate, except in the area of the missing segment [21]. In addition, Russian paint 'AC-8a' remained on the surface of both sides of reactor cover plate and on ¾ of surface of the base plate [21] suggesting that the high temperature was localized. It could be concluded that the main part of the reactor core and shaft were not affected by high temperatures for any appreciable amount of time. Presumably, steam releases occurred through fissures between the steel walls of the reactor core and the base plate. Several unusual observations such as graphite blocks in between metal pipes, indentations from cast iron balls hitting the walls can be explained by rather localized impact of steam jets entraining pieces of the corium and other particles.

The emptiness of the reactor shaft, localized pattern of high temperature and the distribution of debris on the roof led to an alternative scenario of the active phase of the accident [12, 21, 43, 44]. This scenario assumes two explosions, and the first had two phases, an explosion (at 1 h 23 min 46 s after the activation of the emergency button) corresponded to an extreme localized temperature excursion in the core followed by a further explosion one second later where the reactor core and cover plate were ejected at least 30 m from their original location. The second very strong explosion (equivalent to 100–250 t of trinitrotoluene (TNT)) happened two seconds later about 6 m northeast of the central hall [43, 44].

Estimates of the amount of fuel dispersed outside the unit, inferred from Pu content in soil samples, range from 3.5 to 6 wt% of the total inventory [16]; in today's European part of the former Union of Soviet Socialist Republics (USSR) [47]. The estimated amount of fuel remaining inside the sarcophagus is extremely controversial from at least 90 wt% [29, 30] to 23–36 wt% [43]. During a reactor entry in 1992, based on lava measurements, the amount was reported to be 11–15 wt% [56] which was later revised down to 9–13% [43, 44], after a 2001 entry. Measurements based on the volume of lava are biased due to the presence of fresh concrete produced during construction of the sarcophagus. These estimates, however, do not provide any explanation where the rest of the fuel is located, since soil sampling for Pu [48] does not account for an order of magnitude error in the reported values.

After the explosion a fraction of the dispersed fuel, corium (Zr–U–O), molten steel and silicate materials (serpentinite and sand) had been injected into room No. 305/2. Room No. 305/2 is the main source of Chornobyl lava [25, 31]. Studies of lava samples [25, 29—33] suggest lava pool formation and further melt stratification into layers of black and brown lava[5] occurred over several days [39] (Fig. 10). This correlates with the increase in the radionuclide releases between the 1–6 May (Fig. 9) and the sudden fall in discharges on 6 May. According to KRI's version of events, the common stratified lava in room No. 305/2 remained intact until 5 May at an initial temperature 1773−1873 K [39], which decreased to 1573–1773 K before the lava spread. Gravitational lava stratification almost certainly occurred, but compositional differences between the brown and black varieties suggest that they might have formed in different parts of room No. 305/2, being separated by remains of the base plate, pedestal structure and other materials [25]. Since lava precursor materials are highly variable, changes in relative fractions will influence the final melt. When the walls of the melt reservoir were broken (or melted through), three separate lava streams spread out (Fig. 11) and solidified relatively quickly (over 1–3 h). This explanation is consistent with the sudden fall of radionuclide release on 6 May.

A recent study [66], however, observed different fractional contributions of $UO_2$ fuel and Zr cladding, respectively, for the black and brown lava, suggesting the formation of two distinct initial sources of corium melt that served as a precursor for the further melt evolution (Fig. 12). The composition of the black and brown lava relates to the melting and assimilation of different local construction

[5] The composition and further information on black and brown lava is provided in Section 3.2.

materials [66]. For the brown lava, the high concentration of Mg was explained by a fractional contribution of 23 % serpentinite originating from the base plate. The composition of the black lava matrix showed a high fractional contribution of concrete (43%). The idea of the formation of two spatially separated sources of melt has already been proposed by Bugatov et al. [25].

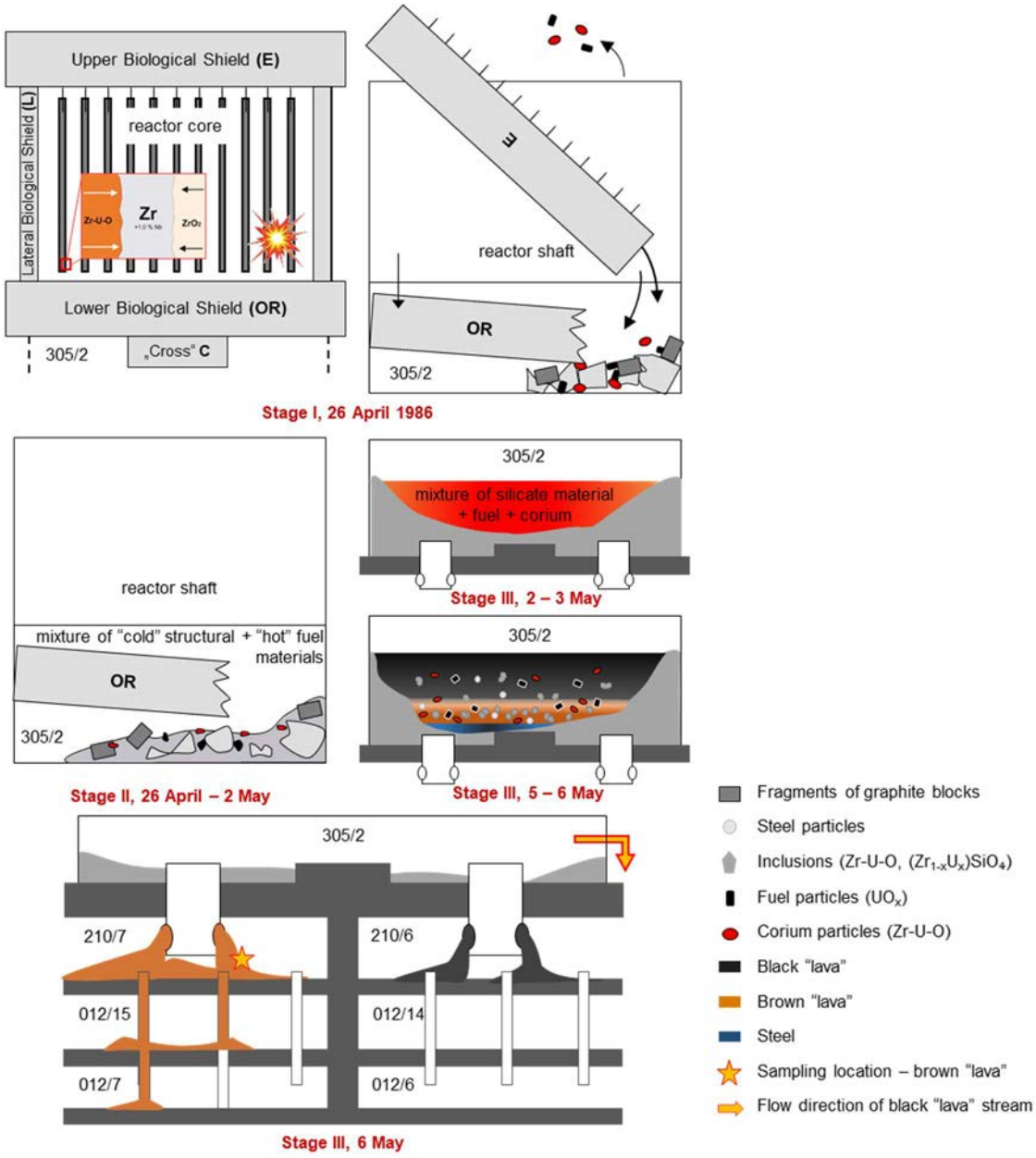


*FIG. 10. Schematic sketch of the Chornobyl accident sequences at Unit 4 (reproduced from Ref. [66] with permission courtesy of M.I. Lönartz et al.).*
*Where:*
***Stage I**: Interaction between $UO_2$–fuel, Zr–cladding, and steel in local parts of the reactor core, prior to the explosion. Release of hot particles and dislocation of the base plate (OR) due to the explosion. Structural materials, fragments of graphite blocks, fuel, corium, and mixtures of Zr–U–O + $UO_x$, + Fe–Cr–Ni + $Fe_3O_4$) enter room 305/2.*
***Stage II**: MCCI in places of fuel conglomerations.*
***Stage III**: Formation of one homogenous melt, 2–3 May, followed by the stratification into three layers of molten steel, brown and black lava (5–6 May). Formation of solid solutions and crystallization of high uranium zircon until breakthrough from room 305/2 to the reactor basement (6 May).*

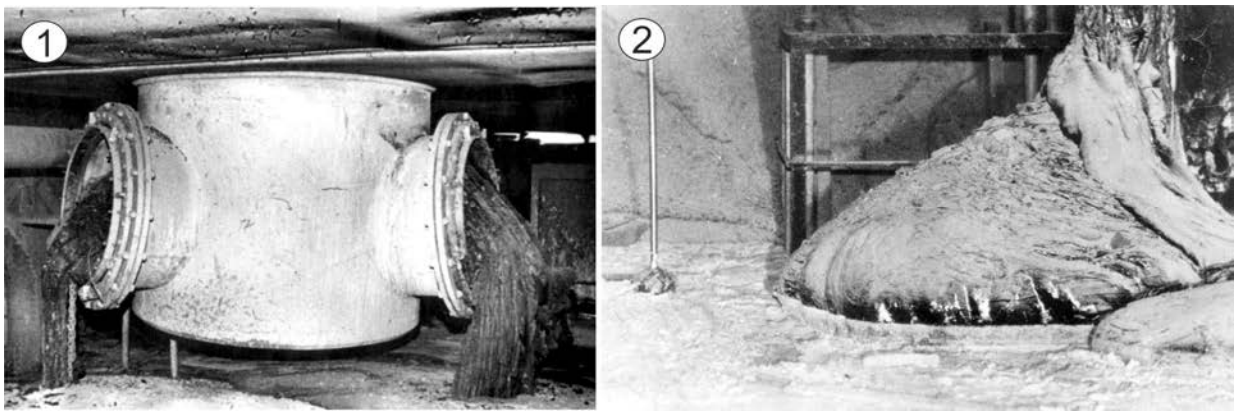


*FIG. 11. Two historical photos of Chornobyl lava [30]: (1) in steam discharge corridor (room No.210/6) and (2) 'Elephant foot' (room No.217/2). Photos were taken in 1990 (courtesy of Kurchatov Institute).*

We note that an alternative version advanced by Checherov et al. exists [21] in which very fast formation and extremely rapid spreading of lava during only 8–10 s immediately after explosions is described.

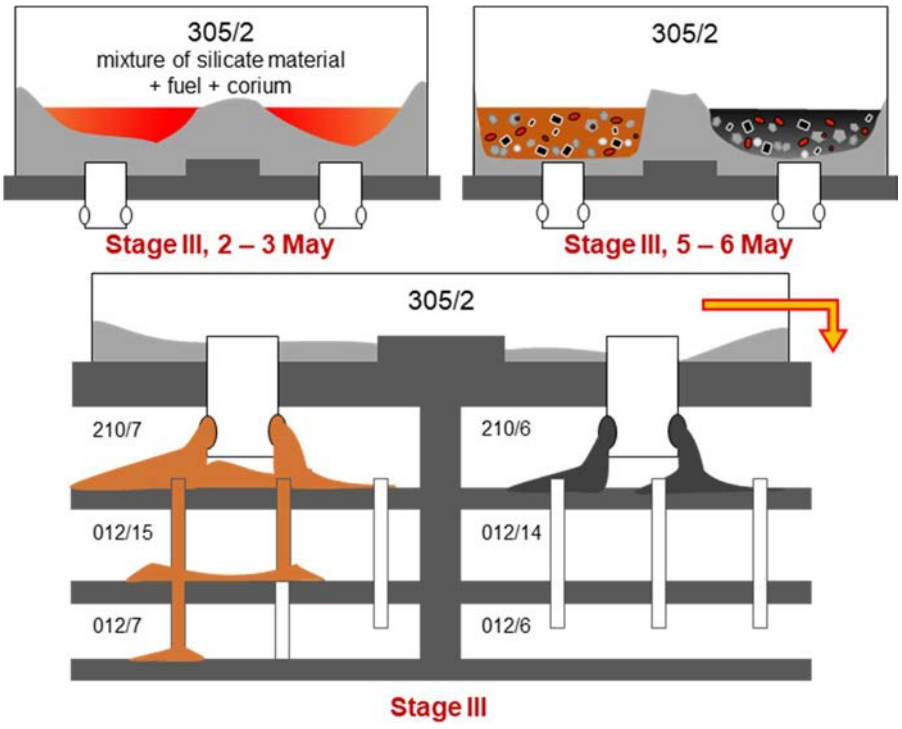


*FIG. 12. Black and brown Chornobyl lava formation process (courtesy of M.I. Lönartz et al.).*

Two lava streams penetrated into the steam-discharge corridor through steel pipes located in room No. 305/2, which have diameters of 1.2 m [43] and also spread horizontally though breaches in walls of the room No. 305/2. The total volume of black and brown lava remaining in room No. 305/2 is estimated to be 73.5 $m^3$ [43]. The volume of brown lava inside the sarcophagus (including room No.305/2, steam discharge corridor, and bubbler tank) is calculated to be 45.3 $m^3$ [43]. The volume of both streams of black lava (including rooms No. 305/2; 304/3; 301/5; 303/3; 301/6; 217/2 and steam discharge corridor) is calculated to be 124.8 $m^3$ [43].

The sarcophagus was built in Nov. 1986 as a temporary (projected lifespan of 30 years) confinement around the destroyed unit to supress the release of radioactive aerosols into the environment and prevent rainwater penetration and its further contact with fuel containing materials. However, the sarcophagus was not hermetically sealed, in 1990 it was estimated that there was 1000 $m^2$ of gaps in the roof and walls [30].

In Apr. 1990, newly formed yellow coloured phases were found on the surface of the black lava (room No. 305/2 and steam discharge corridor) [50] (Fig. 13), the volume increased over time. The investigation of this material carried out by KRI showed it to be a mixture of uranyl phases, secondary uranium minerals [50], due to chemical alteration with water and air. In the same year a decrease in the mechanical durability of the black lava of the 'Elephant foot' stream (room No. 217/2) was also observed. Compared to 1987 where extreme measures had to be adopted to collect samples [30, 49], sampling was no longer a problem [30]. In some areas of the 'Elephant foot' mechanical degradation was observed in a 1–3 cm thick lava surface layer.

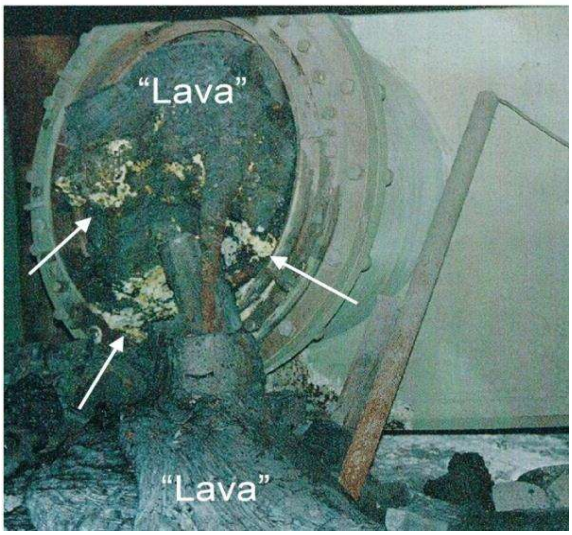


*FIG. 13. Yellow new formed uranyl phases (marked by arrows) discovered on the surface of black lava in steam discharge corridor (room No. 210/6) in April 1990 (reproduced from Ref. [67] with permission courtesy of Kurchatov Institute).*

To secure the unit a new safe containment was built around the old sarcophagus in 2016. Dismantling of the old sarcophagus that covers the reactor and recovery of the debris is pending.

## 2.3. FUKUSHIMA DAIICHI (JAPAN)

The accident at Fukushima Daiichi NPP (1F), unlike previous severe accidents at NPPs, was triggered by natural events and highlighted the need for provisions against beyond design basis events and multiple mode failures to be incorporated into reactor design/site selection.

Site selection and the requirements in place when 1F was planned in the early 1960s contributed to the accident, as this resulted in both flooding of the reactors and flood water being held within the space between the natural terrain at 30—35m above sea level at Onahama Peil (OP), Units 1—4 at OP +4 m and OP +10 m and the sea.

The 1F comprises 6 BWR reactors of a General Electric (GE) design; Units 1, 2 and 6 were manufactured by GE and the remaining units by Toshiba and Hitachi. Units 5 and 6 are off set from Units 1—4 on higher ground (Fig. 14). Between Units 1—4 and Units 5, 6 was located a dry cask

storage facility. Behind Units 3, 4 was located a common pool. The first reactor was connected to the grid in 1971 and the last (Unit 6) in 1979.

### 2.3.1. Reactor description

Descriptions are limited to Units 1—4, designs of which are based on BWR—3 design for Unit 1 and a BWR—4 design for Units 2—4. Under normal operation pressurized coolant water (typically at a pressure of 7.5 MPa) is boiled in the core to produce steam which is used to drive the turbines. The steam is cooled in condensers that are cooled by sea water and returned to the core in a closed loop system.

The reactor pressure vessel (RPV), made from high strength alloy steel, is lined with 6 mm stainless steel (grade 304). Internal reactor parts which cannot be clad are made from solid Ni–Cr–Fe alloys. The various structures and components inside the RPV are shown in Fig. 15 (Unit 1) and Fig. 16 (Units 2—4).

The reactors use a mark 1 type of containment, a steel dry well, which is a 30 mm thick steel vessel (primary containment vessel (PCV)) in the shape of an inverted light bulb, surrounded by reinforced concrete. The dry well is linked by vents to a torus shaped wet well that contains the suppression pool. The suppression pool acts as an energy absorber in the event of an accident. Secondary containment is provided by the concrete reactor building.

The atmosphere in the dry and wet wells contains mostly nitrogen. Hydrogen produced by radiolysis is managed using recombiners. The system, however, is inadequate to control hydrogen produced during a LOCA where Zr—steam interaction takes place.

One of the main differences between the BWR–3 and BWR–4 designs are the systems used to manage residual heat when the reactor is isolated[6] under high pressure conditions. In the BWR–3 design an isolation condenser is used, which can be maintained for eight hours before intervention is required, in comparison a reactor core isolation cooling system is used in the BWR–4 design. Reference [68] provides further details of these systems and their operation.

[6] A loss of external power supply would trigger the Main Steam Isolation Valves (MSIV) to shut off, preventing steam generated by the reactor from reaching the turbines. Under these conditions of reactor shutdown, isolated, and at high pressure, BWR-3 and BWR-4 designs have different systems to cool the reactor.

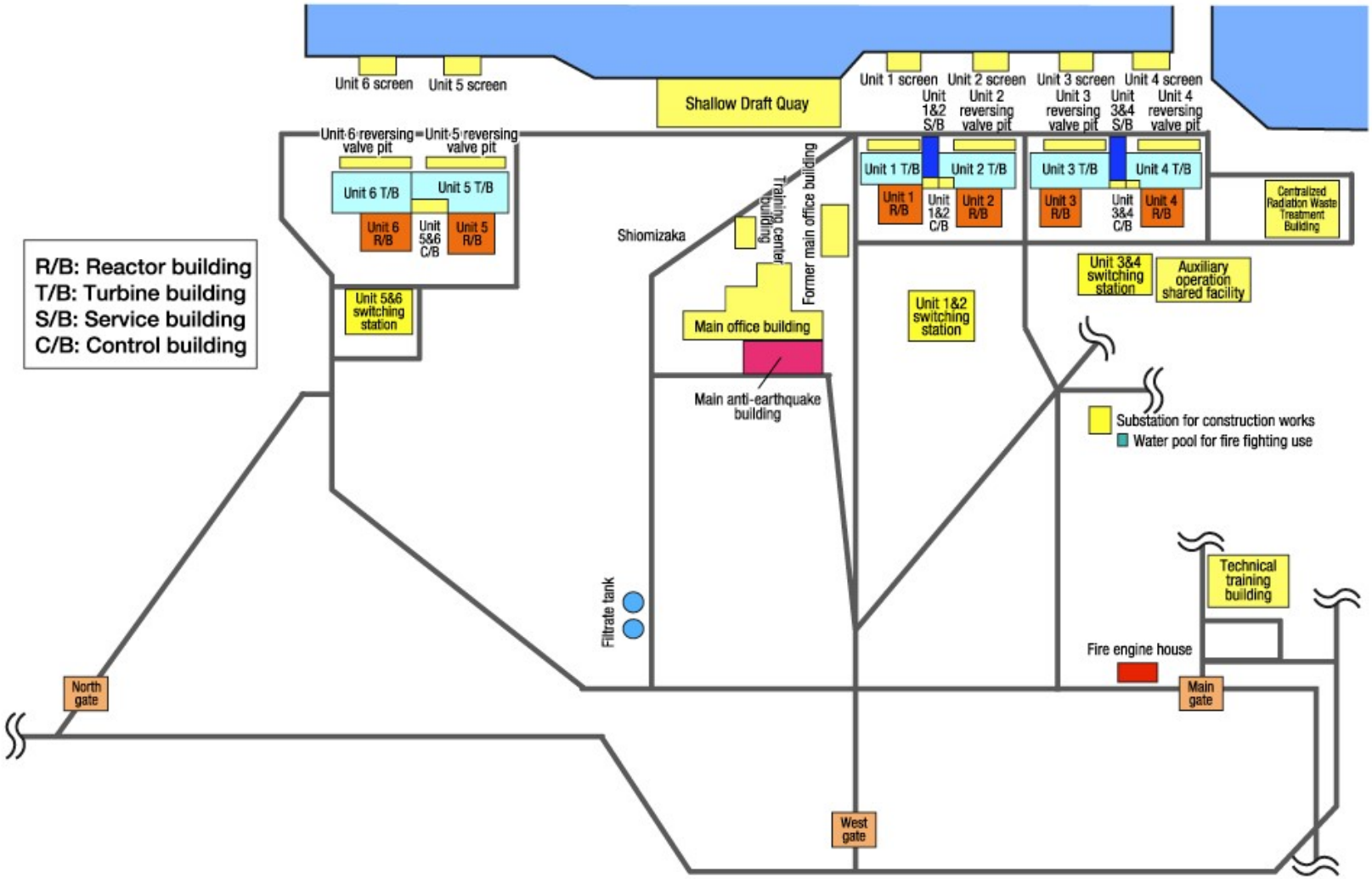


*FIG. 14. Site map of 1F (courtesy of TEPCO).*

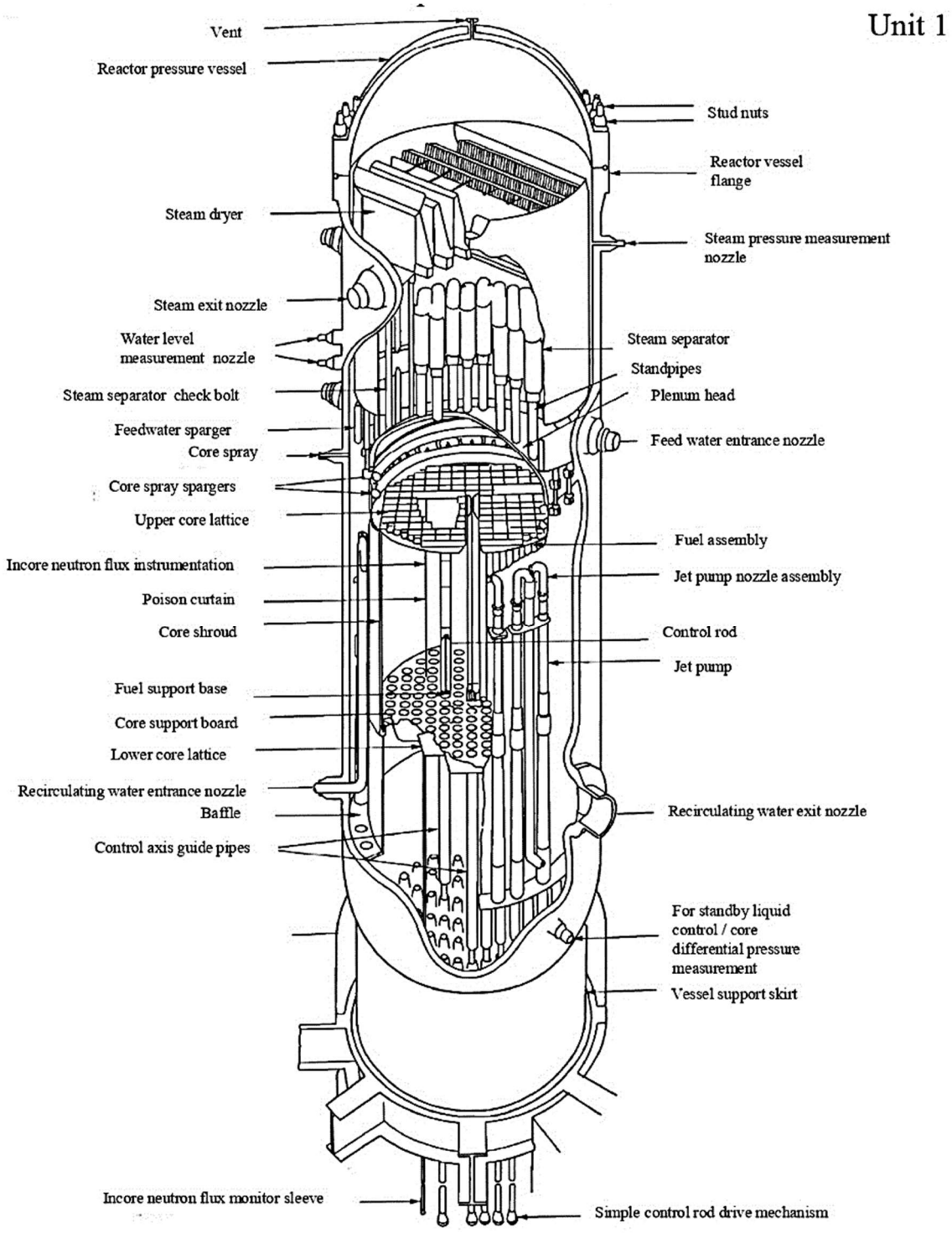


*FIG. 15. Structures and components inside the reactor pressure vessel (reproduced from Ref. [69] with permission courtesy of TEPCO).*

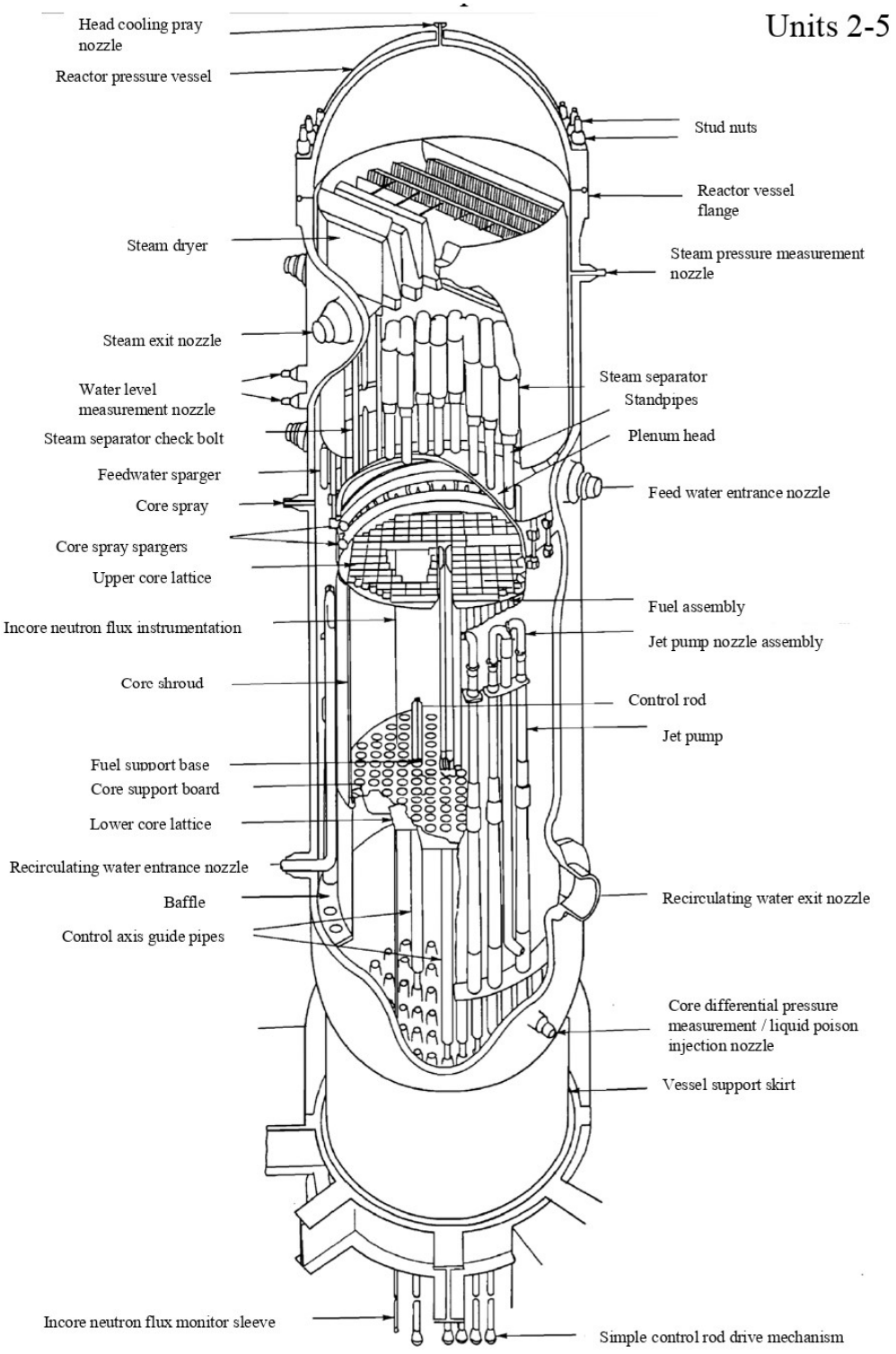


*FIG. 16. Structures and components inside the reactor pressure vessel (reproduced from Ref. [70] with permission courtesy of TEPCO).*

The specific designs of the FAs used in the 1F units is proprietary information. A typical BWR fuel assembly consists of fuel rods and several water rods held in position by spacer grids, tie rods and top and bottom fittings (Fig. 17). Each fuel rod is up to 4 m long, is typically fabricated from Zircaloy–2 and has a zirconium liner. The enriched $UO_2$ pellets are stacked inside the fuel rod to form an active length (see Table 2), are held in place with a spring (Fig. 17) and the rod is filled with an inert gas

(typically helium). A removable fuel channel or water box is fitted to the outside of the FA when in–core. The different structural components of the fuel assembly, such as spacers, water tubes, fuel channels are manufactured mainly from zirconium–based alloys, stainless steel, and Inconel.

The base designs in use are reported to have consisted of 60 fuel rods bundled in either an 8 × 8 or 9 × 9 arrays with fuel enrichments between 3.4—3.8 wt.% for $UO_2$ fuels [68]. The number of assemblies loaded to each reactor is shown in Table 2. Cruciform control blades are inserted between individual assemblies.

Table 2 summarizes the main design details.

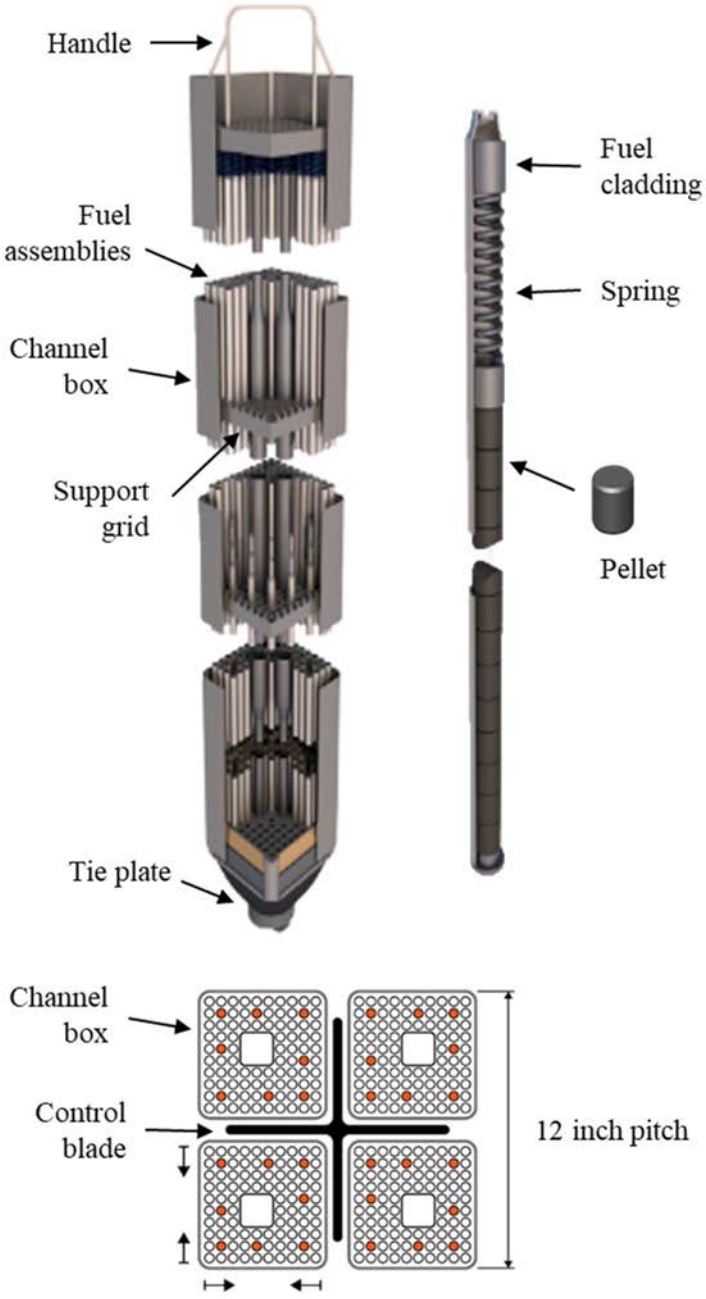


*FIG. 17. Boiling Water Reactor fuel assembly.*

TABLE 2. OVERVIEW OF THE UNITS 1–4 REACTOR FACILITIES AT THE FUKUSHIMA DAIICHI NPP (adapted from Ref. [71])

| | Unit 1 | Unit 2 | Unit 3 | Unit 4 |
|---|---|---|---|---|
| Electric output (MW(e)) | 460 | | 784 | |
| Thermal output (MW(th)) | 1380 | | 2381 | |
| Start of construction | Sep. 1967 | May 1969 | Oct. 1970 | Seep. 1972 |
| Commissioning | Mar. 1971 | Jul. 1974 | Mar. 1976 | Oct. 1978 |
| Reactor type | BWR 3 | | BWR 4 | |
| RPV inside diameter (mm) | approx. 4 800 | approx. 5 600 | approx. 5 570 | |
| RPV overall height (mm) | approx. 20 000 | | approx. 22 000 | |
| RPV total weight (t) | approx. 440 | | approx. 500 | |
| RPV design pressure | approx. 8.62 MPa (87.9 kg/cm$^2$) | | approx. 8.62 MPa (87.9 kg/cm$^2$) | |
| RPV design temperature (℃) | | 302 | | |
| Number of FAs | 400 | | 548 | |
| Number of high burnup 8 × 8 fuels | 68 | | — | |
| Number of 9 × 9 fuels (type A) | — | — | 516 | — |
| Number of 9 × 9 fuels (type B) | 332 | 548 | — | 548 |
| Number of high MOX fuels | — | — | 32 | — |
| Effective fuel rod (active) length (m) | approx. 3.66 | | approx. 3.71 | |
| Number of control rods | 97 | | 137 | |
| Containment type | | Mark 1 | | |
| Containment overall height (m) | 32 | 34 | 34.1 | |
| Containment diameter (m) | 17.7 (sphere) 9.6 (cylinder) | | 20.0 (sphere) 10.9 (cylinder) | |
| Pool water volume in suppression chamber (m$^3$) | 1750 | | 2900 | |
| Containment design pressure | approx. 0.43 MPa (4.35 kg/cm$^2$) | | approx. 0.38 MPa (3.92 kg/cm$^2$) | |
| Containment design temperature (℃) | | | | |
| Spent fuel pool volume (% full core) | | 225 | | 290 |
| Spent fuel pool working temperature (℃) | | ≤65 | | |
| Spent fuel pool length (north south, parallel to coastline) (m) | approx. 7.2 | | approx. 9.9 | |

### 2.3.2. Accident description

On 11 March 2011, the Fukushima Daiichi and Daini NPPs of Tokyo Electric Power Company Holdings (TEPCO) were hit by the magnitude 9.0 (Richter scale) Pacific Ocean earthquake. This was followed by an accompanying tsunami which had an inundation height at 1F exceeding 15 m above OP.

At the time of the earthquake, Units 1—3 were in operation, and Units 4—6 were in maintenance modes for scheduled outage (Table 3).

> "*It is believed that Units 1 to 3 were automatically scrammed at the earthquake, but external power supplies and almost all in-house AC power supplies were lost due to the earthquake and the tsunami*" [72].

TABLE 3. OPERATIONAL STATUS OF 1F UNITS DURING THE TOHOKU PACIFIC OCEAN EARTHQUAKE [73]

| Unit | Output (MW)t | Status when the earthquake occurred | Aftermath Status |
|---|---|---|---|
| Unit 1 | 460 | Operating at rated output | Automatic shut down |
| Unit 2 | 784 | Operating at rated output | Automatic shut down |
| Unit 3 | 784 | Operating at rated output | Automatic shut down |
| Unit 4 | 784 | Under regular inspection | – |
| Unit 5 | 784 | Under regular inspection | – |
| Unit 6 | 1100 | Under regular inspection | – |

About 50 minutes after the earthquake, the tsunami hit the NPP, and all electrical power system functions were lost except for the combination of Unit 6 air cooled emergency diesel generators and the power panel. In addition, a lot of equipment such as electrical equipment, pumps, fuel tanks, and emergency batteries was damaged or lost due to spillage, resulting in total power loss (station blackout (SBO)). This disabled the reactor monitoring and cooling operations at the main control room. The water injection was stopped, part of the reactor core was not submerged in water and nuclear fuel melted [68] presumably due to decay heat. Explosions occurred on Units 1, 3 and 4, which were caused by ignition of hydrogen released from the damaged cores (melted fuel zirconium–steam reaction) that had filled the reactor buildings. The reactor core of Unit 2 was also damaged but the building remained largely intact. Photographs of damaged Units 1–4 and reactor site after tsunami are presented in Figs. 18–21.

The sequence of events at Units 1—3 is reported in detail in Annexes 1—3 of Ref. [68].

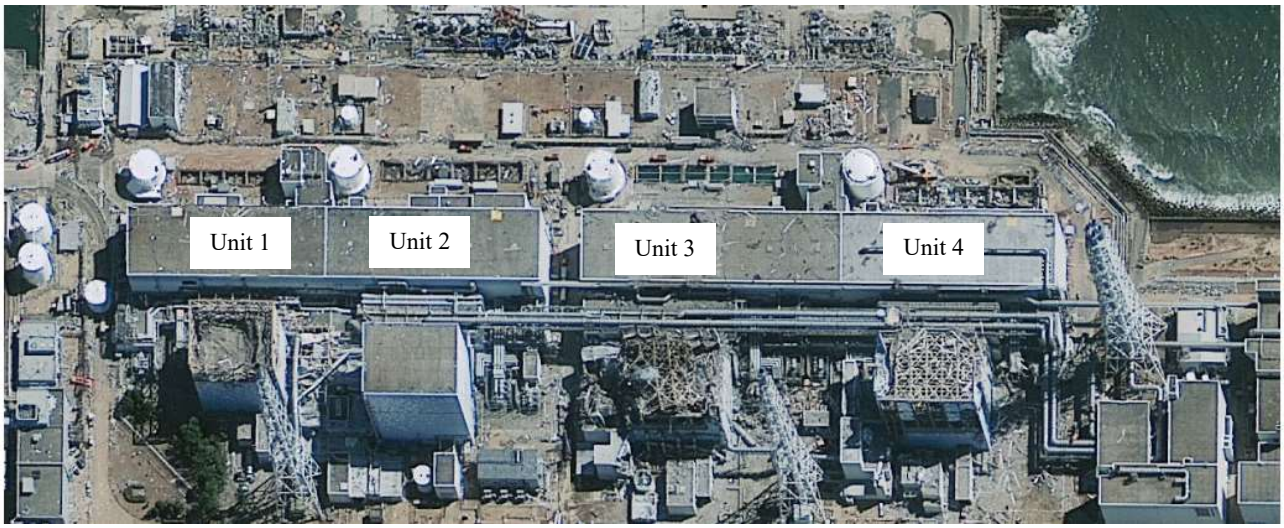


*FIG. 18. Aerial view of Fukushima Daiichi NPP after explosion (courtesy of TEPCO).*

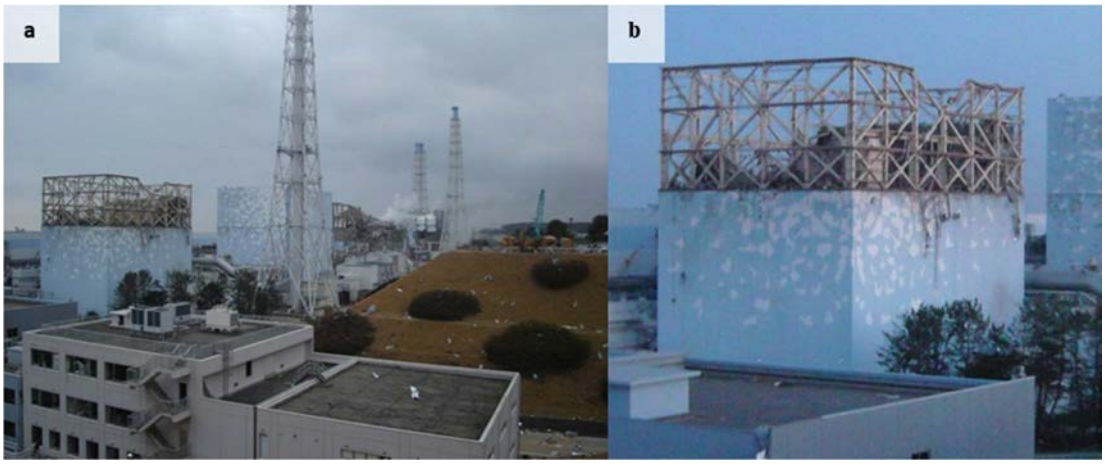


*FIG. 19. Fukushima Daiichi NPP Units (a) 1–4 and (b) Unit 1 after Explosion (courtesy of TEPCO).*


*FIG. 20. Fukushima Daiichi NPP (a) Unit 3 and (b) Unit 4 after explosion (courtesy of TEPCO).*


*FIG. 21. Tsunami that struck 1F, (a) the east side of Unit 5 taken from the southern side of the unit and (b) the north side of centralized radiation waste treatment building taken from 4th floor. Photographed on 11 March 2011 (courtesy of TEPCO).*

Many radioactive materials were released and spread from 1F. The amount and percentage of radionuclides released are shown in Table 4. The zone up to 20 km from the site was designated as an access ‘Restricted Area’ and no entry was allowed unless authorized. Some areas outside the 20 km zone from the site were also designated as the ‘Deliberate Evacuation Area’. More than 110 000 people were evacuated.

Since April 2012, these areas have been reorganized into an ‘Preparation zone for lifting evacuation order’, a ‘Restricted zone for habitation’, and a ‘Difficult to return zone’ depending upon the amount of radiation (in principle entry is prohibited in the Difficult to return zone). In addition, since April 2014, evacuation orders have been gradually lifted in some areas, and all Preparation zones for lifting evacuation order and Restricted zones for habitation’ were lifted in March 2020, except in some areas where it is difficult to return. Still many people are forced to remain evacuees, and radiation contaminations have caused serious impacts on extended areas.

TABLE 4. THE AMOUNT AND PERCENTAGE OF RADIONUCLIDES RELEASED FROM THE REACTOR CORES TO THE ENVIRONMENT AT THE FUKUSHIMA DAIICHI NUCLEAR POWER STATION (1F) ACCIDENT (based on data from [74])

| Radionuclides | Half-life [75] | Boiling point K | Melting point K | Amount of environmental release [PBq] [76] | Percentage released [77] |
|---|---|---|---|---|---|
| Xe–133 | 5 days | 165 | 161 | 11000 | ~60 % |
| I–131 | 8 days | 457 | 387 | 160 | ~2–8 % |
| Cs–134 | 2 years | 951 | 301 | 18 | |
| Cs–137 | 30 years | 951 | 301 | 15 | ~1–3 % |
| Sr–90 | 29 years | 1653 | 1042 | 0.14 | |
| Pu–238 | 88 years | 3508 | 913 | 1.9 E-5 | |
| Pu–239 | 24100 years | 3508 | 913 | 3.2 E-6 | |
| Pu–240 | 6540 years | 3508 | 913 | 3.2 E-6 | |

The combination of earthquake, accompanying tsunami and scale, in terms of the number of units involved, has made the decommissioning of 1F a complex task. Some of the initial operations have involved restoration of services, securing the site to a further tsunami (Fig. 22 (a)), removal of rubble/debris both on site and in the harbour, and building of tanks (Fig. 22 (b)) and cleanup systems to capture contaminated water.

(a)

(b)

*FIG. 22. (a) New sea barrier to secure site against a further tsunami, (b) New tanks for holding contaminated/treated water.*

In response to a direction from the Minister of Economy, Trade, and Industry (METI) and the Minister of Restoration from and Prevention of Nuclear Accident issued on 9 Nov. 2011 a 'Mid−and−Long−Term Roadmap towards the Decommissioning of Fukushima Daiichi Nuclear Power Station Units 1–4' was issued on 21 Dec. 2011 by the government of Japan and TEPCO. The road map developed a set of goals to be achieved within the first 2, 10 and 30+ years. The road map has been revised on a periodic basis to incorporate new information obtained during the decommissioning process.

Some of the achievements to date include:

- The recovery of dry storage cask from the cask storage building, inspection and transport to a temporary cask custody facility at OP +30—35 m;
- Removal of rubble and building of a new export route from Unit 4, removal of AR pool stored fuel from Unit 4 and transport to the common pool;
- Removal of rubble and structures from Unit 3 reactor floor, building of a new fuel route from Unit 3 and remote export of AR pool stored fuel from Unit 3;
- Preparations are underway to collect fuel debris from Unit 2 PCV using a robotic arm and other remotely operated devices;
- Internal investigations of the PCV have been undertaken to establish the location and debris in Unit 1.

# 3. CHARACTERIZATION OF CORIUM

Section 3 provides an account of the experiences, tools, techniques, analysis, and interpretation of results in characterizing materials (including corium) taken from accident sites or melted cores.

## 3.1. CHARACTERIZATION OF THREE MILE ISLAND UNIT 2 SAMPLES

The characterization of the melted core had aspects regarding technical issues concerning the extent and progression of the accident. The technical issues addressed were:

- What part did the thermal-hydraulic phenomena in the reactor systems play in the meltdown?
- What was the core damage progression?
- In what modes could the reactor pressure vessel have failed?
- What were the mechanisms of fission product release and transport?

The characterization of the melted core also established the basis for safe handling and interim storage of the debris regarding chemical and physical material stability, potential for contamination spread, pyrophoricity and criticality. Ultimately, characteristics important to long term storage and potential disposal like leachability were identified when the debris was transferred to dry storage by measuring the constituents in the canister water in which the debris had been immersed for ten years. This data is provided in Table 5.

The characterization of the melted core included:

- In situ examination of the core and vessel by video camera and acquisition of samples of loose material accessible within the axis of the leadscrew nozzle (grab samples) were performed prior to the reactor vessel head removal;
- Following removal of the upper head, the surface contour mapping using ultrasonic sensors was performed, individual discrete components were recovered, and core bore samples were extracted and analysed;
- Examination of cooling system artifacts, including debris from the plenum cover and filters from the makeup and letdown system and control rod components such as leadscrews and support tubes;
- Chemical analysis (gamma and mass spectrometry to establish radiological retention and elemental composition) of rubble bed grabs samples, fuel rod segments and other identifiable control rod cluster and fuel assembly components, as well as control rod leadscrews and the core melt samples;
- Optical and electron microscopy as well as microprobe analysis to identify chemical constituent distribution and localized inclusion composition within samples;
- X ray diffraction (XRD) and neutron diffraction to identify sample crystal form;
- Microprobe analysis to identify chemical composition of sample.

Based on the video work, debris samples were removed from the vessel using a rotating point cup sampler and a narrow clamshell tool, inserted through the control rod drive penetrations, as illustrated in Fig. 23 (a). Figure 23 (b) shows elevation and plan views of the sampling locations.

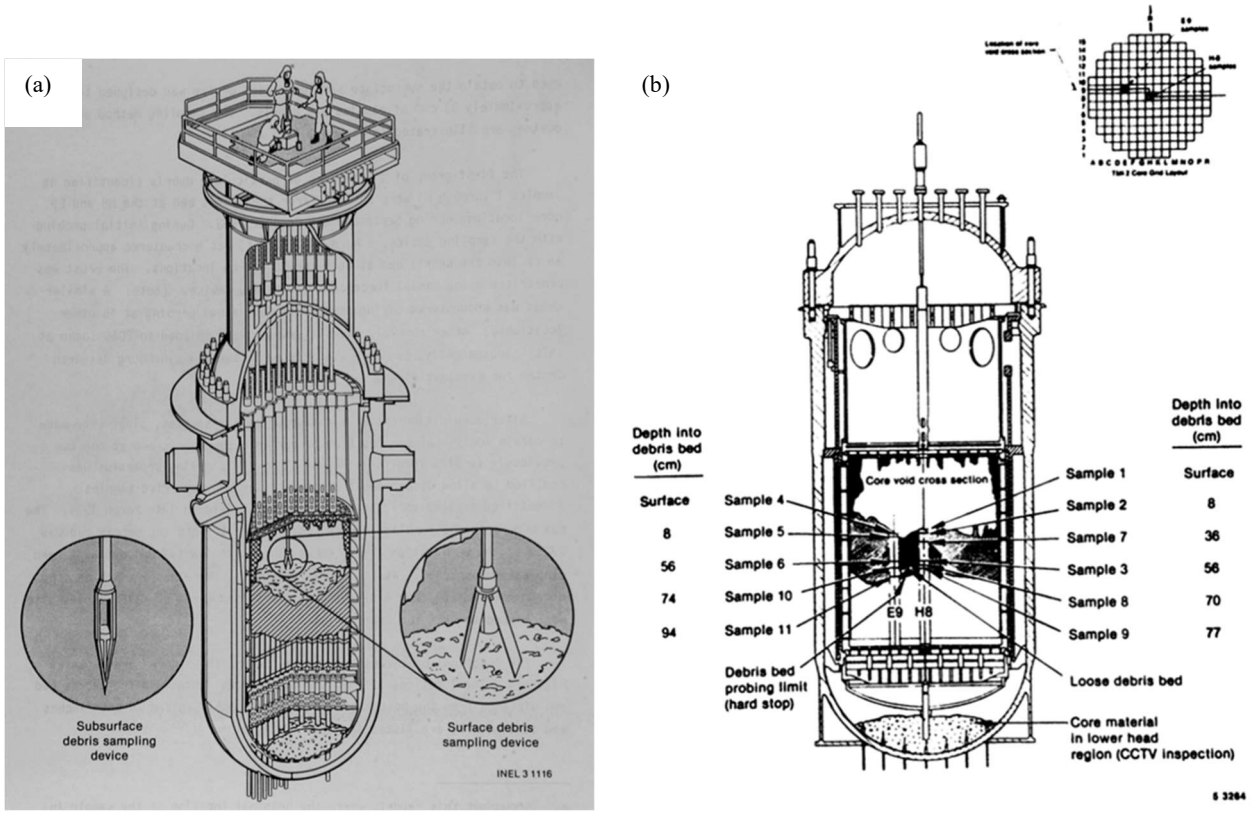


*FIG. 23 (a). Loose debris grab sampling, (b) Sampling locations (reproduced from Ref. [78] with permission courtesy of INL).*

### 3.1.1. Initial grab sampling

Eleven samples of loose material lying on the top of the melt were recovered before the reactor vessel head was removed. These grab samples provided indications of the highly varied nature of the loose debris. Material was acquired from the centre and midradius positions normally occupied by fuel assemblies H8 and E9. In the centre location, the sample tool was pushed into the loose debris to a depth of 77 cm from the top of the debris bed and to 94 cm at the midradius position. The sample tools included a clamshell device and a pointed penetrator with a cup into which loose material flowed. The samples were taken from the debris surface as well as at depths of 8 cm and 56 cm from the surface [78]. Figure 24 shows one type of sampler with granular material recovered.

*FIG. 24. Clamshell grab sampler with recovered material (courtesy of INL).*

### 3.1.2. Analysis of grab samples

The eleven loose material (grab) samples recovered 1.37 kg of material. Ten of the samples were analysed at Idaho National Engineering Laboratory (INEL). Sample density and particle size distribution measurement allowed initial classification of the sample material and gave the recovery design teams information on the material to be recovered. The bulk samples were also tested for the presence of pyrophoric and magnetic material. Gamma ray spectrometry was used to establish fission product retention while neutron activation analysis was used to determine fissile material content. The solid samples were dissolved to the extent possible and inductively coupled optical emission spectroscopy (ICP–OES) was employed to determine elemental composition of the samples, specifically for silver, aluminium, boron, cadmium, chromium, copper, iron, gadolinium, indium, manganese, molybdenum, nickel, niobium, silicon, tin, tellurium, uranium, and zirconium. XRD was performed to identify crystal structure. Metallographic mounting, polishing, and etching revealed grain structure, and electron microscopy was able to identify elemental distribution in the exposed prepared sample surfaces.

#### *3.1.2.1. Sample preparation*

Dissolution of the samples for wet chemical analysis was initially attempted using nitric and hydrofluoric acids, which left a significant fraction of undissolved solids. The remaining solids were made soluble following high temperature treatment using a potassium bisulphate fusion. The pyrosulfate technique included use of a caustic (sodium hydroxide) vapour trap to collect volatile iodine to establish the retention fraction for $^{129}I$.

Strontium was separated from the solutions as a carbonate precipitate, which was counted for beta emissions to evaluate $^{90}Sr$ content of the samples.

Selected particles greater than 1 mm in diameter were mounted and polished for optical metallographic imaging at between 15 and 500 ×. These samples were also examined at up to 2000 × using scanning electron microscopy (SEM) with energy dispersive spectroscopy (EDS) for elemental analysis. Boron and oxygen content were quantified using Scanning Auger Spectroscopy. One sample was sent to the B&W research centre for investigation by the reactor vendor. Fractions of seven particles were analysed with differential thermal analysis at the Rockwell Hanford Operations (US DOE operation at Hanford Washington) laboratories. Twenty-two particles were selected and sent to Argonne National Laboratory. The bulk material was quite radioactive, having dose rates reported as 1 Sv/h [78].

The results of the various analyses determined that most of the loose particles had inclusions that were previously molten uranium–zirconium oxide. This composition provided definitive indication that the core temperature had exceeded 2800 K at various points. Some particles containing exclusively $UO_2$ had morphology consistent with having been melted, resulting in the hypothesis that temperatures might have exceeded 3100 K. Aluminium, chromium, iron, and nickel were present at levels ranging from minimum detection to majority constituent in most samples in voids and at grain boundaries. An estimated 10% of the silver component of the control rods was projected to have been retained in the core based on the grab samples.

#### *3.1.2.2. Sample particle size*

In physical size distribution, the grab samples ranged from 30 to 6000 $\mu$m with a size bias toward large particles on top of the debris field and smaller particles at the depth of the impenetrable (hard stop) layer. Particles were observed to have a general appearance that included that of discrete fuel

pellets, pieces of cladding, porous material, metallic surfaces, and particles that included fuel, clad and structural material. An example of a fuel piece is shown in Fig. 25. Particles with dimensions between one and five thousand $\mu$m accounted for ~90% of the samples.

*FIG. 25. Fuel piece retrieved from surface of the debris field in the centre of the core void (courtesy of INL).*

Examples of the general size distribution, discrete character and shape recovered from samples of loose debris material are shown in Fig. 26.

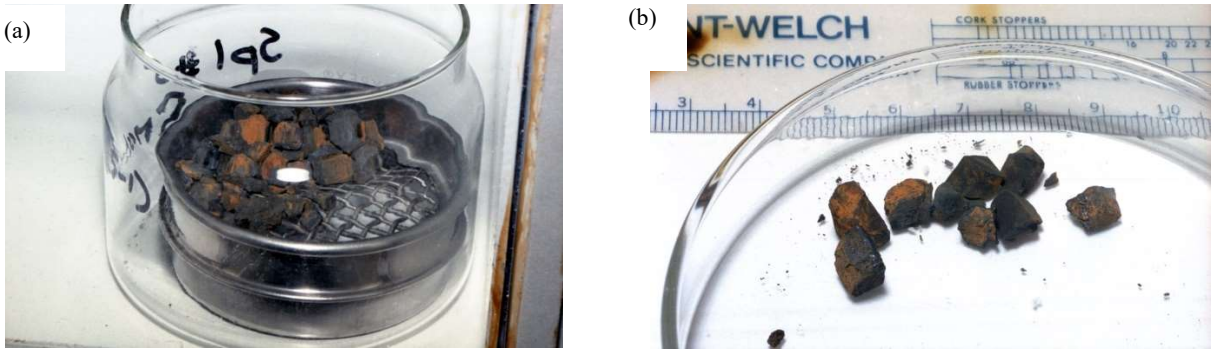


*FIG. 26. (a) Loose material retained on sieve for size analysis, (b) Typical debris pieces (courtesy of INL).*

### *3.1.2.3. Grab sample optical evaluation*

The grab sample material was generally categorized according to the constituents that could be identified and the apparent phases that were present. Samples were frequently described as foamy, presumably resulting from gas production during the reaction from metal to oxide. The combination of composition and physical properties was used to evaluate the range of possible temperatures that had been reached for various materials. The dominant constituents were uranium and zirconium, which were present in almost all samples, either exclusively or in combination with metals from control rods or structural material. This determination involves more than single component melt temperatures such as Zircaloy, which melts at 2030 K and uranium dioxide, which melts at 3120 K. The various expected melt temperatures can be found in temperature composition phase diagrams. Because diverse materials are present in the core, each combination might represent a eutectic alloy, in which the reaction between the two materials lowers the melt temperature appreciably. Uranium dioxide and zirconium might have formed single phase liquids that solidify into zirconium and zirconium–uranium metallic components in the absence of oxygen. Steam oxidation of solidified formerly molten material can convert zirconium metal to zirconium dioxide and uranium zirconium

oxide as discrete phases. Oxidation while molten material is at temperatures below 2800 K generally results in a single phase uranium–zirconium oxide solid solution with little porosity. Melting and formation temperatures of the core materials involved in the melt are shown in Table 5. Qualitative temperature projections were made based on the grab samples as shown in Table 6. Note that these samples were taken from the top of the debris field and are the first retrieved material.

TABLE 5. RELATIVE MELTING POINTS OF CORE CONSTITUENTS (based on data from [79])

| Melt Constituent | Melting Temperature (K) | Formation Temperature (K) |
|---|---|---|
| $UO_{2.0}$ | 3120 | |
| $ZrO_{2.0}$ | 2960 | |
| $UO_{2+x}$ | 2900 | |
| (U, Zr)$O_2$ liquid ceramic phase | | 2810 |
| (U, Zr)$O_2$–$Fe_3O_4$ ceramic phase | 2695 | |
| α-Zr(O)/$UO_2$ and U/$UO_2$ monotectic | | 2670 |
| α-Zr(O) | 2245 | |
| α-Zr(O)–$UO_2$ eutectic | | 2170 |
| Zircaloy–4 | 2030 | |
| Stainless Steel | 1720 | |
| Inconel | 1650 | |
| Inconel–Zircaloy | 1500 | |
| Liquid U from $UO_2$–Zircaloy interaction | | 1400 |
| Fe–Zr and Ni–Zr eutectic | | 1220 |
| Ag–In–Cd | 1073 | |

The melting progression of when the core became uncovered was led by reaction of the Inconel grid spacers with exposed Zircaloy cladding, followed by eutectic reactions between the stainless steel control rod cladding and the Zircaloy guide tubes. When the control rod tubes failed, the silver–indium–cadmium neutron absorber had already melted. The cadmium evaporated from the alloy, leaving the silver and indium to join the iron–zirconium/nickel–zirconium metal flowing at 1220 K to the bottom of the vessel. This flow solidified at intact grid spacers, interfering with coolant flow, further complicating the problem of circulating water in the core. As temperatures continued to rise, the zirconium oxide external surface began to break down allowing a steam–zirconium metal reaction to progress exothermically, further driving the heat load. A similar exothermic reaction occurred between steam and the stainless steel components. Metallic Zircaloy began melting as temperatures exceeded 2030 K, and at 2170 K partially oxidized alpha zirconium oxide and uranium oxide began to have a eutectic relationship, leading to a fully liquid ceramic at 2810 K. Core reflooding solidified the majority of the melt and shattered some previously intact fuel [80].

An image of ballooned clad described in the first entry (Particle 1A) of Table 6 is shown in Fig. 27 and Fig. 28 is a multiphase sample that illustrates some of the different reactions that occurred at fuel–clad interface. It includes metallic Zircaloy with uranium and zirconium oxides at one surface and apparent uranium dissolution into the Zircaloy at the lower surface.

TABLE 6. TMI-2 GRAB SAMPLE PEAK TEMPERATURE ESTIMATES [78]

| Particle | Temperature Range (K) | Comment |
|---|---|---|
| 1A | 2170–2245 | No melting of $UO_2$; ballooned α-Zr(O); eutectic Zr–U interaction. |
| 1B | 2170–2600 | No melting of $UO_2$; slight grain growth; eutectic Zr–U interaction. |
| 1E | 2810–2960 | No melting of $UO_2$; melting of α-Zr(O) cladding; prior molten (U, Zr)$O_2$. |
| 1H | >2810 | Dissolution of (U, Zr)$O_2$ by porous heterogeneous U–Zr–O melt. |
| 3L | >2850 | Above the liquidus temperature for U–Zr–O ceramic. |
| 3M | >2850 | Areas of (U, Zr)$O_2$ melt; contains trace Cr, Ni, Fe. |
| 4A | ~2810 | Foamy U–Zr–O molten ceramic contacting $UO_2$; might be slightly lower due to impurities. |
| 4B | ~2810 | Foamy U-Zr–O molten ceramic contacting $UO_2$ fuel; might be slightly lower due to impurities. |
| 4D | >2850 | Molten (U, Zr)$O_2$; dense. |
| 5E | ~2810 | Foamy U-Zr-O molten ceramic contacting fuel. |
| 6B | <2245 | No melting of α-Zr(O). |
| 6C | 2170–2960 | No melting of $UO_2$; $UO_2$-$Al_2O_3$ eutectic interaction. |
| 6D | 2170–2810 | No fuel melting: metallic U-Zr-O melt, oxidized to (U, Zr)$O_2$, by reducing oxidized fuel to $UO_2$. |
| 6E | ~2000 | Oxidized cladding fragment; no melting. |
| 6F | 2170–2810 | Porous heterogeneous U-Zr-O melt attached to (U, Zr)$O_2$, ferromagnetic ingots. |
| 7A | ~2810 | Foamy U-Zr-O molten ceramic; might be lower due to impurities. |
| 7B | 2170–2245 | No melting of $UO_2$ or α-Zr(O); eutectic U-Zr interaction. |
| 7E | ~2810 | Foamy U-Zr-O molten ceramic. |
| 8A | ~2810 | Foamy U-Zr-O molten ceramic. |
| 8C | >2170 | Oxidized U-Zr-O melt. |
| 8E | ~2810 | Foamy U-Zr-O melt contacted later by metallic Zr melt. |
| 8H | >2850 | Areas of dense (U, Zr)$O_2$ melt containing trace Fe. |
| 9D | ~2810 | Foamy U-Zr-O ceramic melt. |
| 9G | >1233 | Molten Ag. |
| 10A | ~3100 | Areas of dense (U, Zr)$O_2$ melt with 5% $ZrO_2$. |
| 10E | >2810 | U-Zr-O ceramic melt on $UO_2$ fuel pellet. |
| 10F | >2850 | Regions of dense and foamy U-Zr-O melt. |
| 11B | >2810 | Foamy U-Zr-O melt. |
| 11C | 2170–3100 | No melting of $UO_2$; small region of prior molten (U, Zr)$O_x$. |

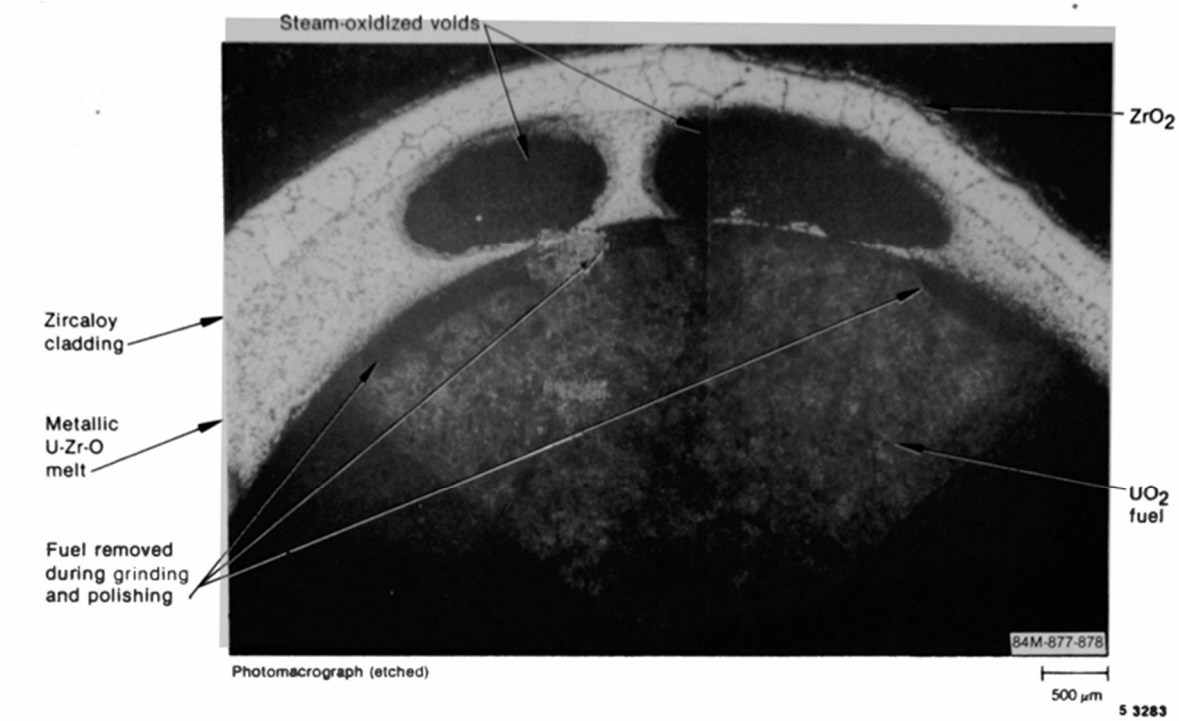


*FIG. 27. Cross section of partially intact fuel clad section (reproduced from Ref. [78] with permission courtesy of INL).*

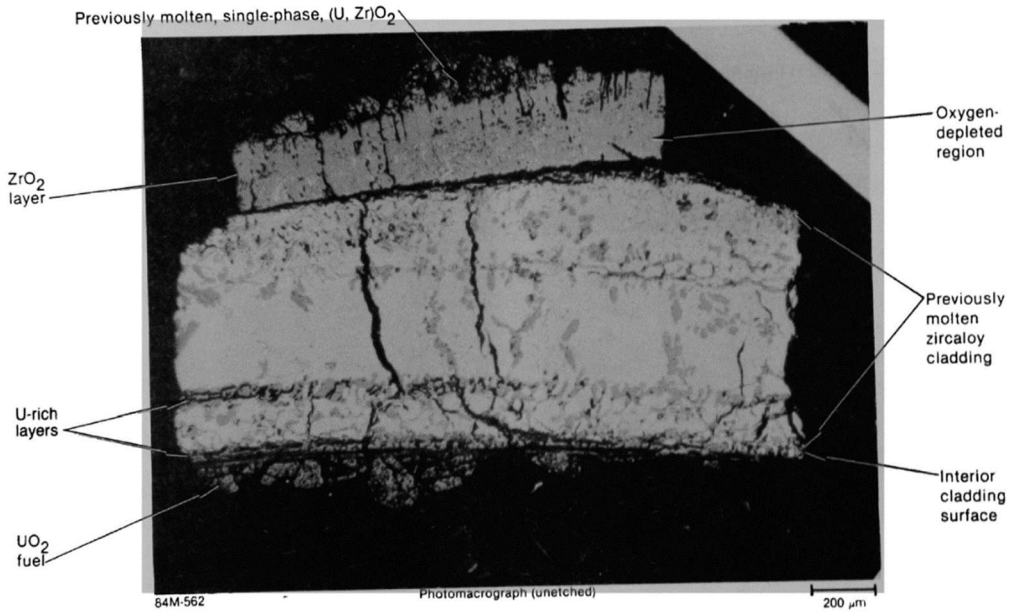


*FIG. 28. Macrograph of grab sample showing uranium diffusion into cladding (reproduced from Ref. [81] with permission courtesy of INL).*

Optical and electron micrographs show an example of grain structures and phases of the uranium–zirconium grab sample melt fragments in Fig. 29.

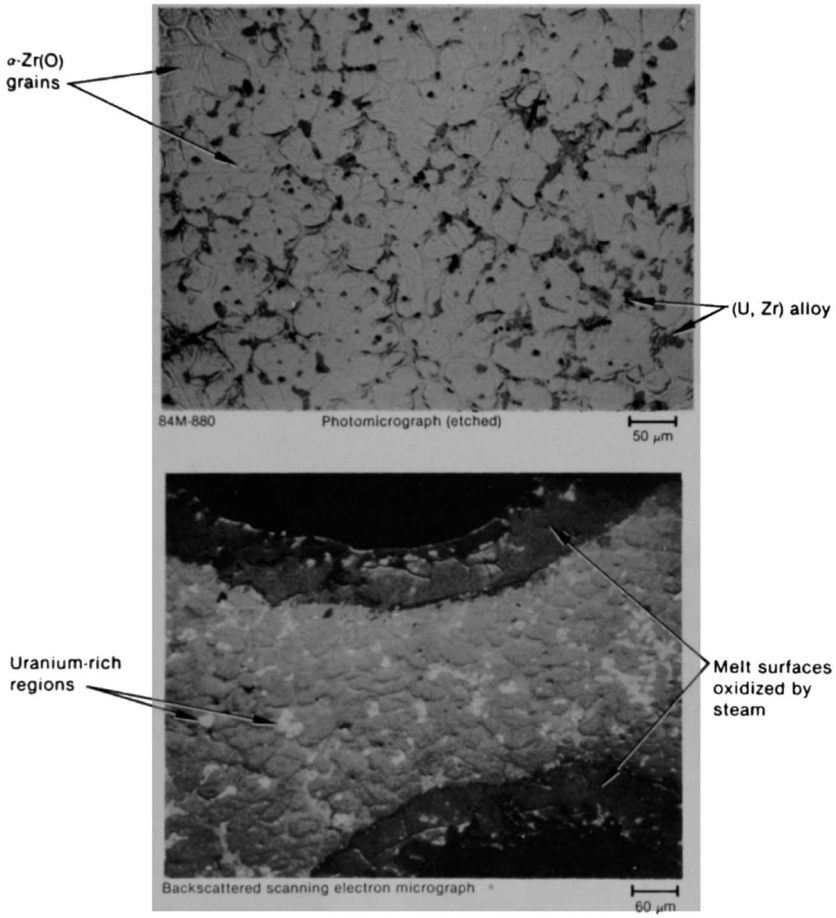


*FIG. 29. Photomicrographs displaying grain type and phases (reproduced from Ref. [81] with permission courtesy of INL).*

### *3.1.2.4. Radionuclide data*

Gamma ray spectra were used to identify and quantify primary fission products in the grab sample and to extrapolate the relative quantities as an indication of retention in the core. Due to the extreme high temperatures, fission gases such as $^{85}$Kr and several xenon isotopes were released quite uniformly, having negligible retention in the samples. Caesium and iodine species are among the most readily released, having relatively low vapour temperatures, and being highly soluble in water, both in the elemental form as well as in the form of oxides and other compounds.

Caesium-137 is a direct fission product with a single 662 keV gamma emission from its decay product, short lived metastable $^{137m}$Ba, and a 30 year half-life, which is consistently produced in a reactor, making it a dominant isotope in nuclear evaluation. The grab samples taken at the centre of the core had $^{137}$Cs values which varied by only approximately 5% from the mean value of the group. Those taken at the midradius had as much as a fivefold range and were as much as 85% higher than the centre sample location.

Strontium-90 is produced by fission at a rate nearly directly proportional to that of $^{137}$Cs with a similar 28 year half-life, but its mobility is much less, due to a higher melting and vaporisation temperature (1050 K/1655 K) as a pure substance, and lower solubility as an oxide. Comparison of the types of samples indicated that $^{90}$Sr was more selectively found in relation to the uranium phase. Antimony-125 was generally retained at ~21% of the predicted value.

As the core was melting, multiple reactions occurred between the ceramic and metal components in the fuel and core structure. Between the initial loss of primary coolant to the containment and the later injection of cooling water into the core, as much as 80% of the caesium that has been anticipated to be present in the core inventory leached out of the debris. This estimate was developed by comparing the core inventory calculated using an ORIGEN–2 model against the average values of nuclides found in the grab samples. From this comparison, ~22% of $^{137}$Cs was retained while at least 98% of the $^{90}$Sr was retained. A tabulated reporting of the data taken from Table 25 from Ref. [78] for the two locations is shown as Table 7.

TABLE 7. RETENTION OF RADIONUCLIDES IN TMI-2 BASED ON GRAB SAMPLE GAMMA SPECTRA DATA [78]

| Nuclide | Total Core Inventory (TBq) calculated by ORIGEN-2 | H8 (Central Location) Average Concentration (MBq/g) Decay corrected to Apr 1, 1984 | Fraction of Inventory Retained (%) | E9 (Midradius Location) Average Concentration (MBq/g) Decay corrected to Apr 1, 1984 | Fraction of Inventory Retained (%) |
|---|---|---|---|---|---|
| Sr–90 | 2.45E4 | 2.05E4 | 105* | 2.15E4 | 110* |
| Ru–106 | 4.26E3 | 1.84E3 | 54 | 2.59E3 | 76 |
| Sb–125 | 1.37E3 | 3.40E2 | 31 | 2.31E2 | 21 |
| I–129 | 8.47E-2 | 1.74E-3 | 26 | 1.54E-3 | 23 |
| Cs–134 | 1.37E3 | 2.21E2 | 20 | 2.68E2 | 24 |
| Cs–137 | 2.81E4 | 4.88E3 | 22 | 6.29E3 | 28 |
| Ce–144 | 1.02E4 | 1.09E4 | 134* | 1.03E4 | 127* |
| Eu–154 | 2.36E2 | 2.23E2 | 98 | 1.52E2 | 81 |
| Eu–155 | 5.96E2 | 3.33E2 | 70 | 3.39E2 | 71 |

* The values more than 100% are assumed to be due to higher core burnup at the sample locations.

Based on these data, strontium, cerium, and europium are retained in the sample material at values more than that expected. The higher burnup anomaly was compared against the initial $^{235}$U enrichment values for the fuel that would have been at the sampling locations. The measured sample enrichment for the centre core location was consistent with the expected value, but the midradius sample enrichment was higher than the original value. This difference at the midradius was presumed to indicate that higher enriched fuel had relocated and become mixed with the debris from the expected value.

Regarding $^{154}$Eu and $^{155}$Eu, the ORIGEN–2 model of the time had a large uncertainty in calculating the rate at which these isotopes were produced. Although $^{106}$Ru retention in the core is less than 100%, specific metallic samples with high nickel content were observed to have disproportionately high $^{106}$Ru concentrations. To a lesser extent, the same nickel affinity phenomenon was noted for metallic samples with higher than expected concentrations of $^{125}$Sb.

*3.1.2.5. Sample crushing tests*

To evaluate the potential for increased release because of mechanically pulverizing the debris, 50 g of the combined bulk material from one sample were crushed to reduce the particle size and expose greater surface area. The crushed material was then placed in deionized water to simulate conditions

expected during debris removal. One result was that the $^{137}Cs$ concentration in the water increased by nearly an order of magnitude, indicating that increased surface area allowed more effective leaching.

The other concern for crushing was the possibility that an increase in airborne contamination would result. Based on the test procedure, exposure of nearly dry pulverized sample resulted in an increase in airborne activity; however, in the case of a fully wetted sample, no increase occurred. For defuelling operations, it was recommended that controls be applied to prevent drying of the core debris.

*3.1.2.6. Sample pyrophoricity*

The potential presence of pyrophoric zirconium fines was tested by attempting to ignite samples using spark ignition and direct flame. Neither wet nor dry samples were found to be ignitable, much less pyrophoric.

### 3.1.3. Core bore characterization

The core stratification sampling programme adapted a commercial core boring machine for the job of confirming the composition of the melt below the upper surface. In 1986, ten cores were bored at selected locations in the core. The drilling machine was instrumented to monitor changes in drive motor torque as an indication of changes in material composition. The core samples were shipped to INEL to be analysed for chemical and radiological composition. From the core data, it was possible to determine that the melt varied in thickness from 1.5 m in the core centre to 30 to 60 cm toward the outer edge of the core. The solidified melt amounted to approximately 10% of the core.

The system was mounted to the defuelling platform in a manner that allowed radial and rotational position of the drill location to be precisely controlled. That position was confirmed by use of a surveyor's theodolite. Figure 30 shows an elevation view of the drill orientation on the platform and its position in the vessel. Figure 31 shows a plan view of the locations in the core where samples were taken, and visual inspection performed.

As with the loose debris samples, analysis of core bore samples included density measurements, gamma spectrometry, chemical composition by mass spectrometry, metallographic mounting with optical and electron microscopy to identify grain structure and chemical distribution and XRD to establish crystal structure. These analyses yielded identification of the various ceramic and metallic phases, which produced a basis for correlating control room temperature indications with timing of the materials that melted, relocated, solidified, remelted or fractured. The primary melt located below the loose debris field was evaluated according to its composition, being the upper crust, the central region, peripheral crust and lower crust. Figure 32 shows the range of material types encountered and observations from a core bore from the periphery of the main core region.

Samples were selected for examination by US DOE operators as well as multiple international laboratories, including Japan, Germany, Canada, and France. The analysis included inductively coupled plasma, optical emission spectroscopy as well as microprobe to determine elemental chemical composition, scanning electron microscopy to determine surface topography, and transmission electron microscopy and XRD to identify chemical constituents and crystalline structure [83]. Other testing included furnace tests to measure the release of volatile fission products from the various samples.

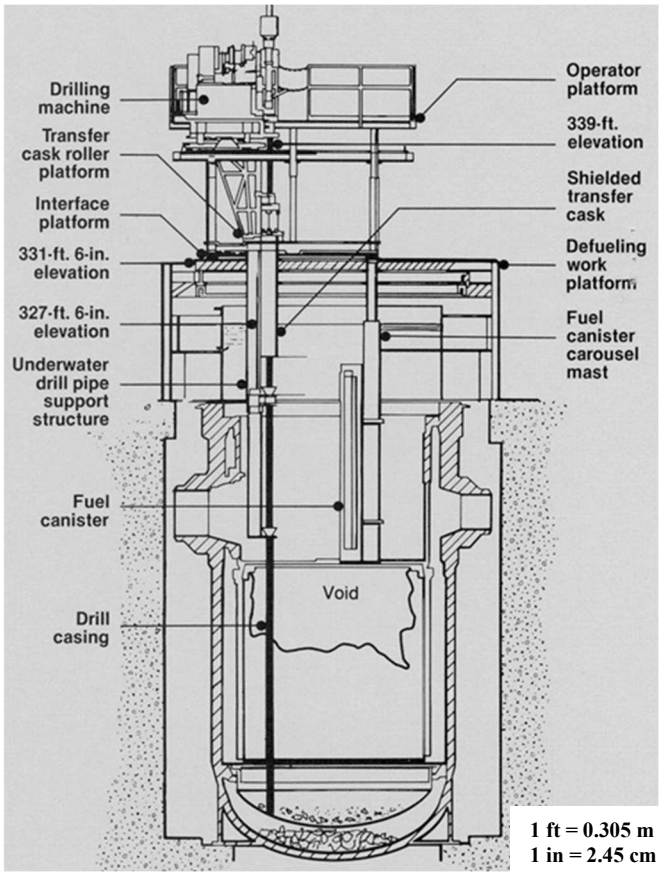


*FIG. 30. Elevation view of core stratification core bore system (courtesy of INL).*

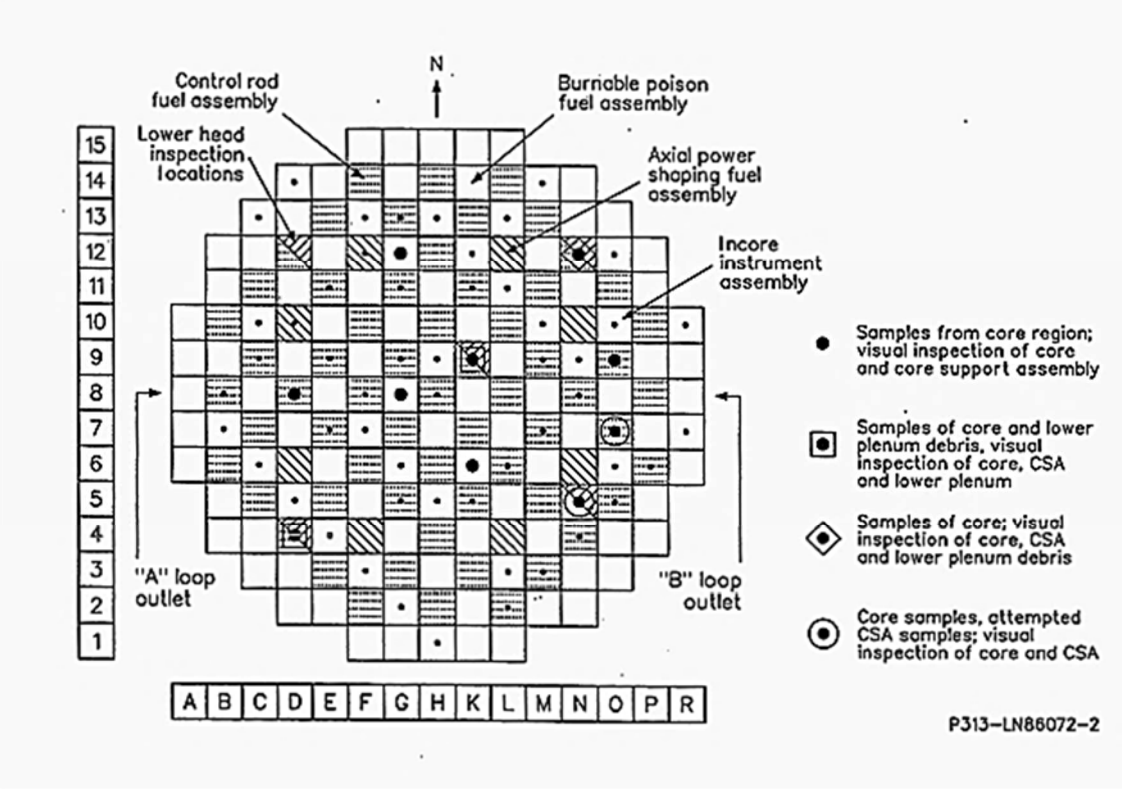


*FIG. 31. Plan view of core-drilling locations (reproduced from Ref. [82] with permission courtesy of US DOE).*

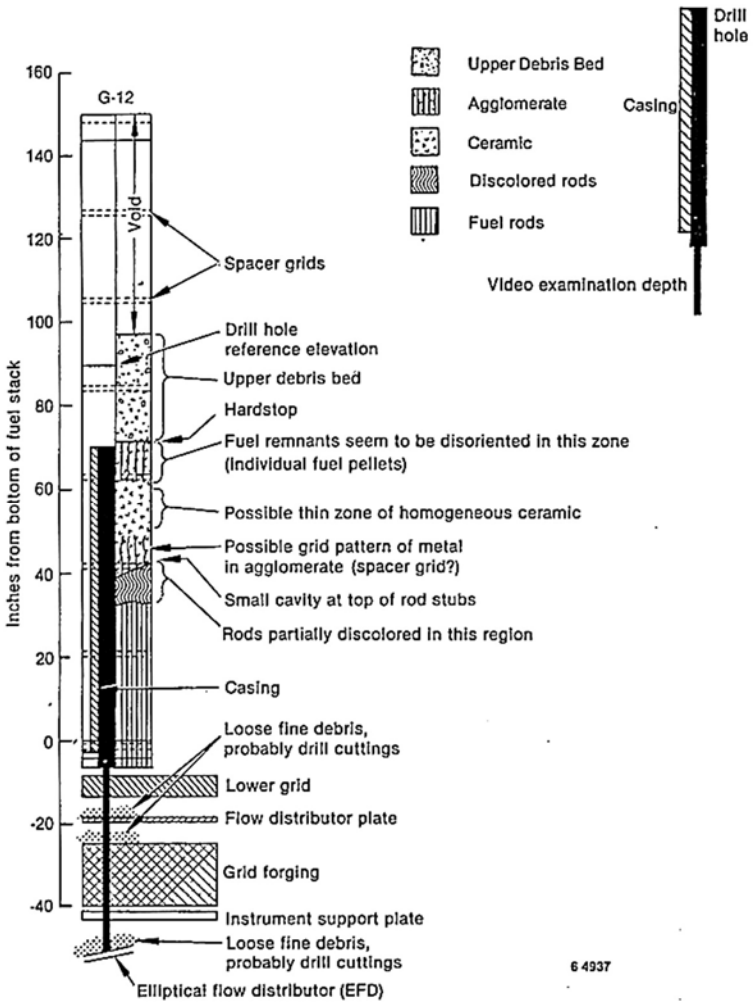


*FIG. 32. Example of core bore material diversity (reproduced from Ref. [84] with permission courtesy of US DOE).*

### *3.1.3.1. Upper crust*

The upper crust of the central melt contained ceramic and metal phases, with the ceramic consisting of various fuel material ratios of uranium–zirconium oxide and the metallic phase being primarily iron–nickel–aluminium from melted structural components and control rods. Metallic phases were present in cracks within the ceramic phases. This suggested that the ceramic phase had solidified, and low melting temperature metal filled the cracks, flowing from above into the established ceramic. Approximately one-fourth of the upper crust was metallic in nature.

The upper crust samples were examined using SEM and optical metallography. Distinct phases of high uranium (U, Zr)$O_2$ and high zirconium (Zr, U)$O_2$ were identified. FeCrO spinel crystals were found at grain boundaries in the ceramic phases. Using XRD, crystal structures identified were found to include cubic $UO_2$, and monoclinic and tetragonal $ZrO_2$. The presence of these phases indicates that the melt cooled relatively slowly, allowing multiple crystalline phases to form. Rapid quenching would have been expected to leave the (U, Zr)$O_2$ cubic form as a single phase.

Metallic phases that had penetrated cracks in the ceramic melt included: (a) Silver and indium from control rods; (b) Iron, nickel, and tin from structural steel and Zircaloy; (c) Inclusions of silver, indium, nickel, and tin as individual elemental constituents. One investigator found nickel–tin alloy precipitates that were approximately 40% tin, and iron–nickel morphologies, both of which have

specific formation temperatures of 1500 and 1700 K, respectively. Some of the melt material broke up into granular fragments that can be seen in the core bore tube as Fig. 33 (a).

*3.1.3.2. Central melt*

The central region of the melt was composed primarily of relatively homogeneous uranium–zirconium (U, Zr)$O_2$ ceramic or metal–ceramic agglomerates. A section of the core bore indicating the progression of particles melting together into an integrated melt is shown as Fig. 33 (b).

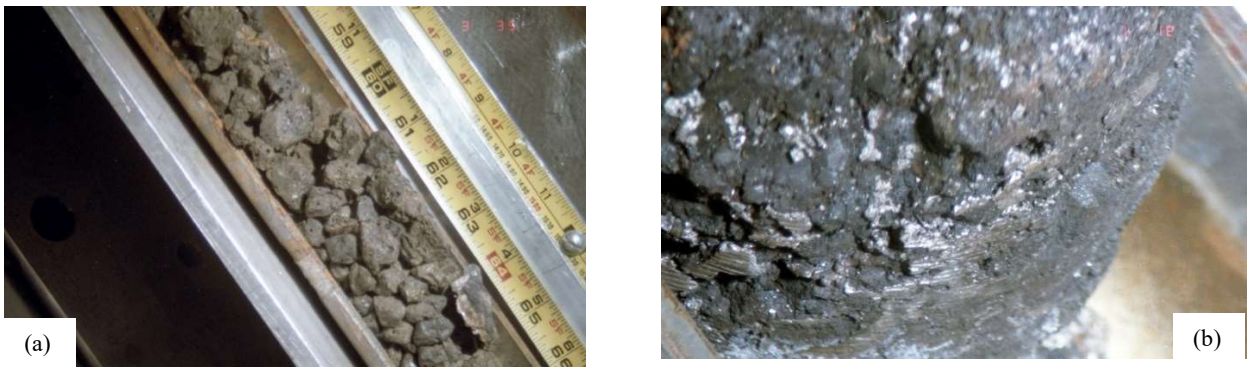


*FIG. 33. (a) Core bore section with loose U-ZrOx gravel. (b) Core bore section consolidated melt material (courtesy of INL).*

Variations in composition resulted in phases with higher uranium as well as those with higher zirconium. The homogeneous ceramic types were predominately uranium–zirconium oxide, the relative concentrations varied widely ($UO_2$ 62–82 wt%, $ZrO_2$ 18–53 wt%) over the melt volume. Confirmation of the ceramic characteristics was done using XRD; this showed the fluorite face centred cubic form of $UO_2$ and the monoclinic of $ZrO_2$. Cubic spinel phases containing iron, nickel, chromium, aluminium, and tin in the homogeneous melt material appear at the grain boundaries and, in some cases, as discrete inclusions in void spaces. In other cases, silver spheres were identified within metallic phases. In general, it appeared that the central melt remained at a high temperature for a longer period than the upper crust, allowing the various constituents to become more uniformly mixed. The presence of aluminium in the central melt is indicative that the aluminium–boron oxide burnable poison rods had melted at an early stage in the process, prior to the formation of the upper crust. A scanning electron micrograph of a sample from the central portion of the melt (Core bore G12–P9–B) with iron–nickel and iron–chromium inclusions is shown as Fig. 34 (a) [85]. Some of the silver–indium control rod material alloyed with tin from Zircaloy appeared as discrete metallic inclusions in which chromium oxide particles were present in voids [79]. Figure 34 (b) is a SEM image of a spherical silver inclusion within a multiphase material.

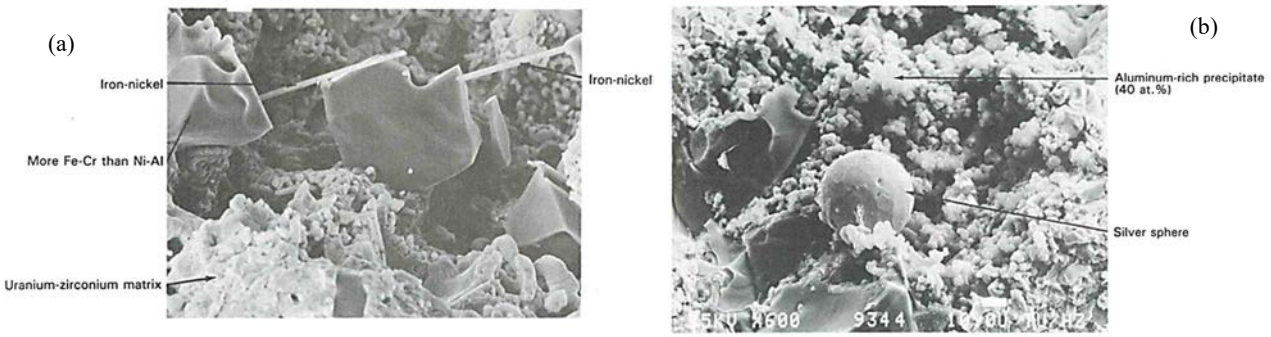


*FIG. 34. (a) Iron–nickel crystals in uranium–zirconium central melt sample. (b) SEM image of spherical silver inclusion [85] (reproduced from Ref. [85] with permission courtesy of Taylor & Francis Group).*

Volatilization tests were unable to detect krypton, xenon, or iodine, but the expected caesium, europium and ruthenium isotopes were released after heating a core sample to 2273 K. An unusual observation of this testing was the higher release of $^{134}Cs$ relative to $^{137}Cs$. Partial volatilization of the fission products was noted with complete release at 2773 K.

*3.1.3.3. Lower crust*

The lower crust of the central melt included stacks of fuel pellets that were encapsulated in a metal phase. The metal composition included three alloys that had a high percentage of zirconium, primarily Zr–Fe–Ni–Cr and Zr–Ni–In, as well as silver–indium [79]. A cross–section image of the lower crust sample showing the fuel rod stacks is shown in Fig. 35 (a) [86]. This image graphically illustrates how lower melting point materials such as Inconel (rod spacers) and control rod stainless steel melted when the core became uncovered and flowed to a lower level to solidify when sufficient heat was absorbed by the cooler bulk material at the depths of the core. In some cases, a thin shell of Zircaloy remained surrounding the uranium dioxide fuel pellets, while in other cases, the Zircaloy had either dissolved into the metallic phase or reacted with the $UO_2$.

Figure 35 (b) is a photomicrograph of a previously molten, primarily uranium oxide sample with Cr, Al, Fe, and Ni accumulation at grain boundaries.

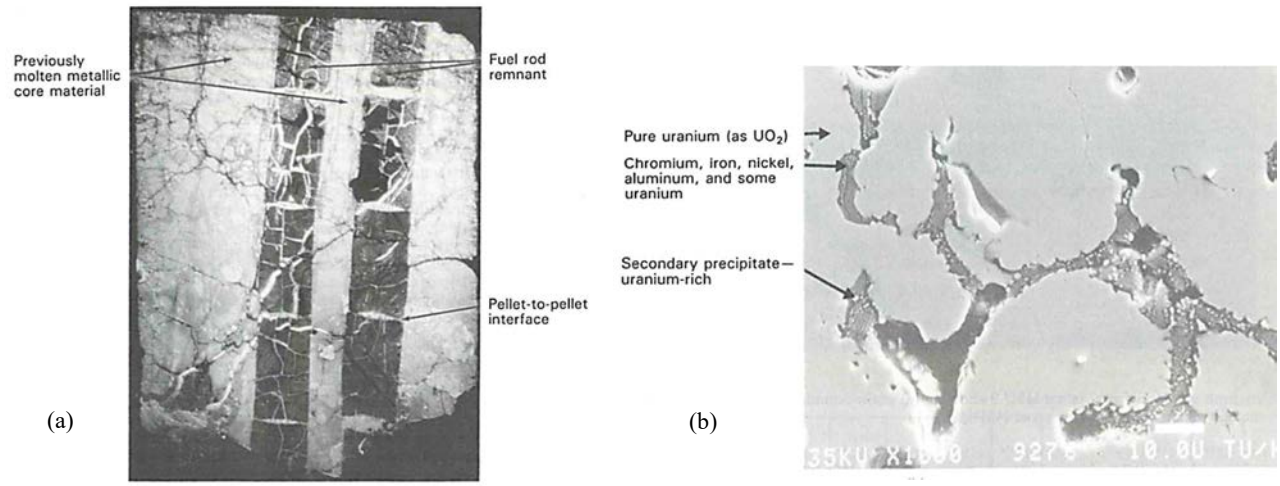


*FIG. 35. (a) Encapsulated fuel rod pellets in sample from lower crust core bore. (b) Uranium phase with metallic inclusion (reproduced from Ref. [82] with permission courtesy of Taylor & Francis Group).*

For fuel rod sections immobilized in the lower level of the melt, such as that taken from nearly in the centre of the core (position K9 Fig. 36), significant alteration of the Zircaloy clad at the location of the melt partition, with a wide range of zirconia thicknesses, was observed. Hydride formation was noted as relatively uniform, with a circumferential uniform hydride surface.

Sections of clad that did not undergo gross oxidation exhibited the expected beta phase of zirconium. In the highly oxidized zones, alpha phase zirconium oxide (Zr[O]) was overlaid by a 14–52 $\mu$m layer of zirconia ($ZrO_2$). The large variation in zirconia thickness is indicative of the effect of a large thermal gradient. The oxygen ratio measured at the alpha zirconium oxide/zirconium beta phase interface indicated that temperatures might have exceeded 1370 K [87].

Fission products $^{137}Cs$ and $^{134}Cs$, and activation products $^{125}Sb$ and $^{60}Co$ deposition were detected by gamma ray spectrometry. Surface scrapings showed $^{238}U$ that might have been deposited during the samples' years long exposure to uranium containing water in the reactor vessel [1].

To establish these characteristics, core bores were subjected to axial gamma ray spectrometry to identify the concentration and distribution of gamma emitting fission products. The cores were examined for chemical content to determine what constituents had reacted to produce the melt.

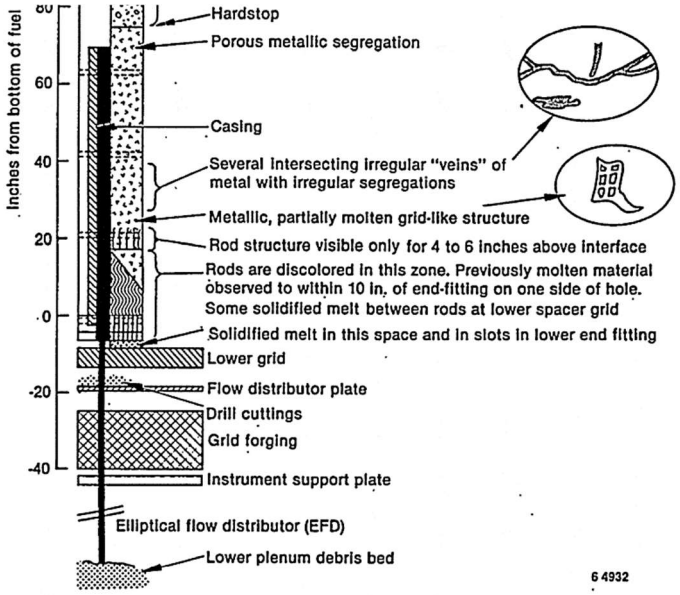


*FIG. 36. Section of core bore K9 (reproduced from Ref. [84] with permission courtesy of US DOE).*

Chemical analysis was performed to establish chemical composition, radionuclide content, and provide a basis for nuclear material accountancy. Several approaches were used to dissolve the samples for analysis. These included grinding the samples to get a sample mass that could be readily dissolved, dissolution with sequential application of nitric acid to dissolve metal and uranium, followed by hydrofluoric acid to dissolve remaining silicates and oxides of niobium, tantalum, titanium and zirconium, then any remaining undissolved material was melted in a pyrosulfate fusion, which was used to provide a solution for to be used for mass spectrometry and scintillation counting analysis.

An example of a metallographic image of mounted debris showing $ZrO_2$ as a separate phase as well as a uranium–aluminium–zirconium oxide phase appears as Fig. 37.

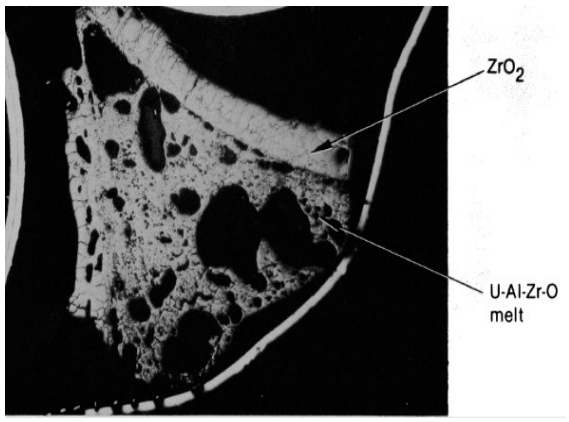


*FIG. 37. Optical metallograph of melted core sample (reproduced from Ref. [78] with permission courtesy of INL).*

In those zones of the core where the lower sections of the fuel assemblies were largely intact, the core bore samples retained that configuration with some distortion due to the twisting action of the core bit passing through that material. A section of the intact rod structure is shown as a composite image in Fig. 38, and detailed views in Fig 39.

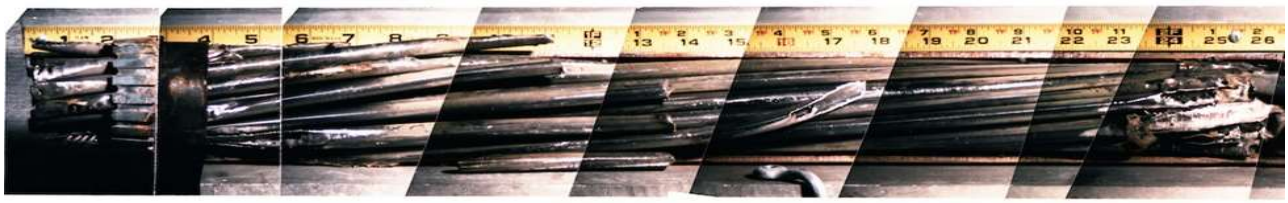

*FIG. 38. Composite image of intact rods in core bore (courtesy of INL).*

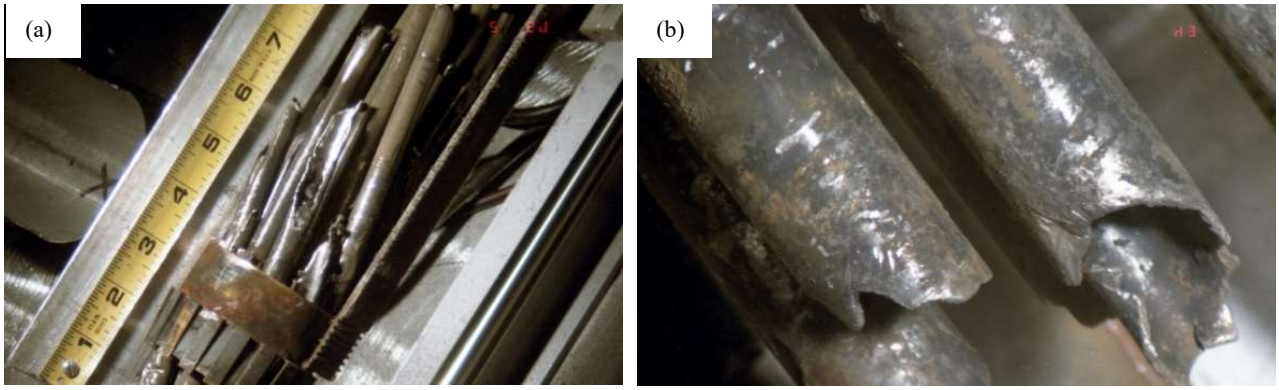


*FIG. 39. (a) Partially intact rods core bore. (b) Rods showing discoloration and melted ends (courtesy of INL).*

By combining the composition averages from the core bores and recovery actions, it was possible to develop a tabular inventory of where fuel ultimately resided at the point the melt was stabilized. The general mass inventory is shown in Table 8.

Characterization of the various sampled materials provided an indication of the distribution of radionuclides that were retained in the core according to their relative volatility as shown in Table 9.

*3.1.3.4. Lower head debris characterization*

Evaluation of the fuel debris material recovered from the lower head was done according to the protocol used for characterising the loose grab sample debris and the core samples. Radiological, chemical, and physical properties were measured. The data indicate that all the samples were uranium zirconium oxide which had solidified in the lower head. The investigation identified both uranium predominant and zirconium predominant phases, which suggested a relatively slow cooling process with fully oxidized zirconium. Average elemental composition was generally 70 wt% uranium and 13.75 wt% zirconium. Approximately 3 wt% of the melt was stainless steel and Inconel from core structural materials. Porosity identified in the material was presumed to result from trapped steam or metal vapour [89].

TABLE 8. DEBRIS COMPOSITION AND DISTRIBUTION [88]

| Core material repositories | Core material distribution of fuel material [a] | | | Core material distribution of control rod materials [a] | | |
|---|---|---|---|---|---|---|
| | Uranium | Zirconium | Tin | Silver | Indium | Cadmium |
| Upper reactor plenum | (b) | (b) | (b) | 1.0 | (b) | (b) |
| Upper core debris | 24 | 13 | (c) | 1.8 | (c) | (c) |
| Upper crust region | | | | | | |
| Ceramic | 1.3 | 1.2 | 2.3 | 1.2 | 3.6 | 0.65 |
| Metallic | – | 0.3 | 6.1 | 2.4 | 3.3 | 0.39 |
| Consolidated region | | | | | | |
| Ceramic | 12 | 18 | – | 10 | 27 | 6.1 |
| Metallic | – | 0.2 | 5.8 | 1.6 | 2.1 | 1.1 |
| Lower crust region | | | | | | |
| Ceramic | 3.6 | 2.8 | 9.3 | 7.3 | 7.2 | 1.4 |
| Metallic | – | 5.6 | 26 | 11 | 16 | 2.9 |
| Intact fuel rods (d) | 33 | 33 | 33 | 11 | 11 | 11 |
| Lower reactor vessel head | 15 | 11 | (c) | (c) | (c) | (c) |
| Lower core support assembly | 4.36 | 3.3 | (c) | (c) | (c) | (c) |
| Upper core support assembly | 3.3 | 2.4 | (c) | (c) | (c) | (c) |
| TOTAL | 97 | 91 | 82 | 47 | 70 | 23 |

a. Percentage of the total amount of the element originally present in the core.
b. Insignificant amount (<0.1 wt.%) based on the upper plenum measurements.
c. Elemental constituent not detected based on detection limits of approximately 0.1 wt%.

### 3.1.4. Distinct component examination

Distinct components were shipped to the Test Area North (TAN) 607 Hot Cell (USA) and opened in specialized handling fixtures that facilitated controlled removal of items for inspection and selection for analysis. Figure 40 shows a view of the handling carriage that was used to receive, open and sort through the various parts that were forwarded to INL for examination.

Once the canisters were unloaded in the TAN-607 hot cell at INEL, the various distinct components were photographed, subjected to neutron radiography, and gamma spectroscopy. An example of an upper end fixture with retained fuel rods is shown as Fig. 41 (a) [1]. Stubs of melted control rods and guide tubes were recovered and photographed as seen in Fig. 41 (b). Note that the silver–indium–cadmium neutron control material has melted and drained out of the rod. Figure 42 (a) shows metallographic images of cross–section and axial mounts of a control rod section that retained a portion of its control medium at the level of the plenum spring at the top of the rod. A partially melted control rod spider is shown in Fig. 42 (b).

TABLE 9. REACTOR SYSTEM FISSION PRODUCT DISTRIBUTION [88]

| Fission product repositories | Fission product distribution Low volatility fission products Percent of inventory [a] | | | Fission product distribution Medium volatility fission products Percent of inventory [a] | | | Fission product distribution High volatility fission products Percent of inventory [a] | | |
|---|---|---|---|---|---|---|---|---|---|
| | Ce–144 | Eu–154 | Eu–155 | Sr–90 | Ru–106 | Sb–125 | Cs–137 | I–129 | Kr–85 |
| *Ex–vessel* | | | | | | | | | |
| Containment atmosphere, basement, and tanks | 0.01 | (b) | (b) | 2.1 | 0.5 | 0.7 | (b)<br>47 | (b)<br>(47) (c) | 54<br>(b) |
| Reactor coolant system | (b) | (b) | (b) | 1 | (b) | 0.2 | 3 | 1 | (b) |
| Auxiliary building | (b) | (b) | (b) | 0.1 | (b) | 0.7 | 5 | 7 | (b) |
| *In–vessel* | | | | | | | | | |
| Upper reactor plenum | (b) | (b) | (b) | (b) | (b) | (b) | (b) | (b) | (b) |
| Upper core debris A | 26 | 30 | 24 | 23 | 14 | 13 | 5.3 | 5.9 | 6 |
| Upper core debris B [c] | 20 | 19 | 19 | 19 | 16 | 24 | 4.3 | 5.3 | (b) |
| *Upper crust region* | | | | | | | | | |
| Ceramic<br>Metallic | 1.4 | 2.0 | 1.6 | 0.73<br>(b) | 0.8<br>3.8 | 0.5<br>7.8 | 0.41 | 0.27 | (b) |
| *Consolidated region* | | | | | | | | | |
| ceramic<br>metallic | 24 | 32 | 22 | 8.3<br>(b) | 2.2<br>9.0 | 3.1<br>6.9 | 0.77 | 2.1 | (b) |
| *Lower crust* | | | | | | | | | |
| ceramic<br>metallic | 5.9 | 7.9 | 5.1 | 4.5<br>(b) | 5.7<br>24 | 7.4<br>36 | 1.4 | 3.5 | (b) |
| Intact fuel rods | 30 | 30 | 30 | 30 | 30 | 30 | 30 | 30 | 30 |
| Upper core support assembly | 3.4 | 4.5 | (d) | 3.9 | 0.23 | 0.22 | 0.46 | 0.12 | (b) |
| Lower core support assembly | 4.7 | 6.3 | (d) | 5.3 | 0.32 | 0.30 | 0.63 | 0.16 | (b) |
| Lower head–reactor vessel | 16 | 21 | (d) | 18 | 1.1 | 1.0 | 2.1 | 0.54 | (b) |
| TOTAL | 105 | 122 | 110 [d] | 93 | 94 | 119 | 95 | 97 | 91 |

a. Percentage of total amount of the fission product inventory calculated from comparisons with ORIGEN2.
b. Insignificant amount (<0.1 wt.%) based on the upper plenum measurements.
c. Two sets of bulk sample measurements were performed on the upper debris bed. The A series was performed on 16 $cm^3$ sample from near the centre of the core at a variety of depths whereas the B series were bulk samples from near the bottom of the debris bed. The data provide a range. For the totals, the B series data were used.
d. Measurements not performed for this radionuclide at this core location. The total shown value in parenthesis is a total which assumes the same distribution as Eu-154 for the repositories where measurements were not performed.

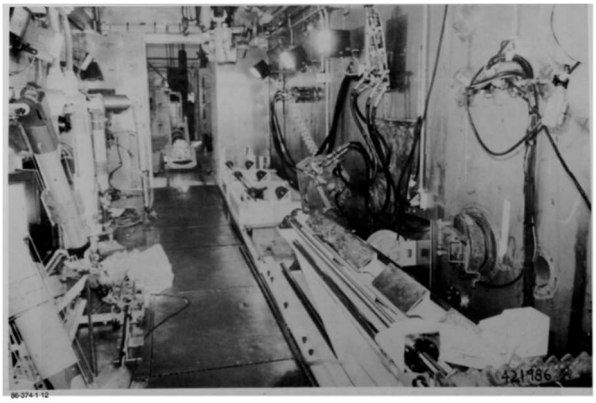

*FIG. 40. Canister unloading table in TAN hot cell (reproduced from Ref. [1] with permission courtesy of INL).*

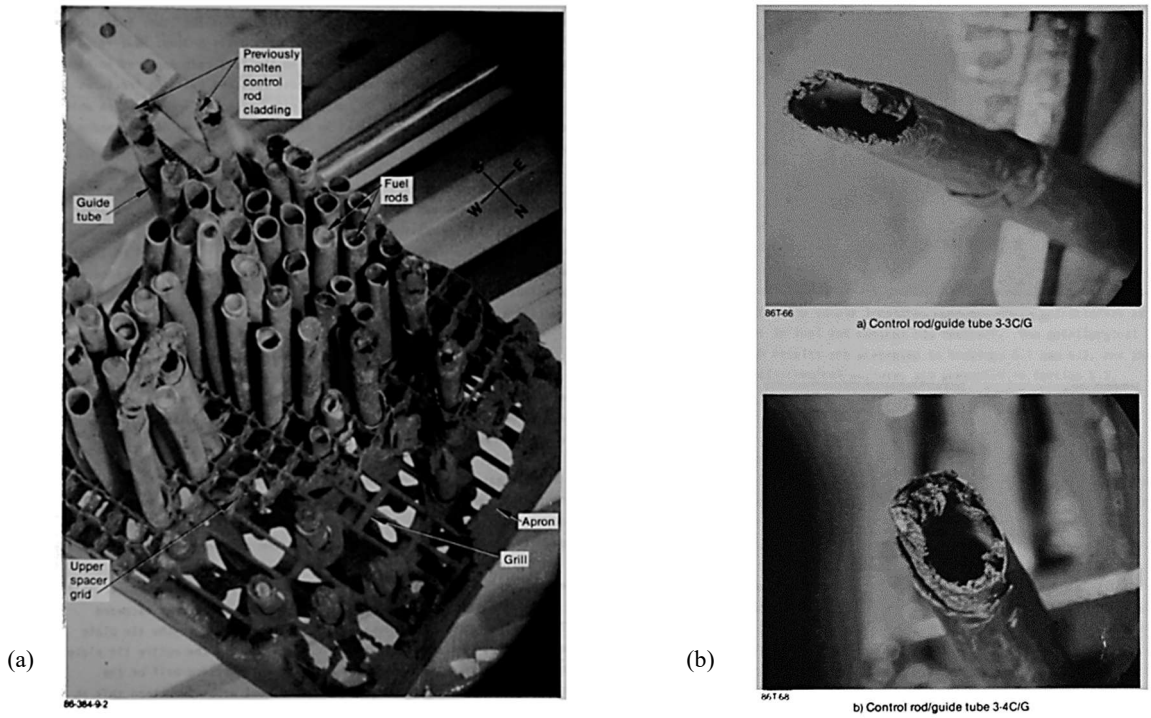


(a) (b)

*FIG. 41. (a) End fitting recovered from debris canister D-153 photographed in the INEL TAN-607 hot cells. (b) Melted stubs of control rods and guide tubes (reproduced from Ref. [1] with permission courtesy of INL).*

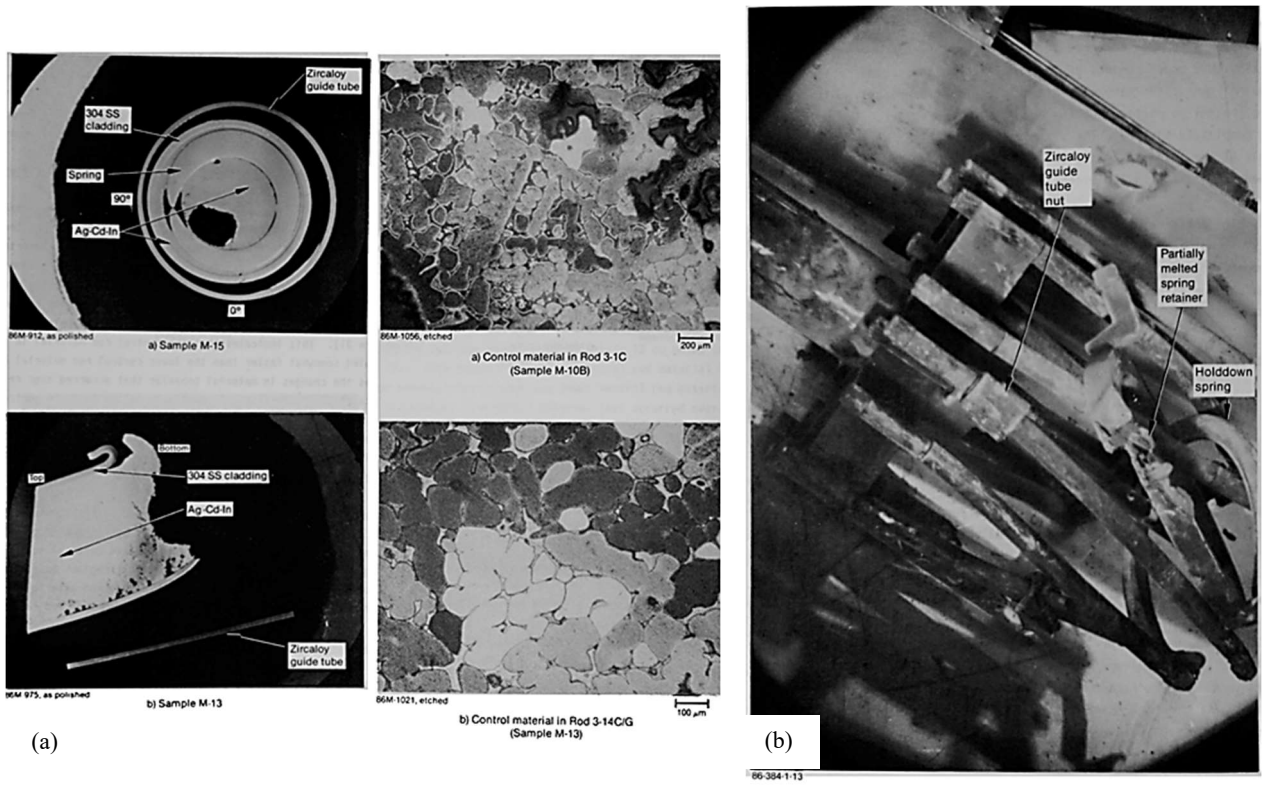


(a) (b)

*FIG. 42. (a) Metallographs of Control Rod 3-14C/G showing partially retained silver-cadmium-indium alloy, right; Dendritic structures in micrographs of etched mounts. (b) Partially melted control rod spider (reproduced from Ref. [1] with permission courtesy of INL).*

## 3.2. CHARACTERIZATION OF CHORNOBYL CORIUM SAMPLES

Investigation of the internal areas of the sarcophagus (or shelter) and collection of highly radioactive samples between 1986–1990 was undertaken by the Kurchatov Institute (now National Research Centre (Kurchatov Institute)), outlined in [31]. The first samples of lava from the 'Elephant foot' were collected in 1987 [26, 49], the main aim of examinations before 1990 was to determine the basic radionuclide and chemical compositions [51, 52]. The status of the collection at the Kurchatov Institute is unclear, and it is assumed that the collection has been disposed of as a radioactive waste. Some lava and corium samples are stored at the Institute of Nuclear Safety at Chornobyl.

V.G. Khlopin Radium Institute was invited by Kurchatov Institute to collaborate on research inside and outside the destroyed unit from the first days of the accident, a small group of KRI scientists collected samples including lava between 1989 and 1991. The main part of KRI's Chornobyl lava and corium collection was collected under extremely dangerous conditions. In addition to collecting samples, some were partly dissolved in hydrofluoric acid (HF) inside the sarcophagus to obtain representative concentrates of artificial minerals (high uranium zircon (Zr, U)$SiO_4$, solid solutions $ZrO_2$–$UO_2$, etc.).

People involved in this sampling work accumulated radiation doses exceeding the recommended limits[7]. The accumulated individual dose of some KRI researchers during sampling in Chornobyl area reached 4–5 Sv. Individual dose uptake during a single lava sampling operation was up to 0.8 Sv. Highly radioactive samples were packed into plastic bags inside the sarcophagus (Fig. 43) and then placed into heavy lead containers for transport to KRI (former Leningrad, Russian Soviet Federative Socialist Republic, now St. Petersburg, Russian Federation) by special arrangements. After arrival at KRI samples were repacked and then stored under normal conditions i.e., room temperature, air without humidity control.

*FIG. 43. Wrapping a big Chornobyl lava sample inside the sarcophagus for transportation to KRI, 1990 (courtesy of B.E. Burakov, Ioffe Institute).*

[7] Reference level for public exposure 20-100 mSv as given in INTERNATIONAL ATOMIC ENERGY AGENCY, Radiation protection of the public and the environment, IAEA Safety Standards Series No. GSG-8, IAEA, Vienna (2018) and recommended limits for nuclear workers as given in ICRP Publication 96 (20 mSv/year, maximum of 100 mSv in five consecutive years, a maximum of 50 mSv in any one year. A maximum dose of 500 mSv to skin contact. A one off dose of 5 Sv will cause death to half of those receiving it in a month).

The KRI collection includes corium, black and brown lava from the main streams, pumice, and secondary uranium minerals (Fig. 44). Currently, this is the only representative collection of highly radioactive samples of corium and lava in the world available for international research and training.

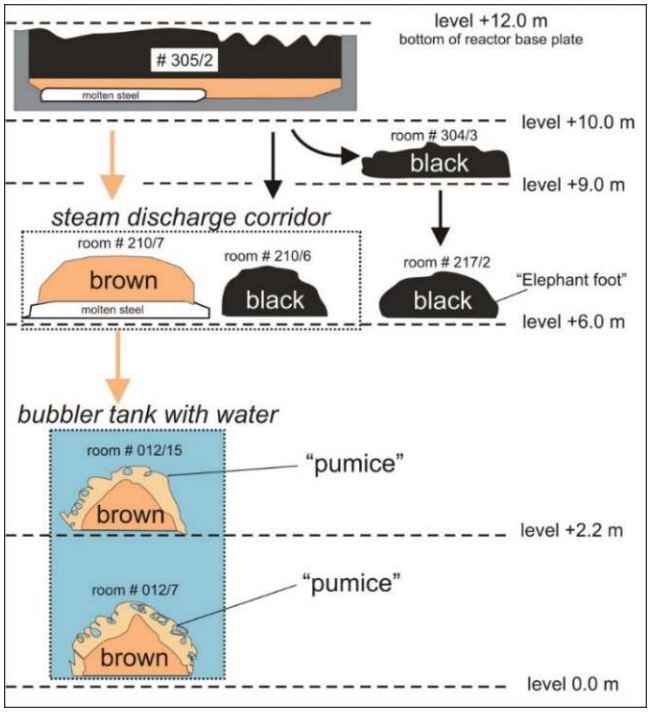


*FIG. 44. Simplified main streams of Chornobyl lava showing major locations (based on data from Ref. [37], courtesy of B.E. Burakov, Ioffe Institute).*

Several samples of Chornobyl lava and highly radioactive molten steel were sent to Atomic Energy Commission (CEA) at Saclay (France) in 1991 for joint material studies [36], the current status of these samples is unclear. In 2012 some fragments of brown lava (from the steam discharge corridor) and black lava from the 'Elephant foot' (room No. 217/2) and two unique hot particles (analysis reported in Refs [41, 45]) were sent to the Institute for Transuranium Elements (ITU, now Joint Research Centre (JRC) Karlsruhe, Germany) for joint studies using SEM, electron probe micro analysis (EPMA), transmission electron microscopy (TEM) and Raman methods, under an agreement between KRI and ITU. Some small samples (about 3–5 mm in size) of brown lava (from steam discharge corridor); black lava from the 'Elephant foot' (room No. 217/2); massive corium (room No. 305/2); mineral grains extracted from lava matrices and some hot particles have been shared with the Radiochemistry Division of the Department of Chemistry, Lomonosov Moscow State University and A.N. Frumkin Institute of Physical Chemistry and Electrochemistry, Russian Academy of Sciences (RAS) (Moscow, Russian Federation) for joint research [38, 40, 46, 53].

A brief summary of the KRI collection is provided in Table 10. Examples of the samples retained at KRI are presented in Figs. 45–47. All samples have been stored in uncontrolled air at room temperature since 1990, and alteration was observed on the samples in 2011.

### 3.2.1. Principal characteristics of samples

Systematic material study of lava and hot particles started at KRI at the beginning of 1990. The results obtained at KRI in cooperation with CEA in Saclay, Radiochemistry Division of the Department of Chemistry, Lomonosov Moscow State University, A.N. Frumkin Institute of Physical Chemistry and Electrochemistry RAS and ITU (JRC Karlsruhe) have been published in numerous papers [32–41,

45, 46, 53], including two detailed summaries [31, 39]. Examination of large samples from room No. 305/2 was started only recently, mainly due to the extremely high gamma radioactivity of the samples in 1990, due to the short lived gamma emitter $^{106}$Ru, precluded safe sample handling and preparation for SEM–EPMA analyses.

TABLE 10. MAIN TYPES OF CHORNOBYL SAMPLES AVAILABLE AT KRI

| No. | Type of sample(s) | Sampling location (room inside sarcophagus or location outside) |
|---|---|---|
| 1 | Brown lava with secondary uranium minerals on the surface | 305/2 |
| 2 | Massive corium | |
| 3 | Brown lava from steam discharge corridor | |
| 4 | Concentrate of minerals after dissolution of brown lava matrix in HF | 210/7 |
| 5 | Molten steel | |
| 6 | Black lava | 304/3 |
| 7 | Concentrate of minerals after dissolution of black lava matrix in HF | |
| 8 | Black lava from steam discharge corridor | 210/6 |
| 9 | Concentrate of minerals after dissolution of black lava matrix in HF | |
| 10 | Black lava from ‘Elephant foot’ | |
| 11 | Concentrate of minerals after dissolution of black lava matrix from ‘Elephant foot’ in HF | 217/2 |
| 12 | Aggregate of molten steel, corium, and secondary uranium minerals | |
| 13 | Pumice from bubbler tank | 012/7 |
| 14 | Concentrate of minerals after dissolution of pumice matrix in HF | |
| 16 | Hot particles extracted from contaminated soils | Western plume at distance from 0.5 to 12 km from sarcophagus |

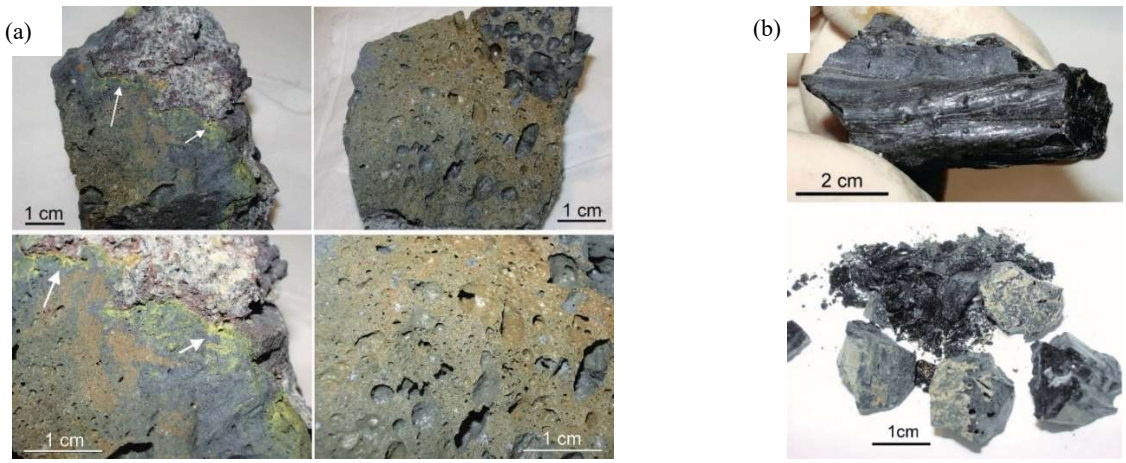


*FIG. 45. (a) Sample of brown lava in contact with a piece of partially molten concrete from room No. 305/2. A secondary uranyl phase, indicated by arrows, was observed in 2011 along the interface between the lava and concrete. (b) Fragments of black lava from the ‘Elephant foot’ room No. 217/2. Sample observed to have fragmented in 2011 (reproduced from Ref. [35] with permission courtesy of B.E. Burakov, Ioffe Institute).*


*FIG. 46. Samples of brown lava from steam discharge corridor, room No. 210/7 (reproduced from Ref. [35] with permission courtesy of B.E. Burakov, Ioffe Institute).*

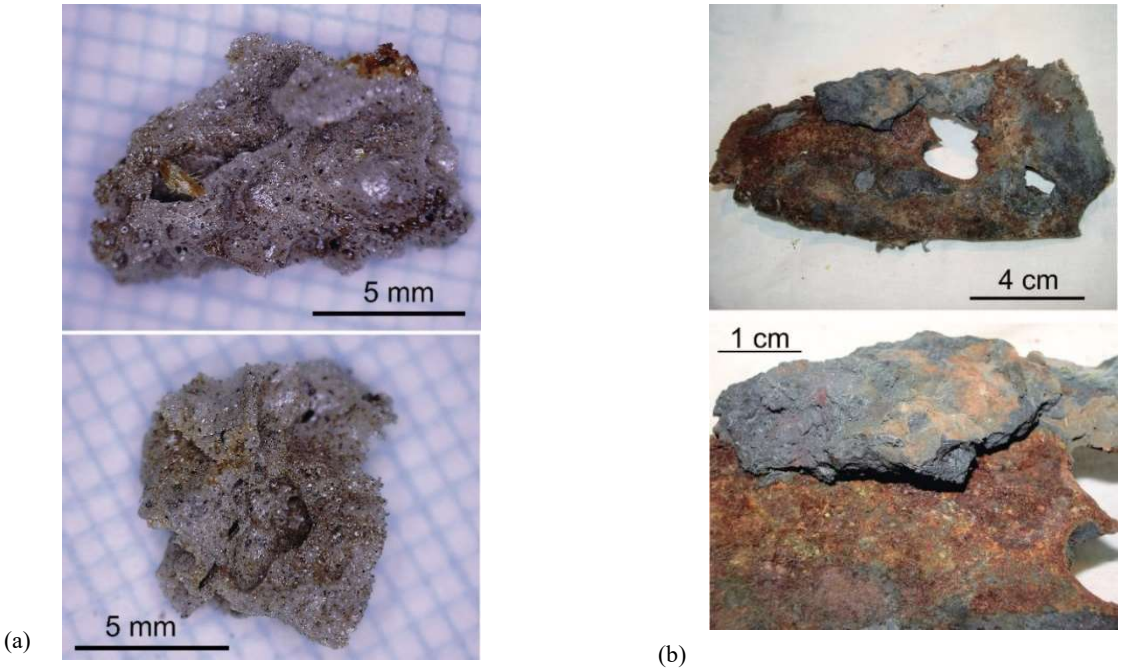


(a) (b)

*FIG. 47. (a) Samples of pumice (result of brown lava melt falling into water) from bubbler tank, room No. 012/7. (b) Product of interaction between massive corium and metal (dark colour) on the surface of corroded waterpipe, room No. 305/2 (reproduced from Ref. [39] with permission courtesy of B.E. Burakov, Ioffe Institute).*

Bulk radionuclide and chemical composition of samples are summarized in Table 11 and Table 12. Results of EPMA of lava silicate glass like matrices (avoiding inclusions) are summarized in Table 13. Micrographs (SEM and optical microscopy in reflected light) pictures of samples are shown in Figs 48–54. According to chemical analysis using EPMA, Raman and Infrared spectroscopy, the lava represents a metaluminious anhydrous silicate glass with rather depolymerized structure (Q2 units dominate) and numerous inclusions and bubbles. Speciation of uranium and zirconium was assessed using X ray absorption spectroscopy.

TABLE 11. PRINCIPAL MATRIX RADIONUCLIDES OF CHORNOBYL LAVA, CORIUM–METAL INTERACTION PRODUCTS AND CORIUM OF HOT PARTICLES [39]

| Material | Radionuclide content, MBq/g (recalculated for April 1986) | | | | | | | | | | |
|---|---|---|---|---|---|---|---|---|---|---|---|
| | Cs–137 | Cs–134 | Ce–144 | Eu–154 | Eu–155 | Cm–244 | Am–241 | Am–243 | Pu–239,240 | Pu–238 | Sr–90 |
| Black lava | 20–40 | 10–30 | 1000–2000 | 1–3 | 2 | 0.1 | 1 | 0.03 | 1 | 0.5 | 10 |
| Brown lava | 50–60 | 30 | 2000–3000 | 3–4 | 5 | 0.2–0.3 | 3 | 0.06 | 2 | 1 | 30 |
| Pumice | 50 | 30 | 3000 | 4 | 5 | 0.2–0.3 | 3 | 0.06 | 2 | 1 | — |
| Corium hot particles | 600–1500 | 200–600 | 30000–100000 | 30–300 | 0–200 | — | — | — | — | — | — |
| Corium-metal interaction product (room No. 305/2) | 0.1–30 | — | — | 0.2–5 | 0–1 | 0.03–0.07 | 0.1–1 | 0.01–0.04 | 1–4 | 0.4–1.6 | — |

TABLE 12. MATRIX ELEMENTAL COMPOSITION OF CHORNOBYL LAVA, PUMICE AND LARGE CORIUM SAMPLES (EXCLUDING OXYGEN) [39]

| Material | Element content, wt% | | | | | | | |
|---|---|---|---|---|---|---|---|---|
| | U | Zr | Na | Fe | Mg | Ca | Si | Al |
| Black lava | 4–5 | 2–6 | 2–10 | 0.3–6 | 1–5 | 3–13 | 19–36 | 3–8 |
| Brown lava | 7–10 | 5–6 | 4 | 1–2 | 4 | 5 | 31–33 | 4 |
| Pumice | 8–9 | 3–6 | 1 | 1 | 5 | 5 | 33–37 | 3 |
| Corium–metal interaction products (room No. 305/2) | 1–40 | 0.2–20 | – | 40–95 | – | – | – | – |

TABLE 13. LOCAL ELEMENTAL COMPOSITIONS OF GLASS-LIKE MATRICES OF CHORNOBYL LAVA AND PUMICE AVOIDING INCLUSIONS (EXCLUDING OXYGEN) [39]

| Material | Element content, wt% | | | | | | | | |
|---|---|---|---|---|---|---|---|---|---|
| | U | Zr | Na | Fe | K | Mg | Ca | Si | Al |
| Black lava | 3–4 | 3–4 | 0.4 | 0.3–7 | 1–3 | 1–3 | 5–7 | 30–40 | 3–4 |
| Brown lava | 2 | 2–3 | 0.6 | 0.2–0.4 | 1–2 | 4 | 5–8 | 40 | 3–4 |
| Pumice | 3 | 4–5 | 0.4–0.7 | 0.2–0.3 | 2 | 4–5 | 7–8 | 30–40 | 4 |

Data are summarized and simplified EPMA results.

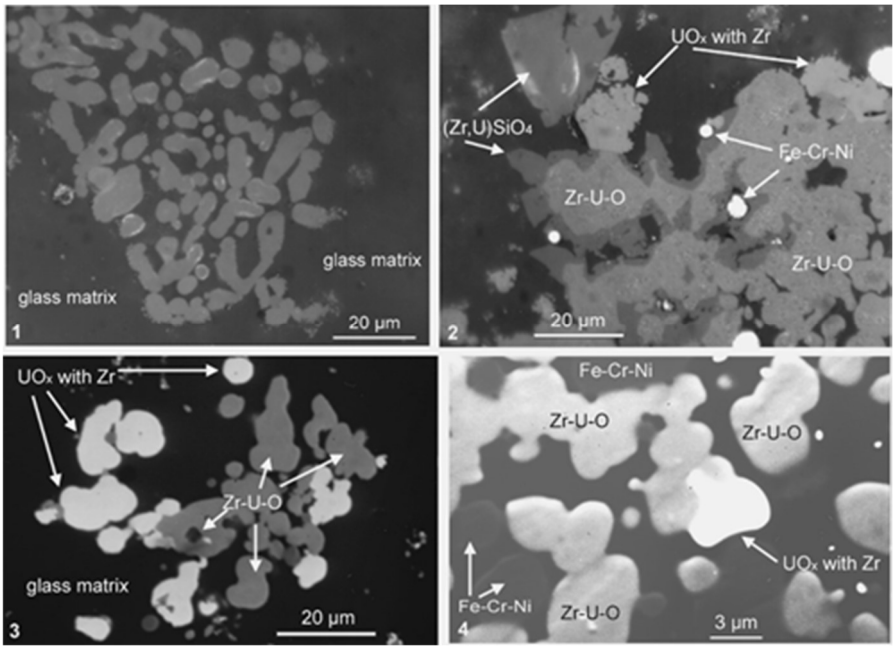


*FIG. 48. Inclusions of $UO_2$-$ZrO_2$ phases with high zirconium content (marked as Zr-U-O) and high uranium content (marked as $UO_x$ with Zr); zircon, $(Zr_{1-x}U_x)SiO_4$, in glass like matrix (marked as glass matrix) of brown lava from steam discharge corridor (room No.210/7). Inclusions of molten stainless steel are marked as Fe-Cr-Ni. Photo 1) and 2) – microphotograph in reflected light in optical microscope; 3) and 4) – microphotograph in backscattered electrons (BSE) on SEM. In photo 2) zircon phase, $(Zr_{1-x}U_x)SiO4$, substitutes Zr-U-O as a result of chemical interaction between Zr-U-O and silicate melt (reproduced from Ref. [35] with permission courtesy of B.E. Burakov, Ioffe Institute).*

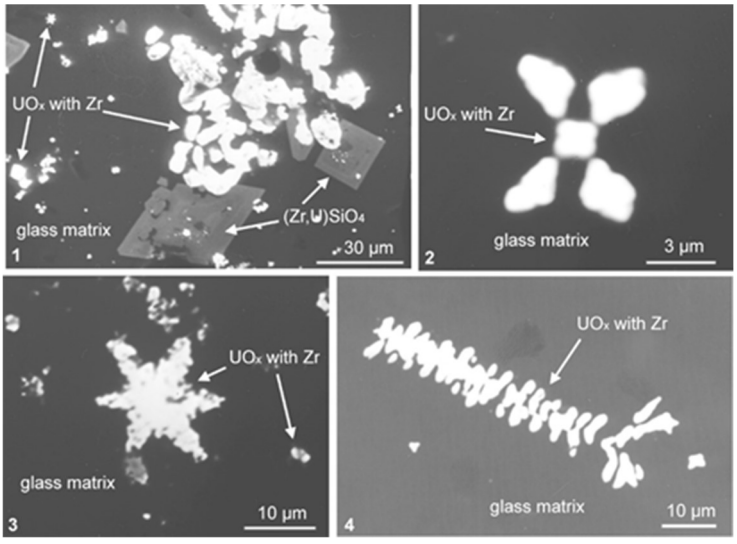


*FIG. 49. Different phases of $UO_2$-$ZrO_2$ with high uranium content (marked as $UO_x$ with Zr) and zircon, $(Zr_{1-x}U_x)SiO_4$, in glass like matrix (marked as glass matrix) of 1) and 2) black lava from steam-discharge corridor (room No.210/6); 3) brown lava from steam discharge corridor (room No.210/7); 4) black lava from the "Elephant foot"(room No.217/2). All photos – microphotographs in BSE on SEM. It is assumed that all small dendrite like inclusions of $UO_x$ with Zr formed during lava melt cooling as a result of segregation of excessive U and Zr from oversaturated silicate melt (reproduced from Ref. [35] with permission courtesy of B.E. Burakov, Ioffe Institute).*

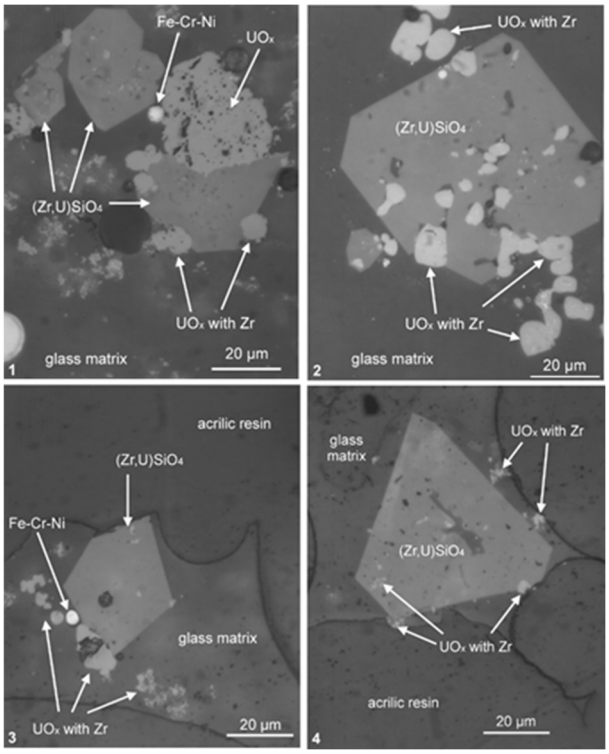


*FIG. 50. Crystalline inclusions in matrices (optical microscopy in reflected light): 1) brown lava from steam discharge corridor (room No. 210/7); 2) black lava from the 'Elephant foot' (room No .217/2); 3) and 4) – pumice from bubbler tank (room No.012/7). Polished sample embedded in epoxy resin. In all samples of crystals of zircon, $(Zr_{1-x}U_x)SiO_4$, associate with phases of solid solutions $UO_2$-$ZrO_2$ with high uranium content (marked as $UO_x$ with Zr). Relict of fuel particle (free of Zr admixture, marked as UOx). White round inclusions – particles of molten stainless steel (marked as Fe-Cr-Ni). Glass-like matrix of lava and pumice (marked as glass matrix) (reproduced from Ref. [35] with permission courtesy of B.E. Burakov, Ioffe Institute).*

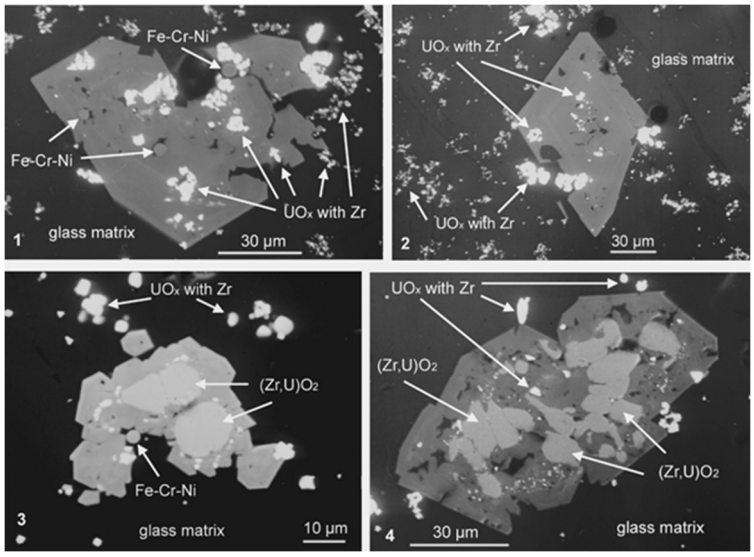


*FIG. 51. Inclusions of artificial zircon, $(Zr_{1-x}U_x)SiO_4$, which associates with solid solution $UO_2$-$ZrO_2$ phases with high uranium content (marked as $UO_x$ with Zr) and U-bearing (4–6 wt% U) monoclinic zirconia or baddeleyite $(Zr_{1-x}U_x)O_2$ (which is one of products of Zr-U-O crystallization) in glass-like matrix (marked as glass matrix) of: 1) and 2) –brown lava of steam discharge corridor (room No .210/7); 3) and 4) – black lava from steam discharge corridor (room No. 210/6). All microphotographs in BSE on SEM (reproduced from Ref. [35] with permission courtesy of B.E. Burakov, Ioffe Institute).*

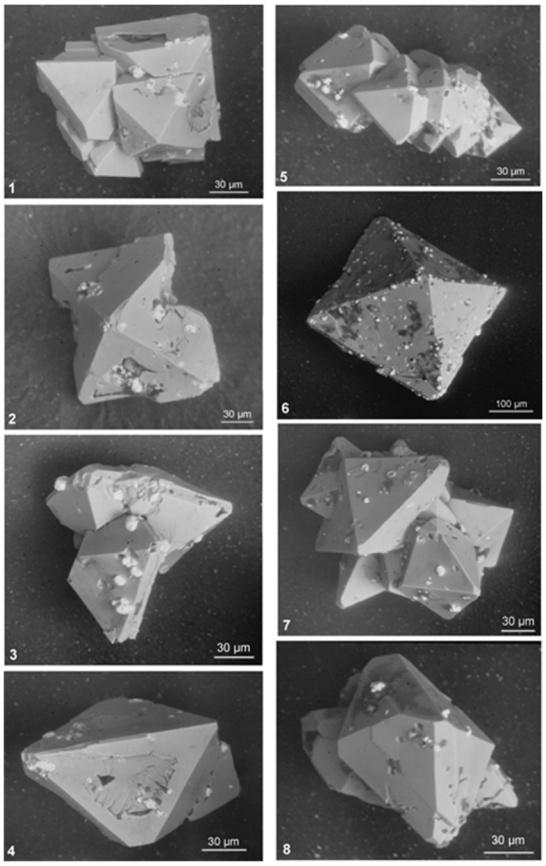


*FIG. 52. Crystals of artificial zircon, $(Zr_{1-x}U_x)SiO_4$, obtained by partial dissolution of lava fragments in HF: 1)–4) – brown lava from steam-discharge corridor (room No. 210/7) and 5)–8) – black lava from steam-discharge corridor (room No.210/6). All microphotographs in BSE on SEM (reproduced from Ref. [35] with permission courtesy of B.E. Burakov, Ioffe Institute).*

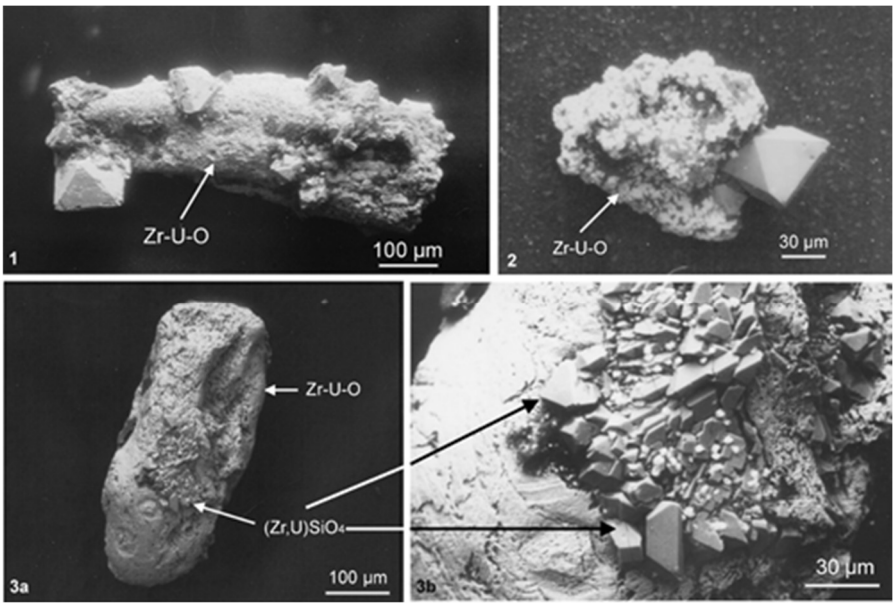


*FIG. 53. Crystals of artificial zircon, $(Zr_{1-x}U_x)SiO_4$, on particles of $UO_2$-$ZrO_2$ solid solution phases with high Zr content (marked as Zr-U-O). Samples have been obtained by partial dissolution in HF of brown lava fragments from steam-discharge corridor (reproduced from Ref. [35] with permission courtesy of B.E. Burakov, Ioffe Institute).*

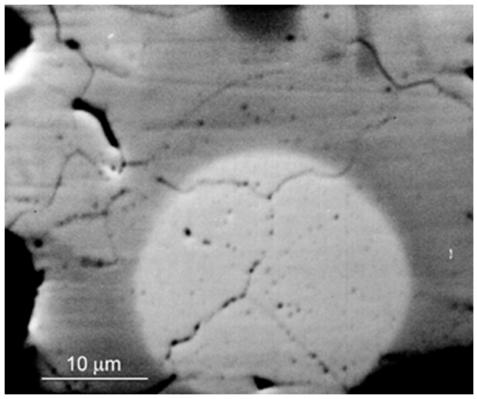


*FIG. 54. Corium hot particle extracted from soil sample collected at western plume, 12 km from ChNPP Unit 4. Contents of elements (in wt%): U – 40–44 and Zr – 39–36 in grey matrix; U – 54–55 and Zr – 26 in round white area. SEM–BSE) micrograph of polished sample. Black surrounding area is acrylic resin (reproduced from Ref. [35] with permission courtesy of B.E. Burakov, Ioffe Institute).*

Electron probe microanalysis, powder and single crystal XRD, Raman spectroscopy and focused ion beam assisted TEM of inclusions extracted from lava matrices and pumice allowed identification of the following U–Zr-phases:

- Cubic, tetragonal and monoclinic solid solutions (U, Zr)$O_2$ with Zr content from 0.5 to 20 wt% (unit cell parameter a decrease with increasing zirconium concentration from 5.468 to 5.318 Å). Chemical composition of these phases varies from $(U_{0.985}Zr_{0.015})O_{2.000}$ to $(U_{0.895}Zr_{0.105})O_{2.000}$. Admixture of uranium is one of the possible reasons for stabilisation of the high temperature tetragonal and cubic modifications;
- Cubic $UO_x$, with structure and chemical composition close to stoichiometric $UO_2$. These inclusions are relicts of undissolved fuel particles and phases formed by precipitation of excess uranium upon cooling of the lava. According to Raman spectroscopy for all $UO_{2+x}$ inclusions the deviation from ideal stoichiometry is minor: $x < 0.07$;
- High uranium artificial zircon with chemical composition in the range $(Zr_{0.95}U_{0.05})SiO_4$–$(Zr_{0.90}U_{0.10})SiO_4$ from homogeneous crystal areas. This phase is fully crystalline (a = 6.617(2) and c = 5.990(2) Å) with U content in solution of up to 12–13 wt%. TEM reveals presence of multiphase submicron inclusions; numerous $UO_{2+x}$ inclusions are also present. At the same time, steel droplets are never captured;
- Tetragonal phase Zr–U–O with chemical composition varies from $(Zr_{0.86}U_{0.14})O_{2.00}$ to $(Zr_{0.89}U_{0.11})O_{2.00}$. This phase is likely stabilized by uranium. Transformation of this phase into low temperature baddeleyite, either in situ due to contact with moisture or already on cooling of the lava, is accompanied by large volume effect (expansion) and thus appears to be a significant factor leading to thermomechanical destruction of the lava;
- Monoclinic phase with chemical composition close to artificial baddeleyite (monoclinic zirconium dioxide). Calculated composition varies from $(Zr_{0.995}U_{0.005})O_{2.000}$–$(Zr_{0.967}U_{0.033})O_{2.000}$ with up to 6 wt.% of U.

The results from the material studies on Chornobyl samples are very important to predict the main properties of fuel debris at 1F. Expected similarities and differences of Chornobyl fuel debris in comparison with 1F are summarized below:

- Mechanically destroyed fuel — similar to 1F;
- Black and brown lava — expected at 1F;
- Pumice — expected at 1F in a larger volume;

- Hot particles with fuel and corium matrices — similar particles were already found at 1F;
- Molten steel enriched with $^{106}Ru$ — expected at 1F;
- Massive corium that reacted with oxidized steel — possibly formed at 1F;
- New formed uranyl phases (products of chemical alteration and uranium oxidation) — greatly expected at 1F;
- Not available inside the sarcophagus but very probable at 1F: huge amount of low radioactive $ZrO_2$ (oxidized Zircaloy as a result of steam–zirconium reaction);
- Pu-oxide phases and solid solutions $ZrO_2$–$UO_2$–$PuO_2$ are not available in Chornobyl but very probable at Unit 3 of 1F.

### 3.2.2. Sample chemical alteration and physicochemical properties of the newly formed phases

Chemical alteration of lava inside the sarcophagus was observed several years after the accident. In 2011 newly formed uranyl phases were observed on the surface of some lava samples at KRI (Fig. 55). It indicates that at high humidity the chemical durability of lava and corium decreases in air. X ray diffraction analyses showed that newly formed yellow stains on the surface of black lava from the steam discharge corridor (room No. 210/6) consisted of crystalline phases [50]. Some of these phases are chemically close to natural minerals: $UO_3 \times 2H_2O$ (analogue of epiianthinite), $UO_4 \times 4H_2O$ (analogue of studtite), $UO_2CO_3$ (analogue of rutherfordine). Other phases such as $Na_4(UO_2)(CO_3)_3$, and sodium carbonates $Na_3H(CO_3)_2 \times 2H_2O$ and $Na_2CO_3 \times 2H_2O$ were also identified.

Fluorescence of secondary phases under ultraviolet (UV) light confirms that uranium in these phases is partly oxidized from U(IV) to U(VI) (Fig. 55). Slow oxidation of uranium by $O_2$, $H_2O$ and $CO_2$ take place even under laboratory conditions, and it was confirmed by chemical alteration of corium and lava where uranium is dissolved in a matrix (Fig. 54). However, uranium related to solid solution phases $UO_2$–$ZrO_2$ and high uranium zircon $(Zr_{1-x}U_x)SiO_4$, is not oxidized as these phases have a high chemical durability even in acids. On the contrary, newly formed uranyl minerals on the surface of Chornobyl lava and corium have low mechanical and chemical durability. This crystalline material can be easily dehydrated in dry air, destroyed and dispersed even under insignificant mechanical impact (see, e.g., Fig. 11 in [38]). All uranyl phases can be easily dissolved at room temperature in acid solution, most of them are soluble in alkaline solutions and even in distilled water.

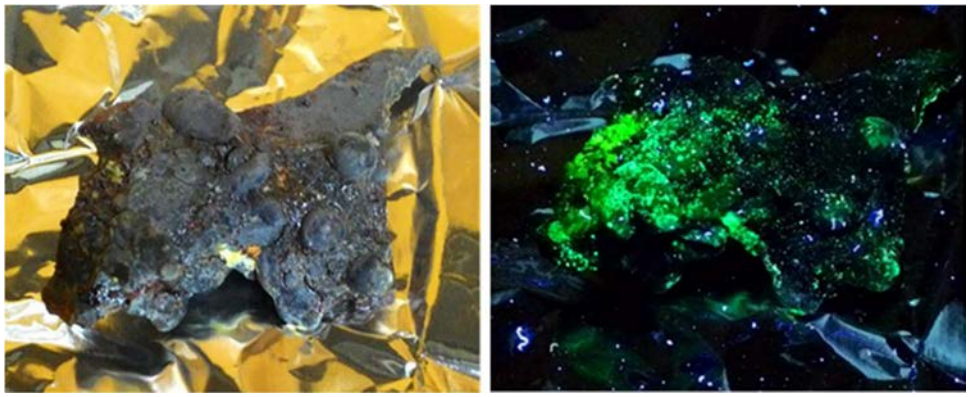

*FIG. 55. Alteration of the surface of Chornobyl corium–metal products (aggregate of corium and molten steel from room No. 217/2) with formation of secondary uranyl minerals in the light (left) and UV luminescence of alteration products (right). KRI Collection (courtesy of B.E. Burakov, Ioffe Institute, and Yu.Yu. Petrov, KRI).*

At KRI long term leaching and alteration experiments started in 2016 to evaluate leach rates of various radionuclides from matrices of 30 years old lava samples. The normalized leach rates of Pu and Cs

in distilled water are presented in Table 14. The radionuclide release rate might increase significantly at higher temperature and for leaching solutions with different chemical compositions. For example, the normalized mass loss of $^{137}Cs$ from black lava taken from the 'Elephant foot', after 4 months in simulated seawater (Fukushima Daiichi accident's related conditions) and increasing temperature from 25 to 363 K, resulted in increased loss by a factor of 25. For brown lava taken from steam discharge corridor (within the same period) a factor of 40 was observed. Detailed results of leaching experiments are summarized in KRI publications [90, 91].

TABLE 14. NORMALIZED LEACH RATES OF PU AND CS IN DISTILLED WATER AFTER 270 DAYS AT ROOM TEMPERATURE [90] AND AFTER 1 YEAR AT 363 K

| Sample | Normalized Leach Rate (NR)(Pu), $g \times m^{-2} \times day^{-1}$ | | NR(Cs), $g \times m^{-2} \times day^{-1}$ | |
|---|---|---|---|---|
| | 298 K, 270 days | 363 K, 1 year | 298 K 270 days | 363 K, 1 year |
| Black «lava» | $2.6 \times 10^{-3}$ | $5.8 \times 10^{-3}$ | $2.0 \times 10^{-4}$ | $6.0 \times 10^{-2}$ |
| Brown «lava» | $5.2 \times 10^{-3}$ | $6.1 \times 10^{-3}$ | $8.1 \times 10^{-4}$ | $5.9 \times 10^{-2}$ |
| Corium–metal interaction product | $2.3 \times 10^{-3}$ | $3.2 \times 10^{-3}$ | $1.3 \times 10^{-2}$ | $2.7 \times 10^{-1}$ |

After 1 year of contact in distilled water at 423 K, samples of lava and corium–metal interaction products were significantly altered in comparison with samples at 363 K (Figs 56 and 57). Different alteration processes took place on the surface of brown lava: formation of a gel on the surface of the sample, corrosion of metallic inclusions in lava matrix and oxidation of uranium in U bearing phases with formation of secondary uranyl minerals. At lower temperatures (298 and 363 K) dissolution of the glass like matrix of lava was not accompanied with a gel formation, in contrast to nuclear waste glasses [92].

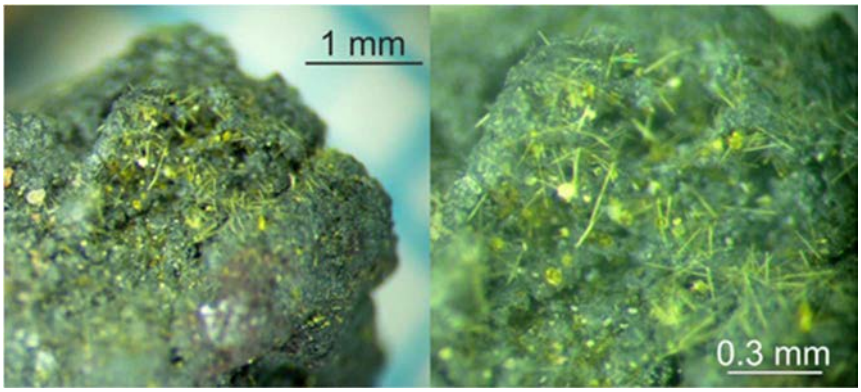


*FIG. 56. Formation of secondary phases on the surface of corium–metal interaction products (from room No. 305/2) after 1 year contact with distilled water at 423 K. Phase with needle shaped crystals was not observed in alteration experiments at lower temperature (363 K) [93] (courtesy of B.Yu. Zubekhina, KRI, and B.E. Burakov, Ioffe Institute).*


*FIG. 57. Brown lava from steam discharge corridor used for alteration experiment: original sample (left) and after 1 year contact with distilled water at 423 K (right) [93] (courtesy of B.Yu. Zubekhina, KRI, and B.E. Burakov, Ioffe Institute).*

## 3.3. CHARACTERIZATION OF FUKUSHIMA DAIICHI FUEL DEBRIS

During the course of the severe accident at 1F, the failure to refill the cooling system resulted in the large scale meltdown of Units 1–3 cores. The accident situation was different from other severe accidents at TMI–2 and ChNPPs, apart from fuel debris was generated in all cases. The fuel debris consists of solidified melt materials, the composition and phase are dependent on accident scenario, i.e., affected reactor core materials, accident progression and cooling conditions. Examples include: the injection of sea water into the reactors to provide emergency cooling in the early stages of the accident; material melting through the PCV; and falling melted debris reacting with the concrete floor in the PCV pedestal. At the time of the accident mixed oxide fuel (MOX) was loaded in Unit 3, therefore it is also necessary to investigate the behaviour of plutonium under accident progression.

### 3.3.1. Estimated amount of Fukushima Daiichi fuel debris

Reactor core damage in Units 1–3 depended on the accident progression. Some parts of the core are assumed to have melted and reached the bottom of the PCV through the lower end of the RPV and reacted with the concrete to produce MCCI products (see Fig. 58). The current state of the fuel debris depends on the accident events and sequence. The total amount of fuel debris, for Units 1–3, has been estimated based on the reactor core configuration (i.e., number of FAs, control rods, channel boxes). Table 15 shows the estimated weight of the core materials [94].

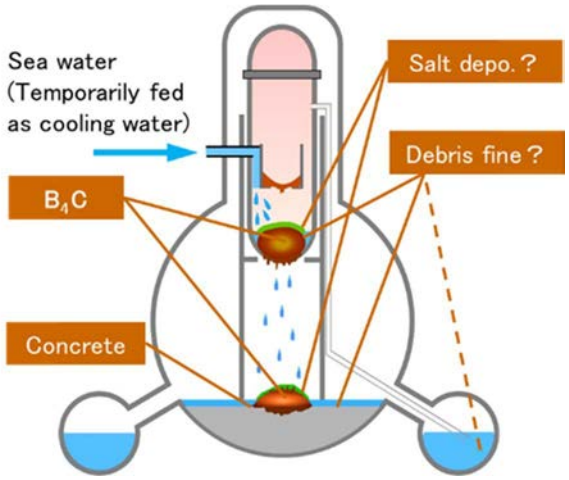


*FIG. 58. Sequence of events of the 1F accident that have the potential to impact fuel debris properties (courtesy of Japan Atomic Energy Agency (JAEA)).*

TABLE 15. AMOUNT OF ESTIMATED CORE MATERIALS IN 1F (based on data from [95])

| | Unit 1 (t) | Unit 2, Unit 3 (t) |
|---|---|---|
| Stainless Steel (Control rod drive (CRD) housing, CR guide tube, etc.) | 18 | 25 |
| $UO_2$ | 79 | 107 |
| Zircalloy | 32 | 43 |

### 3.3.2. Preparation for Fukushima Daiichi fuel debris analysis and retrieval

The recovery of fuel debris is quiet a challenging issue in the decommissioning of 1F for TEPCO. In order to proceed safely and steadily with the decommissioning, conditions inside the reactor, such as the location and characteristics of fuel debris and fission products (FP), and the characteristics of damaged structural materials in the reactor need to be determined. Information on the conditions inside the reactor can be obtained from inspections, monitoring and analysis of fuel debris [96]. Such information is also necessary to assess criticality safety and containment measures required to prevent the spread of radioactive contamination, that needs to be incorporated in the design for retrieval, storage, and disposal of the fuel debris. Moreover, it is also necessary to design the overarching processes relating to the transport, storage, processing, and disposal of retrieved fuel debris [96].

It should be noted that the RPVs of Units 1–3 have been damaged during the accident, and as a result, the vessels cannot be filled completely with water. Unlike TMI–2, where the core recovery was done with the RPV filled with water, recovery of the core material from 1F might need to be done without the RPV being completely underwater. If the recovery is to be done under dry conditions, dispersal of aerosols and fine particles of radioactive contamination would be a very significant issue to deal with.

#### *3.3.2.1. Priority of fuel debris analysis*

Systematic acquisition of 1F samples, including fuel debris, is necessary to develop the knowledge and information required for process design and management of the 1F decommissioning (retrieve method of fuel debris, formulating plans and methods for storage, disposal and dismantlement of the facilities), the information will be acquired from sample analyses, reactor investigations and understanding of the accident phenomena for ascertaining cause of the accident [94]. TEPCO and the Nuclear Damage Compensation and Decommissioning Facilitation Corporation (NDF) are examining how to carry out internal investigations of PCV, trial retrievals and analyses (Fig. 59) to enable methods for retrieving fuel debris to be developed and to prepare plans for, and methods of, storage, processing and disposal of fuel debris and dismantlement of facilities.

The Mid–and–Long–Term Roadmap for Decommissioning [98] includes carrying out a small fuel debris sampling trial from Unit 2 in 2022. The reactor investigation including retrieval of fuel debris samples is expected to follow shortly after. It is important to understand how to analyse fuel debris and interpret the analysis results to ensure that the results are of most use for planning decommissioning operations. To achieve this, it is important to get a consensus between stakeholders. Safe decommissioning is the highest priority in the 1F decommissioning, but understanding the phenomenon involved in the accident and its causes is also valuable as this can lead to safety improvement of future light water cooled reactors (LWRs) [99].

*3.3.2.2. Analysis issues of fuel debris*

Figure 59 summarises the many challenges associated with fuel debris recovery, safeguards, storage management, processing and disposal that will need to be overcome to underpin decommissioning and to provide insights into the cause of 1F accident. Prioritization of fuel debris analysis is important and the framework for understanding the purposes for analysing fuel debris is shown in Fig. 60.

Having established the aims of the analyses, it is necessary to consider what samples are to be taken and how the fuel debris samples will be analysed to solve those issues (identify the items subject to analysis). The items subject to analysis were evaluated and identified by a rigorous review of feasible analysis methods. Figure 61 shows that the process of acquiring knowledge necessary for solving issues is through interpreting, analysing, and evaluating the analysis results. However, the details of the individual activities in this process will depend on the results derived as the work progresses. Therefore, this process was considered based on basic ideas and concepts.

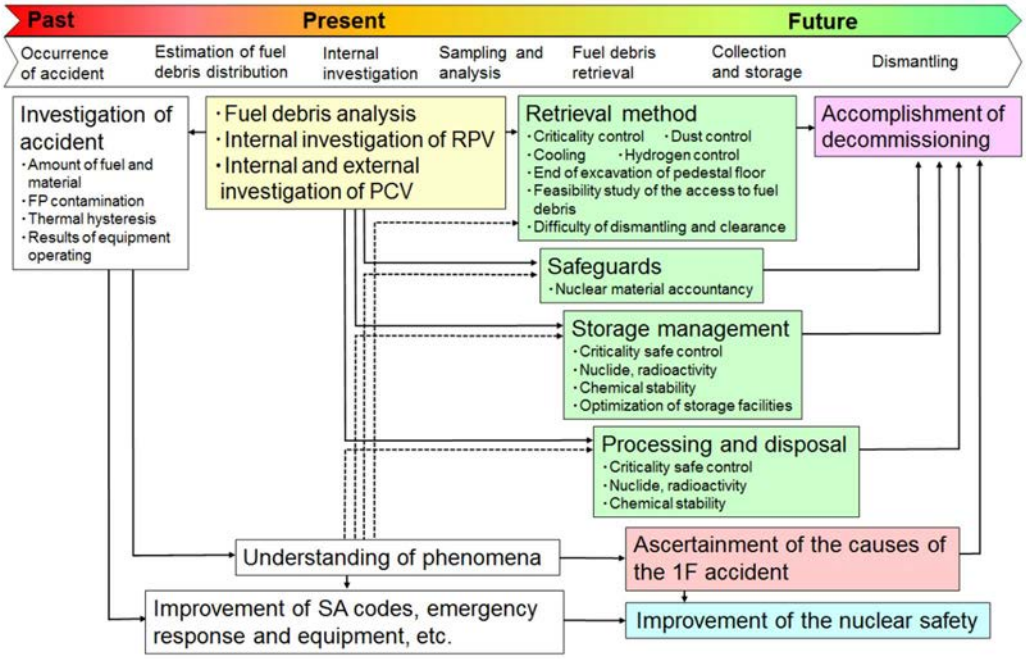


*FIG. 59. Purpose of fuel debris analysis and investigations items of fuel debris (reproduced from Ref. [96] with permission courtesy of JAEA).*

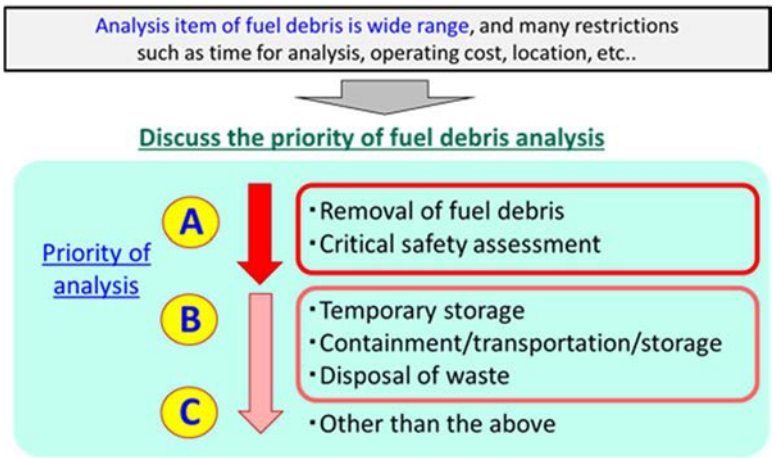


*FIG. 60. Priority on analysis items of fuel debris (courtesy of JAEA).*

The data from the debris analysis will be used directly to evaluate the fuel debris properties, or it will be evaluated and applied to understand more comprehensive evaluation subjects. Table 16 [96] shows the data obtained from the analyses and the evaluation subjects using the analysis results.

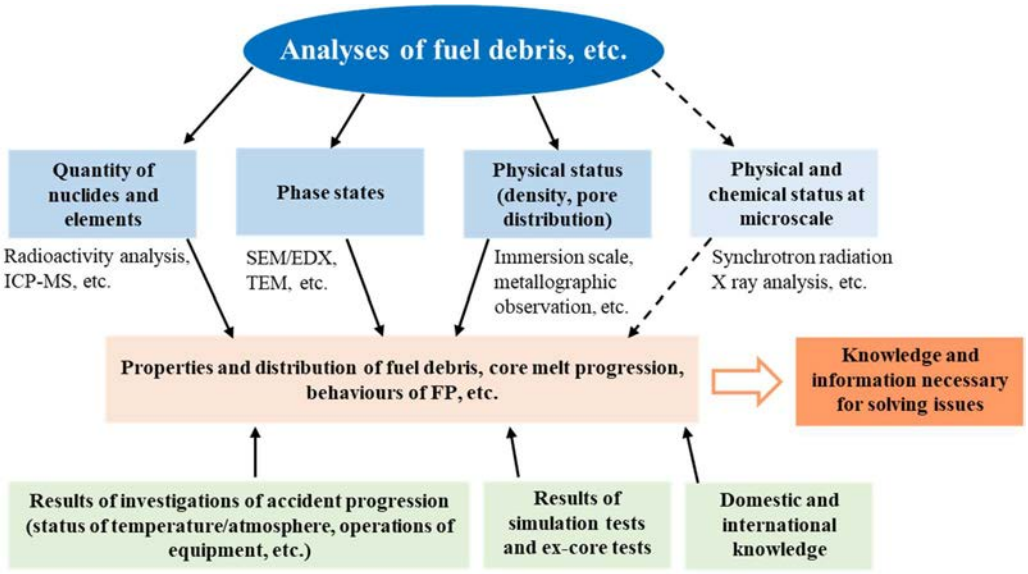


*FIG. 61. Flow of acquiring knowledge and information necessary for solving issues based on the analysis results of fuel debris (reproduced from Ref. [96] with permission courtesy of JAEA).*

*3.3.2.3. Guideline for fuel debris characterization*

Guidelines for fuel debris characterization with respect to the preferential R&D took into consideration: that the previous severe accident studies, technical attention, were focused mostly on the analysis of the accident progression. Data on debris properties were primarily limited to the items related to heat transfer and material mobility, melting point, heat capacity, and thermal conductivity.

Very few physical and mechanical properties have been reported, except for those of TMI–2 debris. Physical properties such as shape, size, and density depend on the conditions under which the accident progressed, e.g., the temperature history and atmosphere, such as the $H_2/H_2O$ concentration ratio. It is difficult to obtain highly reliable estimates without onsite observation and sampling because detailed information on the reactor and accident progression is unavailable.

Therefore, before sampling from the actual reactors begins, the mechanical properties of the fuel debris need to be estimated preferentially by simulated debris tests using a uranium dioxide and zirconium dioxide solid solution, zirconium alloys, stainless steel, and so on. Hardness is measured by the indentation method as the Vickers hardness. The elastic modulus can be measured by the ultrasonic wave pulse echo method, and the fracture toughness can also be measured using a Vickers hardness tester. All these methods require very small samples. Because very small samples can be obtained early in the sampling operations, it will be possible to use the listed techniques to summarize the mechanical properties of the debris. Further, simulated debris properties will be compared with the actual properties enabling the guidelines for preparation of the 1F debris for retrieval to be reviewed.

### 3.3.3. Analysis of actual samples from the Fukushima Daiichi site

To inform fuel debris retrieval process requirements, deposits from inside the 1F reactors were collected and characterized. Although the number of samples obtained is extremely limited due to

differences in the acquisition sites and targets of the samples in the PCV of each unit (Fig 62), the following general highlights can be shared based on the sample analysis results obtained to date:

- Fe content ratio is large, and a lot of rust like material is present in the PCV;
- Core components, non–core components, and control rod grade components were detected, and the type of component sampled could be obtained;
- U containing particles were present in the samples in the PCV of Units 1 and 3;
- Regarding the U containing particles, the sample in PCV of Unit 2 had a larger proportion of zirconium than the samples from the PCVs of Units 1 and 3, and there was a difference between Unit 1 and 3 samples (Fig. 63). Information about molten core fuel could be available;
- The sampling analysis results will contribute to verifying the results of estimation of interiors of PCV at Units 1—3, obtained in the previous project, which was entitled Advanced comprehensive estimation of inside of PCV.

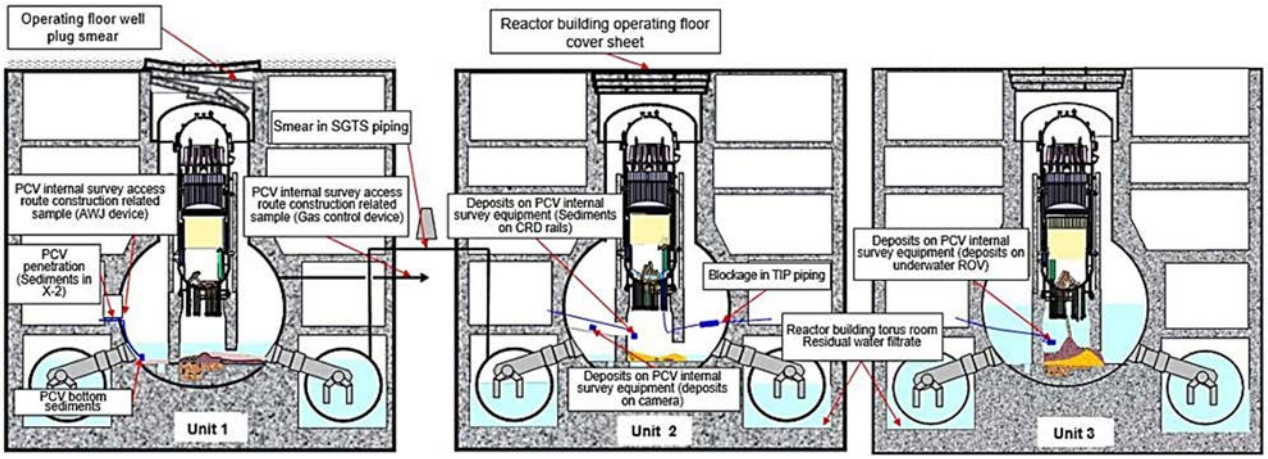


*FIG. 62. Schematic locations of the retrieved samples in the damaged units (adapted from [100, 101] courtesy of JAEA).*

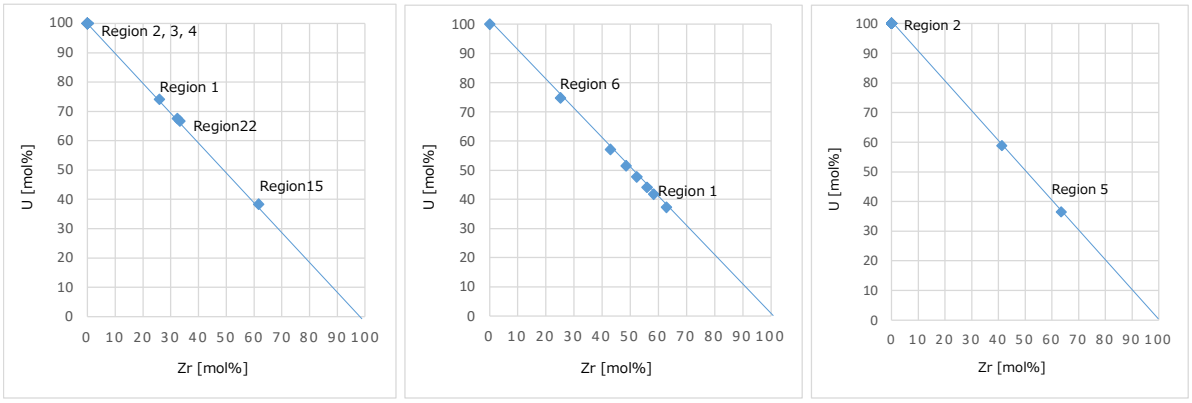


(a) Unit 1 (Muddy sample)

(b) Unit 2 (Sample from pedestal floor inspection)

(c) Unit 3 (Sample from pedestal floor inspection)

*FIG. 63. Normalized mole ratio between U and Zr for U rich regions/particles contained in samples from (a) Unit 1, (b) Unit 2, and (c) Unit 3. The mole amount of U and Zr detected/evaluated in U rich regions by the FE-SEM/energy-dispersive x ray spectroscopy (EDX) point analysis is normalized. The marked regions are further analysed by TEM (adapted from [100, 101] courtesy of JAEA).*

TABLE 16. INFORMATION AND EVALUATION ITEMS OBTAINED THROUGH ANALYSIS AND CONTRIBUTION POINTS OF THE FUEL DEBRIS ANALYSIS (based on data from Ref. [96])

| Analysis item | Examination/ Equipment (Items that are not required but can be expected to obtain detailed data are underlined.) | Information to be obtained | Evaluation items that use analysis values | Contribution points | | | | |
|---|---|---|---|---|---|---|---|---|
| | | | | Retrieval | Storage management | Processing and disposal | Core melting progress | Source term |
| Metallography | Optical microscope | Morphology<br>Structure<br>Oxide layer thickness | Thermal behaviour and chemical reaction at accident<br>Particle size distribution | + | | + | + | + |
| Element/ Impurity | SEM–EDX<br>SEM– wavelength-dispersive x ray spectroscopy (WDX)<br>EPMA-WDX | Appearance/ Microstructure<br>Structure/Phase<br>Elemental composition | Criticality safety<br>Long term integrity<br>Thermal behaviour and chemical reaction at accident | + | + | + | + | + |
| Compound/ Phase | Infrared spectrometer<br>Raman spectrometer<br>Hard X ray photoelectron spectroscopy (HAXPES)<br>Scanning transmission x ray microscope (STXM)<br>Synchrotron radiation X ray analysis (SR-XA) | Chemical form/ state | Long term integrity<br>Chemical behaviour at accident | + | + | | | + |
| Crystal structure/ Phase | Powder XRD<br>TEM-EDX<br>SR-XA<br>– Powder $\mu$-XRD (synchrotron radiation)<br>– X ray absorption fine structure (XAFS) (synchrotron radiation) | Crystal structure/Chemical form<br>Crystal structure/Chemical form of microstructure<br>Amorphous phase structure | Long term integrity<br>Thermal behaviour and chemical reaction at accident<br>Fuel debris properties at sampling location | + | + | | + | + |

TABLE 16. INFORMATION AND EVALUATION ITEMS OBTAINED THROUGH ANALYSIS AND CONTRIBUTION POINTS OF THE FUEL DEBRIS ANALYSIS (contd.) based on data from Ref. [96]))

| Analysis item | Examination/ Equipment (Items that are not required but can be expected to obtain detailed data are underlined.) | Information to be obtained | Evaluation items that use analysis values | Contribution points | | | | |
|---|---|---|---|---|---|---|---|---|
| | | | | Retrieval | Storage management | Processing and disposal | Core melting progress | Source term |
| Density/ Porosity | Immersion type balance | Porosity | Water content<br>Cooling effect during water injection<br>Mechanical properties | + | + | + | + | |
| Qualitative analysis | X ray fluorescence (XRF) | Non-destructive identification/ abundance ratio of elements<br>Screening of main components | Criticality safety | + | | + | | |
| Elemental analysis (FP & structural materials) | ICP–OES | Quantitative analysis results of metal elements (B, Gd, Zr, Fe, Cr, Ni etc. ~ ppm) | Criticality safety<br>Thermal behaviour and chemical reaction at accident | + | + | + | | + |
| Elution element | Ion chromatograph | Chloride ion content (~ppm) | Storage can corrosion<br>Hydrogen generation | + | + | | | + |
| Organic matter content | Total organic carbon (TOC) | Organic impurity content | Stability/Reactivity<br>Gas generation through radiolysis | | + | + | | + |

TABLE 16. INFORMATION AND EVALUATION ITEMS OBTAINED THROUGH ANALYSIS AND CONTRIBUTION POINTS OF THE FUEL DEBRIS ANALYSIS (contd.) based on data from Ref. [96]))

| Analysis item | Examination/ Equipment (Items that are not required but can be expected to obtain detailed data are underlined.) | Information to be obtained | Evaluation items that use analysis values | Contribution points | | | | |
|---|---|---|---|---|---|---|---|---|
| | | | | Retrieval | Storage management | Processing and disposal | Core melting progress | Source term |
| Nuclide analysis (Nuclides and isotopes from B to Cm) | Inductively coupled plasma mass spectrometry (ICP–MS) | Actinide isotopic composition<br>FP isotopic composition | Criticality safety<br>Burnup<br>Radiation dose<br>Heat generation<br>Inventory | + | + | + | | + |
| α emitting nuclide analysis | α ray spectrometer | Quantitative analysis (U, Np, Pu, Am, Cm) | Criticality safety<br>Heat generation<br>Inventory | + | + | + | | + |
| β emitting nuclide analysis | Liquid scintillation counting (LSC) | Quantitative analysis (H-3, C-14, Ni-63, Sr-90, Zr-93, Mo-93, Tc-99 etc.) | Inventory<br>Heat generation | + | + | + | | + |
| γ emitting nuclide analysis | γ ray spectrometer | Quantitative analysis (Ca-41, Cs-134, Cs-137, Eu-152, Eu-154, Ni-59, Co-60, Nb-94, Sm-151 etc.) | Dose rate<br>Heat generation<br>Inventory | + | + | + | | + |
| Radiation dose distribution | Imaging plate | Radioactivity distribution | FP release behaviour at accident | | | | | + |
| Water content measurement | Karl Fischer moisture meter | Water content | Recriticality<br>Steam generation<br>Gas generation through radiolysis<br>$H_2O_2$ generation | + | + | + | | |
| Gas release characteristics such as FP | Gas chromatograph | Amount of gas release during heating | FP release behaviour at accident<br>Hydrogen generation | | | | | + |

TABLE 16. INFORMATION AND EVALUATION ITEMS OBTAINED THROUGH ANALYSIS AND CONTRIBUTION POINTS OF THE FUEL DEBRIS ANALYSIS (contd.) based on data from Ref. [96]))

| Analysis item | Examination/ Equipment (Items that are not required but can be expected to obtain detailed data are underlined.) | Information to be obtained | Evaluation items that use analysis values | Contribution points | | | | |
|---|---|---|---|---|---|---|---|---|
| | | | | Retrieval | Storage management | Processing and disposal | Core melting progress | Source term |
| Hardness and toughness | Vickers hardness tester<br>Micro Vickers hardness tester | Hardness | Toughness | + | + | | + | |
| Melting point | Melting point measurement device | Thermophysical properties (solidus and liquidus temperature) | Melting point | + | | | + | |

## 3.4. PROGRESS ON THE COMPARISON OF SIMULANTS WITH ACTUAL MATERIALS

Material science examination of actual samples from nuclear accidents is indispensable for understanding the progression of events and to develop countermeasures to mitigate future accidents. At the same time, laboratory experiments need to be designed to replicate the thermomechanical conditions experienced during the accidents to provide a consistent explanation of observed features. Numerous experiments on different scales have been performed to understand LOCA and RIA, respectively and subsequent interaction of corium with construction materials (such as MCCI). In the following sections a comparison of some of the features observed in actual samples from ChNPP and experimental investigations is provided along with some results from the experiments performed during the CRP in preparing 1F simulants.

### 3.4.1. Simulated Chornobyl corium and lava

In this section some of the features observed in real samples from ChNPP and those obtained through experimental investigations are compared.

#### *3.4.1.1. Conditions of formation of real hot particles and Chornobyl lava*

Temperatures during the reactivity transient in ChNPP Unit 4 could have reached several thousand Kelvin. Finding unambiguous temperature markers in real materials is a difficult task, but some estimates have been made.

Results obtained from experimental investigation of $^{90}Sr$ and $^{137}Cs$ loss from undamaged ChNPP fuel in the temperature range between 673 and 1173 K were used to estimate the temperature and duration of annealing experienced by fuel ejected as hot particles during the reactor explosion (i.e. those collected in the western plume) [61, 62]. Depending on the exact model used, the average temperature experienced by large fuel hot particles is between 2400–2630 K. However, the maximum inferred temperatures are in the region of 4200 K. These values are comparable with those reported in some experimental RIA transients [102]. Temperatures above 3138 K should lead to (partial) melting of $UO_2$. Hints for such behaviour could be found in ChNPP fuel particles, see for example Fig. 2b from [103]. As expected, these particles are deficient in $^{125}Sb$ and Cs isotopes.

Examination of some fuel particles showed elongated pores [46, 103], which are apparently like microstructures found in fuel with moderate burnup that has experienced a temperature ramp. The concentration of Cs isotopes in such particles vary, most likely reflecting differences in the location of the given fuel pellet within the reactor core and, consequently, in the duration of the transient.

Detailed microstructural examination of complex hot particles [46] revealed features corresponding to the decay of Zr–U–O solid solution (Fig. 64), leading to formation of oriented lamellae closely resembling samples from CORA–13 and CORA–16 experiments at JRC Karlsruhe. Such features were observed only in those parts where complete melting of fuel and Zircaloy or very extensive Zircaloy oxidation had occurred. For the CORA–13 experiment temperatures at the corresponding elevations were 2123 K during the transient and up to 2473 K during the quench. Presumably, the heating rate in ChNPP accident was much higher than the experimental 1 K/s, suggesting that during the accident the peak temperatures were significantly higher. Temperatures of at least 2673 K were also inferred from investigation of another complex U–Zr–O particle [41].

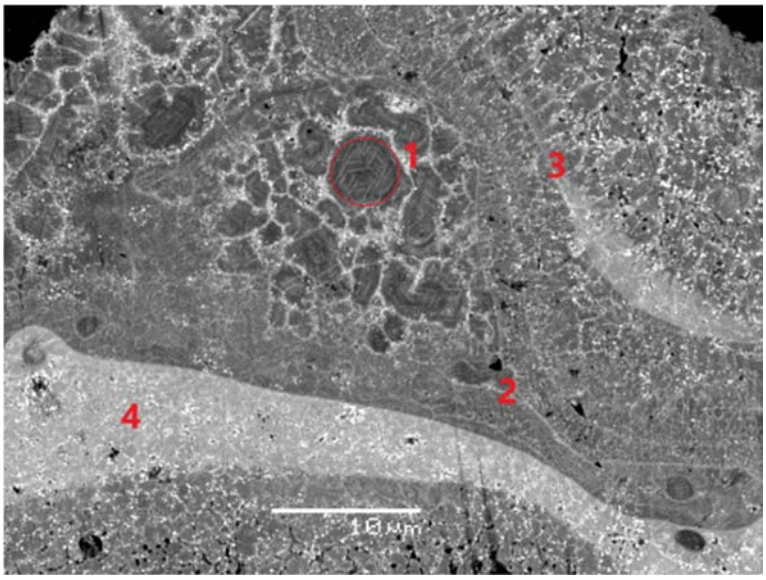


*FIG. 64. Features corresponding to decay of supersaturated Zr–U–O solid solution in a hot particle from ChNPP, described in detail in Ref. [46] (courtesy of B.E. Burakov, Ioffe Institute).*

1. *Domain with oriented lamellae produced by decomposition of Zr–U–O solid solution see text for detail.*
2. *A pore.*
3. *Region with columnar structures suggesting crystallization in a temperature gradient.*
4. *A U rich intrusion. Numerous tiny white dots – precipitates of U rich phase, presumably $UO_{2+x}$.*

It is very likely that the temperature in room No. 305/2, the lava source, was non–uniform and varied in rather wide range as a function of proximity to pieces of fuel, its burnup degree and other factors. Nevertheless, some estimates of the ChNPP lava temperature can be made. The simplest evaluation is based on the presence of numerous steel droplets in lava matrix, indicating a minimum temperature consistent with the melting point of the steel, i.e., ~1723 K. Temperature in room No. 304/3 adjacent to the inferred lava source (room No. 305/2) is estimated to have been at least 1773 K from concentration of $^{125}Sb$ on its walls [104]. Semi-quantitative measurements of composition of pyroxene dendrites formed by quenching of brown lava suggest that the initial temperature of the parent melt exceeded 1823 K [38]. At the same time, formation of rather numerous U rich zircon crystals (Chornobylite) [105] indicates that zircon decomposition temperature of 1943 K was not reached. However, the zircon formation temperature remains debatable and values as low as 1523 K have been given [106]. Zircon normally forms from $ZrO_2$ and $SiO_2$ between 1573 and 1873 K and the rate of the synthesis increases rapidly between 1698 and 1808 K. An increase of zircon nucleation rate around 1473 K is probably due to the Hedvall effect, i.e., an increase in the nucleation rate related to phase or polymorphic transformation in the substrate. A zircon displacive phase transition occurs between 1123 and 1423 K and this effect can be responsible for changes in kinetics and rates of zircon formation in the lava (see Ref. [38] for details).

Once more, it is important to stress that the local U content of the molten material could vary considerably and thus the temperature field might have been very heterogeneous; the values given above reflect observations made for several abundant phases and might reflect different stages of the lava evolution.

According to experimental observations, the lava solidifies between 1073 and 1123 K [107], thus giving the lowest limit of the phase formation. Although the appearing of secondary phases on some of the lava formations is well known to occur both in the sarcophagus and under laboratory conditions, it is unlikely that phases trapped in the lava matrix underwent transformations. For example, all studied inclusions of urania are always very close to stoichiometric $UO_2$ [38, 40]. The only potentially

important alteration is spontaneous, or moisture induced polymorph transition of U containing zirconia inclusions, which might lead to mechanical destruction of the lava accumulations [38, 40].

*3.4.1.2. Synthesis of lava analogues*

Several studies have attempted to synthesise analogues of ChNPP lava. Synthesis of lava simulants using a wide range of starting materials, oxidizing and inert atmospheres and a broad temperature range is reported in Refs [108, 109]. These studies reproduced many important textural and morphological features of real lava, but the absence of chemical analyses makes detailed comparison problematic.

A close analogue of Chornobyl lava, reproducing several important features such as the presence of U rich zircon (Chornobylite), was synthesized by Barlow et al. [110]. In this study, prolonged synthesis at rather high temperatures (4 h at 1773 K and 72 h at 993 K) in reducing atmosphere was employed. While it is tempting to suggest that Chornobylite formation requires a long synthesis time, the duration presumably reflects the need to achieve the required supersaturation. On the other hand, Chornobylite has also been obtained in common MCCI experiments where this phase was found in a thin layer roughly in the centre of a lava flow [111]. Cooling of the melt in experiments described in Ref. [111] were relatively fast (minutes), implying that U rich zircon might be obtained over shorter timeframes.

Most published works on MCCI and Chornobyl simulants with actual lava present discrepancies in the selection of the starting materials. In most experiments, a mixture of pure starting Zr and U oxides are used, whereas in actual lava the principal sources of U and Zr are usually a mixed (U, Zr) oxide, sometimes with Fe admixture. During the CRP, an attempt to mimic the multistep approach for lava formation was made. At first, an actual fuel pellet was placed into an Zr + 1%Nb (E110) tube and heated up to 2223 K in a vacuum. The resulting material represents an irregular black lump shown in Fig. 65. The specimen was cut into half and polished, allowing the changes in structure and contact zone between the cladding and fuel to be examined. Characterized by a very complex structure at the $\mu$m scale. Corresponding SEM images are shown in Fig. 66.

*FIG. 65. Result of interaction of a fuel pellet placed in Zr + 1%Nb (E110) tube and heated at 2173 K for 10 min in vacuum, optical photograph taken on top of a 1 mm grid paper (courtesy of B.E. Burakov, Ioffe Institute).*

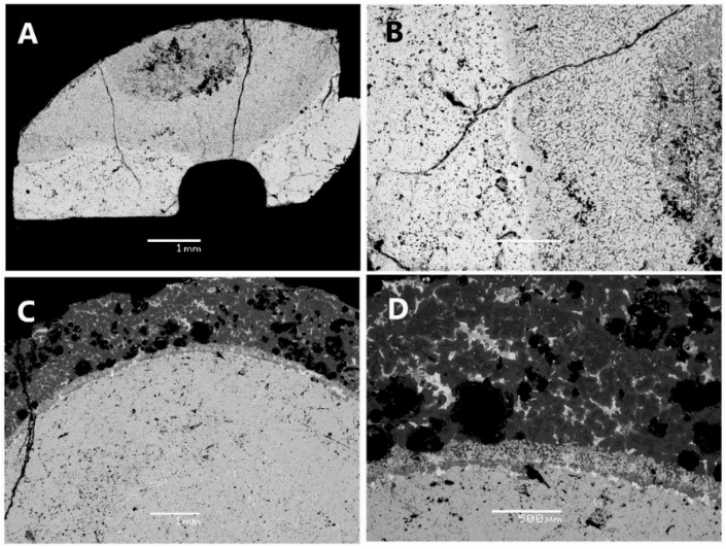


*FIG. 66. SEM images of fuel products – cladding interaction at various scales. (courtesy of A. A. Shiryaev, A.N. Frumkin Institute of Physical Chemistry and Electrochemistry).*
*Notes:*
*A, B – Piece of a $UO_2$ fuel pellet after the interaction at different magnifications. Bottom – central part of the pellet with a central hole typical for Russian fuel; upper part was in contact with the cladding. Variations of composition (roughly fraction of in diffused Zr) are apparent from changes in intensity of grey hue. Reasons for the very heterogeneous pattern of the diffusion front are not yet fully understood. Dendrites in B are reflected quench products. C, D – a different cross-section at different magnifications. Dark grey layer in the upper part corresponds to cladding, bottom to fuel pellet. Extensive porosity in the cladding (black holes) and manifestations of mutual diffusion are seen.*

The other half of the specimen was reacted with a mixture of K–Al–Si oxides and melted at 1673 K for 5 h in air. Samples mimicking black and brown ChNPP lava were obtained and subject to detailed examination (Figs. 67 and 68).

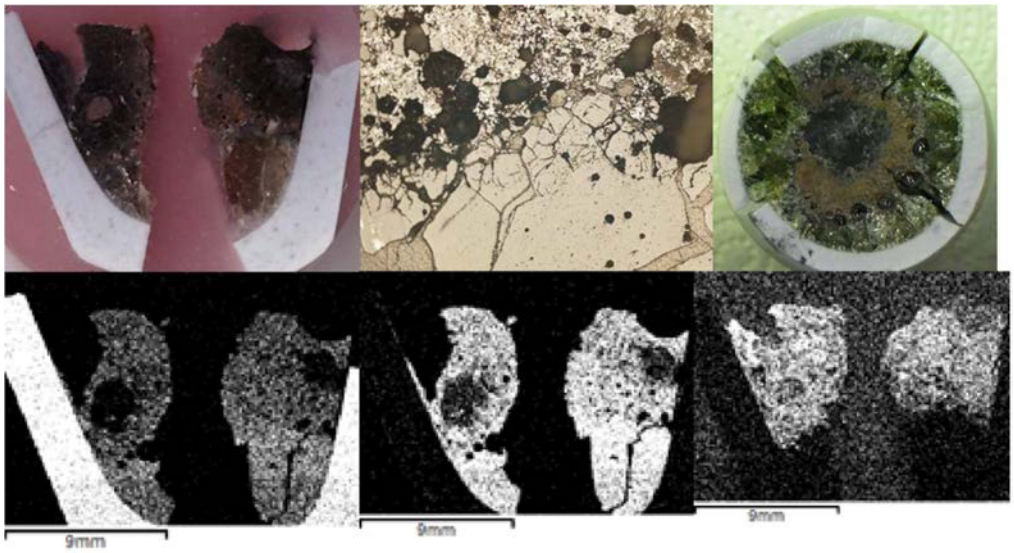


*FIG. 67. Samples obtained by reaction between the fuel and E110 product with K–Al–Si oxide mixture. Upper row shows the optical photographs; bottom row shows the μ-XRF maps of (from left to right) Al, Si, and U distributions (courtesy of B.E. Burakov, Ioffe Institute).*

*FIG. 68. $ZrO_2$-based dendrites and spheres in the molten sample (courtesy of A. A. Shiryaev, A.N. Frumkin Institute of Physical Chemistry, and Electrochemistry).*

### 3.4.2. Fukushima Daiichi fuel debris simulant

In this section the efforts into fabricating and analysing 1F simulants are reported.

#### *3.4.2.1. Fabrication of simulated fuel debris*

Fuel debris generated in a nuclear accident that involves a core melt is non-uniform and has a variety of characteristics that depend upon the accident conditions. The most typical fuel debris at high temperatures is molten oxide (U, Zr)$O_2$ of uranium and zirconium. In addition, metallic debris might have been generated under 1F accident conditions. Several experimental methods have been investigated to synthesize simulated fuel debris in the laboratory. Fabrication methods included:

(a) Sintering method

Sintering is used in the fabrication of oxide fuel pellets. Powdered material components (such as $UO_2$, Zr, $ZrO_2$, etc.) are mixed and moulded into pellets. The pellets are sintered in an electric furnace at about 1973 to 2073 K, to produce simulated fuel debris (Fig. 69). $UO_2$ is eutectic with $ZrO_2$ to form a melt of (U, Zr)$O_2$. Using this method, various fuel debris can be easily fabricated through changing the atmosphere and components.

Features:

- Same as fuel pellet fabrication;
- Mixing, crushing, pelletizing, sintering (Ar, ~2000 K);
- Additive: $Gd_2O_3$, $Fe_2O_3$, Ca;
- Oxygen potential control.

*FIG. 69. Sintering heater unit (left), manufactured pellet with $UO_2$, $ZrO_2$ mixture (right) (reproduced from Ref. [112] with permission courtesy of International Research Institute for Nuclear Decommissioning (IRID)).*

(b) Arc melting method

In the arc melting method, an arc is formed between an electrode and the sample material, the material is heated by electron impact. The sample is melted at high temperature (>2000 273 K) in a short time. However, it needs inert gas atmosphere such as vacuum or Ar, and conductive materials for the material to melt. The sample can be completely melted and mixed with each component in this method (Fig. 70).

Features:

- Entirely uniform heating;
- Required metal rich conditions;
- Simulates core debris, MCCI products;
- ~ 5 g / sample.

*FIG. 70. Arc melting device (left), and sim-fuel debris pellet melted by arc melting (right) (reproduced from ref. [112] with permission courtesy of IRID).*

(c) Heating by light collection method

During the condensed light heating method, the light of halogen heater is focused at one point by a condensing mirror and can heat the object in a short time (Fig. 71). By this method, not only metals but composite materials such as oxides can be melted.

Features:

- Concentrating light as a heat source;
- Erosion under thermal gradient conditions;
- Various atmospheres;
- Small scale MCCI, melting of (U, Zr)$O_2$.

*FIG. 71. Light collection heater device (left), and sim-debris pellet on concreate melted by Light collection method (right) (reproduced from Ref. [112] with permission courtesy of IRID).*

*3.4.2.2. Experimental study of simulated fuel debris*

(a) Reaction with Sea Water

The effect of sea salt on fuel debris was examined at high temperature using simulated debris and salt. In the experiment, pelletized $(U_{0.4}Zr_{0.6})O_2$ simulated debris was heated from 1088 to 1471 K under Ar or flowing air.

(i) Reactions under flowing air

Figure 72 shows SEM and X ray mapping images of cross-sections of simulated fuel debris pellet after heating with salt at 1275 K under a high oxygen partial pressure (air flow) for 12 h. After the heating treatment, U(IV) uranates are formed on the surface of the pellet, resulting in a colour change to orange. According to the X ray analysis, thickness of the layer of (Na, Ca) uranate is about 50 $\mu$m on the surface of the $(U_{0.4}Zr_{0.6})O_2$ pellet. The ratio of U/Zr on the surface of pellet is lower than the initial ratio of 40/60, it suggests that uranium might have dissolved from the surface of the uranium pellet to form U(IV) uranates.

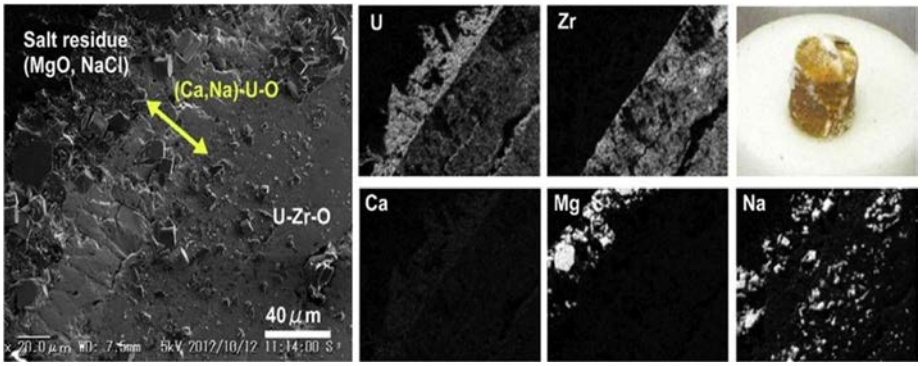


*FIG. 72. SEM and X ray mapping images of the polished cross section of $(U_{0.4}Zr_{0.6})O_2$ pellet heat treated with salt at 1275 K for 12 h under flowing air, together with the specimen appearance (reproduced from Ref. [113] with permission courtesy Elsevier B.V.).*

(ii) Reactions under flowing argon

Figure 73 shows SEM and X ray mapping images of a sample heat treated with salt at 1275 K under Ar flow. The (Na, Ca) uranium layer was not detected on the pellet surface, but MgO was attached to the surface. In the SEM image in Fig. 73 (a) calcium is present along cracks, pores and grain boundaries in the pellet surface. In the SEM image in Fig. 73 (b) fine chips (several μm) consisting of Ca–U–O were scattered in the MgO layer. The Ca/ (Ca + U) fraction was 5–8 at.%. Based on these results, simulated fuel debris forms a layer of calcium and sodium uranate on the surface at around 1170 to 1280 K under high oxygen partial pressure. The main component of simulated debris is orthorhombic (U, Zr)$O_2$, which coexists with $U_3O_8$ and/or Zr-rich monoclinic (U, Zr)$O_2$. Therefore, the effect of sea salt on fuel debris is assumed to be limited to the surface.

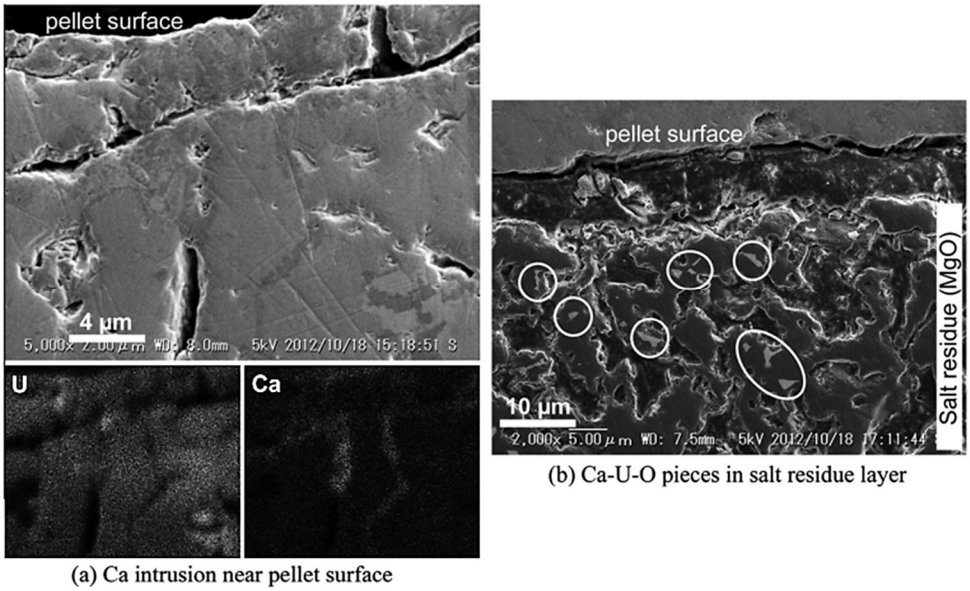


(a) Ca intrusion near pellet surface

(b) Ca-U-O pieces in salt residue layer

*FIG. 73. SEM and X ray mapping images of the polished cross section of $(U_{0.4}Zr_{0.6})O_2$ pellet heat treated with salt at 1275 K for 12 h under flowing Ar (reproduced from Ref. [113] with permission courtesy Elsevier B.V.).*

(b) Reaction with control rod material

The neutron absorber material in 1F was $B_4C$, which differs from Ag–In–Cd alloy used at TMI-2 and in PWRs. The associated material differences have the potential to directly influence the fuel degradation process and the resulting metallic phases in the solidified core melt. The presence of boron in fuel debris is important for criticality control during fuel debris retrieval, but also the chemical reaction between boron and other generated compositions should be considered. In previous examinations, the high temperature reaction between metal structural material and $B_4C$ might have formed hard boride ($(Fe, Cr)_2B$, $ZrB_2$, etc.). This was simulated by mixing powders of (U, Zr)$O_2$ and $B_4C$, stainless steel, and zirconium and arc melting them in an Ar atmosphere, SEM and X ray mapping cross-sections of the resultant are shown in Fig. 74. Figure 75 shows the results of microhardness testing of (U, Zr)$O_2$ dioxides, alloys, and borides. The hardest component is the boride phase such as $ZrB_2$, then the oxide phase of (U, Zr)$O_2$, and the softest phase is the metal phase. Precipitation of these boride phases can be a potential barrier, especially for mechanical cutting or core boring, when considering mechanical treatments to remove solidified core melts.

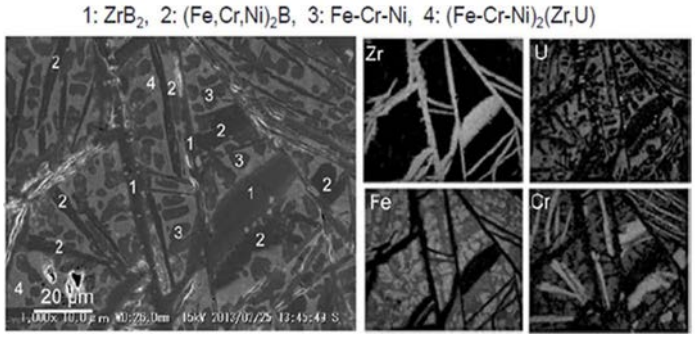


*FIG. 74. SEM and X ray mapping images of the metallic part in arc-melted sample ($B_4C$/SS/Zr/(U, Zr)$O_2$). Phases marked with numbers correspond to $ZrB_2$ (1), $(Fe_{0.56}Cr_{0.42}Ni_{0.02})_2B$ (2), 80Fe–9Cr–11Ni (3), and 65Fe–3Cr–15Ni–4Zr–13U (4) (reproduced from Ref. [114] with permisssion courtesy of Taylor & Francis Group).*

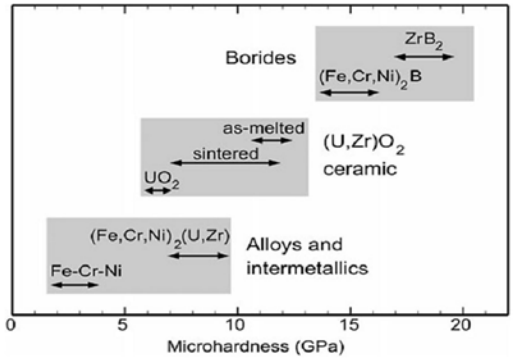


*FIG. 75. Schematic diagram of the measured microhardness ranges for the oxide ceramic, alloys, and borides (reproduced from Ref. [114] with permission courtesy of Taylor & Francis Group).*

(c) Generation of metallic debris

According to the latest accident progression analysis, for Units 2 and 3, the RPV might have been damaged after the core material collapsed to the lower plenum before the core temperature reached the melting point at which the fuel components completely melted. As the temperature of the deposits was increasing, core components with relatively low melting temperatures (Fe, $B_4C$, a mixture of such Zr) melted and might have flowed out of the RPV (Unit 2). When the temperature rose further, oxide components such as fuel would have also melted and might have flowed out of the RPV in a semi–molten state over several hours (Unit 3). Therefore, metallic debris mostly composed of metal components is predicted to have been deposited on the bottom of the PCV (Unit 2), an internal survey of Unit 2 PCV has found deposits with a similar appearance.

Similarly, the internal investigation of Unit 3 helped confirm the assumption made that a deposit had moved over several hours in a semi-molten state. It is very likely that metallic debris will have also formed inside the PCV. Possible metallic debris includes alloys of stainless steel components and Zr, and borides such as $Fe_2B$ and $ZrB_2$.

JAEA Collaborative Laboratories for Advanced Decommissioning Science (CLADS) conducted a high temperature degradation test (CLADS-MADE-01) using a unique large scale equipment for investigation of severe accidents in nuclear reactors (LEISAN) facility (Fig. 76). The purpose of this test was to confirm the degradation behaviour of a BWR FA (Fig. 77) with control blade under Unit 2 accident conditions; i.e., pre–oxidation, transient heating, isothermal heating under steam starvation, and finally cooling.

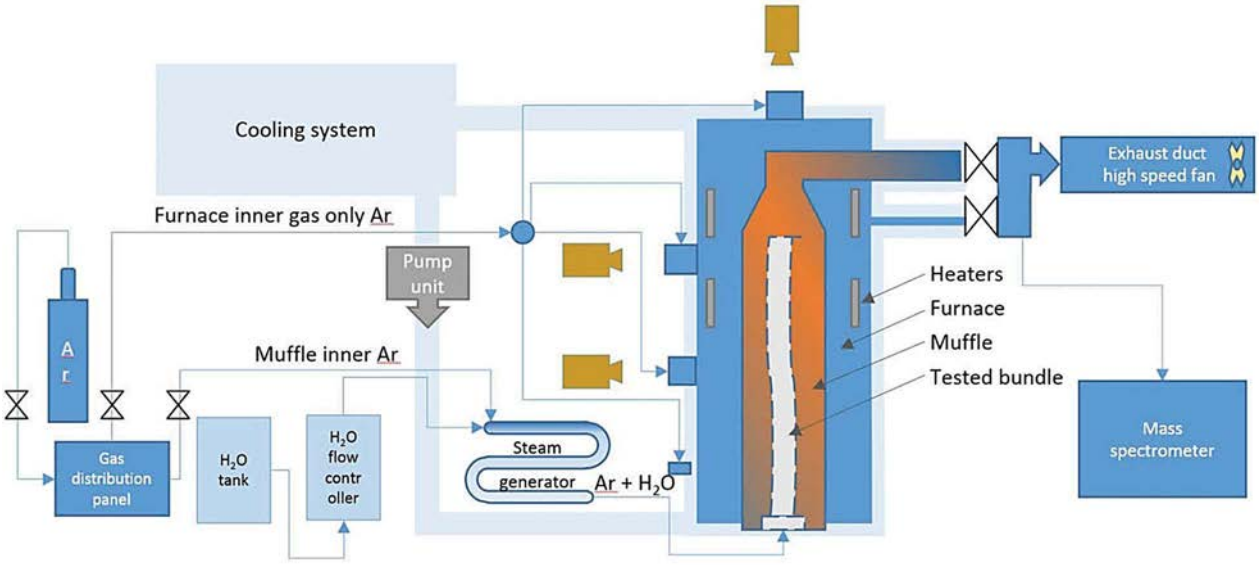


*FIG. 76. Flow diagram of the LEISAN facility (reproduced from Ref. [115] with permission courtesy of Taylor & Francis Group).*

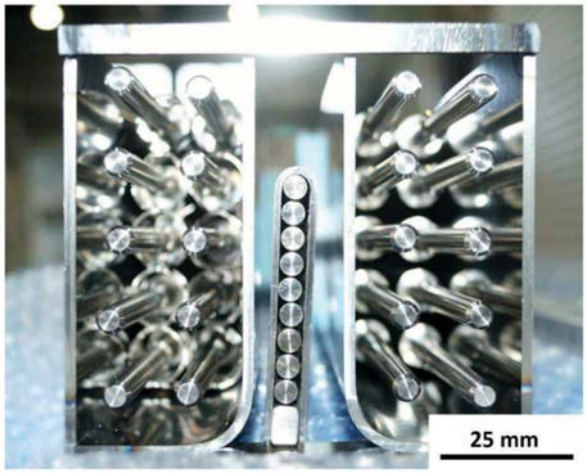


*FIG. 77. Part of simulated fuel assembly (top view), simulated control rod (centre) and simulated fuel pins (left and right) (reproduced from Ref. [115] with permission courtesy of Taylor & Francis Group).*

In Figs 78 and 79 the appearance of the post-test assembly of test components (control rod and FA) simulating a part of the reactor core is shown from various viewpoints. The tests results showed that boron containing metallic melt (approximately 5 wt%) was formed during the initial stage of the core degradation (Fig. 80). However, a significant part of the control blade debris retained $B_4C$ and prevented its oxidation in steam by the mechanism shown in Fig. 81. This debris might be a source of $B_4C$ in the damaged RPV if it moves downwards. If it is stuck in the core, it will be oxidized anyway and, in this case, become a source of boric acid aerosols.

The current most accurate assessment for Unit 2 shows the pedestal is rich in metallic debris. Where fuel debris contains a large amount of metal components, mechanical tools such as core boring used as a fuel debris retrieval tool in TMI–2 will not be suitable, water abrasive jets and thermal cutting might be more effective. For designing and selecting the debris retrieval tools, the potential generation of radioactive fine particles needs to be considered.

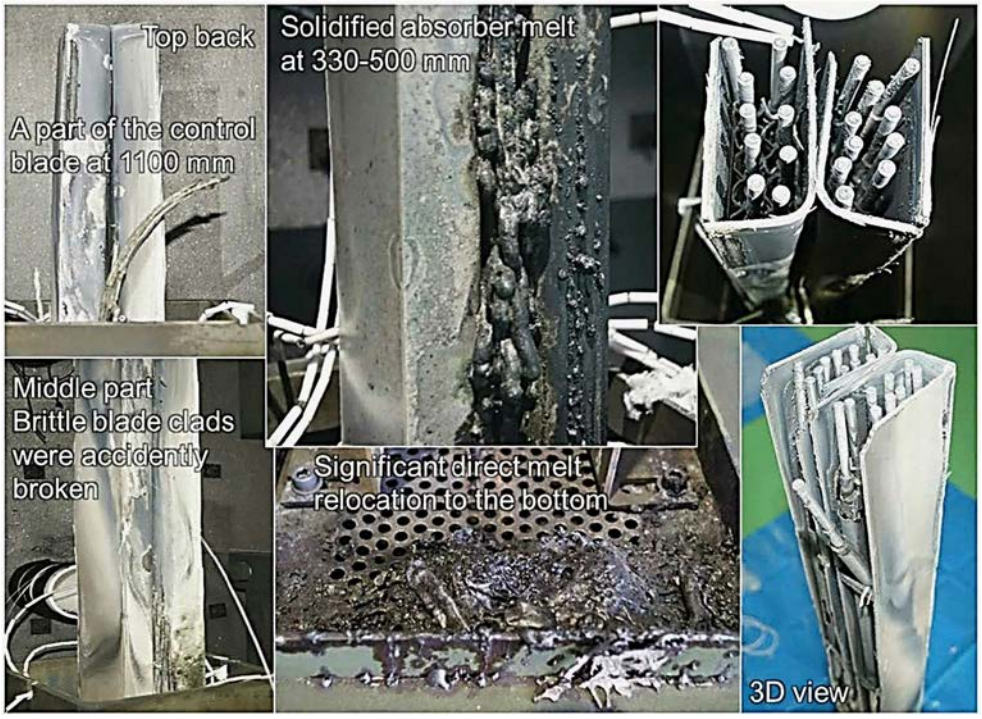


*FIG. 78. Appearance of the post-test assembly of CLADS-MADE-01 test (reproduced from Ref. [115] with permission courtesy of Taylor & Francis Group).*

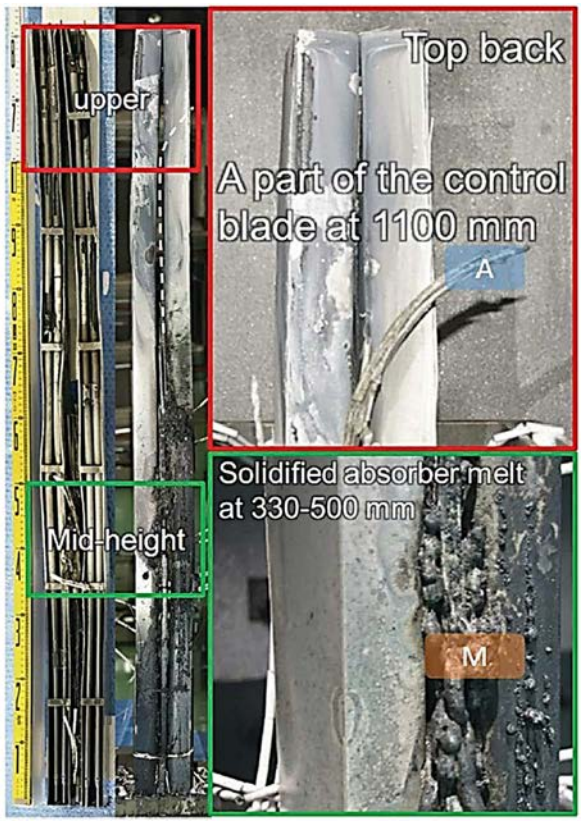


*FIG. 79. Sampling areas for SEM and XRD; A – upper part of the degraded control blade, M – candled material from the blockage area (reproduced from Ref. [115] with permission courtesy of Taylor & Francis Group).*

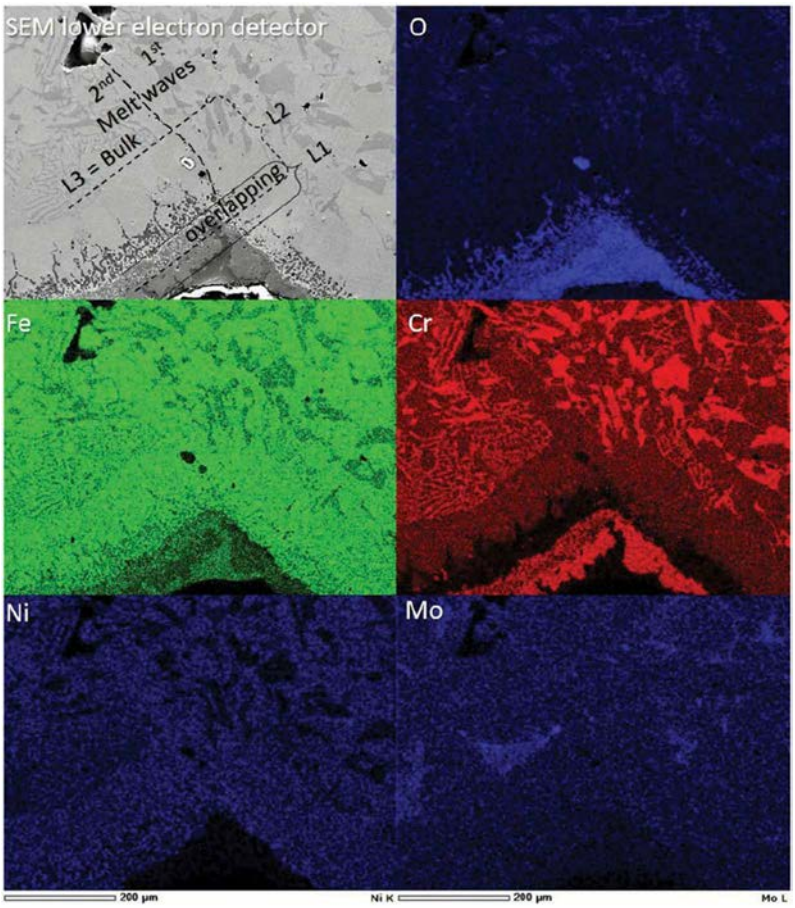


*FIG. 80. SEM image of zone M (Blockage melt area $T_{max}$ = 1515 K) with EDS mapping showing the distribution of Fe, Cr, Ni, Mo, and O (reproduced from Ref. [115] with permission courtesy of Taylor & Francis Group).*

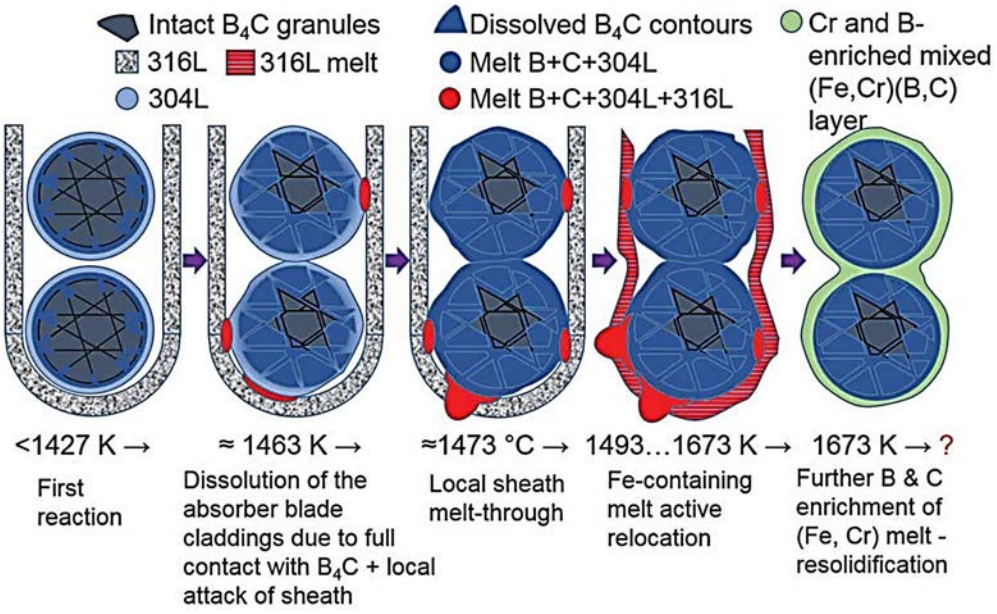


*FIG. 81. Mechanism of control blade degradation at an early phase of nuclear accident under steam-starved conditions (reproduced from Ref. [115] with permission courtesy of Taylor & Francis Group).*

(d) MCCI

In the frame of a JAEA–CEA cooperation under a research programme entrusted to IRID, a MCCI test named VF–U1 on VULCANO was performed using a prototypic metal and oxide corium (58.8% $UO_2$, 16.2% $ZrO_2$, 11.8% Zr, 13.2% stainless steel) representative of 1F Unit 1 conditions. The VF−U1 was carried out on 19 January 2017. The concrete test section (Fig. 82), made with Japanese components, was siliceous of basaltic origin. About 40 kg of a metal and oxide corium pool was made by inductive heating.

The VF–U1 test is the first experiment using a 2D axisymmetric geometry and direct melting of corium using a more powerful inductive heating system compared to previous tests.

The main objective of the test was to get a significant melt leading to a melt volume ratio of 1.6. A ratio of 1.68 was obtained to produce fuel debris with a composition corresponding to expected conditions in the damaged plant (Table 17). Therefore, the corium produced is well representative. Conclusions arising from the material analysis of the selected samples will be relevant for future dismantling operations. A bank of 1F prototypic MCCI debris is thus available for R&D issues linked to future 1F fuel debris retrieval. Figure 83 shows the MCCI products in the concrete test section after the VF-U1 test.

From a phenomenological point of view, it is to be noted that the concrete melt was clearly anisotropic with a predominant melting downwards unlike in previous experiments with silica and limestone concrete. Experiments in large scale experimental facility on MCCI with basaltic concrete also presented a different melt pattern than with other types of concrete.

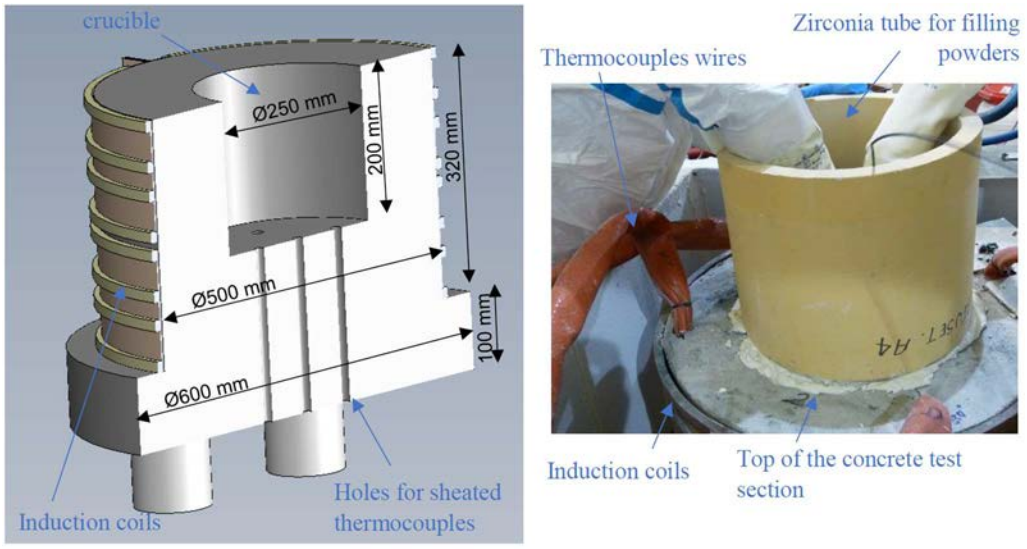


*FIG. 82. Sketch of VF-U1 concrete test section (left). Picture of the top of the test section (right) (reproduced from Ref. [116] with permission courtesy of Bouyer, V., et al.).*

TABLE 17. INITIAL CORIUM AND CONCRETE COMPOSITION OF VF-U1 TEST (based on data from [116])

| Corium initial composition (kg) | | | | |
|---|---|---|---|---|
| Zr | CaO stabilized $ZrO_2$ | | $UO_2$ | steel |
| 5.5 | 7.5 | | 27.3 | 6.1 |
| Concrete initial composition (wt%) | | | | |
| $SiO_2$ | CaO | $Al_2O_3$ | $Fe_2O_3$ | $H_2O$ |
| 66.9 | 11.8 | 12.2 | 5.8 | 3.3 |

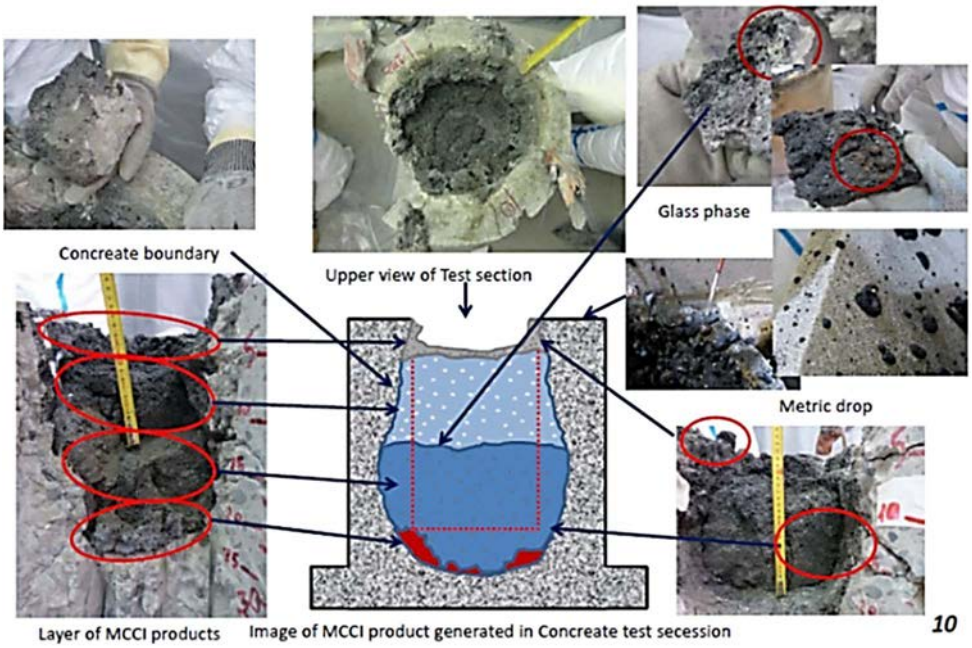


*FIG. 83. Outline of MCCI products in concrete test section of the large MCCI test (VF-U1) (adapted from [117], courtesy of JAEA).*

*3.4.2.3. Results of sample characterization*

Figure 84 shows the SEM micrographs of all samples. The micrographs were taken in BSE mode. In the SEM photographs, the light grey area contains heavy elements (U and Zr), the dark grey area contains light elements (Si etc.), and around the sample materials, the voids and resin are shown as black.

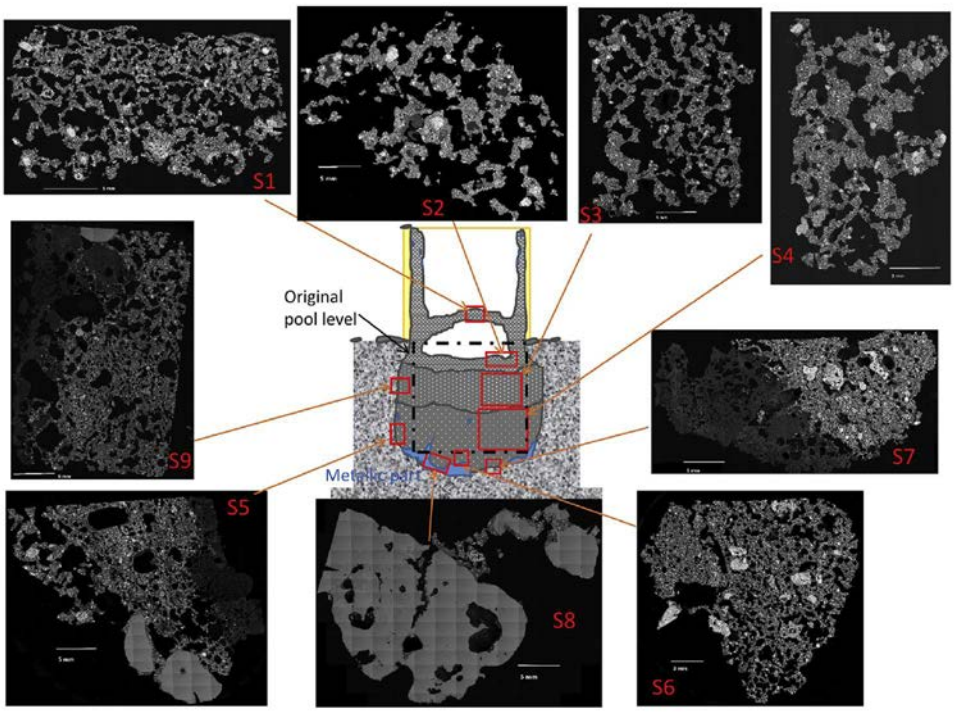


*FIG. 84. Location and SEM/BSE micrographs of the nine samples analysed for the VF-U1 tests [118] (courtesy of Brissonneau, L., et al.).*

(a) Corium core sample (S4)

Figure 85 (a) shows the EDS elements mapping for sample 4. This sample is very porous, and its pore diameter is hundreds of $\mu$m to mm. This sample consists of a matrix area (dark grey) containing fine nodules (light grey) but is divided into four areas due to structural characteristics: (i) Silicon rich region (including unmelted aggregates), green colour in EDS mapping; (ii) Zirconium rich region, light blue; (iii) Uranium rich region, lilac; (iv) Iron rich region, orange. The dark grey matrix is called the 'Concrete element rich matrix (CEM), and the light grey area is called the 'Corium element rich nodules (CRN). Figure 85 (b) shows the microstructure of a sample in two typical regions.

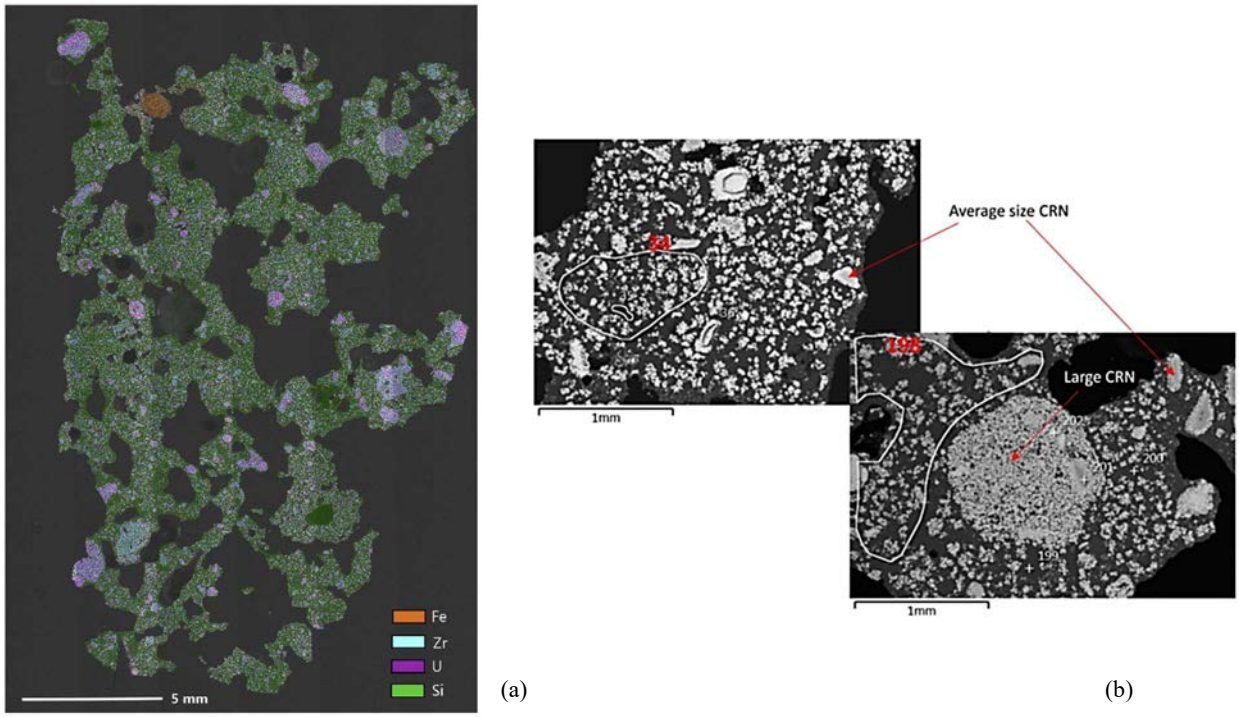


(a) (b)

*FIG. 85. (a) EDS elements mapping of sample S4. (b) Microstructure of matrix rich zone of sample S4 [118] (courtesy of Brissonneau, L., et al.).*

(b) Corium concrete interface sample (S9)

Figure 86 (a) shows an EDS elements mapping of a sample vertical interface with concrete. In the boundary between concrete (left) and corium (right), large pores (up to 5 mm) are observed. Such type of pores is found in other interface samples. On the right side of the picture, some small pores are seen in the corium area. The size of the smaller pores are tens of $\mu$m to a few mm. The U and Z are partially rich in the sample (pale blue or lilac), and a metal particle (orange) can be observed in the upper part of this mapping. Figure 86 (b) shows a microstructure of the corium area in the molten pool.

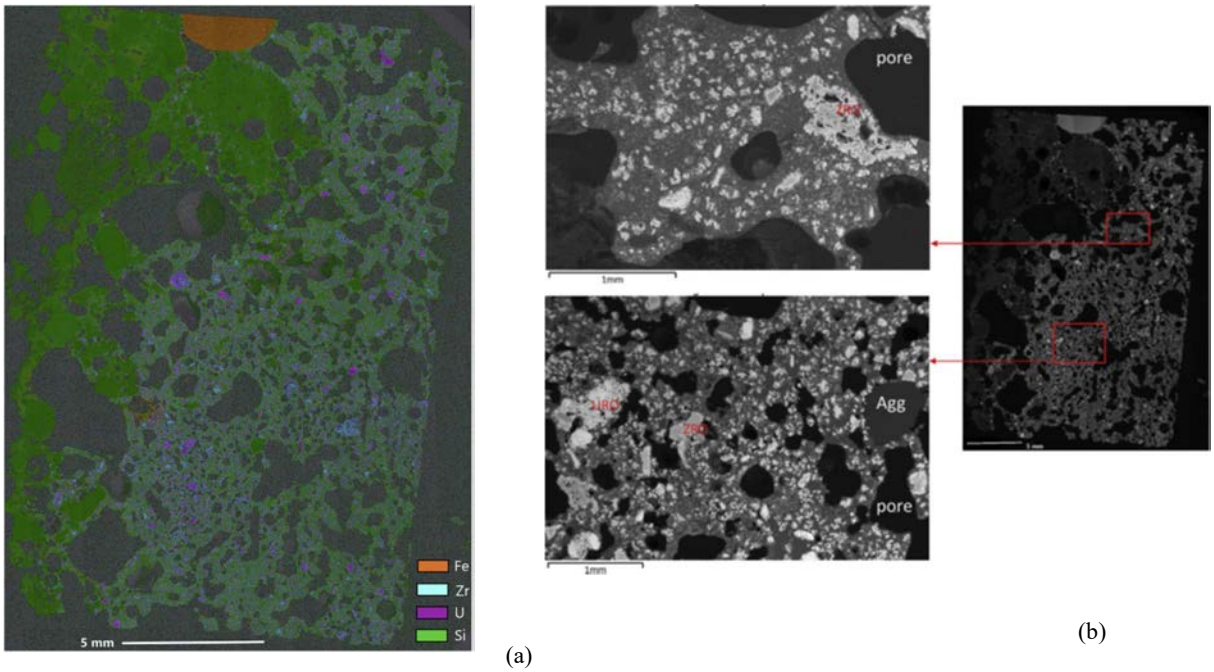


*FIG. 86. (a) EDS elemental mapping of sample S9. (b) Example of microstructures of the pool zone in sample S9 (SEM/BSE) [118] (courtesy of Brissonneau, L., et al.).*

(c) Metal horizontal interface sample (S8, S10)

An EDS elements mapping of the metallic sample at the horizontal interface area is shown in Fig. 87 (a). The main element in this sample is Fe, which has internal pores (a few mm). A microstructure of the metallic part is shown in Fig. 87 (b). The dominant elements in this metallic area are Fe and Ni. The Ni ratio of the area is low as 1/7 to 1/8.5 of Fe. The other miner elements are S, P, Al, Si, Cr and FeS phases, but the amounts are very small.

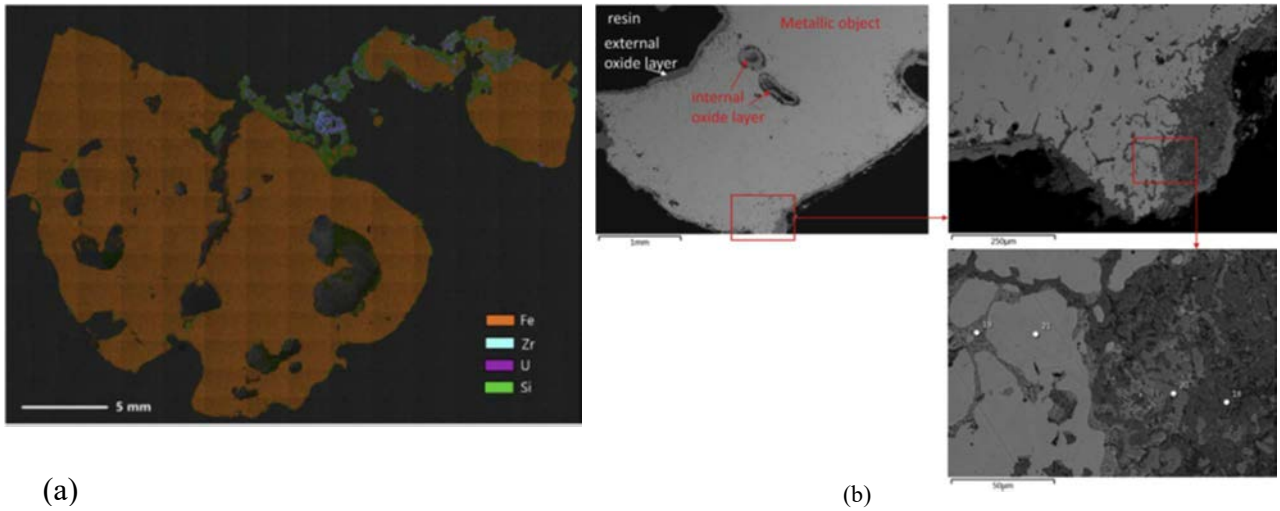


*FIG. 87. (a) EDS elemental mapping of sample S8. (b) Microstructure of the metal zone in sample S10 [118] (courtesy of Brissonneau, L., et al.).*

(d) Hardness

Vickers hardness (HV) was measured on the phases of each sample. The hardness depends on the phase location. Table 18 shows the measured hardness for each sample. The maximum values are obtained in the more uniform phase. The CRN phases were found to be is the hardest material and the metallic blocks the softest.

TABLE 18. AVERAGE AND MAXIMUM HARDNESS OF THE DIFFERENT PHASES IN SAMPLES S4, S8 AND S9 [118]

| Phase | Average hardness (HV) | Maximum hardness (HV) |
|---|---|---|
| CEM | 750 | 900 |
| Biphasic CRN | 1100 | 1250 |
| Zr rich CRN | 850–1350 | 1855 |
| U rich CRN | 1100 | 1600 |
| PP* | 1500 | 2250 |
| Metallic blocks | 290 | 330 |

*PP: Polyhedral Precipitates

### *3.4.2.4. Summary of research findings into simulating 1F MCCIs*

An MCCI test to simulate the 1F unit1 corium concrete interaction was carried out in the VULCANO facility.

Analysis of the simulants showed that most samples (except metallic phase) were very porous and mostly consisted of a matrix of Si, Ca, and Al in concrete. The majority of MCCI products were composed of uranium zirconium mixed oxide (uranium rich zirconium oxide (faced–centred cubic) and zirconium rich uranium oxide(tetragonal)). The samples were also found to contain a small amount of spinel and lamella, containing chromium and silicon. Scattered in the MCCI molten pool were metallic droplets of unmelted aggregate ($SiO_2$), and a small amount zirconium silicon lath.

The metallic phase located at the base/boundary between the corium pool and concrete, contained iron and nickel, and trace amounts of sulphur and phosphorus. In the MCCI, the concrete was eroded by the high temperature of the molten corium, upon cooling the depth of the corium penetration into the concrete phase was measured as <1 mm. The hardest phase in the samples is spinel (depending on the amount of chromium), CEM the main constituent of the samples was found to be the softest after the metal.

# 4. DEGRADED, SEVERELY DAMAGED AND FAILED SPENT FUEL MANAGEMENT

This section aims to share the experiences of managing a wide spectrum of non-intact and damaged spent fuel scenarios including:

- Pinhole puncture and cut pins due to planned PIE;
- Cladding cracks and broken pins during operations;
- Penetration of cladding due to in-pool corrosion during storage;
- Larger scale severe mechanical damage to pins and whole assemblies due to operational incidents.

These types of damage present a challenge for the handling, packaging, storage, and transportation arrangements for such fuel. The fuel might be leaking and require special containment, the structural integrity might be compromised and require bespoke solutions to lift and remediate the fuel for transport and storage or reprocessing. Transport might require specialist flasks to be deployed.

Aspects covered in detail in this chapter include:

- Characterization, treatment and repackaging of long stored (40 years) PIE fuel (arisings from prototype advanced gas cooled reactor (AGR) fuel) and associated corrosion product sludge;
- Assessment of potential hazards associated with uranium metal fuel corrosion (heat generation and hydrogen generation);
- Inspection techniques used in post-irradiation examination;
- Inspection techniques used for examination of damaged fuel in situ;
- Solutions developed to access damaged fuel for retrieval purposes;
- Segregation of fuel and non-fuel items;
- Fuel drying techniques to prepare fuel for sealing in canisters for storage, transport and reprocessing;
- Packaging of damaged fuel assemblies in various special containers for containment, transportation, storage (wet or dry), and reprocessing;
- Packaging of non-fuel items in waste containers;
- R&D / technology development required to achieve optimum results;
- Collaboration required to achieve optimum results.

## 4.1. MANAGEMENT OF DAMAGED FUEL AT CHORNOBYL NUCLEAR POWER PLANT

In Apr. 2016, ChNPP transferred all severely damaged spent fuel from Units 1 and 2 to the intermediate spent fuel storage No.1 facility (ISF–1); ISF–1 is a temporary wet spent fuel storage facility. A new dry spent fuel storage facility (ISF–2) was commissioned in 2020 and ChNPP has started transferring spent fuel from ISF–1 to ISF–2 for long-term storage (100 years). The damaged fuel is stored in ISF-1 and a separate project will be developed to facilitate the possibility of placing it in ISF-2.

### 4.1.1. Fuel assembly description

A description of RBMK–1000 FAs is given in Section 2.2.1 and a FA is shown in Fig. 8.

### 4.1.2. Severely damaged spent fuel at the Unit 1 and 2

Before transportation to the ISF-1, severely damaged spent fuel (SDSF) was stored at the AR storage pools of Unit 1 (32 FA) and 2 (20.5 FA) in special containers, denoted Type 1, 2, 3, 4 and 5 (Figs 88 and 89).

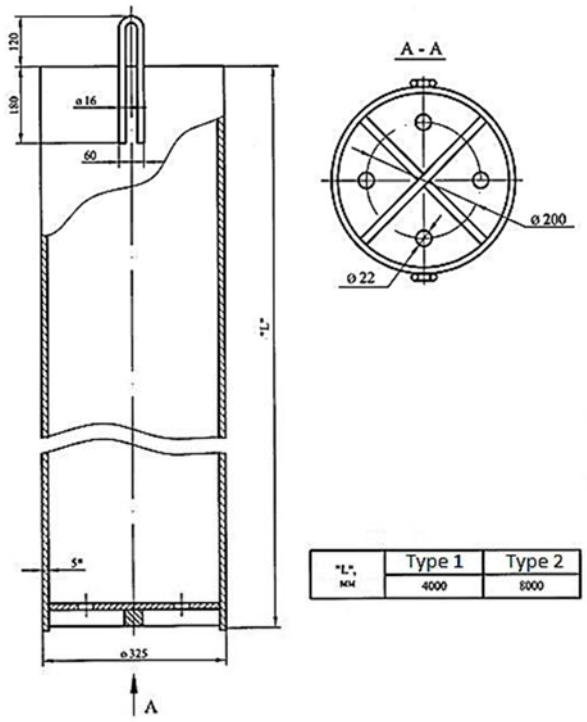


*FIG. 88. Special containers, Type 1 and 2 (courtesy of State Specialized Enterprise (SSE) ChNPP).*

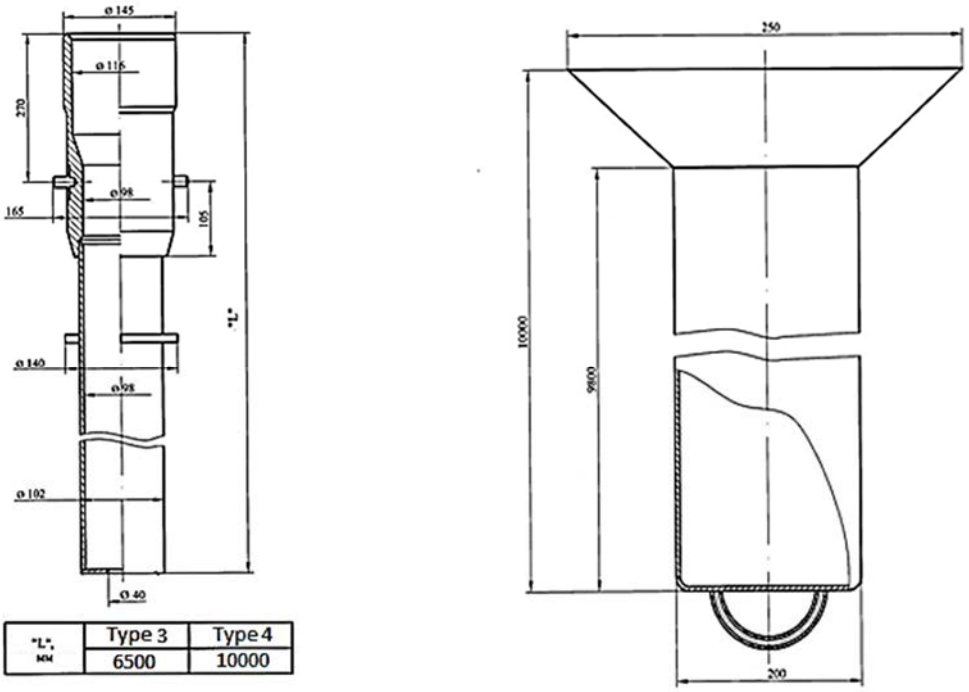


*FIG. 89. Special containers, Type 3, 4 and 5 (courtesy of SSE ChNPP).*

To gather more information about the SDSF, video inspection of it was performed using a handheld remote video inspection system. The results of the video inspection (Figs 90 and 91) showed that the main mechanical defects of the SDSF were:

- Deformation of the upper spacer grids of the FA or their absence;
- FA deformation (bending and kinks);
- Individual fuel rod deformation;
- Central rod damage (breakage and bending).

Video inspection also showed that in addition to fuel, the special containers contained graphite rings, ropes, and other non-fuel objects.

*FIG. 90. Results of video inspection on the Unit 1 SDSF (courtesy of SSE ChNPP).*

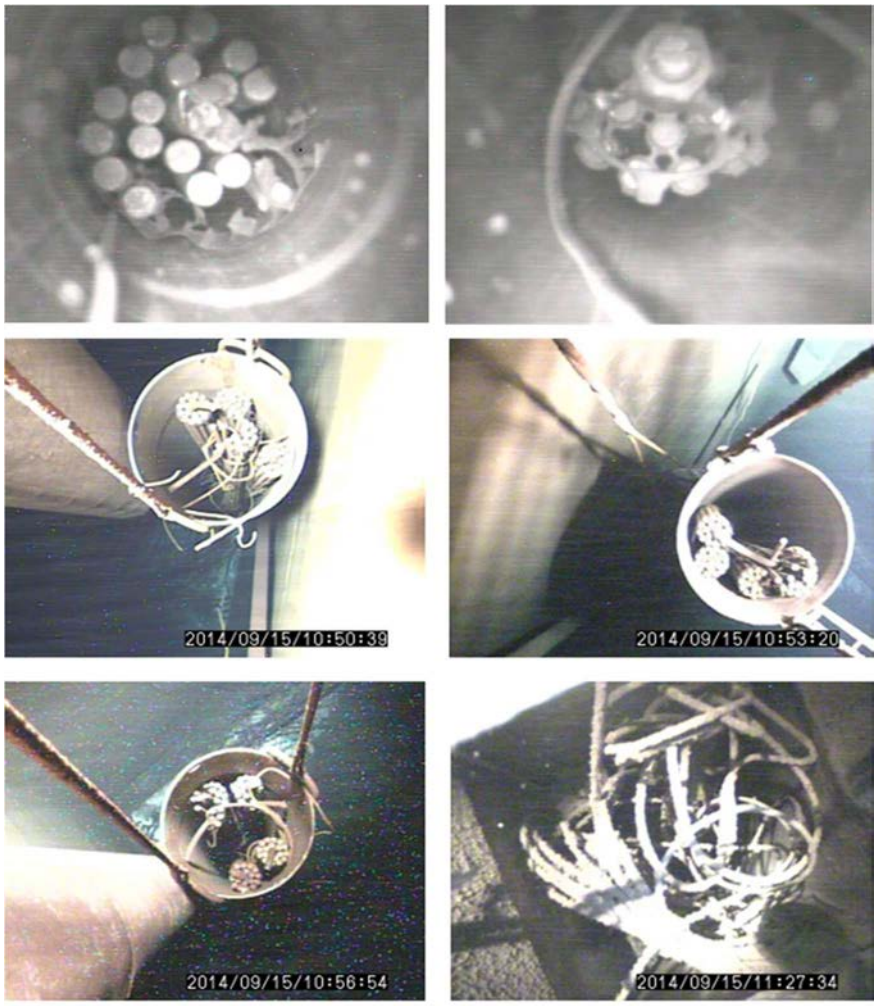


*FIG. 91. Results of video inspection on the Unit 2 SDSF (courtesy of SSE ChNPP).*

### 4.1.3. Transport and storage of severely damaged spent fuel at Chornobyl Nuclear Power Plant

For stabilization and transport of special containers from Units 1 and 2 to ISF–1, a universal special cask (USC) and special cask basket (SCB) were used. The USC and placement options for the special containers in the USC are shown in Figs 92 and 93.

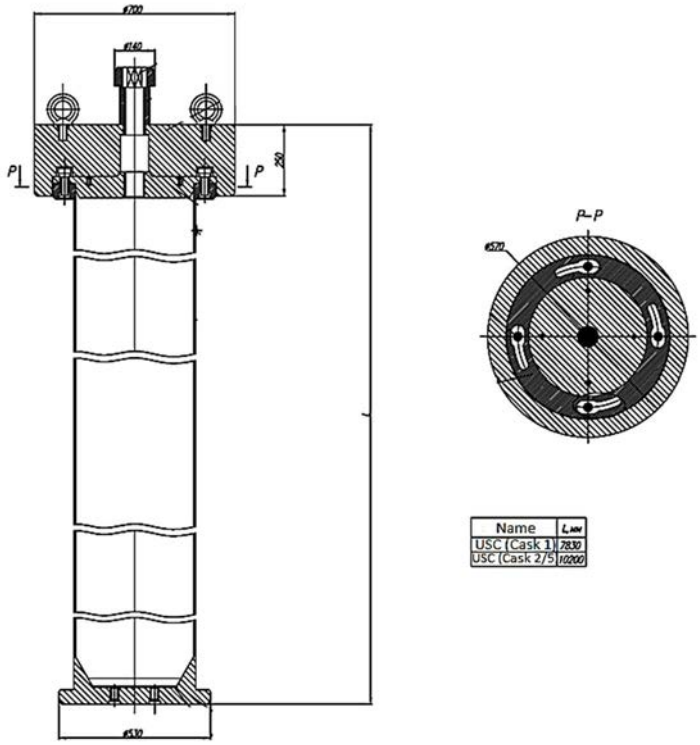


*FIG. 92. Universal special cask (courtesy of SSE ChNPP).*

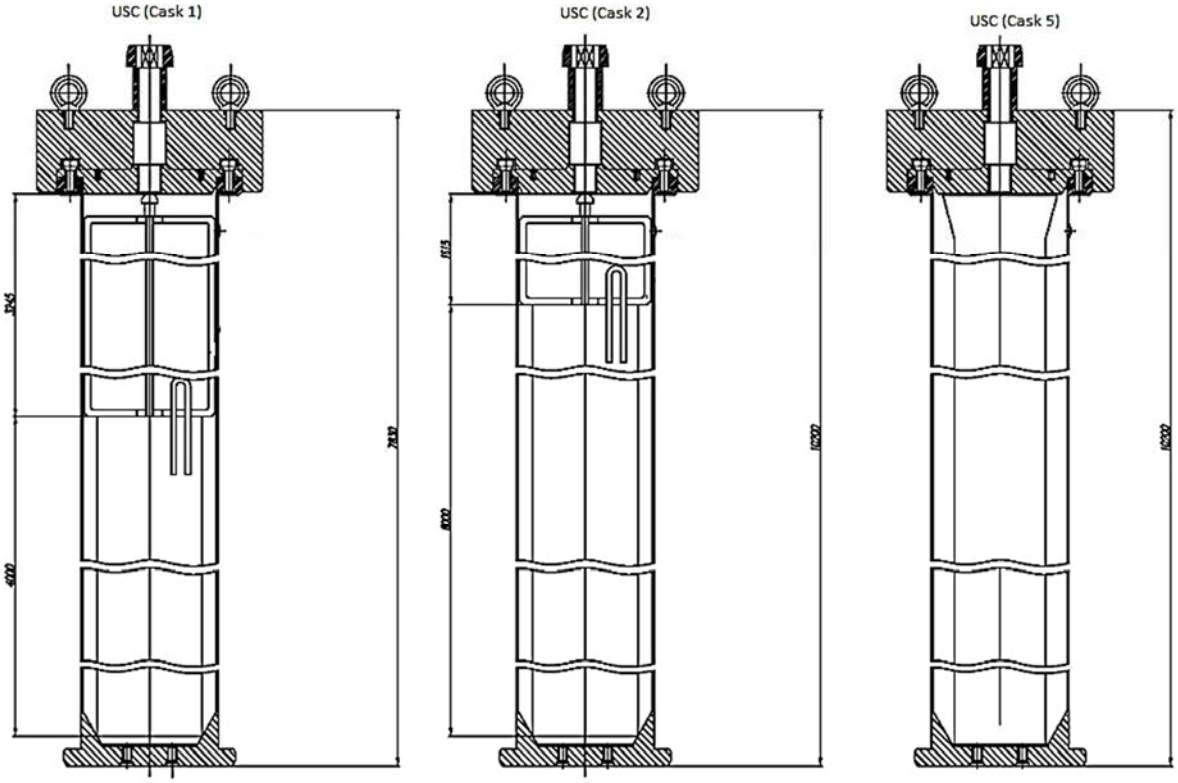


*FIG. 93. Placement options of the special containers in the USC (courtesy of SSE ChNPP).*

The special cask basket can accommodate up to four special containers (Fig. 94 (a)). Special container placement options in the SCB are shown in Fig. 94 (b).

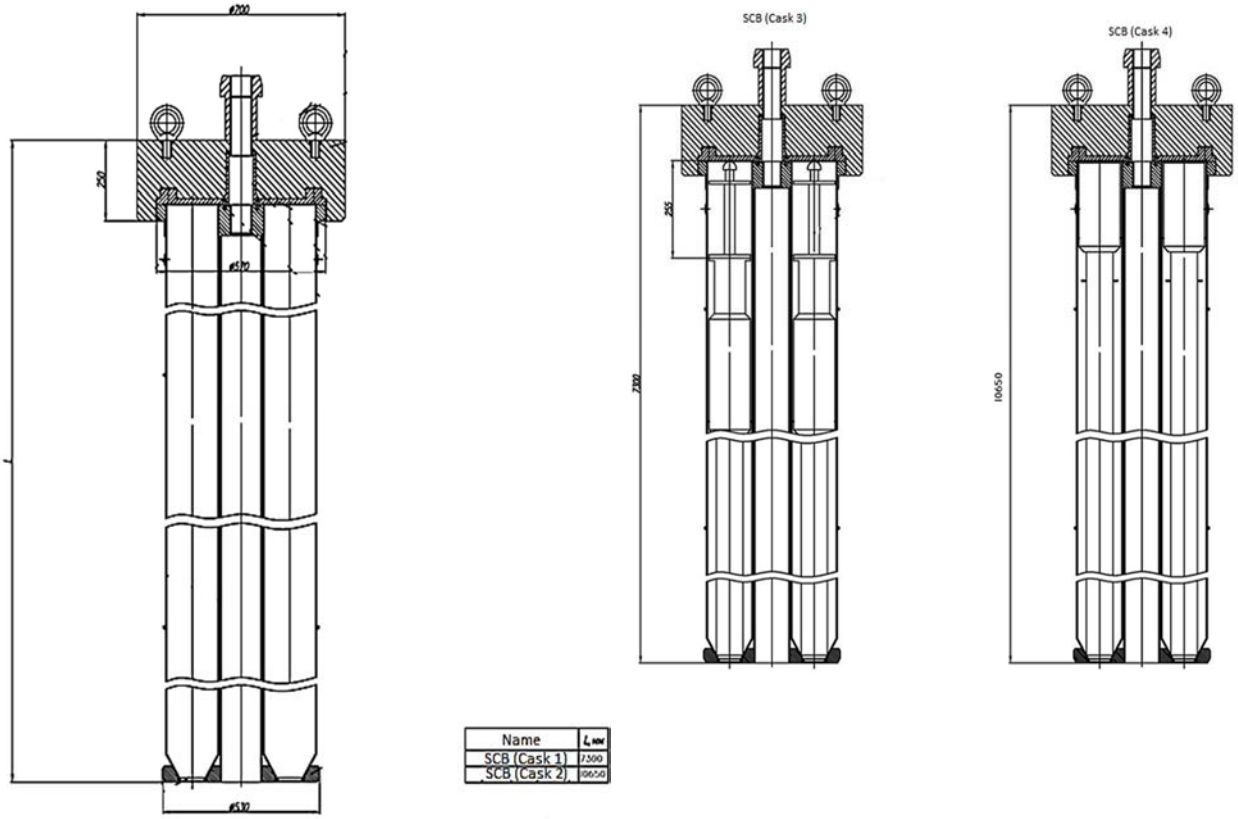


*FIG. 94. (a) Special cask basket. (b) Placement options of the special containers in the SCB (courtesy of SSE ChNPP).*

A railcar (Fig. 95) was used to transport either a USC or a SCB with SDSF in the internal transport package (Fig. 96) from Units 1 and 2 to ISF–1. There were two means of transport, one with the use of a universal basket the other without basket.

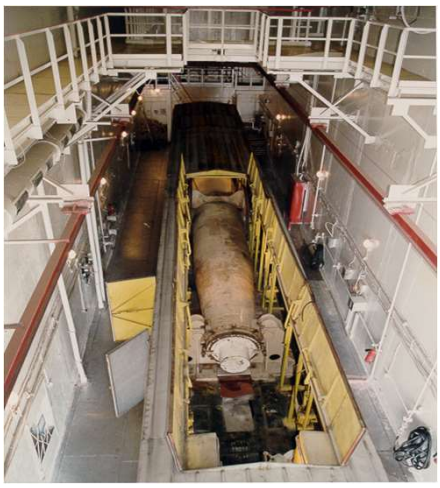

*FIG. 95. Railcar with internal transport package (courtesy of SSE ChNPP).*

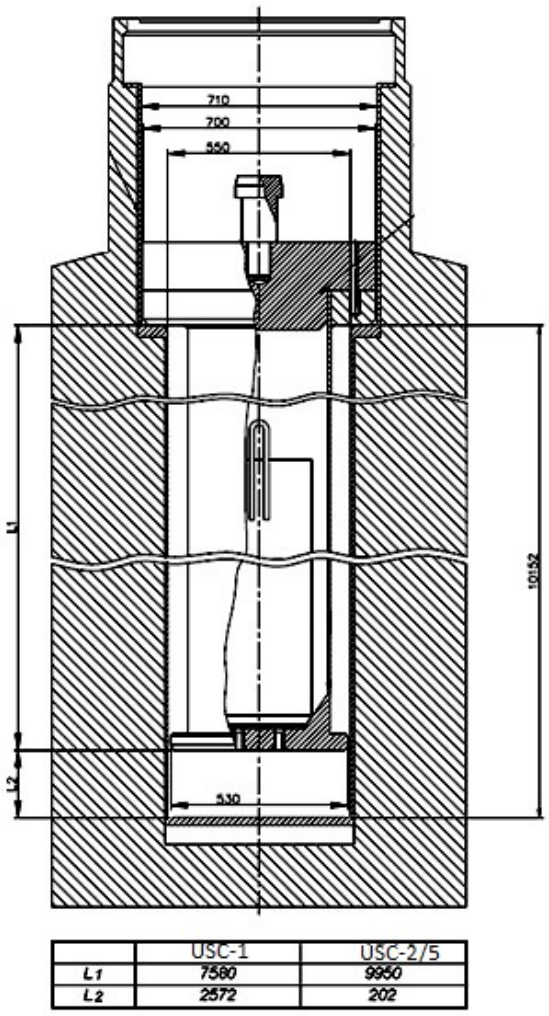


| | USC-1 | USC-2/5 |
|---|---|---|
| L1 | 7580 | 9950 |
| L2 | 2572 | 202 |

*FIG. 96. Internal transport package with USC (courtesy of SSE ChNPP).*

### 4.1.4. Severely damaged spent fuel storage in intermediate spent fuel storage number 1

The ISF−1 (Fig. 97) is designed to receive, store and transport spent fuel assemblies (SFAs) to ISF−2.

*FIG. 97. Intermediate Spent Fuel Storage No.1 (courtesy of SSE ChNPP).*

In ISF–1 the spent fuel is stored in five spent fuel pools (Fig. 98 (a)). There is a separate pool for transport casks and canyon.

To transfer SDSF from Units 1 and 2 to the ISF–1, it was necessary to make changes to the ISF–1 project and perform safety calculations. The canyon (Fig. 98 (b)) was designed for the storage (placement) of 29 USC (or SCB) with SDSF. The canyon consists of a reinforced concrete tank in which the walls and floor are lined with stainless steel and a rack for hanging SDSF in either a USC or SCB.

(a)

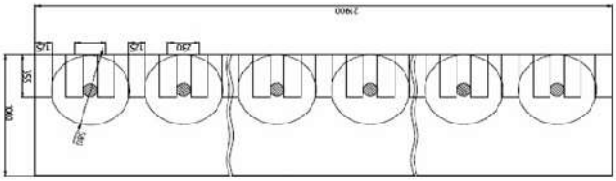

(b)

*FIG. 98. (a) Intermediate Spent Fuel Storage No.1 spent fuel pool. (b). Canyon with USC (SCB) (courtesy of SSE ChNPP).*

ISF–1 has a visual control system (VCS) that is designed to inspect (or monitor) the condition of spent fuel and performs the following functions:

- Surface condition inspection (monitoring) of SFA at a distance up to 100 m from the operator's station which is protected from ionizing radiation;
- Remote control of radiation using radiation resistant cameras;
- Digital video processing and estimation of the dimensions of SFA fragments.

Monitoring of the SFA is performed using 3 cameras. The VSC allows the detection of the following potential defects:

- SFA cladding cracks, breaks;
- Missing fuel rod plug;
- Edge fins and breaks of spacer grid;
- Gap between the bundles less than 8 mm;
- Extraneous object in the SFA overall volume;
- Visually observed bending of SFA;
- Absence of a fuel rod (one or more);
- Extension rod detached from SFA;
- Missing tailpiece and/or nuts;
- SFAs or fuel rods cut/broken along the thermal gap.

SFAs with the following damage will not be transported to the ISF-2:

- SFA cladding cracks, breaks;
- Missing fuel rod plug;
- Extension rod detached from SFA;
- Missing tailpiece and/or nuts;
- SFAs or fuel rods cut/broken along the thermal gap.

Examples of VCS results are presented in Figs 99–101.


*FIG. 99. Spent fuel assembly cladding breakage (a), bending (b) (courtesy of SSE ChNPP).*

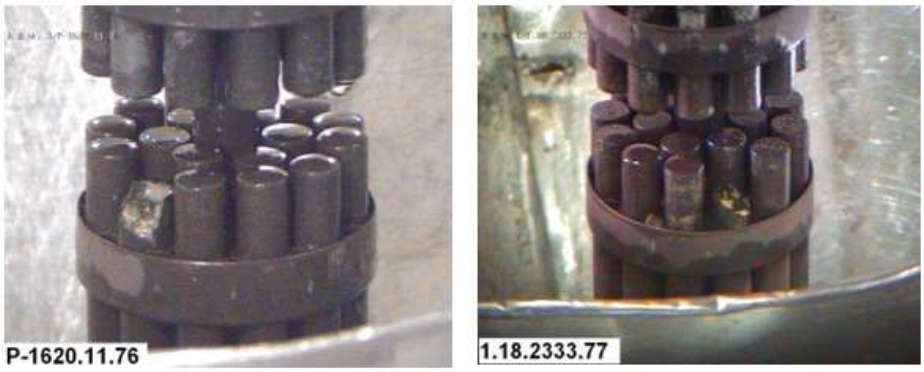


*FIG. 100. Missing fuel rod plug (courtesy of SSE ChNPP).*

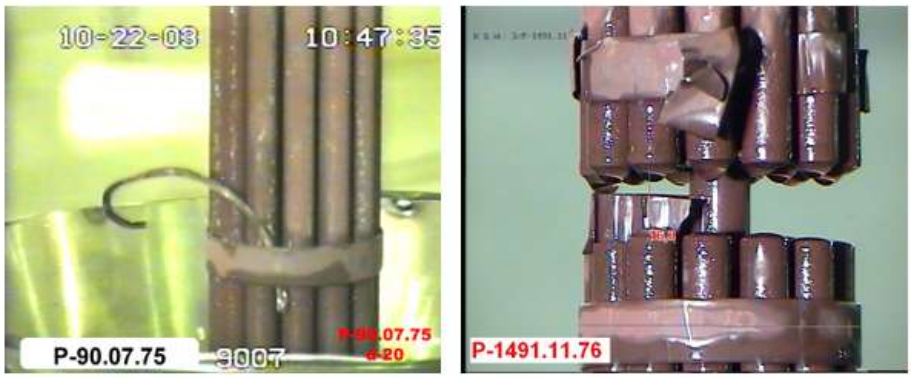


*FIG. 101. Extraneous object in the SFA overall volume (courtesy of SSE ChNPP).*

### 4.1.5. Spent fuel management at intermediate spent fuel storage number 2

The ISF–2 is designed for processing and storage of the spent nuclear fuel (SNF) of ChNPP RBMK–1000 reactors. The facility contains:

- Area for fuel acceptance, unloading and processing at the spent fuel processing facility (SFPF);
- Spent fuel storage area (canisters in concrete storage modules (CSMs));
- Storage area (tubes storehouse);
- Exclusion area with checkpoint building.

The spent fuel processing facility (Fig. 102) is designed to receive, separate, and pack SFAs into canisters before exporting for storage, for up to 100 years.

*FIG. 102. Spent fuel processing facility (courtesy of SSE ChNPP).*

The main systems within the SFPF are:

- TK–700 transfer wagon handling system;
- SFA handling system;
- Fuel tube handling system;
- Forced gas drying system (FGDS);
- Double wall canister (DWC) handling system.

The TK–700 transfer wagon handling system performs the following functions:

- Receiving and shipment of TK–700 transfer wagon;
- Unloading of the transport transfer basket (Fig. 103) with SFA from TK–700 to the hot cell;
- Loading of the transport transfer basket with extension rods from hot cell to TK–700 (Fig. 104).

*FIG. 103. Transport transfer basket (courtesy of SSE ChNPP).*

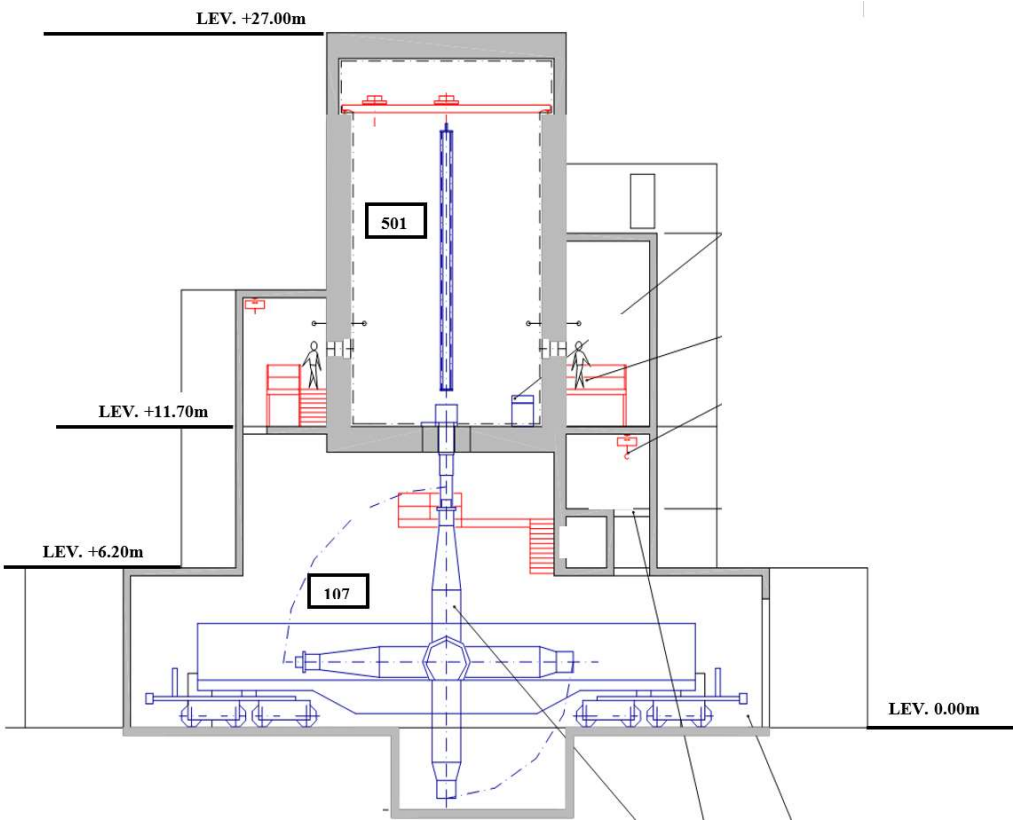


FIG. 104. TK-700 transfer wagon handling system (courtesy of SSE ChNPP).

The SFA handling system provides the following functions:

- SFA extraction from the transport transfer basket in the hot cell;
- SFA handling in the hot cell (Fig. 105 (a)), cutting SFA into fuel bundles and detachment of extension rod by SFA cutting device (Fig. 105 (b));
- Loading fuel bundles into fuel tubes.

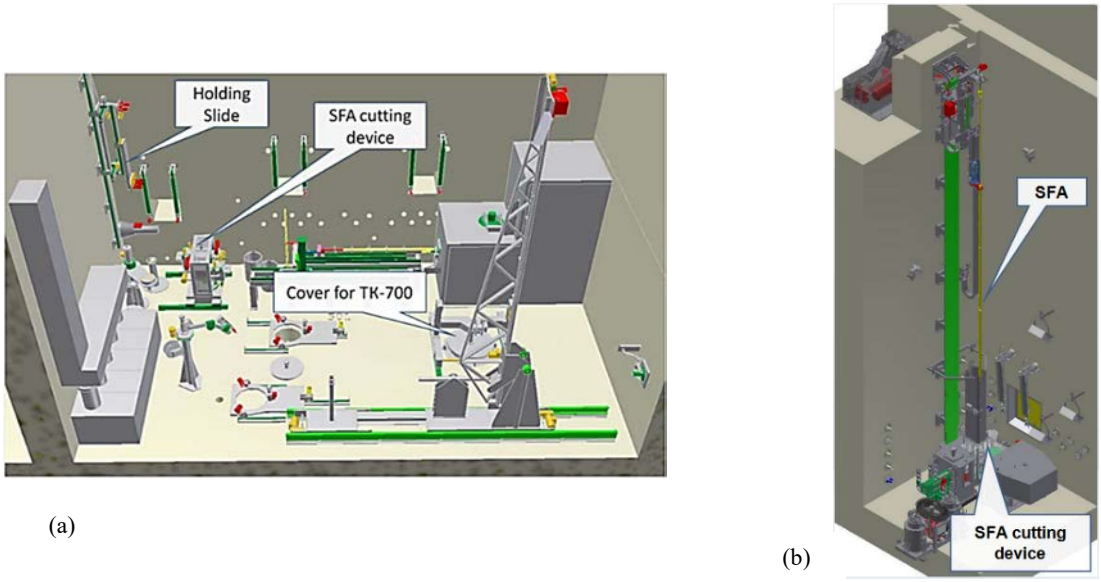


(a) (b)

*FIG. 105. (a) Hot cell. (b) SFA cutting device (courtesy of SSE ChNPP).*

The fuel tube handling system performs the following functions:

- Receipt of fuel tubes into the SFPF;
- Loading fuel bundles into fuel tubes (Fig. 106);
- Fuel tubes transfer and loading into DWC.

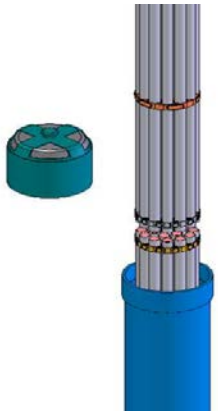

*FIG. 106. Fuel tube handling system (courtesy of SSE ChNPP).*

The purpose of the FGDS is to remove water from the SFA central tube and remove moisture from all fuel bundles in the DWC (Fig. 107) by circulating nitrogen gas in a closed loop. The gas saturated with water vapour enters the air cooled condenser, where moisture is removed, after which the dry heated gas is again fed into the DWC through the outlet of the main FGDS module.

The circulation of hot dry gas provides moisture removal through two phenomena. First, the high gas temperature contributes to the heating of moisture in the DWC, causing it to evaporate and increase the pressure of water vapour. Secondly, the constant flow of gas with low vapour pressure (dry gas) creates strong thrust due to the pressure difference between moisture and gas. A significant difference in pressure means that even moisture located in hard to reach areas of the internal structures of the DWC and the central pipe/SFA defects will turn into a gaseous form and will be captured and removed by the circulating gas flow.

The criteria for the successful completion of drying were a steady condensate level in the collection tank remains over 4 hours and a minimum drying time of at least 58 hours.

After removing moisture using FGDS, the pressure in the internal cavity of the EAEP is released through the drain valve separator and the FGDS is disconnected from the canister. The drainage hole of the DWC is hermetically welded, after which a vacuum drying system (VDC) and a helium filling system are connected to the ventilation hole of the DWC, which removes residual nitrogen and water vapour from the inner cavity of the DWC, checks the drying efficiency and fills the DWC with high purity helium.

The VDC lowers the pressure in the DWC using a vacuum pump. The vacuum pump includes a cooler that circulates water through the vacuum pump to prevent overheating. The vacuum pump creates a vacuum in the inner cavity of the DWC, after which the case is cut off by fittings. The vacuum pressure in the DWC is monitored to confirm the absence of residual moisture in the canister, which passes into the gaseous phase, causing an increase in pressure in the DWC. If the pressure in the DWC remains below the set limit, dehydration is considered effective and the internal cavity of the DWC is filled with helium.

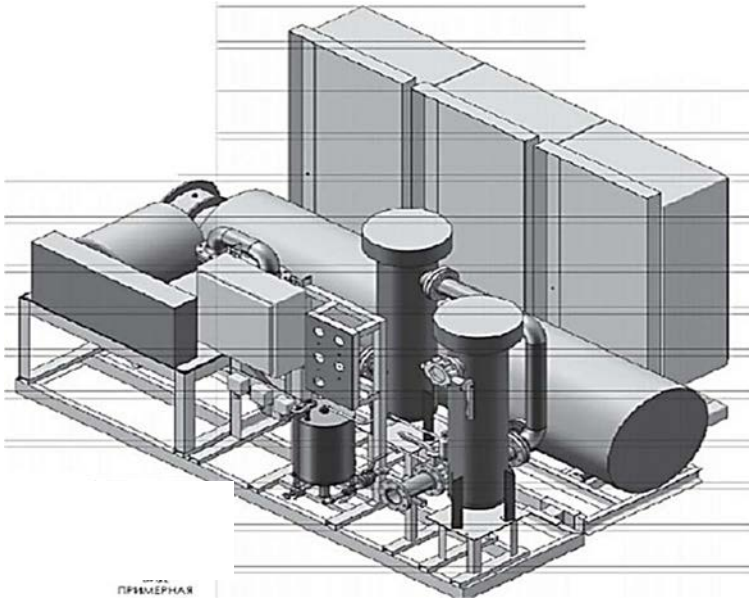


*FIG. 107. Forced Gas Drying System (courtesy of SSE ChNPP).*

The DWC, shown in Fig. 108, is designed to hold 186 FAs in fuel tubes. The canister has three main components: sealed vessel, inner basket, and fuel tubes.

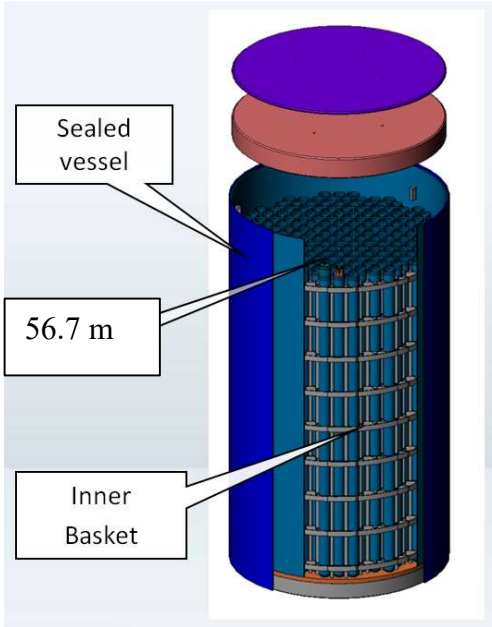


*FIG. 108. Double wall canister (courtesy of SSE ChNPP).*

The DWC handling system performs:

- Receiving of empty DWC in SFPF;
- Loading of fuel tubes in DWC;
- Drying SFA using FGDS;
- DWC leak control;
- DWC shipment and installing (Fig. 109 (a)) into CSM;
- Storing DWC in CSM for 100 years (Fig. 109 (b)).

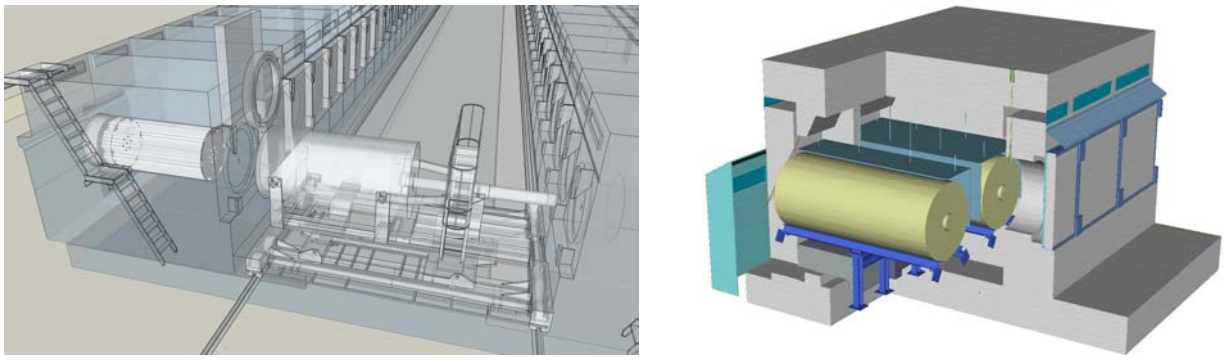

*FIG. 109. (a) Installation of double wall canister from on-site transfer cask to concrete storage modules by means of canister transportation and handling system. (b) Double wall canister storage in the CSM (courtesy of SSE ChNPP).*

The spent fuel storage area consists of 58 CSM × 4 cells (232 cells in total) with a design basis of 100 years (Fig. 110).

*FIG. 110. Spent Fuel Storage Area (courtesy of SSE ChNPP).*

### 4.1.6. Planned management of severely damaged spent fuel in intermediate spent fuel storage number 2

Fuel assemblies might have been damaged to an extent which does not allow the holder slide, cutting machine and fuel tube double lid system in ISF–2 to be used. Current studies indicate that handling severely damaged spent fuel could be performed in ISF–2, but it requires development of additional processes and equipment for the transfer of severely damaged fuel into the ISF–2 hot cell, and handling on a new damaged SFA handling table (damaged fuel table (DFT)).

Any SFA which is considered defective, in accordance with input control criteria, would be subjected to additional inspection to determine the method of handling. Additional inspections may include physical measurement of the thermal gap, the estimation of the SFA bend, the degree of spacer grids damage etc. Any SFA which, following additional inspection, is considered to be impossible to handle using regular means, would be delivered to a DFT. Handling the SFA at the DFT (Fig. 111) would be performed using special tools and equipment, which are intended to have the following functions:

- Receive the defective SFA from the hot cell crane in a vertical position;
- Tilt the defective SFA into horizontal position;
- Cut off the extension rod of the SFA;
- Cut separate upper bundle from lower bundle of SFA (dismantling fuel bundle);
- Load separated SFA bundles into auxiliary fuel tubes (AFT);
- To handle and transport AFT to holder slide.

Currently, development and deployment of the equipment and processes requires approval of a new project.

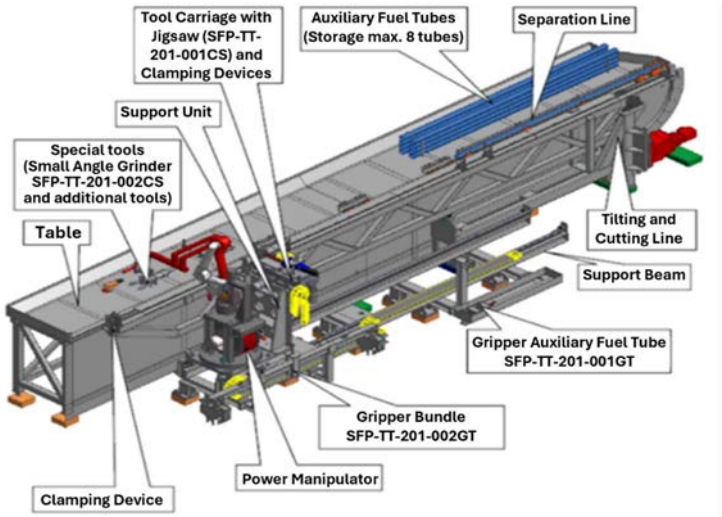


*FIG. 111. Damaged SFA handling table (courtesy of SSE ChNPP).*

## 4.2. CHARACTERIZATION OF CORROSION PRODUCTS FROM DEGRADED ADVANCED GAS COOLED REACTOR URANIUM DIOXIDE FUEL

In 1962, the UK began operating the Windscale advanced gas cooled reactor (WAGR), the prototype reactor for the UK's second generation of commercial power plants. Like the first generation Magnox reactors upon which it was based, WAGR was graphite moderated, and carbon dioxide cooled but to improve thermal efficiency the operating temperature was increased to up to 850℃. To enable higher operating temperatures, magnesium alloy clad metallic uranium fuel elements were replaced with niobium stabilised stainless steel clad uranium dioxide fuel.

In the WAGR, fuel elements consisted of 12–18 pins in two concentric circles surrounded in a graphite sleeve. Four elements were held together to form the fuelled section of an arrangement known as a stringer which was loaded into each reactor channel. As a prototype reactor WAGR was used to carry out a wide number of irradiation experiments to test differences in fuel design in order to inform the design of the commercial AGR reactors that were to follow. This required a large quantity of fuel to undergo PIE. Elements that were designated for PIE were transferred to the co-located PIE facilities at Windscale. Although differing between elements, the basic process for PIE was as follows:

- Visual examination of the entire fuel element;
- Removal of individual pins and macroscopic examination of each pin and support materials;
- Pin length measurement of all pins;
- Gamma scanning of all pins;
- Leak testing of all pins;
- Radiography of all pins;
- Diameter measurements ~eight pins per element;
- Fission gas release (FGR) testing of ~six pins per element;
- Metallography examination of two sections typically from one pin.

The majority of pins that underwent PIE were generally intact or had only punctures from FGR measurements, whilst a much smaller number were cut following the removal of sections for metallography. After PIE cut or punctured fuel was segregated from intact fuel and placed into screw top cans. The cans were then transferred into the Pile Fuel Storage Pond for storage ahead of reprocessing.

Forty years later approximately 2 t of this fuel had not been reprocessed and between 2012 and 2016 a project was undertaken to recover, dry and repack this fuel into welded cans ahead of continued long term storage.

During the repackaging campaign in the National Nuclear Laboratory's (NNL) hot cells it was found that all the cans had become flooded. Subsequent modelling and hydraulic tests on cans of similar design indicated that the cans would have flooded rapidly, most likely in a matter of weeks.

The condition of the fuel removed from these cans differed widely. Most of the fuel was in good condition, however in some cases the cans contained significant quantities of sludge which had not been expected. The remainder of this section describes work to characterise, treat and repackage these materials for a further period of storage.

### 4.2.1. Sludge examination

In order to characterize the airdried sludge, to permit treatment of the sludge for storage, samples were taken from three different cans for examination and testing.

*4.2.1.1. Scanning electron microscopy*

Electron microscopy was carried out with a FEI Quanta 200 FEG environmental SEM fitted with an Oxford Instruments X act energy dispersive X ray detector (Fig. 112).

All samples were found to contain broadly the same phases:

- Acicular particles rich in Fe and O;
- Facetted (cuboid/octahedral) Fe and O rich material;
- Spherical Fe rich material;
- Diffuse Fe and O rich material;
- Sharp fragments of uranium oxide.

The Fe rich material appears to have come from solution, (unlike the uranium containing material) and is likely to consist of a mixture of iron oxides, hydroxides and oxyhydroxides. Energy dispersive X ray spectroscopy analysis of the facetted material shows it to contain more Fe (relative to O) than the acicular material. Based on EDX and morphology the facetted material is thought to be magnetite while the acicular material is believed to be goethite.

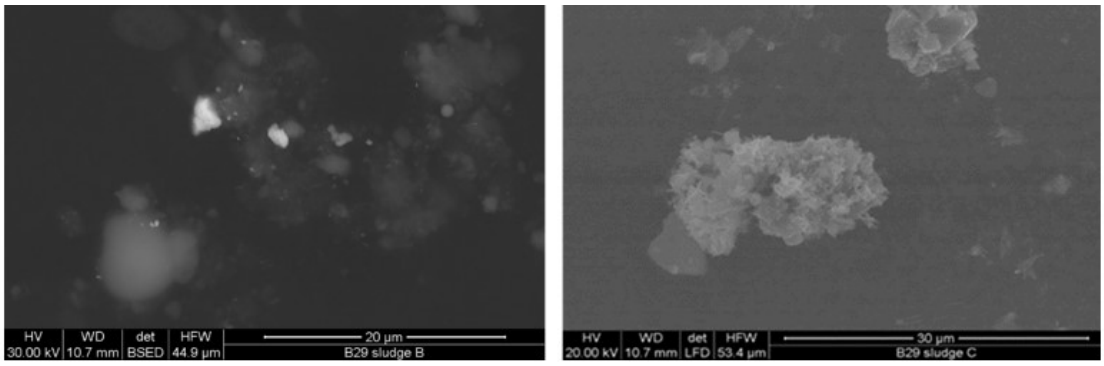


*FIG. 112. SEM images of different phases observed in sludge. (Left) $UO_2$ fragments, facetted, spheroidal and acicular Fe rich phases. (Right) Facetted, acicular and diffuse Fe rich fragments (courtesy of NNL).*

*4.2.1.2. Elemental composition*

Samples of sludge were taken and analysed for their elemental composition by ICP–MS. The composition varied somewhat between cans but was found to be predominantly uranium. There were also significant quantities of iron, silicon, aluminium, and zinc. Aluminium is likely to be from Sintox pellets and the screw topped cans used for storing cutting fines. Figure 113 shows images of corroded aluminium. Silicon is believed to be from the polishing compound using in the preparation of metallographic samples. The source of the iron is unclear as it did not contain significant nickel or chromium which would be expected if it resulted from spalled cladding oxide (formed in reactor), or corrosion of the cladding or storage can. Similarly, the source of zinc is unknown. These may be due to fittings used on experimental fuel.

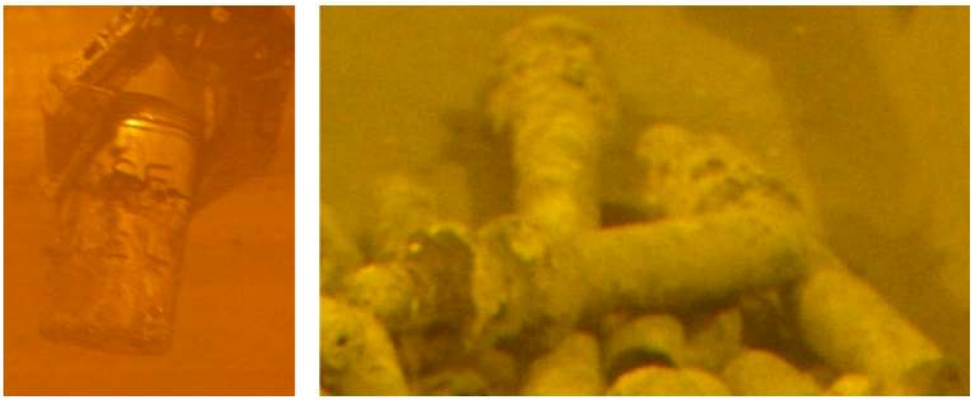

*FIG. 113. Corroded aluminium can holding cutting fines and additional fittings on an experimental fuel pin (courtesy of NNL).*

### 4.2.2. Fuel condition

The majority of the fuel recovered was found to be in reasonably good condition. While there was evidence of some general corrosion, the ribs were still visible, and end caps showed no evidence of significant deterioration (Fig. 114). In general, cans which contained only punctured or long lengths of fuel pin were found to be in this condition.

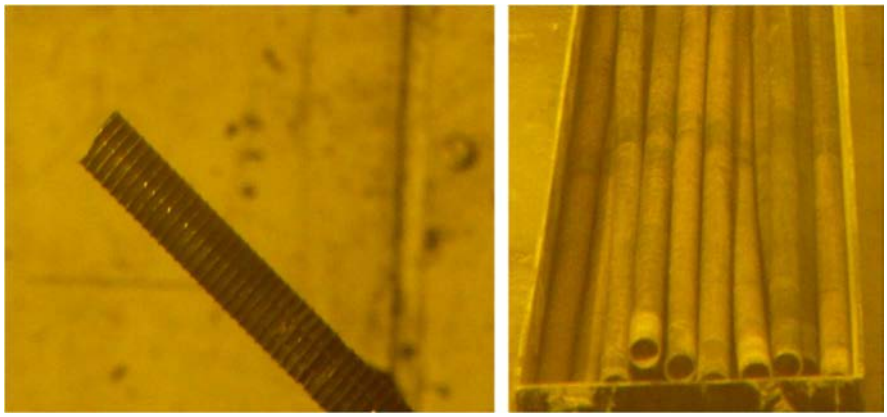

*FIG. 114. Intact WAGR pins recovered from cans containing mainly whole pins (courtesy of NNL).*

A small number of cans were found to contain substantial quantities of sludge. This was an unexpected finding and led to a concern regarding possible water carryover in future storage.

Examination of the records indicated that when packed, such cans had been filled predominantly with smaller sections of cladding left over from metallography mounts (Fig. 115).

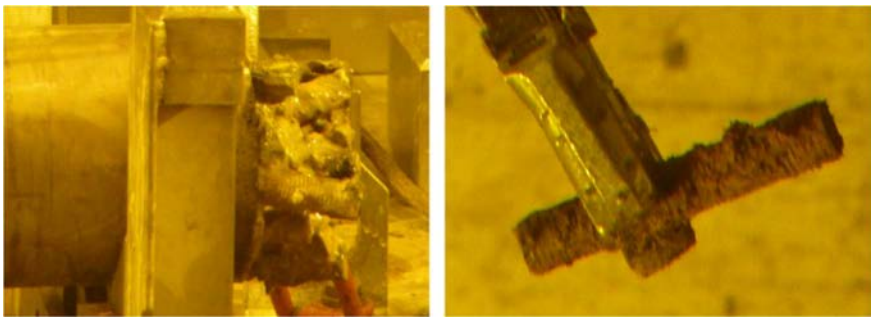

*FIG. 115. Sludge found in can packed with small pin sections. (left) As received; (right) After storage in cave (courtesy of NNL).*

It was considered to be inconceivable that the sludge to have migrated into the can from the pond water and there was no evidence of significant differences in the storage environments associated with the can with and without sludge, therefore it was concluded that the differences in sludge formation were associated with conditions within the cans themselves.

After weighing the fuel pin remnants, there was found to be a discrepancy between the mass of recorded and the mass of fuel expected within the can based on record. Inspection of the cut fuel sections indicated that in some cases substantial quantities of fuel were missing from the cut end of pins (Fig. 116).

*FIG. 116. Cut fuel pin with missing fuel (courtesy of NNL).*

After removal from the cans the sludge was passively air dried in the warm air within the cave system. After drying, the mass of dried sludge (Fig. 117) in each can was recorded and found to be between 1 and 8.2 kg, significantly more than would be expected based on the loss of fuel from fuel pins. There was, however, no apparent correlation between the mass of sludge and either fuel burnup or exposed surface area. In many cases the sludge included other debris, such as thermocouple fittings.

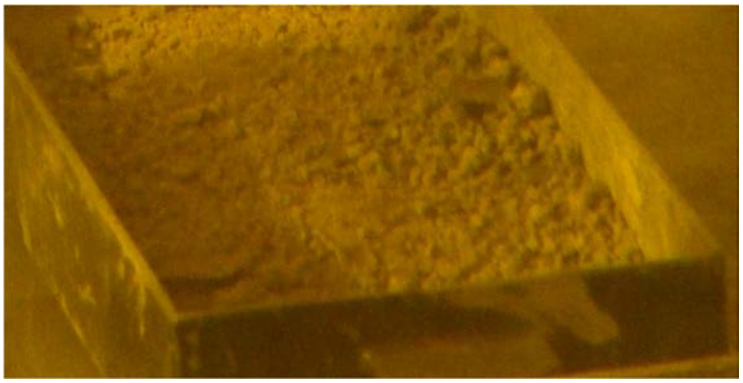

*FIG. 117. Sludge recovered from a single can of cut WAGR fuel pins (courtesy of NNL).*

Observations of the screw top cans did not indicate any signs of substantial corrosion.

*4.2.2.1. X ray diffraction*

The XRD results generally confirmed the findings of SEM analysis. The sludge contained a mixture of iron oxides and hydroxides, while the uranium was present only as crystalline $UO_2$.

*4.2.2.2. Thermogravimetric analysis*

Since the major concern with sludge was water carryover samples were examined by thermogravimetric analysis (TGA). The results showed a mass loss of between 10 and 57% although the behaviour varied between the samples (Fig. 118). Two sample showed large mass losses before heating indicative of surface moisture however all samples were found to contain chemisorbed water although there was no characteristic drying temperature. Detailed analysis of the mass loss supports heterogeneity between samples and even within samples.

*4.2.2.3. Leach testing*

A series of leach tests were carried out with the sludge to ascertain sludge behaviour during pond storage. Sludge was immersed in a solution of demineralised water dosed to pH 11.4 with NaOH to represent the caustic dosing used to inhibit corrosion in the majority of the UK's spent fuel ponds. The samples were immersed for a total of 30 days with samples being taken for analysis after increasing intervals.

Uranium and caesium were leached in detectable levels from all three samples as shown in Fig. 119. The release behaviour was similar in all three samples showing a high initial leach rate followed by continued leaching at greatly reduced rates. This is typical of the leach behaviour observed for spent fuel and indicates the initial loss of material from precipitates and oxidised fuel followed by release from the fuel matrix.

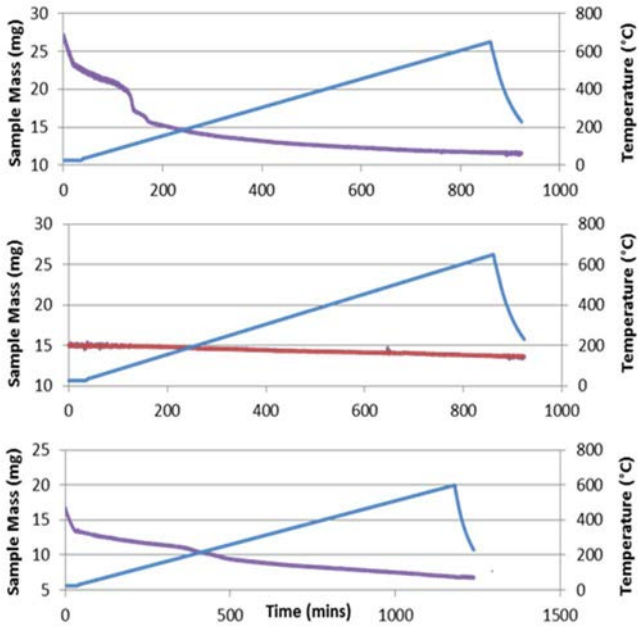


*FIG. 118. Thermographs of the three samples examined by TGA (courtesy of NNL).*

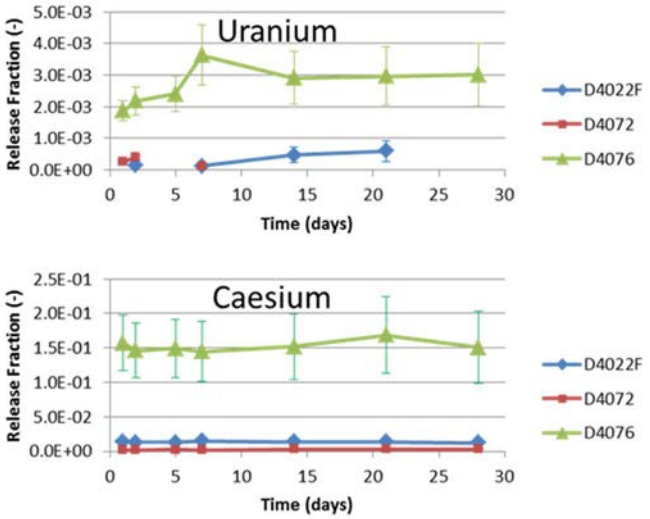


*FIG. 119. Leach behaviour of the samples examined (courtesy of NNL).*

### 4.2.3. Conclusions on sludge formation

The quantity of corrosion product sludge associated with cut, irradiated oxide fuel was related to the size of the fuel pin sections within the can, with cans containing intact pins being free from sludge while the cans containing small pin remnants had significant quantities of sludge. No direct correlation was established between the quantity of corrosion product sludge and either burnup or exposed surface area, however the presence of particulate material derived for fuel cutting during PIE is likely to have added additional variability in the material form that affected the local corrosion processes.

Scanning electron microscopy examination and XRD indicated that the sludge predominantly consisted of shards of uranium with various phases of precipitated iron oxides. The most likely explanation for this is the preferential corrosion of the cladding and disintegration of uranium dioxide

fuel which is released into the can. The lack of nickel or chromium in the sludge is believed to be due to these having remained in solution when the can was emptied.

The observed leaching behaviour of the recovered sludge samples is consistent with the expected behaviour of surface oxidised, crystalline $UO_2$ rather than that of precipitated uranium compounds.

### 4.2.4. Fuel identification

Records indicated that the retained fuel was from cans containing the remains of pins that underwent PIE in the 1960's. Records also suggested that the burnup of these pins varied from 5–20 GWd/tU and had different geometries, since WAGR was an experimental reactor used to trial different fuel designs. Despite having a somewhat lower burnup than current fuel, the highest burnup section of the recovered fuel (20 GWd/tU) fuel was felt to be the most valuable. This fuel is also geometrically similar to modern LWR fuel (~10 mm diameter). It was also considered to be worthwhile to examine a section of fuel which was geometrically similar to modern commercial AGR (CAGR) fuel (~15 mm diameter with a hollow bore) even though it was of lower burnup.

Interrogation of the original PIE records indicated that the high burn fuel recovered came from stringer 4 of irradiation experiment 221B (IE 221B/4). Unfortunately, the can also contained sections of fuel pin from stringer 2 of the same irradiation experiment which contained identical fuel pins but were removed with a burnup of only ~5 GWd/tU. It was therefore necessary to carry out gamma spectroscopy to identify the high burnup pins.

For completeness all 18 of the recovered fuel sections underwent spot gamma spectroscopy (Fig. 120) and a low power visual examination. In order to identify the pin section most likely to have been wetted, the higher burnup fuel sections underwent axial gamma scans to reveal any indications of caesium loss due to water leaching (Fig. 121). From the axial gamma scan of high burnup pin section B206/41/C11 (C11) it was possible to see evidence of apparent caesium leaching at the wetted ends, the presence of a Sintox pellet and some clearly defined pellet—pellet interfaces. The axial gamma scan of hollow pin B206/41/C5 (C5) showed no evidence of caesium leaching most likely because the bore had allowed water access along the entire length of the fuel sections and almost equal leaching along the pin length. Pellet—pellet interfaces (PPI) were not discernible in this pin although the anti-stacking grooves (ASG) are evident. Pin C11 had only one ASG however since the groove was in the Sintox pellet it is not apparent.

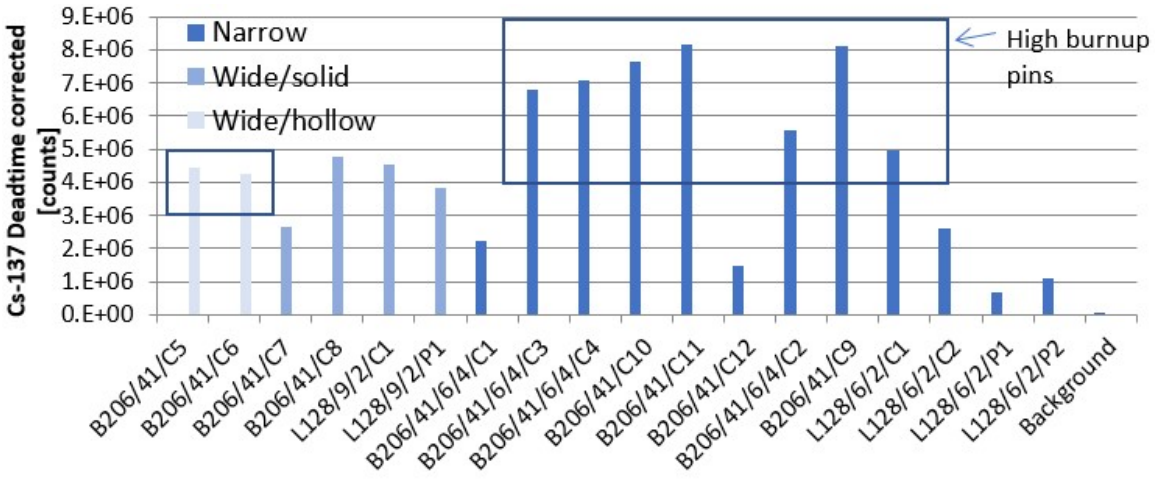


*FIG. 120. Spot gamma spectroscopy of fuel pins recovered from extended pond storage (courtesy of NNL).*

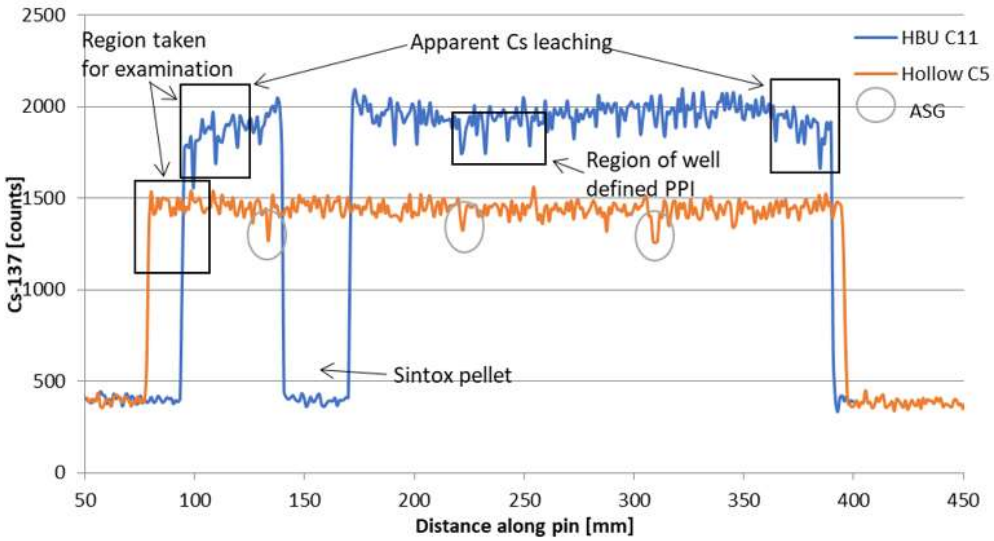


*FIG. 121. Axial gamma scans of the two sections examined showing some well-defined PPI, ASG, caesium leaching, and the regions selected for examination (courtesy of NNL).*

Images of the two sections examined are shown in Fig. 122.

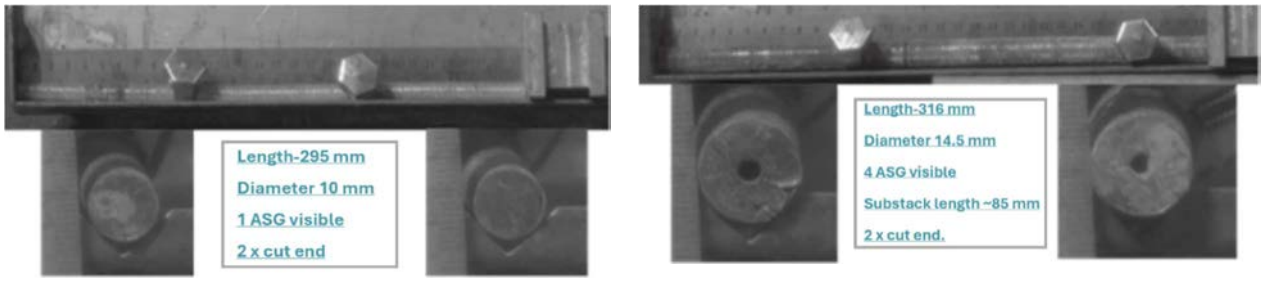


(a) (b)

*FIG. 122. (a) Solid fuel pin segment C11. (b) Hollow fuel pin segment C5 (reproduced from Ref. [119] with permission courtesy of NNL).*

### 4.2.5. Optical examination for fuel

The mounted sections of pins C11 and C5 are shown below. cut sections of fuel pin were mounted in resin and polished before being examined by optical microscopy. The samples were then exposed to a mixture of sulphuric acid and hydrogen peroxide to reveal grain boundaries in the fuel and a cladding etch in oxalic acid.

Figure 123 shows the wetted and non-wetted ends of the section cut from high burnup pin C11 in the 'As Polished' state and following the fuel etch. There is no evidence of, and difference in oxidation between the wetted and non-wetted ends. Similar results were observed for hollow pin C5, as shown in Fig. 124. There was no evidence indicating formation of higher oxides ($U_3O_7/U_3O_8$). The small amount of interlinked, intergranular porosity at the PPI/pellet bore in hollow pin C5 (Fig. 125) was not deemed to be significant.

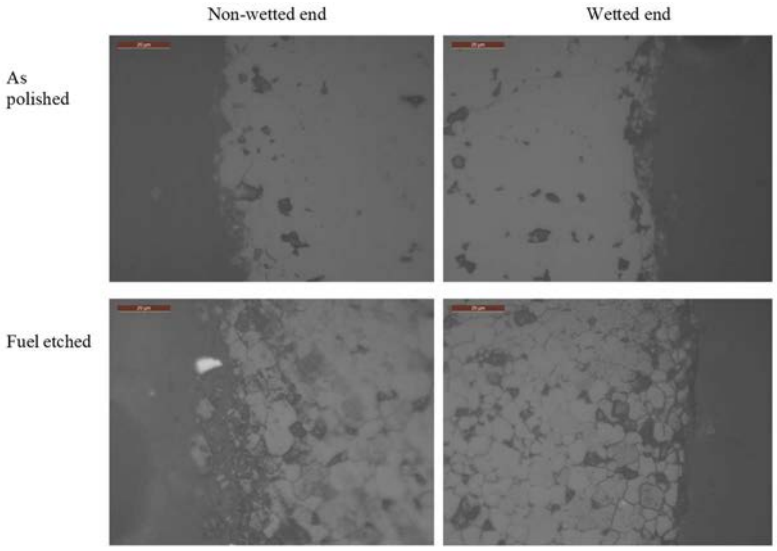


*FIG. 123. Non wetted and wetted ends of solid pellet pin C11 (element burnup of 27.1 GWd/tHM)) (reproduced from Ref. [119] with permission courtesy of NNL).*

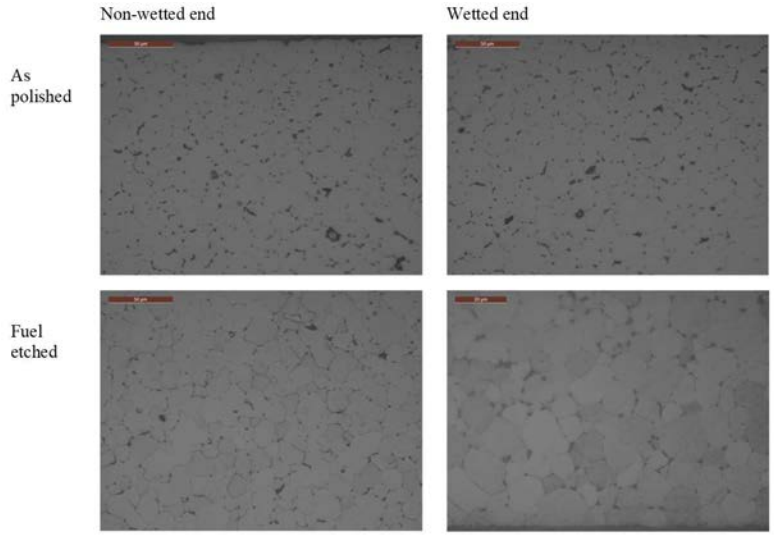


*FIG. 124. Non-wetted and wetted ends of hollow pin C5 (element burnup of 8.9 GWd/tHM) (reproduced from Ref. [119] with permission courtesy of NNL).*

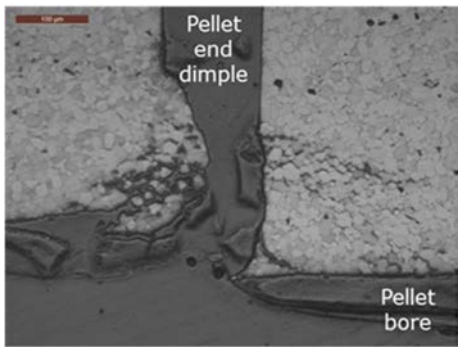


*FIG. 125. Interlinked intergranular porosity in hollow pin C5 (reproduced from Ref. [119] with permission courtesy of NNL).*

Figure 126 shows the observed fuel microstructure during a recent examination and that observed during the original PIE in the 1960's. Comparison of the microstructures yields no evidence of increased oxidation or degradation. As expected, based on the irradiation conditions, the cladding appearance was likewise unchanged, as shown in Fig. 127.

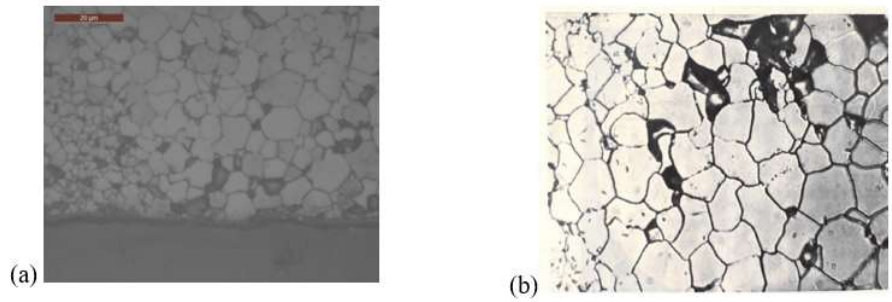


*FIG. 126. Fuel microstructure from solid fuel pin C11. (a) Recent examination (reproduced from Ref. [119] with permission courtesy of NNL). (b) Historic examination (courtesy of NNL).*

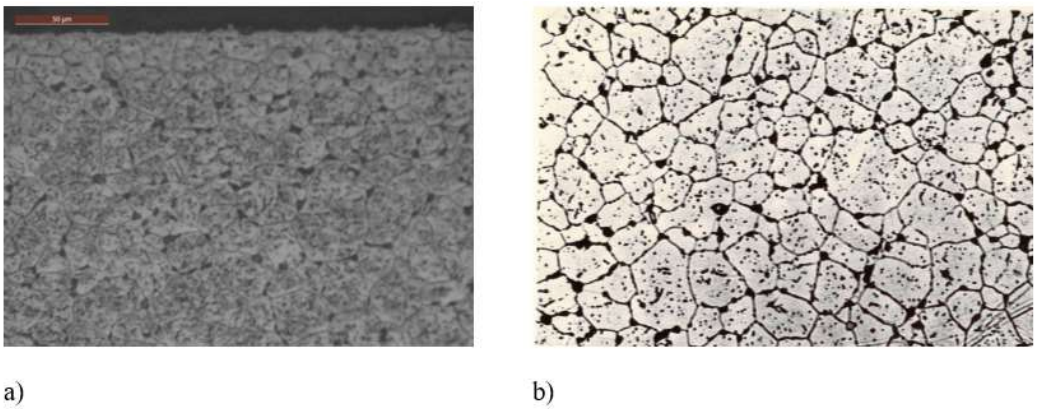


*FIG. 127. Cladding from high burnup pin C11. (a) Recent examination and (b) Historic examination (courtesy of NNL).*

Optical microscopy of $UO_2$ fuel known to have been exposed to water for over 40 years shows no signs of degradation, with wetted and non-wetted sections both appearing much the same. Comparison of recent images with those collected prior to water exposure showed no significant differences, despite indications of localised loss of caesium in some sections.

Small subsamples from of the fuel sections have been extracted from adjacent fuel pellets. Examination by SEM and wavelength dispersive X ray spectroscopy is planned but data are not available for reporting.

### 4.2.6. Final treatment for repackaging

Prior to of repacking, long pin sections were broken to check whether there was any bulk water within the fuel pins and to ensure that the fuel matrix was definitely exposed to the cave air to allow drying. No pin appeared to contain bulk water.

Fuel sludge was packaged into individual screw top cans ahead of placement into welded cans for return to pond (Fig. 128) to provide additional containment for the easily dispersible material.

*FIG. 128. Screw top sludge container with cap removed prior to repackaging (courtesy of NNL).*

To prevent over pressurisation due to radiolysis of the remaining water adsorbed on the fuel and dried sludge, small holes were drilled into the welded can lid to allow radiolytic hydrogen to be released. The small diameter was specified to prevent water ingress due to surface tension when the fuel was returned for pool storage alongside other PIE remnants pending disposal. Operational experienced, evidenced from pool water activity monitoring, however, has shown this provision to have failed. The failure is believed to be due to the effects of varying atmospheric conditions not being taken into account.

## 4.3. MANAGEMENT OF DAMAGED FUEL AT PAKS NUCLEAR POWER PLANT

In the early 2000's magnetite deposits formed on FAs in three units of Paks NPP. The investigations concluded that it had resulted from a mass decontamination campaign of the steam generators prior to modification of one of them.

In 2003, during the outage period of Unit 2, a chemical cleaning programme of FAs was carried out (10 April). Thirty *Voda–Vodyanoi Energetichesky Reaktor*, i.e. water–water power reactor, (VVER)−440 SNF assemblies were significantly damaged due to inadequate cooling (total mass of SNF > 6 t, $UO_2$ > 3.5 t, $^{235}U$ > 70 kg, Pu > 20 kg, the fuel was severely damaged, but not molten).

The chemical cleaning of assemblies was carried out in a specially designed cleaning tank, placed in a service shaft (pit No. 1) near the reactor (Fig. 129). The plant's systems and services were not affected, but it was necessary to encapsulate the damaged fuel and to clean up shaft No. 1, as the cleaning tank constituted an obstacle to the transportation of fresh and spent fuel to and from the reactor.

In Paks NPP's case the full recovery of the consequences of the incident took more than 11 years.

The recovery time can be split into 3 phases. The goals of the first phase were:

- To investigate the cause of the accident, to understand the condition of the fuel and of the pit. The investigation showed the cause of the accident to be a design error since the removal of the residual heat was not properly ensured in all regimes. The tank contained more than 6 t of fuel, which was severely damaged in the centre, at the edges there was almost intact fuel (the status of the fuel is demonstrated in Fig. 130);
- To stabilize the fuel and to ensure safe condition of the damaged fuel and the units, including cooling, chemical treatment, and monitoring of main parameters (i.e., temperature, boron concentration and other chemical parameters, neutron flux and subcriticality, radiation, and potential releases).

The work was mostly carried out by the NPP's specialists and domestic research institutes and design organizations.

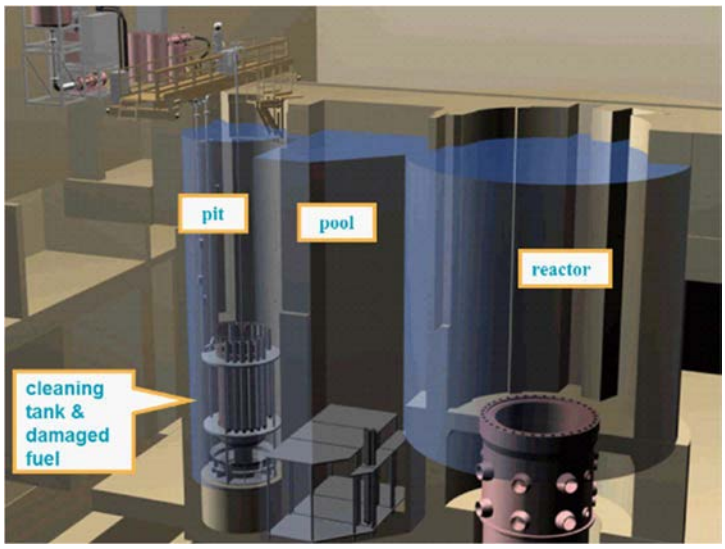


*FIG. 129. The location of the cleaning tank (courtesy of Paks NPP).*

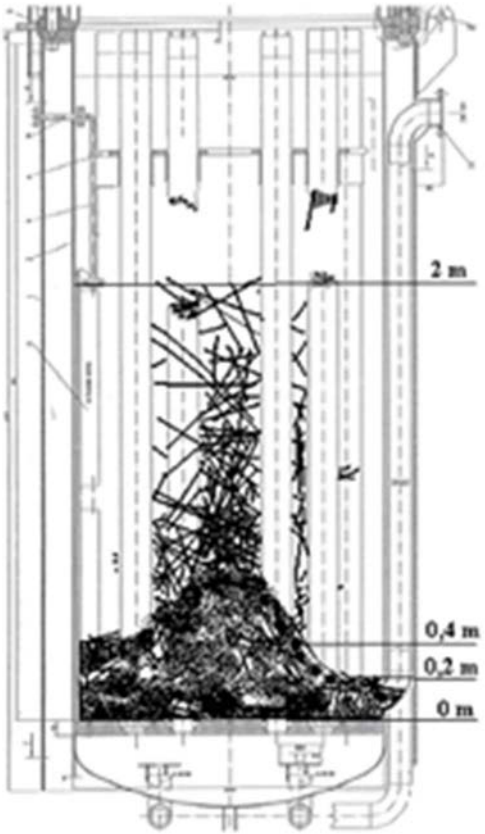


*FIG. 130. The condition of damaged fuel in the cleaning tank (courtesy of Paks NPP).*

After completion of the first phase the second phase commenced. The goals of this phase were the preparation for fuel removal, licensing, and the fuel removal from the cleaning tank.

Neither the NPP operator, nor Hungary were in possession of suitable technology and did not have enough experience to remediate the consequences of the incident. In 2003 the Russian Federation's TVEL Fuel Company and Paks NPP concluded a contract, whereby Russian specialists, in compliance with all requirements of nuclear and radiation safety, would develop technology for the removal of the damaged fuel assemblies from the cleaning tank, empty pit No. 1 and undertake the recovery operations. The work was carried out by leading companies in the industry in Russian Federation and Hungary.

Two types of canisters were designed for storing the damaged fuel and a cask for solid radioactive waste, a broad (28 type) canister (Fig. 131 (a)) and a narrow (29 type) canister (Fig. 131 (b)). The broad type of canister was used for most intact FAs and the narrow type for debris.

Canisters had to meet the following requirements:

- Safe interim storage in the spent fuel pool of the plant. There was a significant number of positions for containers with the size of normal fuel, but positions for storing extra large containers with fuel fragments or for storing canisters with heads and tails of the fuel assemblies were limited;
- To ensure appropriate cooling of the stored materials;
- To ensure all potential internal and external transport operations using existing fuel transport capabilities;
- Withstand all potential mechanical loads for all possible operational modes;
- Since the first period of storage was planned with water filled canisters it was necessary to ensure sufficient leak tightness to limit releases from the containers into the spent fuel pool, but at the same time to have internal pressure change compensation capability to cope with the effects of normal and abnormal temperature changes;
- To handle the hydrogen generated by radiolysis inside the canisters;
- To ensure future drainage, internal drying and full leak tightness (applicability for further possible treatment of the canned fuel).

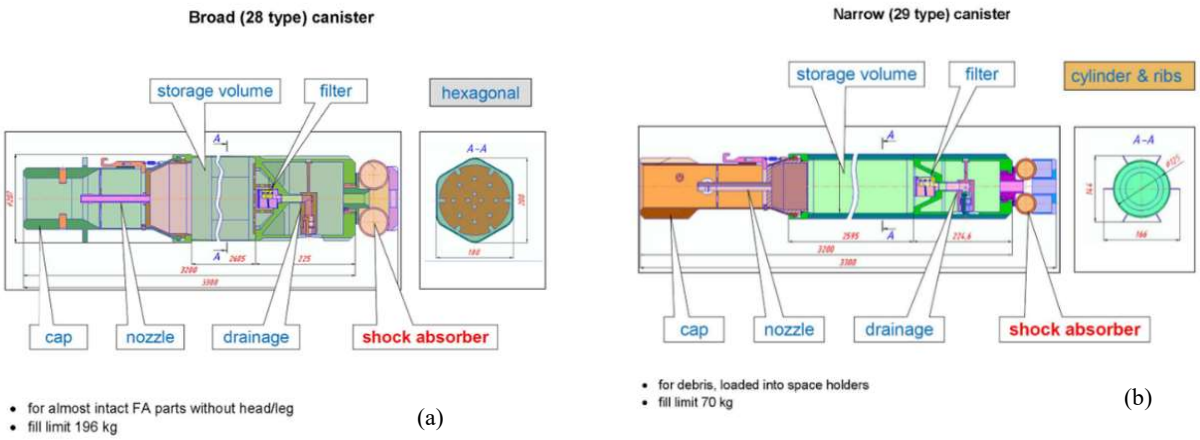


*FIG. 131. (a) 28 type canister, (b) 29 type canister (courtesy of Paks NPP).*

In addition, the large recovery equipment such as the working and lifting platform and tools were also designed and manufactured. The platforms were placed into pit No. 1 above the cleaning tank containing the damaged fuel.

The major recovery equipment is presented in Fig. 132.

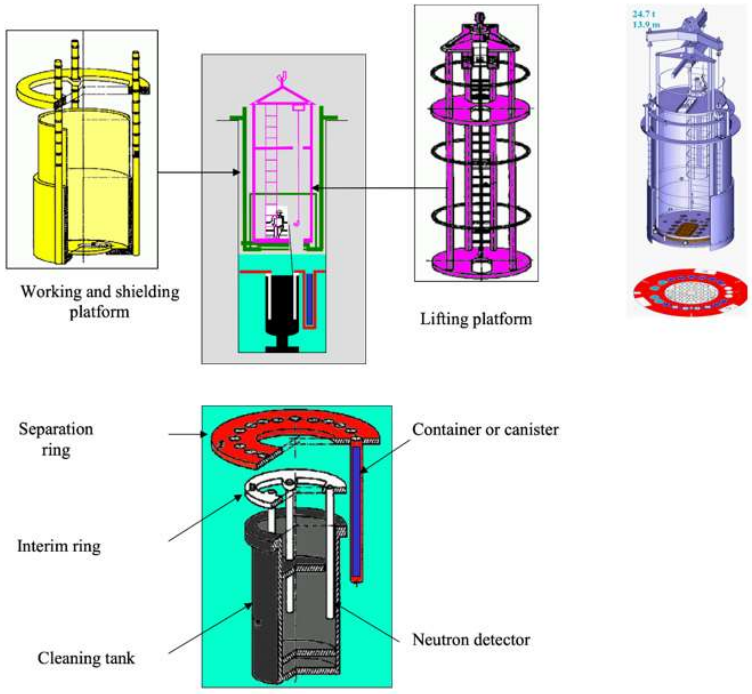


*FIG. 132. Major equipment of the recovery (courtesy of Paks NPP).*

A working platform had to provide a safe working area with the following features:

- Shielding against radiation;
- Ventilation to assure comfortable working environment and necessary air flow direction to avoid inhalation of radioactive gases, if any;
- Hoisting equipment to handle tools and canisters;
- Adjustability to assure optimum distance for appropriate shielding by water and adequate manoeuvrability of tools;
- Washing of the used tools to avoid spread of contamination;
- Adequate illumination, continuous video observation and recording, and radio connection;
- Easy relocation from the shaft to facilitate transfer operations of loaded containers into the spent fuel pool and emergency removal from the shaft in case of any kind of unforeseen event in the shaft by the available 32 t crane in the reactor hall.

After the extensive preparations, lasting some 3.5 years, at the end of 2006 the encapsulation of the damaged fuel was performed as planned over 3 months without any problems.

The fuel was safely reloaded under water by personnel with hand operated tools (Fig. 133). The almost intact assemblies, after cutting off the stainless steel top and bottom end parts were placed into broad canisters (Fig. 134), fuel debris was loaded into holders and placed into the narrow canisters, and end pieces without fission material were placed into solid waste casks, which were treated as radioactive waste.

The process steps consisted of (Fig. 134):

- Cleanup of the upper plate (removal of the top and bottom end pieces from the FAs, the fragments of FAs and the fragments of the fuel rods);
- Opening of the upper plate by drilling, cutting and crown boring;

— Debris removal from the central area of the cleaning tank (removal of the fuel rod fragments and the fuel in bulk form);
— Debris removal from the lower plate;
— Opening of the lower plate by crown boring;
— Debris removal from areas under the lower plate.

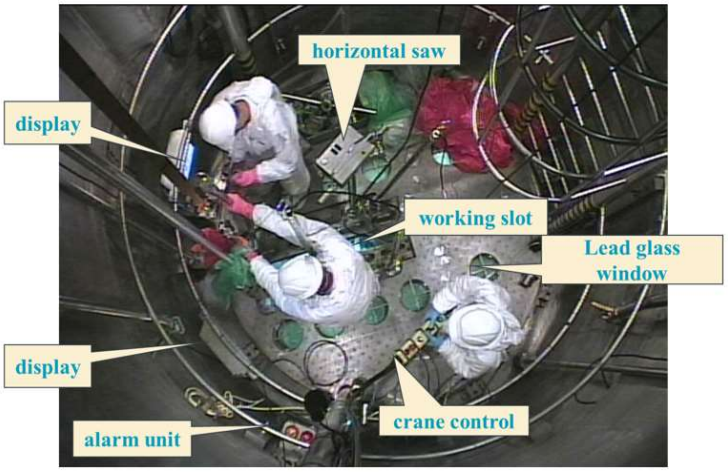


*FIG. 133. Personnel on the working platform (courtesy of Paks NPP).*

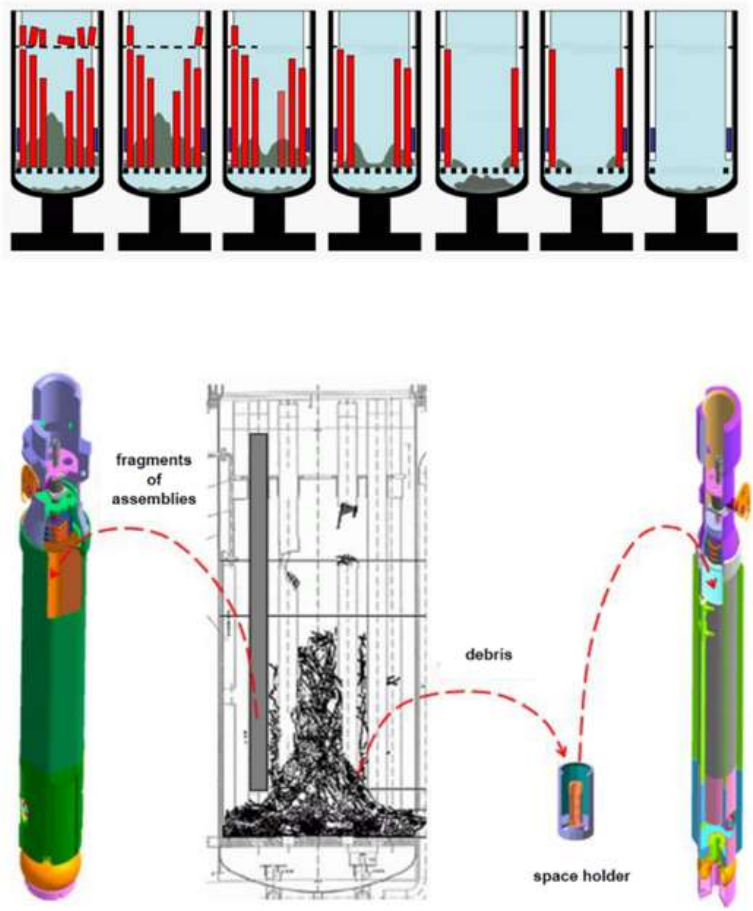


*FIG. 134. Fuel/debris removal (courtesy of Paks NPP).*

Three operators worked on the platform at the same time (Fig. 133). They had excellent views of the fuel and tools, using video systems and by viewing directly (through the water and via the bottom windows). The fourth operator and the two shift leaders supervised their actions from the reactor hall at a nearby control panel and display (Fig. 135).

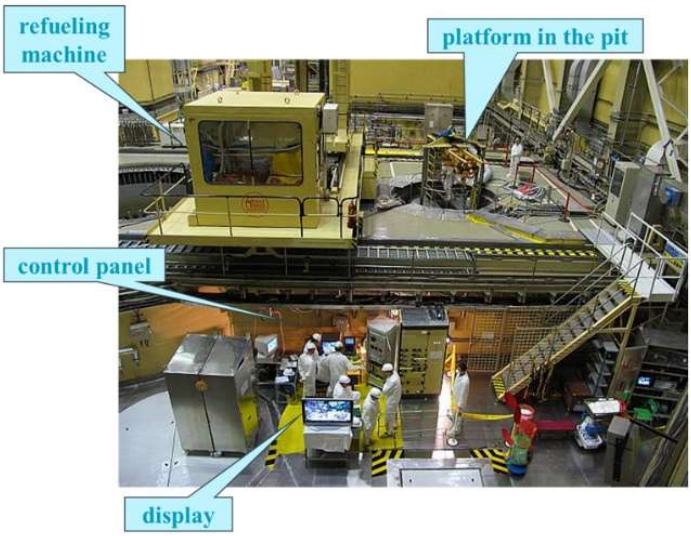


*FIG. 135. Overview of the recovery works location (courtesy of Paks NPP).*

At the end of the second phase all fuel was encapsulated. Sixty-eight ventilated canisters filled with water were stored in the spent fuel pool (a special device was developed to allow venting of gas to the pool and to prevent the release of water from the canister). The main result of this phase was that the fuel was stored in a safe and controlled manner, allowing time for long term management solutions to be developed.

From this point the third phase of full recovery commenced. The objective was to restore plant conditions to those prior to the incident. To achieve this goal, it was necessary to develop a method for drying and hermetically sealing the canisters (which didn't impact normal operations of Units 1 and 2), to substantiate the transport of the canisters, to dry the canisters, and then to transport them to a reprocessing facility.

The main challenge was to ensure and justify the safety of shipment of damaged SNF (transport of the wet damaged SNF is difficult due to radiolysis of the water in the canisters).

It was necessary to carry out experiments with real spent fuel to study the behaviour of damaged nuclear fuel in canisters and to confirm the feasibility of the drying technology. Since Hungary does not have the technical base and hot cells for such experiments, these experiments were carried out in the Russian Federation by R&D company Sosny and research institute of atomic reactors (RIAR) in Dimitrovgrad.

The results became the basis for the basic technology for preparation of the canisters containing damaged spent fuel for transportation to Mayak (Russian Federation), for reprocessing (there is no reprocessing plant in Hungary, and the existing spent fuel interim storage facility is licensed only for normal spent fuel).

The overall process of canisters management for transportation included three key stages (shown in Fig. 136):

– Handling of the canisters at Paks;
– Transport of the canisters from Paks to Mayak;
– Reprocessing of the fuel at Mayak.

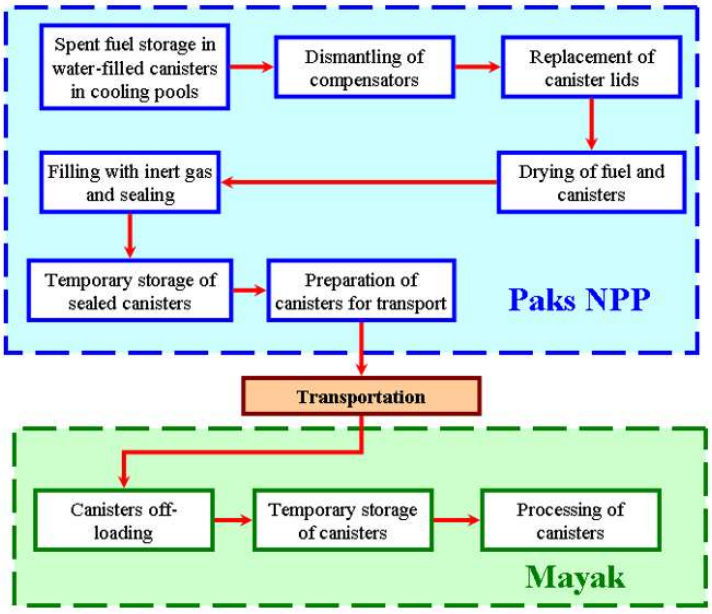


*FIG. 136. Generalized schematic of canisters management (courtesy of Paks NPP).*

The main challenge with the assurance and justification of safety of transport of wet damaged spent fuel is the need to keep the canister leak tight over an extended period. This duration includes the period during which the leak tight canisters were kept at the plant site, transported to and received at Mayak and stored at Mayak before being reprocessed.

Transport of wet damaged SNF differs from the traditional way of handling intact SNF due to the presence of radiolysis of residual water inside the canisters. Radiolysis results in an increase of pressure inside tight canisters and generation of an explosive gaseous mixture.

During development of the basic technology, analysis was carried out considering the safety requirements for the management of damaged SFAs at the reprocessing plant, and a justification was produced for transportation of failed spent fuel from the Paks site to Mayak. All key safety aspects of transport were considered: nuclear and radiation safety, structural integrity and leak tightness of the canisters, thermal conditions, explosion, and fire safety.

### 4.3.1. Choice of canister drying method

The water must be removed from the canisters before they are sealed and shipped to Mayak. Before the research activities, only one requirement from the Mayak reprocessing facility regarding the water content was known – the residual water in the canisters must not exceed 5% of the fuel mass.

The goal of the experiments was to select the best method for drying and to confirm the achievement of the sufficient level of drying.

Three water removal methods were considered:

— Water removal without additional drying, filling with inert gas and sealing of the canisters;

- Water removal, drying of spent fuel, filling with inert gas and sealing of the canisters;
- Drying of spent fuel without prior water drainage, filling with inert gas and sealing of the canisters.

Additional difficulties:

- Sixty-eight unique objects with two different geometries (unique = the content of canisters is different);
- Design of canisters (2 types), it was not possible to close canisters in a leak tight manner (new types of lids were needed).

To select the optimum technology, experimental equipment was designed and fabricated, and tests were carried out to investigate the three approaches to water removal on reduced height simulators of type 29 canisters, loaded with irradiated VVER–440 fuel, and on full scale type 28 and 29 canisters loaded with dummy spent fuel.

The experiments were carried out in a hot cell on mock-up canisters each loaded with 8.75 kg $UO_2$ fuel pellets ground to 0.1 mm < d < 2.5 mm fragments, the fuel had been soaked in 24 g/L boric acid water for 3 and 4 months.

The irradiated fuel from a VVER-440 FA with the following parameters was used for the experiments:

- Initial enrichment by $^{235}U$ (3.6% W%);
- Average burnup along FA (27.6 MWd/kgU);
- Maximum burnup along FA height (32.0 MWd/kgU);
- Total FA operation time (649.1 effective days);
- Date of discharge of FA from the reactor (18 June 1999).

Logical sequence of experiments is provided in Fig. 137.

Within the scope of experiments carried out at the level one stage, the conservative state of nuclear fuel from the point of view of radiolysis was determined for the whole spectrum of canister contents.

A test rig was created to examine the behaviour of damaged VVER–440 fuel under conditions simulating SNF storage in leak tight canisters, to perform level two experiments. Measurement of the rate of the generated hydrogen, oxygen, and gaseous fission products was carried out within the canister cavity, depending on the amount of residual water (after water removal by various methods), at ambient temperature. These results were conservative with regard to Paks NPP fuel loaded into type 28 and 29 canisters.

Based on the results of the experiments the following conclusions were made.

- Safety justification for all management stages after canister sealing and water drainage is not possible, as over six months the volumetric concentration of hydrogen in a type 29 canister, with a free cavity volume of 20 l, will reach 8.7%;
- Canister thermal vacuum drying, based on the residual pressure in the canister not exceeding 0.6 kPa, after two years of storage led to the volumetric concentration of hydrogen of <0.05% in a type 29 canister (free cavity volume 18 L), and <0.04% in a 28 canister (free cavity volume 50 L);

— The amount of hydrogen that would accumulate inside the canister over twice the storage period would be two orders of magnitude below the level of self-ignition for a oxygen–hydrogen mixture;
— For leak tightness class IV (permissible leakage up to $6.7 \times 10^{-7}$ Pa·m$^3$·s$^{-1}$), the time needed for the excessive pressure in the canister to drop is many times greater than double the duration of time from the beginning of sealing of the first and completion of processing of the last canister;
— Since there is a lack of oxygen in the canisters after sealing and thermal vacuum drying, it would not be efficient if catalysts are installed in them.

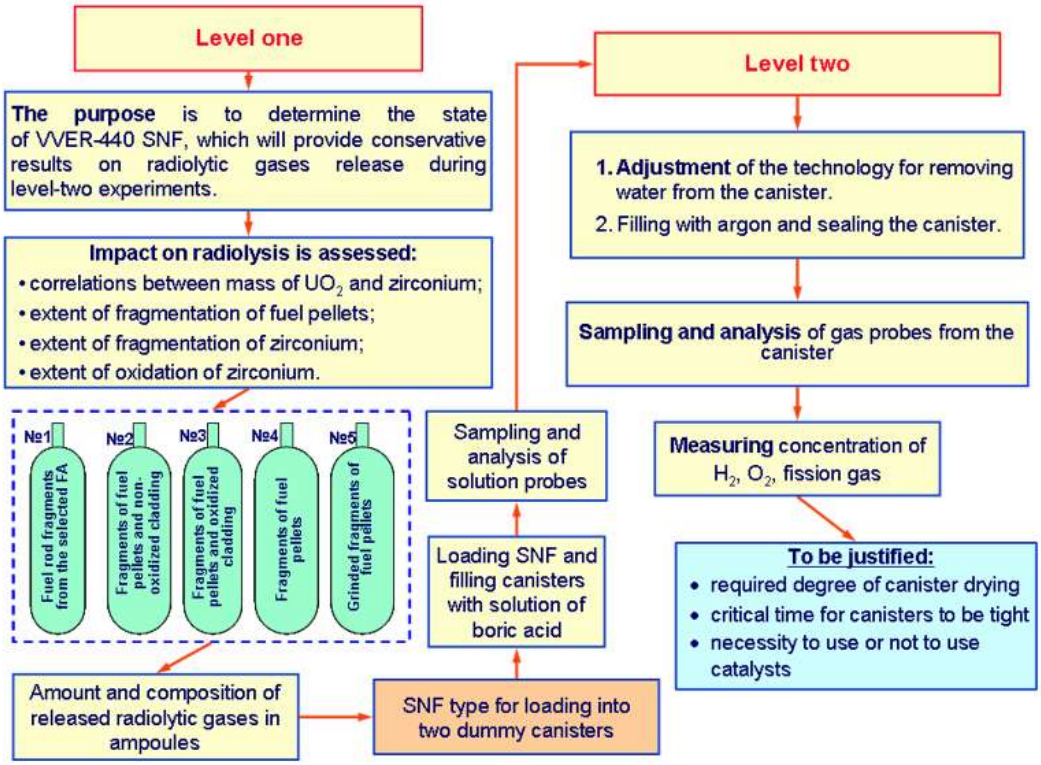


*FIG. 137. Logical sequence of experiments (courtesy of Paks NPP).*

The objectives set for the full scale experiments were:

— Selection of the drying method (drying using hot gas or thermal vacuum drying);
— Determination of the effective drying temperature;
— Examination of the effect from the presence of boric acid;
— Determination of drying time in the event of drying with drainage and without preliminary drainage;
— Determination of the method to be used for filling with noble gas.

On full scale experiments an electro–technical casting porcelain (ECP) was selected to simulate damaged SNF. The heat capacity per unit volume of ECP and $UO_2$ are close in values, i.e., the amount of heat required to heat ECP and $UO_2$, and consequently heating time are comparable. Thermal conductivity of ECP is 3 times less than the thermal conductivity of irradiated $UO_2$ that gives an opportunity to simulate $UO_2$ drying conservatively using ECP. Fuel pellet simulants fabricated using ECP are shown in Fig. 138.

*FIG. 138. Fuel pellet simulants using electro–technical casting porcelain (courtesy of Paks NPP).*

The density of ECP is lower than the density of $UO_2$ and $ZrO_2$, i.e., particles of ECP of the same size are lighter than particles of $ZrO_2$ and $UO_2$. Therefore, there will be more small particles entrained in the steam flow from the canister during drying process when compared to drying the full scale type 28 and 29 canisters.

ECP was also used for simulating damaged $ZrO_2$, since thermal conductivity of ECP and $ZrO_2$ coincide and the difference in heat capacity per unit volume of these materials is not more than 20%. For conservative simulation of drying of a spillage consisting of damaged pellets of $UO_2$ and oxidized fuel claddings, pellets from ECP were milled to the particle size <2.5 mm (Fig. 139 (a)).

To obtain ground $ZrO_2$ standard non-irradiated claddings of VVER–440 fuel rods fabricated from Zr 1%Nb alloy were oxidized in a muffle furnace at the temperature of 1000°C and then ground as shown Fig. 139 (b).

(a)

(b)

*FIG. 139. (a) Electro–technical casting porcelain with the particle size <2.5 mm. (b) Ground $ZrO_2$ (courtesy of Paks NPP).*

Based on three years of research, the option of drying fuel and its transport to a reprocessing facility in the Russian Federation became feasible and by means of these experiments it was possible to confirm that the drying of canisters can be performed without draining. The results of the R&D activities were used for designing the drying equipment, canister sealing and for licensing the process.

### 4.3.2. Technology used for drying and hermetic sealing of the canisters

The drying technology and equipment used for the removal of spent fuel from the cleaning tank were used to the maximum extent possible. Additionally, a lot of unique equipment and tools were designed and produced.

The thermal vacuum drying was carried out in pit No. 1. The drying equipment is presented in Fig. 140 (a) and b) and the shielding technological module in Fig. 140 (c).

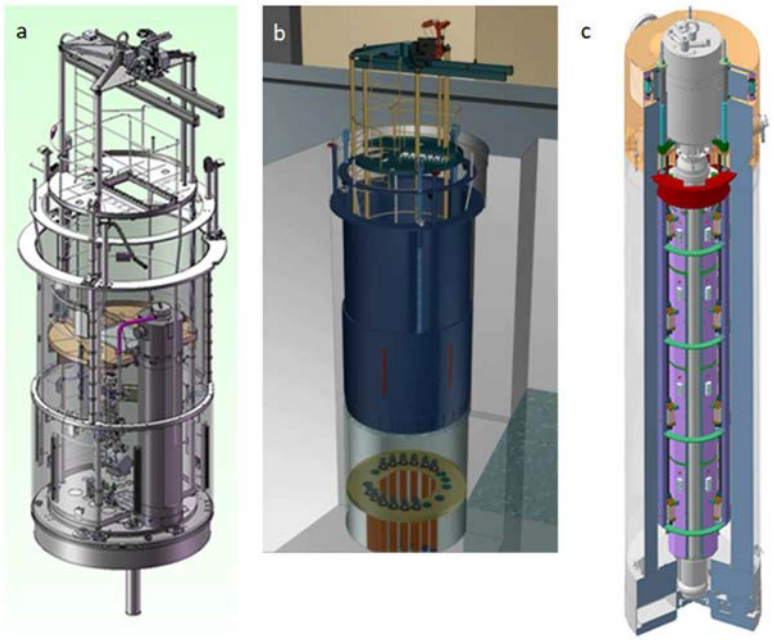


*FIG. 140. (a) Drying equipment for Paks–2 damaged fuels. (b) Pit No.1 and the drying equipment. (c) Shielding technological module (courtesy of Paks NPP).*

The main drying steps were:

- Canisters that had been stored in the spent fuel pool were transferred to the protective flange that was located beneath the working platform during drying operations. The total number of canisters that could be stored was 12;
- Canister lids were replaced with the new lids appropriate for the drying procedure, the sealing and maintaining of the canister leak tightness after drying was carried out;
- The work platform was inserted and fixed within the pit. The main equipment such as shielding technological module (STM), condensers, steam lines, condensate receiver tank had been equipped;
- One canister was lifted into the STM and secured;
- A combined filtering unit (UFK) was installed on the top of the canister. During drying the UFK had two roles: a buffer tank for water expansion within the canister and the filtration of radioactive contamination entrained in the steam. The main steam pipeline was connected to the UFK. During the drying process, the steam pipelines were heated to prevent solidification of boron;
- The water from the canister was removed by means of boiling, then the canisters were fully dried by means of a vacuum pump (the drying criteria was canister pressure $\leq$ 0.6 kPa, 573 K);
- Condensed water from condensers was collected in the condensate receiver tank;
- After the completion of thermal vacuum drying, injection of inert gases, and seal inspection, the canister was lowered onto the protective flange;
- The same operations were applied to other canisters. After completion of drying a batch of 12 canisters, the canisters were transferred to the pool;
- Transport of the canisters between the pool and pit were performed by the re-fuelling machine.

In the second half of 2013 with the assistance of Sosny all 68 canisters were successfully dried.

Transport of the canisters was carried out using a TK–6 cask that had been previously used at Paks NPP for the routine shipments of SNF, up to 1998. The transport cask was filled with nitrogen (the goal was to prevent water access to dried canisters under emergency conditions). Substantiation of safe transport was carried out in accordance with IAEA Safety Standard TS-R-1[8] [120] and domestic regulations. Licensing process of the transport means, and mode was completed in each country of concern: Russian Federation, Ukraine, and Hungary. In summer 2014 the capsules were successfully shipped to Mayak.

Through this project a full recovery of the consequences of the 2003 accident was completed.

## 4.4. EXOTHERMIC BEHAVIOUR OF DEFECTIVE URANIUM METAL FUELS AND IMPLICATIONS FOR STORAGE

Uranium metal has been used since the early days of the nuclear industry. In the UK, a number of storage facilities were built in the 1960s that now contain varying amounts, and forms, of irradiated metallic uranium. The NNL and Sellafield Limited have undertaken work to understand the potential hazards associated with the management of such materials and the conditions under which significant hazards may arise. This section describes some of the important aspects of uranium corrosion and associated exothermic hazards.

The main hazards associated with the storage and treatment of metallic uranium fuel and wastes are a result of the corrosion/oxidation reactions uranium metal undergoes with water, hydrogen, or oxygen, producing a number of corrosion products. There are four areas particularly important for understanding the rate of corrosion/oxidation of uranium metal:

- Determining the inventory of uranium metal remaining after prolonged under water storage and the inventory of corrosion/oxidation products formed;
- Assessing the thermal stability of uranium and its corrosion products, which may give rise to:
  - A pyrophoric reaction, thermal excursion or thermal transient in the uranic material;
  - Propagation of heating to other wastes;
  - Enhanced corrosion rates or ignition.
- Determining the rate of hydrogen production, which may cause a deflagration or explosion. The hydrogen arising from corrosion of metal by anoxic water or water vapour;
- Understanding the effect of the volume expansion resulting from corrosion of uranium metal on the stability of a package and consequently the waste package lifetime. This is particularly important for encapsulated uranium, e.g., in grout.

Most of the factors that influence the risk arising from these hazards are determined by the local chemical environment of the uranium, which is specific to a particular scenario. Therefore, whilst it is necessary in principle to develop technical and safety cases individually for each scenario, or group of closely related, scenarios, in practice evidence and arguments often draw on a common understanding of fundamental mechanisms that apply in similar contexts.

Figure 141 illustrates the important reactions uranium metal, and its corrosion / oxidation reaction products may undergo in the context of metallic uranium fuel handling and storage facilities; note that the stoichiometry of the reactions is not maintained in the figure. The local environment, and

[8] This publication was superseded by SSR-6 (Rev. 1) in 2020.

most importantly oxygen and hydrogen exposure to the metal, determine the dominant reaction pathways during storage and the extent of oxidation that occurs over time.

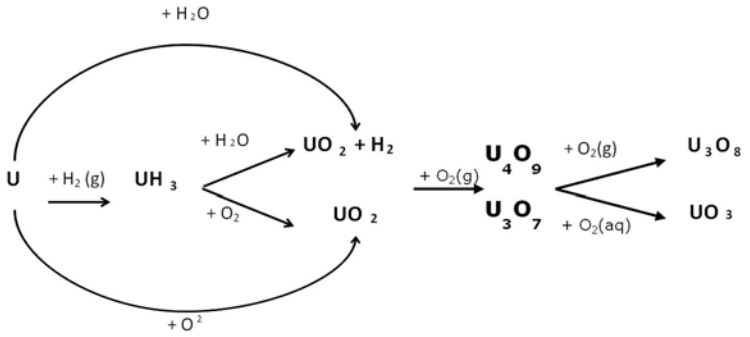


*FIG. 141. Schematic reactions of uranium metal and its reaction products with oxygen gas, hydrogen gas and water in the context of handling and storing of uranium metal at ambient pressure and temperature (courtesy of NNL).*

Thus, the main uranium corrosion products of relevance are [121]:

- Stoichiometric uranium dioxide, $UO_2$, formed by the reaction between uranium and anoxic water;
- Hyper-stoichiometric uranium dioxide, represented as $UO_{2+x}$, where *x* can be a value typically between 0.06 and 0.1 and the oxide is a mixture of $UO_2$, $U_3O_7$ and $U_4O_9$ formed by the reaction between uranium and oxygen at relatively low temperatures below ~473 K (or uranium corroded in anoxic liquid water or water vapour then exposed to oxygen at low temperatures);
- $U_3O_8$ formed by the oxidation of uranium dioxide in air at elevated temperatures above ~523 K;
- $UO_3$, formed as metaschoepite (hydrated $UO_3$), for corrosion of uranium in aerated water, or from oxidation of uranium dioxide formed during anoxic corrosion that is subsequently exposed to aerated water;
- Uranium hydride, $UH_3$, formed by the reaction between uranium and hydrogen gas or uranium and water under sealed conditions. Uranium hydride can be oxidised by water to form stoichiometric uranium dioxide and hydrogen gas [122];
- Uranium dioxide can be oxidised to higher oxides up to uranium trioxide [123].

Under aqueous conditions with a significant radiation field from spent fuel additional oxidation reactions are possible due to reaction with water radiolysis products, principally hydrogen peroxide, that perturb the solution chemistry and lead to the formation of a range of uranium hydroxy and peroxy minerals which have low solubility and generally form as precipitates.

Not all the corrosion products of uranium are of great interest during waste processing and decommissioning, those that are, are generally the more reactive species:

- Uranium metal, primarily due to hydrogen production during corrosion, expansion associated with corrosion when encapsulated and generation of reactive corrosion products;
- Uranium hydride, primarily due to its potentially pyrophoric behaviour and particulate release. Other metallic uranium derived waste materials, such as stoichiometric uranium dioxide or higher oxides of uranium, are of lesser concern due to their lower reactivity and lower heats of reaction;

- Uranium oxides, the potential for self-heating in air is limited to stoichiometric uranium dioxide, which is considerably less energetic than uranium hydride. Stoichiometric uranium dioxide oxidises readily to marginally higher oxides which are much more stable. Therefore, in many operational situations, uranium oxides do not pose a significant hazard but may contribute to aerial activity release or dispersion of colloidal uranium oxide in under water storage;
- Sub-stoichiometric uranium dioxide is sometimes suggested as a potentially self-heating material. The conditions required for the formation of sub-stoichiometric uranium dioxide are extreme; requiring very high temperatures that are not relevant during storage of metallic uranium fuel and associated wastes. Formation of $UO_{2-x}$ during corrosion in oxygen or water appears unlikely since $UO_{2-x}$ would be expected to continue to oxidise to uranium dioxide during the initial oxidation phase, rather than stop an intermediate stoichiometry before further oxidation at a change of environment. For example, oxidation is observed when uranium dioxide surfaces are ion sputtered to create oxygen vacancies, and therefore reduced uranium sites equivalent to $UO_{2-x}$, are subsequently exposed to water vapour [121, 122]. Therefore, sub-stoichiometric uranium dioxide is not considered a significant cause for concern for management of stored irradiated uranium fuels and residues.

### 4.4.1. Uranium corrosion rate

Environmental factors having most influence on the corrosion rate metallic uranium and derived corrosion products [124]:

- Temperature, the corrosion rate of uranium increases with increasing temperature;
- Presence of oxygen (oxic conditions), the corrosion rate is much lower when oxygen is present, i.e., under oxic conditions;
- Water vapour pressure, the corrosion rate increases with an increase in water vapour pressure.

Other less important factors include:

- Oxide layer, the presence of a thin adherent oxide layer reduces the corrosion rate compared with bare metal by acting as a diffusion barrier for oxidising species, however this forms very rapidly compared with practical storage times and most practical measurements of the corrosion rate are made after this adherent layer has formed. In the long term, the accumulation of corrosion products offers no further protection as it is highly porous. Certainly, consideration of the initial formation of the oxide layer on the metal is not required in assessments of metallic uranium derived waste originating from long term storage;
- Water content of the grout, there is apparently a slight reduction in the corrosion rate of encapsulated uranium versus corrosion in water;
- pH, a rapid increase in the corrosion rate of uranium is observed in pH range between 1 and 3, then pH does not show a significant effect, until a pH reaches a range between 7 and 14 where a small decrease in the corrosion rate is observed.

Corrosion data for uranium metal shows considerable variability. The scatter of the experimental data is illustrated by Fig. 142, which shows a plot of corrosion rate constant for uranium metal in anoxic water vapour.

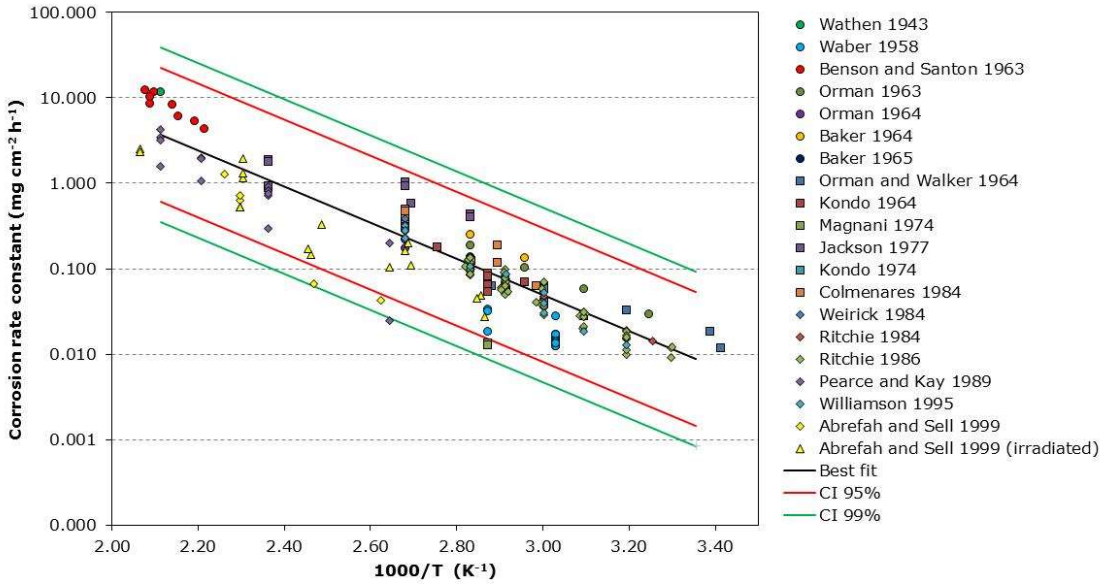


*FIG. 142. Linear regression fit for uranium oxidation rate in anoxic water vapour (adapted from [125-137], courtesy of NNL).*

Potential sources of variability in the experimental results arise from:

- Errors in experimental measurements of the corrosion rate or surface area of uranium samples;
- Variability in the local environment (or poor control of conditions) in the experiments, both chemical environment and temperature;
- Variability in the uranium composition or microstructure used in the various studies.

The corrosion rate of any piece of uranium selected at random could deviate significantly from the mean rate suggested by the linear regression of the experimental data. In principle, the calculated confidence limits from experimental data can be used to estimate this variation assuming a log−normal distribution about the line of best fit in the Arrhenius plot. Following the argument further, where a very large number of uranium pieces are corroding, the average of the logarithm of the corrosion rate $ln\,\overline{k(T)}$ of the uranium pieces will be close to the mean rate determined using linear regression of the experimental data population.

The values of $\overline{ln\,k(T)}$ and $ln\,\overline{k(T)}$ (mean of the corrosion rate) for a log–normal distribution are not equal, the latter being somewhat larger. This difference can be accounted for using the logarithmic transformation shown in Eq. (1). This equation can be used to estimate the average corrosion rate of a large number of uranium items.

$$ln\ \overline{k(T)} = \overline{ln\,k(T)} + \tfrac{1}{2}\,\sigma^2_{ln\,k(T)} \qquad (1)$$

When a small number of uranium items are being considered the deviation from the true mean rate could be large and a stochastic modelling approach can usefully be used to predict the extent of corrosion of finite number of uranium items assumed to possess a distribution of corrosion rates.

The conclusions that uranium items possess a distribution of corrosion rates has the practical consequence that initially the corrosion rate of any individual uranium piece will fall within a wide range, with faster corroding pieces of uranium reaching complete corrosion before slower corroding pieces. This results in the average rate of corrosion reducing with time as the faster corroding pieces in the distribution become completely corroded.

Another important question to address is whether the best fit and $\frac{1}{2}\sigma^2$ calculated from Arrhenius plots of the collated literature data are representative for any particular uranium alloy. Important points to note are:

- Literature data are derived from a wide variety of sources, sometimes with little or no information on the uranium composition, and there is comparatively little data for specific uranium alloys, that may be used in specific reactor types. Therefore, it may not be possible to determine whether there is a systematic difference between alloy specific rates and the general population of literature data;
- There is potential for bias when calculating the best fit line from literature data using unweighted linear least squares regression because:
  - In datasets where there isn't a uniform distribution of data as a function of temperature the best fit may be biased by a small number of data points in the sparsely populated regions;
  - Fits may be biased by studies that reported a large number of measurements for a particular source of uranium because uniform weighting of data points is assumed.

From the available data it is not possible to give a definitive answer to how significant these effects might be, so the impact of this uncertainty needs to be considered, and suitable sensitivity analyses carried out to assess the potential effect of changes in the corrosion rate and standard deviation. If possible, a representative sample should be taken, or observations made of the waste to confirm and support the predictions of modelling before extrapolating models.

Finally, it is important to recognise that the rate of corrosion of uranium may be perceived to decrease with time as a smaller mass of the corrosion product is formed per unit time. With time the surface area of uranium metal available for oxidation decreases, and thus the mass of the corrosion product formed per unit time will decrease for any piece of uranium and eventually it will become of low significance. However, the corrosion rate does not change, and it remains constant. This is applicable to both corrosion of uranium metal corroding in under water storage (e.g., pool) or silo storage and in the immobilised form.

There are many sources of data on corrosion rates for uranium metal. When using these rates in technical assessments the discussion of uncertainties in the data should be carefully considered and fitting of data in the range of most relevance for the particular application may be prudent.

### 4.4.2. Uranium hydride formation

The important conclusions of experimental studies of uranium corrosion chemistry are summarised below:

- Uranium hydride formation from the reaction between uranium metal and hydrogen gas has an induction period, followed by a non–linear period of increasing rate, before the bulk hydriding reaction occurs. The duration of this induction stage is increased by the presence of water vapour and oxygen but cannot be predicted with any accuracy for a given water vapour and oxygen pressure. Furthermore, it is currently not possible to underpin a limiting water vapour and/or oxygen pressure that will prevent the formation of uranium hydride. Consequently:
  - The potential for uranium hydride formation must be considered to occur in any environment where uranium is exposed to a hydrogen gas partial pressure;
  - Technical assessments cannot assume that a specific induction period occurs or exposure to water vapour and/or oxygen prevents uranium hydride formation.

- The potential for bulk uranium hydride formation cannot be ruled out under conditions where uranium metal is exposed to a stable hydrogen partial pressure. However, the resulting uranium hydride may not be stable and may not persist for a long period of time, therefore does not necessarily pose a self–heating hazard;
- Uranium hydride may also form at the metal–oxide interface during corrosion of uranium in water. In open storage, it presents a small fraction of the corrosion products and is not considered to pose a self–heating hazard, however in sealed conditions a stable hydrogen over pressure may be established that can lead to formation of larger quantities of hydride. Once formed, hydrolysis of such hydride is expected to occur;
- Uranium hydride formation will be inhibited by oxygen and water vapour, delaying the onset of bulk hydriding, but it is not possible to define an accurate timescale or bounding water/oxygen concentration to prevent uranium hydride formation;
- For uranium hydride to remain present in a waste for extended periods would require limited exposure to oxygen or water, which will oxidise the uranium hydride.

Hydrogen gas required for the formation of bulk quantities of uranium hydride can be produced from the reaction of the uranium metal with water, uranium hydride with water or water with another waste material such as Magnox. In regions where hydrogen is present with little water or oxygen to oxidise any uranium hydride formed then significant accumulations of uranium hydride are able to form and persist.

In the experiments by Baker et al., uranium waste was sealed with water vapour inside a glass vessel and the quantity of uranium hydride remaining in the corrosion product at the time of analysis (based on hydrogen release during thermal decomposition) was typically low, between 2 and 9 wt% of the corrosion products, and was dependant on the relative humidity and temperature during aqueous corrosion of uranium metal [125, 138]. Historically these values were often quoted in industry documents when describing the proportion of uranium hydride found in the corrosion products of uranium, which was then assumed to be pyrophoric even for aqueous corrosion. This is not the correct general interpretation and conclusion to make from these experiments. It is quite possible that the uranium hydride was a consequence of an accumulation of hydrogen in the vessel that reacted with the metal, rather than direct formation as part of the water corrosion mechanism. For example, in other experiments where the gas was continually vented uranium hydride has not been observed. The latest study [139] using atom probe tomography to analyse the oxide layer on uranium corroded in anoxic water vapour appears to provide conclusive evidence for the hydride layer to be present (between 3 nm and 5 nm thick) and evidence that it forms from $OH^-$ reacting at the metal surface. However, this would not account for percent quantities of uranium hydride in the corrosion products observed by Baker et al.

From a practical point of view the formation of uranium hydride during water corrosion, in the absence of hydrogen accumulation in contact with the metal, should be recognised in assessments of potential uranium hydride formation. However, the potential impact on, for example, the self–heating behaviour of corrosion products is expected to be minimal given its level of dispersion within corrosion products and degree of oxidation from exposure to water.

From the above arguments it can be seen that, the main corrosion product of long stored uranium metal in pond water can be expected to be stoichiometric uranium dioxide, or hyper–stoichiometric $UO_2/UO_3$ depending on the extent of oxygen ingress. Uranium hydride formation will not be widespread within storage facilities, as it only forms under specific conditions that favour the uranium metal–hydrogen reaction.

### 4.4.3. Thermal hazards

Exothermic reactions of uranium and related compounds can lead to a range of behaviours, which can be described by five related terms; two of which describe general behaviours, i.e., self–heating and ignition whilst three describe relatively specific transients, i.e., pyrophoricity, thermal excursion, and thermal transient. The relationship between these five terms is summarised in Fig. 143, and the qualitative temperature vs. time dependence is described graphically in Fig. 144.

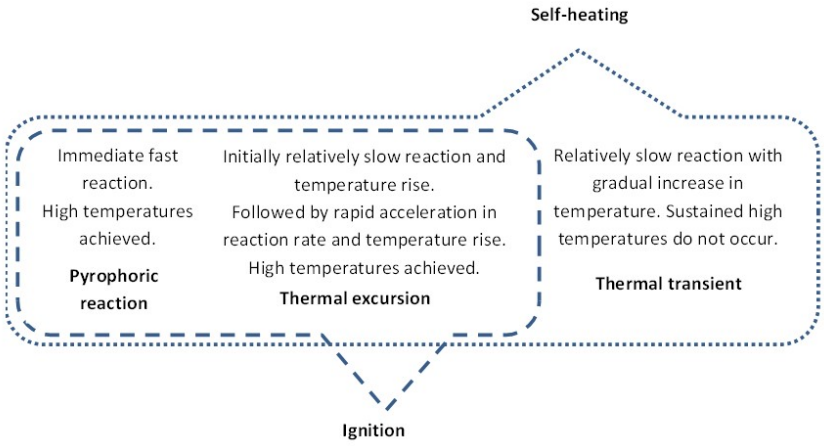


*FIG. 143. Summary and interrelationship between self–heating terms (reproduced from Ref. [140] with permission courtesy of Nuclear Waste Services (NWS)).*

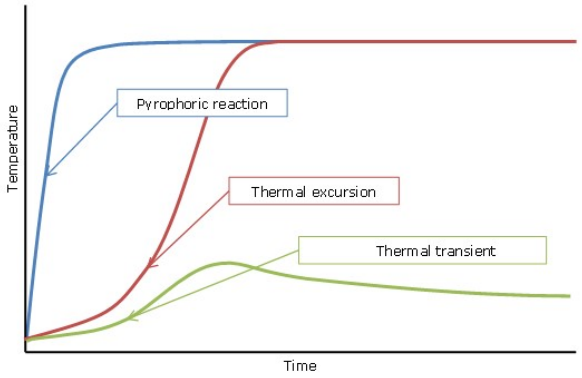


*FIG. 144. Schematic graph showing the difference in relationship between temperature and time depending on the nature of an event. In all cases the temperature would eventually decay as uranium (or oxidant) was consumed (reproduced from Ref. [140] with permission courtesy of NWS).*

#### *4.4.3.1. Self–heating*

Fundamentally, self–heating results from an in balance between heat generation and heat loss. For reacting uranium materials this heating is generally dominated by the exothermic reaction of the material[9] where the material bulk temperature increases without the application of an external heat source. Self–heating doesn't inherently imply anything about the magnitude or timescale of heating.

[9] In general, radiogenic heating is of lesser importance as it is very low for long cooled, low burn-up fuels and because the heat generation rate is independent of the temperature, unlike chemical reactions which generally become more rapid as the temperature increases.

The extent of heating depends upon the mass and distribution of the reacting substance, the nature of the surrounding materials and the temperature of the environment. This process might lead to the emission of light and result in ignition. Subsets of self–heating include ignition (either as a result of a pyrophoric reaction or a thermal excursion) and thermal transients, which reflect differences in the peak temperatures and rate of change of temperature.

*4.4.3.2. Thermal transient*

The heating generated by an exothermic reaction is referred to as a thermal transient when the heating results in a relatively small rise in the material bulk temperature, which is too low to ignite the material, and tails off as the reactants are consumed. Thermal runaway does not occur because the rate of reaction is either too slow[10], the quantity of reactant is inadequate, or the reactant is consumed before a thermal runaway is established.

*4.4.3.3. Ignition*

The onset of a rapid temperature rise is referred to as ignition. Ignition occurs when the rate of heat generated by an exothermic reaction far exceeds the rate heat is transferred to its surroundings. The nett difference between generation and loss drives the thermal runaway, in which the rate of reaction increases sharply until the supply of one of the reactants, either material being oxidised or oxidant, prevents the reaction rate increasing further. At this point, the material is considered to be burning.

Material ignition is caused when its thermal equilibrium is changed to one where there is a rapid increase in net heat generation. Initiating events include:

- Removing a large heat sink (e.g., water);
- Change of atmosphere from inert to oxidative, for example exposure to oxygen;
- Introducing an external heat source (e.g., sparks);
- Changing the geometry of the materials in such a way as to reduce the amount of heat that than can be transferred to the surroundings;
- A rise in the temperature of the material's surroundings.

Ignition can involve more than one exothermic reaction mechanism, operating together or in sequence.

Ignition can be differentiated by different rates of changes, e.g. as thermal excursion or pyrophoric ignition. Drawing a distinction between the two cases is useful as the ability to control and respond to the scenarios are quite different. Typically, different materials are also involved. The cases are described in the following sections.

*4.4.3.4. Thermal excursion*

A thermal excursion starts with a relatively slow rate of reaction, often at ambient temperature, which generates a slow rise in temperature. This rate of rise will gradually increase as the temperature rises until thermal runaway occurs. The difference between the temperature dependence of heat generated by oxidation and the level and rate of change of heat dissipation controls whether a thermal excursion occurs and, if so, at what temperature it occurs. The delay between the start of an exothermic reaction

[10] Or, conversely, the heat removal mechanisms are highly effective.

and initiation of a thermal runaway can be considerable. It will not, however, affect the maximum rate of reaction as this is controlled by the supply of oxidant.

*4.4.3.5. Pyrophoricity*

A material that ignites immediately when exposed to air is called pyrophoric. Unlike a thermal excursion, there is no period of relatively slow temperature rise before ignition. Pyrophoricity depends mainly upon the materials surface area to mass ratio, not the fundamental properties of the material. Other factors that can influence this include:

- Amount of material;
- Spatial distribution;
- Surrounding materials;
- Ambient temperature.

For example, uranium hydride may or may not exhibit pyrophoric behaviour depending on the factors outlined above, furthermore partial oxidation of the hydride may avoid or delay otherwise pyrophoric behaviour. It should be noted that some materials do not display pyrophoric characteristics under any conditions, e.g. aluminium oxide. It should, therefore, be clear that simply saying that "uranium hydride is pyrophoric" is incorrect.

In some documents pyrophoric materials are also defined as those that spark on scratching, however, this is not part of the definition used here.

*4.4.3.6. Self–heating of metallic uranium derived materials*

Self–heating of metallic uranium derived materials occurs as a result of heat being generated by radioactive decay, oxidation reactions, heat from other processes in the surroundings, and poor dissipation of this heat to the surroundings. The oxidant of concern for self–heating is usually oxygen in the air, but liquid water or water vapour can also be important oxidants. The degree of self–heating, with the outcome ranging from a thermal transient through to pyrophoric behaviour, depends on the heat balance of heat production form oxidation and dissipation to the surroundings that in turn depends on the:

- Exact chemical reaction which defines the heat release and the dependence of the rate of heat generation on the temperature;
- Effect of the heat generation on the waste, e.g., water loss, phase changes, etc.;
- Heat capacity and thermal conductivity of the materials;
- Spatial arrangement of the material and loss of heat to the environment;
- Ambient temperature.

The main hazards resulting from the self-heating event are heat/burning, activity release and hydrogen gas generation. All of these may also be affected by propagation of the self–heating to adjacent waste material such as Magnox metal.

*4.4.3.7. Heat generation*

The dynamic self–heating of metallic uranium and derived waste arises mainly from exothermic oxidation reactions of uranium, uranium dioxide, and uranium hydride. Table 19 summaries the heat generated per gram of metallic uranium derived waste being oxidised.

Self–heating depends on the energy released by reactions, and the rates of reactions. The latter depends on the reaction rate and specific surface area of the material. The high specific surface area of uranium hydride makes it prone to self–heating, whereas the low specific surface area of bulk uranium make ignition and sustained burning very unlikely at ambient temperatures. In the case of uranium dioxide formed from metal corrosion, it has a very high surface area, but the oxidation reaction produces much less heat than uranium/uranium hydride and it, therefore, poses a much lower potential for self–heating than uranium hydride.

*4.4.3.8. Self–heating and ignition of uranium hydride*

Uranium hydride can show a wide range of self–heating behaviour when exposed to air. It can:

- Ignite as a pyrophoric reaction upon immediate exposure to air;
- Initially appear stable but ignite at a later time through a thermal excursion;
- Initially appear stable but ignition could be triggered by mechanical disturbance, spark ignition[11] or another local heat source;
- Remain stable for an extended period of time.

Measurements of the reaction rate of uranium under isothermal conditions have allowed an understanding of the origin of these different behaviours.

TABLE 19. ENTHALPY OF REACTION FOR OXIDATION OF METALLIC URANIUM DERIVED WASTE MATERIALS OF INTEREST (based on data from [121])

| Material | Reaction | Heat of reaction (kJ/g (uranic material)) |
|---|---|---|
| Uranium metal | $U(s) + O_2(g) \rightarrow UO_2(s)$ | -4.558 |
| | $U(s) + 2H_2O(g) \rightarrow UO_2(s) + 2H_2(g)$ | -2.527 |
| | $U(s) + 2H_2O(l) \rightarrow UO_2(s) + 2H_2(g)$ | -2.157 |
| Uranium dioxide | $3UO_2(s) + O_2(g) \rightarrow U_3O_8(s)$ | -0.395 |
| Uranium hydride | $2UH_3(s) + 2O_2(g) \rightarrow 2UO_2(s) + 3H_2(g)$ | -3.973 |
| | $2UH_3(s) + 4H_2O(g) \rightarrow 2UO_2(s) + 7H_2(g)$ | -1.967 |
| | $2UH_3(s) + 4H_2O(l) \rightarrow 2UO_2(s) + 7H_2(g)$ | -1.602 |

*4.4.3.9. Reactivity of uranium hydride in air, oxygen, and water*

Uranium hydride shows different oxidation behaviour for the reaction with oxygen/air, liquid water or water vapour; that is, whether ignition or thermal runaway occurs, and different burning kinetics are observed. However, the observed behaviour can be understood in terms of the reaction kinetics of uranium hydride as a function of oxidation extent.

The reaction kinetics of uranium hydride with liquid water and water vapour have been investigated in some detail under controlled isothermal conditions and therefore without thermal runaway [141—146]. The observations from these studies illustrate the main characteristics that determine the overall reaction behaviour in different scenarios.

[11] Spark ignition is defined as an ignition caused by a small hot particle or electrical discharge through a gaseous atmosphere.

The oxidation rate of uranium hydride with water under isothermal conditions exhibits three distinct kinetic regions:

- Initial phase characterised by a rapid oxidation rate that rapidly decreases with oxidation extent;
- Intermediate phase characterised by a steady decrease in the oxidation rate;
- Final phase with the oxidation rate close or below the limit of detection. During this stage the reaction progresses very slowly until either the uranium hydride or the oxidising species is completely reacted.

The change in the oxidation kinetics of uranium hydride is illustrated schematically in Fig. 145.

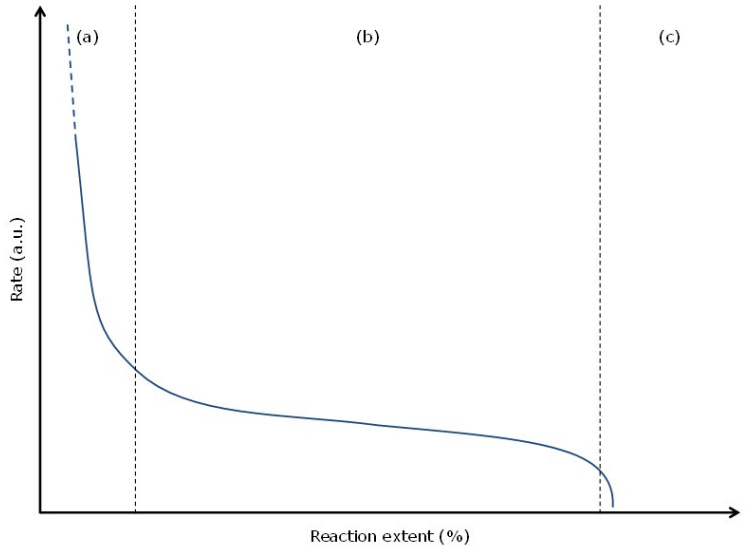


*FIG. 145. Schematic illustration of the uranium hydride oxidation (a) initial phase, (b) intermediate phase, and (c) final phase (reproduced from Ref. [140] with permission courtesy of NWS).*

During the rapid phase the uranium hydride initially reacts as fast as oxidant reaches the surface, causing rapid heat generation. The rate decreases due to the formation of a surface oxide layer on each particle of uranium hydride that produces a barrier to further oxygen ingress. Thus, there is a transition from the reaction rate being limited by the supply of oxidant, to being limited by oxidant diffusion through the oxide layer. This results in a decreasing reaction rate with oxidation extent. Interestingly the reaction rate appears to decrease to a very low value before complete oxidation is approached (70% to 90% reaction extent); the cause of this behaviour is not well understood. As expected, the oxidation rate increases with temperature [141].

A further interesting observation is that uranium hydride formed at a lower temperature (below 353 K), which contains a larger fraction of α–$UH_3$ compared to the thermodynamically more stable of β–$UH_3$, shows a higher oxidation rate than uranium hydride formed at a higher temperature. This has implications for the persistence of uranium hydride formed under waste storage conditions.

The kinetics of the reaction between uranium hydride and oxygen has been investigated in less detail. However, the general features of the kinetics are believed to be similar.

The consequences of this variation of reaction rate with extent of oxidation are that the uranium hydride that has not had prior exposure to oxidant is much more reactive, and therefore more prone to ignition or thermal excursions. After partial oxidation the reaction rate is much reduced, and

therefore the rate of heat generation is much reduced and the propensity for ignition or thermal runaway is reduced. However, a large amount of hydride can remain present at the core of each particle and ignition can still be triggered by:

- A thermal excursion;
- Local heating from spark ignition;
- Local heating from a small amount of residual unoxidized uranium hydride or another localised heat source;
- Mechanical disturbance.

These mechanisms are discussed further below.

*4.4.3.10. Active uranium hydride and surface oxidised uranium hydride*

As uranium hydride oxidises the rate of reaction decreases rapidly, it is therefore, useful to differentiate between oxidised and unoxidized material.

Uranium hydride that has previously been partly oxidized is commonly referred to as ‘passivated’, whereas unoxidized uranium hydride is often referred to as ‘pyrophoric’. This terminology can be misleading as it can lead to an assumption that uranium hydride that is ‘passivated’ is stable and would not ignite. Experience from numerous laboratory studies and events during processing operations has, however, shown that this not to be the case. The term ‘passivated uranium hydride’ is, therefore, no longer recommended.

The following definitions of ‘active uranium hydride’ and ‘surface oxidised uranium hydride', were developed to distinguish key stages in the evolution of uranium hydride properties [147].

Active uranium hydride is uranium hydride that has experienced minimal oxidation and is in a condition where the oxidation kinetics are very rapid. The rapid reaction rate means it will immediately undergo an oxidation reaction on exposure to air or oxygen, resulting in uranium oxides, heat, and hydrogen gas. The exact stoichiometry of the oxidation products depends on the temperature and oxidants. Pyrophoric behaviour is normally occurring in air and violent reaction occurs in water unless limited amounts of materials are involved. Where there are no oxidants present to react with the uranium hydride, active uranium hydride is expected to persist.

Surface oxidised uranium hydride is defined as uranium hydride that has undergone some degree of oxidation and formed a surface oxide layer. This form of uranium hydride may still self–heat on exposure to air, oxygen, or water but, exhibits significantly decreased reactivity when compared to active uranium hydride. Surface oxidised uranium hydride, therefore, may exhibit gradual self-heating rather than pyrophoric ignition in most conditions. External heating or mechanical disturbance could, however, lead to ignition of this type of material.

In practice the definitions are qualitative describing the different possible types of uranium hydride behaviour that can occur in waste streams, rather than a quantitative classification based on the extent of a specific reaction. This is partly due to ignition being dependent on other factors (such as geometry, total mass of uranium hydride, ambient temperature, etc.) and not just the reaction rate. Importantly, predicting whether uranium hydride has formed, and the extent of subsequent oxidation, cannot be done with any accuracy because the wastes history and the environments it has been exposed to are often unknown. In such cases, it is only credible to identify whether there was potential for uranium hydride to form and not whether it will occur in all cases. Assessment, therefore, must consider whether:

- Uranium hydride formation is possible;
- Oxidation can be guaranteed to ensure that all uranium hydrides are partially oxidised to the surface oxidised state or the final phase, which has a very low oxidation rate under all conditions. This must be based on conservative but reasonable assumptions about the storage environment.

*4.4.3.11. Pyrophoric ignition of uranium hydride*

The conditions that promote a pyrophoric reaction of uranium hydride most importantly include:

- A large surface area to volume ratio of active uranium hydride particles;
- A rapid[12] introduction of an ongoing supply of an oxygen or air;
- The presence of active uranium hydride as the major fraction of the total amount of uranium hydride present.

It is important to recognise that the effect of individual oxidising conditions is heavily influenced by the relative amount and rate of supply of an oxidant. For example, low concentrations of oxygen (for example low percent oxygen in an inert gas) in a controlled supply would limit the rate of oxidation of uranium hydride to levels that prevent generation of a large amount of heat, and consequently uranium hydride does not ignite. Instead, controlled self-heating can be achieved.

In general:

- Air, as it contains a relatively high concentration of oxygen gas (20.95%) will trigger a pyrophoric reaction for active uranium hydride;
- Oxygen gas in argon or other inert gas, will trigger a pyrophoric reaction of uranium hydride if the amount of oxygen is sufficient to sustain a significant burn rate. The onset of ignition and burn rate can therefore be controlled by limiting the supply of oxygen. The supply of oxygen depends on both the flow rate, which determines the boundary layer thickness at the surface of the powder, and the concentration of oxygen. A simple threshold level to prevent ignition cannot be specified from available experimental data.

Experiments by Hawes [148] studied the ignition of uranium hydride in static reduced oxygen atmospheres and observed that:

- A static inert gas blanket of nitrogen with less than 2% oxygen prevented pyrophoric ignition of uranium hydride;
- Layers of dry uranium hydride powder did not ignite in an atmosphere of argon containing oxygen below 5%. It was noted that significant oxidation occurred, but the resulting temperature rise was insufficient for visual recognition of an ignition.

Small additions of water to active uranium hydride may cause what appears to be a pyrophoric ignition (strictly hypergolic ignition since the reaction is not with air); for example, Fig. 146. Here, the amount of water is too small to act as an effective heat sink and allows transient burning to occur (before the water reacts and probably largely evaporates and the reaction ceases). The large volume of gas generated is notable and contributes to the significant dispersal of powder.

[12] Rapid is taken to mean conditions where the supply is not restricted or controlled to prevent substantial heating, it should not be taken to mean that ignition requires rapid exposure to air.

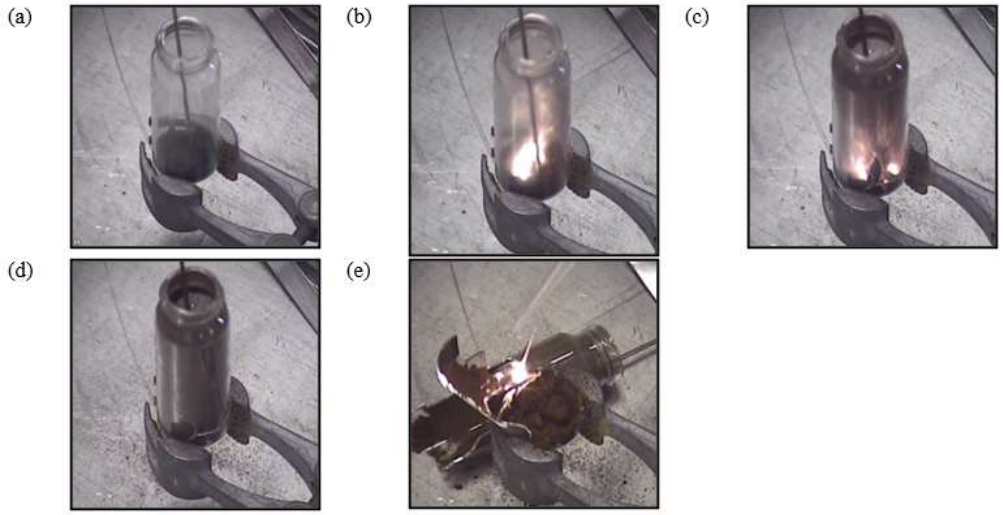


*FIG. 146. Subsequent stages of reaction of ~1 g of uranium hydride with a small number of water droplets under an argon atmosphere, starting from (a) addition of water to uranium hydride to (e) an end result of the reaction (courtesy of NNL).*

*4.4.3.12. Ignition of uranium hydride through a thermal excursion*

Uranium hydride that does not react with pyrophoric ignition on exposure to air, typically seen for surface oxidised uranium hydride, may still ignite through a thermal excursion due to the heat from oxidation exceeding the dissipation of heat to the surrounding. This is dependent on the:

- Amount of uranium hydride present;
- Presence of other materials that can either act as diluents or be combustible;
- Thermal conductivity of the materials in the vicinity;
- Heat dispersion capabilities of the given environment;
- Availability and concentration of oxygen.

Therefore, it is not possible to describe simple generic bounding conditions for a safe mass of hydride or a safe time in air that can be used to define process operations. However, it may be possible to use thermal modelling to understand the potential for thermal excursions to occur if appropriate assumptions about mass transfer of oxidant and the surrounding environment are made.

Water will oxidise active uranium hydride to surface oxidised uranium hydride and, with time, to uranium dioxide. A water reaction can lead to a thermal excursion. As mentioned above, a vigorous reaction is possible with water, similar to the pyrophoric reaction in air, if relatively small volumes of water are added quickly to the active uranium hydride or a relatively large volume of active uranium hydride is added to water. This is because the supply of oxidant is rapid yet the heat dissipation by thermal conduction and convection in the water is limited. In contrast, a small mass of uranium hydride added to a large volume of water shows little reaction. For example:

- A small quantity of uranium hydride can be added to a large quantity of water without large amounts of heat generation taking place, even for uranium hydride with no prior oxidation. This is because the water acts a heat sink, preventing a sustained temperature rise during the initial very rapid reaction of the uranium hydride such that the intermediate phase is reached without self–heating;

- A large quantity of uranium hydride added to a comparable amount of water (i.e., a similar bulk volume) all at once could cause a very rapid oxidation reaction accompanied by sudden heat and hydrogen gas (and steam) generation, causing uranium hydride to glow red hot and dispersing material. In this situation the initial rapid reaction releases heat that is not effectively dissipated to the surroundings leading to thermal runaway;
- At the other extreme, the slow addition of very small quantities of water to a large amount of uranium hydride can be safely performed without large bulk heating. In this case, the slow addition of water allows for the dissipation of heat to the surroundings so that significant self-heating does not occur.

Whilst a qualitative description can be given for the likely behaviour of uranium hydride in contact with water it is not possible to provide quantitative guidance on the threshold ratios of water to hydride and rates of addition that would determine the behaviour observed because no experimental studies have been undertaken. Arguments are based on qualitative observations [148], anecdotal observations and reasonable argument.

*4.4.3.13. Ignition due to a localised heat source (spark or active uranium hydride)*

A localised heat source, such as a spark or ignition or a small amount of active uranium hydride, may be sufficient to cause ignition of nearby surrounding surface oxidised uranium hydride that was otherwise stable with respect to ignition. Once even a small fraction has ignited it could propagate to the remaining surface oxidised uranium hydride. Consequently, the potential for even a small fraction of active uranium hydride to remain present must be considered in assessments.

*4.4.3.14. Ignition of uranium hydride due to mechanical disturbance*

The consequences of mechanical disturbance of uranium hydride can depend on whether the material consists of only active or surface passivated material or whether there is a mixture of active and surface oxidised uranium hydrides. Where an accumulation of uranium hydride has had a limited exposure to oxidate it is important to distinguish between a bulk layer of oxidised uranium hydride surrounding the external surface of an accumulation of active uranium hydride and surface oxidation of all uranium hydride particles in the accumulated hydride.

As well as the above definitions of active and surface oxidised, a distinction should also be drawn between the accumulations of/with:

- Corrosion products containing only surface oxidised uranium hydride;
- Active and intimately mixed surface oxidised uranium hydride;
- A layer of surface oxidised uranium hydride forming a barrier around a core of active uranium hydride.

These cases are illustrated in Fig. 147 for clarity.

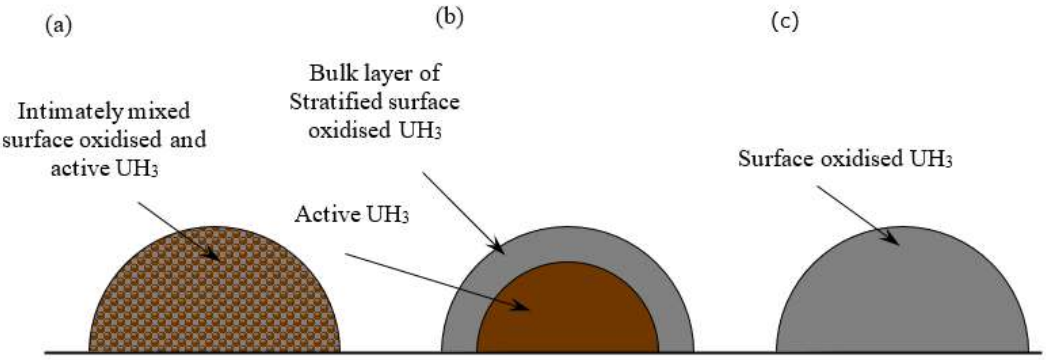


*FIG. 147. Potential distributions of active and surface oxidised uranium hydride: (a) accumulation of intimately mixed surface oxidised and active uranium hydride, (b) accumulation of uranium hydride with a stratified surface oxidised uranium hydride surface layer and core of active uranium hydride and (c) accumulation of surface oxidised uranium hydride (reproduced from Ref. [140] with permission courtesy of NWS).*

Generally:

- Surface oxidised uranium hydride which is intimately mixed with active uranium hydride is expected to ignite in air, without mechanical disturbance;
- A stratified surface oxidised uranium hydride layer and a core of active uranium hydride particles will only undergo a thermal excursion if the oxide covering is disturbed, and the active uranium hydride is exposed to air. In such an event vigorous disturbance of the uranium hydride would not be required, just disturbance of the powder bed;
- Surface oxidised uranium hydride may ignite if is aggressively disturbed. Based on practical laboratory experience this required mechanical grinding. Breakdown of the surface oxide layer on particles is believed to lead to local rapid reactions and heating. Frictional heating or static discharge, however, may also influence this process. A precise description of the conditions under which rapid oxidation occurs cannot be made with current information.

*4.4.3.15. Burning behaviour of uranium hydride*

Following ignition in air, uranium hydride glows red hot, and, under quiescent dry conditions, it is a relatively gentle reaction appearing similar to burning charcoal. This arises from the burning being limited by the supply of oxidant to the powder bed. More vigorous reactions can take place if a disturbance that disperses the powder or another event results in a large proportion of the uranium hydride being suddenly exposed to oxidant; an example being the addition of water (Fig. 148).

*4.4.3.16. Ignition of uranium metal*

Bulk uranium metal does not readily ignite and sustain burning and in practice bulk uranium is generally difficult to ignite from a localised source, owing to conduction of heat away from the source [147]. Ignition of uranium metal and sustained burning requires a high ambient temperature (> 573 K) and a constant supply of oxidant. Ignition is also favoured by the material having a high specific surface area, for example in porous uranium.

Assessments will need to consider the form and mass of the uranium metal including its porosity, the form and mass of the ignition source, the ambient temperature and the concentration of oxygen and its rate of supply.

*FIG. 148. Burning of 100 g uranium hydride in air with water dripped from above at 7.5 ml/min (courtesy of NNL).*

*4.4.3.17. Uranium hydride*

For activity release from uranium hydride ignitions there are two main exposure pathways, namely:

- Atmospheric, originating from a uranium hydride ignition in air: the reaction produces a substantial amount of heat that forms a thermal plume able to entrain fission product gases and particulate leading to a release to the intermediate surroundings. A hydrogen plume may also form in the absence of ignition, leading to dispersion of active particulate;
- Aqueous, originating from a uranium hydride thermal excursion in water: the reaction produces heat that may form a plume that will disperse particulate into the body of the water. In addition, hydrogen generation and some boiling will entrain fission products and fine particulate that can be transported to the surface and hence the atmosphere. Some of the particulate released in this manner may become trapped within the liquid film as the bubbles burst, although reliable data on retention factors at a scale relevant to local conditions and their dependence on bubble size, particulate size and gas properties are not currently available.

The addition of water to uranium hydride burning in air causes a substantial increase in the non-volatile particulate release compared to burning in air alone.

In some assessments, consideration may be given to the rate of release during burning. The burning rate is scenario dependent but typically the reaction in air lasts several minutes for gram quantities of uranium hydride and for 100 g lasts tens of minutes. However, the release rate is not uniform. For static beds of uranium hydride in air the total releases of particulate are very small and may be dominated by the initial release around the point of ignition. With water addition the release rate does not appear to be uniform with time; additional details will be included once these experiments are complete.

The activity release behaviour when uranium hydride is mixed with bulk water has yet to be investigated.

*4.4.3.18. Action to be taken in the event of uranium hydride ignition*

Historically, uranium hydride ignitions were dealt with in a number of different ways, each specific to the conditions experienced during the event. Some ignition events were controlled, and others were left to reach completion naturally. No generic advice can be given on how to manage uranium hydride ignitions because the appropriate response depends on the associated waste materials in the stream, and the tolerance of the facility to burning. However, comments on the possible responses to aid in the planning of the actions by a plant to a uranium hydride ignition can be given.

In general, in previous events the control of the ignition was achieved by:

- Removing the supply of oxidant(s). This could be purging with argon or in other cases application of a eutectic fire powder or powder bags to cover the area affected and smother the uranium hydride;
- Providing conditions that rapidly dissipated the heat produced by the oxidation reaction of uranium hydride and hence affected the heat balance. Thus, on some occasions uranium hydride ignitions were quenched using a large quantity of water applied by a fire brigade or an operator.

In a scenario when an item such as an element, can, or bottle is identified and /or suspected of containing active uranium hydride, it may be appropriate to take pre–emptive action by opening the item in a reduced oxygen atmosphere.

Opening the item in a low oxygen atmosphere provides a limited and controlled supply of oxygen to the contents of the item: provision of a small volume of oxygen, preferably in argon, at a low rate will slowly and safely oxidise the active uranium hydride to surface oxidised uranium hydride avoiding an immediate ignition on subsequent exposure to air. Some agitation of the uranium hydride may be required to ensure that it all has been sufficiently exposed to the oxygen. However, as noted previously this does not fully remove the risk of ignition and mechanical disturbance or other sparks could still initiate ignition.

The levels of oxygen needed to be used to prevent or extinguish ignition is determined by the total rate of oxygen supply to the corrosion products, i.e., determined by both the concentration of oxygen and the flow rate. Therefore, typically low percent concentrations of oxygen will be required. The chemical nature of the oxygen diluting gas should also be considered. In the past carbon dioxide was considered, however, after ignition has occurred it has been observed to sustain burning. Similarly, nitrogen can react with uranium hydride that has already ignited. Therefore, an inert gas, such as argon, is recommended as being the best diluent.

Although initially a violent reaction between the uranium hydride and water may occur when an item is immersed in a large volume of water it will probably cease reacting relatively quickly if it is dispersed in the water. The heat generated will be dissipated by the water, but a substantial volume of water needs to be provided to adequately quench the reaction.

#### *4.4.3.19. Conclusion*

Corrosion of uranium metal in sealed conditions in the presence of moisture can lead to the formation of high reactive corrosion products. These products have the capacity to generate high temperatures, release of hydrogen gas and radioactive particulate. The risk posed by such materials is mitigated in part by the narrow range of conditions under which such materials form and the residual risks can be managed by careful consideration of any opening, treatment, and handling operations.

Whilst the oxidation behaviour of uranium and its corrosion products can be understood generically, experience has shown that the level of risk posed in particular operation situations normally requires specific assessment to take account of the particular fuel, storage systems and environments.

## 4.5. CHARACTERISTICS OF IN-POOL LIGHT WATER REACTOR FUEL CORROSION

In 2018, a small cohort of Pressurized heavy water research reactor FAs stored in–pool at Sellafield was being repackaged in readiness for transfer to the reprocessing facility. During routine inspection the FAs were all observed to have suffered localised corrosion of the cladding in the area where they had been in contact with the supporting grid within the skip in which they were stored (Fig. 149 (a)). In most cases the cladding was fully penetrated exposing the fuel pellets beneath (Fig. 149 (b)). Apart from this very localised corroded area (approximately 10 $cm^2$ × 10 $cm^2$), the condition of the fuel cladding was otherwise very good (Fig. 150 (a)). This particular fuel type was a remnant (44 FAs) of a larger fuel campaign which had been reprocessed in the 1970's. This small amount of fuel remaining, which could not be reprocessed at the time for operational reasons, was placed in pool storage in an open skip with ad hoc grid inserts of painted mild steel fitted for support (Fig. 150 (b)).

(a)  (b) 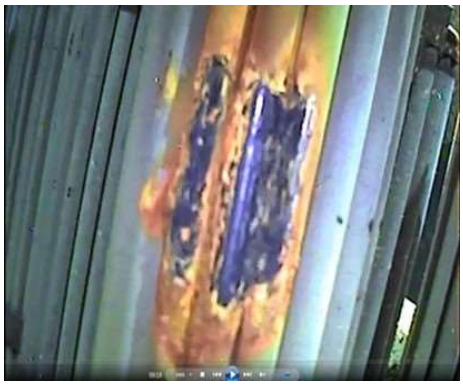

*FIG. 149. (a) Pressurized heavy water reactor (PHWR) fuel assembly in contact with mild steel grid in storage skip (in-pool). (b) Corroded area of PHWR fuel assembly where assembly was in contact with mild steel grid (courtesy of Nuclear Decommissioning Authority (NDA)).*

(a)  (b) 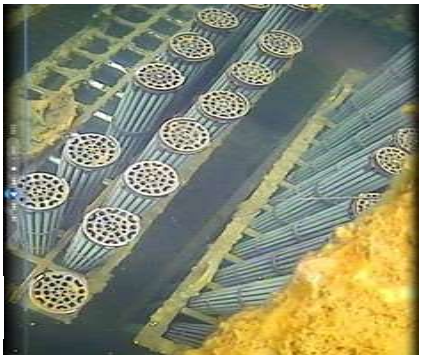

*FIG. 150. (a) Pressurized heavy water reactor fuel assemblies showing good condition of fuel where not in contact with mild steel grid. (b) Grid inserts in open skip used to store 44 PHWR fuel assemblies (courtesy of NDA).*

LWR fuel received into the pool was normally stored in lidded skips or multi–element bottles with dedicated fuel channels to contain each fuel assembly, providing isolation from the bulk pool water and protection from aerial debris.

The ad hoc arrangement provided for the PHWR fuel was required as the assemblies were of smaller dimensions than commercial fuel and it was intended to be a short term storage solution only, however the fuel was ultimately stored for over 40 years before it was reprocessed in 2018.

A preliminary literature search [150–157] confirmed the widely held view that Zircaloy cladding is not expected to corrode in pool storage under normal circumstances. However, a small number of conditions were cited under which Zircaloy corrosion may occur. Some examples given were sustained loss of the protective oxide layer on the cladding and the presence of aggressive ions in the water (particularly chloride). These can lead to localized corrosion which could then have been exacerbated by the contact load imposed by the close fit of the fuel assemblies in the grid within the storage skip.

As this first generation pool is open to the elements and historically has been exposed to transient conditions such as increased chloride (due to biocide dosing), seasonal algal bloom, and mechanical disturbance of the FAs within the skip, it was evident that these conditions could have caused superficial damage to the cladding/oxide layer and the deterioration of protective paint on the mild steel grid could all have conspired to promote corrosion.

However, given the well defined area of corrosion (bounded by the dimensions of the grid contact area) and the otherwise corrosion free condition of the rest of the assembly surfaces, the corrosion observed was concluded to be due to galvanic coupling of the Zircaloy cladding with the mild steel support grid, initiated, or exacerbated by variable chemistry conditions in the pool. No other instance of such corrosion has been observed on any other fuel type stored in this pool (or any other oxide fuel storage pool at Sellafield).

The lifting feature and overall structural integrity of the FAs were not impacted by the corrosion therefore handling and repackaging operations were able to proceed as planned.

The fuel was successfully repackaged into purpose built sheaths (Figs. 151) designed to contain four assemblies per sheath for ease of handling and batch feeding to shear for reprocessing. Reprocessing was completed without any issues and none of these assemblies remain in storage. Other examples of fuel packaged in sheaths for reprocessing are given in Section 7.

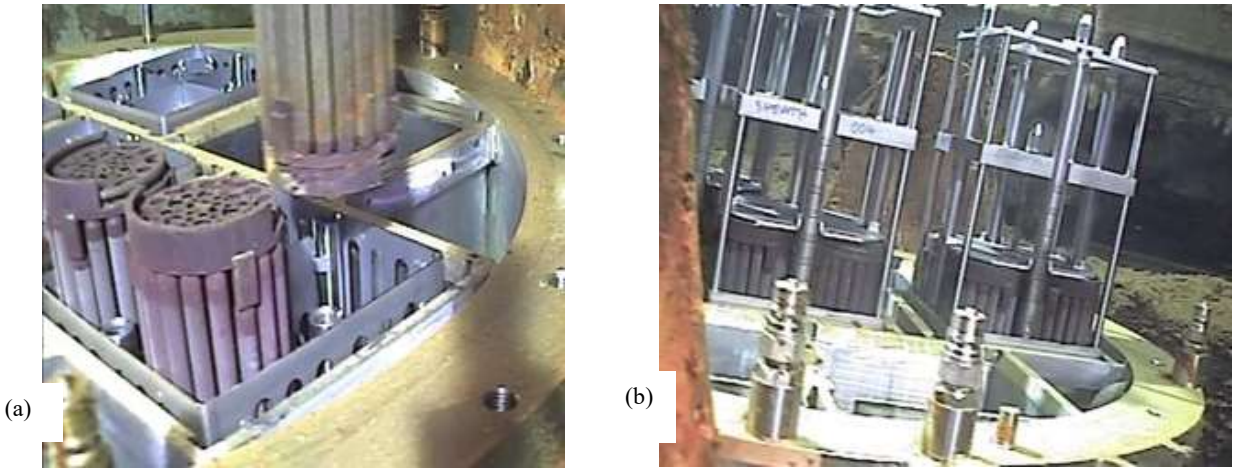


*FIG. 151. (a) Pressurized heavy water reactor FAs being placed in sheaths, 4 per sheath to batch for reprocessing. (b) Pressurized heavy water reactor fuel assemblies in sheaths with sheath lids in place (courtesy of NDA).*

Further research into Zircaloy cladding corrosion is currently underway with fresh Zircaloy samples immersed in water with varying concentrations of chloride, some in contact with mild steel samples. Results are expected in early 2021[13].

## 4.6. LEARNING

The experiences described in this Section demonstrate the advances made in the examination, handling, packaging and treatment of damaged fuel and the variety of ways in which it can be approached, covering:

- Characterization and passive drying of PIE debris to allow segregation of sludge from full size fuel pins and thus optimized packaging for ongoing storage;
- Understanding the rate of corrosion/oxidation of uranium metal fuel to assess the inventory of fuel versus corrosion/oxidation products after prolonged wet storage;
- Understanding the rate of hydrogen production due to corrosion of uranium metal and the effect of volume expansion on package stability;
- Characterization of corroded pool stored LWR fuel resulting from off normal storage conditions;
- Development of equipment and working platforms to safely access and retrieve damaged fuel from its storage location;
- Development of in situ cutting equipment to separate end appendages from fuel to allow fuel and non-fuel waste to be segregated and packaged separately and minimize the size of fuel canisters required for ease of storage and transportation;
- Development of different canister types to accommodate fuel and non-fuel items and maximise storage capacity;
- Development of different drying techniques to minimize risk of radiolytic gas build up in sealed containers (force gas drying system (ChNPP), Thermal vacuum drying (Paks NPP);
- Importance of collaboration between different nuclear parties (nuclear facility operators, R&D specialists, equipment design specialists) to achieve optimum results in recovery from off normal conditions or accidental damage scenarios;
- Appreciation of the extensive preparation time required to ensure recovery operations proceed smoothly and safely with the minimum disruption to normal plant operations.

The forced gas and thermal vacuum fuel drying techniques may have applications in the future for existing pool stored fuels that will ultimately require to be retrieved and dried for storage in underground repositories.

The techniques described for accessing and remediating/repackaging severely damaged fuel may be applicable to other remnant fuels that are still in pool storage in various facilities and are known to have suffered accidental damage to a greater or lesser degree during their storage period.

[13] Attempts to replicate the observations seen in pool did not lead to Zircaloy corrosion using standard unirradiated Zr-2 material.

# 5. COMPUTER MODELLING FOCUSED ON RADIONUCLIDE PROGRESSION WITH TIME

Following the accident at 1F the Japanese Ministry of Education, Culture, Sports, Science and Technology (MEXT) made a request to the Organization Economic Co-operation and Development (OECD) Nuclear Energy Agency (NEA) to model the accident using severe accident codes to gain an understanding of the status of the reactor cores at 1F. The study (benchmark study of the accident at Fukushima Daiichi nuclear power plant (BSAF)) was undertaken by 14 partners from 11 countries using a variety of codes. The final report of this working group was issued in 2021, a summary of their findings is provided in Ref. [158].

This Section describes an approach to understanding the nuclide inventory of a degraded reactor core and its subsequent evolution over the first 50 years of cooling. With the assistance of JAEA, the base assumptions and data used in the BSAF programme have been applied and the results compared with measured data at 1F and the outputs from the BSAF studies.

Knowing the nuclide inventory at the end of irradiation, and its subsequent evolution, is important for understanding many of the fuel characteristics and how these evolved with time.

This Section is divided into five parts:

- Modelling and simulation of spent fuel using Monte Carlo N-Particle (MCNP) code;
- Source term pathways in different stages using HOTSPOT code;
- Time dependent behaviour of the fuel inventory;
- Thermal modelling and analysis of the reactor core using reactor excursion and leak analysis program/severe core damage analysis package (RELAP/SCDAP) code;
- Thermal analysis of the corium using RELAP/SCDAP code.

All times given in Section 5 are in local time.

## 5.1. MODELLING AND SIMULATION OF SPENT FUEL USING MONTE CARLO N-PARTICLE CODE

This Section outlines the approach taken to modelling the 1F accident at Unit 1 using an Monte Carlo N-Particle (MCNP) code.

### 5.1.1. Assumptions and uncertainties upon Fukushima Daiichi core model

The 1F core model uses data generated by the working party on nuclear criticality safety, expert group on burnup credit criticality at the OECD NEA 2016 and the published data of the evaluation of fuel composition of the last core of 1F prepared by the division of nuclear data and reactor engineering, JAEA 2012 [159—161].

The core of 1F was modelled as one FA (using Unit 1 data as given in Table 2) irradiated at the core average rating power at the time of the shutdown (1380 MW(th)) to reach the core average burnup at the scram time. The earthquake caused the shutdown system to initiate, resulting in the core becoming subcritical. Due to the failure of the cooling system, the accumulation of decay heat led to fuel melt down. The nuclide inventory of the melted fuel was calculated using MCNP extended (MCNPX) code.

The concentration, activity, and specific activity of the actinides and non–actinides were calculated for different cooling times, starting from the time of the accident in 2011 and ending in the year 2061.

The model inputs assumptions such as enrichment, uranium loaded mass, and the average core burnup are presented in Table 20.

TABLE 20. MODEL ASSUMPTIONS (based on data from [159—161])

| Item | Value |
|---|---|
| Assembly average enrichment | 3.7% |
| Amount of loaded uranium (tonne) | 68 |
| Core average void fraction | 48% |
| Operational pressure (MPa) | 6.89 |
| Average burn-up/ cycle (GWd/tU) | 25.8 |

### 5.1.2. Neutronic core modelling

The fuel design and reactor core arrangements evolved over the years. The assumed core arrangement at the time of the accident and technical data of the fuel are presented in Table 21.

TABLE 21. TECHNICAL DATA OF FUKUSHIMA DAIICHI UNIT 1 (based on data from [159–163])

| Core configuration | | Fuel rod | |
|---|---|---|---|
| Hydraulic equivalent diameter (cm) | 344 | Diameter of pellet (cm) | 0.94 |
| Total amount of uranium (tonne) | 68 | Diameter of cladding (cm) | 1.1 |
| Steam flow rate (t/h) | 2480 | Thickness of cladding (thickness of zirconium liner) (cm) | 0.07(0.01) |
| Core temperature (K) | 558 | Number of fuel rods in one fuel assembly | 9 × 9–9 (water channel) |
| Thermal power output (MW(th)) | 1380 | Gap radius (cm) | 0.48 |
| Total flow rate of coolant (t/h) | 21,800 | Cladding material | Zircaloy–4 |
| Steam flow rate (t/h) | 2480 | Fuel rod pitch (cm) | 1.43 |
| Fuel assembly | | Fuel rod active length (cm) | 366 |
| Total number of fuel assemblies | 400 | Fuel density (97% of theoretical density) (g/cm$^3$) | 10.63 |
| Inner channel of assembly (cm) | 12.87 | Enrichment (approximate (%)) | 3.7 |
| Outer channel of assembly (cm) | 13.9 | Cladding density (g/cm$^3$) | 6.5 |
| | | Water density (g/cm$^3$) | 0.45 |
| Water channel box | | | |
| Channel box material | Zircaloy–4 | | |
| Water channel width (cm) | 3.75 | | |

#### *5.1.2.1. Model Description*

The core model of 1F assumes the last core contained 400 BWR fuel assemblies of 9 × 9–9 type B with an average enrichment of 3.7%.

The last core configuration consists of six batches of fuel assemblies with different burnup values. This core was operated for 165 days to an average burnup of 25.8 GWd/tHM at the time of the reactor scram with thermal power 1 380 MW(th) [159] ending on 11 Mar. 2011. The last core arrangement is illustrated in Table 22.

TABLE 22. ESTIMATION FOR 1F CORE ARRANGEMENT (based on data from [160])

| | |
|---|---|
| Start of last reloading | 27 Sept. 2010 |
| Operation days | 165 |
| Number of batches | 6 |
| Total number of fuel assemblies | 400 |

*5.1.2.2. Fuel modelling using Monte Carlo N-Particle Extended code*

This Section outlines the Monte Carlo N-Particle Extended (MCNPX) code studies.

(a) MCNPX description

MCNPX is a general purpose Monte Carlo radiation transport code that tracks nearly all particles at nearly all energies from birth until it is lost from the system due to fission, capture, or leakage. MCNPX depletion/burnup capability is a linked process involving steady state flux calculations and nuclide depletion calculations in CINDER'90 as shown in Fig. 152 [164, 165].

Calculations were performed using MCNPX 2.7 and the Evaluated Nuclear Data File branch seven (ENDF/B–VII) cross section data library with CINDER'90 for calculation of burnup and the core inventory of radionuclides at the time of the accident [166].

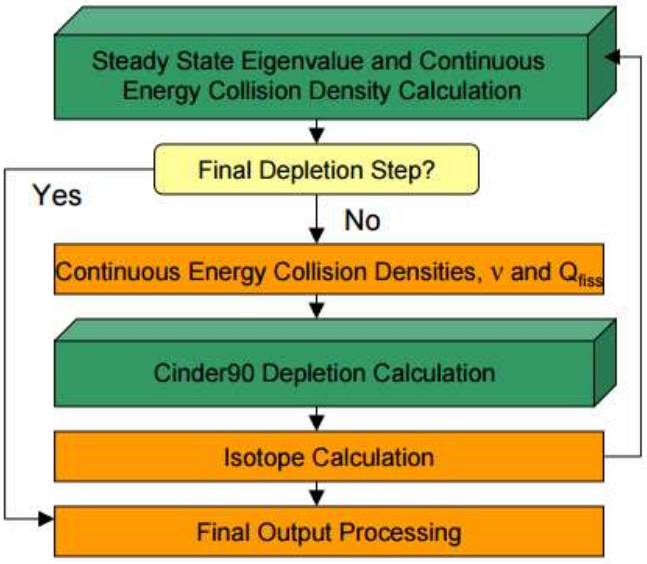


*FIG. 152. MCNPX and CINDER'90 Calculation Process (based on data from [166] courtesy of Egyptian Atomic Energy Agency (EAEA)).*

(b) Geometrical model

The modelling of the fuel rod cell geometry and the fuel assembly are shown in Figs 2 and 3 of Ref. [167].

(c) Initial Material Composition

The initial atomic densities for fuel matrix, cladding and moderator are tabulated in Tables 23—25 [161, 168].

TABLE 23. ATOM DENSITY OF FUEL MEAT (wt% = 3.7)

| Element | Atom density ($10^{24}$/cm$^3$) |
|---|---|
| U–235 | 8.82E-4 |
| U–238 | 2.27E-2 |
| O–16 | 4.71E-2 |

TABLE 24. ATOM DENSITY OF ZIRCALOY–4 CLADDING (based on data of [168])

| Element | Atom Density ($10^{24}$/cm$^3$) |
|---|---|
| Cr | 0.000076 |
| Fe | 0.000141 |
| Zr | 0.042520 |
| Sn | 0.000464 |
| O–16 | 0.000295 |

TABLE 25. ATOM DENSITY OF MODERATOR ($H_2O$)

| Void% | Nuclide | Atom fraction |
|---|---|---|
| 48% | H–1 | 0.111894 |
| | O–16 | 0.888106 |

### 5.1.3. Validation of experimental data within the model

The MCNPX model outputs were compared with experimental measurements [161]. This experiment used samples of BWR 9 × 9–9 FA. The isotopic dilution mass spectrometry was applied to Nd, U and Pu isotopes with spikes in the forms of $^{150}$Nd, $^{233}$U and $^{242}$Pu, respectively. The measured sample results of U and Nd were compared with calculated data as given in Tables 26 and 27. It was found that the results were in good agreement with an uncertainty of ~ 1% globally, due to some assumptions and approximations.

TABLE 26. COMPARISON OF ISOTOPIC INVENTORIES OF URANIUM CONTENT FOR C3 ROD

| Isotope ID | MCNPX (atoms/b.cm) | MCNPX (atoms/total U atoms) | Measured atoms/total U atoms [160] |
|---|---|---|---|
| U–233 | 8.70E-11 | 3.88E-9 | – |
| U–234 | 5.94E-6 | 2.65E-4 | 3.00E-4 |
| U–235 | 2.39E-4 | 1.07E-2 | 1.03E-2 |
| U–236 | 1.54E-4 | 6.85E-3 | 7.00E-3 |
| U–237 | 1.30E-7 | 5.81E-6 | – |
| U–238 | 2.20E-2 | 9.82E-1 | 9.82E-1 |
| U–239 | 5.98E-9 | 2.67E-7 | – |
| Total density | 2.24E-2 | | |

* barn (b) = $10^{-24}$ cm$^2$

TABLE 27. COMPARISON OF ISOTOPIC INVENTORIES OF NEODYMIUM CONTENT FOR C3 ROD

| Isotope ID | MCNPX (atoms/b.cm) | MCNPX (atoms/total U atoms) | Measured atoms/total U atoms [160] |
|---|---|---|---|
| Nd–142 | 1.01E-6 | 4.51E-5 | 5.67E-5 |
| Nd–143 | 3.25E-5 | 1.45E-3 | 1.85E-3 |
| Nd–144 | 5.62E-5 | 2.51E-3 | 3.51E-3 |
| Nd–145 | 2.98E-5 | 1.33E-3 | 1.69E-3 |
| Nd–146 | 3.16E-5 | 1.41E-3 | 1.73E-3 |
| Nd–147 | 7.98E-8 | 3.56E-6 | – |
| Nd–148 | 1.56E-5 | 6.96E-4 | 8.92E-4 |
| Nd–150 | 6.13E-6 | 2.74E-4 | 4.04E-4 |
| Total density | 1.73E-4 | | |

### 5.1.4. Verification

The actinides and non–actinides activities for different cooling times using MCPNX code were compared with JAEA calculations using ORIGEN2 [160] and the comparison was found to be in good agreement (Figs 153 and 154). The small changes in the actinides are due to their long half−lives.

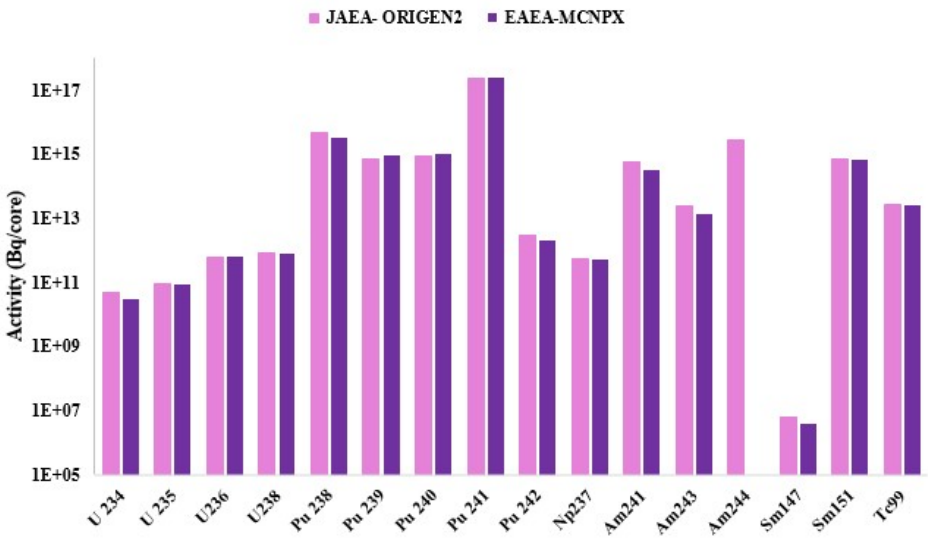


*FIG. 153. Activity of selected radionuclides after 0 days (courtesy of EAEA).*

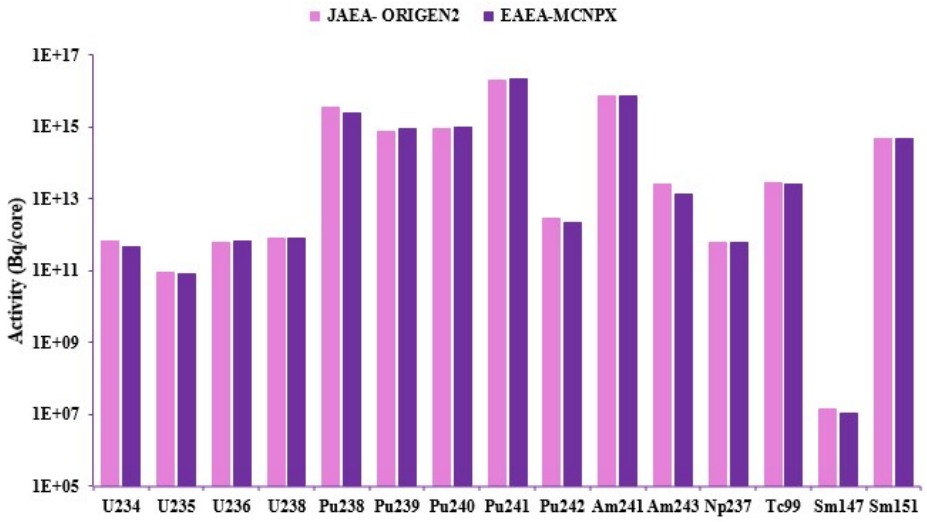


*FIG. 154. Activity of selected radionuclides after 50 years (courtesy of EAEA).*

## 5.2. SOURCE TERM PATHWAYS IN DIFFERENT STAGES USING HOTSPOT CODE

The accident caused a month long discharge of radioactive materials into the atmosphere. This section will present the results of atmospheric and ground activity calculations within 80 km of 1F. Simulations were made with a HotSpot Gaussian plume model [169].

The radiation dose evaluation resulting from the radioactive release depends mainly on two parameters, the number of radioactive materials releases and the meteorological conditions at the time of release. A comparison was made between HotSpot code results and some previous studies of radioactive releases from 1F plant [162, 170, 171].

### 5.2.1. Release heights

The source term used simulated atmospheric releases between 12 Mar. and 13 Apr. 2011, as shown in Table 28. Two main release heights were considered:

- 20 m (representative of the top of the reactor pressure vessel) was used whenever a pressure decrease happened in the unit;
- 120 m (exhaust stack) for specific venting actions.

The hydrogen explosions (events 3 and 6, as given in [172, 173]) source was assumed to be diluted by the heat and momentum of the explosion, resulting in effective release heights of 100 m and 300 m.

After 15 Mar. 2011 (events 15–30, as given in [172, 173]), releases were detected by on–site monitoring devices, but could not be associated to specific units or events.

### 5.2.2. Source terms

The following section covers the calculation of source terms by TEPCO and EAEA.

*5.2.2.1. Tokyo Electric Power Company source term calculations*

The quantity of radioactive I and Cs released during the 1F accident has been determined using the measurements of the concentrations of radioactive I and Cs in the air around the plant undertaken by TEPCO and atmospheric data [174, 175].

Studies using reverse methods to derive the atmospheric release of $^{131}$I and $^{137}$Cs using atmospheric dispersion models concluded that the release began on 12 Mar. 2011, the largest release occurred on 15 Mar. 2011 and during other periods the releases were one or two orders of magnitude smaller than that on 15 Mar. 2011 [172, 175, 176]. The release rates for $^{131}$I and $^{137}$Cs, release time, and release duration are tabulated in Table 28.

*5.2.2.2. Egyptian Atomic Energy Authority source term calculations*

Source terms were calculated using the inventory data provided in Section 5.2.4 and the release fraction from NUREG–1465 [177], which are relevant for most LWRs. Based on the radioactive material characteristics released from the core into the containment, it is assumed that the releases consist of 100% of the core inventory of noble gases, 50% I, and 1% of the remaining solid FPs [178].

The atmospheric releases were dominated by the volatile isotopes of iodine and caesium. The contamination was dominated by the deposition of $^{131}$I, $^{134}$Cs and $^{137}$Cs during the first days and weeks of the accident and afterwards by $^{134}$Cs and $^{137}$Cs. Xenon–133 is a considerable contributor for the external dose after the accident. Table 29 presents the calculated results for the abovementioned nuclides.

The largest contributors to the activity released to the environment were two radionuclides ($^{131}$I and $^{137}$Cs). Many other radionuclides were released in the accident, and some were measured in the environment; but very few were released in sufficient amounts to contribute significantly to the human health [176]. Iodine–131 tends to accumulate in the thyroid gland for a few weeks after the release and delivers a dose primarily to thyroid. Caesium–137 was deposited on the ground following its release and can deliver a dose to the whole body for many years.

Therefore, HotSpot code calculations were focused on estimating the deposition densities for these isotopes and comparing the results with the available measurements and verified models. Evaluation of deposition density (Bq/m$^2$) is essential for determining the ground shine dose for $^{137}$Cs (long $T_{1/2}$), and the time integrated concentration in air (Bq·s·m$^{-3}$) of $^{131}$I is essential to determine the inhalation dose (internal dose).

TABLE 28. RELEASE START TIME, RELEASE DURATION, RELEASE RATES OF $^{131}I$ AND $^{137}CS$, $^{131}I/^{137}CS$ RADIOACTIVITY RATIO, AND RELEASE HEIGHT FOR THE PERIOD FROM 2011-03-12-05:00 JAPAN STANDARD TIME (JST) AND 2011-05-01-00:00 JST [172]

| No. | Start time, JST | Duration (h) | I–131 (Bq/h) | Cs–137 (Bq/h) | I–131/ Cs–137 | Height (m) |
|---|---|---|---|---|---|---|
| 1 | 2011-03-12-5:00 | 4.5 | 3.70E13 | 3.70E12 | 10 | 20 |
| 2 | 2011-03-12- 9:30 | 6 | 1.70E13 | 1.70E12 | 10 | 120 |
| 3 | 2011-03-12-15:30 | 0.5 | 3.00E15 | 3.00E14 | 10 | 100 |
| 4 | 2011-03-12-16:00 | 31 | 8.40E13 | 8.40E12 | 10 | 120 |
| 5 | 2011-03-12-23:00 | 12 | 3.60E13 | 3.60E12 | 10 | 120 |
| 6 | 2011-03-14-11:00 | 0.5 | 3.00E15 | 3.00E14 | 10 | 300 |
| 7 | 2011-03-14-11:30 | 10 | 2.30E13 | 2.30E12 | 10 | 20 |
| 8 | 2011-03-14-21:30 | 2.5 | 1.30E15 | 1.30E14 | 10 | 120 |
| 9 | 2011-03-15-00:00 | 7 | 3.50E14 | 4.00E13 | 8.8 | 120 |
| 10 | 2011-03-15-07:00 | 3 | 3.00E15 | 3.00E14 | 10 | 20 |
| 11 | 2011-03-15-10:00 | 3 | 8.00E13 | 8.00E12 | 10 | 20 |
| 12 | 2011-03-15-13:00 | 4 | 4.00E15 | 4.00E14 | 10 | 20 |
| 13 | 2011-03-15-17:00 | 37 | 2.10E14 | 3.00E12 | 70 | 20 |
| 14 | 2011-03-17-06:00 | 57 | 4.10E14 | 1.00E13 | 41 | 20 |
| 15 | 2011-03-19-15:00 | 36 | 3.80E14 | 3.50E13 | 11 | 20 |
| 16 | 2011-03-21-03:00 | 18 | 1.40E14 | 1.40E13 | 10 | 20 |
| 17 | 2011-03-21-21:00 | 26 | 4.10E14 | 4.70E12 | 87 | 20 |
| 18 | 2011-03-22-23:00 | 25 | 7.10E14 | 8.90E12 | 80 | 20 |
| 19 | 2011-03-24-00:00 | 24 | 1.90E14 | 2.90E12 | 66 | 20 |
| 20 | 2011-03-25-00:00 | 35 | 5.60E13 | 1.20E12 | 45 | 20 |
| 21 | 2011-03-26-11:00 | 47 | 4.00E12 | 1.70E11 | 23 | 20 |
| 22 | 2011-03-28-10:00 | 35 | 7.50E12 | 4.70E12 | 1.6 | 20 |
| 23 | 2011-03-29-21:00 | 14 | 1.50E13 | 8.80E12 | 1.7 | 20 |
| 24 | 2011-03-30-11:00 | 13 | 1.80E14 | 1.40E14 | 1.3 | 20 |
| 25 | 2011-03-31-00:00 | 22 | 2.40E13 | 4.50E12 | 5.3 | 20 |
| 26 | 2011-03-31-22:00 | 35 | 1.80E12 | 1.60E12 | 1.1 | 20 |
| 27 | 2011-04-02-09:00 | 48 | 1.80E12 | 5.80E11 | 3.1 | 20 |
| 28 | 2011-04-04-09:00 | 80 | 7.00E11 | 1.40E11 | 4.9 | 20 |
| 29 | 2011-04-07-17:00 | 150 | 0 7.0E11 | 3.50E11 | 2 | 20 |
| 30 | 2011-04-13-23:00 | 409 | 0 7.0E11 | 1.80E11 | 4 | 20 |

TABLE 29. MAIN EFFECTIVE ISOTOPES RELEASED TO THE ENVIRONMENT

| Isotope | Core activity (Bq) | Release fraction | Release activity (Bq) |
|---|---|---|---|
| Xe–133 | 2.64E18 | 1 | 2.64E18 |
| Cs–134 | 1.93E17 | 0.01 | 1.93E15 |
| Cs–137 | 1.64E17 | 0.01 | 1.64E15 |
| I–131 | 1.26E18 | 0.5 | 6.30E17 |
| I–132 | 1.84E18 | 0.5 | 9.20E17 |
| I–133 | 2.63E18 | 0.5 | 1.32E18 |
| Te–132 | 1.81E18 | 0.01 | 1.81E16 |

*5.2.2.3. Meteorological data*

There is no published data on the wind strength or other meteorological data for the 1F site during the accident. Having reviewed meteorological data used in previous publications, stability class D was chosen to simulate the meteorological condition around 1F in this study, with a wind speed of 3 m/s [172, 173].

*5.2.2.4. HotSpot code for dispersion and deposition calculations*

A HotSpot Gaussian plume model was used for the simulations. HotSpot health physics codes were created to provide emergency response personnel and emergency planners with a fast, field portable set of software tools for evaluating incidents involving radioactive material. It is also used for safety analysis of facilities handling nuclear material. It is a first order approximation of the radiation effects associated with the atmospheric release of radioactive materials [179].

HotSpot uses the radiation dosimetry methodologies recommended by the International Commission on Radiological Protection (ICRP)[14]. These methodologies are summarized in United States Environmental Protection Agency federal guidance reports No. 11 [180], No. 12 [181], and No. 13 [182]. Reference 178 also provides dose coefficients in the form of 50 year integrated dose equivalents for acute inhalation of radionuclides and is based on the biokinetic and dosimetric models of ICRP Publication 30 [183]. Reference [179] provides dose coefficients in the form of dose per unit time integrated exposure for external exposure to radionuclides in air, water, or soil. Reference [180] provides dose coefficients using the new ICRP–66 lung model [184] and ICRP series 60/70 methodologies [185, 186].

*5.2.2.5. Results*

Figure 155 shows HotSpot calculated dose rate distributions after the accident from plume air submersion and ground shine from radioactive deposits on the soil surface, using TEPCO and EAEA data. The calculations assume that the release of radioactive materials was at a constant rate (between 11 Mar. and 11 Apr. 2011). The maximum dose rates resulting from the air submersion and ground shine are 0.03 and 0.005 Sv/h at a distance of 0.27 km from the plant.

Figure 156 shows the calculated deposition density of $^{137}$Cs around 1F (in the northwest direction) at distances less than 20 km (the emergency evacuation zone during the accident). Surface activities for $^{137}$Cs varied between 0.02 kBq/m$^2$ and $5.7 \times 10^4$ kBq/m$^2$. The calculated data is in good agreement with the measured data.

Surface activities levels of $^{137}$Cs measured in the soil samples since Jun. 2011 vary between less than 30 kBq/m$^2$ and $1.5 \times 10^4$ kBq/m$^2$. The difference between EAEA results and measured TEPCO values are due to the wind direction variability (not included in the calculations), which has evened out the contamination in the plume affected areas.

Iodine–131 and $^{137}$Cs deposition density were evaluated for some locations around 1F by HotSpot. The results were compared with MEXT's measurements [170], the verified models of the National

[14] While, extensive reference is made here to ICRP recommendations and methodologies, as used in HotSpot, guidance is also provided by the IAEA in the Safety Standards and Report Series. For example, internationally agreed dose coefficients are provided in INTERNATIONAL ATOMIC ENERGY AGENCY, Assessment of doses to the public from ingested radionuclides, IAEA Safety Report Series No. 14, IAEA, Vienna (1999).

Oceanic and Atmospheric Administration (NOAA), and the Institute for Radiological Protection and Nuclear Safety (IRSN) [171].

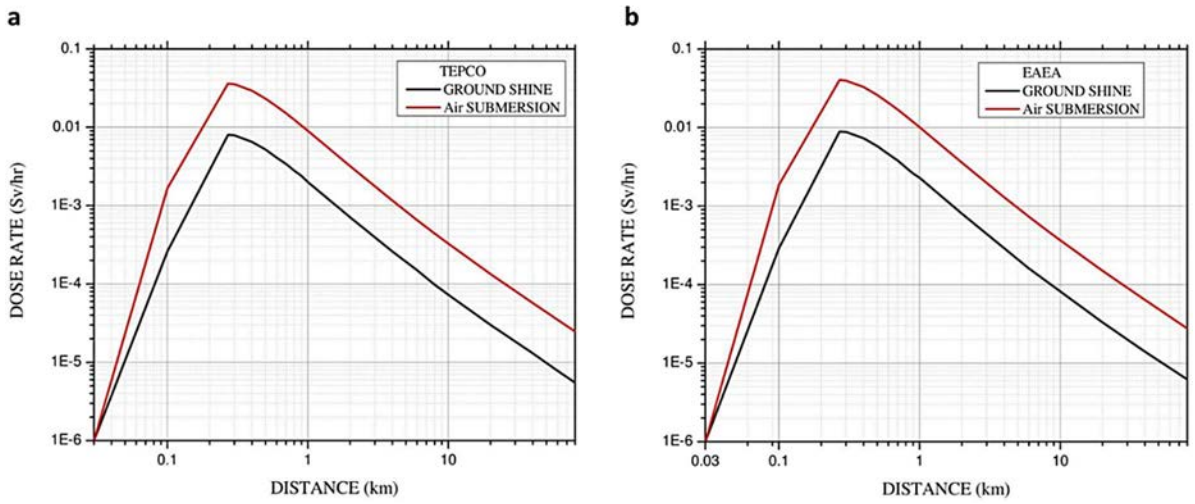


*FIG. 155. The dose rate resulting from the atmospheric dispersion of releases from the Fukushima accident. (a) Dose rate vs distance using TEPCO data; (b) Dose rate calculations vs distance using EAEA data* (courtesy of EAEA).

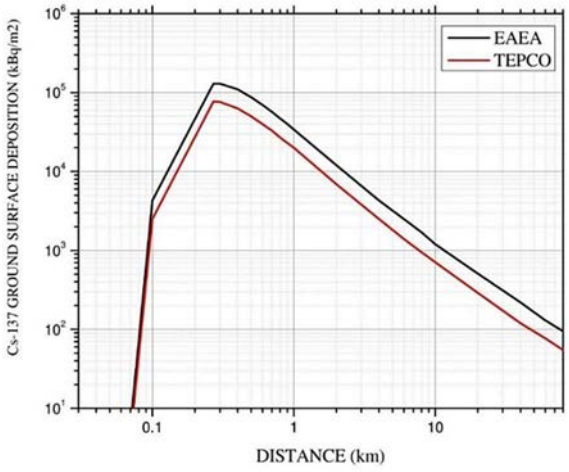


*FIG. 156. Comparison between calculated (blue) and measured (red) $^{137}$Cs deposition density after 1F accident, between 11 March and 11 April 2011 (*courtesy of EAEA).

The $^{137}$Cs deposition pattern was compared with the measured deposition in locations of Kawauchi village, Minami–Soma city, Katsurao, Tamura, and Iwaki city. HotSpot estimates for $^{137}$Cs deposition density were between a factor of 0.36 and 1.25 of MEXT measurements, as shown in Table 30.

HotSpot estimates for $^{131}$I deposition density are within a ratio of 0.7 and 3.6 of MEXT measurements, as shown in Table 30. HotSpot results were considered to be in reasonable agreement with the measured values, taking into account the limitations of the code, i.e., the short term (less than 24 hours) release duration in unobstructed terrain, simple meteorological conditions, near surface releases, and short range (less than 10 km) dispersion.

TABLE 30. THE SURFACE DENSITY OF $^{137}$CS AND $^{131}$I AT SOME LOCATIONS ESTIMATED BY HOTSPOT RESULTS THAT COMPARED WITH AVERAGE MEXT MEASUREMENTS, 15 MARCH 2011

| Location | MEXT Cs-137 deposition density (Bq/m$^2$) | HotSpot code Cs-137 deposition density (Bq/m$^2$) | HotSpot/ MEXT for Cs-137 | MEXT I-131 deposition density (Bq/m$^2$) | HotSpot code, I-131 deposition density, (Bq/m$^2$) | HotSpot/ MEXT for I-131 |
|---|---|---|---|---|---|---|
| Kawauchi Village (20 Km West-South) | 1.01E5 | 6.4E4 | 0.65 | 1.16E6 | 1.2E6 | 1.04 |
| Minami-Soma City (25 km north) | 1.06E5 | 4.8E4 | 0.45 | 1.2E6 | 8.4E5 | 0.7 |
| Katsurao Village (25 km west-west-north) | 2.56E5 | 9.2E4 | 0.36 | 2.875E6 | 2.8E6 | 0.9 |
| Tamura City (35 km west) | 3.78E4 | 3.2E4 | 0.85 | 4.3E5 | 1.6E6 | 3.6 |
| Iwaki City (40 km south) | 2.15E4 | 2.7E4 | 1.25 | 1.6E6 | 1.3E6 | 0.8 |

HotSpot code was used to evaluate the time integrated concentration of $^{131}$I in air and the results were compared with those obtained by NOAA's Global Data Assimilation System (GDAS) and IRSN's European centre for medium range weather forecasts (ECMWF), shown in Table 31. The NOAA−GDAS data is a combination of source term meteorology data generated by reverse modelling environmental measurements (concentrations in air, deposition densities, dust samples, dose rates). The IRSN–ECMWF is a source term meteorology combination based on inverse modelling of generally continuous dose rate measurements from 57 monitoring stations in Japan.

TABLE 31. COMPARISON OF THE TIME INTEGRATED CONCENTRATION OF $^{131}$I IN AIR AND DEPOSITION DENSITY ESTIMATED BY NOAA, IRSN, AND HOTSPOT CODE

| Location | Time period | | NOAA | | IRSN | | HotSpot code | |
|---|---|---|---|---|---|---|---|---|
| | From | To | Time integrated concentration in air (Bq s/m$^3$) | Deposition Density (Bq/m$^2$) | Time integrated concentration in air (Bq s/m$^3$) | Deposition Density (Bq/m$^2$) | Time integrated concentration in air (Bq s/m$^3$) | Deposition Density (Bq/m$^2$) |
| Kawauchi Village (20 Km west-south) | 2011-03-12 11:00 | 2011-03-16 08:00 | 3.4E7 | 4.1 E5 | 4.0 E8 | 2.9 E6 | 4.2E7 | 1.2E6 |
| Minamisoma City (25 km north) | 2011-03-11 00:00 | 2011-03-15 10:00 | 1.3E5 | 9.3 E5 | 2.7 E8 | 5.7 E5 | 3.0E7 | 8.4E5 |
| Katsurao Village (25 km west-west-north) | 2011-03-11 00:00 | 2011-03-21 12:00 | 2.4 E8 | 5.5E6 | 2.4 E8 | 4.0 E6 | 1.0E8 | 2.8E6 |
| Tamura City (35 km west) | 2011-03-12 08:00 | 2011-03-31 08:00 | 9.4 E6 | 3.6 E5 | 9.4 E7 | 2.5 E6 | 5.7E7 | 1.6E6 |
| Iwaki City (40 km south) | 2011-03-12 13:00 | 2011-03-31 12:00 | 2.9E8 | 2.5E6 | 1.5 E8 | 8.1 E5 | 4.5E7 | 1.3E6 |

As shown in Table 32, the comparison of HotSpot results with NOAA estimates for integrated time concentration of $^{131}I$ in air varied between about 0.155 and 6, except of one extreme overestimated value of 150. The comparison of HotSpot results with IRSN estimates were within 0.1 and 0.6. The main point is that Hotspot results lie between the values predicted by the other two codes.

TABLE 32. THE RATIOS OF HOTSPOT RESULTS TO NOAA AND IRSN ESTIMATES (TIME-INTEGRATED CONCENTRATION OF $^{131}I$ IN AIR)

| HotSpot/NOAA | HotSpot/IRSN |
|---|---|
| 2.23 | 0.1 |
| 150 | 0.2 |
| 0.4 | 0.42 |
| 6 | 0.6 |
| 0.155 | 0.3 |

## 5.3. TIME DEPENDENCE OF THE RADIONUCLIDE SOURCE TERM

The inventory of the radionuclide source term in 1F between the time of the accident and the year of 2061, which is the time range declared in TEPCO's cleanup plan, was calculated using MCNPX. The results are given in Fig. 157.

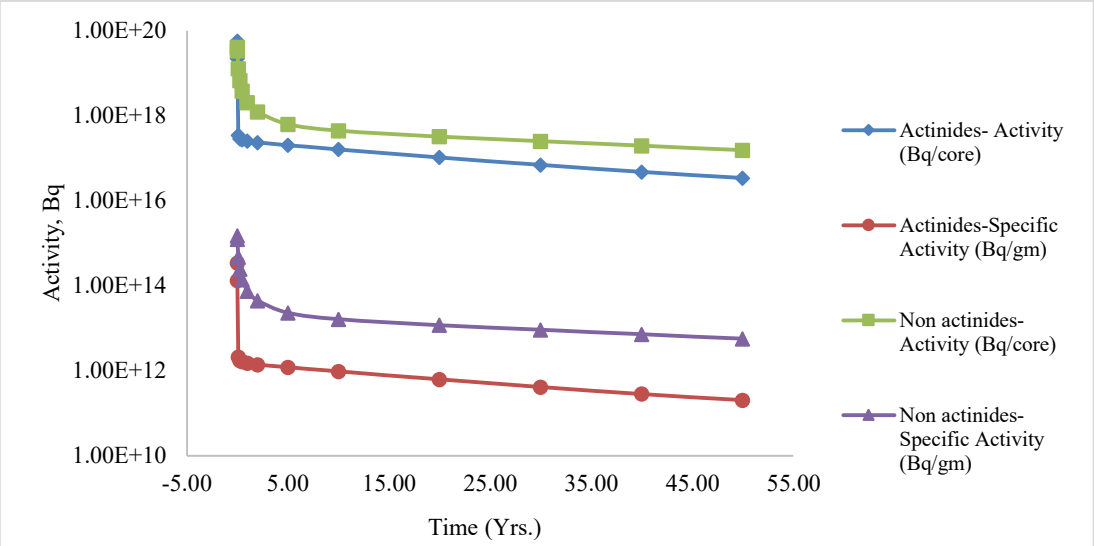


*FIG. 157. Total activity and total specific activity of the radionuclides in the corium at different times* [187] *(courtesy of EAEA).*

The total specific activity of the radionuclides in the corium in 2011, 2021 and 2061 are $1.84 \times 10^{15}$ Bq/g, $1.73 \times 10^{13}$ Bq/g and $5.86 \times 10^{12}$ Bq/g respectively. The total activity of the radionuclides in the corium in 2011, 2021 and 2061 are $9.86 \times 10^{19}$ Bq, $6.09 \times 10^{17}$ Bq and $1.89 \times 10^{17}$ Bq, respectively.

Figures. 158–164 present the variation in radionuclide activities for selected isotopes.

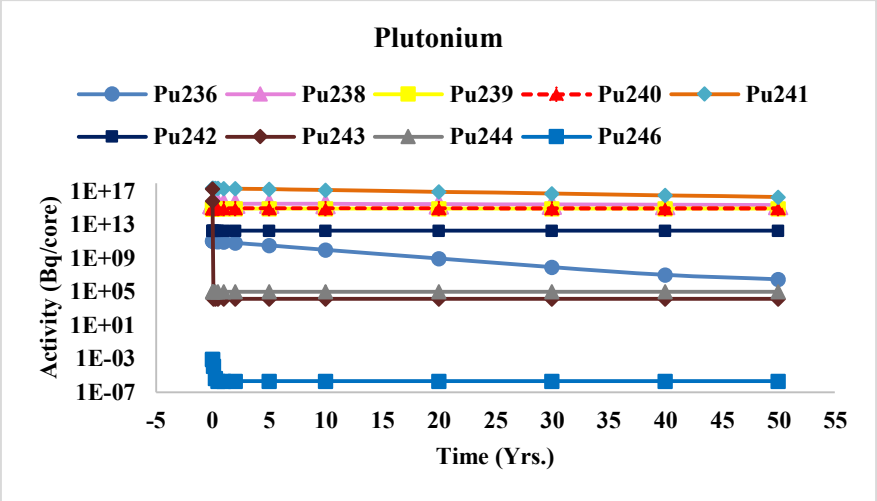


*FIG. 158. Plutonium isotopes activity during different times (courtesy of EAEA).*

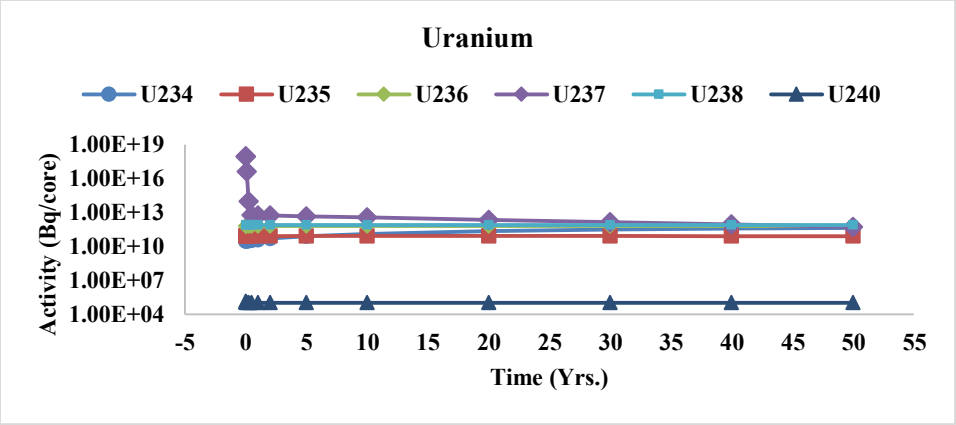


*FIG. 159. Uranium activity during different times (courtesy of EAEA).*

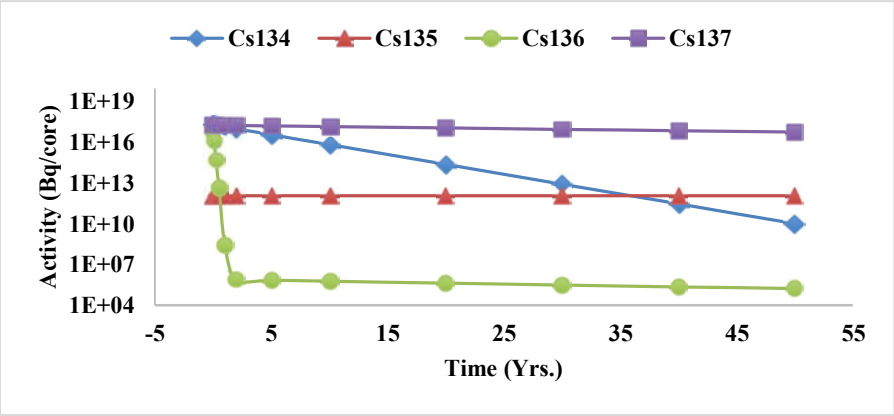


*FIG. 160. Caesium isotopes activity during different times (courtesy of EAEA).*

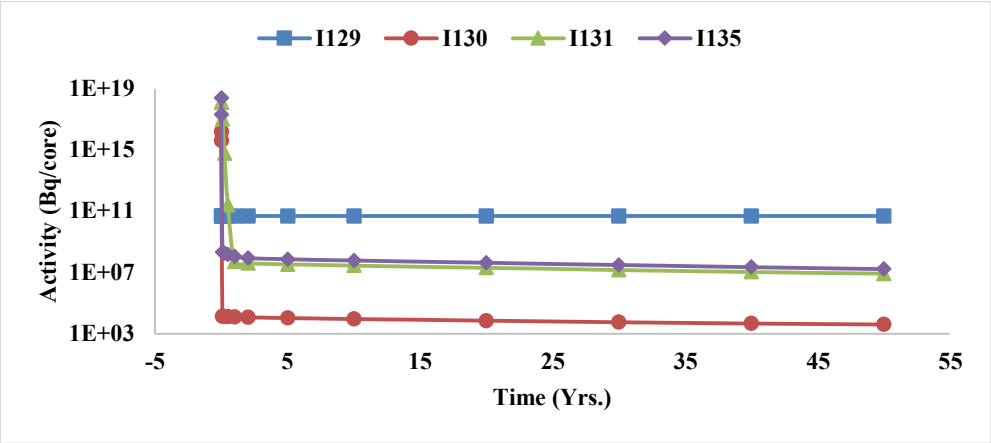


*FIG. 161. Iodine isotopes activity during different times (courtesy of EAEA).*

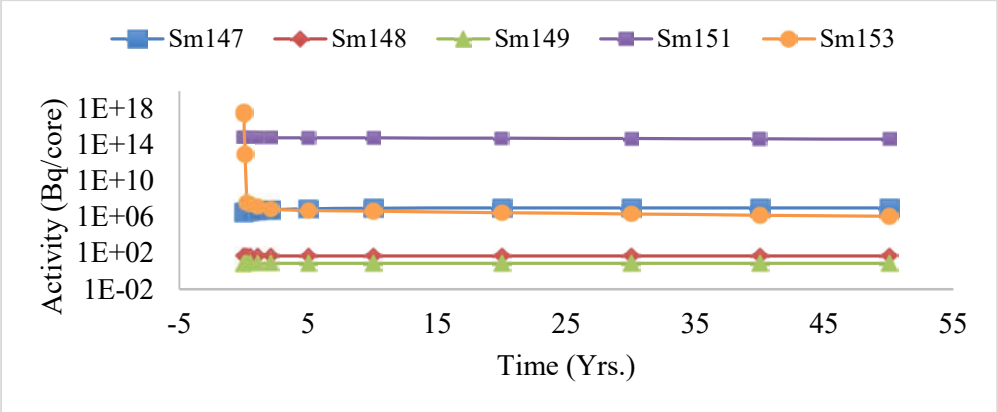


*FIG. 162. Samarium isotopes activity during different times (courtesy of EAEA).*

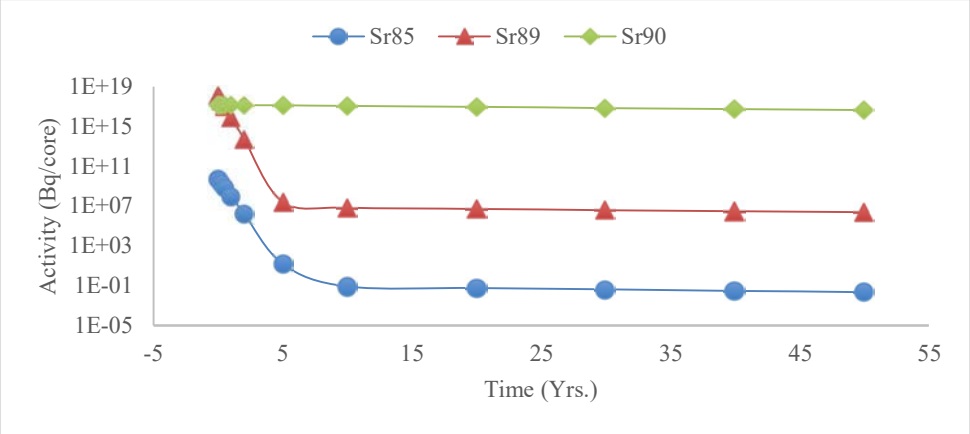


*FIG. 163. Strontium isotopes activity during different times (courtesy of EAEA).*

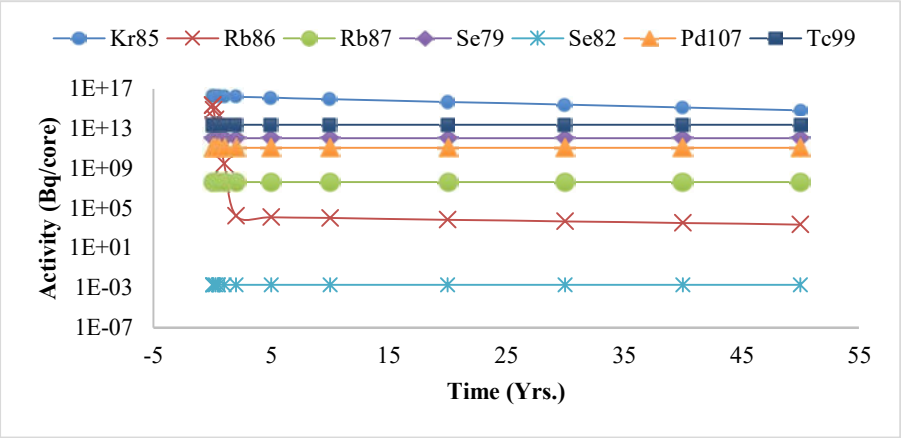


*FIG. 164. Isotopes of Krypton, Rubidium, Selenium, Palladium and Technetium activity during different times (courtesy of EAEA).*

## 5.4. THERMAL MODELLING AND ANALYSIS OF CORE EVOLUTION DURING THE ACCIDENT USING SEVERE CORE DAMAGE ANALYSIS PACKAGE/ REACTOR EXCURSION AND LEAK ANALYSIS PROGRAM 5 CODE

The event sequence from reactor scram on 11 Mar. 2011 and injection of water on 12 Mar. 2011 is shown in Table 33.

The conclusions for 1F based on the assessment and information available were:

- Within the first one or two weeks of the accident, it was probable that significant fuel melting occurred in Unit 1 due to the loss of cooling;
- The vessel failure in Unit 1 was likely event given the large uncertainties in the accident [188].

TABLE 33. CHRONOLOGICAL SEQUENCE OF EVENTS USEFUL IN THE THERMAL ANALYSIS [189]

| Before earthquake: Operating | | |
|---|---|---|
| 2011-03-11 | 14:46 | Reactor scram |
| | 14:47 | All control rods fully inserted, turbine trip, loss of external power supply, emergency diesel generator start-up, main steam isolation valve close |
| | 14:52 | Emergency condenser (IC) automatic start-up |
| | ~15:03 | IC shut down and repeatedly reactivated until~15:03 (reactor pressure was controlled by IC) |
| | 15:07 | Reactor containment spray system pumps were started to cool the suppression chamber (S/C) |
| | 15:37 | All alternating current (AC) power supplies lost |
| | 18:25 | IC (A) system MO-3A valve was closed |
| | 21:30 | IC 3A valve was opened and steam generation was observed |
| | 22:00 | Reactor water level effective fuel top (top of active fuel (TAF)+550mm |
| 2011-03-12 | 0:30 | Water is being supplied to IC (A) body side by fire extinguishing system |
| | 5:46 | Fresh water injection by fire pumps was started |

### 5.4.1. Methods of calculations

Two methods were used to calculate the core performance after reactor scram. The first method used analytical calculations to estimate the times at which the surface of the fuel was uncovered, the whole fuel assembly was uncovered, when the fuel started to melt, and the hydrogen started generating. The second method used RELAP5/SCDAP SIMulation (SCDAPSIM) code which is designed to describe the overall reactor coolant system (RCS) thermal hydraulic responses and core behaviour under normal, design basis or severe accident conditions. The code was used to model Fukushima Unit 1 and simulate the SBO that occurred during the accident.

The RELAP5 part of the code calculates the RCS thermal hydraulic responses, control system behaviour, reactor kinetics and the behaviour of system components, for example valves and pumps.

The SCDAP models core and vessel structure behaviours for different operating conditions. Apart from general core and vessel structures, the code includes user selectable components for LWR fuel rods, control rods ($B_4C$, Ag–In–Cd), BWR control blade/channel boxes, and electrically heated fuel rod simulators. There are also features to introduce debris and molten pool formation, debris–vessel interactions, and structural failure (creep rupture) of vessel structures to simulate the later stages of a severe accident [190].

The model was also used to calculate various parameters for SBO scenarios and curtailing the emergency core cooling system injection, including: the progression of fuel and core damage; maximum surface temperature; fuel cladding melting; hydrogen generation; height of debris; quantity of molten material in the lower head.

*5.4.1.1. Analytical Method*

Assuming the water level above the fuel was about 10 m before the accident, the reactor was divided into three sections, as shown in Fig. 165 (a).

- The top: consisting of the upper plenum, modelled as half a sphere, and the part above the fuel, modelled as a cylinder with 9.38 m height. In the top, the water density is 0.2 g/cm$^3$;
- The core: consisting of the part that contains the fuel, cladding and coolant, represented by a cylinder 4.63 m high. The density of the water changed in this section, as shown in Fig. 165 (b), resulting in an average water density of 0.45 g/cm$^3$;
- The bottom: represented as half a sphere containing only water with density of 0.74 g/cm3.

At a pressure of 7.92 MPa (absolute), the water density is 0.7236 g/cm$^3$ for the saturated liquid and 0.042 g/cm$^3$ for the saturated vapour. Table 34 gives the volumes and masses of water in the reactor. The amount of fuel and clad used were taken from Tanabe [191] and are given in Table 35.

The average temperatures were assumed to be 900 K for the fuel, 600 K for the cladding and 567 K for the coolant.

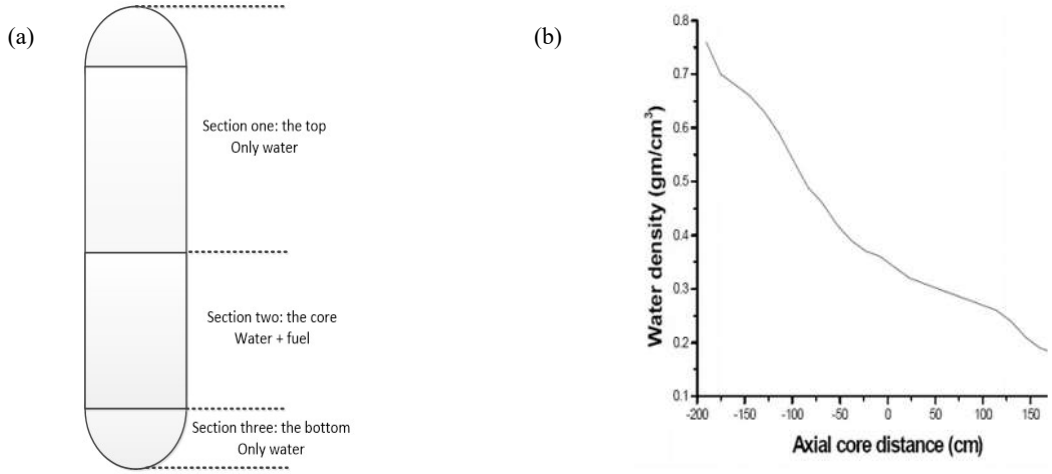


*FIG. 165. (a) The three sections of the reactor. (b) Change of water density with reactor height (courtesy of EAEA).*

TABLE 34. VOLUMES AND MASSES OF WATER AND STEAM IN THE REACTOR VESSEL

| | Head (above core) | Core | Bottom |
|---|---|---|---|
| Shape | Half sphere (upper plenum) + Cylinder | Cylinder | Half sphere (lower plenum) |
| Height (m) | 2.4 + 9.38 | 4.36 | 2.4 |
| Volume($m^3$) | 198.69 | 64.58 | 28.95 |
| Total mass (water + steam) (Kg) | 3.974E4 | 2.906E4 | 2.171E4 |
| Liquid mass (kg) | 3.334E4 | 2.797E4 | 2.171E4 |
| Steam mass (kg) | 6.398E3 | 1.09E3 | — |
| Total mass of water in reactor vessel = 90.51 t | | | |

TABLE 35. FUEL AND ZIRCONIUM INVENTORY AND SPECIFIC HEAT

| Material | Mass(kg) | Specific heat (kJ/kg K) |
|---|---|---|
| $UO_2$ | 7.83E4 | 0.251 |
| Zr | 3.27E4 | 0.364 |

Other assumptions included:

- Uniform temperature distribution in the fuel, clad and coolant. The temperature in each section was uniform and no temperature gradients were considered;
- The properties were independent of temperature, the decay heat and the heat generated from the Zr–steam reaction was calculated after the complete loss of all power supply and before vessel failure;
- Other oxidation reactions (e.g., with stainless steel) were ignored.

*Heat sources: Decay heat and chemical heat.*

After the reactor shut down, there were only two sources of heat – heat generated due to the decay of radioactive material in the fuel and heat caused by the exothermic reaction of steam with zirconium based fuel bundle/water channel materials. The total heat generated until time ($t$) after shut down, $Q(t)$, can be calculated with Eq. 2 [192]:

$$Q(t) = Q(t)_{decay} + \Delta H \int_0^t R_x \, dt \tag{2}$$

where:
$Q(t)_{decay}$ – decay heat generated;
$\Delta H$ – energy generated from an oxidation reaction;
$R_x$ – reaction rate of oxidation.

*5.4.1.2. Decay heat*

The decay heat is a function of the burnup, reactor power, operation time and reactor type. The calculation of the decay heat can be done by a number of methods from simple equations that are valid for only small periods of time (up to 100 days from shut down) to complicated computer codes (such as ORIGEN) [193].

The American Nuclear Society (ANS) standard 5.1 [194] was used to estimate of the decay heat. Errors up to 50% can result for short (<1000 s) and long (>$10^7$ s) times. In the midrange, errors are of the order of -20% to +10% [193].

It should be noted that the ANS Standard underestimates the decay power for times greater than $10^8$ s (more than 3 years), due to the neglect of some actinides, mainly $^{238}$Pu, $^{244}$Cm, and $^{241}$Am. Figure 166 shows the fractional decay power as a function of time between 100 s and 31 years, the difference is about 40% at $1 \times 10^{10}$ s [195].

The decay energy, $Q(t)_{decay}$ can be obtained from integrating the decay power over time [195]. Figure 167 shows the decay energy accumulation with time between 100 s and 31 years.

For $t_s > 10^8$ s, the decay heat is increasingly underestimated up to about 40% at $10^{10}$ s.

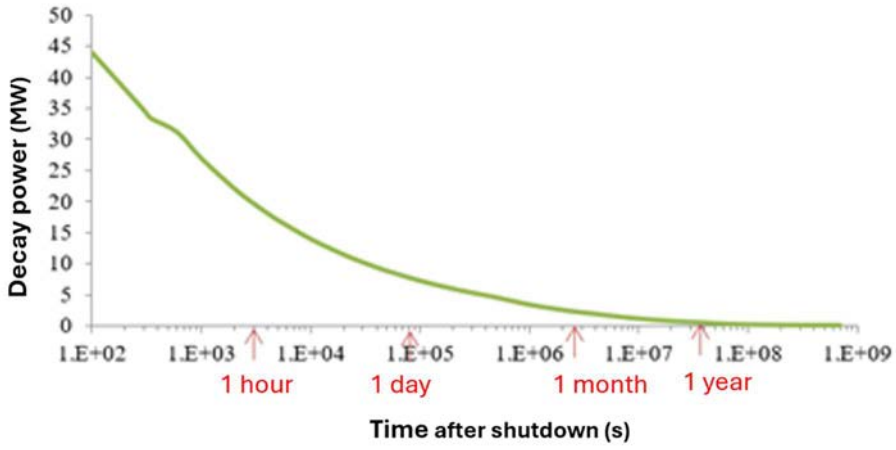


*FIG. 166. Decay power against time after shutdown (100 s to 31 years) (courtesy of EAEA).*

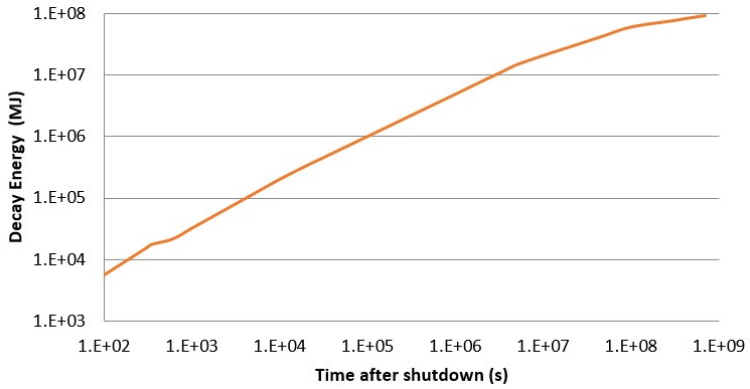


*FIG. 167. Accumulation of decay energy with time after scram (courtesy of EAEA).*

*5.4.1.3. Chemical energy*

During fuel heat up and core damage, hydrogen production is a very important parameter, because it represents an integrated effect of core degradation processes: (1) metal oxidation model; (2) availability of coolant for chemical reaction; (3) fraction of metal surface exposed to coolant [196].

As the heat removal system failed to work appropriately, the primary containment vessel temperature quickly rose to more than 1173 K. Due to the chemical reaction between zirconium based materials and steam/water, pressures increased beyond the design specifications. Hydrogen was produced according to Eq. (3) [197].

$$Zr(s) + 2H_2O(g) \rightarrow ZrO_2(s) + 2H_2(g) + 583.6 \text{ kJ/(mole Zr)} \quad (3)$$

This exothermic reaction starts at around 1173 K and becomes autocatalytic >1473 K [195].

The decision to vent $H_2(g)$ and any other built-up volatile gases inside the primary vessel to the atmosphere when the pressures exceeded the design specifications was made to protect the primary containment vessels' structural integrity [198]. On 12 Mar. 2011 at 14:40 JST, the day after 1F was scrammed, a series of venting procedures took place. Hydrogen released from the PCV accumulated within the superstructures above the core, resulting in a sequence of explosions[198] .

Generally, oxidation of Zr based alloys follows a parabolic rate law above ~1273 K characteristic of a protective or well adhering oxide layer. The prediction of $H_2$ generation requires the knowledge of the time dependent temperature, Zr inventory, steam, and interface distributions in the degraded core [198, 199].

Robb et al. [200] proposed that 30–100% of the zirconium was oxidized. We assumed that 50% of the zirconium was oxidized before the hydrogen explosion. Therefore, if the total mass of Zr was $3.27 \times 10^4$ kg, then the total chemical energy generated after the core exposure is given by Eq. (4).

$$Q_{chem} = 583.6 \times (3.27 \times 10^4 / 91.224 \times 10^{-3}) \times 0.5 = 1.05 \times 10^5 \text{ MJ} \quad (4)$$

Comparing the value of $Q_{chem}$ to that of the decay energy, $Q_{decay}$, we can see that the contribution of both types of energy to the situation in Unit1 were of the same order of magnitude between 1 hour and 1 day. After the total failure of AC power 2011-03-11-15:37, the decay heat was not removed for fourteen hours and nine minutes [189].

The decay heat generated during that time was $5.58 \times 10^5$ MJ, about five times the energy released from chemical oxidation. Figure 168 shows the heat accumulation in the core after the reactor shutdown until the water injection, assuming the chemical reactions had a steady rate.

Although only a small proportion of the total heat generated is associated with chemical energy as outlined above, the heat generated from chemical reactions is crucial in determining the corium temperature. Though it is not believed that these made a significant contribution to fuel melting.

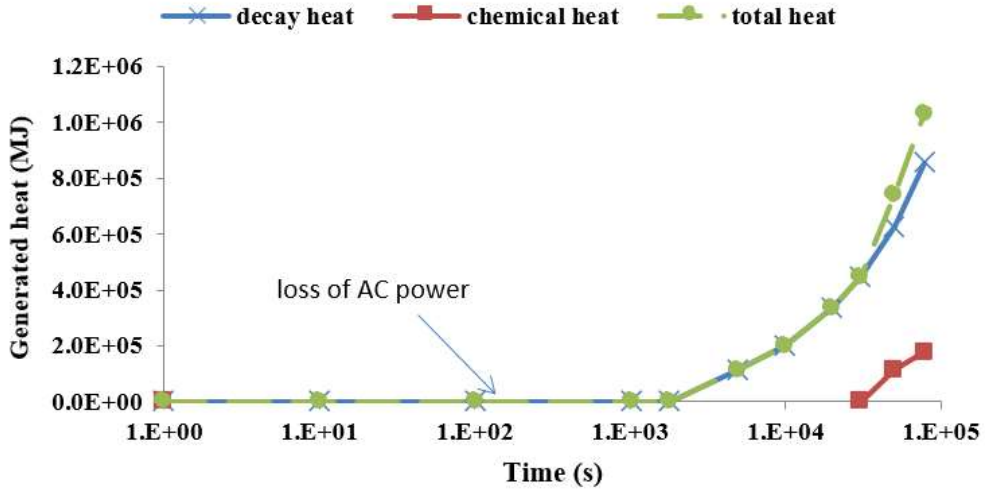


*FIG. 168. Accumulation of heat after reactor shutdown from decay heat and clad–coolant reaction until cooling was supplied (courtesy of EAEA).*

*5.4.1.4. The water level in the core*

According to the Nuclear and Industrial Safety Agency (NISA) assessments [189], the fuel was exposed as a result of a reduction in the water level at around 2011-03-11-17:00 and core melting began subsequently. Based on the assumption of uniform temperature in the three sections of the reactor, the water level was calculated assuming that all the heat was used to vaporise water.

Note that there was no chemical heating at that time because the temperature was still low (567 K), so radioactive decay was the only significant heat source.

The change in water level with time is shown in Fig 169. The calculated start time of fuel top exposure was at 2011-03-11-16:24, which is in reasonable agreement with the time calculated by NISA (17:00), within about half an hour [189], and Bonneville et al. [201]. However, there was a disagreement between the calculated time when the whole fuel was exposed (17:08) compared to Bonneville et al (18:14) [201].

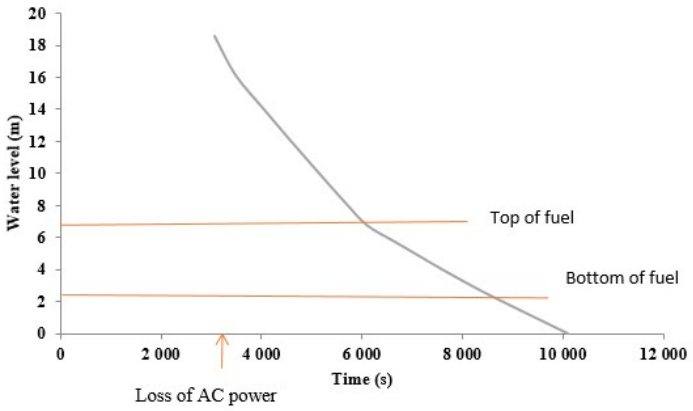


*FIG. 169. Drop of the water level in the core against time from scram (courtesy of EAEA).*

*5.4.1.5. Start time of hydrogen generation*

As mentioned earlier, Zr reacts with steam (autocatalytic reaction) to produce $H_2$ gas at about 1473 K [195, 197]. According to the calculations, at 2011-03-11-17:34, all the water has evaporated. The amount of energy required to increase the temperature inside the reactor to 1473 K can be divided into three parts: the energy associated with the fuel ($E_f$), the energy associated with the fuel cladding ($E_c$) and the energy associated with steam ($E_f$). The energy required to increase the temperature to 1473 K can be calculated simply from component masses and specific heats using the adiabatic assumption, which yields a heat requirement of $2.19 \times 10^5$ MJ.

From Fig. 169 the time at which the hydrogen generation started from the Zr—steam reaction was about 2011-03-11-22:44.

*5.4.1.6. Fuel melting*

The melting temperatures used were 3113 K for the fuel and 2960 K for the cladding. Following the same method as above, the energy required to start melting the cladding is $1.77 \times 10^3$ MJ as the clad temperature rises from 1473—2960 K. In this case, chemical and decay heat generation were both important throughout this time span. It was 22:47 when the cladding began to melt.

The energy required for the fuel to reach its melting point was $3.22 \times 10^4$ MJ which was reached at 2011-03-11-23:30.

*5.4.1.7. Reactor excursion and leak analysis program/severe core damage analysis simulation*

The model was based on the benchmarked Laguna Verde (LV) model [188] incorporating the main reactor features: Core; Vessel; Associated emergency cooling and containment systems. Model nodalization included: RPV; Water (safety) injection components of the emergency core cooling system: Main steam line [188].

Four sets of BWR assemblies and related control blades were used to describe the core at various power levels and burnup histories. The flow between the grouped fuel assemblies was represented by four vertical flow channels. The flow in the regions outside the channel boxes and surrounding the control blades were depicted by four additional vertical flow channels. The BWR assemblies consisted of a fuel rod bundle, Zircaloy channel box, and $B_4C$ control blade element. A SCDAP card was used to model fuel rods along with the radial and axial power peaking [188].

The model included the following main elements: feed water (FW), turbine, suppression pool, CRD system, and emergency core cooling systems (ECCS) such as low pressure core Spray system (LPCS), high pressure core spray system (HPCS), low pressure core injection system. All of them were defined by the boundary conditions with the reactor core isolation cooling system [188].

A few modifications to the LV model were made to adapt the model to reflect Unit 1 of 1F. The modifications included:

(a) Modifying some parameters such as system pressure, type of internal recirculation jet pumps, and adding two recirculation loops;
(b) Increasing the number of jet pumps (262, 263);
(c) Modifying the emergency core cooling system by adding another independent cooling system LPCS (163, 380, 168). Table 36 contains a list of the changes made to the LV model.

The model is shown in Fig. 170. The initial RELAP/SCDAPSIM calculations performed using the LV model included depressurization scenarios and a station blackout transient incorporating emergency core cooling. A two dimensional finite element heat conduction COUPLE code was used to model the lower head phenomena and debris and/or surrounding structures heat up.

The model considers decay heat and the internal energy from recently fallen or formed debris. Heat transported by conduction in the radial and axial directions to the surrounding walls and water is calculated. Lower head vessel heat up, as a result of core material slump, was also used to establish when the lower head core materials ruptured [202].

TABLE 36. A LIST OF THE CHANGES IN THE MODIFIED MODEL

| Item | Laguna Verde model | our model |
|---|---|---|
| System pressure | 7.0327 MPa | 6.930 MPa |
| Internal recir. jet pumps | Five nozzle | Single nozzle |
| Forced circulation | 2 recirculation loops (N/A) | Adding 2 recirculation loops |
| Jet pumps | Not applicable | Two jet pumps added, 262, 263 |
| ECCS | High pressure and low pressure cooling systems | Adding two independent cooling system (LPCS) composed of three pipes, 163, 168, 380 connected by two junctions, 164, 169 (see Fig. 170) |

An estimate of the heat removed from the lower head debris was made from the sum of the heat generated in the accumulated corium in the lower plenum/core material and heat transfer to the reactor vessel and the outer vessel [188].

The modified RELAP/SCDAPSIM Fukushima model was verified by comparison to other models [188, 203] and showed to be in good agreement with the Fukushima like LV model [188]. The verification of the model was made by comparing core depressurization against time after reactor scram with that of the methods for estimation of leakages and consequences of releases (MELCOR) code calculation [203], as shown in Fig. 171.

The following transients were modelled:

- The loss of cooling instantly after scram with depressurization and the lack of an emergency water injection;
- Closing the main steam isolation valve (510);
- Disabling the emergency cooling and Automatic Depressurization System (610, 670, 665, and 626);
- Depressurization by opening two safety relief valves (SRV) with:
  - Termination of all water addition through emergency cooling systems;
  - All water addition through emergency cooling systems were terminated;
  - Nominal CRD flows of 2.3 kg/s;
  - Termination of all water addition following reactor scram.
- SRVs continued closed—high pressure fluctuating between relief valve set points.

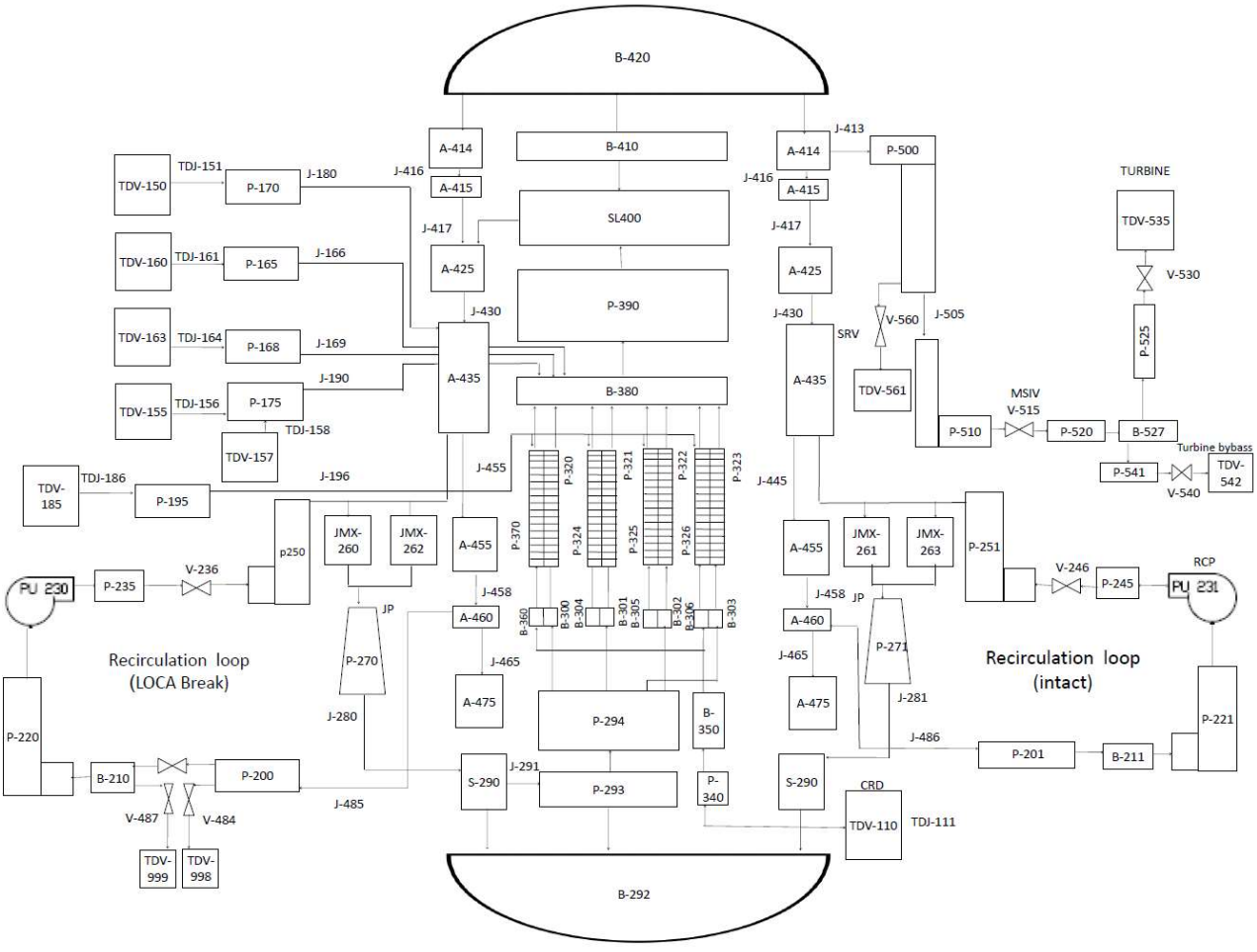


*FIG. 170. Nodalization of Fukushima, Unit 1 — modified from Laguna Verde (reproduced from Ref. [188] with permission courtesy of C. M. Allison et al.).*

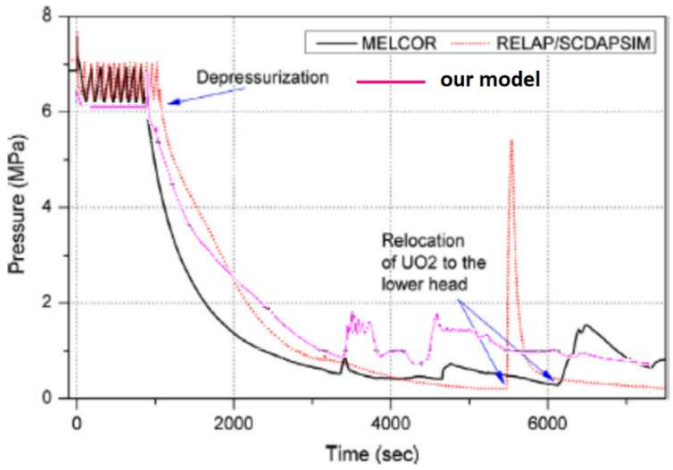


*FIG. 171. Comparison between the depressurization simulated occurring using Laguna Verde model, MELCOR [203] and RELAP/SCDAPSIM model for the SBO scenario [188] (courtesy of EAEA).*

To calculate the time required for the fuel and the clad to start melting, their corresponding melting temperatures (3113 K, for fuel and 2960 K, for clad) must be considered. Using the same approach, with the clad temperature changing from 1473 to 2960 K, the energy required to start melting the clad is equal to $1.77 \times 10^3$ MJ.

During this period chemical and decay heat generation were both significant. The time at which the clad started to melt was at 22:47.

The COUPLE code was used to calculate the thermal behaviour of core materials in the lower plenum by assuming the complete evaporation of the lower plenum water during the first relocation process of the core material.

The damage progression stages predicted were:

- Embrittlement of cladding due to oxidation;
- Oxidation induced the cladding embrittlement;
- Melting of metallic cladding and dissolution of fuel in contact with liquefied cladding;
- The fuel dissolved and metallic cladding melted in contact with liquefied cladding;
- Slumping of liquefied cladding and dissolved fuel due to failure of the oxide shell containing the liquefied mixture;
- Due to the collapse of the oxide shell enclosing the liquefied mixture, liquefied cladding and dissolved fuel are slumping;
- Solidification of the slumped mixture at a lower and cooler location in the core and concurrent formation of a nonporous debris region that blocks the flow of coolant;
- The slumping mixture solidifies at a lower and cooler position in the core, resulting in the creation of a nonporous debris area that restricts coolant flow;
- Meltdown of the reactor core into a molten pool supported by the frozen previously molten ceramic material;
- Melting through or structural failure of the crust of frozen material that supported the molten pool and slumping of the molten pool to the bottom of the reactor vessel.

*5.4.1.8. The station blackout scenario*

The depressurization happened immediately after the reactor scram (note that 500 s simulation time is equivalent to real scram time 2011-03-11-14:46, and each 5500 s simulation time are equivalent to 17:00 hours real time from reactor scram), see Figs 5 and 6 in Ref. [167], and resulted in core uncovering, melting of the fuel, relocation of the fuel into the lower plenum, and lower head failure. The decay heat continued to be generated after the scram. A conservative assumption was applied in that before reactor scram the reactor power was kept at 2370 MW(th), as LV model, this slightly increases the decay heat and the core temperature compared with the real values.

It was found that the reactor core was completely melted after 4000 s (i.e. 2011-03-12-04:58) when the temperature reached 2700 K, Fig. 8 in Ref. [167]. It was deduced that the temperature began to rise after the coolant failed to remove the decay heat.

The sharp rise in the temperature (a jump) was associated with the release of hydrogen (Eq. 3) which resulted in additional heat being generated in the core. This decreased suddenly when the fuel fell to the bottom of the pressure vessel.

After 5000 s, the molten pool extended to the periphery of the core. It was found that a molten pool containing about 19.3 t of liquefied (U, Zr)$O_2$ slumped to the lower head after 4500 s. Figure 9 in Ref. [167] showing hydrogen production versus time after scram confirms that the hydrogen production was the cause of the sharp increase in the core temperature.

According to [167], hydrogen production began at 1900 s (2011-03-11-22:15), when the temperature was around 1300 K. The highest temperature in the lower head vessel wall had exceeded the melting point for steel (2800 K).

The timeline of the SBO scenario modelled with a 6000 s simulation time is shown in Fig. 172 and Table 37. The Couple code results are summarized in Table 38.

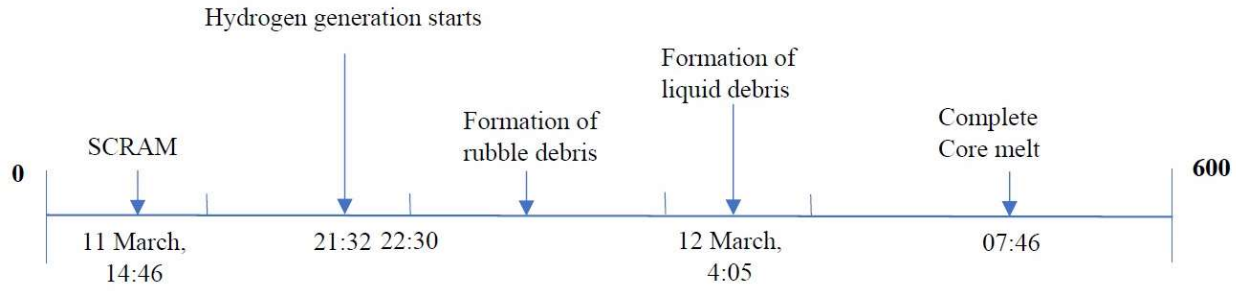


*FIG. 172. Timeline of Fukushima SBO model within simulation time of 6000 s (courtesy of EAEA).*

TABLE 37. SUMMARY OF TIMES THE MAIN EVENTS CALCULATED BY RELAP/SCDAPSIM

| Real time (simulation Time) | Event |
|---|---|
| 2011-03-11-14:46 (500 s) | Scram, depressurization, and termination of water injection |
| 2011-03-11-21:32 (1900 s) | Hydrogen generation starts |
| 2011-03-11-21:53 (2000 s) | Maximum temperature at the core surface |
| 2011-03-11-22:30 (2170 s) | Formation of rubble debris (start of clad melting then fuel) |
| 2011-03-12- 04:05 (3740 s) | formation of liquid debris started |
| 2011-03-12-07:46 (5500 s) | Maximum temperature at control rod (Complete clad, fuel and control rods melt and core failure) |

TABLE 38. COUPLE CODE RESULTS

| Couple code output | Value |
|---|---|
| Debris nuclear heat generation at each axial node at 2500 s | 1.7231 MW/$m^3$ |
| Mass of liquefied material in partially liquefied porous debris | 601 kg |
| Cumulative mass of $UO_2$ added to molten pool | 16.45 t |
| Cumulative mass of Zr added to molten pool | 542.1 kg |
| Cumulative mass of $ZrO_2$ added to molten pool | 2355 kg |
| Total oxidation heat generation at 5000 s | 1.1992 MW |
| Cumulative overall hydrogen production | 280 kg |
| Debris temperature at each axial node | 2808 K |
| Formation of liquid debris started | 3741 s |
| Temperature of location at time of degradation to rubble | 1092.5 K |

*5.4.1.9. Comparison between analytical model, simulation codes and operator analysis*

Table 39 contains the timeline of the main events calculated analytically using the RELAP/SCDAPSIM simulation. It also includes some timepoints found in the literature for comparison. It shows that the times predicted by using analytical methods tended to be sooner than those found in the literature and those calculated using code simulation. For example, the calculated TAF and bottom of active fuel were half an hour and two and half hours before the time values predicted in published data. One of the explanations can be that we assumed that the core included only fuel and clad but not structural materials.

TABLE 39. COMPARISON OF TIMELINE OF THE MAIN EVENTS ACCORDING TO TEPCO PUBLISHED DATA, RELAP/SCDAPSIM AND ANALYTICAL CALCULATIONS

| | TEPCO | Analytical Method | RELAP/SCDAPSIM |
|---|---|---|---|
| Top of fuel exposure | 17:00 [187], 18:10 [203] | 16:24 | -- |
| Bottom of fuel exposure | 18:14 [199], 19:40 [203] | 17:08 | -- |
| Start of hydrogen generation | | 22:44 | 22:15 |
| Clad started to melt | | 22:47 | 22:30 |
| Fuel started to melt | | 23:30 | 23:00 |

In addition, the generation of 280 kg of hydrogen estimated by RELAP/SCDAPSIM could not be calculated by analytical methods, in which we estimated that half of the zirconium reacted with the steam to generate hydrogen. Since the reaction with 1 kg of zirconium generates $4.42 \times 10^{-2}$ kg of hydrogen [191], we estimated that 1365 kg of zirconium would produce only about 72.27 kg of hydrogen.

This difference may be due to: (1) either more than half of the zirconium oxidized; (2) other elements in the reactor reacted with the hydrogen; or (3) the assumed amount of zirconium used in the calculations is incorrect. Yanez et al. [204] used an amount of zirconium in the reactor equal to 4.5 t and calculated the amount of hydrogen generated between 50—270 kg, depending on the method of calculations.

In summary, the analytical calculations and the code simulation estimates were very close in predicting the start of hydrogen generation. They also estimated similar times for fuel cladding melting, however, there was a significant difference in the estimated time for when the fuel started to melt.

## 5.5. THERMAL ANALYSIS OF THE CORIUM FOR FUKUSHIMA DAIICHI UNIT 1 ACCIDENT USING REACTOR EXCURSION AND LEAK ANALYSIS PROGRAM/SEVERE CORE DAMAGE ANALYSIS PACKAGE

The factors which affected the rate of cooling, spread and corium composition found on the base mat included composition and corium in–vessel behaviour, bottom of the lower plenum of the RPV degradation/failure and rate and time of the corium drop from the RPV [206]. To simulate the ex−vessel corium, it is necessary to simulate the in–vessel molten pool.

Several models were made to represent the molten pool in the RPV lower head. The models suggested that the molten pool was formed in different layers and compositions. The formation and total number of layers present depended on the amount of water in the lower head when the slump occurred, slump characteristics, and the materials present [201].

### 5.5.1. Corium characterization and composition

Generally, a molten corium pool, comprising metallic materials (for example, Zircaloy and fuel assembly structural materials) and oxide materials (such as $UO_2$) is likely to have formed during the initial accident stages [207]. The corium then divided into different phases that combined to form two layers, due to their density differences and related dynamic effects as shown in Fig. 173 [208]. The upper metallic layer without a volumetric heat source and a lower oxide layer with a volumetric decay heat source [201, 207, 209, 210].

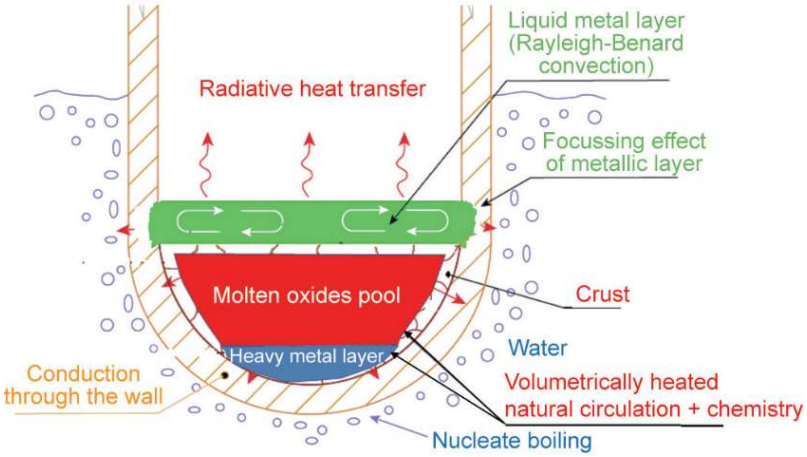


*FIG. 173. Corium with different layers (reproduced from Ref. [208] with permission courtesy of Ma et al.).*

The major materials in the corium are nuclear fuel ($UO_2$), cladding and fuel channel ($ZrO_2$), control rods ($B_4C$) and different varieties of steel, from the control rod cladding, sheaths, and the vessel. The melted control rod material was more soluble in the metal rich region therefore, most of the $B_4C$ was concentrated there. The reduction of $UO_2$ by Zr produced some amounts of uranium [211]. Between the molten pool and the RPV, some models proposed the presence of a crust [208, 212—214].

Over time, the different phases may have combined, because of density differences and related dynamic effects [200, 201, 215—217]. Other published simulations usually use a two layer formation with an upper metallic layer without a volumetric heat source and a lower oxide layer with a volumetric decay heat source [210, 211].

The decay heat generated in the oxide layer is predicted [218] to radiated to the internal of the RPV and side walls by natural circulation. The heat flux distribution depended on many aspects, including

melt pool constitution and configuration, internal decay power, RPV external boundary conditions, pool top state and crust formation [219].

The fuel, control rods, and a portion of the structural elements fell to the bottom part of the lower plenum as a result of the water evaporating in the RPV, exposing the fuel, and causing it to melt. This resulted in the RPV's bottom degrading and eventually failing [215].

Different codes have been used to simulate the corium in the lower plenum and to verify the time of failure. The predicted time for failure was between 8–15 hours after scram, depending on the code used and assumptions made [200, 201, 215—217].

The codes predicted that different quantities of corium at different temperatures fell from the RPV to the drywell. For example, Robb et al. calculated the quantity of corium to be around 140 t and between 1850–2100 K [200] while Luxat et al. calculated the temperature to be 2751 K [216]. The heat of decay was calculated to be between 86–110 W/kg, model dependent [200, 201, 220].

The corium is composed of uranium and zirconium oxides, structural steel and iron oxide (FeO) [200]. $ZrO_2$ and Zr masses depend on the oxidation fraction. Strizhov suggests that the degree of zirconium oxidation is around 50%, the U—Zr ratio is 0.8 and steel ratio is 0.3 [210].

The relocated $B_4C$ control rods masses are 1.4 t. The stainless steel structure was estimated to be 50 t [221, 222]. Table 40 presents the corium composition used in different models such as, MELCOR, modular accident analysis program–low pressure (MAAP–LP) and modular accident analysis program–high pressure (MAAP–HP). It can be noticed that the values are nearly the same.

TABLE 40. COMPOSITION OF MOLTEN CORIUM IN THE RPV USED IN DIFFERENT MODELS (based on data from [200])

| Total Pour Mass of Melt Constituent (kg) | MELCOR | MAAP-LP | MAAP-HP | MCNPX[b] |
|---|---|---|---|---|
| $UO_2$ | 69400 | 76153.2 | 76153.4 | 75770 |
| Zr | 25800 | 16594.1 | 16616.0 | 17800 |
| $ZrO_2$ | 16600 | 14141.5 | 14112.7 | 13820 |
| Cr | 5900 | 1135.9 | 1099.4 | 1130 |
| $Cr_2O_3$ | 30 | 2732.0 | 2765.5 | 2730 |
| Fe | 20430 | 16095.1 | 15928.4 | 12500 |
| FeO | 230 | 11210.5 | 11369.5 | 11210 |
| Ni | 2530 | 555.7 | 534.8 | 556 |
| NiO | 30 | 1208.2 | 1229.1 | 1210 |
| $B_4C$ | 0 | 502.0 | 502.0 | 590 |
| Fission Product[a] | – | – | – | 2490 |
| Inconel[c] | – | – | – | 1000 |
| Total | 140950 | 140328.3 | 140310.8 | 140806 |

a. MCNPX calculations.
b. EAEA Model Estimations.
c. Ref. [191]

Since no data is available on the instruments and structures below the vessel, most models either have not included them or made assumptions. Also, the initial condition of the existence of the amount of water on the drywell floor has not been defined, which could affect spreading behaviour.

Because most of the corium that fell was molten, it started spreading and cooling after hitting the base mat. The final spread area of the corium on the base mat was estimated by Robb et al to be between 30–110 $m^2$, depending on the code used, model scenario and assumptions [200].

Table 40 presents the total mass of the core composition at the time of the accident (before core melt) using MCNPX code.

After the core slumped and relocated to the lower vessel head, melting was complete by 2011-03-12-07:46, the composition and masses of the core materials involved were: FeO, 11.21 t; Cr, 1.13 t; $Cr_2O_3$, 2.73 t; Ni, 0.556 t; NiO, 1.21 t. The total mass of corium was 140.806 t.

### 5.5.2. Corium interaction with concrete primary containment vessel (outside pressure vessel)

The corium began to interact with the concrete due to its high temperature. The MCCI resulted in the ablation of the concrete base mat and he release of a combination of fission products, combustible gases, and steam into the containment [222].

A variety of chemical reactions can occur between the corium and the base mat concrete. Some of the reactions are exothermic while others are endothermic. Thus, some of these reactions were a heat source and contributed to further heating of the corium or were a heat sink and contributed to corium cooling [223].

According to Robb et al. the amount of $H_2$ released was between 75.4–701.5 kg, the CO was between 103.4–753.47 kg and the $CO_2$ gas was between 0.44–493 kg [200]. In a study by Kitagaki et al. [222], most of the uranium and zirconium in the melt was found to form (U, Zr)$O_2$ and (Zr, U)$SiO_4$, depending on the rate of cooling. The release of fission gases led to a decrease in the decay heat by about 20–25% [200, 225].

The time taken by the corium to solidify ranged from less than 3 hours after scram, when the models included the addition of water to cool the corium to two days when calculations assumed no water was added. The addition of water also significantly decreased the concrete ablation because of the decrease in temperature [200].

### 5.5.3. Thermal modelling of corium

Currently, there is no accepted criterion or correlation that can establish whether there is one homogeneous liquid pool or two stratified pools. Hence, the SCDAP model was assumed to be two stratified layers [213].

#### *5.5.3.1. Calculation of material properties*

The thermal properties of the various layers have been calculated to establish the temperature distributions, heat flows, and chemical interactions between the layers of the complex multiphase multicomponent corium mixture. Other properties such as density, thermal conductivity, viscosity, and heat capacity have also been derived.

As there is more than one material present in the corium the properties of the mixture and the corium layers in liquid and solid states need to be known.

The molar fraction of species *i* and density of the mixture as a function of temperature, *r(T)*, can be calculated by correlations. The following examines the properties of the oxide and metallic layers [226, 227].

(a) Uranium dioxide

The density of solid $UO_2$ can be obtained by Eq. 5 [228]:

$$\rho_{UO2}(T) = 10970 \times (9.9672 \times 10^{-1} + 1.179 \times 10^{-5}\mathrm{T} - 2.429 \times 10^{-9}\mathrm{T}^2 + 1.219 \times 10^{-12}\mathrm{T}^3)^{-3} \quad (5)$$

The specific heat (J/mol·K) can be calculated using Eq. 6:

$$C_P = \frac{2.457 \times 10^7 e^{548.68T}}{T^2(e^{548.68T}-1)^2} + 4.57 \times 10^{-3}T + \frac{4.37 \times 10^{11} e^{-1.853 \times 10^4/T}}{T^2} \quad (6)$$

For 298 < T < 3120 K, there are many equations that can be used for the 100% dense $UO_2$.

The IAEA–TECDOC–1496 [225] recommended that Fink's equation (Eq. 7) was the most complete [226]:

$$k(T) = \frac{1}{0.95} + \left[\frac{100}{6.548 + 23.533 \times 10^{-3}T} + \frac{6400\, e^{-16.35 \times 10^3/T}}{(T \times 10^{-3})^{5/2}}\right] \quad (7)$$

For 300 < T < 3100 K, Kim et al. predicted the thermophysical properties of liquid $UO_2$ up to 5000 K. The formulas they obtained are shown in Ref. [227].

(b) Zirconium dioxide

The thermal conductivity of solid $ZrO_2$ can be obtained from Eq. 8:

$$k(T) = \frac{1}{0.0893 + .0002T} + 1.3 \times 10^{-10} \times T^3 \quad (8)$$

For 300 < T < 2982 K

The density of $ZrO_2$ is almost independent of temperature, Eq. 9:

$$\rho_{ZrO2} = 6.1 \times 10^3 \ (g/cm^3) \tag{9}$$

For the heat capacity, Eqs 10–12 can be used [229]:

$$C_P = 565 + 6.11 \times 10^{-1} \ T - 1.14 \times 10^7 T^{-2} \tag{10}$$

For 300 K < T ≤ 1478 K

$$C_P = 604.5 \tag{11}$$

For 1478 < T ≤ 2000 K

$$C_P = 171.7 + 0.2164 \ T \tag{12}$$

For 2000 K < T < 2973 K, the thermophysical properties of liquid $ZrO_2$ for temperatures up to5000 K are found in Table 41.

TABLE 41. THE DENSITY, HEAT CAPACITY, DYNAMIC VISCOSITY AND THERMAL CONDUCTIVITY OF LIQUID $UO_2$ AND $ZrO_2$ IN CORIUM (based on data from [227])

| Property (units) | $UO_2$ | $ZrO_2$ |
|---|---|---|
| Density (ρ) (g/cm$^3$) | $\rho(T) = 4.40 - 8.31 \times 10^{-4}(T - 3120)$ | $\rho(T) = 7.56 - 2.86 \times 10^{-4}(T - 2988)$ |
| Heat capacity ($C_v$) (J/kg·K) | $C_v(T) = 390 - 0.900 \times 10^{-4} T$ | $C_v(T) = 940 - 3.36 \times 10^{-2} T$ |
| Dynamic viscosity (μ) (mPa·s) | $\mu(T) = 0.520 \ e^{8.26 \times 10^3/T}$ | $\mu(T) = 0.320 \ e^{8.79 \times 10^3/T}$ |
| Thermal conductivity (k) (W/m·K) | $k(T) = 1.64 + 4.74 \times 10^{-2} T e^{-1.45 \times 10^4/T}$ | $k(T) = 2.11 + 4.46 \ T e^{-2.75 \times 10^4/T}$ |

(c) Zirconium

The Zr density for temperatures up to 4000 K can be calculated using Eq. 13 [230]:

$$\rho_{Zr}(T) = 6844.51 - 0.609898\,T + 2.05008\ \times 10^{-4}T^2 - 4.47829\ \times 10^{-8}T^3 + 3.26469 \times 10^{-12}T^4 \quad (13)$$

The heat capacity of liquid Zr (J/kg·K) between 1825 and 2200 K, Eq. 14 [166]:

$$C_P(T) = 39.72 - 7.42\ \times 10^{-3}(T - T_m) \quad (14)$$

The heat capacity of solid Zr between 1400 and 2100 K, Eq. 15 [166]:

$$C_P(T) = \varepsilon_{Ts}[123.42 - 1.51\ \times 10^{-2}(T - T_m)] \quad (15)$$

Where $\varepsilon_{Ts}(T)$ is calculated using Eq. 16:

$$\varepsilon_{Ts}(T) = 0.29 - 9.91\ \times 10^{3}(T - T_m) \quad (16)$$

The thermal conductivity of solid Zr between 298 and 2000 K, Eq. 17 [169]:

$$k(T) = 8.8527 + 7.0820\times10^{-3}T + 2.5329\times10^{-6}T^2 + 2.9918\times10^{3}T^{-1} \quad (17)$$

The viscosity of liquid Zr (Pa·s) between 1850 and 2200 K, Eq. 18 [166]:

$$\mu(T) = 5.83 - 5.31\ \times 10^{-3}(T - T_m) \quad (18)$$

*5.5.3.2. Corium modelling using couple and severe core damage analysis package code*

The COUPLE code was used to simulate the thermal behaviour of core materials in the lower plenum, assuming full evaporation of the lower plenum water during the first relocation process of core material.

The COUPLE model determines the transient temperature distribution in a reactor vessel's lower head as well as the solid and molten debris supported by it. The model consists of two parts, a homogeneous or a stratified molten pool. The homogeneous part in COUPLE deals with heat transfer in the region using an existing algorithm if the pool has partial or completely molten core material.

The COUPLE calculates the heat transfer behaviour through applying the effective thermal conductivity concept for every computational cell. The transient temperature distribution for the lower head and for the regions with liquefied or solidified debris is determined through the heat conduction equations and correlations for natural convection heat transfer at the liquid–solid interface.

The liquid–solid interface includes the following locations: (1) molten corium pool facing sides of solidified crust at the inner surface of the lower head; (2) molten corium pool facing side of solidified material on top of corium pool [213].

From the modelled scenario, reactor scram occurred at 500 s equivalent to 2011-03-11-14:46, the reactor pressure started to decrease immediately from 7 MPa until it reached 0.9 MPa on 2022-03-12-03:00 as shown in Fig. 6 of Ref. [167]. The results of RELAP/SCDAP are in close agreement with MELCOR results. In addition, the model calculated the start time of hydrogen formation, rubble debris and core melt and the corresponding temperatures.

The hydrogen generation started at time 21:32, the formation of rubble debris at 22:30, the formation of liquid debris started at 04:05 the following day (12 Mar. 2011), and finally, the complete core melt was at 07:46. The temperatures correspond to the start of hydrogen generation, rubble debris, liquid debris and complete core melt were 505, 505, 1400 and 2700 K respectively, as shown in Fig. 174.

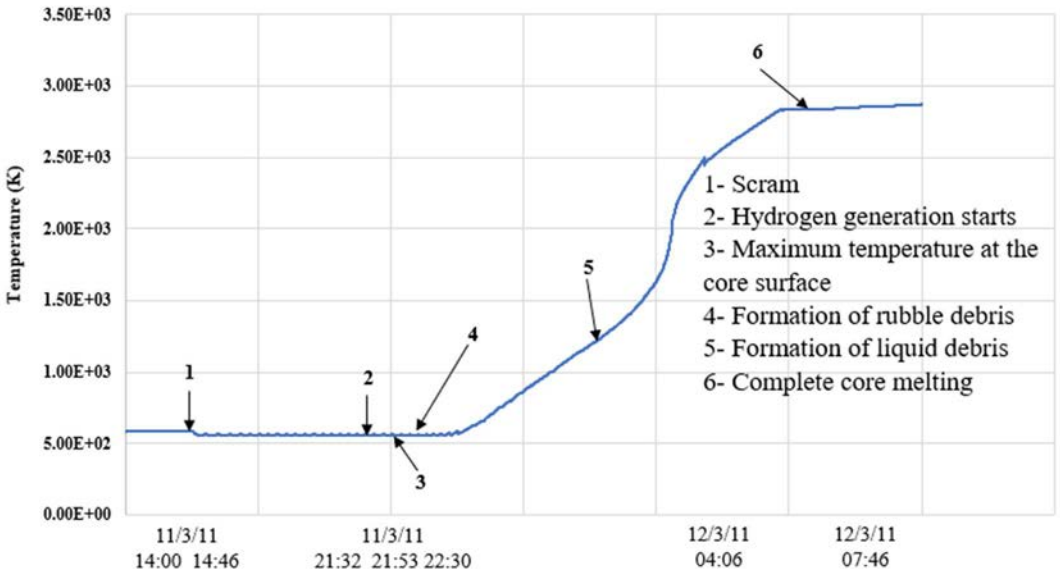


*FIG. 174. Time history against temperature of core melt for 1F (courtesy of EAEA).*

The complete melting of the reactor core ended on 2011-03-12-04:58 when the temperature reached 2700 K, as shown in Fig. 174. It can be concluded that the temperature started to rise when the coolant was no longer capable of removing the decay heat. This corresponded with the release of hydrogen as a result of the Zr reaction with steam/water and caused additional heat to be generated in the core.

*5.5.3.3. Activity and specific activity of the corium melt*

The corium radionuclides activities and masses were calculated after 10 years and 50 years from the time of the accident using MCNPX code, the results after 10 years are shown in Table 42.

The total corium activity after 10 years is $6.09 \times 10^{17}$ Bq as shown in Table 42. After 50 years the corium activity reduces to $1.89 \times 10^{17}$ Bq and is dominated by the long lived radionuclides. For safety considerations in partitioning and handling, we assumed that the corium is a heterogeneous mixture, its specific activity is the same for the highest radionuclide which is $^{137}$Cs with a value of $3.21 \times 10^{12}$ Bq/g.

TABLE 42. CORIUM RADIONUCLIDES ACTIVITIES AFTER 10 YEARS

| Radionuclide | Activity (Bq) | Mass (g) | Radionuclide | Activity (Bq) | Mass (g) |
|---|---|---|---|---|---|
| Cs-137 | 1.57E17 | 4.88E4 | Zr–93 | 3.52E12 | 3.78E4 |
| Pu-241 | 1.53E17 | 4.00E4 | Pu–242 | 2.14E12 | 1.46E4 |
| Sr-90 | 1.22E17 | 2.34E4 | Cs–135 | 1.22E12 | 2.86E4 |
| Kr-85 | 9.58E15 | 6.60E2 | U–238 | 8.11E11 | 6.52E7 |
| Cs-134 | 7.34E15 | 1.53E2 | U–236 | 6.44E11 | 2.69E5 |
| Am-241 | 3.45E15 | 2.72E4 | Np–237 | 5.32E11 | 2.04E4 |
| Pu-238 | 3.39E15 | 5.35E3 | U–234 | 1.29E11 | 5.61E2 |
| Pu-240 | 1.00E15 | 1.19E5 | U–235 | 8.31E10 | 1.04E6 |
| Pu-239 | 9.18E14 | 4.00E5 | Rb–87 | 4.38E7 | 1.38E4 |
| Sm-151 | 6.29E14 | 6.46E2 | | | |
| Total Activity | 6.09E17 | | | | |

## 5.5.4. Modelling of accident progression summary

The radioactive inventory of 1F core was modelled by simulating one assembly to reach the core conditions at last operation on 11 Mar. 2011. The melted fuel inventory and the variation of activities over the period 2011 to 2061 were then calculated using MCNPX code.

The atmospheric releases of key radioactive materials originating from 1F were calculated and compared with TEPCO's sampling results. The calculation of the dose rate distribution resulting from the air plume submersion and shine from radioactive deposits on the soil surface was performed using the HOTSPOT code (Gaussian plume model). The results showed that:

- The maximum calculated dose rates resulting from air submersion and ground shine are 0.03 and 0.005 Sv/h at a distance of 0.27 km from the reactor;
- HOTSPOT results for integrated time concentration of $^{131}$I in air were compared with NOAA estimates to be varied around 0.155 and 6 apart from an extremely overestimated value of 150. The comparison with IRSN estimates also varied around 0.1 and 0.6 which is regarded as an acceptable agreement (see Table 32).

The thermal performance of the core was performed by two methods:

- The first method by using analytical calculations to estimate the times at which the surface of the fuel was uncovered, the whole fuel was uncovered, the fuel started melting, and for the hydrogen to start being generated;
- The second method by using RELAP/SCDAPSIM code to model and simulate the station blackout that occurred during the accident. The RELAP/SCDAPSIM results were compared with the results of TEPCO and MELCOR code and found in close agreement.

# 6. TECHNOLOGIES FOR THE INSPECTION OF POST ACCIDENT CONDITIONS

Section 4 introduced some of the advances in technology to inspect and remediate severely damaged FAs. For example, the image in Fig. 149 was captured by an off the shelf non radiation tolerate high definition video camera, available at a relatively modest cost. The following Section provides an account of the technologies that have been used in the past to inspect/remediate the consequences of severe accidents and then goes on to look at the advances been made in support of 1F inspections.

## 6.1. THREE MILE ISLAND EXPERIENCE

Visual examination was performed using video cameras to identify specific locations to derive an estimate of volume of debris in a location and compare sample data to establish a fuel content value. Poor lighting, lack of water clarity and limited access contributed to fuel estimate uncertainty regarding items identified in video. Due to the nature of all of these systems, substantial uncertainty exists due to the heterogeneity of the material. It should be remembered that even in a reprocessing facility where fuel is dissolved to the maximum extent practical resulting an essentially homogeneous product, uncertainty will be present due to the cumulative effect of analytical measurement error, sampling error and mass measurement error.

Radiometric methods such as several types of dosimeters were used to establish the location of displaced core material. Techniques including ultrasonic surveying were used to establish the contours of the main core melt.

### 6.1.1. Water treatment and reactor and auxiliary building cleanup

Prior to entry to the reactor buildings, the initial response required cleanup of approximately 2.12 million liters of water from the flooded reactor containment and auxiliary building. This first involved the Cuno (brand) filter system, in which the filter vessels were specially constructed with lead weights in the bottom to assure that they did not float when submerged. The Cuno filters were a part of the submerged demineralizer system, which was installed in the TMI–2 fuel pool. This was followed by processing through a series of filters and ion exchange media developed by Epicor Inc. The EPICOR–II system used a three stages system of prefilters and inorganic and organic resins to remove particulate and dissolved fission products.

Although it is common to focus on the mechanical and logistical heroics involved in removing the melted core material from the reactor vessel that occurred years after the accident, a major part of the initial post–accident recovery was decontamination of various parts of the reactor, auxiliary, and fuel handling buildings. Contaminated water was released to the reactor building sump in the early minutes of the accident when the primary coolant being dumped to the reactor coolant drain tank caused the overflow valve to open and then the rupture disc to burst. This sump water was transferred to the auxiliary building sump tank. Other systems, including the makeup and purification system, also received highly radioactive core material. A relatively small quantity of core debris, estimated to be less than 10 kg, was spread through these systems following the opening of the PORV.

Reactor building dose reduction started with processed water flushes of all surfaces of the accessible areas between the 93 and 106 m levels. This was followed by mechanical scabbling of painted and concrete surfaces to remove embedded activity. Many remote technologies were developed and deployed to minimize personnel exposure and speed up the cleanup. Numerous documents including EPRI-NP-6931 [231] report the types of techniques used. Cleaned areas were sealed with epoxy paint and other coatings to minimize recontamination potential.

Due to the material's porosity, some concrete block wall surfaces were scarified using a remotely operated water lance. The internal voids of the block were flushed to remove sediment that had settled inside.

The water generated by the flushing, scabbling and scarification was processed through the submerged demineralizer and Epicor–II filtration and ion exchange systems (Fig. 175). The surface cleaning operations generated an estimated 4900 kg of sludge. A remotely operated sludge suction system was able to remove sludge from approximately 40% of the accessible reactor building basement floor area. An estimated 4 kg of fuel were contained in the sludge.

Fuel material and contamination in the reactor cooling system were removed using spray nozzles and submersible pumps during the first phase, followed by a remotely operated submersible that was used to pick up large discrete pieces that were present in the pressurizer vessel.

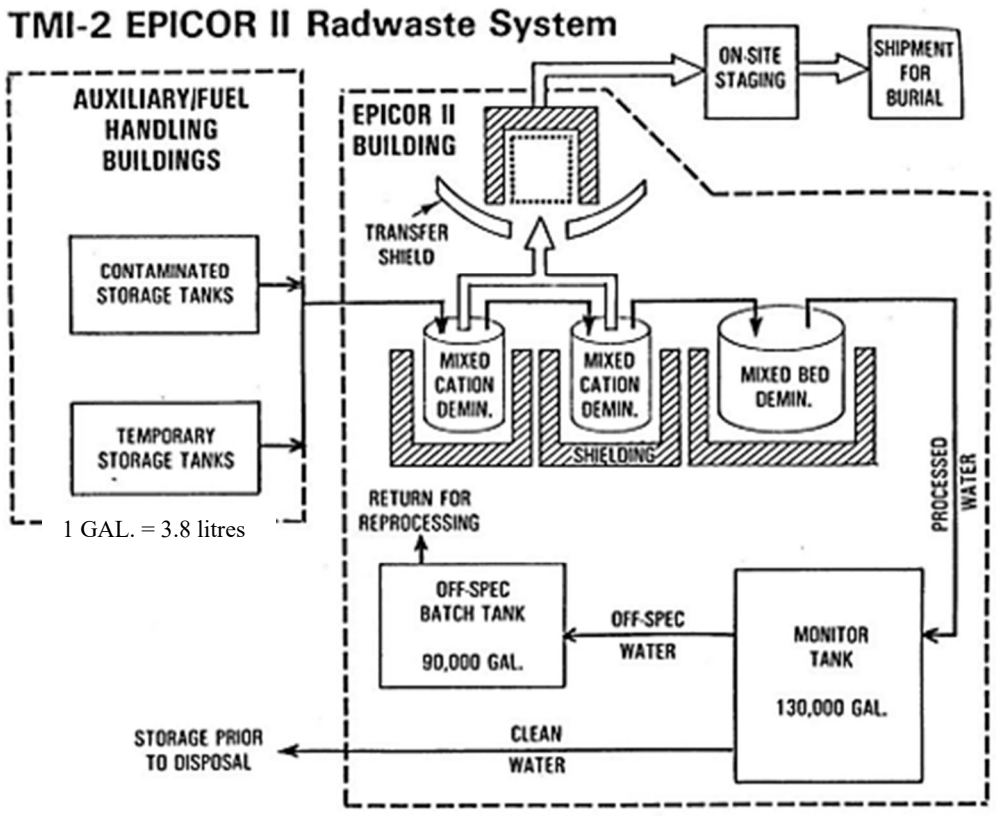


*FIG. 175. Water cleanup schematic (courtesy of INL).*

Following treatment, the water was contained onsite in two 1.9 million L epoxy coated welded carbon steel tanks. In some instances, the water was recycled to be used for decontamination purposes.

In accordance with the supplement to the environmental impact statement, 8.7 million L of treated water was disposed of by evaporation through the processed water disposal system. This unit was a closed cycle evaporator that discharged the vapour through the facility's 30.5 m tall exhaust stack. Included in the vapour released to the environment was an estimated 37.74 TBq of $^{3}H$ and 0.09 TBq of other nuclides including $^{90}Sr$, $^{14}C$ and $^{137}Cs$. An estimated 136 t of boric acid was included in the effluent [232].

### 6.1.2. Vessel internal inspection

Several options were considered for doing a visual inspection of the reactor vessel, but logistics of crane availability and equipment movement limited the alternatives, which ultimately would have led to multiyear delays. Core characterization began in earnest in 1982 with the quick look programme, which amounted to insertion of a Westinghouse Model ETV–1250 black and white analogue video camera into the reactor vessel through the 35 mm ID control rod drive mechanism penetrations following the removal of the leadscrew [233]. The camera was 31.75 mm OD × 355.6 mm long. Figure 176 illustrates the video camera insertion approach, and Fig. 177 (a) shows video images of the debris from that camera: and the view of fuel components still attached to the lower side of the upper grid plate.

The initial plan was to insert the camera at centre, midradius and outer diameter positions in the core, but removal of the B–8 control rod proved impossible, so no outer diameter location was available. The camera was suspended by its cable and used a second wire that could be used to change the camera angle for a lateral view. The camera could also be fitted with a right angle lens for lateral viewing. In-vessel views showed a 1.2 m deep void in the centre of the core. A steel probe could be inserted into the debris 30 cm before encountering a rigid layer hard stop. Pivoting the camera to look at the lower side of the core upper grid plate showed the remains of partial rods as seen in Fig. 177 (b). Suspended particulate in the water limited visibility, meaning only a limited amount of information about core conditions could be determined.

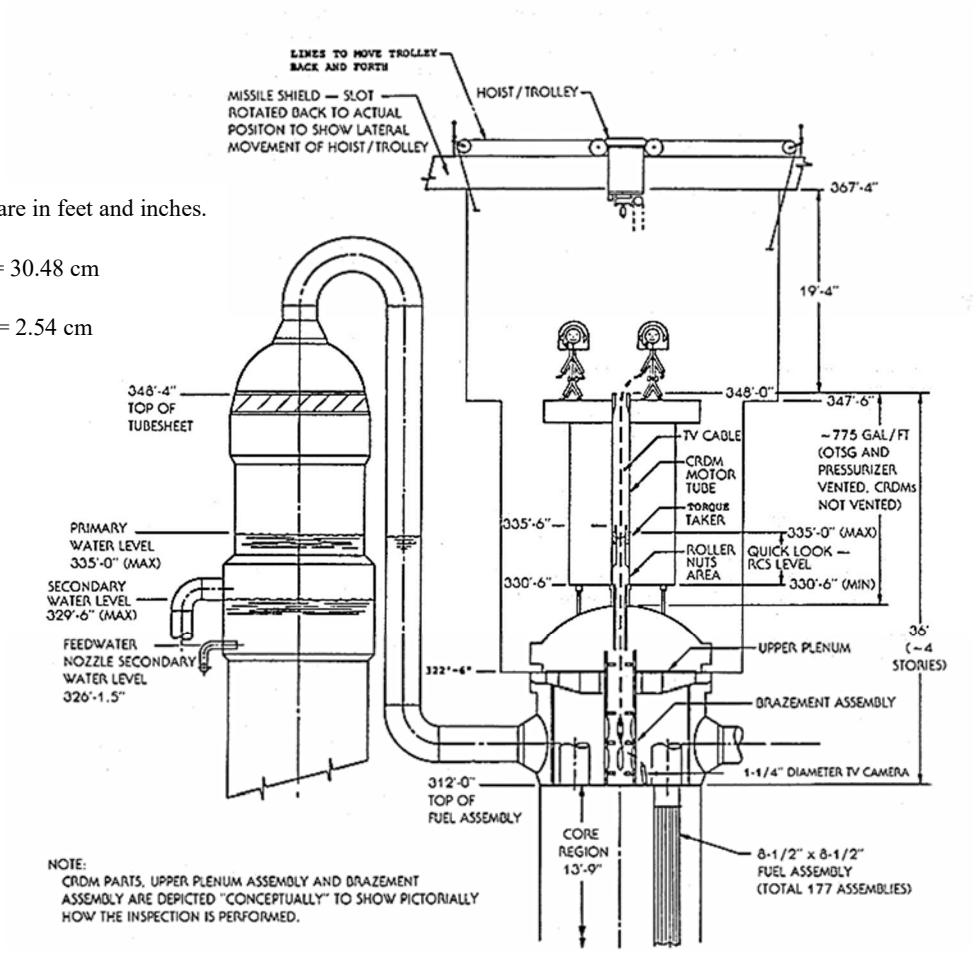


*FIG. 176. Quick look video schematic cartoon (reproduced from Ref. [231] with* permission *courtesy of EPRI).*

Additional video work was done after the vessel head was removed and the plenum was jacked up. A Rees model R–93 black and white analogue video camera 40 mm in diameter was lowered through the downcomer area between the vessel wall and the core former barrel to inspect the area below the core support structure. This inspection required additional lighting to be able to clearly see the debris that had relocated to the bottom head. After the plenum was removed a more controlled video survey of the lower head was done, again with a Rees model R–93 camera. Improved control was achieved by using an aluminium pole with an articulating joint to position the camera rather than just allowing it to hang from its cable. A significant amount of the main debris recovery work in the vessel was done using the R–93 camera that had been fitted with a zoom lens and remote light and focus controls as well as a pan and tilt function.

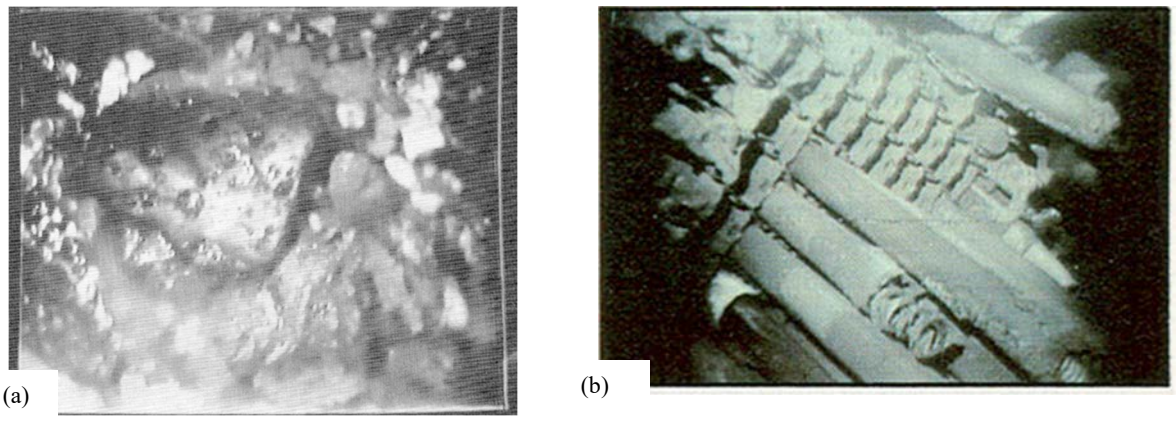


*FIG. 177. (a) Quick look video image of debris bed (reproduced from Ref. [231] with permission courtesy of EPRI). (b) FA remnants hanging from upper grid plate (courtesy of INL).*

The underside of the plenum and the upper grid plate were imaged both with the camera submerged, and after the water level was lowered, in air so that damage and fuel debris presence could be assessed.

As the standing fuel assembly fragments were removed from the periphery of the core, damage to the baffle plates was visible, and a Welch–Allyn video probe as well as a Diaguide fiber optic camera were used. These cameras had higher resolution than the Westinghouse and Rees cameras and could operate in lower light. These views helped recovery engineers develop estimates of the amount of fuel present behind the baffle plates and design retrieval methods.

A Rees R-93 camera was inserted into the holes created during the core boring in the stratification investigation to get images at various depths inside the melt.

Eventually, colour video technology was provided in the form of a fixed focal length lens Bore Tech BT2020 camera that produced high resolution analogue images. Despite the lack of a zoom lens this unit was a significant improvement in that being able to visualize colour allowed the team to distinguish different aspects of the components being disassembled in 1988 and 1989.

The final accountability inspection to estimate the amount of fuel debris remaining in the vessel was primarily done with the Bore Tech model BT2020 colour camera to evaluate the size of residual accumulations. A Rees model R–93 camera was used to inspect the inaccessible areas under the lower core support assembly (LCSA). The camera was dropped through holes in the LCSA with a right angle lens mounted to look laterally around the perimeter of the assembly. Thirty hours of video were recorded to provide evidence of the thoroughness of the recovery effort.

### 6.1.3. Radiation detection for fuel location determination

Quartz crystal solid state track recorders were inserted into the space between the biological shield and the reactor vessel for approximately three weeks in 1983 to do neutron dosimetry to map the flux profile of the vessel. Seventeen dosimeters mounted at specific elevations on a cable indicated that the equivalent of four FAs was present in the lower head of the reactor vessel. The parameter being measured was fission rates of fissile $^{235}U$, $^{239}Pu$, and $^{237}Np$ [234].

Other efforts to measure the mass of fuel in the lower head included insertion of a Westinghouse miniature ionization detector into the core through one of the accessible in-core detector tubes on the bottom of the reactor pressure vessel.

Thermoluminescent dosimetry (TLD) combined with a shielded, collimated Geiger Müller detector were used to establish a gross radiation profile of the material behind the core baffle plates by lowering a unit containing the detector and several TLDs in the lower head region.

### 6.1.4. Containment building general radiological conditions

Because it was possible to keep the reactor pressure vessel filled with water for shielding, at the time that the video inspections and grab sampling were performed, general body fields within the containment building had dropped from approximately 4.3 to 1.5 mSv/h at the entry level and to approximately 0.6 mSv/h at the top of the reactor vessel as shown in Fig. 178.

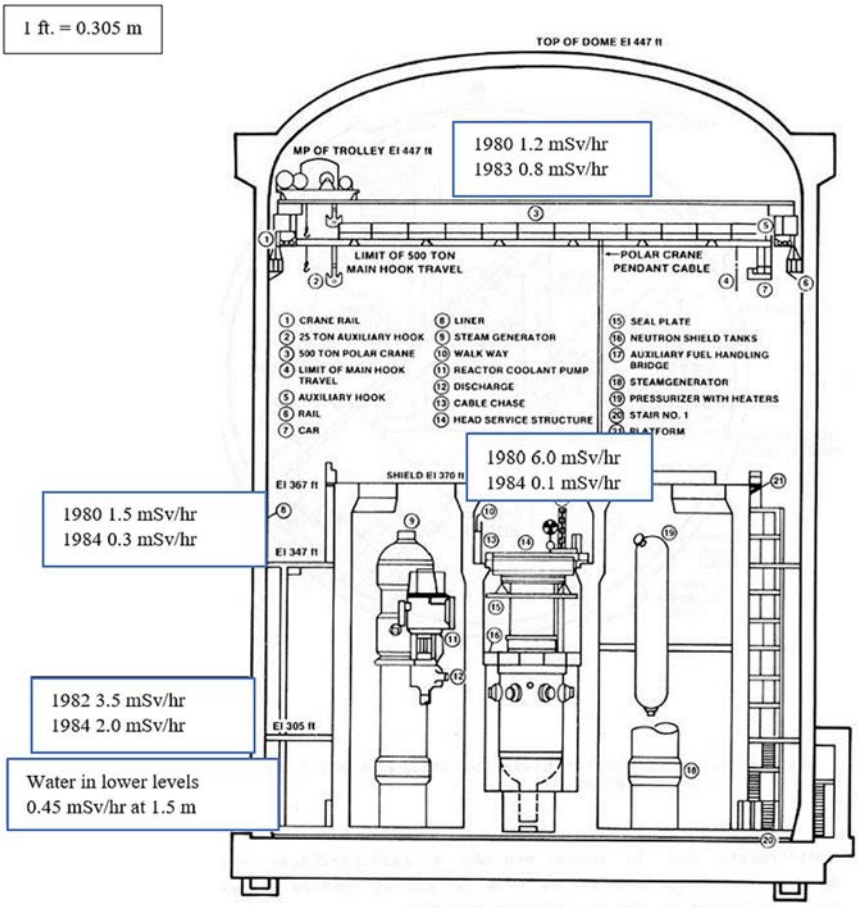


*FIG. 178. Containment building dose rates, 1980 and 1983 (courtesy of INL).*

### 6.1.5. Ultrasonic core topography mapping

A multiple-transducer underwater ultrasonic system was developed at INEL to provide a detailed survey of the contours of the irregular melt structure. The system was deployed in 1983 and collected data from two downward facing 2.25 MHz transducers that were positioned using a 13 m long tool. The transducers were lowered to within 15 cm of the surface and then raised in 2.5 cm increments. At each increment, a horizontally oriented transducer was rotated 360 degrees, providing a range indication of the contour, as shown in Fig. 179.

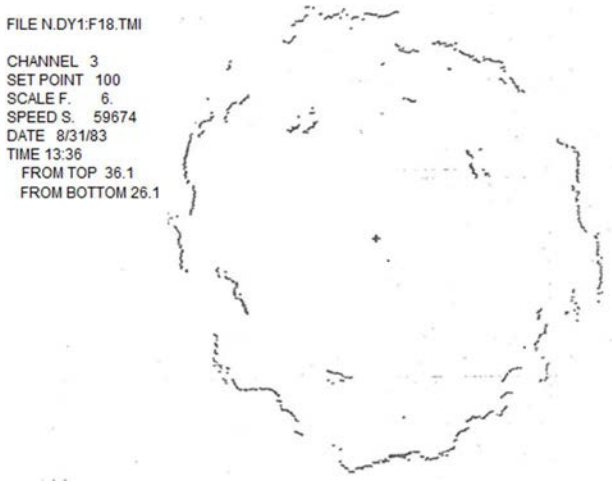


*FIG. 179. Range bearing plot from ultrasonic survey (reproduced from Ref. [235] with permission courtesy of INL).*

Compilation of the various elevation plots allowed the plots to be converted into an iso-height map (Fig. 180) and then three dimensional physical model (Fig. 181) that was used to evaluate recovery options.

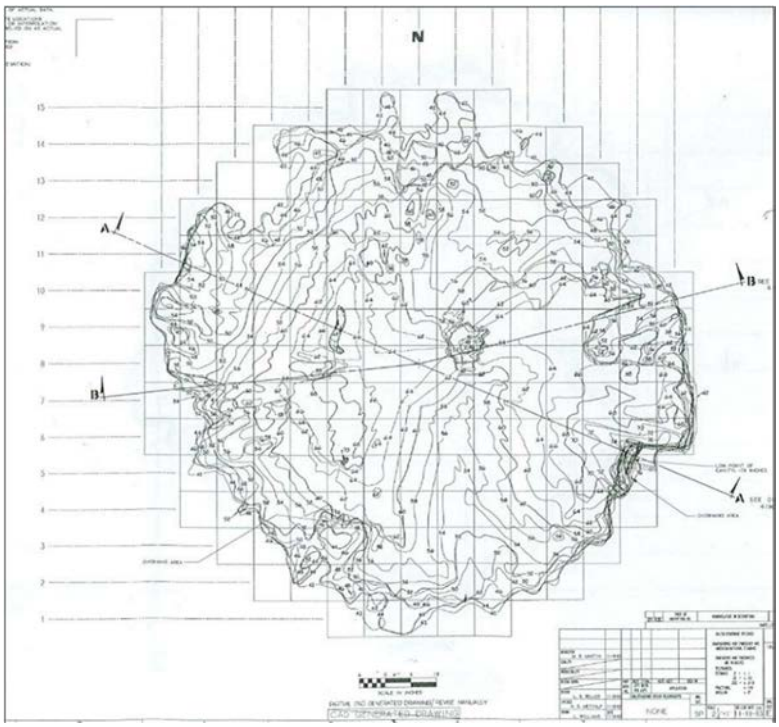


*FIG. 180. Iso–height map of core melt contour (reproduced from Ref. [235] with permission courtesy of INL).*

*FIG. 181. Acrylic layer 3D model reconstruction cross section (courtesy of INL).*

### 6.1.6. Reactor pressure vessel head removal

One of the most significant efforts in the process of recovery was to gain access to the internals of the RPV. Large scale efforts went into planning, engineering, and training to remove the reactor vessel head. A shielded location for storing it was constructed, a special shielded control booth for the crane operations was built, and monitoring and control systems were engineered. As part of the stabilization efforts, the system was filled with water, including the pressurizer, which is substantially higher than the top of the pressure vessel. The water level needed to be lowered to allow the head to be removed. By mid-1984, the polar crane certification was completed; the RPV head could be jacked up a small distance, allowing conditions to be evaluated. One of the most significant efforts in the process of recovery was to gain access to the internals of the RPV. Large scale efforts went into planning, engineering, and training to remove the reactor vessel head. The head was carefully removed and stored, allowing the internals indexing fixture to be installed so that the plenum could be removed while under water. The upper plenum was inspected, and it was determined that it had only sustained a small amount of damage. By late 1984, the plenum was raised and inspected, and by mid–1985, it was removed, allowing inspection of the bottom side of the upper spacer grid. The upper spacer grid had remnants of fuel elements stuck in it, requiring operators to push the stubs back into the vessel prior to removing it. A view of the underside of the upper spacer grid fuel bundle removal is shown in Fig. 182. Some melting of the highest temperature central area of the grid is visible.

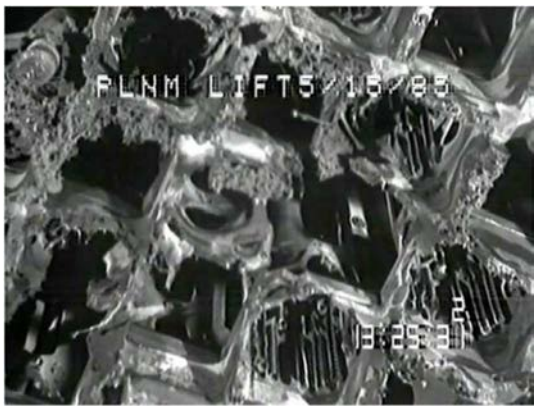


*FIG. 182. Underside of upper fuel grid showing evidence of melting (reproduced from Ref. [236] with permission courtesy of INL).*

Fig. 183 shows a diagrammatic view of the grid plate with regard to areas where fuel assembly top temperatures caused melting by exceeding 1750 K.

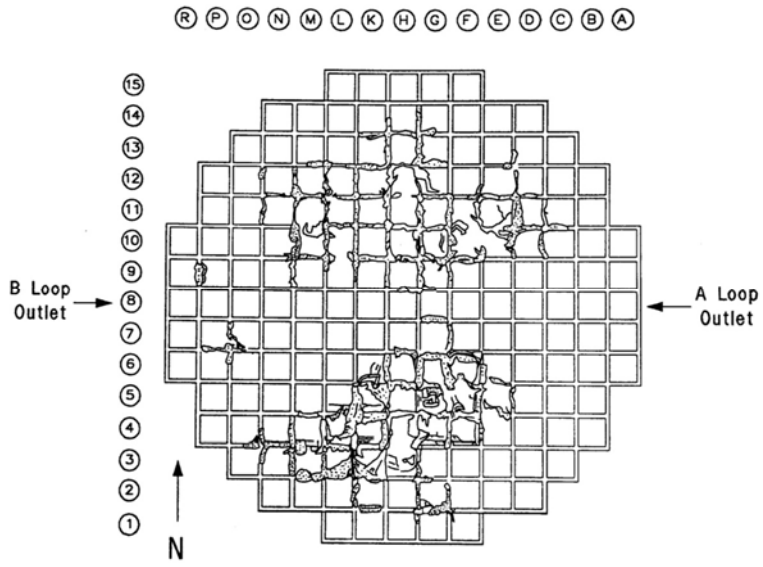


*FIG. 183. Areas of upper fuel grid plate where melting occurred (reproduced from Ref. [1] with permission courtesy of INL).*

Once the RPV upper head was removed, it was possible to evaluate the degree of damage more completely. Around the perimeter of the vessel, 42% of the 177 FAs were recognizable. Of the standing assemblies, all were damaged, with two that had damage to only ten percent of their rods. Various views of damaged fuel rods are shown as Fig. 184.

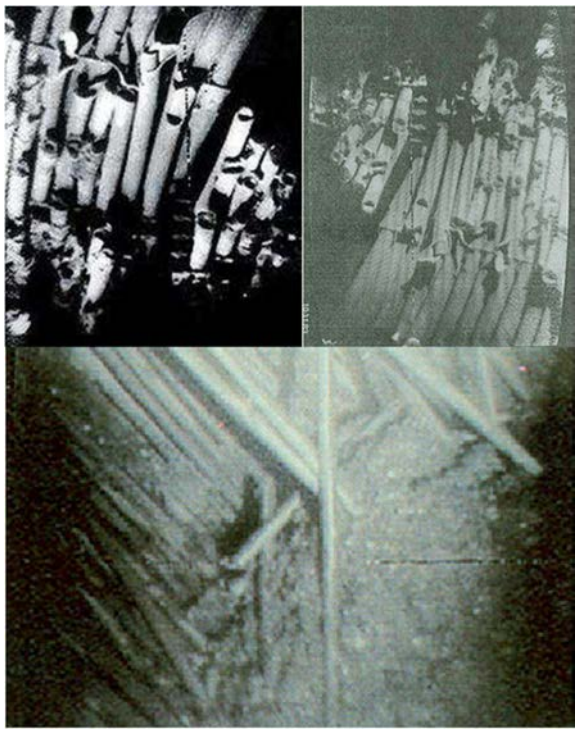

*FIG. 184. Remains of FAs (upper view, hanging rods; lower view, rods fallen into debris bed (courtesy of INL)).*

### 6.1.7. Distinct component recovery

After removal of the upper head, the plenum assembly was removed. To achieve this result, the upper end fittings from numerous fuel assemblies had to be dislodged from the upper grid. Fourteen of the end fittings were melted to such a degree that four could not be removed and ten could only be partially removed. The plenum was also washed down using a water jet, which was able to displace fines and pieces that were approximately the size of fuel pellets.

The first material removed from the RPV included 110 upper end fittings as well as control rod and burnable poison rod components. Five partial FAs were included in the eighteen debris canisters that were shipped to INEL for examination.

### 6.1.8. Core stratification sampling programme

An overview of the core stratification sampling programme is provided in Section 3.1.2. This Section provides further information on the technology deployed in the programme.

To accommodate materials ranging from metallic to ceramic, the core boring system that was used was based around a bit that used a combination of industrial diamond and tungsten carbide, silver soldered into the drill body. The drill bit type is shown in Fig. 185. This type of bit is hollow and creates a hole with a cylindrical centre core that is removed with the drill, resulting in an elevation representative section of the material it bores through. In this case, it is a sample core that was extracted by boring through the formerly melted reactor core.


*FIG. 185. Core sample core drill bit (courtesy of INL).*

The drive unit for the core boring system used a hydrostatically driven spindle and hydraulic drill string raising and lowering mechanism. A 37 KW electric motor drove a hydraulic pump that ran the spindle as well as the hydraulic pump for raising and lowering. Drill operations were monitored for rotational speed and torque applied, as well as vertical force applied to the bit. The drill could operate from 0 to 500 rpm, with a torque from 0 to 4067 Nm and a vertical force of up to 4535 kg applied to the bit. The system was designed to work with the shielded defuelling platform and reach any position within the central 2.4 m of the core diameter. The system was constructed in modules to allow it to be transported into the containment via the 1 m × 1.9 m airlock doors.

The core bores were acquired using an 89 mm OD core barrel attached to a sectional drill string that allowed the bit to be driven to the full depth of the reactor vessel to extract a 63.5 mm OD core. During operation, the drill bit was cooled, and chips flushed by using a 23 L/min flow of the borated water that filled the reactor vessel. The selected equipment was a Longyear Corporation 38EHS unit, and used a Megalo head spindle, which allowed for adjustment of the jaw diameter to the required

diameter of the drill string casing. A 114 mm OD casing was inserted into each hole that was bored to provide stability for the drill string and keep the hole open if video viewing was to be performed. The core barrel length was 3.35 m to assure that it would be able to fit inside the debris canister.

Due to preinstallation testing using mock materials, the spindle torque and vertical force values provided an indication of whether the drill was running through standing fuel arrays, loose rubble, metal, or ceramic debris.

The system was mounted to the defuelling platform in a manner that allowed radial and rotational position of the drill location to be precisely controlled. That position was confirmed by use of a surveyor's theodolite. Figure 30 shows an elevation view of the drill orientation on the platform and its position in the vessel. Figure 31 shows a plan view of the locations in the core where samples were taken, and visual inspection performed.

Following the receipt and analysis of the grab samples and the core bore samples, it was possible to combine that information with the video and ultrasonic probe data to reconstruct the post–accident melt profile. Additional information regarding the material that accumulated in the lower plenum was the result of removal of the lower core support structures. The reconstructed melt image has been included in every general explanation of the melt outcome and is repeated here as Fig. 186.

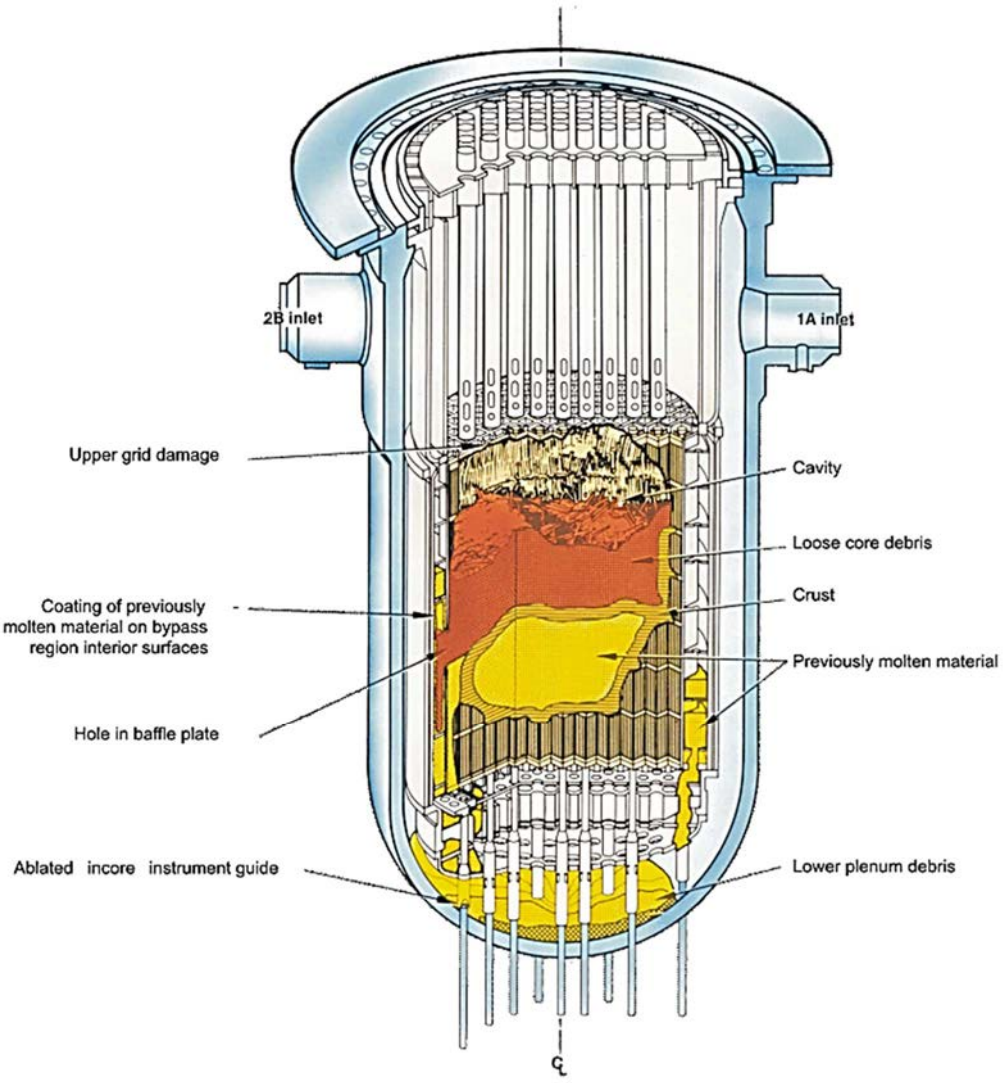


*FIG. 186. Final reconstruction of post-accident in-vessel debris configuration (courtesy of INL).*

### 6.1.9. Vessel investigation project

As a result of the determination that a significant part of the melt had relocated to the lower head of the reactor pressure vessel, a separate effort was organized to evaluate its effects. Fifteen samples of the head material were acquired with reach tools from the top head work platform after the solidified core material had been removed. Other samples included sections of instrument guide tubes. The steel samples were analysed using tensile, microhardness, Charpy V–notch impact, and creep testing. Analysis of the samples' chemical composition was also performed. Temperature effects were evaluated using optical metallography. The estimated temperatures from several locations ranged from a local maximum of 1373 K to a general maximum of 1000 K. Some cracking was observed around instrument nozzles, but no through wall penetration occurred. It was concluded from various calculations that the vessel could have sustained the local maximum temperature for thirty minutes if heat could be dissipated to relatively cool sections of the vessel [89].

### 6.1.10. Core removal

Multiple approaches for core removal were considered prior to receipt of the first characterization data. Five official predictions of the degree of core damage were compiled into a single report [237]. This report was used as a basis for development of design concepts for defuelling. These were the dual telescoping tube/manipulator system, the manual defuelling cylinder system, the indirect defuelling cylinder system, the flexible membrane defuelling system, and the dry defuelling system. The dual telescoping tube system would have mounted two telescoping tubes on the TMI–2 defuelling bridge and remotely operated them by closed circuit video. The manual defuelling system was a design with a rotating cylinder supported on the top flange of the reactor vessel with a slot through which operators would perform manual removal of the core. The indirect defuelling cylinder system was to have inserted an X–Y bridge with a telescoping tube in place of the manual tools of the previous design. The flexible membrane defuelling system would have incorporated an X–Y bridge using a single telescoping tube operating through a conical contamination control membrane and used a separate tank whose support arms were to have pivoted out over the reactor vessel to hold manipulators canisters, buckets, and tools in support of the manipulation function of the telescoping tube. The dry defuelling system was to insert an indexable shield ring on the top flange of the reactor vessel that used an access port to remove debris via a heavily shielded transport cask (Section 8.2.2 of Ref. [231]) .

Considerable discussion about the merits of manual versus automated core removal included the possibility of using the Westinghouse remotely operated service arm (ROSA) to shred the melted core and transfer the result by vacuum to canisters outside the reactor vessel. One of the negative aspects of this approach was the dispersal of the core nuclides, increasing the dose potential and placing a greater demand on the water cleanup systems. Several variations of the remote and manual core recovery systems were proposed, but all had problems of complexity and delays due to development and testing of tools to size materials that were poorly understood and not well characterized.

Due to the expected delay in the automated tool system development and the cost and availability of the polar crane, it was decided that the manual defuelling approach was the most expedient. The manual shielded defuelling platform was fabricated and installed on the top of the reactor vessel to perform core recovery. The platform was a shielded turntable with slots through which extended reach tools could be used to pick up individual pieces of debris and accumulate them in baskets that were used to fill the fuel debris canisters. The platform also supported the canister handling system and included specific ports for canister removal. An isometric view of the platform is shown in

Fig. 187. The work elevation was 2.75 m above the upper flange of the reactor vessel, as seen in Fig. 188 (a). Figure 188 (b) is a photograph of the deployed system from above.

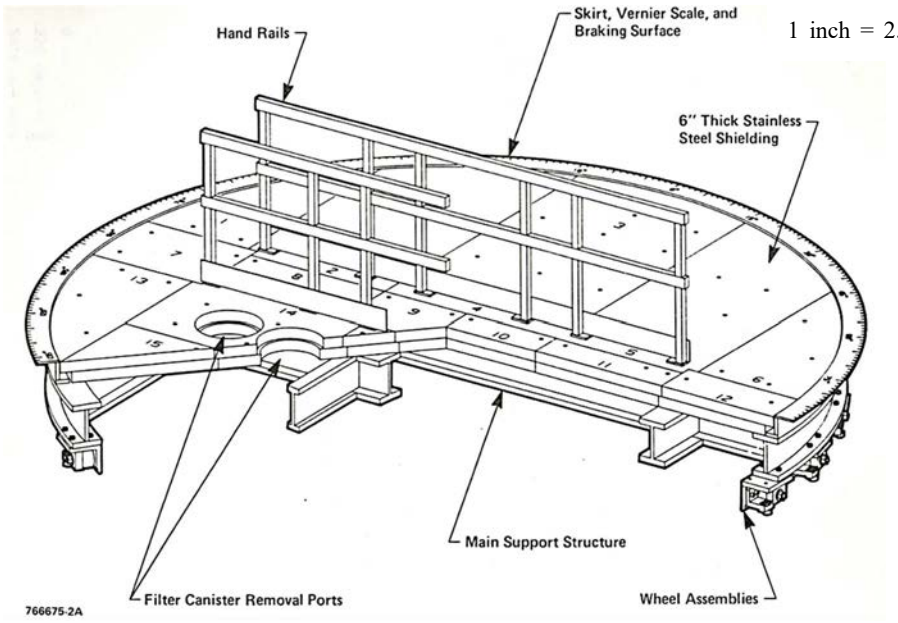


*FIG. 187. Manual shielded defuelling platform* (*reproduced from Ref. [238] with permission courtesy of US DOE).*

(a)

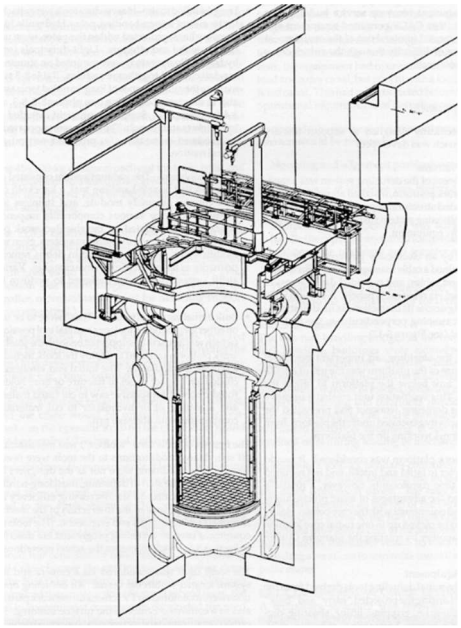

(b)

*FIG. 188. (a) Defuelling platform schematic in position on reactor vessel (reproduced from Ref. [231] with permission courtesy of EPRI). (b) Photos of shielded defuelling work platform (courtesy of INL).*

The platform also supported a five canister turret system that allowed multiple canisters to be loaded, as shown in Fig. 189. Once loaded, the canisters were weighed and then selectively transferred to the fuel pool for dewatering prior to loading into the transport cask.

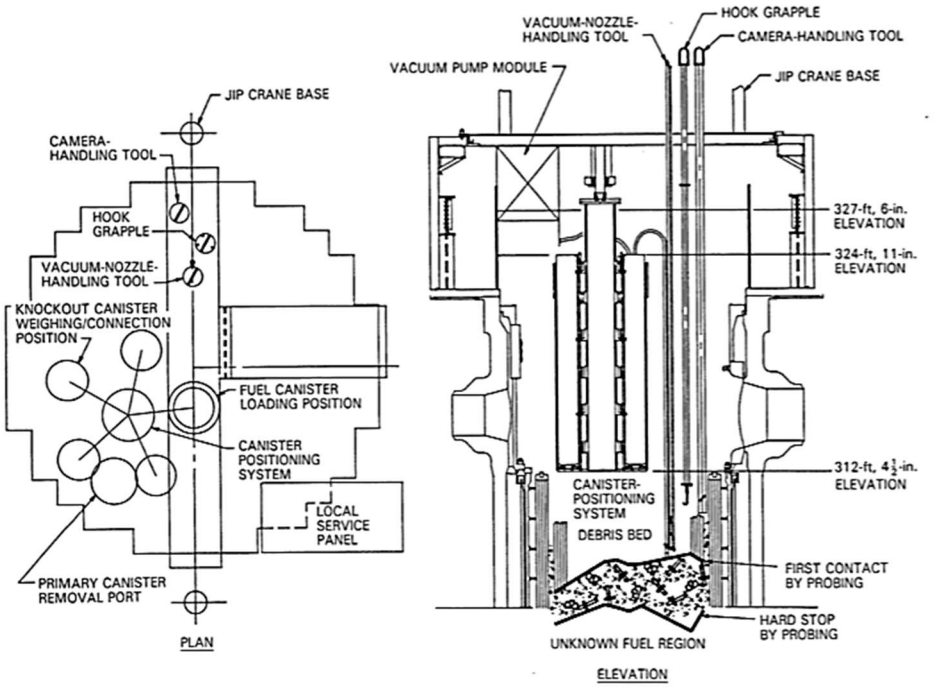


| Elevation conversion | |
|---|---|
| (ft.– in.) | (m) |
| 327 – 6 | 99.82 |
| 324 – 11 | 99.03 |
| 312 – 4.5 | 95.21 |

*FIG. 189. Canister positioning system (reproduced from Ref. [239] with permission courtesy of INL).*

Once a canister had been filled to the desired limit, it was closed, lifted out of the reactor vessel through the penetration in the defuelling platform, wiped down, and raised into the shielded transfer device, which then transferred the canister to the refuelling canal within the reactor building. As shown in Fig. 190, the canister would be loaded into an up ender that rotated it to the horizontal orientation, allowing it to be moved through the fuel transfer tube to the fuel handling building pool.

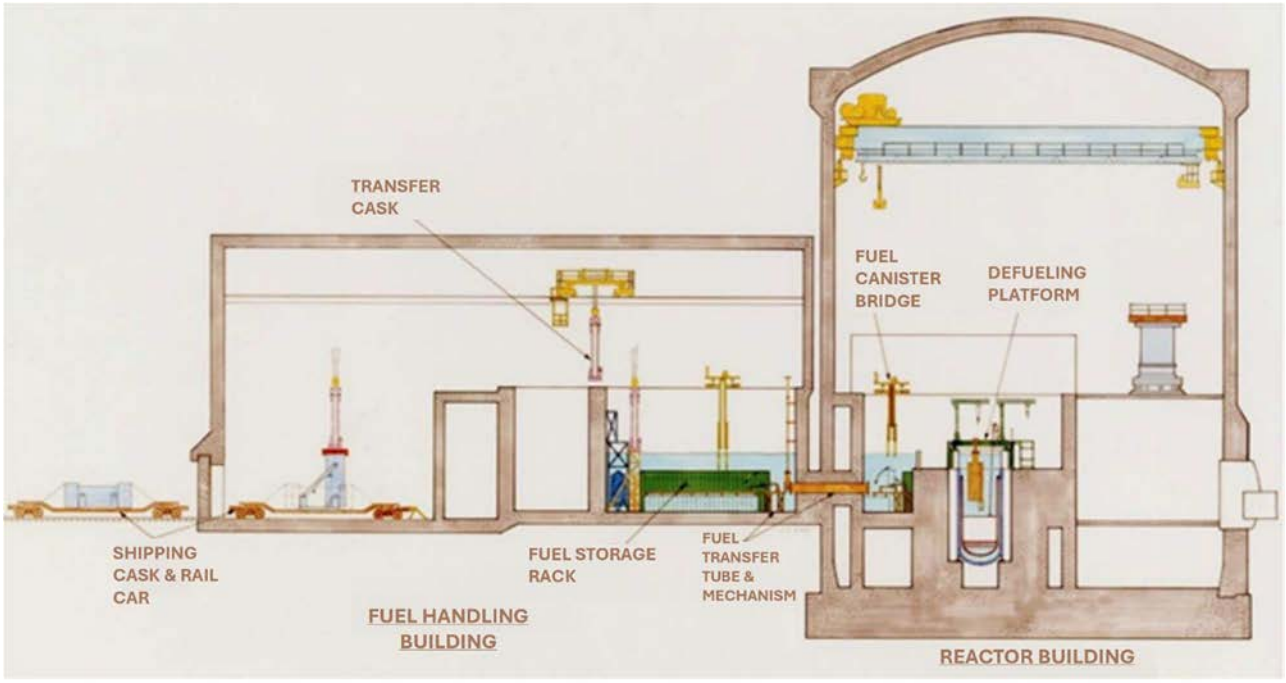


*FIG. 190. Schematic of canister transfer from reactor to fuel handling building (courtesy of INL).*

Debris canisters were filled piecewise by filling buckets, which were then transferred to the canisters. A graphic (Fig. 191) shows operator notes on filling a canister, including the location from which material was retrieved (shown as depth from the platform and radial position as well as the type of material added to Canister D-188 (in this example all material is identified as loose debris).

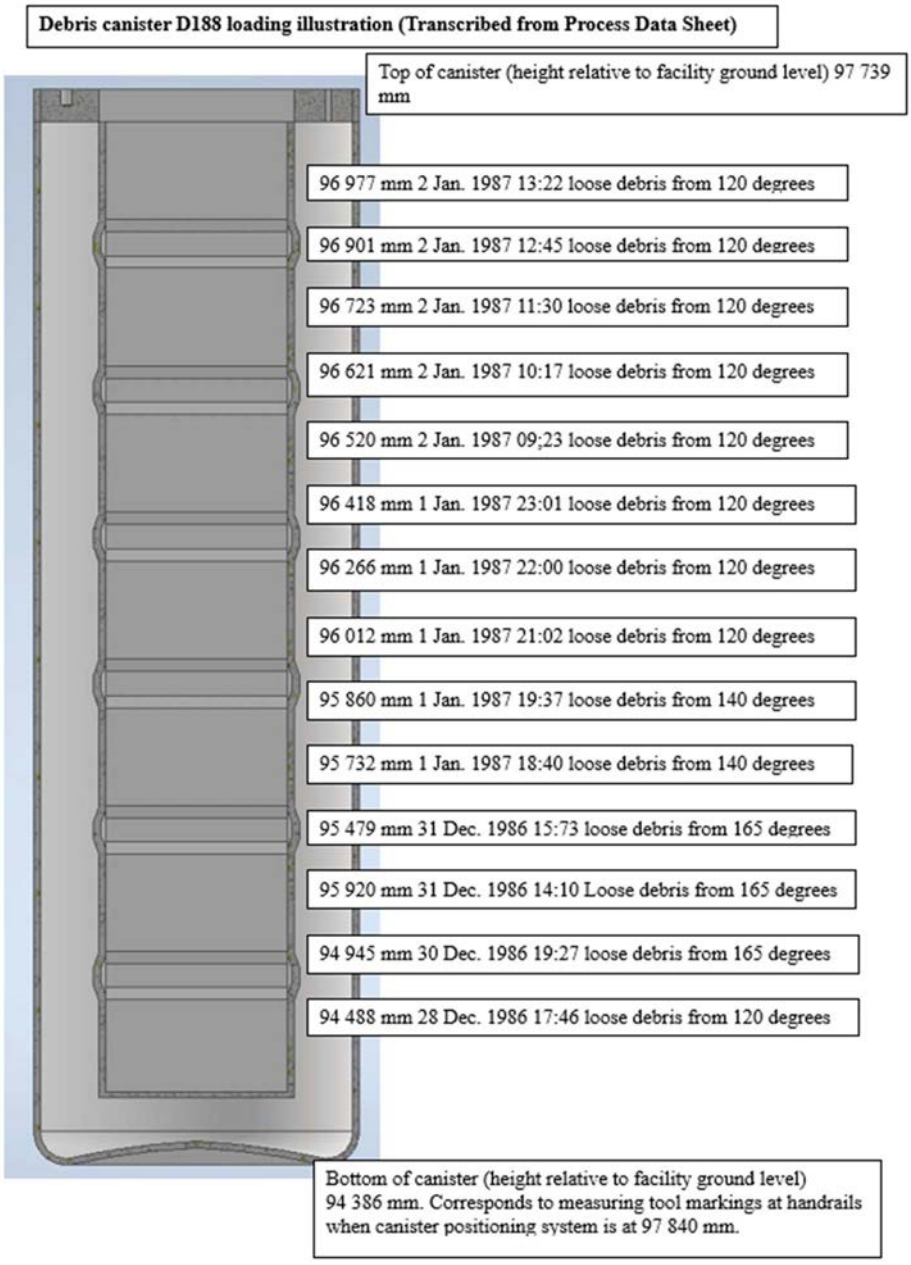


*FIG. 191. Operator log for canister D-188 loading (reproduced from Ref. [238] with permission courtesy of INL).*

### 6.1.11. Defuelling tools and equipment

A variety of specialized tools were developed for debris retrieval and sectioning of the melted core, including a water jet cutter, an abrasive saw, bolt and bale cutters, hooks, pliers, and an underwater plasma torch. Numerous changes in tool design occurred as the core conditions became better understood. Early design bases assumed a degree of consistency in the material to be retrieved when, in fact, the diversity of melted, broken, and shattered material was significant. Only 15% of the fuel

retained a recognizable rod and assembly configuration. Examples of the tools, including a clamshell spade bucket, chisel, and shears, are shown in Fig. 192.

The debris was recovered by manual tools, including scoops, pliers, and hook tools. The material was collected in reusable buckets or baskets [240], which were transferred to the debris canisters using a funnel.

The canisters were weighed during loading to assure that the design weight limit was not exceeded as well as to provide a running total of fuel recovered.

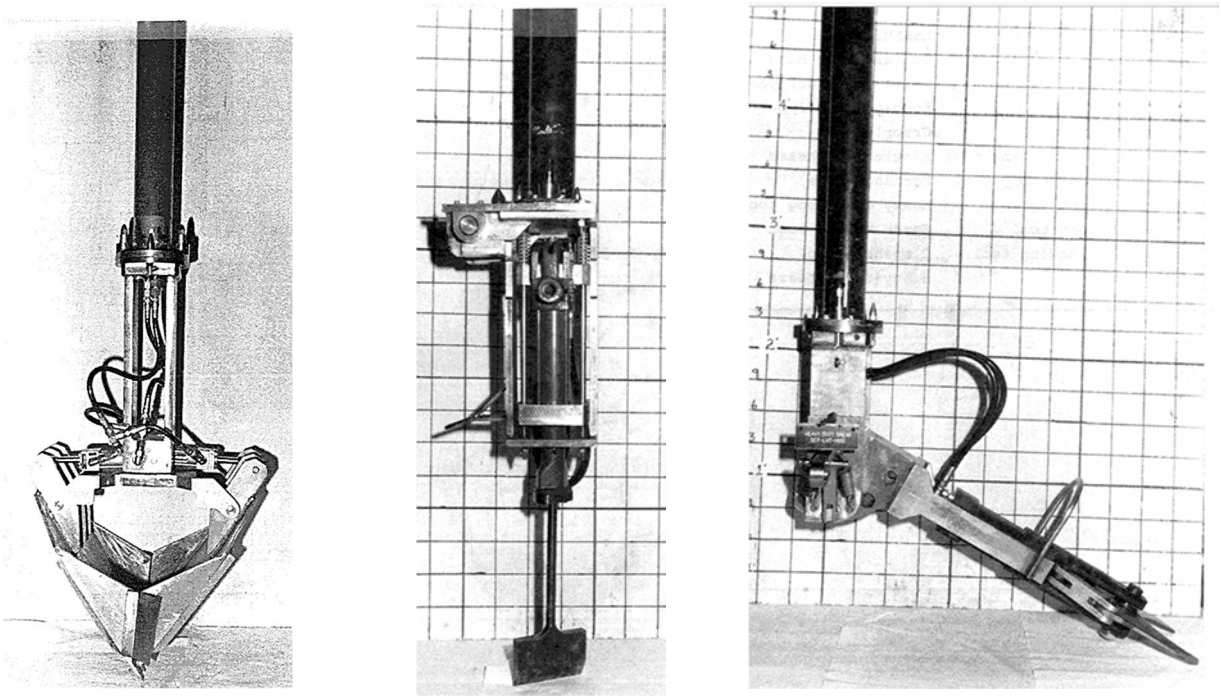

*FIG. 192. Examples of tools (reproduced from Ref. [231] with permission courtesy of EPRI).*

### 6.1.12. Debris removal

Primary fuel removal operations began on 30 Oct. 1985 and concentrated on making room for installation of the canister positioning system. Much initial effort amounted to removal of fuel end fittings. The process of loose debris removal using a spade bucket tool proceeded until Apr. 1986 when the hard layer of formerly molten fuel was reached. Several tools, including a hydraulic impact chisel and a 135 kg impact tool, were tried on the crust, but none was able to penetrate it.

The core boring machine that had been developed for the purpose of taking ten characterization cores was fitted with a 11.4 cm solid face bit with Stratapax cutter inserts for cutting through the ceramic melt [241], and in Oct. 1986, it was used to begin the process of boring 409 holes to break up the centre of the solidified melt. This operation was made more difficult by poor visibility conditions due to a loss of water clarity that resulted from microbial growth and small particulates that plugged the water cleanup sintered metal filters. The microbial bloom was attributed to the introduction of river water during the early recovery response.

Following the breakup of the central monolith, water clarity was improved by use of an additional water filtration system. At that time, it was possible to see that there was a ring of large pieces that had been only partially broken up. These pieces were estimated to weigh as much as 1200 kg. Thus,

they weighed too much to be handled with the manual long reach tools. Because the pieces were overlaid on debris, hammering, and chiselling them in place was ineffective; the loose material absorbed most of the impact energy. A special thick walled funnel was designed for the canister top. Large chunks were placed in the funnel and broken up using a 198 kg jackhammer fitted with a 3.6 m long chisel.

Pieces as large as 5 cm were retrieved using an underwater suction system that used an air driven diaphragm pump connected to a 10 cm diameter suction pipe. The schematic and isometric sketches of the configuration are shown in Fig. 193. This suction system worked with the knockout and filter canister system to recover pieces too small to be easily picked with manual grab tools. The system had a maximum flow rate of 288 L/min. A flow rate of 227 L/min was demonstrated to be sufficient to pick up 9.5 mm OD × 16 mm long $UO_2$ fuel pellets. Operator care was needed to prevent plugging of the suction uptake due to the random size and geometry of the material that could be moved. Using this system, as much as 14 500 kg of debris was removed in a single month [239]. This system was operated from late 1986 to mid–1987.

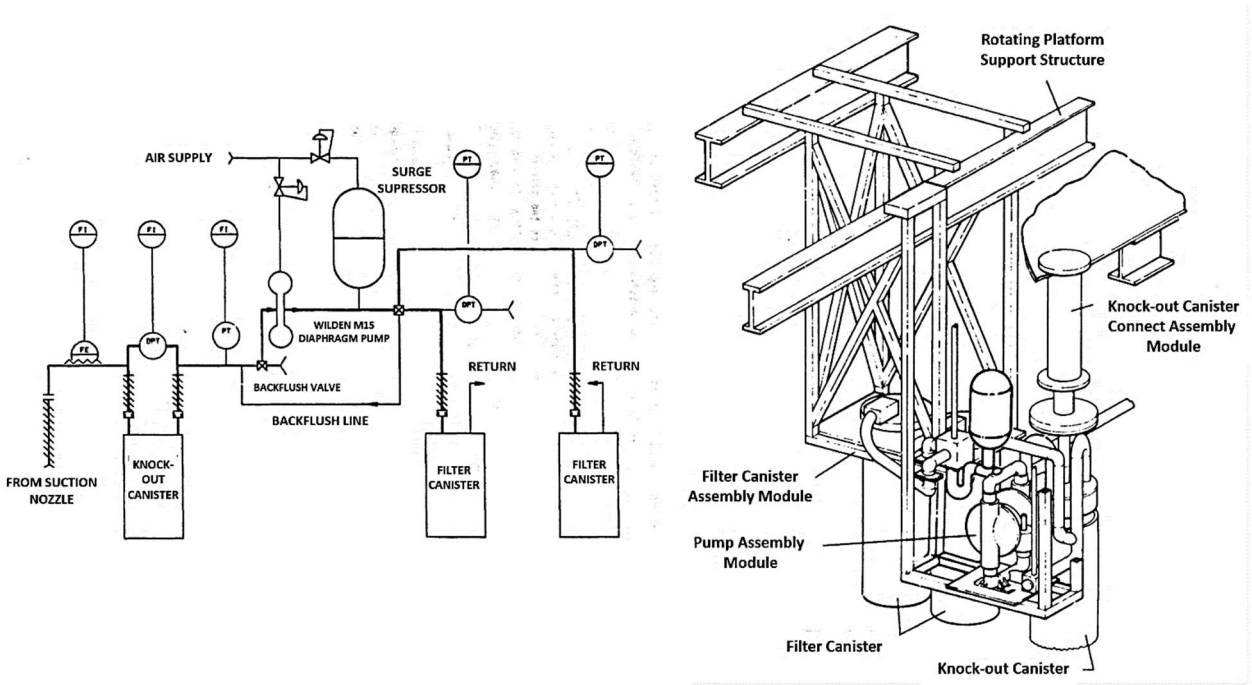


*FIG. 193. Suction System Schematic (reproduced from Refs [239, 241] with permission courtesy of INL).*

For recovery of particulate from the area below the lower core support assembly, an airlift system was developed by EG&G Inc. Idaho. This system uses entrained air injected into a vertical pipe that has a specific submergence to create a density differential that causes lower density (due to air entrainment) liquid in the lift leg to flow up that pipe to a separation chamber that allows solids to be collected, and the liquid returned to the vessel while venting the air through a filter. Airlifts are used in highly hazardous chemical and radiological process plants because there are no moving parts and the motive force is remote from the material being transported, allowing maintenance without risk to personnel. An image of that design is shown as Fig. 194.

*6.1.12.1. End fitting disposal*

Due to distortion of the end fittings of some assemblies, a decision was made separate those discrete non-fuel components to the extent possible and dispose of them separately from the fuel debris that were placed in canisters. The separated end fittings were shipped to the US DOE site at Hanford, Washington, and buried as low level waste.

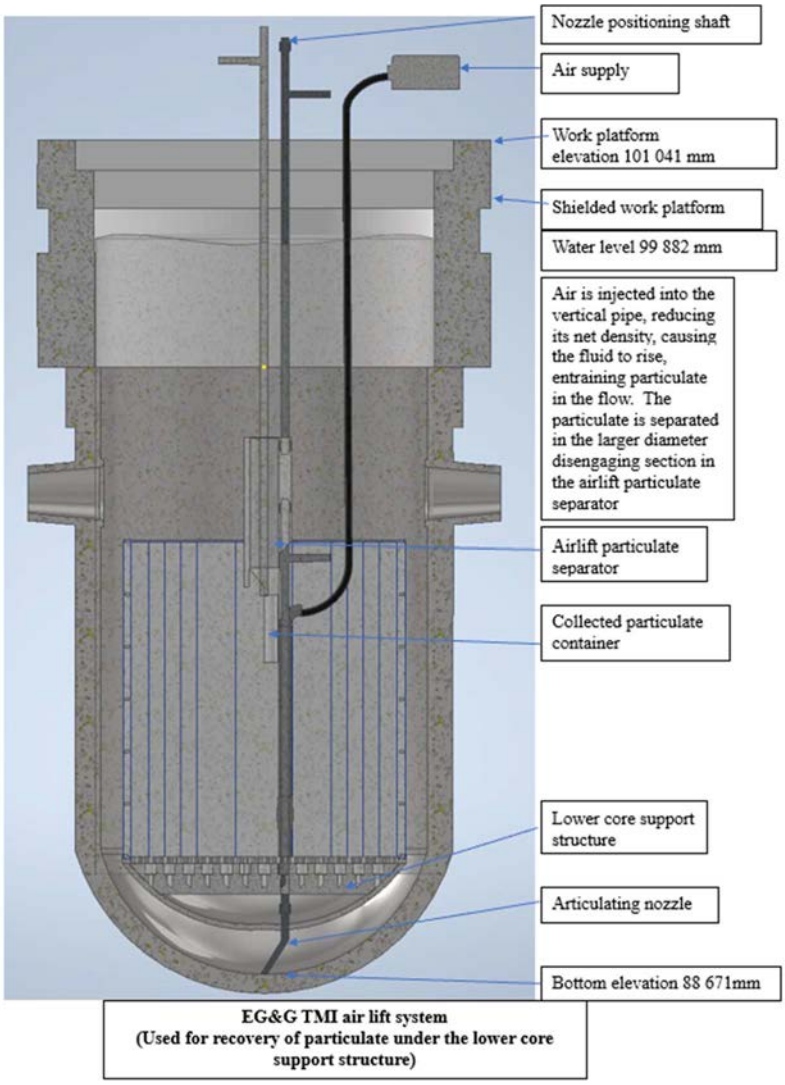


*FIG. 194. Airlift system schematic (courtesy of INL).*

*6.1.12.2. Stub or partial assemblies*

The next type of fuel debris remaining after the central monolith and perimeter melted zones were removed was the partial or stub assembly region around the periphery of the reactor vessel and the pieces remaining below the melt. Some sections were partially stuck together. Most of this material was removed using long handled tools that screwed into the top, attached as a clamshell, and then using pry tools to tilt partial assemblies away from each other. In some cases, largely intact assemblies could be removed after a spike was pressed into the top of the assembly and a tool with two fingers grasped it at the base. Except for two significantly melted locations, all of the stub assemblies were removed by Nov. 1987.

*6.1.12.3. Lower core support assembly*

Once the stub assemblies were removed, it was possible to see that between 9000 and 18 000 kg of debris had fallen through the lower core support framework. Initial design assumptions had been that only easily suctioned pieces would be present under this structure. Video revealed that, in addition to the debris that fell through during the stub assembly and nozzle removal, a substantial quantity of melted, solidified core mass was present under the LCSA.

Because its purpose was to support the entire core, the LCSA was massive: 3 m in diameter and fabricated in five stainless steel plates, 90 cm deep. The components included the lower grid top rib, lower distributor plate, lower-grid forging, in-core guide support plate, and in-core guide tubes, as shown in Fig. 195.

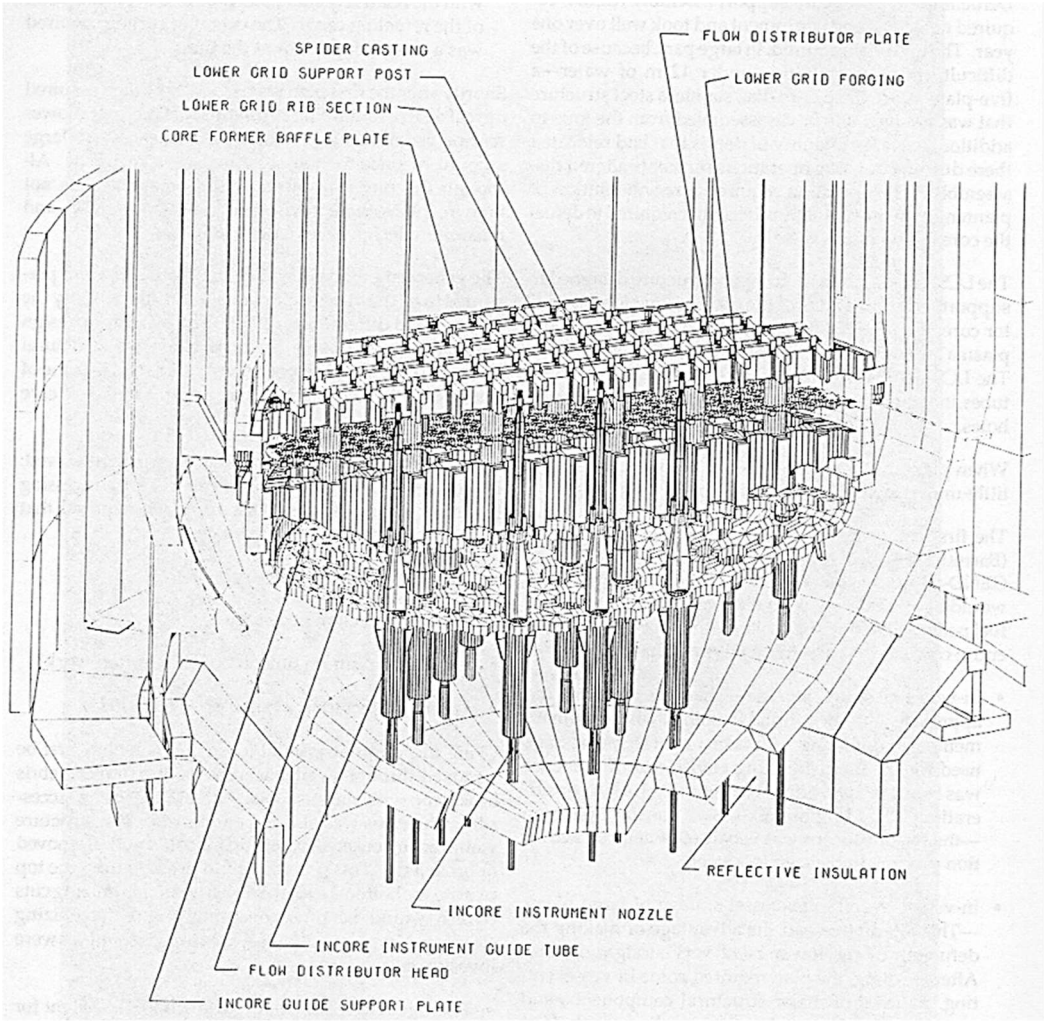


*FIG. 195. Lower core support assembly model (reproduced from Ref. [231] with permission courtesy of EPRI).*

A large number of alternatives was considered for the removal and sizing process, ranging from sawing and shearing to thermal, abrasive, plasma, and explosive cutting. After additional demonstration testing, the plasma arc cutter was applied for the primary portion of this task. The work was performed under 12 m of borated water. It was estimated that opening an access hole with an area of 1.2 $m^2$ would require 890 cuts. Because of the large number of cuts necessary to create an opening through which the debris could be removed, an automated cutting equipment system (ACES) was developed to deploy the plasma torch.

The ACES system is shown in Fig. 196. One alternative design included a multi-axis dual arm system (MANFRED) that ultimately was not used due to its complexity and the expected problems of decontaminating the multitude of hoses and cables that operated the arms. The plasma torch was deployed using an X–Y bridge, which was lowered into the reactor vessel to a short distance above the lower core support to position the torch.

Prior to deployment of the plasma arc torch, numerous concerns were raised, including problems of maintaining subcriticality, potential for hydrogen evolution, pyrophoric reaction of zirconium in water, the potential to damage the reactor vessel lower head, and unexpected spread of contamination. Through analysis, these concerns were discounted, and the torch was deployed.

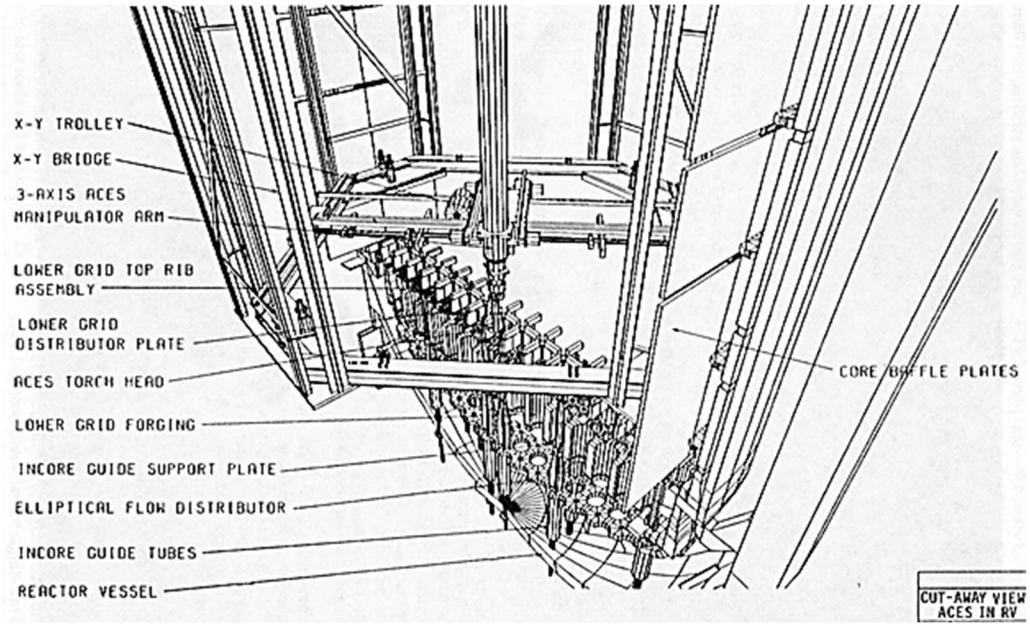


*FIG. 196. Automated cutting equipment system (reproduced from Ref. [231] with permission courtesy of EPRI).*

Prior to using the plasma torch, the plan was that the core-boring machine would be used to drill out 15 of the 52 in-core guide tubes and all 48 distributor plate support posts. The core bore drill was fitted with two different types of bits (trepanning and junk mill) to perform this task (see Fig. 197). Due to the problem of discharging drilling chips, the bits became fouled, and not all of the in-core tubes were able to be cut. Despite that setback, the core-boring machine was used to cut the lower-grid rib plate into thirteen pieces.

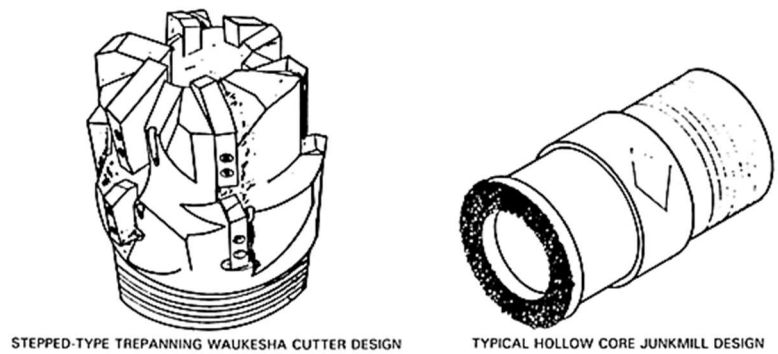


*FIG. 197. Trepanning and junk mill bits (reproduced from Ref. [241] with permission courtesy of Taylor & Francis Group).*

The lower-grid distributor plate was disassembled and removed in four pieces in June and July 1998. Due to problems with torch failures attributed to adherent debris, the torch controls were redesigned. Cutting of the 34 cm thick lower grid forging plate required the use of an abrasive saw to perform vertical cuts while the plasma torch completed the horizontal cuts. The forging was removed during Aug. to Dec. of 1988.

The in-core guide support tube plate was removed in four pieces between Dec. 1988 and Feb. 1989. The flow distributor plate was removed as 26 pieces during Feb. through Apr. of 1989. Prior to removal of the core former baffle plates, it was necessary to remove debris generated by previous defuelling activities.

*6.1.12.4. Lower Head Debris Removal*

The primary tools used for core removal were long-handled grippers, scoops, and tongs. Between pic and place actions with these tools and vacuuming using the airlift, 12 400 kg of debris were removed from the lower head in May 1989. This cleanup revealed a molten monolithic mass on the bottom head of the reactor vessel. Although this mass was as much as 0.6 m thick at the centre, it was determined to be brittle as it was fractured using an impact hammer. Figure 198 is a schematic view of the melt.

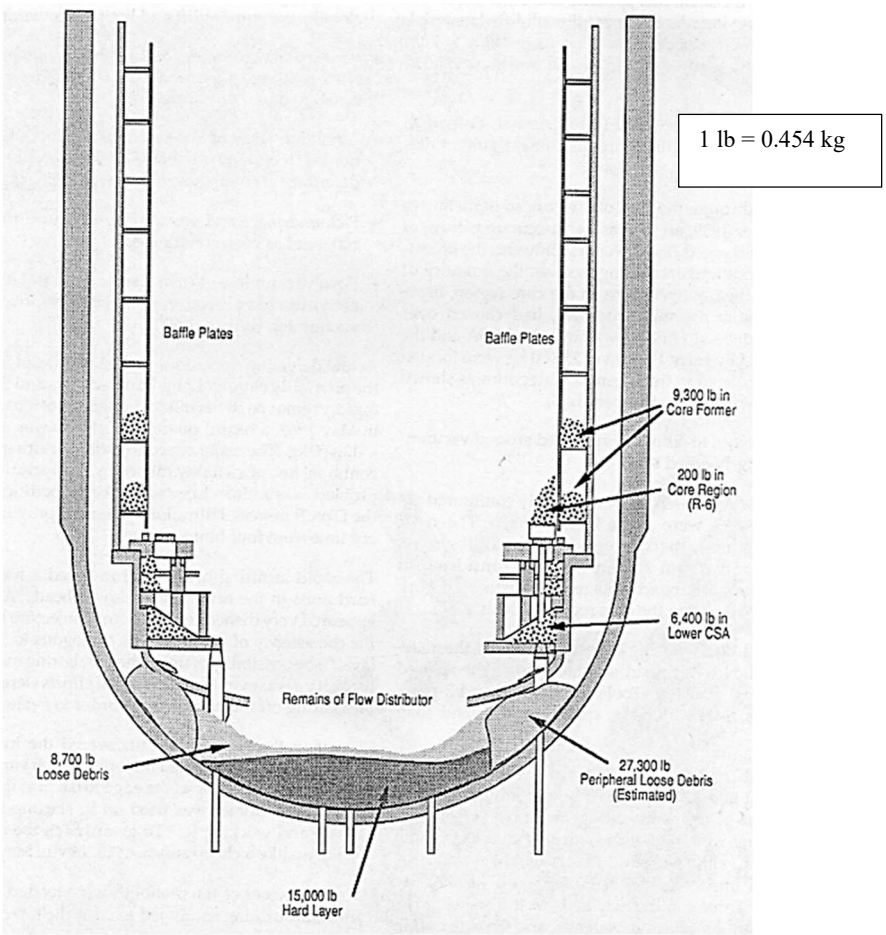


*FIG. 198. Debris located below the lower-core support assembly (reproduced from Ref. [231] with permission courtesy of EPRI).*

It had been estimated that 4000 kg of debris was located behind the core former baffle plates. Removing the 4 m long baffle plates involved removing the bolts that held them in place and moving

the eight pieces out of position to allow vacuuming of the debris. An airlift and cavitating water jet were used to recover the debris.

In all, the debris at the bottom of the vessel were tabulated as follows: 4218 kg behind the core former plates, 2903 kg was found in the lower core support area, and 3946 kg of central and 12 383 kg of peripheral loose debris, and 6804 kg of previously molten monolithic hard layer, adding up to 30 254 kg.

## 6.2. CHORNOBYL EXPERIENCE

In the first days after the accident, high radiation levels and severe damage to the reactor and building hampered all attempts to find damaged fuel and corium at Unit 4. For this purpose, special detectors based on NaI (Tl) with a lead collimator were manufactured and installed on a helicopter (Fig. 199). When scanning from 200 m heigh it captured a field with a diameter of 30 m. In this way, the first map of radioactive sources was created over the damaged reactor, roofs of the on–site buildings and around the reactor site. In total, about 2000 measurements were made. The first measurements inside Unit 4 were made using radiometer Kirzhach–3 with a dose rate measurement limit of up to 30 Sv/h, however the dose rate near melted fuel locations quickly exceeded this limit. The method allowed the first lava accumulations like the one in room No. 217/2 (‘Elephant's foot’) to be discovered. Later, dehydrated pipelines were used for radiation measurements, which made it possible to find another accumulation of molten fuel in room No. 305/2. The location was also confirmed by temperature measurements (Chapter 1 of Ref. [49]).

*FIG. 199. Inspection of the destroyed ChNPP Unit 4 using helicopter (courtesy of Kurchatov Institute).*

By the time the sarcophagus construction was completed, the dose rates at Unit 4 had decreased hundreds of times. Most samples of corium were taken inside the sarcophagus in 1990–1991. At the time, the gamma dose rate at the perimeter of the sarcophagus was around 4–6 Sv/h, but on the lava surface (for example, at ‘Elephant foot’) irradiation levels exceeded 10 Sv/h. Even so, all corium samples of KRI collection were taken manually using hands and hammers.

Investigation of the post-accident conditions in the destroyed unit continued during the construction of the sarcophagus. Various remote sensing methods were used to study the radiation environment and characteristics of damaged fuel (Chapter 2 of Ref. [49]):

— *Gamma vizor* to identify areas with strongest gamma radiation [243—245] (Fig. 200, left). The principle of the gamma vizor combines the optical image from the video camera and scintillator glowing converted into an analogue signal (Fig. 200, right). Use of the gamma vizor helped to find fragments of nuclear fuel inside Unit 4 and on the roofs of Units 3 and 4.

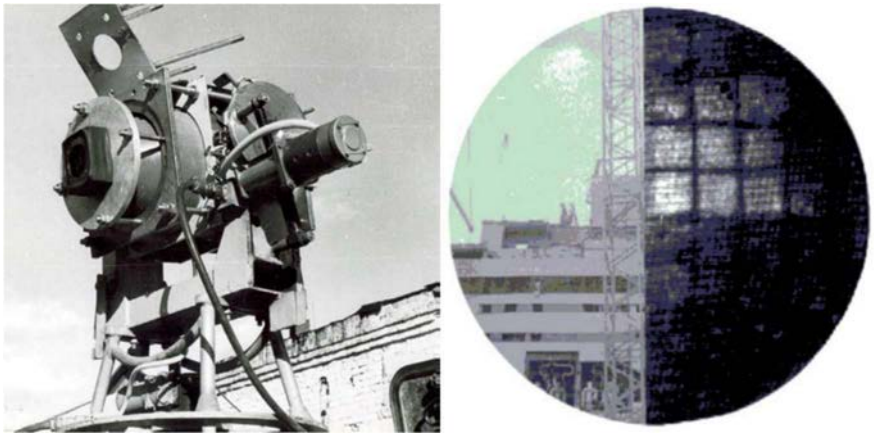

*FIG. 200. Gamma vizor (left) and combined optical and gamma image of destroyed reactor from the western side (right) taken in 1988 (courtesy of Kurchatov Institute).*

— *Buoy programme*. The buoy was a truncated cone shaped 300 kg device, which had been installed directly into the reactor shaft using a helicopter or crane (Fig. 201). Each buoy was equipped with two sensors for measuring temperature and heat flux density, and it also had a gamma radiation detector and six anemometers in the upper part. The buoy cable was brought into a room with radiation background of 0.1–0.2 mSv/h where recording equipment was installed. In total, 15 buoys were installed with 160 different sensors and detectors.

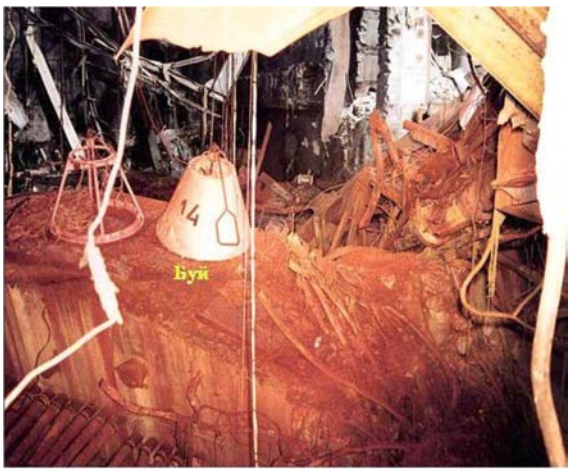


*FIG. 201. One of the buoys installed on damaged reactor lid (scheme E) (courtesy of Kurchatov Institute).*

— *Measurements using thermoluminescent dosimeters DPG-03 and IKS-A*, placed in various thickness filters made of lead, iron, sand and graphite. Packages of dosimeters had been placed on the crane and exposed for 30 minutes at a height of 1.5 m from the geometric centre of the reactor hall ceiling. The use of filters enabled the contribution of gamma emitters with different energies to the integral dose rate to be identified and hence enabled optimisation of the radiation protection measures for further works at the sarcophagus.

In 1988 boreholes drilling had begun in places near expected accumulation of damaged fuel (Chapter 3 of Ref. [49]). The aim of the boreholes was to:

- Carry out visual observations using photo and video documentation;
- Measure characteristics of damaged fuel and corium using gamma, thermal and neutron detectors (Chapter 4 of [49], [246]);
- Assess the threats (including nuclear safety issues) of melted fuel accumulations and undertake control measures.

Most of the holes were horizontal with a diameter of 60–150 mm and length up to 26 m. Cores and samples taken during drilling were firstly analysed by spectroscopic and radiometric methods directly at the Sarcophagus. A hot cell for dissolution of the samples and further analysis was installed in room No. 207/3. Small amounts of liquid samples were analysed in a radiochemical laboratory in Chornobyl town. More than 10 000 gamma spectrometry measurements were carried out by KRI [247].

Periscopes, portable photo and video cameras were used for visual inspection. The visual observation showed for the first time that the reactor shaft was almost empty (Fig. 202) and did not contain any fuel or graphite.

*FIG. 202. Photo of the reactor shaft made by periscope through the borehole (courtesy of Kurchatov Institute).*

Dose rate measurements in the holes were carried out mainly using an ionization chamber Splav with an interval of measured exposure dose from 0.1–1000 Sv/h. In particular, these measurements confirmed the location of the fuel melt in room No. 305/2.

To measure the heat flux, a heat probe with an operating temperature range of -30 to 130℃ and recording a heat flux up to 10 $kW/m^2$ was used. By rotating the probe around its axis, it was possible to determine the maximum heat flux. The heat measurements showed confirmed the location of molten fuel under reactor base plate.

The study of neutron fluxes was carried out using neutron detectors of three types:

- Sentry neutron detector for monitoring the long term stability of the neutron flux. These detectors were equipped with an additional 15 mm Plexiglas moderator to increase the camera sensitivity;
- Reconnaissance neutron detector for operational research of neutron field distributions. It was equipped with standard fission chamber in a thin stainless steel casing (total weight less than 2 kg);

– Neutron detector with removable filters (boron carbide powder) for registration of spectral distributions of neutron fluxes. The results of neutron flux measurements have shown that damaged fuel is deeply subcritical and there is no threat of supercriticality process.

In addition to boreholes, researchers from the Kurchatov Institute and KRI used different methods, such as dosimetry cords for the study of distributions of major gamma radiation sources in the central hall of the Sarcophagus [248, 249], and remote controlled collimated gamma detector for estimation of the amount of fuel on the upper biological protection of the reactor central hall (Chapter 6 of Ref. [49]) and melted fuel in the bubbler tank [250]. Many of these systems and technologies for investigation of post-accident situation were subsequently used for monitoring inside the Sarcophagus (Chapter 9 of Ref. [49]).

One of the main features of the Chornobyl accident was the release of radioactive aerosols with a total activity of quadrillions of Becquerels. The first measurements of radiation levels over the collapsed reactor were carried out using helicopters and an AN–24rr laboratory aircraft. In May 1986 helicopters and special equipment were employed to sample air directly from the plume of radioactive release from the destroyed Unit 4 (Helicopter programme) [251]. Aerosol measurements taken over Unit 4, the reactor site and over a 30 km zone (Chapter 10 of Refs [252], [253]) used special filter gondolas (containers with filters from which air was evacuated) fixed to airplanes and helicopters. More accurate data on the characteristics of aerosols was obtained in Sept. 1986 when a steel cable was connected from one of the upper-level premises of Unit 3 to the remaining part of the western wall of Unit 4, using harpoon cannon. A device for sampling air moved along this cable, provide measurements to allow calculation of the average daily release of radioactive substances into the atmosphere. After the Sarcophagus construction was completed, the aerosol monitoring system was moved to the internal premises. Aerosol monitoring, decontamination and dust suppression technologies are detailed in Chapters 11–13 of Ref. [252].

Since the Sarcophagus was not hermetically sealed, and due to the use of dust suppressing solutions in some places inside the Sarcophagus, the molten fuel regularly interacted with water. Water samples were taken regularly by hand from the surface layer (Chapter 14 of Ref. [67]) (Fig. 203). After the decision was made in 1992 to transform the Sarcophagus into a new safe containment, detailed measurements of the dose rate, soil and groundwater contamination in the local area of the Sarcophagus were carried out (Chapter 15 of Ref. [67]).

*FIG. 203. Water sampling inside the Sarcophagus (courtesy of Kurchatov Institute).*

As noted earlier, most of the samples inside the Sarcophagus were taken manually. The use of robotics during the post-accident examination has not met with much success for three main reasons (Chapter 17 of Ref. [67]):

- Robots could not negotiate destroyed sections of the facility and operators had to pull them out by hand;
- High radiation level caused interference in electronic circuits, which made the mechanisms unreliable;
- The movement of the robot was accompanied by the rise of radioactive dust, and their decontamination led to significant dose uptake by personnel.

However, some handmade robots were used inside Unit 4. For example, a self-propelled toy tank equipped with a dosimeter, temperature sensor, flashlight, and a 15 m cable (Fig. 204). Development, testing and improvement of robots continued during the operation of the Sarcophagus, where they were used to clean the air from aerosols and take samples of contaminated concrete [254].

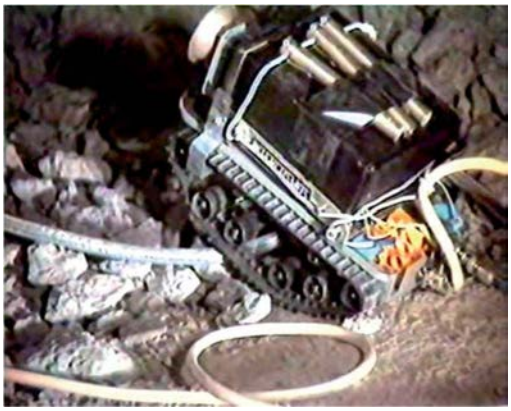

*FIG. 204. Toy tank equipped with a dosimeter, temperature sensor and flashlight inside the Sarcophagus (courtesy of Kurchatov Institute).*

## 6.3. FUKUSHIMA EXPERIENCE

The following section provides an account of the various investigation robots and equipment for debris retrieval that have been developed in support of the cleanup of 1F.

### 6.3.1. Important properties of Fukushima Daiichi fuel debris

The important properties required to support debris retrieval processes are discussed in Ref. [255]

Based on information about 1F and experience gained from the TMI–2 accident, the most important R&D items for fuel debris characterization were identified. The fuel debris physical properties to be measured were determined by considering their influence on the performance of candidate retrieval tools.

Although the damaged reactor core of 1F will be different from that of TMI–2, similar tools can be used to remove the fuel debris. The differences between fuel debris retrieval at 1F and TMI–2 are:

- In TMI–2, fuel debris did not melt through RPV, most of the fuel debris remained inside the RPV. However, in 1Fs case the RPV is assumed to be damaged, and the molten core has melted through the RPV and fallen down to the bottom of the PCV;
- In terms of 1F PCV conditions, some water leakage has occurred at penetration tubes or

cracks, so the PCVs are not fully covered with water (like TMI–2), therefore, the fuel debris retrieval will need to operate under dry or semidry conditions.

The fuel debris retrieval tools have been selected and categorized into six groups according to working principles (Table 43).

The core boring machine is a mechanical tool which played an important role at TMI–2 and was the most effective and reliable tool throughout retrieval operations. In the case of 1F decommissioning, modification of such a machine and tools to meet the required mechanical properties for 1F debris retrieval therefore has been assumed.

TABLE 43. CATEGORIZATION OF EXPECTED DEBRIS RETRIEVAL TOOLS [255]

| Tools | | Working principle | Tools (Representative) |
|---|---|---|---|
| Cutting tools | A | Impact | Air chisel |
| | | | Cavitating water jet |
| | B | Shearing | Heavy duty shears |
| | C | Fusion cutting | Plasma arc cutting |
| Pick and place tools | | Pick and place | Spade bucket tool |
| | | | Vice grips |
| Aspiration system | | Aspiration | Airlift |
| | | | Pump lift vacuum |
| Core boring system | | Grinding | Core boring machine |

During TMI–2 defuelling the core boring machine was used to survey the core configuration and to break up the massive resolidified (previously molten core) pool, which had a hard crust. Its operating principle is complex, but it seems that the main action is grinding. It is generally easier to grind soft and brittle material, therefore, grinding is thought to be influenced by material hardness and fracture toughness. In addition, because elastic deformation and friction heat are involved, the elastic modulus and thermal properties such as heat capacity and thermal conductivity are believed to also affect grinding.

Three types of cutting tools were used in TMI–2 defuelling depending on the situational demands. Type A cutting tools were used to break up massive ceramic debris by impact. This type of tool breaks up bulk ceramics by a cracking procedure. Therefore, the fracture toughness of debris is thought to be important for type A cutting tools. To cut comparatively thin metallic plates and rods, type B cutting tools, or shearing devices, were used. The major mechanisms of shearing are blade biting, elastic/plastic deformation, and crack progression. Thus, it is postulated that the mechanical properties of the debris, such as hardness, elastic modulus, and fracture toughness, affect the performance of type B cutting tools. Fusion cutting by type C cutting tools was used for complex and heavy duty metallic structures. Their performance depends on the thermal properties of the target materials, such as melting point, heat capacity, and thermal conductivity.

For pick and place tools, it seems obvious that the important properties of the debris are physical properties such as shape, size, and density (bulk weight). They are also important for the ventilation system, considering that the settling velocity is essential for flow phenomena of debris particles in water.

The important properties of fuel debris to aim debris retrieval were selected based on the possibility of undertaking measurements on small samples of actual debris. Table 44 shows the properties, shape, size, density, hardness, elastic modulus, fracture toughness, thermal conductivity, specific heat (heat capacity), and melting point, which affect the choice of retrieval tool. The highest priority was given

to mechanical properties; hardness, elastic modulus, and fracture toughness, because little data has been obtained in the past from severe accident studies.

TABLE 44. IMPORTANT PROPERTIES OF FUEL DEBRIS [255]

| | **Property** | **Physical** | | | **Thermal** | | | **Mechanical** | | | |
|---|---|---|---|---|---|---|---|---|---|---|---|
| Tools | | Shape | Size | Density | Melting point | Heat capacity | Thermal conductivity | Hardness | Elastic modulus | Fracture toughness | |
| Cutting tools | A | | | | | | | | | √ | |
| | B | | | | | | | √ | √ | √ | |
| | C | | | √ | √ | √ | √ | | | | |
| Pick and place tools | | √ | √ | √ | | | | | | | |
| Aspiration system | | √ | √ | √ | | | | | | | |
| Core boring system | | | | | | √ | √ | √ | √ | √ | |

### 6.3.2. Estimated condition inside each primary containment vessel

As mentioned above, three units melted, however, their condition is different depending on the unit. An overview of the estimated conditions of Units 1—3 is given in Table 45 and the conditions inside each PCV in Fig. 205. In Unit 1 it is estimated that most of melted fuel fell to the bottom of the RPV. Moreover, there is a possibility that fuel debris exists outside of the pedestal. The PCV is filled with cooling water, to a level of about 1.9 m from the bottom. In Unit 2 and Unit 3, some of the melted fuels is expected to have fallen to the bottom of the RPV lower plenum and PCV pedestal, the remainder may have been left inside the RPV. The water level of Unit 2 is 0.3 m, and that of Unit 3 is 6 m.

TABLE 45. ESTIMATED CONDITIONS UNITS 1–3

| | Core | Lower plenum | PCV | D/W water level | S/C water level |
|---|---|---|---|---|---|
| Unit 1 | Almost none | Almost none | Almost all | ~2 m | Almost full |
| Unit 2 | Little | A lot | Little | ~0.3 m | Low level |
| Unit 3 | < Unit 2 | < Unit 2 | > Unit 2 | ~5 m | Full |

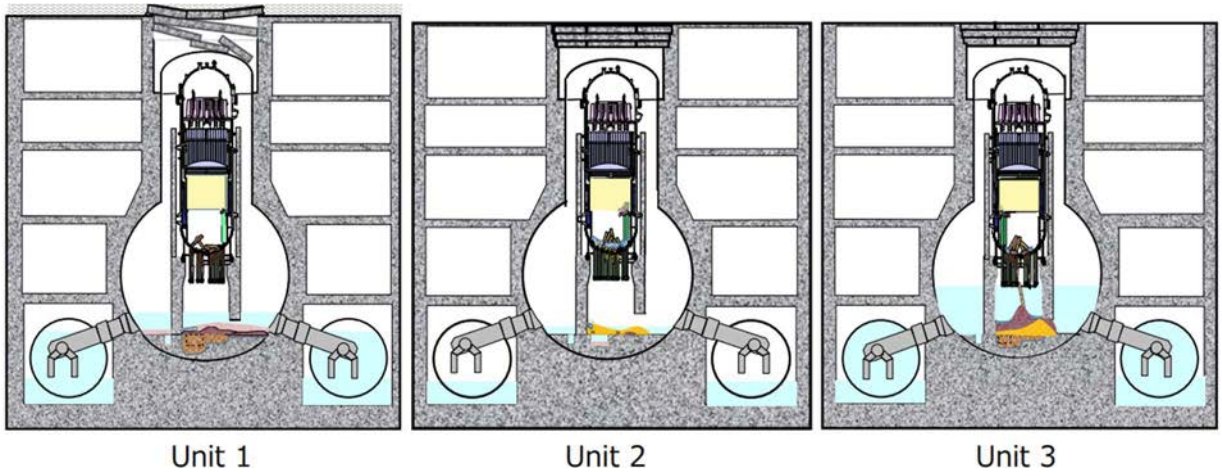


*FIG. 205. Estimated condition of inside of the PCV (reproduced from Ref. [256] with permission courtesy of TEPCO).*

### 6.3.3. Investigation of pressure containment vessel interiors

The following Section provides an account of the robots developed in support of the inspection of Units 1–3 PCVs.

#### *6.3.3.1. Unit 1*

Inspection of the pedestal was conducted as a priority because the existence of fuel debris was presumed. Primary containment vessel penetration X100–B22[15] was selected to access the inside of the PCV. The penetration is at a height of 8.6 m from the bottom of the PCV and is a very narrow pipe (100 mm diameter). To investigate the PCV a robot was inserted into the penetration and travelled over the grated floor, which is 3.5 m high from the bottom. The robot moved around the grated floor so the conditions inside the PCV could be recorded.

The robot developed to undertake this task PMORPH–1 is shown in Fig. 206. Images of the condition of the grating in Unit 1 pedestal taken by the robot are shown in Fig. 207.


*FIG. 206. PMORPH-1 (reproduced from Ref. [257] with permission courtesy of IRID).*


*FIG. 207. Photographs of the grating in the Unit 1 pedestal made by investigation robot PMORPH-1 (reproduced from Ref. [258] with permission courtesy of TEPCO).*

The robot is shape changeable maintaining an I shape when travelling through narrow pipes and transforming into a U shape when travelling across the grated floor. It is 600 mm long (I shape), 75 mm wide, 95 mm high, and weighs approximately 10 kg. The robot was operated in April 2015. Since 2015 PMORPH–2 has been developed, it has a similar structure to PMORPH–1 and has a sensor unit that can be lowered. Although PMORPH–1 only operated on the grated floor,

[15] Please refer to Fig. 216.

PMORPH−2 can operate under the floor and in the retained water by lowering the sensor unit between the gaps in the grated floor. The robot was operated in March 2017.

*6.3.3.2. Unit 2*

As it's possible that fuel debris has spread outside of the pedestal, i.e., to a lower level in comparison with Unit 1, the ability to investigate inside the pedestal was developed as a priority. A CRD rail was used to access the inside of the pedestal as shown Fig. 208 (left). An investigation robot called SCORPION was developed to undertake the task, shown in Fig. 208 (right). This robot also has a shape changeable mechanism so that it can pass through a narrow pipe. The dimensions are 90 mm (length) × 90 mm (width) × 90 mm (ht) when in the I shape, and 260 mm (length) × 90 mm (width) × 220 mm (ht) when in investigatory operation. The weight is approximately 5 kg. Before introducing the robot, preliminary observations using a pan tilt camera with a telescopic mechanism was done (Fig. 209). SCORPION was operated in February 2017. Unfortunately, the robot got stuck on the CRD rail because of crawler trouble.

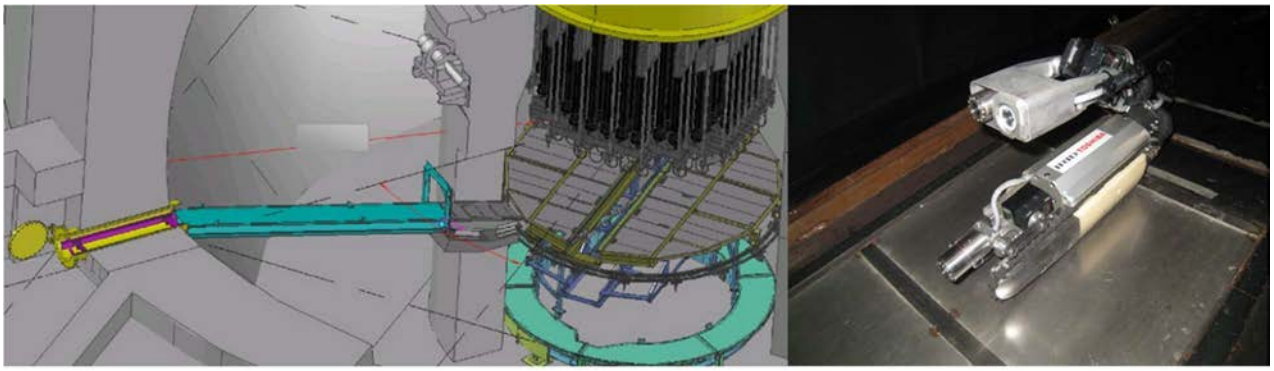

*FIG. 208. Investigation inside the pedestal at Unit 2 (left: Access route to inside pedestal; Right: Investigation robot (reproduced from Refs [259, 260] with permission courtesy of TEPCO/IRID).*

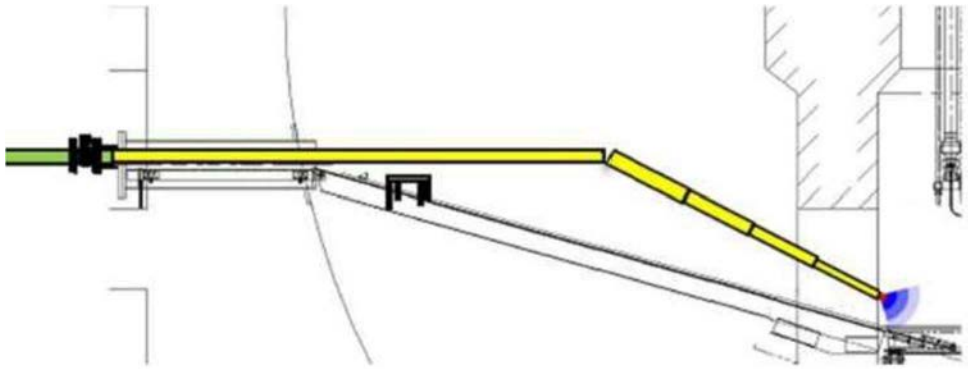

*FIG. 209. Preliminary observation (reproduced from Ref. [261] with permission courtesy of TEPCO).*

Figure 210 shows the condition of the grating in Unit 2 pedestal, observed using the robot system. In addition, a part of a handle of a FA was observed at the bottom of the pedestal and at the bottom of the RPV; the CRD mechanism was also damaged (Fig. 211). Based on the photographs taken of the lower part of the RPV, it was estimated that there was a large amount of damage to the RPV that had allowed damaged FA to pass through it. The photos will provide valuable information for investigating the location and cause of the damage to the bottom of the RPV.

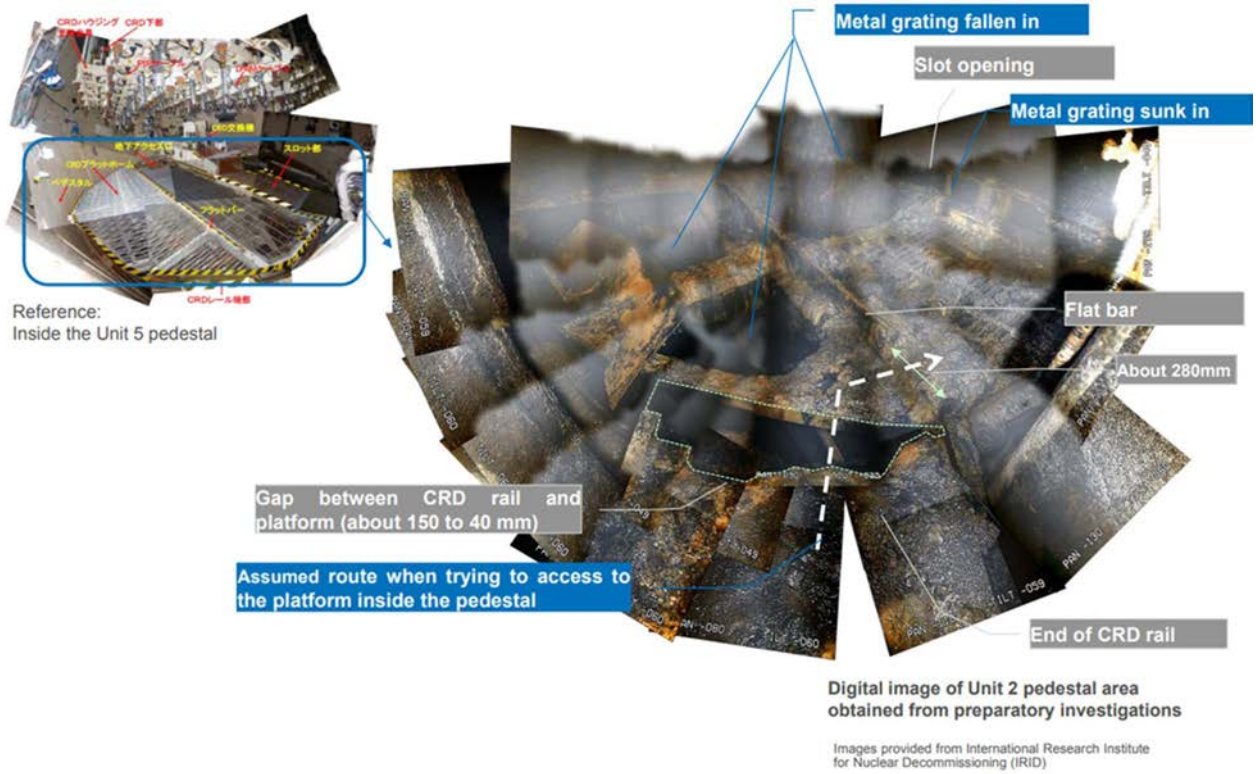


*FIG. 210. Image of installed camera on grating around pedestal inside Unit 2 PCV (reproduced from [261] with permission courtesy of IRID/TEPCO).*


*FIG. 211. Image of pedestal bottom (left) and lower part of control rod drive (right) in Unit 2 PCV (reproduced from Ref. [262] with permission courtesy of IRID).*

To investigate the debris observed at the pedestal bottom a new investigative device/robot that could be lowered from the platform inside the RCV was developed; the deployment mechanism and route are shown in Fig. 212, and the investigative device is shown in Fig. 213. The robot, in addition to its video and image capture capabilities, features robotic fingers for investigating the debris, a dose meter and temperature sensor. The device has been deployed in 2018 and 2019. In 2019 physical contact was made with the debris to establish temperature, dose and whether the debris could be easily moved. Photographs of the fingers in action are shown in Fig. 214. It was established that some material could be easily moved, and other material could not.

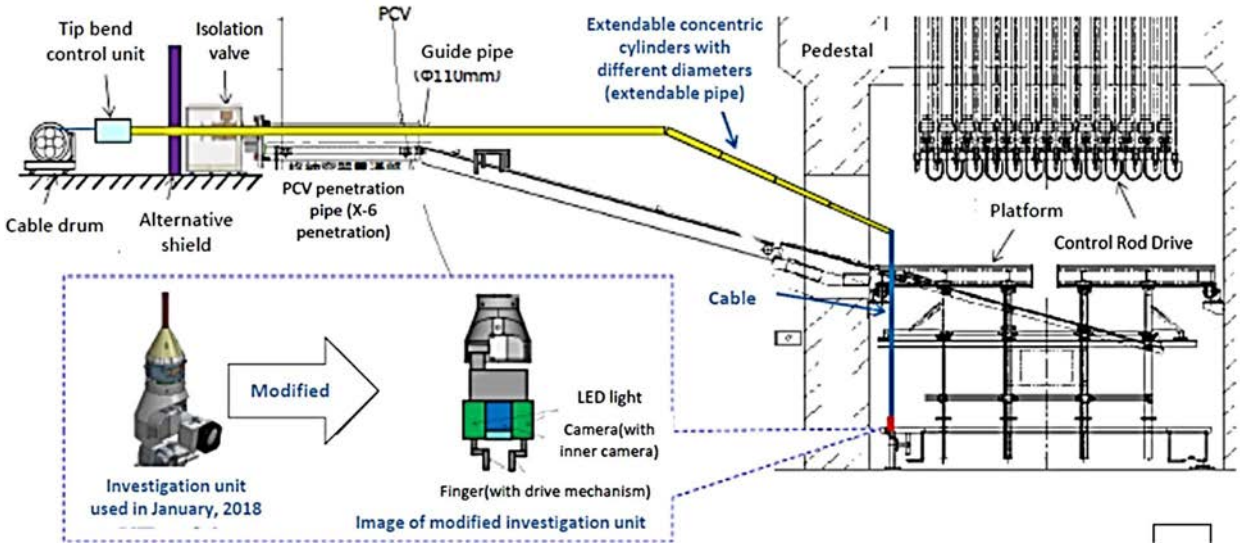


*FIG. 212. Observation system for debris contact (reproduced from Ref. [263] with permission courtesy of Toshiba).*

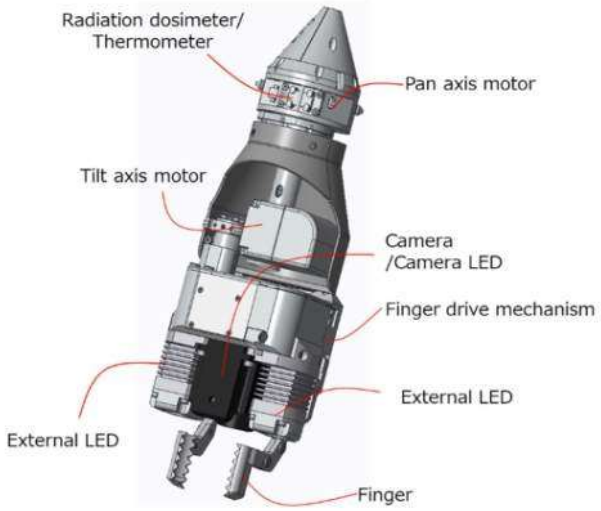


*FIG. 213. Remote operated robot to investigate debris in the bottom of Unit 2 PCV (reproduced from Ref. [263] with permission courtesy of Toshiba).*

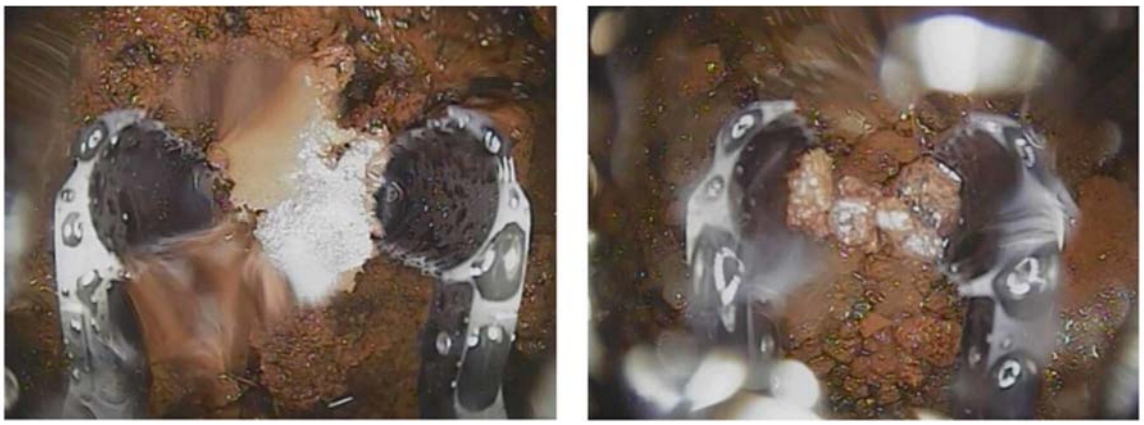

*FIG. 214. Image of fuel debris contacted by remote-operated robot in Unit 2 PCV (reproduced from Ref. [257] with permission courtesy of TEPCO).*

*6.3.3.3. Unit 3*

As the water level inside Unit 3 PCV is high, a submersible inspection robot was developed, shown in Fig. 215. It has five thrusters, four are for forward motion and one is for up/down motion. The robot can also pass through a narrow pipe (150 mm diameter) to enter the PCV. The size is approximately 130 mm (diameter) × approximately 300 mm (length), and weighs around 2 kg (in air), and neutral buoyancy (in water). It is equipped with two cameras, light emitting diodes (LED) lights, and a dosimeter. The robot operated in July 2017, entered the PCV through penetration X–53 and travelled into the RPV (Fig. 216).

*FIG. 215. Submersible inspection robot (reproduced from Ref. [265] with permission courtesy of IRID).*

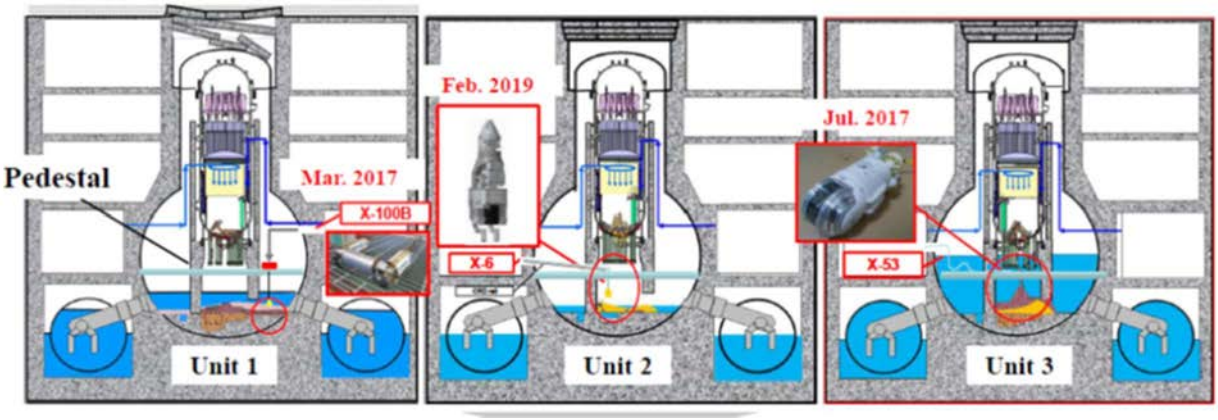


*FIG. 216. Inspection robot systems Unit 1–3 PCVs (reproduced from Ref. [266] with permission courtesy of TEPCO, Japan).*

### 6.3.4. Planned investigations inside Unit 1 primary containment vessel

Figure 217 shows a new boat type submarine. It has been developed to access and investigate the inside of Unit 1 PCV. This equipment has a total length of approximately 1 m, a cylindrical shape with a diameter of 25 cm, and various sensors to obtain information: A scanning type ultrasonic distance meter to acquire data on the shape of the sediments accumulated on the bottom of the PCV; A high power ultrasonic sensor to measure the thickness of the sediments; A radiation measuring instrument to understand the distribution of fuel debris etc.

### 6.3.5. Robot system development for fuel debris retrieval and sampling

The fifth revision of the Mid–and–Long–Term Roadmap for Decommissioning in December 2019 [98] indicated the following regarding fuel debris retrieval: The method for removing fuel debris from Unit 1 has been decided and trial removals at Unit 2 will start during 2021; After that, the scale of removals will be gradually expanded. The development of a robotic arm is currently being progressed

as the removal method. Although this will be the first unit to start fuel debris removal, it is the second unit from the viewpoint of safety, it however can be undertaken quicker and allows optimization of the entire decommissioning work while avoiding the overall spent fuel removal work being affected.

TEPCO had planned to collect a small sample (few grams of debris) from Unit 2 containment vessel by the end of 2021, but due to the influence of the Coronavirus disease 2019 (COVID-19), the development and manufacture of equipment was delayed. In Dec. 2021, it was announced that the start of collection would be postponed to fiscal year (FY) 2022 or later. In Aug. 2022, TEPCO and the Japanese government reannounced that the date would be postponed to the latter half of FY2023 or later, due to modifications to robotic arm system.

In support of the test retrieval of fuel debris from Unit 2, an arm type access equipment is being developed by IRID and others. It is made of stainless steel, ~22 m long, ~40 cm high, ~25 cm wide, weighs ~4.6 t (Fig. 218), and is radiation resistant to ~1 MGy [268]. The arm can be folded for storage in a box (enclosure) connected with the exterior of the PCV and sequentially unfolded to enter the PCV when used. Figure 219 shows an illustration of the investigation inside the PCV using arm type access equipment X–6.


*FIG. 217. Boat type access equipment with submersible functions (reproduced from Ref. [267] with permission courtesy of IRID).*

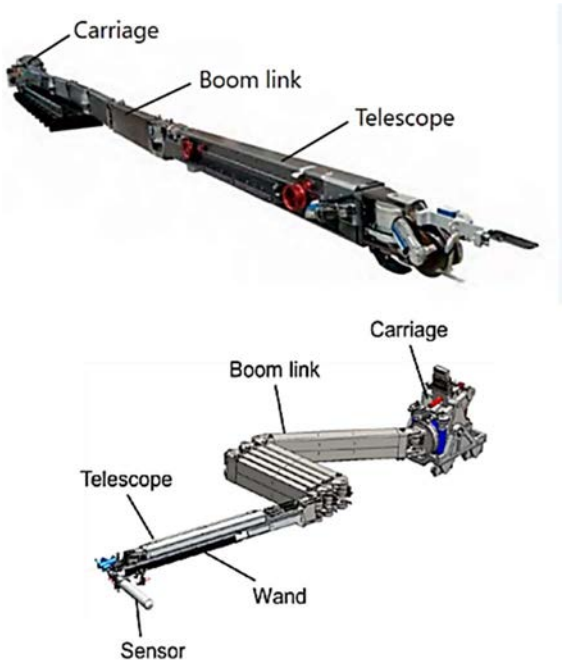


*FIG. 218. Arm type access equipment (reproduced from Ref. [266] with permission courtesy of IRID).*

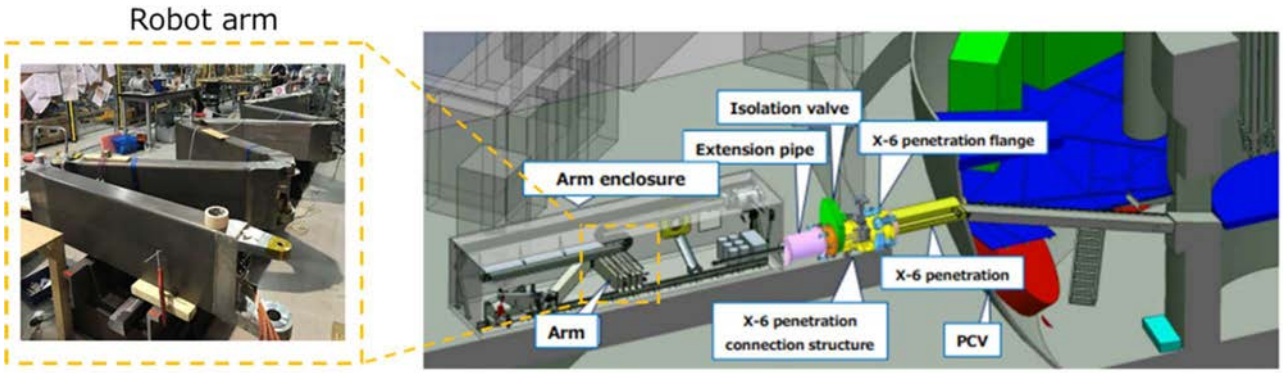


*FIG. 219. Access route to fuel debris in pedestal by arm type access equipment (courtesy of Agency for Natural Resources and Energy (ANRE)).*

There is a plan to attach a metal brush to the tip of the arm and rub the debris to take out about 1 g in several batches. After that, the plan is to increase the amount of fuel debris handled in stages. At that time, the tool will be changed as shown in Fig. 220. The provisional process of retrieval of fuel debris from the PCV is shown in Fig. 221.

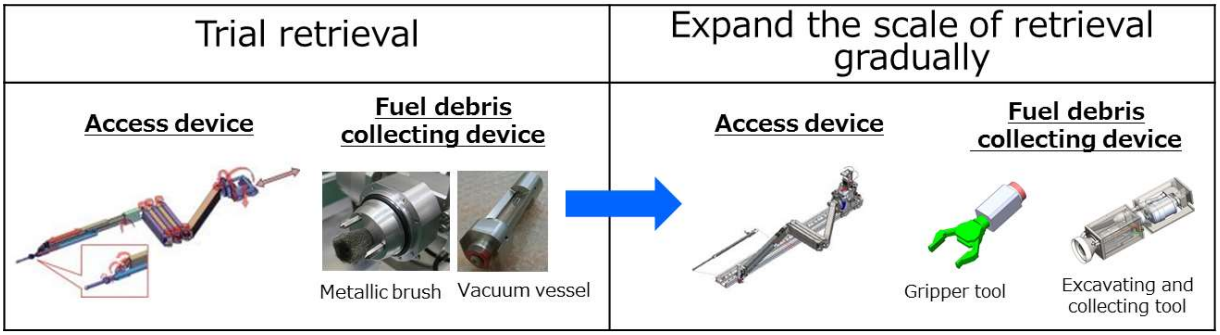


*FIG. 220. Illustration of fuel debris collecting devices due to increasing amount of retrieval fuel debris (courtesy of ANRE).*

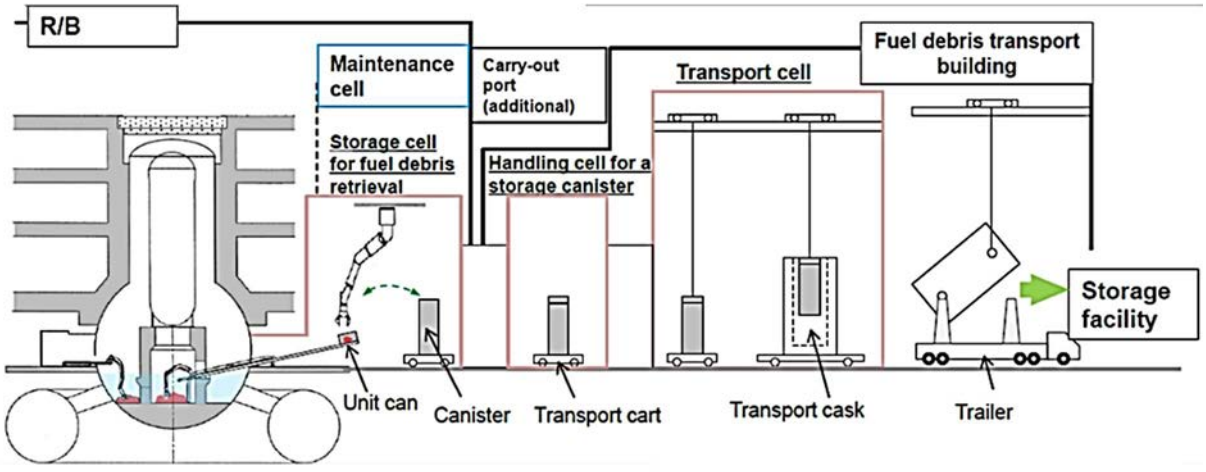


*FIG. 221. Illustration of fuel debris retrieval process from inside PCV (reproduced from Ref. [255] with permission courtesy of IRID).*

# 7. PREPARING FOR TRANSPORT, STORAGE, AND FINAL DISPOSITION

The following Section outlines the performance criteria required of severely damaged spent fuel debris packages and how these criteria were met in the case of conditioning TMI–2 debris. An account of conditioning TMI–2 and an update on the status of the packed TMI–2 debris is also provided. Recognizing that fuel cycle closure for this type of material has not been achieved yet, available strategies/options are explored.

## 7.1. BEHAVIOUR OF SEVERELY DAMAGED SPENT FUEL IN PACKAGES

The purpose of the drying and storage is to isolate the radioactive material from the environment for a defined (long) period of time at minimum cost in a manner that, in the general case, does not preclude either recovery of the fuel at the end of storage or subsequent disposal to a geological disposal facility. The requirements of such a concept include:

(a) Compliance with regulatory requirements;
(b) An acceptable outcome in terms of national policy for radioactive waste management, i.e., for higher activity wastes, passively safe waste suitable for disposal in a geological repository;
(c) Consistency with national and international standards of radioactive waste management;
(d) Clarity and minimisation of interdependencies on other stages in the generation and management of radioactive waste.

Given the long timescales involved and large radioactive inventories, multiple containment barriers are normally incorporated in the design. The principal barriers that prevent the radioactive material causing hazards are identified in Fig. 222.

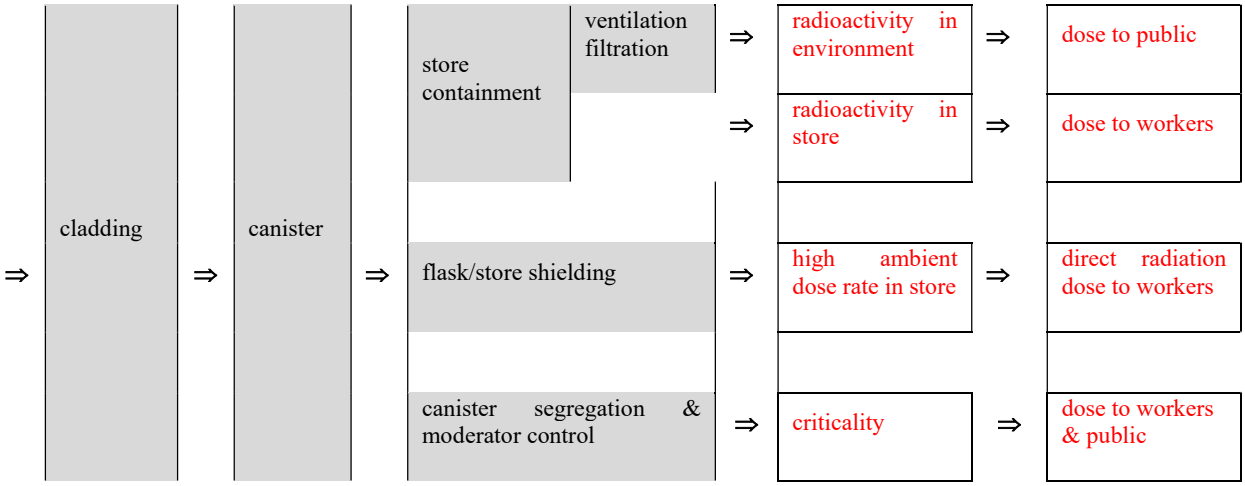


*FIG. 222. Principal barriers for preventing hazards from radioactive material (courtesy of NNL).*

Although the above figure focuses on doses to people, release of radioactive materials or high levels of radiation will also have adverse consequences on the environment.

The principal drivers for canister performance are:

— To prevent any radioactive release during storage;
— To ensure that the contents remain in a form suitable for recovery or disposal after an extended period of storage;
— To ensure that the canister remains in a condition where after storage, it can be handled, overpacked, opened or otherwise incorporated into a process or engineered barrier system.

These drivers can be further developed by considering, at a top level, the potential challenges faced by the canister during proposed operations. This leads to the following additional performance drivers:

- To retain integrity for foreseeable fault conditions, including:
  - Drop/impact;
  - Pressurisation/self-heating;
  - Pressurisation in the event of failure/bypass of drying;
  - Degradation over time.

During handling, transport and storage:

- To eliminate the potential for an in-canister flammable hydrogen–oxygen mixture because the low ignition energy of such mixtures makes elimination of ignition sources problematical;
- To be consistent with a passive store design, i.e., there should be no/minimal release of hazardous substances from the canister during long term storage, which in turn requires a very low level of surface contamination on the welded canister;
- To remain subcritical under all conditions;
- To maximise proliferation resistance.

The assessment of canister performance therefore must address a range of behaviours associated with the different constituent parts of the stored canister, which depends on:

- Fuel type (e.g., cladding, fuel, and implications of degraded items);
- Internal components;
- Canister;
- Gas space;
- Pressure control options;
- Fuel residual enrichment, and criticality.

For degraded fuels the following characteristics are of particular concern with respect to storage:

- Variation in composition due to material interactions during accident conditions;
- Increased surface area, which affects:
  - The rate of reaction per unit mass, hence rate of generation of heat and reaction products;
  - Surface area available for water adsorption, affecting water carryover;
  - Generation of more dispersible and/or more soluble species.
- Prior exposed to an aqueous environment, which affects:
  - The quantity of free water, either inside failed but largely intact fuel or within debris;
  - The quantity of bound water associated with corrosion products and precipitates;
  - Increase in path length between sources of water and drying environment.
- Close contact between water and fuel matrix, leading to:
  - High local alpha dose rate at fuel surface;
  - Increased beta dose rates around debris.
- For certain fuels, the potential for formation of high reactive corrosion products must be considered, prior to and during storage.

The principal concern with severely damaged fuel arises from hydrogen generation, either from radiolysis of water or hydrated compounds or from corrosion reactions leading to hydrogen formation.

In a sealed storage environment, this can lead to pressurisation and either an immediate or delayed potential for explosion. In the presence of materials that form readily oxidisable hydrides, e.g., U and Th, the formation of readily oxidisable materials with a large exothermic yield are particularly of concern, see Section 4.

In a vented system, the rate of formation of flammable gasses must be managed to prevent the formation of a flammable mix and the rate of corrosion must be sufficiently low as to not lead to a thermal runaway or to a significant degradation in the capacity of the fuel to retain fission products during subsequent management steps. Vented storage, therefore, is generally limited to low heat output fuels.

The requirements for drying of irradiated fuel are well described in ASTM C1553 [269] and include the need to understand all potential sources of water, the maximum permissible water carryover into the storage container and the effectiveness of drying. For poorly characterised fuel debris, with a potential range of compositions demonstrating adequate drying can be challenging. An example of a case where this was successfully applied is the Hanford N–reactor fuel [270].

However, residual uncertainties on the extent of drying can be such that a case for safe, sealed storage cannot be made and a vented storage configuration can be used, examples include TMI debris (see below) and legacy uranium fuel storage at Sellafield [271].

## 7.2. PACKAGING AND TRANSPORT OF THREE MILE ISLAND CORIUM MATERIALS

The following section provides an account of how TMI-2 material was packaged and transported to INEL.

### 7.2.1. Canister design

As a matter of system integration, the common component from the reactor to the current storage configuration was the canister. The canisters function as a discrete fuel handling unit, provide confinement of fission and activation products, and maintain subcriticality. Design requirement specifics are provided in the Appendix.

The canisters were designed by B&W and fabricated to American Society of Mechanical Engineers (ASME) pressure vessel standards [270]. The canisters were central to the retrieval process at the reactor, needed to be compatible with the INEL interim storage pool, and were initially expected to be a confinement barrier in transport.

Canisters for general debris, granular material, and filtered water were designed to be handled by the fuel handling equipment at the reactor while being compatible with the interim storage pool at INEL.

The fuel debris canister was designed to accommodate partial fuel assemblies as well as debris. Some initial design assumptions considered the possibility that a significant fraction of assemblies was intact. The original approach was to use 457 mm diameter canisters, but that was reduced to 456 mm due to handling limitations within the reactor vessel.

The knockout canisters were used to receive pieces suctioned from the reactor vessel that were too small for remote manual pick and place recovery; these ranged from fuel pellet size to 140 $\mu$m.

The filter canister was designed to remove particulate as small as 0.2 $\mu$m from the suction stream. Cross sectional views of the canister types are shown in Figs 223–225. The canisters were designed

to allow remote dewatering and prevent hydrogen buildup resulting from radiolysis of retained water during transportation.

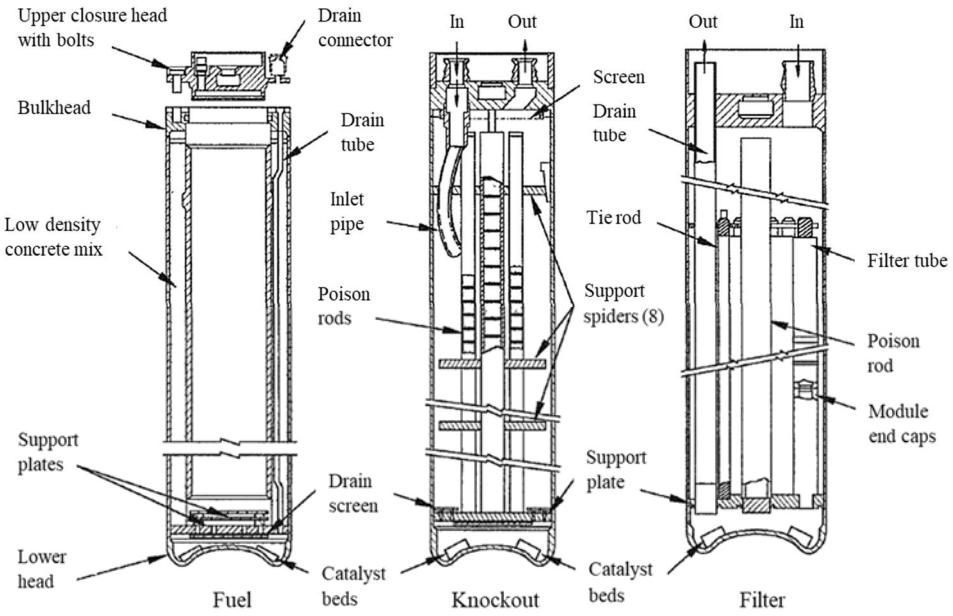


*FIG. 223. Fuel debris, knockout, and filter canisters elevation view (courtesy of INL).*

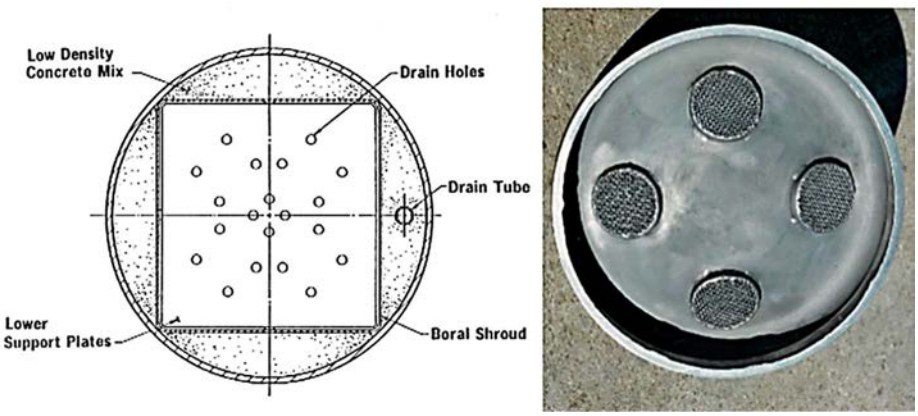


*FIG. 224. Cross-section view of fuel debris canister and lower head with catalyst bed (reproduced from [240] with permission courtesy of INL).*

*FIG. 225. Internal structure of knockout canister (reproduced from Ref. [240] with permission courtesy of INL).*

Concerns were raised regarding the properties of the debris being recovered. One uncertainty was the potential for pyrophoric reaction of unoxidized Zircaloy in air. This was determined to be unlikely because the debris were submerged in water, which would oxidize any zirconium surface immediately. To address this as a transportation issue, the canisters were backfilled with argon during dewatering. There was also the possibility of achieving a flammable concentration of radiolytically produced hydrogen. Numerous alternatives were suggested, but the choice was a platinum–palladium catalyst recombiner material that would convert hydrogen and oxygen back into water.

Assuring subcriticality ($k_{eff}$ <0.95) in the nonhomogeneous mass of debris, whether as a single canister or in an array, was achieved by the use of boron neutron poisons in several configurations. The square tube of the fuel debris canister was constructed by sandwiching a layer of stainless steel over plates of borated aluminium. The structure of the filter canister includes a centre rod that is filled with $B_4C$ pellets. In the knockout canister, four rods arranged around a large central rod, all filled with $B_4C$ pellets function to prevent criticality.

### 7.2.2. Canister shipping process

As part of the defuelling, it was decided that a sort of post-mortem examination of the fuel needed to be performed. The core needed to be removed and stored to allow completion of the reactor building cleanup.

To achieve a resolution of the final destination for the debris, negotiations in 1981 between US NRC and US DOE led to a memorandum of agreement under which US DOE would take a portion of the debris for research, and the balance would be retained onsite. In 1982, the decision was made to transfer the entirety of the core to the US DOE for research and storage until the national high level waste repository was operational.

It was determined that INEL had the requisite combination of facilities that could store the core debris and do the necessary research on the materials that were recovered. The laboratory also had experience doing research on severe accidents for the US NRC and the nuclear industry.

To move the core and debris 3540 km from Pennsylvania to Idaho, it was decided to design and construct two specialized rail casks. Rail was chosen to limit the number of shipments, allowing seven canisters to be shipped at once, versus one in a legal weight truck cask. The shipping cask was designed and fabricated by Nuclear Pacific (NuPac).

Because the fuel cladding was damaged or absent, the debris canisters were initially designed to be the primary barrier to dispersal. Due to concerns about the ability to achieve adequate sealing with the bolted head canister design, it was concluded that the cask would need to provide double containment. The cask design provided two barriers in the form of internal and external cask modules, complete with individual impact limiters for the canisters. Double containment was mandated because the primary fuel clad barrier was no longer present, and the transportation regulation requires double containment for Pu containing materials. Three casks were fabricated for rail service. Forty-nine cask loads were transferred in 22 shipments.

Once a canister was identified for shipping, it was dewatered using argon purge gas and loaded into the fuel transfer cask. The cask was moved to the fuel handling building loading area, where the shipping cask was staged. The shipping cask was rotated from its horizontal transport position, and a loading collar was installed. A mini hot cell was mounted to the loading collar and used to remove the shield plug from the shipping cask position designated to receive the canister that was ready for shipping. The fuel transfer cask was mated to the loading collar, the canister was lowered into the

position in the shipping cask, and the shield plug was replaced. The loading collar and mini hot cell configuration is shown in Fig. 226, and the upended rail shipping cask with the fuel transfer cask attached is shown in Fig. 227.

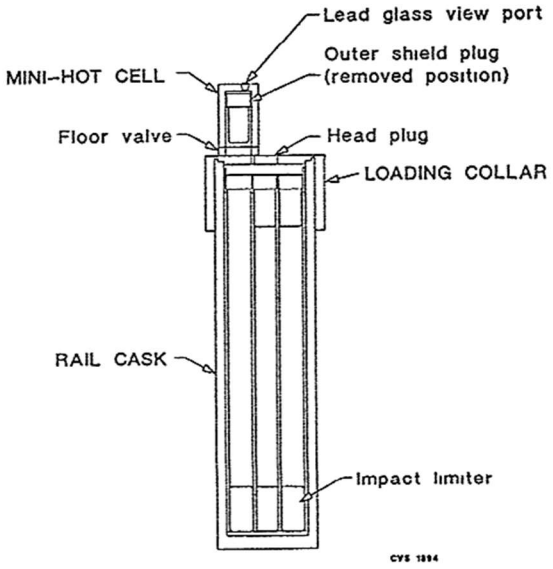


*FIG. 226. Schematic of mini hot cell with rail cask and loading collar (courtesy of INL).*

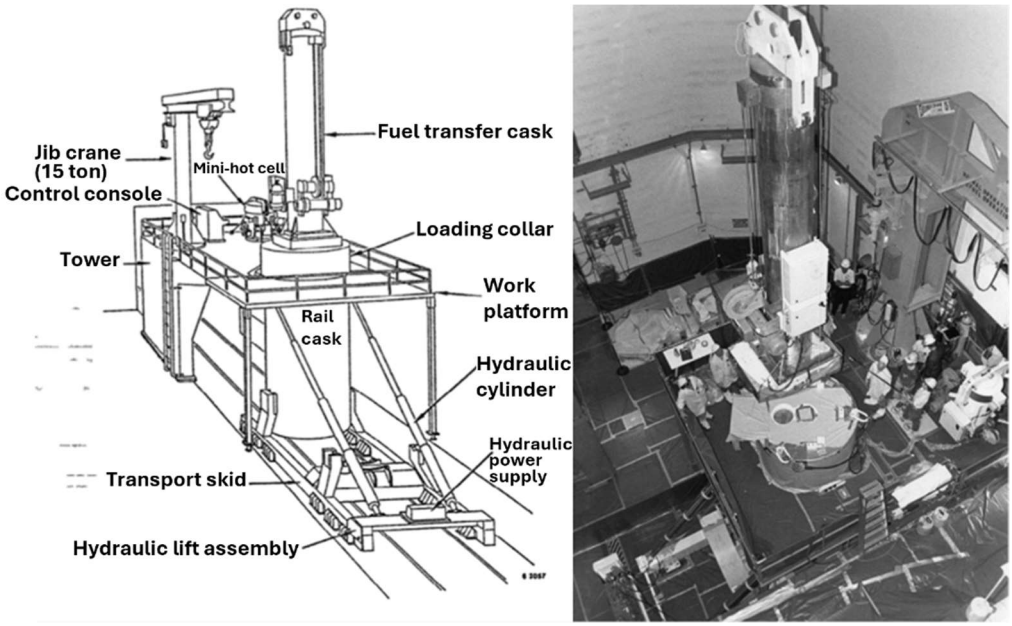


*FIG. 227. Equipment for dry transfer of debris canisters to rail cask (courtesy of INL).*

On arrival of the empty cask, the impact limiters were removed before pushing the rail car into the fuel handling building's truck bay. Then the rail car was pushed into a specific location in the truck bay under the cask unloading station, where four screw jacks raised the cask and skid from the rail car. The rail car was then removed from the truck bay. The cask unloading station was then removed from the skid and set aside using an overhead crane. The cask hydraulic lift assembly was attached to the railcar skid to rotate the empty cask from a horizontal position to a vertical orientation. This unit comprised a pair of hydraulic cylinders that pushed on the upper trunnions to rotate the cask. A work platform was attached around the cask, allowing removal of the outer and inner cask lids using a jib crane.

Loaded debris canisters were operationally limited to a gross dewatered weight of 1272 kg, with a typical debris load of 750 kg.

Concerns about residual water retention were validated based on differences between empty and loaded, dewatered containers, as shown in Table 46. As may be expected, the filter canister (F–462) has the greatest remaining water.

TABLE 46. EXAMPLE CANISTER WATER RETENTION [239]

| Canister ID | Canister Weight Empty (kg) | Full (kg) | Dewatered (kg) | Core Debris (kg) | Water Remaining (L) | Total PayLoad | Void Volume (L) |
|---|---|---|---|---|---|---|---|
| D-180 | 542 | 1,393 | 1,315 | 743 | 29 | 772 | 72 |
| D-188 | 542 | 1,405 | 1,317 | 746 | 29 | 775 | 81 |
| D-330 | 538 | 1,406 | 1,327 | 767 | 22 | 789 | 78 |
| F-462 | 662 | 1,218 | 1,101 | 310 | 111 | 439 | 120 |
| K-506 | 458 | 1,471 | 1,324 | 842 | 23 | 865 | 146 |

As part of the validation process for specifying transport conditions for potential radiolytic hydrogen production, eight of the canisters were sealed and monitored for pressure and periodically sampled for headspace composition. The test canisters remained sealed for between sixteen to 205 days. Pressure values reached as high as 198 kPa in as few as 16 days for the D–188 debris canister. The headspace gas was analysed at INEL and indicated that, over time, the hydrogen concentration could reach as much as 9 vol.% with only 0.2 vol.% oxygen in 87% argon after 205 days sealed. The values are tabulated as shown in Tables 47 and Table 48.

TABLE 47. CANISTER PRESSURE SAMPLES SEALED TEST [272]

| Canister Number | Rail Shipment | TMI (kPa) | First Sample | | Second Sample | | Third Sample | | Fourth Sample | |
|---|---|---|---|---|---|---|---|---|---|---|
| | | | kPa | Days Closed | kPa | Days Closed | kPa | Days Closed | kPa | Days Closed |
| D-144 | – | 203.67 | 188.54 | 147 | – | – | – | – | – | – |
| D-148 | 4 | 203.53 | 200.84 | 26 | 198.78 | 48 | – | – | – | – |
| D-145 | 5 | 141.62 | 202.22 | 27 | – | – | – | – | – | – |
| D-180 | 6 | 202.57 | 126.38[a] | 27 | 133.28 | 205 | – | – | – | – |
| D-162 | 7 | 201.81 | 202.22 | 36 | 195.33 | – | – | – | – | – |
| D-188 | 7 | 202.43 | 200.50 | 16 | 198.78 | 181 | 195.33 | 88 | 188.43 | 168 |
| D-207 | 8 | 202.29 | 198.78 | 20 | 188.43 | 56 | – | – | – | – |

### 7.2.3. Transport cask

The transport cask was designed by NuPac as a multiple barrier system. In a normal fuel shipment, intact fuel clad can be credited as a containment barrier. Per transportation regulations, the fuel debris contained sufficient plutonium to require double containment. In this design, the canisters were not considered a containment barrier because the debris canisters had removable heads. To provide the necessary barriers, the NuPac 125-B casks were designed with an inner and outer vessel to provide double containment. The inner vessel weighed 15.4 t and the outer vessel weighed 43.5 t.

Seven canisters were fitted inside the cask, each having its own upper shield plug and upper and lower internal impact limiter. The casks were shipped cross country by rail as a dedicated shipment with as many as three rail cars, each cask on its own car. Figure 228 shows the cask with impact limiters in place.

The 125–B cask was mounted to a skid (or transport frame) that was in turn attached to a rail car. To perform the loading of the transport cask in the fuel handling building, it was necessary to remove the 125–B cask and its transport skid from the rail car. This was performed using the cask unloading station.


*FIG. 228. NuPac 125–B cask on a rail car (courtesy of INL).*

### 7.2.4. Offloading at Idaho National Engineering Laboratory

When the casks reached INEL there was no rail spur available to complete the journey to the TAN−607 hot shop and pool system. This meant that the casks needed to be unloaded from the rail cars and transported by truck approximately 48 km from the rail terminal at the INEL Central Facilities Area to TAN; as shown in Fig. 229.

*FIG. 229. Gantry crane removing 125-B Cask from rail car (left). 125-B cask on transport skid, loaded on trailer (right) (courtesy of INL).*

### 7.2.5. Idaho National Engineering Laboratory storage site Test Area North 607

The TAN–607 building included a hot shop, which was originally designed for handling test nuclear reactors for a conceptual nuclear airplane. The hot shop was 15.5 m × 50 m × 16.76 m. It was a high bay cell with a large entry lock sufficient to accommodate a large truck trailer unit or a rail engine using rail tracks. It featured a 100t bridge crane, nine shielded viewing windows, and one bridge mounted and three wall mounted electromechanical manipulators. The main overhead crane was used to lift and position the cask upright (Fig. 230 (a)) before placing into a work platform (Fig. 230 (b)). After cask preparations and lid bolt removal, the manipulators were used to open the cask and retrieve the contents.

TABLE 48. SEALED CANISTER HEADSPACE COMPOSITION [271]

| | Hydrogen (Vol.%) | | | | Nitrogen (Vol.%) | | | | Oxygen (Vol.%) | | | | Argon (Vol.%) | | | |
|---|---|---|---|---|---|---|---|---|---|---|---|---|---|---|---|---|
| Canister Number | 1st | 2n$^{d}$ | 3r$^{d}$ | 4t$^{h}$ | 1s$^{t}$ | 2n$^{d}$ | 3rd | 4th | 1st | 2nd | 3$^{rd}$ | 4th | 1st | 2nd | 3rd | 4th |
| D–144 | 0.77 | – | – | – | 0.90 | – | – | – | 0.08 | – | – | – | 98.20 | – | – | – |
| D–148 | 1.15 | 1.47 | – | – | 0.36 | 0.70 | – | – | 0.07 | 0.13 | – | – | 98.40 | 97.70 | – | – |
| D–145 | 0.74 | – | – | – | 0.585 | – | – | – | 0.09 | – | – | – | 98.6 | – | – | – |
| D–180 | 1.23 | 9.05 | – | – | 1.07 | 3.75 | – | – | 0.13 | 0.02 | – | – | 97.5 | 87.19 | – | – |
| D–162 | 1.005 | 1.01 | – | – | 4.36 | 2.22 | – | – | 1.02 | <0.01 | – | – | 93.53 | 96.74 | – | – |
| D–188 | 1.165 | 2.43 | 3.30 | 5.09 | 0.50 | 1.95 | 2.16 | 1.81 | 0.05 | 0.305 | 0.26 | <0.01 | 98.26 | 95.29 | 94.25 | 93.1 |
| D–207 | 0.20 | 0.46 | – | – | 0.475 | 3.82 | – | – | 0.04 | 0.72 | – | – | 93.40 | 89.66 | – | – |
| D–267 | 0.12 | 0.25 | – | – | 0.90 | 0.52 | – | – | 0.17 | 0.01 | – | – | 98.80 | 99.17 | – | – |

(a)

(b)

*FIG. 230. (a) Cask unloading in TAN-607 hot shop, (b) NuPac 125-B cask on the work platform (courtesy of INL).*

The hot shop had a vestibule that provided access from the dry area to the storage pool. The pool was 14.6 m wide, 21.3 m long, and 7.3 m deep.

The TAN–607 hot shop also had a hot cell 3.05 m wide × 10.7 m long×6.1 m high. It was directly connected to the hot shop, which facilitated receipt of the TMI–2 canisters that contained core bores for inspection. An additional set of four hot cells allowed handling of subdivided samples for further analysis. Pictures of the canister being removed from the casks and being loaded to the storage rack are shown in Fig. 231 and the racks stored in the pool in Fig. 232.

(a)

(b)

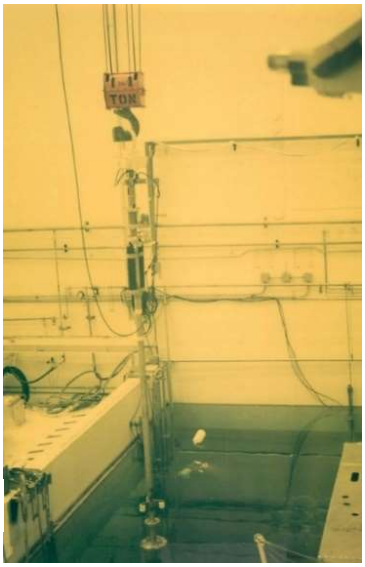

*FIG. 231. (a) Canister being removed from 125-B cask prior to transfer to TAN-607 pool. (b) Six pack canister rack for storage in TAN-607 pool (reproduced from Ref. [271] with permission courtesy of INL).*

Storage of canisters in the TAN-607 pool used the six pack array, with each canister having an individual vent tube extending above the pool surface. The canister internals, including debris, were isolated from the pool water. The canisters were backfilled with deionized water through the vent tube. During the early stages of storage, release of gas from radiolytic hydrogen production caused the water in the canister to be kinetically expelled through the vent tube. Following observation of

this phenomenon, the tops of the vent tubes were covered with plastic caps that diverted any expelled water back into the pool (see Fig. 232).

FIG. 232. TAN-607 pool, showing six pack racks and individual canister vent ports (orange caps divert water back into pool) (courtesy of INL).

### 7.2.6. Drying of fuel debris and nuclear materials and transfer to dry storage

At least in part due to legal action by the state of Idaho regarding the US DOE management of nuclear material, a decision was made to transfer the fuel debris from wet to dry storage. This decision was made on the basis that dry storage is less expensive to operate and represents a lesser environmental risk; the TAN-607 pool was known to leak. Contaminated water could have eventually reached the Snake River aquifer.

### 7.2.7. Drying

Design alternatives led to selection of the concrete shielded Pacific Nuclear Fuel Services NUTECH Horizontal Modular Storage System (NUHOMS) design. One primary consideration was the relatively low cost of the concrete shield and shielded canister design when compared to metal shielded multipurpose cask designs.

A total of 342 stored canisters were dried and repackaged for dry storage in the hot shop. A larger number of canisters, 344, were originally shipped from TMI to INEL, but two of the canisters were handled separately because various epoxy containing metallographic mounts that were produced during the characterization phase were loaded into these canisters. The two separate canisters contained a minimal amount of fuel debris, and they are stored in one of the 125–B transport casks located on the CPP-2707 dry cask storage pad. The canisters were retrieved from storage, dewatered, and brought into the dry hot cell for final drying in the heated vacuum drying system (HVDS).

Dewatering was performed by removing the vent tube and attaching a gas line to the Hansen connector on the canister and displacing the water with air or nitrogen. The gas released during the dewatering purge process was vented through a high efficiency particulate air (HEPA) filter and the TAN–607 air handling system before being released through the TAN–734 stack. Sintered metal filters were installed on 1.905 cm vent and 1.27 cm purge lines of the filter and knockout canisters in place of Hansen quick connect fittings. This was a precaution to reduce the chance of fines being released from the canisters during drying. The sintered metal filters were removed from the canisters prior to placement in the dry shielded canister. Installation and removal are shown in Fig. 233.

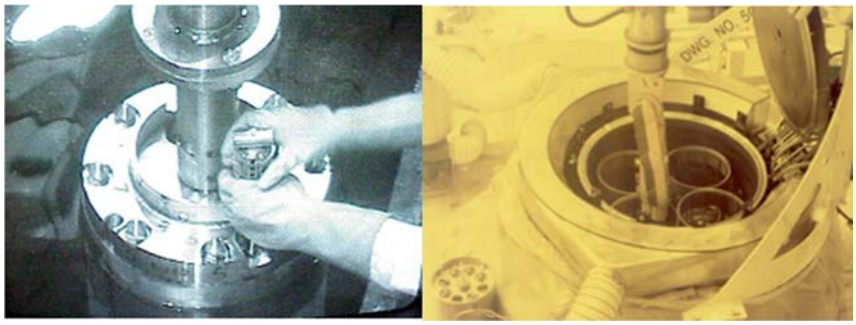

*FIG. 233. Installation and removal of sintered metal filters (courtesy of INL).*

It was calculated that there could be up to 80 L of water retained in the canister following dewatering. The displaced water was not discharged into the pool to avoid the introduction of contamination. The water from selected canisters was sampled and analysed for dissolved chemical species to determine the degree of leachability of the debris. Canister sample pH was 8.0, except for D–330 (pH 8.5). Canister data are shown in Table 49. The analysis is shown in Table 50. Table 51 shows tabulated radionuclide concentrations measured in the water. A calculated average radionuclide leach value for all sampled canisters is shown in Table 52.

TABLE 49. LEACH WATER FROM SAMPLED CANISTERS, DESCRIPTION [274]

| Canister | Description | Contained Solid Mass (kg) | Contained Volume (L) | Solid Void Fraction | Volume of TMI Water Shipped (L) | Present Water Volume (L) |
|---|---|---|---|---|---|---|
| D–180 | Fuel | 742 | 191 | 0.404 | 29.02 | 77.21 |
| D–188 | Fuel | 745 | 191 | 0.458 | 29.02 | 87.53 |
| D–330 | Fuel | 766 | 191 | 0.411 | 21.77 | 78.55 |
| F–462 | Filter | 309 | 281 | 0.416 | 110.66 | 117.07 |
| K–508 | Knockout | 841 | 304 | 0.482 | 23.2 | 146.43 |

TABLE 50. CHEMICAL CONSTITUENTS OF CANISTER WATER [274]

| Species or elemental component | D–180 (moles/L) | D–188 (moles/ L) | D–330 (moles/ L) | F–462 (moles/ L) | K–506 (moles/ L) |
|---|---|---|---|---|---|
| Boron | 9.03E-5 | 7.24E-2 | 6.84E-2 | 7.97E-2 | 1.02E-1 |
| Sodium | 1.24E-2 | 1.07E-2 | 1.44E-2 | 1.16E-2 | 1.67E-2 |
| Calcium | 4.19E-6 | 4.07E-6 | 3.78E-4 | 1.25E-5 | 6.94E-6 |
| Chloride | 4.26E-5 | 9.00E-5 | 2.06E-4 | 1.35E-4 | 7.87E-5 |
| Silicon | 2.34E-5 | 2.16E-5 | 7.09E-5 | 1.24E-4 | 3.20E-5 |
| pH (pH paper) | 8.00 | 8.0 | 8.5 | 8.0 | 8.0 |
| Hydroxyl | 1.00E-6 | 1.0E-6 | 3.2E-6 | 1.0E-6 | 1.0E-6 |
| Barium | 1.49E-7 | 3.93E-7 | 7.03E-7 | 6.19E-7 | 2.37E-7 |
| Cadmium | 1.87E-7 | 1.78E-7 | 3.02E-7 | 5.16E-7 | 1.60E-7 |
| Lithium | 8.65E-6 | 1.08E-5 | — | — | — |
| Bromide | 3.30E-6 | — | — | 2.79E-6 | 1.13E-6 |
| Chromium | 1.06E-7 | — | — | 2.02E-7 | 3.37E-7 |
| Arsenic | — | — | — | — | — |
| Lead | — | — | — | — | — |
| Magnesium | — | — | 2.22E-4 | — | — |
| Mercury | — | — | — | — | — |
| Selenium | — | — | — | — | — |
| Silver | — | — | — | 3.4E-7 | 6.00E-6 |
| Uranium | — | — | — | — | — |

TABLE 51. CANISTER WATER RADIONUCLIDE CONTENT DECEMBER 1995 [240]

| Nuclide | Canister D–180 | | Canister D–188 | | Canister D–330 | | Canister F–462 | | Canister K–506 | |
|---|---|---|---|---|---|---|---|---|---|---|
| | Max (mg/L) | Min (mg/L) | Max (mg/L) | Min (mg/L) | Max (mg/L) | Min (mg/L) | Max (mg/L) | Min (mg/L) | Max (mg/L) | Min (mg/L) |
| Pu–238 | 4.92E-6 | 0 | <4.53E-8 | 0 | 2.75E-6 | 0 | 4.67E-6 | 2.71E-6 | <1.74E-7 | 0 |
| Pu–239 | 6.10E-4 | 0 | 1.18E-3 | 0 | 3.57E-4 | 0 | 7.67E-5 | 0 | 9.41E-4 | 4.62E-4 |
| Np–237 | 1.02E-1 | 5.99E-2 | 1.79E-3 | 0 | 2.07E-1 | 1.47E-1 | 1.90E-3 | 0 | 1.88E-2 | 0 |
| Am–241 | 3.40E-6 | 0 | 1.26E-5 | 0 | 1.22E-5 | 0 | 9.65E-6 | 4.16E-6 | 5.73E-6 | 0 |
| Th–228 | 1.11E-9 | 0 | 2.53E-8 | 0 | 2.06E-8 | 0 | 2.27E-8 | 0 | <5.11E-9 | 0 |
| Th–230 | 3.93E-4 | 0 | 9.85E-4 | 0 | <1.27E-4 | 0 | 8.23E-4 | 0 | 7.46E-4 | 0 |
| Th–232 | 1.14E2 | 0 | <2.22 | 0 | <2.22 | 0 | <2.21 | 0 | 1.05E2 | 0 |
| Tc–99 | 6.48E-3 | 2.86E-3 | 5.94E-2 | 5.50E2 | 1.93E-2 | 1.54E-2 | 3.49E-3 | 0 | 4.27E-2 | 3.86E-2 |
| Sr–90 | 7.60E-3 | 7.60E-3 | 3.79E3 | 3.79E3 | 9.08E2 | 9.08E2 | 2.14E3 | 2.14E3 | 2.00E3 | 2.00E3 |
| H–3 | 1.09E-6 | 1.09E-6 | 1.58E-6 | 1.58E-6 | 9.52E-7 | 9.52E-7 | 1.26E-6 | 1.26E-6 | 1.11E-6 | 1.11E-6 |
| Cs–134 | 4.22E-6 | 3.56E-6 | 5.37E-6 | 4.57E-6 | 1.73E-6 | 1.52E-6 | — | — | 3.80E-6 | 3.31E-6 |
| Cs–137 | 3.60E-2 | 3.30E-2 | 4.47E-2 | 4.11E-2 | 1.41E-2 | 1.29E-2 | 9.90E-4 | 9.16E-4 | 2.90E-2 | 2.66E-2 |

TABLE 52. CALCULATED MAXIMUM AVERAGE RADIONUCLIDE LEACH RATES [240]

| Radionuclides | Average leach rate ($g \cdot cm^{-2} \cdot d^{-1}$) |
|---|---|
| Pu–238 | 3E-16 |
| Pu–239 | 8E-14 |
| Np–237 | 9E-12 |
| Am–241 | 1E-15 |
| Th–228 | 2E-18 |
| Th–230 | 8E-14 |
| Th–232* | < 3E-10 |
| Tc–99 | 3E-12 |
| H–3 | 2E-16 |
| Cs–134 | 5E-16 |
| Cs–137 | 3E-12 |

* Excluding canister D-180 and K-506 for $^{232}Th$.

The data noted in the reference letter indicate that only a negligible amount of calcium was leached from the light weight concrete in the debris canisters (i.e., D–180, 188 and 330). This may be related to the limited communication and surface area within the canisters.

In addition, the dewatering skid was fitted with a collimated sodium iodide gamma ray spectrometer that was calibrated for $^{154}Eu$ detection. A correlation to uranium carryover was used to assure that minimal transfer from the canister to the dewatering system occurred during the water removal process.

Following dewatering, the canisters were raised out of the pool into the main hot shop, where the canisters were placed either into a shielded silo or directly into one of the four positions in the HVDS.

The HVDS was built by Exolon Systems under contract to VECTRA[16] and was designed to receive four canisters at a time. The vacuum furnace vessel had a 388.62 cm internal length and was 96.52 cm internal diameter. It was equipped with five thermocouples and heated by 54 kW of axial heating elements. The initial vacuum drying vessel was installed in the REA–2023 cask to provide shielding in the cell in the event that personnel entries were required. A second furnace was eventually procured and installed in one of the NuPac 125–B casks. The process schematic is shown in Fig. 234. The control screen and skid configuration are shown in Fig. 235.

[16] VECTRA Technologies, Inc. (USA).

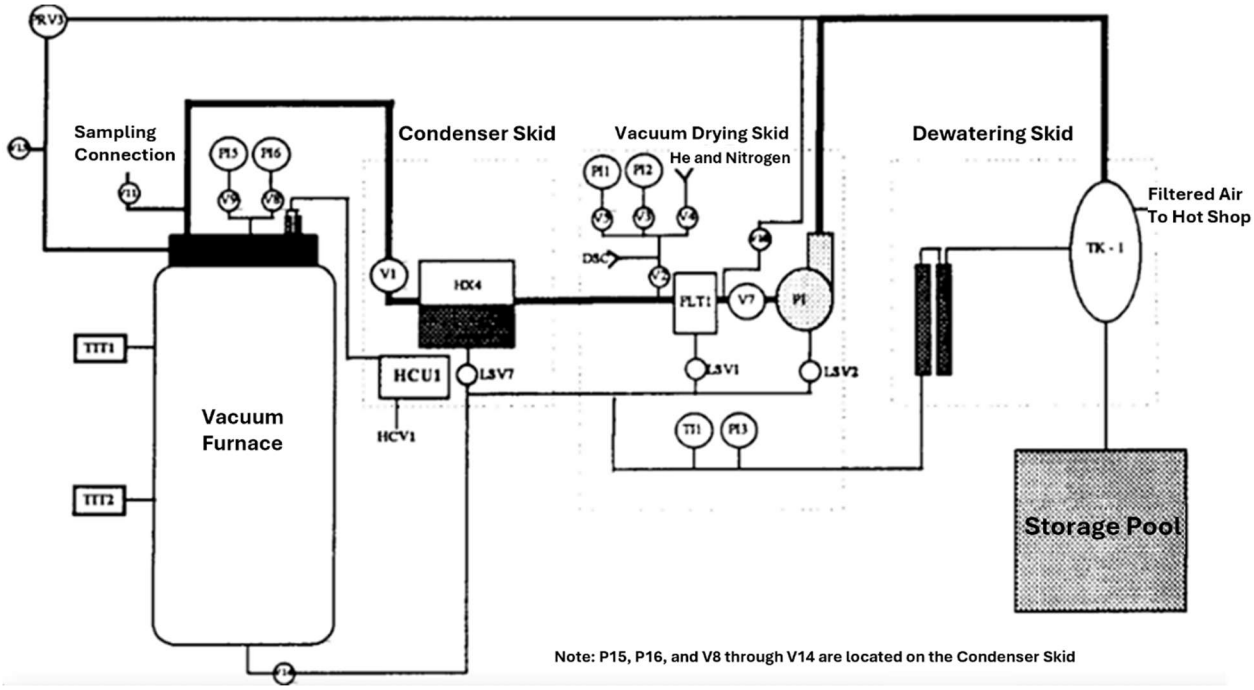


*FIG. 234. General schematic of dewatering and vacuum drying processes (courtesy of INL).*

*FIG. 235. Dewatering skid (courtesy of INL).*

Groups of four canisters were loaded into the HVDS, and the lid was secured. The system heated to 588 K and evacuated. The heater control temperature was a maximum of 755 K, and the debris temperature was estimated to be ~573 K. Because the heater was attached to the vacuum vessel, not to individual canisters, the temperature of the canister was determined by mathematical models. Design temperature was limited to minimize the potential for release of fission products such as $^{137}Cs$, which becomes volatile >773 K. When a vacuum level of $4 \times 10^{-4}$ MPa was reached, the vacuum pump was isolated, and the vessel pressure was monitored. The drying cycles initially were expected to be able to maintain the standard identified in NUREG–1536 [275] of $4 \times 10^{-4}$ MPa for 30 minutes of isolation. During early operation, these values were not achieved, requiring multiple evacuation cycles that took as many as 96 hours to reach the desired vacuum isolation duration. Because it was impossible to determine whether the inability to maintain vacuum was due to in leakage from incomplete closure of the HVDS vessel head, an alternate approach was used. Due to schedule demand, it was determined that acceptable levels of drying could be achieved by observation of the change in temperature and pressure to identify the change from constant rate drying to falling rate drying. The latter is noted by a rise in bulk temperature and a consistent drop in pressure. Falling rate

drying is an indication that the bulk water has been fully evaporated from among the particles of a granular system such as the fuel debris. The HVDS system included a condenser for water removal and separate pump for removable of incondensable gas. The system design included controls to prevent overtemperature conditions as well as to assure that flammable gas deflagration was not possible. The design allowed for intermittent purge capability, which was used periodically. The canister configuration in the HVDS was also analysed to assure subcriticality.

The original assumptions used by the INEL engineering group [276] were predicated on maintaining the drying temperature below that which would cause failure of the O ring on the fuel/debris canister head. When the drying and packaging contract was awarded to VECTRA, the decision was made only to take credit for the dry shielded canister (DSC) as the confinement barrier; no credit was taken for the fuel debris canister O ring, meaning that there was no need to run at a temperature <423 K. The four canister configuration in the HVDS is shown in Fig. 236.

*FIG. 236. Heated vacuum drying system installed in REA-2023 cask in TAN hot shop (courtesy of INL).*

Prior to award of the drying contract, several tests of different materials were performed at INEL, including thermal measurements of bucketed rods, tests on simulated fuel elements in buckets, canned rods, bucketed sand, and TMI–2 debris canisters containing lava rock using heated forced air and heated vacuum drying. Heated vacuum drying was selected as the preferred option.

### 7.2.8. NUTECH horizontal modular storage system dry shielded canister

The selected design was a modified variant of the standard NUHOMS dry storage system that accommodates 24 FAs per stainless steel DSC. The NUHOMS–12T design uses an internal basket configuration that positions twelve of the TMI–2 canisters in a circular array.

The NUHOMS–12T DSCs were fabricated from SA–517, Grade 70 mild steel. The DSC main shell is fabricated of 1.6 cm thick plate, rolled into a 170 cm diameter, 426 cm tall cylinder. The canister configuration is shown in Fig. 237 (a).

The DSC has a 2.54 cm thick welded top plate and a multiple piece bottom lid that incorporates a, 11.5 cm thick radiological shield plug and two 3.8 cm thick top cover plate that are welded to the shell to complete the final closure. The bottom end also incorporates a ring on which a hydraulic ram is attached that is used to push the DSC into place in the horizontal storage module (HSM) as well as retrieve it at the end of interim storage. The ring is visible in the fabrication photo, Fig. 237 (b).

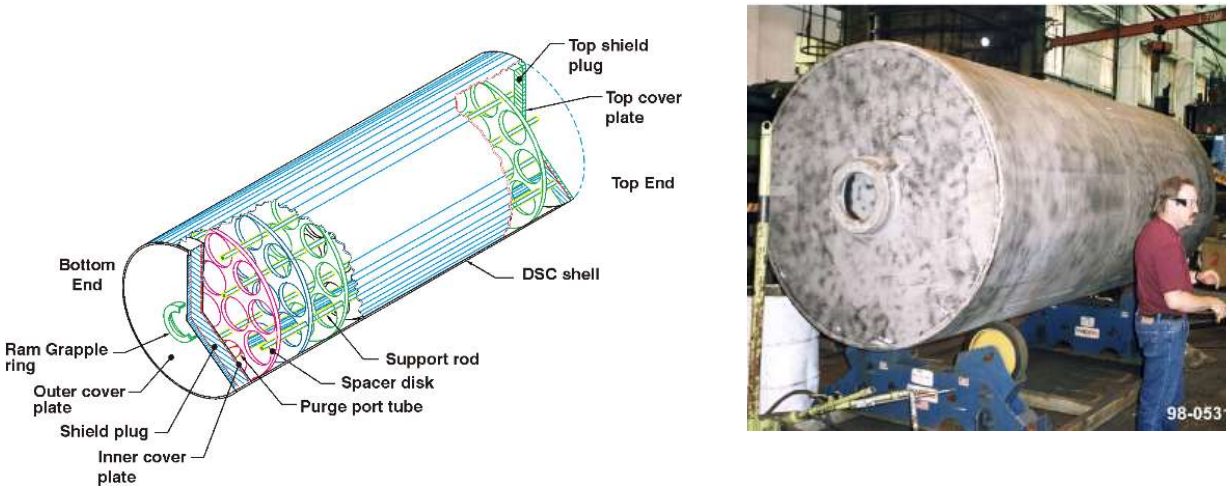


*FIG. 237. (a) NUHOMS dry shielded canister schematic (reproduced from Ref. [277] with permission courtesy of INL). (b) Dry shielded canister during fabrication (courtesy of INL).*

The TMI–2 DSC design required separate certifications from the standard design, at least in part due to its manufacture from carbon steel, which was initially seen as a cost saving measure. This additional certification included confirmation that certain fabrication welds could be made in a fully compliant manner.

The most unique part of the TMI–2 DSC design is the vent that was incorporated to allow any residual water or radiolytic hydrogen to be released from the debris canisters. This vent module is located near the edge of the non-shielded end of the canister and includes four Pall sintered stainless steel filter units as well as an isolation and purge port. If high hydrogen values are observed in a gas sample, the canister can be purged with nitrogen to reduce the concentration to <4 vol.%. If a filter fails to function, the original assumption was that the DSC could be returned to the hot shop, and the filter module replaced. No filters have failed during testing to date.

Criticality control is primarily a function of moderator exclusion by preventing water ingress. The debris canisters have been extensively dried, and the DSC is placed in the HSM above the design flood elevation. Seventy five percent credit is taken for the various fixed neutron absorbers present in the canister components. Canister spacing inside the DSC contributes to criticality safety as well. No burnup credit is considered [278].

Structurally, the entire system was evaluated for specific head load and canister drop potential. Table 53 shows the design criteria.

TABLE 53. NUHOMS DSC DESIGN CRITERIA [278]

| Category | Criteria or Parameter (Dimensions Are Nominal) | Value |
|---|---|---|
| TMI–2 Canister Criteria: | Maximum Canister Weight | 1327 kg |
| | Size (Nominal): Length | 3.81 m |
| | Diameter | 35.6 cm |
| | Initial Maximum Enrichment (w% U-235) | 2.98% |
| | Fuel Burnup (MWd/tU) | 3175 |
| | Gamma Radiation Source (photons/sec/canister) | $6.37\times10^{14}$ (19 yr. cooled) |
| | Neutron Radiation Source | $6.90\times10^{5}$ (19 yr. cooled) |
| | Thermal Characteristics | |
| | Max. Decay Heat/Canister | 60 W |
| | Average Decay Heat/Canister | 15 W |
| | Thermal Design Basis | |
| | Max. Decay Heat per Canister | 80 W |
| | Total Decay Heat for DSC with 12 cans | 860 W |
| Dry Shielded Canister: | Number of TMI-2 Canisters per DSC | Up to 12 |
| | Size (Nominal): | |
| | Overall Length | 4.15 m |
| | Outside Diameter | 1.71 m |
| | Shell Thickness | 15.9 mm |
| | Heat Rejection | 860 W |
| | Internal Atmosphere | Air |
| | Design Pressure | 104 kPa |
| | Equivalent Cask Drop Deceleration | 75 g Vertical (end) & Horizontal (side)<br>25 g Oblique (corner) |
| | Materials of Construction | Carbon Steel |
| | Service Life | 50 years |

*7.2.8.1. Dry shielded canister loading and welding*

Dried canisters were then transferred to the NUHOMS–12T DSC in the TAN hot shop. The DSC was staged in the hot shop, positioned in the OS–197 onsite transfer cask with the lid off. The canister loading is shown in Fig. 238.

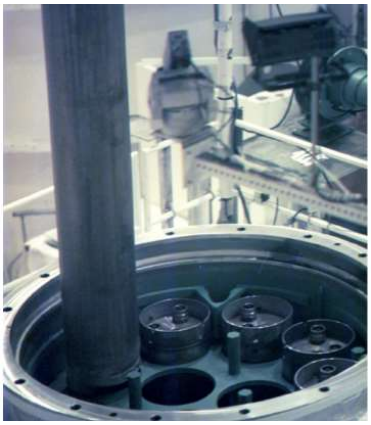

*FIG. 238. Dried debris canisters being loaded into a DSC (courtesy of INL).*

Once the twelve canister payload was inserted into the DSC, the radiological shield plug was inserted, and the final shield plugs were welded into place using the automatic welding machine. Initial welds were performed manually, but in the interest of radiological dose reduction and improved weld consistency, an automatic welding machine was used. When the shield plug weld was completed, the weld was visually inspected by remote camera. Both the welding technique and the remote inspection process were validated using mock up canisters prior to implementation. The DSC was then evacuated to 1.33 kPa using the vacuum drying system and backfilled with helium to a 1.51 kPa pressure, after which a helium leak check was performed. If the DSC failed the helium leak check, the point of leakage would be repaired by grinding and rewelding. The DSC top cover plate was then installed, welded, and visually inspected. The vent and purge ports at the shield plug end of the DSC were then seal welded. Lid placement is shown in Fig. 239 (a).

The less shielded head of the DSC incorporates a replaceable sintered metal HEPA filter that allows any gas that might be produced from water that was not removed during the drying process to be vented without pressurization of the DSC in storage. Following the top cover weld completion, this filter module was installed on the vent and purge ports. This is shown in Fig. 239 (b). A cover was placed over the vent port to seal the canister, and the DSC was then backfilled for transport.

(a) 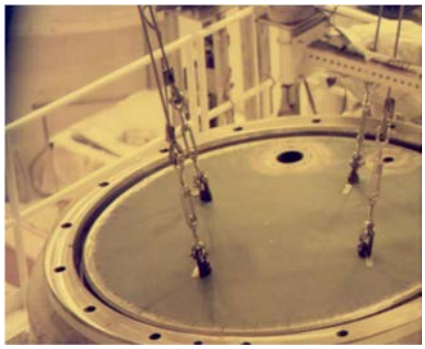 (b) 

*FIG. 239. (a) DSC lid placement. (b) Vent filter installation (courtesy of INL).*

The OS–197 top lid was installed and secured, and helium was leak checked. The cask was lifted, rotated to a horizontal position, and loaded onto the transport trailer. Following survey and decontamination, it was moved out of the TAN–607 hot shop and driven by truck the 30 km to the INTEC.

*7.2.8.2. Dry shielded canister lid closure weld*

The final lid closure weld was performed using gas tungsten arc welding process using a semiautomatic rotary weld unit. This process uses a non-consumable tungsten electrode operating in an argon fill gas with an automatic wire feed for filler metal. The system used dual gas cooled torches mounted on a rotary track that were monitored by video cameras. All communication and power supply cabling were routed outside the cell to allow remote operation. The multi-section lid arrangement is shown in Fig. 240 (a). A photo of the welding apparatus in operation with an observer is shown in Fig. 240 (b). A video capture of the welding machine operation is shown in Fig. 240 (c). and the welding of DSC lid is shown in Fig. 240 (d).

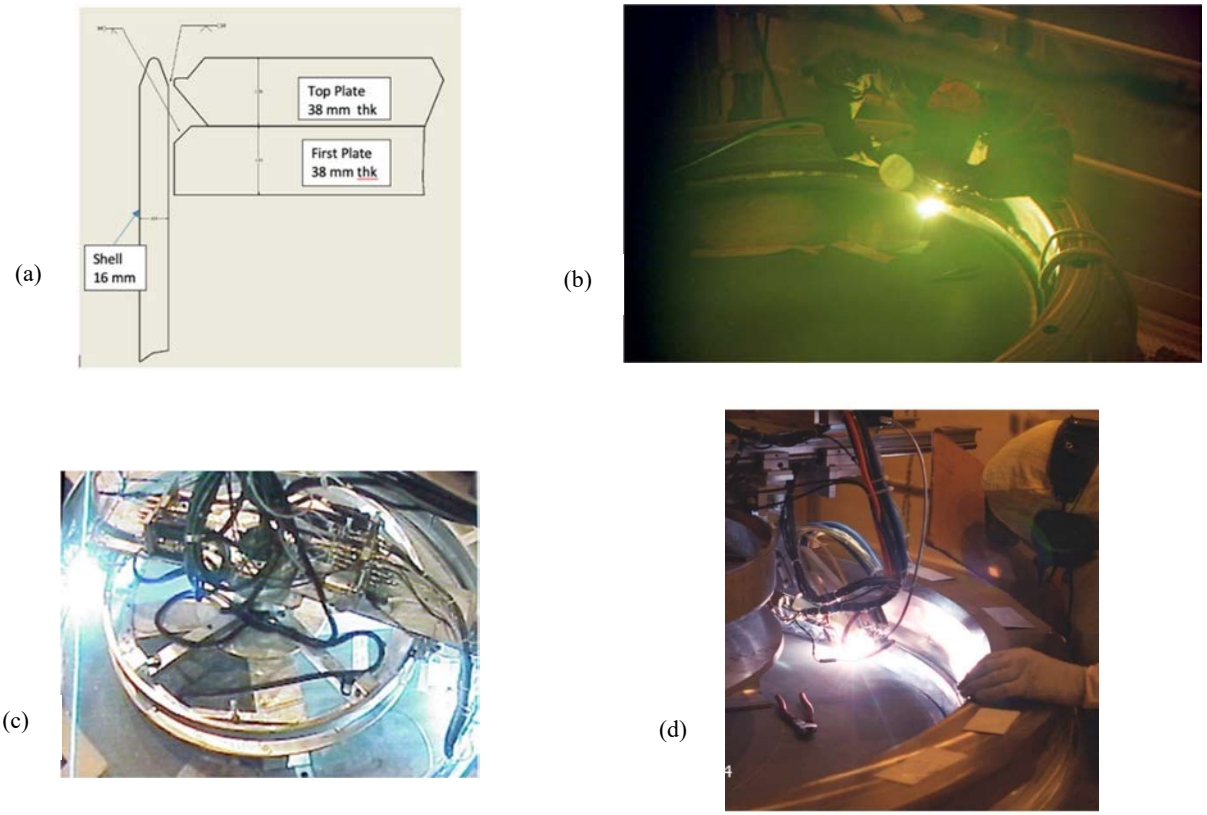


*FIG. 240.(a) Dry shielded canister lid closure weld configuration (based on data from [279]). (b) Manual DSC lid welding. (c) Welding machine operation. (d) Semiautomatic welding of DSC lid (courtesy of INL).*

*7.2.8.3. OS-197 onsite transport cask*

Because the fuel loaded DSC is only radiologically shielded on the end that is exposed following loading into the HSM, shielding is required during transport; this was provided by the OS–197 cask. The design was intended to be adequate to meet US Department of Transportation (US DoT) radiological dose rate values but was not expected to meet transport accident criteria at highway speed because it lacks impact limiters. In the case of the TMI–2 canisters, the dose rate limits were not likely to be challenged because the debris were from a low burnup core. Onsite transport speed was limited to less than 30 km/h to assure that an impact accident would not result in a radiological release.

As in several other respects, the TMI–2 installation was unique in that the DSC had to be placed into the HSM in a precise manner to allow the vent port on the DSC to align with the cutout in the HSM to allow access. Because the debris canisters were not uniformly loaded, it was discovered that certain DSCs tended to rotate out of alignment with the vent port during transport and insertion. Following this discovery, efforts were made to load heavier canisters in positions that would be at the bottom when the DSC was rotated to the horizontal position. The specifications of the OS–197 are shown in TTable 54. Figure 241 (a) shows photograph of the cask in transit between TAN and INTEC and Fig. 242 (b) OS–197 aligned to the HSM for DSC installation. Installation required the HSMs to be exposed on both ends, one for insertion of the DSC, and the other for access to the canister vent.

TABLE 54. OS-197 ONSITE TRANSPORT CASK DESIGN CRITERIA [278]

| | | |
|---|---|---|
| OS-197 Cask | Payload capacity | 37,000 kg |
| | Gross weight | 113,000 kg (handling)<br>109,000 kg (transport)<br>123,000 kg (transport with impact limiters) |
| | Equivalent cask drop deceleration | 75g Vertical (end) & Horizontal (side)<br>25g Oblique (corner) |

(a)

(b)

*FIG. 241. (a) OS-197 in transit between TAN and INTEC (courtesy of INL). (b) Mating OS–197 to HSM at INTEC for DSC placement (reproduced from Ref. [280] with permission courtesy of US DOE).*

### *7.2.8.4. Horizontal Storage Module*

As discussed above the TMI–2 HSM departs from the standard design in that each module has access at both ends to the DSC and to allow for loading as well as access to the vent port. The design also departs in that no convective cooling vents are included in the module due to the low decay heat of the canister contents.

As shown in Fig. 242, the vent module access panel includes the connections necessary for testing the filter, isolating the DSC headspace and headspace gas sampling. The design criteria are shown in Table 55.

TABLE 55. NUHOMS HSM DESIGN CRITERIA [276]

| | |
|---|---|
| Capacity | One DSC per HSM |
| Array Size | Two rows of 15 modules |
| HSM Size (Nominal) | |
| Length | 5.54 m |
| Height | 4.42 m |
| Width | 3.12 m |
| Surface Dose Rate | As low as reasonably achievable (ALARA) |
| Heat Rejection Capacity | 860 Watts |
| Materials of Construction | Reinforced concrete and structural steel |
| Service Life | 50 years |

The resulting ISFSI, a two row HSM configuration, is shown in Fig. 243. There are thirty HSMs, of which 29 contain loaded DSCs. The intent is to provide an additional HSM if one of the DSCs should fail, and an additional position be necessary for any repackaged contents.

Apart from the freeze thaw effects of snowmelt on the bolt pockets that hold the HSM together, no significant degradation has been identified on the structure or systems. The bolt pocket damage was remedied by use of an epoxy filler and covering with stainless steel covers.

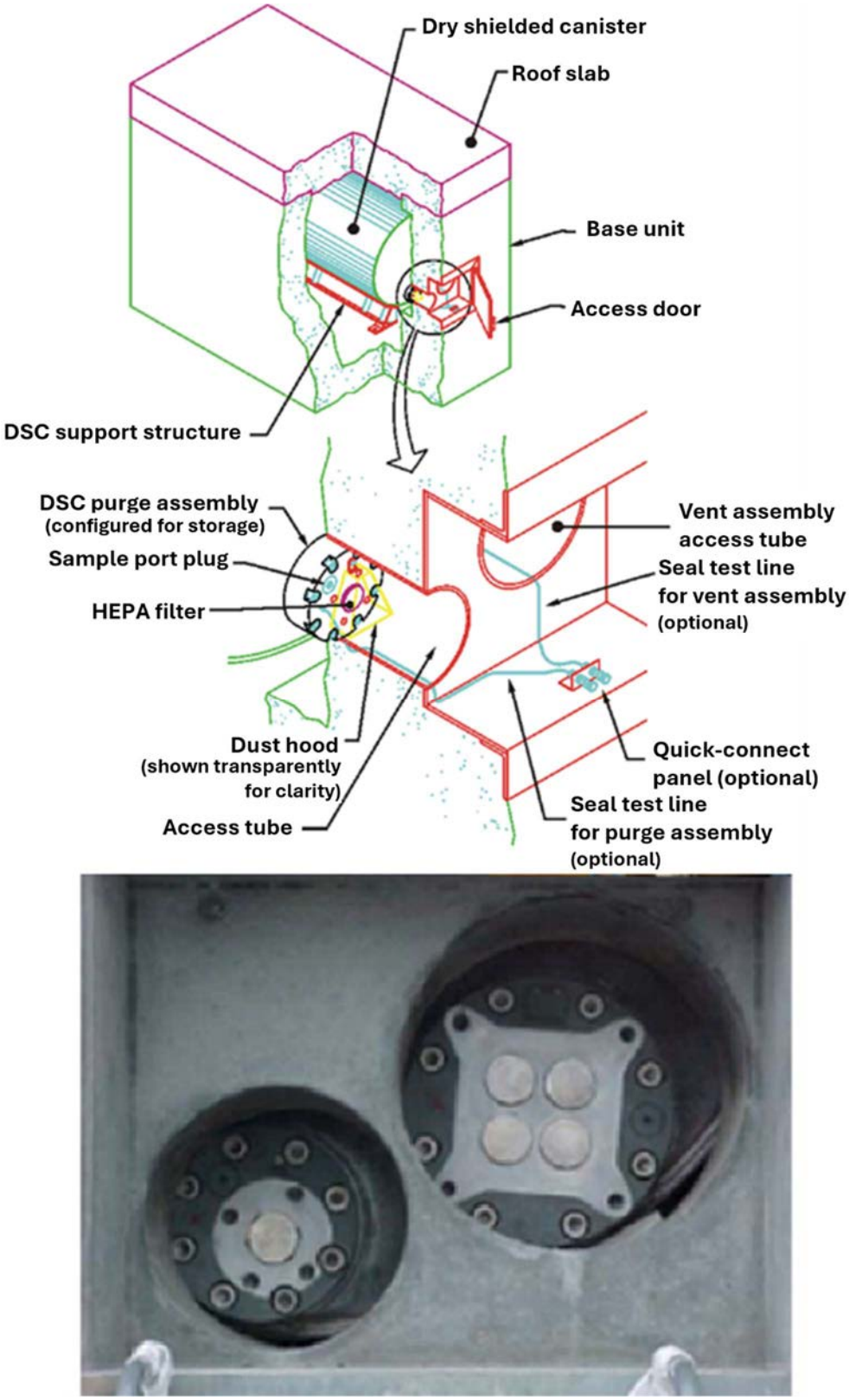


*FIG. 242. Horizontal storage module cutaway diagram (top) and photograph showing purge vent and filter port (bottom) (reproduced from Ref. [277] with permission courtesy of INL).*

*FIG. 243. CPP-1774 ISFSI with HSMs (courtesy of INL).*

## 7.3. MONITORING OF THREE MILE ISLAND FUEL DEBRIS MATERIALS IN DRY STORAGE

In accordance with the safety analysis requirements, a portion of the stored DSCs undergoes headspace gas sampling annually. Due to uncertainty about the effectiveness of the drying process, the canisters were sampled monthly during the first year following loading. Although the canisters are vented, no radiological contamination and no detected release of airborne radiation has been detected by direct smears or air sampling. Gas sampling during the first year resulted in indication of as much as 3% hydrogen, but subsequent samples have stabilized in the range of approximately 0.4 vol.%. Given the SAR assumptions about potential for radiolysis of residual water in the lightweight concrete (LICON), there is no indication that the hydrogen generation rates approach the predicted values (see Fig. 244).

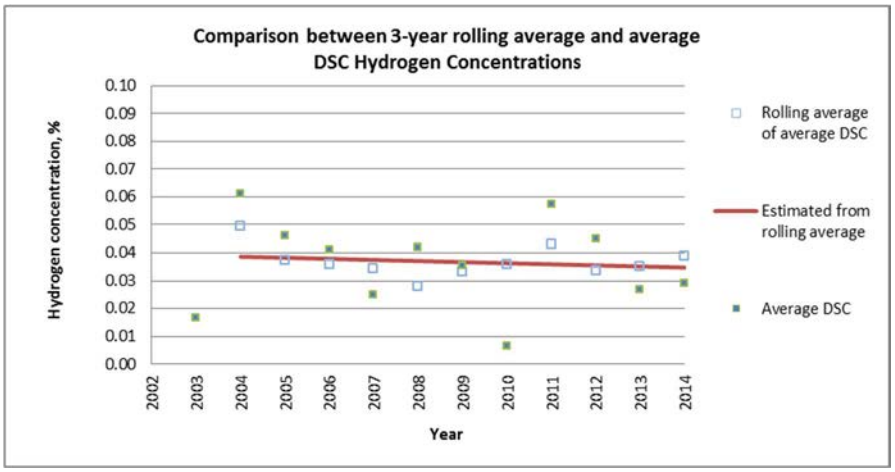


*FIG. 244. Annual DSC hydrogen concentrations, 2003–2014 (courtesy of INL).*

Safety analysis report values were based on hydrogen transport modelled in stored configuration. The analysis assumed hydrogen generation rates included 7 $cm^3$/h due to radiolysis in each canister plus 33 $cm^3$/h due to corrosion in DSC, for a total of 40 $cm^3$/h. Release of the produced hydrogen was assumed to be driven by diffusion, seasonal and diurnal temperature and pressure fluctuations, and wind fluctuations. The resulting analysis concluded that hydrogen concentrations would reach 1.5 vol.% in the DSC, and individual canisters would be as high as 4.5%.

In the interest of time, hydrogen gas concentrations were determined using a flammable gas detection instrument of the type used in industrial hygiene personnel access monitoring. During the first few years of operation, monitoring was performed using a Cannonball unit that was not temperature compensated. This type of instrument measures the temperature change in a catalyst bed as an indication of the presence of flammable gas. For precise measurements, calibration needs to be performed at the same temperature as the measured environment. As a means of getting more consistent results, in recent years, a photo ionization detector system has been implemented. At the present time, canisters are only monitored annually, rather than monthly.

Part of the 2019 US NRC relicensing involved development of a comprehensive ageing management plan. Per the ageing management plan, the HSMs will be monitored for concrete cracking and potential for absorption of water that would lead to cracking in freeze thaw cycles. This monitoring includes use of water absorption testing using a Rilem tube. Other proposed inspections involve insertion of miniature borescope cameras into the accessible openings to view the external surface of the DSC and the structural support rail that supports the DSC. Figure 245 shows examples of HSM cracking.

*FIG. 245. Examples of cracking of HSM concrete (reproduced from Ref. [281] with permission courtesy of US DOE).*

The storage facility safety basis includes full analysis of seismic, tornado, flood, and canister leakage scenarios. Due to its robust construction and the arid remote location, no significant release is expected that would affect offsite population.

## 7.4. STRATEGIES FOR FUEL DEBRIS DISPOSITION

This Section describes a couple of approaches for the disposition of fuel debris.

### 7.4.1. Disposal strategy for Three Mile Island fuel debris materials

In accordance with the terms of the 1995 agreement to settle a lawsuit between the state of Idaho and the US DOE (sometimes known as either the Settlement or Batt Agreement), the TMI–2 debris are to be removed from Idaho by 1 Jan. 2035. To achieve this goal, it will be necessary to specify a package that will be compatible with the proposed disposal approaches. The most developed of the disposal plans was the Yucca Mountain project design, which was suspended in 2008 for 8 years and has not yet been authorized for full construction.

The likely approach for disposal is that the TMI–2 canisters would be removed from the DSC and placed into a unit that has been identified as the US DOE standardized canister. This component would function as an overpack and be either selectively placed in a large disposal canister along with high level waste glass canisters or loaded as a group into specific disposal canisters.

The standardized canister was developed with the intent of accommodating a variety of fuels and debris in a consistent package that was qualified as a component of the overall disposal package. It was designed to be constructed of type 304 stainless steel, available in 457 or 610 mm diameters in either 3.048 or 4.572 m lengths. Packaging of the TMI–2 debris canisters is assumed to use the 610 mm diameter by 4.572 m long variant.

Once disposal design commitments have been made, it will be necessary to have a facility that is capable of receiving the retrieved DSCs. Once received, the DSCs would be cut open, and the TMI−2 canisters removed and placed into the standardized canisters. Independent of the availability of the final repository, the settlement agreement mandates that the fuel be removed from Idaho.

### 7.4.2. Reprocessing of fuel in post irradiation examination cans at Sellafield

There has been a limited amount of reprocessing of ‘debris’ (i.e., not whole fuel assemblies) at Sellafield (UK).

#### *7.4.2.1. Packaging the fuel*

Fuel pins arising from AGR elements and WAGR elements, dismantled for the purposes of PIE, have been stored in PIE cans. This includes intact fuel pins, cut pins and small fragments of fuel resulting from destructive PIE.

Cut pins and fuel fragments were placed in solid walled PIE cans with welded lids (Fig. 246 (a)). Intact pins were placed in slotted cans with loose fitting lids (Fig. 246 (b)). The PIE cans reprocessed to date have all been slotted cans containing full length fuel pins. Welded cans have not been offered for reprocessing due to uncertainty over non-fuel items included with fuel debris, such as sample mounts and other materials associated with PIE operations that may be incompatible with reprocessing operations.

The PIE cans are small (nominally 13 cm in diameter and 0.5 m or 1m in length depending on pin length) compared with a typical fuel assembly (3–4 m length) so the cans are packed in a stack of three within a sheath (Fig. 247) in order to provide a package of suitable dimensions for handling and feeding to shear (to ensure firm gagging) and of suitable fuel mass to ensure an appropriate fuel batch size in the dissolver for feeding forward to the chemical separation area of plant.

Post irradiation examination reprocessing campaigns were carried out in the early 1970s (WAGR) and more recently in 2016 (WAGR and CAGR). These campaigns were all completed successfully with some minor issues overcome as described in the following sections.

(a)

(b)

*FIG. 246. (a) Solid walled (welded) can for cut fuel pins and debris. (b) Slotted can for intact fuel pins (courtesy of NDA).*

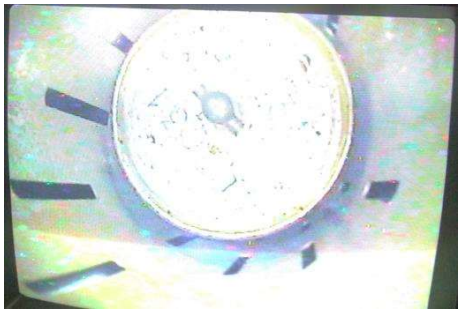

*FIG. 247. Post irradiation examination can inside sheath (courtesy of NDA).*

*7.4.2.2. 1970s campaigns (years 1969, 1971, 1973) conducted in the first generation reprocessing plant*

(a) Handling the PIE cans

The early reprocessing campaigns were conducted with each PIE can fed individually to shear (before the introduction of the sheath to batch them). For example, one campaign included 277 cans (110 × 1 m, 167 × 0.5 m). This impacted on the feed rate which was much lower than for LWR FAs reprocessed in the following campaign.

(b) Shear blade wear

Windscale advanced gas-cooled reactor fuel within the PIE cans caused reasonably rapid shear blade wear leading to incomplete shearing of the cans. In some cases, long lengths of can material (equivalent to several cut lengths) were deposited in the dissolver basket, however, the fuel pins were fully sheared and the fuel dissolved successfully. The long lengths of can material caused some difficulty in emptying the basket.

Removal of the shear pack for refurbishment after the campaign revealed damage due to trapping of can material between the blade carrier and the back plate. The shear pack refurbishment was carried out before proceeding with subsequent LWR fuel reprocessing.

(c) Hulls monitor results

A hulls monitor is used to determine the fuel content retained within the sheared fuel cladding after dissolution. Some difficulty was encountered with interpreting the hulls measurement results for WAGR fuel due to the wide range in irradiation in some batches (1000–18 000 GWd/tU and 1−6 years cooling time). This led to a wide variation in Ce/U ratio (by a factor of 10) which in turn led to difficulty in predicting the amount of uranium retained with the fuel cladding and hence whether to releach or tip the cladding into the silo. The uncertainty associated with the hulls monitor results was supported by subsequent accountancy results yielding figures that were 25% lower than the hulls monitor value.

*7.4.2.3. 2016 Campaign conducted in Thermal Oxide Reprocessing Plant (THORP)*

(a) Handling the PIE cans

After the introduction of multi-element bottles (MEB) in the early 1980s, PIE cans were stored in sheaths designed to contain 3 cans each, with each sheath stored in one channel of a 14 channel MEB. This allowed delivery of the fuel for reprocessing in batches of 42 cans per MEB for maximum efficiency of feeding to shear compared with single can feeding in the early campaigns. Each sheath was handled from the MEB and deposited on the elevator for raising to the shear cave in a similar way to a standard fuel assembly.

(b) Pre-shear monitoring of the fuel

The feed pond fuel monitor (FPFM) is designed to determine the fuel enrichment of each fuel item to be sheared. For PIE cans the FPFM was bypassed due to the variability of pin configurations within the PIE cans which would have led to inaccurate enrichment measurements, based on prior modelling and assessment work. Instead, the FPFM software used the customer declared data for the value of the fuel enrichment in lieu of a measurement. The chemical plants information computer treated the sheath as if it was one long can with all the mass related to the top PIE can within the sheath. This bypass was considered acceptable because the fuel was very long cooled (~40 years) and well within the prescribed initial enrichment limit.

(c) Gadolinium poisoning of the dissolver acid

For normal fuel reprocessing operations, it is standard practice to take account of burnup credit which allows gadolinium poisoning to be tailored to the fuel irradiation history (this leads to less vitrified waste). For fuel in PIE cans the gadolinium poisoning was increased to treat the fuel as unirradiated, representing the worst case scenario. This was considered to have minimal impact on vitrified waste production due to the small amount of PIE fuel being reprocessed.

(d) Blending with fuel of lower enrichment

The PIE fuel had higher residual $^{235}U$ enrichment than was acceptable for feeding the resultant dissolver liquor directly into the chemical separation process therefore blending with fuel of lower residual enrichment was required. This was achieved by retaining product liquor in the buffer storage tanks (BST) from the preceding campaign of lower residual enrichment fuel and topping up with dissolver liquor from the higher residual enrichment PIE fuel. Isolations were placed on the transfer routes out of the BSTs prior to the start of shearing and only removed when the BST sample results had been confirmed and independently verified as being compliant with the chemical separation safety case limit for residual enrichment.

It was also important to adhere to the prescribed feed schedule order to ensure compliance with the target enrichment for each dissolver batch.

(e) Double dipping

Due to the large amount of metal compared to the low fissile inventory in each sheath, ‘double dipping’ operations were implemented in the dissolvers to ensure an appropriate uranium concentration for feeding forward to the chemical separation process. This involved shearing a predetermined number of sheaths per batch into the dissolver, leaching this batch and removing the hulls while retaining the dissolver liquor. A second batch of sheaths was then sheared into a second empty basket. In this way, the uranium concentration was double what it would have been if the dissolver liquor had been fed forward after shearing the first batch of PIE fuel (normal practice for ‘standard’ fuel).

(f) Shear cut length

Post irradiation examination cans reprocessed in 2016 were all of nominal 1 m length but some contained the shorter length pins (0.5 m) stacked within the can (Fig. 248). This gave significant scope for movement of the shorter pins within the can and uncertainty over the pin end locations. For this reason, shear cut lengths were minimised to 25 mm in order to maximise shearing of the shorter pins – this is half the normal cut length employed for standard AGR fuel pins. This shorter cut length resulted in higher than usual volumes of fine material being generated in the decanters which created a degree of restriction when feeding forward to the waste container (which also contained the hulls). The ‘fines’ accumulation issue was successfully managed by additional flushing with acid to clear the decanter pipework.


*FIG. 248. Slotted PIE can with stacked short fuel pins (courtesy of NDA).*

(g) Handling issues

A mechanical issue was encountered during removal of some sheaths from MEBs due to slight deformation of the sheaths from their circular cross section. They presented an oval cross section which the grab could not grapple properly. Similarly, the cohort of sheaths was found to include two different design lengths (varying by 30 cm) which presented an issue when loading on the elevator to the shear cave. In both cases the issues were resolved by design input to effect modifications to the grab head and mast length which allowed the sheaths to be handled and fed forward as required.

### 7.4.3. Reprocessing of damaged fuel assemblies at Sellafield

Over the years, Sellafield has received, by agreement, a number of damaged and/or non-standard FAs for reprocessing. These range from groups of assemblies with components that cannot be reprocessed

to individual assemblies that have been reconstituted or had structural damage and have required remediation prior to reprocessing. Some examples are given below.

*7.4.3.1. Pressurized water reactor 'skeleton' assembly with low number of fuel pins*

This assembly was made up from an accumulation of fuel pins extracted from a number of experimental assemblies and it contained less than half the standard number of fuel pins for an assembly of its type (Fig. 249). The concern was that having so many vacant fuel pin positions it may not be gagged properly during shearing and potentially result in long pieces of fuel pin being dragged into the dissolver. To address this the assembly was positioned early in the campaign before the shear blade suffered any wear and tear and additionally was positioned first in the dissolver batch so that any long pieces of pin would have the greatest time in acid to ensure complete dissolution. The assembly was successfully handled and reprocessed without issue.

*FIG. 249. Pressurized water reactor skeleton assembly view on top nozzle (courtesy of NDA).*

*7.4.3.2. Pressurized water reactor assemblies with broken fuel pins*

A small number of PWR assemblies were received with some broken pins protruding beyond the standard envelope (examples are shown in Fig. 250); these were remediated by placing in a sheath. Each assembly was removed from the MEB in which it was stored by drawing it through a 'catch tray' to capture any loose pieces then loading it into a sheath in an adjacent channel in the MEB. The sheaths had fold over tabs at the top to secure them in position over the assembly.

Issues associated with shearing sheathed assemblies are additional blade wear and more hulls debris being generated than for standard assemblies. To address these issues the assemblies were positioned late in the campaign in batches with a reduced number of assemblies. Each of the sheathed assemblies was positioned as the middle assembly in the batch to allow better assessment of the residual fissile material in the hulls from hulls monitoring.

*7.4.3.3. PWR assemblies with thimble plugs and burnable poison units*

Some types of PWR assembly were received with thimble plugs and burnable poison units (suspended in interstitial positions between the fuel rods on a 'spider' like assembly in the FA top, Fig. 251). These items were incompatible with the THORP process and specialist tools were developed to remove them prior to reprocessing.

In addition, two particular assemblies were received each with a single broken burnable poison rod jammed in the assembly. One of the assemblies also had a marker vane positioned beside the stuck poison rod. In each case the jammed rods (and the vane marker) needed to be removed before reprocessing and this was achieved by using a specially developed tool.

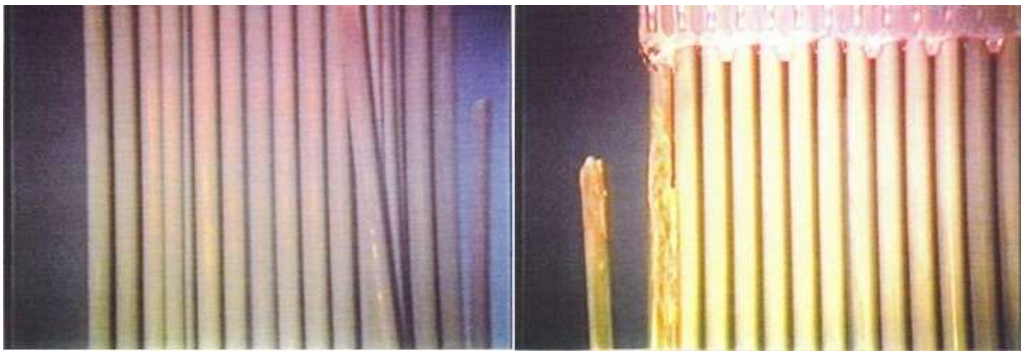

*FIG. 250. PWR assemblies with broken pins visible and broken pin protruding from face of assembly (courtesy of NDA).*

*FIG. 251. PWR Burnable poison unit removed from fuel (courtesy of NDA).*

*7.4.3.4. Pressurized water reactor assemblies with replacement top nozzle*

A number of assemblies were received following PIE which had involved removal of the top or bottom nozzle, removal of a number of pins then replacement of the removed nozzle. To date these have been handled and reprocessed without issue. An example is given as follows:

One PWR assembly had been subjected to PIE which involved removal of the top nozzle and seven fuel pins. The incomplete assembly was then reconstituted using a new top plate with an integral tie-rod running the full length of the FA (Fig. 252). The new top plate/tie rod unit was designed so that the reconstituted assembly would have the same geometry as the original assembly. As these particular FAs were designed with lifting features on both the top and bottom nozzles the replacement top nozzle was made to a simpler design without a lifting feature, instead the assembly was turned around and placed upside down in the MEB channel to enable use of the bottom nozzle lifting feature. Taking this into account the FA was identified as fit for reprocessing with just the requirement for a new specific single use cutting pattern to accommodate the modified top nozzle when processed through shear.

This assembly was successfully handled and reprocessed as part of a campaign of standard assemblies.

A further example is of a PWR assembly that was part of a standard reprocessing campaign but had previously been the subject of PIE in which the top nozzle had been removed and a replacement fitted. It was found that the internal fittings of the replacement top nozzle interfered with the grab legs in Feed Pond and could not be grappled properly. In order to process this fuel at a later date an extension piece to the existing top nozzle was designed to fit over it to provide a lifting feature compatible with the fuel grab and tools to allow it to be fitted in situ. The extension piece results in an overall increase in the FA length thus reducing the clearance for subsequent handling operations therefore additional control supervision/ camera surveillance is required as a precaution during removal of this fuel from the MEB and transfer to shear (this assembly was subsequently successfully reprocessed).

*FIG. 252. View on inverted PWR assembly in MEB channel (replacement top nozzle) (courtesy of NDA).*

*7.4.3.5. Boiling water reactor repaired assemblies*

In a small number of cases BWR assemblies were received following a drop at reactor. One example is an assembly that was dropped at reactor and repaired before packaging for transport. Displaced fuel pins were sprung back into position, modified new top and bottom plates were fitted and the broken tie-rods were replaced with solid bars for strength. The repaired assembly was then sheathed to provide further support. A special canister was made to fit the central position of a modified MEB for transport of this assembly to Sellafield to prevent any movement of it during shipment. The sheathed assembly was successfully reprocessed in a campaign with other standard BWR assemblies from the same reactor. The only variation to standard procedure for reprocessing this assembly was to bypass the FPFM prior to shearing to avoid rotating it and thus prevent imposing additional mechanical stress on it. A further example is of an assembly which was dropped at reactor then wired up (Fig. 253) and transported to Sellafield. Four stainless steel wires were attached to a suspending ring under the bottom nozzle to support the fuel assembly weight. These wires were also fixed to a newly fitted top nozzle by nuts and bolts. With this arrangement the fuel assembly could be handled normally. A sheath was designed at Sellafield to fit over the assembly with holes at the top and base through which cutters could be applied to cut away the wires prior to reprocessing if required.

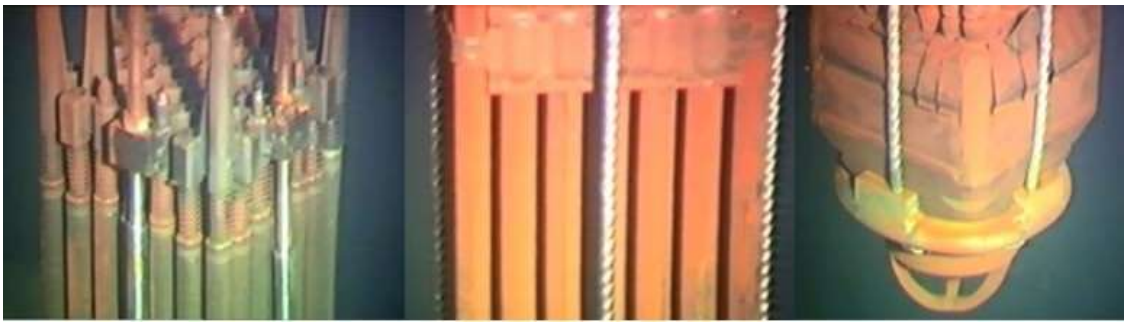

*FIG. 253. Boiling water reactor wired assembly; top nozzle fittings, wires visible on three faces of assembly and base suspending ring (courtesy of NDA).*

*7.4.3.6. Boiling water reactor assemblies in capsules*

Some failed BWR assemblies (leaking) were packaged into capsules at reactor before receipt at Sellafield. The assemblies required to be removed from the capsules prior to reprocessing. On removal from the capsules the assemblies were confirmed to be structurally sound and of standard construction and were reprocessed successfully.

*7.4.3.7. Boiling water reactor assemblies with swivel tops*

Two BWR assemblies that were part of a standard BWR reprocessing campaign had been fitted with non-standard lifting features described as ‘swivel tops’. This meant that the normally fixed ‘goal post’ lifting feature had swivel features at the join with the top nozzle such that it was not firmly fixed in the upright position but could potentially rotate whilst trying to engage the fuel grab. Although they were handled successfully during rebottling into an MEB, the grab design used for fuel removal in a different plant was of a different design and could not grapple them properly. A clamping device was subsequently fitted to fix the position of the lifting feature and the two assemblies were successfully handled and sheared in a later reprocessing campaign with just the requirement for a modified cutting pattern to accommodate the modified top nozzle when processed through shear.

*7.4.3.8. Steam generating heavy water reactor assemblies with damaged basal shrouds or kinked pins*

A small number of assemblies from the prototype steam generating heavy water reactor (SGHWR) were found to have damaged or missing basal shrouds (non-fuel bearing) which presented both a shortened overall assembly length and a potential snagging issue for feeding to shear (Fig. 254). A further two SGHWR assemblies were each found to have a kinked fuel pin (or sparge tube) protruding outside the cross-sectional envelope of the assembly which also presented a potential snagging issue for feeding to shear. A sheath was designed to contain these assemblies to present a uniform package for shearing purposes and to prevent snagging. Figure 255 shows the sheath and a kinked pin assembly being loaded into the sheath with the protruding pin orientated to the corner. All of these damaged assemblies were successfully reprocessed in the sheaths. This sheath design was also used with additional inserts to batch smaller size PHWR assemblies for feeding to shear as described in Section 4.

*FIG. 254. Steam generating heavy water reactor assemblies with twisted or missing basal shrouds (courtesy of NDA).*

*FIG. 255. Sheath designed to contain damaged SGHWR assemblies to facilitate shearing. Kinked pin orientated to corner of sheath (courtesy of NDA).*

### 7.4.4. Long term storage of fast breeder reactor fuel in the United Kingdom

The UK is home to several demonstration reactors in various stages of decommissioning, two of which were fast breeder reactors situated in the north of Scotland at Dounreay. The Dounreay fast reactor was a liquid sodium and potassium cooled experimental fast reactor which operated between 1960–1977. The Prototype fast reactor was operational slightly later than this, between 1975–1994, and had a sodium coolant. Each reactor irradiated driver fuel subassemblies, breeder subassemblies and experimental subassemblies as part of extensive research programmes.

The initial intent in the 1980s was to reprocess the fuel in the UK, however Dounreay reprocessing operations ceased before all the fuel could be processed. The majority of the fuel was initially stored in sealed containers in water filled cooling ponds, however all of it has since been removed and the inventory remains in dry storage at Dounreay. A small proportion of the remaining fuel is suitable for reprocessing through the Magnox reprocessing facility at Sellafield and will be processed through this route until the facility closes, however there will be inventory remaining that cannot be reprocessed and requires ongoing storage. In addition, there is a small amount of other irradiated fuel from commercial contracts which requires interim storage.

A wide range of experimental fuels were irradiated in these reactors under varying conditions, resulting in an inventory of spent fast breeder reactor fuel of various sizes and post–irradiation compositions. Fast breeder fuel is novel compared to other fuel types stored in the UK as it is irradiated to much greater levels in the reactor, subjected to higher operating temperatures and can have much higher enrichment of fissile material. The fast breeder fuel inventory consists of:

— Irradiated uranium oxide;
— Irradiated mixed oxide fuel;
— Irradiated metallic uranic fuel;
— Irradiated carbide fuel.

The majority of fuel has intact stainless steel cladding and a case may be possible for interim storage at Sellafield in an existing pond facility. Some of the fuel has however been cropped or is damaged, requiring further investigation for a transport and storage solution to be identified (see Fig. 256).

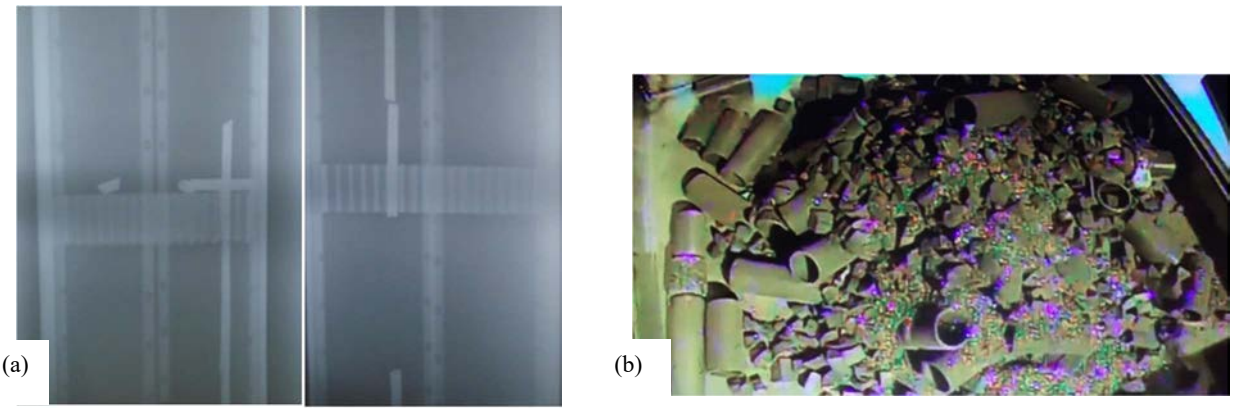


*FIG. 256. (a) Image of failed oxide pins within a Prototype fast reactor subassembly. (b) Image of contents of fuel containers showing fuel debris (courtesy of NDA).*

The UK has enacted a national programme to transfer the remaining fast breeder reactor fuel from Dounreay to the Sellafield site in England. The driver for this movement of fuel is to enable progression of the Dounreay site to interim end state by 2032. The aims of the programme are to:

(a) Remove irradiated fast breeder reactor fuel inventory from Dounreay;
(b) Consolidate irradiated fuel at Sellafield in line with the NDA mission;
(c) Maximise use of existing facilities at Sellafield.

The programme will consolidate fuel at Sellafield for safe and secure storage until approximately 2075 when a geological disposal facility (GDF) will be available in the UK for disposal of the fuel.

The reference case for these irradiated fuels is for it to be consolidated, inspected and packaged in new purpose designed stainless steel Irradiated Fuel Containers for transport to Sellafield. The multi-year collaborative programme has a number of different elements:

— Review the irradiated fuels inventory;
— Design irradiated fuel storage canisters;
— Develop and licence transport packages;
— Develop transport safety cases;
— Design and install packing and flask export facilities at Dounreay;
— Assess and deliver storage solutions at Sellafield e.g., storage in existing facilities, pond storage, dry cask storage;
— Investigate interim storage behaviour of fast breeder fuel in dry storage systems;
— Develop condition monitoring and inspection requirements;
— Develop safety cases for interim storage (pre–GDF).

Traceability of some of the fuel adds extra challenges to the transport and storage case. A number of fuel items are known to have no associated pre-irradiation data and reactor operating conditions are unfortunately not known. A large project is underway at Dounreay to look at historical records including commercial contracts, transport records and PIE records to determine the original manufacturing specifications and conditions it was subjected to within reactor. A programme of work is underway to identify ways to resolve challenges surrounding a lack of historical data. This may require technologies for sampling to determine fissile content. Detailed requirements for acceptance of fuel at Sellafield will be developed as part of this programme.

Due to the differing physical and radiological properties of the fuel, different transport and/or storage solutions will be required for different fuels within the scope of the programme. This is expected to include both wet and dry storage technologies.

# 8. SEVERELY DAMAGED FUEL MATERIALS ACCOUNTANCY AND SAFEGUARDS

While we may simply associate materials accountancy as an obligation under safeguarding protocols to demonstrate that material is not being diverted for non–peaceful applications, materials accountancy information is used for a variety of operational purposes. The information is essential to support operational safety analysis, ensuring sub criticality, and a range of operational limits are not breached; examples include, heat loading, shielding, process requirements.

In Section 3 the subject of characterization, i.e. knowing what we have and how much, was explored. One of the purposes of characterization is to support the design of equipment for material recovery, but also how it will be packaged and eventually managed, either by reprocessing or disposal. If we only have part of the information, then defence in depth leads to over design. Section 7 highlights the issue whereby TMI–2 canister design for fuel debris incorporated neutron absorbers to prevent a potential criticality event.

From a decommissioning aspect of declaring an end state, hazard reduction and down grading security arrangements then the ability to track how much and what is where goes hand in hand with demonstrating that nuclear materials, especially fissile, have been removed from the site.

The following Section takes a brief look at materials accountancy/safeguards with respect to the accidents at TMI–2, ChNPP, and Paks NPP, and then goes on to look at the evolving situation at 1F.

## 8.1. POST ACCIDENT MATERIALS ACCOUNTANCY

Post accident materials accountancy may be considered from two viewpoints. Where the fuel is no longer in its original format but is still present as part fuel assemblies, pins, part pins, pellets or unmodified debris that is still within the normal boundaries of the accountancy regime (i.e. in as designed reactor core, storage module, pool etc.) then existing approaches used for either post irradiation or post storage examination materials accountancy can be adopted. This may require the existing accountancy system to be modified to enable additional information to be added, such as recording material format, number of pins or pieces etc.

Where the fuel has been modified through melting and interaction with other materials and/or has been displaced beyond the normal boundaries of material accountancy then bespoke approaches are likely to be required for both internal accountancy and independent safeguards.

### 8.1.1. Three Mile Island Unit 2

In the case of TMI–2, material accountancy was based on difference. That is a post defuelling survey of the TMI–2 core was undertaken to establish the inventory of special nuclear material (SNM) remaining. Based on the estimated amount of SNM at the time of the accident the delta of the remaining was used as the declared inventory in canisters stored at Idaho.

As such there was no special arrangements, in terms of materials accountancy, put in place during fuel debris recovery operations. The combination of debris analysis (Section 3) can fill procedures (Section 6.1), operator logs (Fig. 191) and weighing filled cans, however, provides a materials account. Can fill procedures segregated the recovered material into three categories: FAs of known lengths; Debris; Structural materials which did not contain SNM.

Refinements of this data, predictive models and assumptions has led to improvements of this account with time [282].

At the time of the accident TMI–2 did not come under international safeguards protocols but was subject to national arrangements. An exemption from the national arrangements, which requires material to be accounted to the nearest gram, was given [282].

### 8.1.2. Chornobyl nuclear power plant

The techniques employed at ChNPP (see Section 6.2) to locate fissile material, primarily to support safety analysis, were visual inspection; temperature and heat flux monitoring; gamma scanning ($^{137}$Cs). The adopted methods had flaws and therefore attempts to undertake a mass balance based on the known inventory and irradiation history of the material before the accident failed. The difficulties encountered related to locating material, for example some material ejected from the reactor had been buried before the inspection. Global thermal measurements were subject to interference from convected heat from the remains of the damaged core and there were large uncertainties in $^{137}$Cs measurements mass balance as not all material was included in the analysis.

Since 1986 ChNPP has been brought under international safeguards. As the location of all the material cannot be verified, the safeguards approach has been based upon containment and surveillance [282].

### 8.1.3. Paks nuclear power plant Unit 2

Unlike TMI–2 and ChNPP, Paks-2 was under international safeguards arrangements at the time of the cleaning accident. Although an entirely different level of challenge compared to reactor core LOCA in terms of the quantity of fuel and materials involved, it still resulted in severe fuel damage but was confined to the cleaning tank. As recovered material was packaged and stored initially in AR pool and then exported via the normal fuel route then existing international safeguards models were not impacted, however, verification of the recovered/packaged material was required.

Materials accountancy was provided through the procedures adopted as part of the recovery operations in combination with bespoke tooling that included spring balances to weigh the recovered material. A mass balance was performed through undertaking burnup measurements on the canisters and then modelling the amount of material which should be present, this was compared with the weighed amount. All recovery operations were videoed for safeguarding purposes.

## 8.2. FUKUSHIMA DAIICHI SAFEGUARDS AND TECHNICAL CHALLENGES

Unlike TMI–2 and ChNPP the 1F site was subject to international safeguards protocols at the time of the accident. The severity of the accident led to restrictions in the months after the accident in accessing the site/damaged reactors and storage facilities due to a combination of radiological and routine safety issues, safeguards inspections were suspended for around 6 months.

As routine safeguards inspection had to be suspended this has led to a requirement for a reverification of the nuclear materials inventory at 1F [283]. The ease of reverification has been placed on a sliding scale where fuel stored in units/facilities which were either not impacted or only partly impacted by the earthquake and accompanying tsunami, i.e. Units 5, 6, the cask custody building and the centralized spent fuel facility, reverification has been relatively straight forward to material in the melted reactor cores of Units 1 to 3 in which it is difficult to do so and will take many years to be resolved.

The other safeguards concern after the accident related to the fuel routes at reactors Units 1, 3 and 4 which were left badly damaged and in principle vulnerable to material being pulled directly from storage and bypassing installed safeguards surveillance systems. The latter has been resolved by the

installation of a remote surveillance and radiation monitoring systems on the hillside overlooking the reactors, namely XCAM surveillance cameras and the IAEA designed open air spent fuel monitor (OASM). The XCAM is a next generation replacement for the standard DCM–14 camera system (which are currently deployed in fuel routes) and the OASM is made up of two neutron slab detectors and two LaBr gamma detectors.

Further information on IAEA Safeguards protocols, requirements and the measures that have been put in place following the accident at 1F are provided in Ref. [283].

### 8.2.1. Transfer of fuel from the at reactor pools to the centralized spent fuel facility

Fuel removal from the AR pools at Units 3 and 4 has now been completed. In both cases fuel removal involved the building of a new fuel route, Unit 3 fuel removal was completed by remote operations due to the high radiation levels. As existing safeguards surveillance systems were by passed then the IAEA installed new XCAM surveillance cameras on the new fuel routes to monitor fuel casks movements. XCAMs were also installed at the receiving facility (CSFS).

Several challenges were encountered when reverifying fuel recovered primarily from Unit 3, these included:

- Normal verification activities, based on Cherenkov light, on some FAs was impaired due deformation, rubble and deposits;
  - A two stage approach was adopted to verify these FAs. A next generation Cherenkov viewing device (XCVD[17]) was used to screen FAs where Cherenkov light was obstructed. The screened FAs were then verified using an IRAT detector[18].
- The serial number of some fresh FAs was obscured by fixed deposits, preventing identification even when using an underwater camera, the issue was subsequently resolved by TEPCO;
  - A fresh fuel attribute test (FFAT) detector, a new instrument that detects the presence of $^{235}U$ was used to confirm FA declared data. The FFAT is a modified IRAT detector.

### 8.2.2. Fuel debris retrieval Unit 2

As outlined in Section 6.3.5. it is planned to retrieve a 1 g sample of debris from Unit 2. If successful a staged approach to increase the amount recovered will be taken. The robotic arm can remove up to a kg of material. As the operations will be undertaken remotely (see Fig. 221), due to the radiation environment, it will not be possible to undertake independent physical verifications until the material has reached its destination.

This presents a few safeguarding challenges as the removal scheme and the material to be removed do not fit within a standard IAEA safeguards reactor model. The amount/composition of the material at the point of removal is an unknown, neither will the packages be weighed, and therefore cannot be declared. The material being removed is not recognized as an IAEA Safeguards material form.

[17] Next Generation Cherenkov Viewing Device (XCVD): Hand-held high sensitivity light intensifying digital device optimized to view Cherenkov light (near ultraviolet) in a spent fuel storage pond. The XCVD can enhance images via real time digital processing (image stacking) and can record individual scans for subsequent re-analysis. The high sensitivity and image stacking enables the verification of long cool and/or low burnup spent fuels, which previously would have required underwater NDA methods.

[18] Irradiated fuel attribute tester (IRAT): CdZnTe based γ ray energy spectra detector system used for verifying fission product presence in an irradiated fuel assembly.

Through early engagement with the site operators and competent authority, it has initially been proposed to:

- Consider Unit 2 as a hybrid facility for safeguarding purposes. Reactor safeguards will be used as a basis but adapted to bring in approaches used in other types of processing facilities such as reprocessing;
- A new material form of fuel debris material (FDM) has been created in the safeguards system, covering corium and MCCIs, to support the reverification of this material;
- A materials accountancy approach like that taken in reprocessing plants between feeding fuel to shear (known) and accountancy after dissolution (known) will be adopted. In this respect the amount of fuel loaded to Unit 2 and its depletion at the time of the accident are known. Material will then be declared on receipt at the storage facility, where it can be weighed, and a ratio applied based on the known. Although there will be uncertainties in this approach it does provide a basis for materials accountancy which can be improved once canister contents are sampled/analysed.

Verifying FDM by standard NDA techniques has the potential to be problematic as behaviour of caesium (low temperature of volatility and has likely to have migrated during the accident) and its ability to mask other gamma rays will impair the ability to establish the plutonium content using standard techniques/potential to contaminate non–nuclear materials which may be present. IAEA Safeguards therefore considers that the only reliable indicator that the fuel debris contained nuclear material would be the presence of a neutron signal. It is proposed to use a combination of gamma dose rate/spectrum and neutron measurements.

# 9. KNOWLEDGE MANAGEMENT RELATED TO COORDINATED RESEARCH PROJECT

The following Section focuses on training and severely damage spent fuel samples.

## 9.1. TRAINING

One of the points highlighted at the 'International Experts Meeting on Decommissioning and Remediation after a Nuclear Accident' [284] was the importance of training:

> *"The use of full scale mock-ups for testing of tools, validation of processes and training of workers is essential".*

This Section provides further information on the training activities in support of TMI–2 clean–up and the handling/analysis of severely damage spent fuel (corium etc.).

### 9.1.1. Training for access to severely damaged facilities

This section provides an account of the training in support of the cleanup of TMI–2.

#### *9.1.1.1. Containment re-entry training*

As in a typical situation where emergency response is required, the first reentry teams that went into the TMI–2 containment building were well rehearsed in the tasks they needed to perform. The personnel involved went through 100 hours of classroom training to familiarize them with the facility details and the concerns of interest in the initial forays into the building.

Classroom training was supplemented with 50 hours of practice exercises working through Unit 1 (TMI–1), which had been shut down at the time of the accident. The personnel were taken through as many scenarios as possible to make clear the recommended responses in the event of emergency conditions.

The practical exercises at TMI–1 included being able to make egress from the building in lights out conditions. All personnel were trained to perform radiation surveying regarding air sampling, general beta gamma body fields, taking loose contamination smears and photographing general conditions. Although this radiological control process is considered routine in present day nuclear facilities, the term ALARA had only been coined three years prior to the accident, and RadCon[19] practices were less well defined.

Numerous critical audits and reviews of the TMI–2 programme led to development of a more rigorous RadCon organizational structure and RadCon programme guidelines that were issued by Institute of Nuclear Power Operations (INPO) four years later.

#### *9.1.1.2. Quick look inspection and vessel head removal*

Prior to attempting the removal of control rod drive mechanism (CRDM) leadscrews from the top of the reactor vessel to insert cameras for the quick look inspection, teams worked through the process using mock-up tools and equipment. Verification of clearances for tools and extraction of the leadscrews was done using the TMI–1 reactor. Everyone had a rehearsed role in which they had

[19] RadCon, radiological control. Measures taken to minimize the dose to workers and public.

demonstrated their ability to perform their assigned tasks safely and efficiently to minimize personnel dose.

Mock-up structures assembled for training and logistic validation included the following:

(a) Control rod drive mechanism service structure (constructed as a full–scale wooden model and using a full length CRDM) used for multiple inspection task walk throughs;
(b) Plenum head mock-up (constructed as a full size wood and plastic structure that represented the head flange area). Used to verify camera positions;
(c) Internals indexing fixture and platform mock-up (constructed as a precise dimension full scale steel cylinder) Used for lifting and positioning the indexing fixture on the vessel upper flange and testing rigging and latching devices. Also used to check out level monitoring equipment;
(d) Reactor vessel stud detensioning mock-up (constructed with full length studs and testing of techniques for loosening the reactor vessel head bolts;
(e) Auxiliary fuel handling bridge (AFHB) mock-up (used a spare crane bridge to practice disassembly and removal of the mast and trolley from the AFHB).

Each of the inspection activities was walked through by personnel using the various mock-ups to confirm their procedures. These included the camera insertion crew that put the first video cameras into the reactor vessel in the quick look programme, as well as the grab sampling team that acquired numerous kgs of loose debris for the first steps of characterization. Likewise, the group that performed the ultrasonic surveys of the core topography had gone through the necessary actions multiple times prior to deploying their equipment.

The teams that lifted and removed the RPV head had worked through the tasks thoroughly prior to detensioning the studs and rigging the head for removal.

The process of first jacking up the reactor plenum, doing video and radiological measurements and then removing it worked through their process according to the procedures and ultimately clearing it of debris and removing it.

Groups that installed the shielded work platform on the reactor upper flange had worked out the rigging and positioning requirements as well as verified platform dimensions to assure that it would fit.

Offsite teams including those developing the core boring equipment were working with full height mock-ups and surrogate material to test equipment that was intended to be able to bore through a large mass of material of unknown composition. Metals, ceramics, and agglomerated materials were tested. The equipment was tested regarding disassembly of the parts to be able to make it fit through the available doorways into the work area and then reassemble it on the reactor head platform. A full walkdown of the task had been done before bringing the equipment into the containment building.

Ultimately the process used at TMI–2 was directed to training:

- On equipment installation;
- On equipment of operations;
- On lifting and rigging operations;
- For anticipated upset condition response;
- For contingency operations.

Classroom work covered basic theory on operation of the equipment, and instruction on operation of equipment within the design limits.

Hands on training followed using the mock-ups and actual equipment as appropriate.

Further development involved coordination of a group for complex actions like lifting of large components. The group training actions were directed by lift control supervision.

Eventually the process had progressed to the stage where routine work proceeded using pre–job briefings that were able to use data and information from each day's experience to define their tasks and minimize dose. Videotape reviews were used to familiarize the workers with the area where work was to be performed and identify areas of concern including high radiation areas.

### 9.1.2. Training needs for research

The scientific experience obtained studying highly radioactive samples related to severe nuclear accidents should be transferred to future generations. Publications summarizing the results of material studies are extremely important for practical use but not completely sufficient when taking into consideration that new methods for analysis become available and the scope of the studies for any new accident. Noting that there is a lack of information concerning material studies on fuel debris samples from the accidents at Chalk River (1952) and Windscale (1957).

Because TMI–2 sample material and debris were shipped across the USA, additional training programmes were developed to familiarize and equip state, local and regional emergency response organizations, and transport crews to understand the risks and actions that could be taken in the event of a transport accident. These programmes have been continued and are periodically reviewed and updated to address shipments of intact defence related fuels through some of the same transport corridors.

Samples of fuel debris from TMI–2 accident (1979) had been studied in many countries but after the accident at Fukushima there are new tasks using those samples to acquire new knowledge for fuel retrieval at 1F.

Therefore, the following is advised:

- Samples of fuel debris collected during the study of any severe nuclear accident should be kept as long as possible and they should be made available when required to support new international laboratory scale studies;
- Experts involved in the study of real fuel debris should transfer their experience to younger international generations. This is particularly important for those who are involved into the study of new severe nuclear accidents.

For example, there was cooperation during the CRP (2019–2020) between KRI, NDF and TEPCO. Japanese experts from NDF, TEPCO and JAEA were invited to KRI to take part in a special two week training seminar accompanied with a demonstration of actual samples of Chornobyl fuel debris (lava and corium). Russian Federation experts from KRI visited 1F and discussed the adoption of KRI experience (in studying Chornobyl samples) by TEPCO for fuel debris retrieval at 1F.

In conclusion, both Japanese and Russian experts agreed that looking at actual samples of fuel debris was beneficial in terms of bringing experts up to speed in the common understanding on how to study

highly radioactive samples, how to minimize risks, and how to provide samples representability minimizing their volumes etc.

## 9.2. CATALOGUING OF SAMPLES

Actual samples play an important role in managing severely damaged spent fuel and corium. They are extremely valuable for understanding the processes that lead to damaged fuel or nuclear accidents, to gain data for modelling codes for severe accident analysis, and for training purposes of researchers and especially early career scientists.

The availability of samples to study, however, is limited to a few institutions. Shipping of samples between laboratories has become costly and complicated. It is therefore important that available samples are collected, characterized, and catalogued as thoroughly as possible. This section is aimed at giving some advice on the data needed on samples, plans for taking samples, analysis methods applicable to sample characterization, and on sharing logistics.

### 9.2.1. Cost, funding, and sample amounts considerations

Samples from severe nuclear accidents are usually difficult to handle and store, their retention is costly and requires a large amount of space. There might be liabilities associated with the samples. They are, however, very valuable from a scientific perspective and can provide important information to the next generation if kept. Because of the cost of storage and handling, it is very important to clarify who is providing the funding and how long the funding body might be interested in keeping the samples. If funding is stopped at some point, it is likely that the samples will be disposed of.

The number of samples taken in the first place or preserved for future use can depend on various factors. Decisions on what and how much to sample to retain are very complex; because a balance must be made between the buildup of samples, retention of skills and knowledge versus cost and space involved. Considering cost and funding, the number of samples has to be limited to the minimum necessary. However, there should be enough samples available for certain analysis techniques and statistical validity; i.e., a trade-off. Other considerations are the availability of sampling methods, the limits and capabilities of the receiving laboratory and funding for analysis, in addition to the funding for storage.

### 9.2.2. Storage and preservation considerations

The retention of samples from severe nuclear accidents has several positive aspects. Not only can those samples be useful for future generations of researchers, monitoring them during storage can also provide valuable data. Periodic examination of the samples provides information on their evolution or long term performance, for example whether they degrade under the applied storage conditions, that can be used for planning of the disposal of similar materials. In addition, such studies maintain skills and knowledge base for future generations.

Preservation of radiological samples of corium or damaged fuel may require several considerations. The samples may undergo alteration due to the material’s inherent radioactivity; for example, alpha emitting material may change morphology due to recoil energy. An example being metamict minerals which were crystalline when formed but become amorphous due to alpha particle effects. This characteristic cannot be avoided.

Metallographic mounted samples might undergo changes due to radioactive decay over time resulting in the mounting media softening, due to local radiation heating, and the need for remounting or

repolishing. This effect has been seen in PIE samples mounted in thermoset epoxy. The same may not be true for samples mounted in metallic or phenolic media.

Liquid samples are particularly prone to change. Oxygen diffuses into the liquid through the walls of poly bottles, altering the dissolved sample. Precipitation may occur if the acidity changes which would result in a change in solution concentration; impacting any repeat analysis. Radiation and exposure to acid will embrittle poly bottles, which would require the liquid to be transferred to a new container, and is likely to introduce contamination.

### 9.2.3. Data to be collected during sampling

Important information to collect starts with the fuel and reactor design and where the samples were taken from. In the case where melting (fuel melting, core melting, or molten core concrete interaction) has occurred, the composition of the melt (if available) is also important. To understand the processes involved in an event, the temperatures (and/or pressures, neutron flux) reached during the event are beneficial In addition, the morphology and the chemical and physical stability of the samples are valuable parameters to know.

### 9.2.4. Sampling plan

Before any sampling is done, it is important to develop a sampling strategy which takes into consideration the following:

- Collecting enough discrete samples to be sure to have a good selection of the material that is available and to be able to determine the maximum possible range of properties of the samples in the laboratory. The selection of samples should be also large enough to facilitate the determination of most compositions present in the host material(s);
- To avoid any cross–contamination and damage, i.e., samples must be collected in a way that their chemistry and morphology is not altered. Samples shall be packed and stored in a way that experimental studies can be conducted on the original unaltered material;
- As much information as possible should be recorded about the provenance of the samples, e.g., the location where the sample was taken, the location of subsamples, what was the surrounding material, date and time, method of collection, orientation;
- How the sample is to be collected. Some situations might require special controls. For example, the material could be under water, or the radiation could be very high. In these cases, special tools must be considered, like robots, special shielding, or radiation protection.

### 9.2.5. Analysis methods

The following non-exhaustive list gives several tools and techniques that provide useful data for sample characterization. There are certainly more techniques available, but the listed techniques have proven to work well for the main characterization of samples and are the more easily available:

- Gamma spectroscopy;
- ICP–MS;
- Strontium isotope analysis;
- Uranium and plutonium isotope analysis;
- Alpha spectrometry;
- Metallography–optical microscopy;
- SEM and EPMA;
- XRD;

— Laser induced breakdown spectroscopy (LIBS);
— TEM;
— BET (Brunauer, Emmett and Teller) analysis;
— Standard (Vickers) hardness;
— Thermal conductivity.

### 9.2.6. Sharing logistics

Sharing samples between laboratories has become difficult in the recent years. Paperwork for licencing transport containers and transports in general has increased; the cost of a sample transport has increased significantly. Nevertheless, sharing samples is still an option, for example when specialist analytical equipment and processes are not available or can be undertaken at the place where the sample is located.

When planning the transport of a sample many things must be considered. Important properties of the sample should be available, such as sample size, weight, composition, radioactive activity, and chemical reactivity. With these properties known, other constraints can be planned. Does the sample require any special handling? Does it, for example, oxidise easily and requires an inert environment? What type of primary and secondary shielding are necessary for packing the sample? As well, the necessary licences for the receiving laboratory should be verified carefully, for example the allowed activity and dose rate.

Other important points to consider are:

— What are the national requirements for the planned transport?
— Who will take or keep ownership of the material, and who will take or keep the disposal liability?
— What type of shipping package or transport container is suitable? Is there a particular interface with a hot cell necessary? Is the sample material identified in the packaging SAR?

### 9.2.7. Examples

Examples are provided below.

#### *9.2.7.1. Three Mile Island Unit 2*

In the case of TMI Unit 2, several categories of samples were acquired. These included components such as the CRD leadscrews, loose debris grab samples from the top of the melt, discrete component samples, core bore samples and sludge samples from the coolant system.

Control rod drive leadscrews were identified based on the control rod location (e.g., H8 and B8). Characterization also included measurements at different lengths of the control rod, so sample sections were catalogued accordingly. Those samples were characterized for changes in hardness indicative of temperature as well as for surface radionuclide measurements as an indication of surface deposition of fuel materials.

Grab samples were catalogued according to the leadscrew penetration from which they were taken and separated into sample sets by particle size and apparent characteristics.

Core bore samples were identified by each of the eleven locations from which they were taken relative to the fuel assembly position that corresponded to each bore. Samples were additionally identified according to depth of sample and type of material present in it.

Metallographic mounts and other destructive analysis samples were identified as subsets of the parent samples, based on location such as core bore location and depth and location within the core section. Metallographic mounts were mounted in epoxy, Bakelite or low melting temperature metals prior to polishing, and type of mount should also be noted for waste management purposes.

Discrete components were catalogued according to locations that they were taken from as well as the canister they were loaded into. They were notated according to canister if no identifying markings could be distinguished. In the case of fuel assembly upper end fixtures, many of the 100 components could be identified by serial numbers on the items and were catalogued accordingly.

Sludge and solution samples were identified according to the system and location from which they were taken, and subsamples used for solution and other destructive samples were identified by the parent location number. Solution samples were not retained for more than one year following analysis due ALARA and waste management concerns.

Following analysis many of the metallographic mounts were placed in one of two debris canisters and placed into cask storage due to a general lack of interest. There is no certainty that the identifying marks placed on the mounts and samples will be legible following numerous years of storage and being dried at somewhat elevated temperatures.

*9.2.7.2. Chornobyl*

The main strategy during sampling was to cover a representative amount of all materials from different locations (rooms and levels) to get a detailed overview of the formed materials. Table 10 provides details of the types of samples collected and the sampling locations. As outlined in Section 2.3, in order to collect more material of the inclusions present in lava like fuel containing masses, some large (hundreds of $cm^3$) samples of the lava (black, brown and pumice) were dissolved in cold HF inside the sarcophagus and the concentrate of undissolved inclusions were collected for later study. Since the sampling was done by hand under extremely dangerous conditions, as quickly as possible, and sometimes with unusual tools (machine gun), there was no detailed sampling plan available to follow. Since 1990, the Chornobyl samples, wrapped in aluminium foil and placed into glass vessels, have been stored in air without humidity control. For over 30 years the samples have been available, been subject to numerous studies and are still providing valuable and unique information (see Section 3.2.1.). In 2012 two pieces of the black (7.8 g) and brown (3.5 g) lava were transported to JRC Karlsruhe and are available for research.

# 10. SUMMARY AND CONCLUSIONS

The final report of the CRP on the management of severely damaged spent fuel and corium consolidates the existing information on the status of and latest developments in the efforts associated with analysing and remediating the melted cores at TMI–2, ChNPP Unit 4 and 1F. In addition, valuable information and experiences are provided on the management of damaged fuel from ChNPP Units 1–3, the remediation of fuel severely damaged during cleaning operations at Paks NPP and conditioning/reprocessing of damaged fuel and fuel debris from PIE operations at Sellafield.

A few areas of interest to Member States are provide in the following Sections.

## 10.1. FUEL DEBRIS DRYING

Drying of wetted damaged fuel/debris is complicated by the significantly greater surface areas involved and the potential for water to be held up within the debris. Four approaches to drying and the issues associated with dried damaged fuel packaging/storage/transport are outlined.

## 10.2. THE EVOLUTION OF FUEL DEBRIS AND CORIUM

Information on the long term behaviour of failed fuel/debris is of great value in remediating and the development of storage safety cases. Reporting is provided on the long term behaviour of 40 year stored water logged fuel debris and the evolution of ChNPP lava samples, held at room temperature in air.

It is interesting that there has been no conversion to higher oxidation states in the waterlogged fuel, suggesting that there was neither the temperature nor oxygen available to drive such a process over the stored period. In comparison it is reported that the long term exposure to heat and moisture has impacted the integrity of Chornobyl lava, i.e. the exposed $UO_2$ is being converted to higher oxidation states of higher molecular weight which is driving the breakdown of the lava structure. There are two sides to every coin, the upside is long term exposure may aid debris removal the downside is containment.

## 10.3. INSPECTION TECHNOLOGIES

The reader is provided with accounts of the approaches to inspection that have been used in the past and can compare these to the latest technological developments. For example, the reported robotic developments by IRID for inspecting containment vessels versus the camera system used on TMI–2, noting that the former is driven by accessibility.

## 10.4. FINAL DISPOSITION STRATEGIES

In common with power reactors, where fuel cycle closure is work in progress, materials, in the case of TMI–2, are in safe storage pending a final disposition route to be defined. In terms of severely damage fuel and debris, reprocessing activities (Russian Federation, UK) have moved this one step further in that it is in the form of products, available for reuse and conditioned waste packages.

## 10.5. INFORMATION EXCHANGE AND COOPERATION

One of the benefits of CRPs is the fostering of information exchange and learning between participants, especially in the case of newcomers. In this CRP Section 5 reports the efforts of EAEA in modelling accident progression, an exercise informed through dialogue with JAEA. Likewise, Section 8 reports cooperation between KRI and JAPAN, and KRI and JRC Karlsruhe on corium.

# APPENDIX

# THREE MILE ISLAND CANISTER SPECIFIC REQUIREMENTS

## A.1. DEBRIS CANISTER DESIGN CRITERIA INCLUDED

(a) Maximum dewatered loaded weight 1270 kg, based on floor loading limits in the TAN-607 water pit with a maximum loaded weight of 1453 kg;
(b) 3.81 m overall length, 356 mm outer diameter, 3.46 m cavity length;
(c) Chemical compatibility with TMI-2 and INEL pools;
(d) Compatibility with fuel-handling tooling and equipment, both at the reactor and the storage sites;
(e) Having a lid that could be removed and placed remotely;
(f) Having provisions for venting, dewatering, inerting and leak testing;
(g) Non-buoyant when empty;
(h) Neutron poison completely encased in stainless steel;
(i) Sized to be compatible with shipping casks;
(j) Providing containment during transport;
(k) 20-micron particle-size limit in effluent when dewatering;
(l) Incorporating hydrogen oxygen recombiner catalyst (control of radiolysis;
(m) Equipped with a removable pressure-relief valve to limit internal pressure to less than 103.4 kPa after loading.

## A.2. STRUCTURAL REQUIREMENTS

(i) Structural integrity for criticality control maintained for all loadings under normal handling and cask loading operations;
(ii) Able to meet ASME Section VIII Subsection UW;
(iii) Internal design pressure: 1034 kPa at 355 K;
(iv) Hydrostatic test pressure 1551 kPa at 273 K;
(v) External Pressure 206.8 kPa at 355 K;
(vi) Sustain design-drop accident 3.5 m in air or 1.87 m in air followed by 5.9 m in water, with impact at any orientation, maintaining criticality control with allowable deformation;
(vii) Cask packaging interface parameters:
  – Maximum impact acceleration 40 g axial;
  – 100 g lateral with continuous support <12.7 mm gap between canister and support cylinder.

## A.3. PERFORMANCE REQUIREMENTS

### A.3.1. Fuel Canister

Canister will be able to:

– Be handled without top closure installed;
– Accept partial-length full cross-section fuel assembly.

### A.3.2. Filter Canister

The filter canister will be able to remove particulates ranging from 800 to 0.5 micron with a flow rate of 473 l/min.

### A.3.3. Knockout Canister

The knockout canister will contain neutron-absorbing material fully encapsulated in stainless steel.

### A.3.4. Criticality Criteria

The criticality criteria include:

- Analyses per 10 Code of Federal Regulations 72.73 and ANSI 8.1, 8.17, 16.5 and 16.9;
- Using optimal fuel size, volume fraction and enrichment;
- Criticality limit $k_{eff}$ <0.95; single or array, faulted or normal;
- Criticality limit without poison $k_{eff}$ <0.95;
- Single canister normal configuration.

## REFERENCES


[1] JENSEN, S.M., AKERS, D.W., GARNER, R.W., ROYBAL, G.S., Examination of the TMI-2 Core Distinct Components, Rep. GEND–INF–082, EG&G Idaho Inc., ID (1987).

[2] UNITED STATES NUCLEAR REGULATORY COMMISSION, Reactor Pressure Vessel Status Report, NUREG-1511, US NRC, Washington (1994).

[3] UNITED STATES NUCLEAR REGULATORY COMMISSION, Calculations to Estimate the Margin to Failure in the TMI-2 Vessel, NUREG/CR-6196/EGG-2733, US NRC, Washington (1994), https://doi.org/10.2172/10144034

[4] OSETEK, D.J., BROUGHTON, J.M., HOBBINS, R.R., TMI-2 Accident Evaluation Program, Rep. EGG-M-89109, EG&G Idaho Inc., ID (1989).

[5] UNITED STATES NUCLEAR REGULATORY COMMISSION, Knowledge Management Library for the Three Mile Island Unit 2 Accident of 1979 (2016), https://tmi2kml.inl.gov

[6] MCCARDELL, R.K, et al., TMI–2: Materials Behavior, Nucl. Technol., **87** 1 (1989).

[7] DISTENFELD, C.H., et al., TMI–2: Health Physics and Environmental Releases, Nucl. Technol., **87** 2 (1989).

[8] PATTERSON, R.L., et al., TMI–2: Remote Technology and Engineering, Nucl. Technol., **87** 3 (1989).

[9] HAYES, G.R., et al., TMI–2: Decontamination and Waste Management, Nucl. Technol., **87** 4 (1989).

[10] MALKO, M.V., "The Chernobyl reactor Design features and reasons for accident", Recent Research Articles About The Chernobyl NPP Accident In Belarus, Ukraine And Russia, KURRI-EKR-10, Research Reactor Institue Kyoto University, Kyoto (2002).

[11] DOLLEZHAL, N.A., EMELYANOV, I.Y., Channel-type nuclear power reactor, Atomizdat (1980) 208 pp (in Russian).

[12] CHERKASHOV, Y.M., NIKITIN, Y.M., STENBOK, I.A., Channel-type nuclear power reactor RBMK, NIKIET (2006) 632 pp (in Russian).

[13] NIGMATULIN, I.N., NIGMATULIN, B.I., Nuclear power reactors, Energoatomizdat (1986) 168 pp (in Russian).

[14] DEMENTYEV, B.A., Nuclear power reactors, Energoatomizdat (1990) 352 pp (in Russian).

[15] SHELEGOV, A.S., LESKIN, S.T., SLOBODCHUK, V.T., Principal features and design of RBMK-1000, MIFI (2011) 63 pp (in Russian).

[16] Information on the accident at the Chernobyl nuclear power plant and its consequences prepared for IAEA, Sov. Atom. Energy **61** 5 (1986) 845–868, https://doi.org/10.1007/BF01122262

[17] UNION OF SOVIET SOCIALIST REPUBLICS STATE COMMITTEE ON THE UTILIZATION OF ATOMIC ENERGY, "The accident at the Chernobyl nuclear power plant and its consequences". paper presented at the IAEA Post-Accident Experts Review Meeting, August 25–29, 1986, IAEA, Vienna (1986).

[18] CHERNOBYL NPP. Technical description of setup, equipment and systems. Part. 1. Entry No. 307/162, Kiev (1975) 144 pp (in Russian).

[19] BYLKIN, B.K., DAVYDOVA, G.B., KRAYUSHKIN, A.V., SHAPOSHNIKOV, V.A., Radiation characteristics of reactor structures after the final shutdown of a nuclear power plant with RBMK reactors, Atom. Energy **97** 6 (2004) 845–850, https://doi.org/10.1007/s10512-005-0071-3

[20] ALMENAS, K., KALIATKA, A., USPURAS, E., "Design of structures, components, equipments and systems", Ignalina RBMK-1500: A Source Book, Ignalina Safety Analysis Group, Lithuanian Energy Institute, Kaunas (1998).
[21] KISELEV, A., SURIN, A., CHECHEROV, K., Confirmed data on dynamics of accident processes at the forth Unit of Chernobyl NPP. Results of post-accident examination, Bulletin on Atomic Energy **4** (2006) 36–42 (in Russian).
[22] STATE COMMITTEE OF STANDARDS OF THE COUNCIL OF MINISTERS USSR, Low-alloyed structural rolled stock for bridge building, GOST 6713-75, Moscow (1975) (in Russian).
[23] STATE COMMITTEE OF STANDARDS OF THE COUNCIL OF MINISTERS USSR, High-alloy steels and corrosion proof, heat-resisting and heat treated alloys, GOST 5632–72 (1975) (in Russian).
[24] MILOVANOV, A.F., SOLOMONOV, V.V., "Effect of high-temperature heating on reinforced concrete capability at Chornobyl NPP accident", Fifteen Years after the Chornobyl Accident Lessons Learned (Proc. Int. Conf. Kyiv, 2001), Anon, Ukraine (2001) (in Russian).
[25] BOGATOV, S., BOROVOĐ, A., GAVRILOV, S., LAGUNENKO, A.S., PAZUKHIN, E.M., Half an hour after the beginning of the accident, Moscow, Russian Federation, (2005).
[26] FLETCHER, C.D., CHAMBERS, R., BOLANDER, M.A., DALLMAN, R.J., Simulation of the Chernobyl accident, Nucl. Eng. Des. **105** 2 (1988) 157–172, https://doi.org/10.1016/0029-5493(88)90337-8
[27] ABAGYAN, A.A., et al., Computational analysis of the initial stage of the accident at the Chernobyl atomic power plant, Soviet Atom. Energy **71** 4 (1991) 785–795, https://doi.org/10.1007/BF01123528
[28] AFANAS'EVA, A.A., et al., Analysis of the Chernobyl accident taking core destruction into account, Atom. Energy **77** 2 (1994) 573–579, https://doi.org/10.1007/BF02407429
[29] PAZUKHIN, E.M., Fuel-containing lavas of the Chernobyl NPP fourth block: Topography, physicochemical properties, and formation scenario, Radiochemistry **36** (1994) 109–154.
[30] BOROVOY, A.A., Inside and Outside Sarcophagus. Preprint of CE IAE, Chernobyl, (1990) (in Russian).
[31] ARUTYUNYAN, R.V., BOLSHOV, L.A., BOROVOI, A.A., VELIKHOV, E.P., KLYUCHNIKOV, A.A., Nuclear Fuel in the 'Shelter' Encasement of the Chernobyl NPP, Nauka, Moscow, Russian Federation (2010) 240 pp.
[32] BURAKOV, B.E., ANDERSON, E.B., GALKIN, B.Y., PAZUKHIN, E.M., SHABALEV, S.I., Study of Chernobyl “hot” particles and fuel containing masses: implications for reconstruction the initial phase of the accident, Radiochim. Acta **65** (1994) 199–202, https://doi.org/10.1524/ract.1994.65.3.199
[33] SHABALEV, S., BURAKOV, B.E., ANDERSON, E.B., General classification of “hot” particles from the nearest Chernobyl contaminated areas, MRS Proceedings **465** (1996) 1343–1350, https://doi.org/10.1557/PROC-465-1343
[34] BURAKOV, B.E., SHABALEV, S.I., ANDERSON, E.B., Principal Features of Chernobyl Hot Particles: Phase, Chemical and Radionuclide Compositions, Proc. Role of Interfaces in Environmental Protection, Springer Netherlands, Dordrecht, 2003 (abstract), https://doi.org/10.1007/978-94-010-0183-0_10
[35] BURAKOV, B.E., Crystalline mineral-like matrices for actinide immobilization (Thesis for DSc), St. Petersburg, Russian Federation, (2013) (in Russian).
[36] TROTABAS, M., BLANC, J.-Y., BURAKOV, B., ANDERSON, E., DUCO, J., Examination of Chernobyl samples. Impact on the accident scenario understanding. Report DMT/92/309, SETIC/LECR-92/36, Report IPSN/93/02, Report RI-1-63/92, (1993).

[37] BURAKOV, B., et al., The behavior of nuclear fuel in first days of the Chernobyl accident, MRS Proceedings **465** (1996) 1297–1308, https://doi.org/10.1557/PROC-465-1297
[38] SHIRYAEV, A.A., et al., Physico-chemical properties of Chernobyl lava and their destruction products, Prog. Nucl. Energy **92** (2016) 104–118, https://doi.org/10.1016/j.pnucene.2016.07.001
[39] BURAKOV, B.E., "Lava-like materials formed and solidified during Chernobyl accident", Comprehensive Nuclear Materials, 2nd ed., Elsevier, Netherlands (2020), https://doi.org/10.1016/B978-0-12-803581-8.11686-8
[40] SHIRYAEV, A.A., et al., Study of mineral grains extracted from the Chernobyl lava, Mineral Petrol. **114** 6 (2020) 489–499, https://doi.org/10.1007/s00710-020-00718-8
[41] PÖML, P., BURAKOV, B., Study of a "hot" particle with a matrix of U-bearing metallic Zr: Clue to supercriticality during the Chernobyl nuclear accident, J. Nucl. Mater. **488** (2017) 314–318, https://doi.org/10.1016/j.jnucmat.2017.01.041
[42] INTERNATIONAL ATOMIC ENERGY AGENCY, INSAG-7 The Chernobyl Accident: Updating of INSAG-1. IAEA Safety Series No. 75-INSAG-7, IAEA, Vienna (1992).
[43] KISELEV, A.N., CHECHEROV, K.P., Model of the destruction of the reactor in the No. 4 unit of the Chernobyl nuclear power plant, Atom. Energy **91** (2001) 967–975, https://doi.org/10.1023/A:1014851218238
[44] KISELEV, A.N., CHECHEROV, K.P., Process of reactor destruction at Chernobyl NPP, Bulletin on Atomic Energy **10** (2001) 40–47 (in Russian).
[45] PÖML, P., BURAKOV, B., Study of the redistribution of U, Zr, Nb, Tc, Mo, Ru, Fe, Cr, and Ni between oxide and metallic phases in the matrix of a multiphase Chernobyl hot-particle extracted from a soil sample of the Western Plume, Radiochim. Acta **106** 12 (2018) 985–990, https://doi.org/10.1515/ract-2018-2957
[46] SHIRYAEV, A.A., et al., Forensic study of early stages of the Chernobyl accident: Story of three hot particles, J. Nucl. Mater. **511** (2018) 83–90, https://doi.org/10.1016/j.jnucmat.2018.09.003
[47] UNITED STATES DEPARTMENT OF ENERGY, Report of the U.S. Department of Energy's Team Analyses of the Chernobyl-4 Atomic Energy Station Accident Sequence, Rep. DOE/NE-0076, US DoE, Washington (1986), https://doi.org/10.2172/7037704
[48] LEBEDEV, I.A., MYASOEDOV, B.F., PAVLOTSKAYA, F.I., FRENKEL, V.Y., Plutonium content in soils of the european part of the country after the accident at Chernobyl Nuclear Generating Station, Atom. Energy **72** (1992) 515–520, https://doi.org/10.1007/BF00760909
[49] BOROVOY, A.A., VELIKHOV, E.P., Experience Of Chernobyl (Vol.1). National Research Center (Kurchatov Institute), Moscow (2012) 168 pp (in Russian).
[50] BURAKOV, B.E., STRYKANOVA, E.E., ANDERSON, E.B., Secondary uranium minerals on the surface of Chernobyl lava, MRS Proceedings **465** (1996) 1309–1311, https://doi.org/10.1557/PROC-465-1309
[51] ABDULAKHATOV, M.K., et al., "4th unit barboter: Complex of postaccident investigations", First International Workshop on Past Severe Accidents and Their Consequences, (Proc. Int. Conf. Sochi, 1989), Nauka, Moscow (1990).
[52] BOROVOY, A.A., et al., New products formed by reaction of fuel with construction materials in the 4th block of the Chernobyl NPP, Soviet Radiochemistry **32** (1990) 659–667.

[53] VLASOVA, I., et al., Radioactivity distribution in fuel-containing materials (Chernobyl lava) and aerosols from the Chernobyl "Shelter", Radiat. Meas. **83** (2015) 20–25, https://doi.org/10.1016/j.radmeas.2015.06.005
[54] BOGATOV, S.A., BOROVOI, A.A., DUBASOV, Y.V., LOMONOSOV, V.V., Form and parameters of the particles of the fuel ejection in the Chernobyl reactor accident, Sov. Atom. Energy **69** (1990) 595–601, https://doi.org/10.1007/BF02086947
[55] DUBASOV, Y.V., KRIVOKHATSKII, A.S., SAVONENKOV, V.G., SMIRNOVA, E.A., State and behavior of dispersed fuel particles ejected from 4th Unit of Chernobyl NPP, Sov. Radiochem. **33** (1991) 96–101.
[56] KISELEV, A.N., NENAGLYADOV, A.Y., SURIN, A.I., CHECHEROV, K.P., Experimental study of lava-like fuel containing masses (FCM) at 4th Unit of ChNPP (Based on results obtained in 1986-1991), IAE, Moscow, Russian Federation (1992) (in Russian).
[57] PAKHOMOV, S.A., KRIVOKHATSKII, K.S., SOKOLOV, I.A., Estimate of the instantaneous energy release in the Chernobyl NPP reactor accident based on the ratio of $^{133}$Xe and $^{133m}$Xe activities in air, Radiochemistry **33** (1991) 685–688.
[58] SINKKO, K., AALTONEN, H., MUSTONEN, R., TAIPALE, T.K., JUUTILAINEN, J., Airborne radioactivity in Finland after the Chernobyl accident in 1986, Rep. STUK-A56, Supplement 1 to Annual Report STUK-A55, STUK, Vantaa (1987).
[59] STRAKHOV, V.N., et al., Seismic phenomena in the area of Chernobyl nuclear power plant, J. Geohpys. **17** (1998) 389–409.
[60] SHIRYAEV, A.A., et al., Products of molten corium-metal interaction in Chernobyl accident: Composition and leaching of radionuclides, Prog. Nucl. Energy **152** (2022) 104373, https://doi.org/10.1016/j.pnucene.2022.104373
[61] KASHPAROV, V.A., IVANOV, Y.A., KHOMUTININ, Y.V., PAZUKHIN, E.M., An estimate of effective temperature and annealing duration of fuel particles ejected from Chernobyl reactor during the accident, Radiochemistry **38** 1 (1996) 84–89.
[62] KASHPAROV, V.A., et al., An estimate of maximal effective temperature and of duration of non-isothermal annealing of Chernobyl fuel particles during the accident, Radiochemistry **39** 1 (1997) 63–67.
[63] PLATONOV, P.A., KRAYUSHKIN, A.V., Process resulting in the destruction of the No. 4 unit reactor at the Chernobyl nuclear power plant, Atom. Energy **104** (2008) 417–427, https://doi.org/10.1007/s10512-008-9050-9
[64] OGORODNIKOV, B.I., BUDYKA, A.K., PAZUKHIN, E.M., V.A., K., Aerosol emission from destroyed 4th block of Chernobyl NPP in 1986 and 2003-2005, Atom. Energy Bulletin **4** (2006) 45–49.
[65] OGORODNIKOV, B.I., PAZUHIN, E.M., KLYUCHNIKOV, A.A., Radioactive Aerosols of the "Shelter" Object 1986-2006, Institute for safety problems of NPP NASU (2008) 456 pp.
[66] LÖNARTZ, M.I., PÖML, P., COLLE, J–Y, MANARA, D., BURAKOV, B.E., Characterization of black and brown Chernobyl lava matrices: The formation process reviewed, Prog. Nucl. Energy **163** (2023) 104796, https://doi.org/10.1016/j.pnucene.2023.104796
[67] BOROVOY, A.A., VELIKHOV, E.P., Experience of Chernobyl (Vol.3). National Research Center (Kurchatov Institute), Moscow (2013) 156 pp (in Russian).
[68] INTERNATIONAL ATOMIC ENERGY AGENCY, The Fukushima Daiichi Accident Technical Volume 1/5 Description and Context of the Accident, IAEA, Vienna (2015).
[69] TOKYO ELECTRIC POWER COMPANY, Fukushima Dai-ichi NPS: Application for reactor establishment permit, TEPCO, Tokyo (2002).
[70] TOKYO ELECTRIC POWER COMPANY, Fukushima Dai-ichi NPS: Application for permit for changes to reactor establishment, TEPCO, Tokyo (2003).

[71] TOKYO ELECTRIC POWER COMPANY, Report to NISA in relation to the impact of Tohoku-Chihou Taiheiyo-Oki Earthquake to Nuclear Reactor Facilities at Fukushima Daiichi Nuclear Power Station (Continued report) (attachment), TEPCO, Tokyo (2012).
[72] INVESTIGATION COMMITTEE ON THE ACCIDENT AT THE FUKUSHIMA NUCLEAR POWER STATIONS, Executive Summary of the Interim Report, 2011.12.26, Invetigation Committee, Tokyo (2011).
[73] TOKYO ELECTRIC POWER COMPANY, Accident Overview of Fukushima, Daiichi NPS (2011), https://www.tepco.co.jp/en/nu/fukushima-np/review/review1_1-e.html
[74] MINISTRY OF THE ENVIRONMENT (Japan) , Comparison of Estimated Radionuclide Release From Chernobyl and Fukushima Daiichi (2021), http://www.env.go.jp/chemi/rhm/h29kisoshiryo/h29kiso-02-02-05.html
[75] INTERNATIONAL COMMISSION ON RADIOLOGICAL PROTECTION, Age-dependent Doses to the Members of the Public from Intake of Radionuclides. Rep. ICRP No. 72. Ann. ICRP 26 (1), ICRP, Ottawa (1995).
[76] GOVERNMENT OF JAPAN, Report of the Government of Japan to the IAEA Ministerial Conference on Nuclear Safety, Government of Japan, Tokyo (2011).
[77] United Nations SCIENTIFIC COMMITTEE ON THE EFFECTS OF ATOMIC RADIATION, Report to the General Assembly, UNSCEAR 2013 Vol. 1 ANNEX 1, UNSCEAR, Vienna (2013).
[78] AKERS, D.W., CARLSON, E.R., COOK, B.A., PLOGER, S.A., CARLSON, J.O., TMI-2 Core Debris Grab Samples-Examination and Analysis, Part 1, Rep. GEND–INF–075–Pt.1, EG&G Idaho Inc., ID (1986).
[79] MCCARDELL, R.K., RUSSELL, M.L., AKERS, D.W., OLSEN, C.S., Summary of TMI-2 Core Sample Examinations, Nucl. Eng. Des. **118** 3 (1990) 441–449, https://doi.org/10.1016/0029-5493(90)90045-Y
[80] AKERS, D.W., et al., TMI-2 Examination Results from the OECD/CSNI Program, Vol. 1, Rep. EGG-OECD-9168, EG&G Idaho Inc., ID (1992).
[81] AKERS, D.W., CARLSON, E.R., COOK, B.A., PLOGER, S.A., CARLSON, J.O., TMI-2 core debris grab samples: Examination and analysis: Part 2, Rep. GEND–INF–075–Pt.2 EG&G Idaho Inc., ID (1986).
[82] HESS, C.J., TMI-2 Technical Information and Examination Program, 1984 Annual Report, Rep. GEND-049, EG&G Idaho Inc., ID (1985), https://doi.org/10.2172/5869135
[83] RUSSELL, M.L., MCCARDELL, R.K., BROUGHTON, J.M., AKERS, D.W., TMI-2 Accident Evaluation Program Sample Acquisition and Examination Plan for FY-1988 and Beyond, Rep. EGG-TMI-7992, EG&G Idaho Inc., ID (1988).
[84] TOLMAN, E.L., SMITH, R.P., MARTIN, M.R., MCCARDELL, R.K., BROUGHTON, J.M., TMI-2 Core Bore Acquisition Summary Report, Rep. EGG-TMI-7385, EG&G Idaho Inc., ID (1987), https://doi.org/10.2172/285489
[85] BOTTOMLEY, P.D., COQUERELLE, M., Metallurgical examination of bore samples from the Three Mile Island unit 2 reactor core, Nucl. Technol. **87** 1 (1989) 120–136, https://doi.org/10.13182/NT89-A27642
[86] HOBBINS, R.R., RUSSELL, M.L., OLSEN, C.S., MCCARDELL, R.K., Molten Material Behavior in the Three Mile Island Unit 2 Accident, Nucl. Technol. **87** 4 (1989) 1005–1012, https://doi.org/10.13182/NT89-A27692
[87] TROTABAS, M., AL., E., TMI-2 Core Materials Examination at CEA, Rep. CEA–DAS–578, CEA, Paris (1989).

[88] AKERS, D.W., MCCARDELL, R.K., RUSSELL, M.L., WORKU, G., TMI-2 Core Materials and Fission Product Inventory, Nuclear Energy Design **118** 3 (1990) 451–461, https://doi.org/10.1016/0029-5493(90)90046-Z
[89] UNITED STATES NUCLEAR REGULATORY COMMISSION, TMI-2 Vessel Investigation Project Integration Report, NUREG/CR-6197/EGG-2734, US NRC, Washington (1994), https://doi.org/10.2172/10140805
[90] ZUBEKHINA, B.Y., BURAKOV, B.E., Leaching of actinides and other radionuclides from matrices of Chernobyl lava as analogues of vitrified HLW, J. Chem. Thermodyn. **114** (2017) 25–29, https://doi.org/10.1016/j.jct.2016.08.029
[91] ZUBEKHINA, B.Y., BURAKOV, B.E., BOGDANOVA, O.G., PETROV, Y.Y., Leaching of $^{137}$Cs from Chernobyl fuel debris: corium and lava, Radiochim. Acta **107** 12 (2019) 1155–1160, https://doi.org/10.1515/ract-2019-0009
[92] OJOVAN, M.I., PANKOV, A., LEE, W.E., The ion exchange phase in corrosion of nuclear waste glasses, J. Nucl. Mater. **358** 1 (2006) 57–68, https://doi.org/10.1016/j.jnucmat.2006.06.016
[93] ZUBEKHINA, B., et al., Long-term aging of Chernobyl fuel debris: Corium and lava, Sustainability **13** 3 (2021) 1073, https://doi.org/10.3390/su13031073
[94] WASHIYA, T., YANO, K., KAJI, N., YAMADA, S., KAMIYA, M., "Study of treatment scenarios for fuel debris removed from Fukushima Daiich NPS", ICONE-23 (Proc. Int. Conf. Chiba, Japan, May 17-21, 2015, JSME, Tokyo (2015), https://doi.org/10.1299/jsmeicone.2015.23._ICONE23-1_447
[95] TOKYO ELECTRIC POWER COMPANY, Core status of Fukushima Daiichi Nuclear Power Station Units 1 to 3, Press release, TEPCO, Tokyo (2011) (in Japanese).
[96] JAPAN ATOMIC ENERGY AGENCY, T.I., Analysis of debris samples of Tokyo Electric Power Company Holdings Fukushima Daiichi Nuclear Power Station (Translated document), JAEA-Review-2020-055, JAEA, Tokai-Mura (2020), https://doi.org/10.11484/jaea-review-2020-055
[97] NUCLEAR DAMAGE COMPENSATION AND DECOMMISSIONING FACILITATION CORPORATION, Technical Strategic Plan 2019 for the Decommissioning of the Fukushima Daiichi Nuclear Power Station of Tokyo Electric Power Company Holdings, Inc., Rep., NDF, Tokyo (2019) 143 pp.
[98] THE INTER-MINISTERIAL COUNCIL FOR CONTAMINATED WATER AND DECOMMISSIONING ISSUES, Mid-and-Long-Term Roadmap towards the Decommissioning of TEPCO's Fukushima Daiichi Nuclear Power Station, Rep., Japanese Government, Tokyo (2019).
[99] THE INTER-MINISTERIAL COUNCIL FOR CONTAMINATED WATER AND DECOMMISSIONING ISSUES, The 67th Secretariat Team Meeting for Countermeasures for Decommissioning and Contaminated Water Treatment, Basic principles toward the planned analysis and investigation on the decommissioning and contaminated water management of Fukushima Daiichi Nuclear Power Station, Tokyo Electric Power Holdings, Japanese Government, Tokyo (2019).

[100] NAKAYOSHI, A., MITSUGI, T., SASAKI, S., MAEDA, K., Analysis of Deposits inside the Reactor at Fukushima Daiichi Nuclear Power Station in JFY 2017-2018 -The Subsidy Programs “Project of Decommissioning and Contaminated Water Management in the FY2016 Supplementary Budget, (Development of Technologies for Grasping and Analyzing Properties of Fuel Debris)”, Rep. 2021-011, J.-D.C., Japan (2022), https://doi.org/10.11484/jaea-data-code-2021-011
[101] BARRACHIN, M., NAKAYOSHI, A., KURATA, M., MORREALE, A., ONDER, N., "Preliminary investigation of samples taken from the PCV inside of Fukushima-Daiichi Nuclear Power Plant and implications on severe accident analysis", NURETH19 (Proc. Int. Conf. Brussels, 2022) SCK CEN, Brussels (2022).
[102] BREITUNG, W., REIL, K.O., Vapor Pressure Measurements on Liquid Uranium Oxide and (U,Pu) Mixed Oxide, Nucl. Sci. Eng. **101** 1 (1989) 26–40, https://doi.org/10.13182/NSE89-A23592
[103] SHABALEV, S.I., BURAKOV, B.E., ANDERSON, E.B., General Classification of “Hot” Particles from the Nearest Chernobyl Contaminated Areas, MRS Proceedings **465** (1996) 13431350, https://doi.org/10.1557/PROC-465-1343
[104] BOROVOI, A.A., LAGUNENKO, A.S., PAZUKHIN, E.M., Radiochemical and some physico-chemical features of samples of lava and of concrete from sub-reactor room 304/3 of 4th unit of ChAES. Their relation with scenario of the accident, Radiochemistry **41** 2 (1999) 197–202.
[105] ANDERSON, E.B., BURAKOV, B.E., PAZUKHIN, E.M., High-uranium zircon from "Chernobyl lavas", Radiochimica Acta **60** 2-3 (1993) 149–152, https://doi.org/10.1524/ract.1993.60.23.149
[106] PÖML, P., et al., Micro-analytical uranium isotope and chemical investigations of zircon crystals from the Chernobyl lava and their nuclear fuel inclusions, J. Nucl. Mater. **439** 1 (2013) 51–56, https://doi.org/10.1016/j.jnucmat.2013.03.031
[107] GONCHAR, V.V., ZHIDKOV, A.V., Behaviour of lava-like fuel-containing materials of the object “Shelter” during thermal treatment, Problems Nucl. Power Plants Saf. Chernobyl **8** (2001) 53–58.
[108] KRASNORUTSKYY, V.S., et al., Microstructural analysis of lava-like fuel containing masses, Problems Atomic Sci. Technol. **95** (2010) 60–67 (in Russian).
[109] KRASNORUTSKYY, V.S., et al., Investigation of interaction of nuclear fuel with construction materials of the core in case of severe accident, Problems Atomic Sci. Technol. **78** (2012) 56–67 (in Russian).
[110] BARLOW, S.T., et al., Synthesis, characterisation and corrosion behaviour of simulant Chernobyl nuclear meltdown materials, npj Materials Degradation **4** 1 (2020) 3, https://doi.org/10.1038/s41529-020-0108-z
[111] JOURNEAU, C., SUDREAU, F., MAGNE, S., COGNET, G., Physico-chemical analyses and solidification path reconstruction of multi-component oxidic spread melts, Mater. Sci. Eng. **299** 12 (2001) 249–266, https://doi.org/10.1016/S0921-5093(00)01404-0
[112] TAKANO, M., “Current status of research and development on fuel debris properties”, paper presented at Project of Decommissioning and Contaminated Water Management – Water Chemistry Subcommittee, 7th Regular Meeting, IRID, Tokyo, 2016.
[113] TAKANO, M., NISHI, T., High temperature reaction between sea salt deposit and (U,Zr)$O_2$ simulated corium debris, J. Nucl. Mater. **433** (2013) 32–39, https://doi.org/10.1016/j.jnucmat.2013.06.039

[114] TAKANO, M., NISHI, T., SHIRASU, N., Characterization of solidified melt among materials of $UO_2$ fuel and $B_4C$ control blade, J. Nucl. Sci. Technol. **51** 78 (2014) 859–875, https://doi.org/10.1080/00223131.2014.912567
[115] PSHENICHNIKOV, A., YAMAZAKI, S., BOTTOMLEY, D., NAGAE, Y., KURATA, M., Features of a control blade degradation observed in situ during severe accidents in boiling water reactors, J. Nucl. Sci. Technol. **56** 5 (2019) 440–453, https://doi.org/10.1080/00223131.2019.1592724
[116] BOUYER, V., JOURNEAU, C., HAQUET, J.F., ET, A., "Large Scale VULCANO Molten Core Concrete Interaction Test Considering Fukushima Daiichi Condition", ERMSAR2019 (Proc. Int. Conf. Prague, 2019), Nuclear Research Czech Republic, Prague (2019).
[117] IKUECHI, H., "Product Phase and Hardness Due to Molten Core Concrete Interaction (MCCI): Insights from Large Scale Test", Annual Meeting of JAEA Sector of Fukushima Research and Development (Proc. Conf. Fukushima, 2018, JAEA, Tokai-Mura (2018) (in Japanese).
[118] BRISSONNEAU, L., et al., Material characterization of the VULCANO corium concrete interaction test with concrete representative of Fukushima Daiichi Nuclear Plants, J. Nucl. Mater. **528** (2020) 151860, https://doi.org/10.1016/j.jnucmat.2019.151860
[119] O'NEILL, R., GOODE, J., HAMBLEY, D., Failed fuel report: Characterisation and secondary alteration products, EU HORIZON 2020 - DISCO - Deliverable 2.2 - NNL 14742 (EU Ares(2019)3542316), NNL, Warrington (2019).
[120] INTERNATIONAL ATOMIC ENERGY AGENCY, Regulations for the Safe Transport of Radioactive Material, IAEA Safety Standards, Safety Requirements No. TS-R-1, IAEA, Vienna (2009).
[121] COLMENARES, C.A., The oxidation of thorium, uranium, and plutonium, Prog. Solid State Ch. **9** (1975) 139–239, https://doi.org/10.1016/0079-6786(75)90016-3
[122] ORR, R., et al., Formation and physical properties of uranium hydride under conditions relevant to metallic fuel and nuclear waste storage, J. Nucl. Mater. **477** (2016) 236–245, https://doi.org/10.1016/j.jnucmat.2016.04.057
[123] MCEACHERN, R.J., TAYLOR, P., A review of the oxidation of uranium dioxide at temperatures below 400°C, J. Nucl. Mater. **254** 2 (1998) 87–121, https://doi.org/10.1016/S0022-3115(97)00343-7
[124] INTERNATIONAL ATOMIC ENERGY AGENCY, Disposal aspects of low and intermediate level decommissioning waste. Results of a coordinated research project 2002 – 2006, IAEA-TECDOC-1572, IAEA, Vienna (2004).
[125] BAKER, M.M., LESS, L.N., ORMAN, S., Uranium + water reaction. Part 2.—Effect of oxygen and other gases, Trans. Faraday Soc. **62** (1966) 2525–2530, https://doi.org/10.1039/TF9666202525
[126] COLMENARES, C.A., Oxidation mechanisms and catalytic properties of the actinides, Prog. Solid State Ch. **15** 4 (1984) 257–364, https://doi.org/10.1016/0079-6786(84)90003-7
[127] WABER, J.T., A review of the corrosion of uranium and its alloys, Rep. LA-1524, LANL, Los Alamos (1952).
[128] RITCHIE, A.G., GREENWOOD, R.C., RANDLES, S.J., The kinetics of the uranium-oxygen-water vapour reaction between 40 and 100°c, J. Nucl. Mater. **139** 2 (1986) 121–136, https://doi.org/10.1016/0022-3115(86)90030-9
[129] CUBICCIOTTI, D., The Reaction between Uranium and Oxygen, J. Am. Chem. Soc. **74** 4 (1952) 1079–1081, https://doi.org/10.1021/ja01124a505

[130] PEARCE, R.J., KAY, P., The reaction of uranium in the U-$O_2$-$H_2O$ and U-$H_2O$ systems, TPRD/B/0954/R87, Berkeley Nuclear Laboratories, (1987).
[131] ORMAN, S., Uranium compatibility studies Part 1: The interaction of uranium with gas free water and water vapour, Rep. AWRE No. O-94/63, AWRE UKAEA, London (1963).
[132] BAKER, M.M., BLELOCH, J.W., LESS, L.N., ORMAN, S., Uranium compatibility studies Part 3: The influence of oxygen on the uranium - water reaction, Rep. AWRE No. 0-40/64, AWRE UKAEA, London (1964).
[133] MAGNANI, N.J., Reaction of uranium and its alloys with water vapor at low temperatures, Rep. SAND-74-0145, SNL, Albuquerque (1974), https://doi.org/10.2172/4258103
[134] JACKSON, R.L., CONDON, J.B., STECKEL, L.M., Uranium/water vapor reactions in gaseous atmospheres, Rep. No. Y-2078, Oak Ridge Y-12 Plant, Oak Ridge (1977), https://doi.org/10.2172/7321252
[135] KONDO, T., BECK, F.H., FONTANA, M.G., A Gas Chromatographic Study on the Kinetics of Uranium Oxidation in Moist Environments, Corrosion **30** 9 (1974) 330–341, https://doi.org/10.5006/0010-9312-30.9.330
[136] WEIRICK, L.J., The oxidation of uranium in low partial pressures of oxygen and water vapour at 100°C, Rep. SAND83-0618, SNL, Albuquerque (1984), https://doi.org/10.2172/6848474
[137] BESSON, J., SANTON, J., Cinetique de reaction de la vapeur deau sur luranium evapore en couches minces, Bull. Soc. Chi. Fr. (1963).
[138] BAKER, M.M., LESS, L.N., ORMAN, S., Uranium + water reaction. Part 1. - Kinetics, products and mechanism, Trans. Faraday Soc. **62** (1966) 2513–2524, https://doi.org/10.1039/TF9666202513
[139] MARTIN, T.L., et al., Atomic-scale Studies of Uranium Oxidation and Corrosion by Water Vapour, Sci. Rep. **6** (2016) 25618, https://doi.org/10.1038/srep25618
[140] GODFREY, H., STRANGE, R., Knowledge Status of Uranium Hydride, internal report RWM/Contr/20/003, RWM Ltd., Harwell (2020).
[141] ORR, R., et al., Kinetics of the reaction between water and uranium hydride prepared under conditions relevant to uranium storage, J. Alloys Compd. **695** (2017) 3727–3735, https://doi.org/10.1016/j.jallcom.2016.11.314
[142] TOTEMEIER, T.C., Characterization of uranium corrosion products involved in a uranium hydride pyrophoric event, J. Nucl. Mater. **278** 2 (2000) 301–311, https://doi.org/10.1016/S0022-3115(99)00245-7
[143] TOTEMEIER, T.C., Oxidation of ZPPR fuel corrosion products : National Spent Nuclear Fuel program FY 1999 final report, Rep. ANL-99/21, ANL, Argonne (1999), https://doi.org/10.2172/816758
[144] TOTEMEIER, T.C., Surface area and chemical reactivity characteristics of uranium metal corrosion products, Rep. ANL/ED/CP-95647, ANL, Argonne (1998).
[145] TOTEMEIER, T.C., PAHL, R.G., FRANK, S.M., Oxidation kinetics of hydride-bearing uranium metal corrosion products, J. Nucl. Mater. **265** 3 (1999) 308–320, https://doi.org/10.1016/S0022-3115(98)00649-7
[146] TOTEMEIER, T.C., PAHL, R.G., HAYES, S.L., FRANK, S.M., Characterization of corroded metallic uranium fuel plates, J. Nucl. Mater. **256** 2 (1998) 87–95, https://doi.org/10.1016/S0022-3115(98)00448-6
[147] PATEL, N., HAMBLEY, D., CLARKE, S., "Influence of uranium hydride oxidation on uranium metal behaviour", International Nuclear Fuel Cycle Conference (GLOBAL 2013) (Proc. Int. Conf. Salt Lake City, 2013), Curran Associated Inc., Red Hook (2014).

[148] HAWES, P.M., Ignition of uranium hydride and Magnox in reduced oxygen atmospheres, Rep. EP/DVW/0786/P20 CPDG(86)P686, BNFL, Warrington (1986).
[149] WARF, J.C., Chemical properties of uranium hydride, Rep. AECD-2997, US AEC, Washington (1949), https://doi.org/10.2172/4419135
[150] ELECTRIC POWER RESEARCH INSTITUTE, BWR Zircaloy Corrosion and Water Chemistry Tests: Joint EPRI/Japan Joint Utility Group/Tokyo Electric Power Company Funded Studies, Rep. TR-106830, EPRI, Palo Alto (1997).
[151] COTTIS, B., et al., Shreir's Corrosion, Vol. 3&4, Elsevier BV, Netherlands (2010), https://doi.org/10.1016/C2009-1-28357-2
[152] HILLNER, E., FRANKLIN, D.G., SMEE, J.D., The Corrosion of Zircaloy-clad Fuel Assemblies in a Geological Repository Environment, Rep. WAPD-T-3173, Bettis Atomic Power Laboratory, West Mifflin, PA (1994).
[153] MOTTA, A.T., COUET, A., COMSTOCK, R.J., Corrosion of Zirconium Alloys Used for Nuclear Fuel Cladding, Annu. Rev. Mater. Res. **45** 1 (2015) 311–343, https://doi.org/10.1146/annurev-matsci-070214-020951
[154] FRAKER, A., Corrosion of Zircaloy Spent Fuel Cladding in a Repository, Rep. NISTIR 89-4114, NIST, Gaithersburg, MD (1989), https://doi.org/10.6028/NIST.IR.89-4114
[155] KENT, R., FITZ, M., CLINE, K., EVANS, S., KENTALA, L., Microbiologically Influenced Corrosion (MIC), MDE Inc., (2007).
[156] LISTER, D., COOK, W., "Nuclear Plant Materials and Corrosion", The Essential CANDU, UNENE, McMaster University, Ontario (2014).
[157] INTERNATIONAL ATOMIC ENERGY AGENCY, Durability of Spent Nuclear Fuels and Facility Components in Wet Storage, IAEA TECDOC No. 1012, IAEA, Vienna (1998).
[158] ORGANISATION FOR ECONOMIC CO-OPERATION AND DEVELOPMENT/ NUCLEAR ENERGY AGENCY, Benchmark Study of the Accident at the Fukushima Daiichi Nuclear Power Plant - Summary Report, Rep. NEA No. 7525, OECD (NEA), Paris (2021).
[159] SUYAMA, K., UCHIDA, Y., KASHIMA, T., ITO, T., MIYAJI, T., Burn-up Credit Criticality Safety Benchmark Phase III-C Nuclide Composition and Neutron Multiplication Factor of a Boiling Water Reactor Spent Fuel Assembly for Burn-up Credit and Criticality Control of Damaged Nuclear Fuel, Rep. NEA-NSC-R-2015-6, OECD (NEA), Paris (2016).
[160] NISHIHARA, K., IWAMOTO, H., SUYAMA, K., Estimation of Fuel Compositions in Fukushima-Daiichi Nuclear Power Plant, Rep. JAEA-Data/Code 2012-018, JAEA, Tokai-Mura (2012), https://doi.org/10.11484/jaea-data-code-2012-018
[161] YAMAMOTO, T., Compilation of Measurement and Analysis Results of Isotopic Inventories of Spent BWR Fuels, Rep., JNES, Tokyo (2009).
[162] INTERNATIONAL ATOMIC ENERGY AGENCY, The Fukushima Daiichi Accident Technical Volume 2/5 Safety Assessment, IAEA, Vienna, (2015).
[163] ORGANISATION FOR ECONOMIC CO-OPERATION AND DEVELOPMENT/ NUCLEAR ENERGY AGENCY, Benchmark Study of the Accident at the Fukushima Daiichi Nuclear Power Plant (BSAF Project) - Phase I Summary Report, Rep. NEA/CSNI/R(2015)18, OECD (NEA), Paris (2015).
[164] PELOWITZ, D.B., MCNPX User's Manual. Version 2.7.0, Rep. LA-CP-11-00438, LANL, Los Alamos (2011).
[165] FENSIN, M.L., HENDRICKS, J.S., MCKINNEY, G.W., Monte Carlo Burn up Interactive Tutorial, LA-UR-09-02051, LANL, Los Alamos (2009).

[166] BRATTON, I.J., Modeling and validation of the fuel depletion and burnup of the OSU Research Reactor using MCNPX/CINDER'90, Master Thesis, Ohio State University, Ohio (2012).
[167] BADAWI, A.A., ELSHAHAT, A.E., MAHMOUD ABOU ALO, R.F., SHAAT, M.K., An Investigation of Corium in Fukushima Daiichi Unit-1 Accident, Appl. Radiat. Isot. **186** (2022) 110264,
https://doi.org/10.1016/j.apradiso.2022.110264
[168] MCCONN, J.R.J., GESH, C.J., PAGH, R.T., RUCKER, R.A., WILLIAMS III, R.G., Compendium of Material Composition Data for Radiation Transport Modeling, Rep. PNNL-15870 Rev. 1, PNNL, Richland (2011),
https://doi.org/10.2172/1023125
[169] SHAAT, M.K., ABDELHADY, A., MAHMOUD, R.F., Radiological Impact due to Atmospheric Releases of the Source Term for F-D, Unit 1, Using HOTSPOT Code, Ann. Ecol. Environ. Sci. **3** 1 (2019) 33–39,
https://doi.org/10.22259/2637-5338.0301005
[170] MINISTRY OF EDUCATION, CULTURE, SPORTS, SCIENCE AND TECHNOLOGY, Results of Third Airbourne Monitoring Survey by MEXT, Rep., MEXT, Tokyo (2011).
[171] INSTITUT DE RADIOPROTECTION ET DE SÛRETÉ NUCLÉAIRE, Fukushima One Year After the Accident, Rep. IRSN-DG-2012-03, IRSN, Fontenay-aux-Roses (2012).
[172] TERADA, H., KATATA, G., CHINO, M., NAGAI, H., Atmospheric discharge and dispersion of radionuclides during the Fukushima Dai-ichi Nuclear Power Plant accident. Part II: verification of the source term and analysis of regional-scale atmospheric dispersion, J. Environ. Radioact. **112** (2012) 141–154,
https://doi.org/10.1016/j.jenvrad.2012.05.023
[173] KORSAKISSOK, I., MATHIEU, A., DIDIER, D., Atmospheric dispersion and ground deposition induced by the Fukushima Nuclear Power Plant accident: A local-scale simulation and sensitivity study, Atmospheric Environ. **70** (2013) 267–279,
https://doi.org/10.1016/j.atmosenv.2013.01.002
[174] CHINO, M., et al., Preliminary Estimation of Release Amounts of $^{131}$I and $^{137}$Cs Accidentally Discharged from the Fukushima Daiichi Nuclear Power Plant into the Atmosphere, J. Nucl. Sci. Technol. **48** 7 (2011) 1129–1134,
https://doi.org/10.1080/18811248.2011.9711799
[175] STOHL, A., et al., Xenon-133 and caesium-137 releases into the atmosphere from the Fukushima Dai-ichi nuclear power plant: determination of the source term, atmospheric dispersion, and deposition, Atmos. Chem. Phys. **12** 5 (2012) 2313–2343,
https://doi.org/10.5194/acp-12-2313-2012
[176] HIRAO, S., YAMAZAWA, H., NAGAE, T., Estimation of release rate of iodine-131 and cesium-137 from the Fukushima Daiichi nuclear power plant, J. Nucl. Sci. Technol. **50** 2 (2013) 139–147,
https://doi.org/10.1080/00223131.2013.757454
[177] UNITED STATES NUCLEAR REGULATORY COMMISSION, Accident Source Terms for Light–Water Nuclear Power Plants, Rep. NUREG–1465, US NRC, Washington (1995).
[178] HOMANN, S.G., ALUZZI, F., HotSpot, Health Physics Codes, Version 3.0, User's Guide, LLNL-SM-636474, Lawrence Livermore National Laboratory, USA, (2014).
[179] MAHMOUD, R.F., ABDU, M.M., SHAAT, M.K., Isotopic Inventory and Activity calculations for Fukushima Daiichi Unit-1 Accident, Arab J. Nucl. Sci. Appl. **54** 3 (2021) 26—33,
https://doi.org/10.21608/ajnsa.2021.40762.1397

[180] UNITED STATES ENVIRONMENTAL PROTECTION AGENCY, Limiting Values of Radionuclide Intake and Air Concentration and Dose Conversion Factors for Inhalation, Submersion and Ingestion, FGR No. 11, US EPA, Washington (1988), https://doi.org/10.2172/6294233
[181] UNITED STATES ENVIRONMENTAL PROTECTION AGENCY, External Exposure to Radionuclide in Air, Water and Soil, FGR No. 12, US EPA, Washington (1993).
[182] UNITED STATES ENVIRONMENTAL PROTECTION AGENCY, Cancer Risk Coefficients for Environmental Exposure to Radionuclides, FGR No. 13, US EPA, Washington (1999).
[183] INTERNATIONAL COMMISSION ON RADIOLOGICAL PROTECTION, Limits for Intake of Radionuclide by Workers, ICRP No. 30, ICRP, Ottawa (1979).
[184] INTERNATIONAL COMMISSION ON RADIOLOGICAL PROTECTION, Human Respiration Tract Model for Radiological Protection, ICRP No. 66, ICRP, Ottawa (1994).
[185] INTERNATIONAL COMMISSION ON RADIOLOGICAL PROTECTION, 1990 Recommendations of the International Commmission on Radiological Protection, ICRP No. 60, ICRP, Ottawa (1991).
[186] INTERNATIONAL COMMISSION ON RADIOLOGICAL PROTECTION, Basic Anatomical & Physical Data for Use in Radiological Protection – The skeleton, ICRP No. 70, ICRP, Ottawa (1995).
[187] MAHMOUD, R.F., ABDU, M.M., SHAAT, M.K., "Core modelling and source term calculations using MCNPX code for Fukushima Daiichi unit-1 nuclear power plant accident", International Conference on the Management of Spent Fuel from Nuclear Power Reactors: Learning from the Past, Enabling the Future (Proc. Int. Conf. Vienna, 2019), IAEA, Vienna (2020).
[188] ALLISON, C.M., et al., Preliminary Assessment of the Possible BWR Core/Vessel Damage States for Fukushima Daiichi Station Blackout Scenarios Using RELAP/SCDAPSIM, Sci. Technol. Nucl. **2012** (2012) 646327, https://doi.org/10.1155/2012/646327
[189] GOVERNMENT OF JAPAN, Report of Japanese Government to IAEA Ministerial Conference on Nuclear Safety - Accident at TEPCO's Fukushima Nuclear Power Stations, Govrnment of Japan, Tokyo (2011).
[190] ALLISON, C.M., HOHORST, J.K., Role of RELAP/SCDAPSIM in Nuclear Safety, Sci. Technol. Nucl. **2010** (2010) 425658, https://doi.org/10.1155/2010/425658
[191] TANABE, F., Analysis of Core Melt Accident in Fukushima Daiichi-Unit 1 Nuclear Reactor, J. Nucl. Sci. Technol. **48** 8 (2011) 1135–1139, https://doi.org/10.1080/18811248.2011.9711800
[192] VALDÉS-PARADA, F.J., ROMERO-PAREDES, H., ESPINOSA-PAREDES, G., Numerical analysis of hydrogen generation in a BWR during a severe accident, Chem. Eng. Res. Des. **91** 4 (2013) 614–624, https://doi.org/10.1016/j.cherd.2013.02.012
[193] GARLAND, W.J., Decay Heat Estimates for MNR, Rep. 1998-03, McMaster Nuclear Reactor, Hamilton (1999).
[194] AMERICAN NUCLEAR SOCIETY, Decay Heat Power in Light Water Reactors, ANS Standard 5.1, ANS, IL (2005).
[195] TODREAS, N.E., KAZIMI, M.S., Nuclear Systems Volume 1: Thermal Hydraulic Fundamentals, 2nd ed., CRC Press, Boca Raton, FL (2011), https://doi.org/10.1201/b14887

[196] ALLISON, C.M., et al., SCDAP/RELAP5/MOD 3.2 Code Manual Volume II: Damage Progression Model Theory, Rep. NUREG/CR-6150 INEL-96/0422, INEEL, Idaho Falls, ID (1997).
[197] HOFMANN, P., HAGEN, S., SCHANZ, G., SKOKAN, A., Chemical interactions of reactor core materials up to very high temperatures, Rep. KfK 4485, KfK, Karlsruhe (1989), https://doi.org/10.5445/IR/270027458
[198] SCHWANTES, J.M., ORTON, C.R., CLARK, R.A., Analysis of a Nuclear Accident: Fission and Activation Product Releases from the Fukushima Daiichi Nuclear Facility as Remote Indicators of Source Identification, Extent of Release, and State of Damaged Spent Nuclear Fuel, Environ. Sci. Technol. **46** 16 (2012) 8621–8627, https://doi.org/10.1021/es300556m
[199] ZHONG, W., et al., Performance of iron–chromium–aluminum alloy surface coatings on Zircaloy 2 under high-temperature steam and normal BWR operating conditions, J. Nucl. Mater. **470** (2016) 327–338, https://doi.org/10.1016/j.jnucmat.2015.11.037
[200] ROBB, K.R., FARMER, M., FRANCIS, M.W., Enhanced Ex-Vessel Analysis for Fukushima Daiichi Unit 1: Melt Spreading and Core-Concrete Interaction Analyses with MELTSPREAD & CORQUENCH, Rep. ORNL/TM-2012/455, ORNL, Oak Ridge (2013), https://doi.org/10.2172/1063828
[201] BONNEVILLE, H., CARENINI, L., BARRACHIN, M., Core Melt Composition at Fukushima Daiichi: Results of Transient Simulations with ASTEC, Nucl. Technol. **196** 3 (2016) 489–498, https://doi.org/10.13182/NT16-27
[202] NUÑEZ-CARRERA, A., CAMARGO-CAMARGO, R., ESPINOSA-PAREDES, G., LÓPEZ-GARCÍA, A., Simulation of the Lower Head Boiling Water Reactor Vessel in a Severe Accident, Sci. Technol. Nucl. **2012** (2012) 305405, https://doi.org/10.1155/2012/305405
[203] POLO-LABARRIOS, M.A., ESPINOSA-PAREDES, G., Comparative study of the hydrogen generation during short term station blackout (STSBO) in a BWR, Ann. Nucl. Energy **83** (2015) 274–282, https://doi.org/10.1016/j.anucene.2015.04.027
[204] YANEZ, J., KUZNETSOV, M., SOUTO-IGLESIAS, A., An analysis of the hydrogen explosion in the Fukushima-Daiichi accident, Inter. J. Hydrogen Energ. **40** 25 (2015) 8261–8280, https://doi.org/10.1016/j.ijhydene.2015.03.154
[205] MIZOKAMI, S., KUMAGAI, Y., "Event Sequence of the Fukushima Daiichi Accident", Reflections on the Fukushima Daiichi Nuclear Accident: Toward Social-Scientific Literacy and Engineering Resilience, Springer International Publishing, NY (2015), https://doi.org/10.1007/978-3-319-12090-4_2
[206] GALUSHIN, S., KUDINOV, P., Sensitivity analysis of debris properties in lower plenum of a Nordic BWR, Nucl. Eng. Des. **332** (2018) 374–382, https://doi.org/10.1016/j.nucengdes.2018.03.029
[207] PARK, R.-J., KANG, K.-H., HONG, S.-W., KIM, H.-Y., Detailed evaluation of melt pool configuration in the lower plenum of the APR1400 reactor vessel during severe accidents, Ann. Nucl. Energy **75** (2015) 476–482, https://doi.org/10.1016/j.anucene.2014.07.055
[208] MA, W., YUAN, Y., SEHGAL, B.R., In-Vessel Melt Retention of Pressurized Water Reactors: Historical Review and Future Research Needs, Engineering **2** 1 (2016) 103–111, https://doi.org/10.1016/J.ENG.2016.01.019

[209] ASMOLOV, V., PONOMAREV-STEPNOY, N.N., STRIZHOV, V., SEHGAL, B.R., Challenges left in the area of in-vessel melt retention, Nucl. Eng. Des. **209** 1 (2001) 87–96, https://doi.org/10.1016/S0029-5493(01)00391-0
[210] STRIZHOV, V.,"Corium debris configurations in course of accident, Russian Academy of Sciences", 1st International Forum on the Decommissioning of the Fukushima Daiichi Nuclear Power Station (Proc. Int. Conf. Iwaki City, 2016), NDF, Tokyo (2016).
[211] MIN, B.T., et al., Phase separation of metal-added corium and its effect on a steam explosion, J. Nucl Mater. **377** 3 (2008) 458–466, https://doi.org/10.1016/j.jnucmat.2008.03.019
[212] MADOKORO, H., MIASSOEDOV, A., SCHULENBERG, T., Assessment of a lower head molten pool analysis module using LIVE experiment, Nucl. Eng. Des. **330** (2018) 51–58, https://doi.org/10.1016/j.nucengdes.2018.01.036
[213] SOHAL, M.S., SIEFKEN, L.J., A Heat Transfer Model for a Stratified Corium-Metal Pool in the Lower Plenum of a Nuclear Reactor, Rep. INEEL/EXT-99-00763, INEEL, Idaho Falls, ID (1999), https://doi.org/10.2172/761806
[214] PANDAZIS, P., HOLLANDS, T., GAUS-LIU, X., MIASSOEDOV, A., Experimental and numerical investigation of molten corium behavior in lower head under external subcooling and boiling conditions, Ann. Nucl. Energy **120** (2018) 888–895, https://doi.org/10.1016/j.anucene.2018.06.020
[215] PARISI, C., DEL NEVO, A., NEGRENTI, E., SEPIELLI, M., Simulation & analysis of the severe accident of the Unit 1 of Fukushima Daiichi NPP, Energia, Ambiente Innovazione **2** (2012) 56–61.
[216] LUXAT, D.L., GABOR, J.R., WACHOWIAK, R.M., YANG, R.L., EPRI MAAP5 Fukushima Daiichi Analysis, Nucl. Technol. **196** 3 (2016) 698–711, https://doi.org/10.13182/NT16-56
[217] SEVÓN, T., NIEMINEN, A., "Thermal hydraulics of severe accidents (TERMOSAN)", SAFIR2014: The Finnish Research Programme on Nuclear Power Plant Safety 2011-2014, Rep. VTT Technology No. 80, VTT Technical Researh Centre of Finland, Espoo (2013).
[218] PARK, R.J., HA, K.S., KIM, S.B., KIM, H.D., Two-phase natural circulation flow of air and water in a reactor cavity model under an external vessel cooling during a severe accident, Nucl. Eng. Des. **236** 23 (2006) 2424–2430, https://doi.org/10.1016/j.nucengdes.2006.03.006
[219] CHEN, L., et al., Three-dimensional experiment of heat transfer for molten oxidic pool, Prog. Nucl. Energ. **103** (2018) 209–216, https://doi.org/10.1016/j.pnucene.2017.11.014
[220] SANDIA NATIONAL LABORATORIES, Fukushima Daiichi Accident Study (Status as of April 2012), Rep. SAND2012-6173, SNL, Albuquerque (2012), https://doi.org/10.2172/1055601
[221] HOFMANN, P., Current knowledge on core degradation phenomena, a review, J. Nucl. Mater. **270** 1 (1999) 194–211, https://doi.org/10.1016/S0022-3115(98)00899-X
[222] AN, S.M., SONG, J.H., KIM, J.-Y., KIM, H., NAITOH, M., Experimental investigation on molten pool representing corium composition at Fukushima Daiichi nuclear power plant, J. Nucl. Mater. **478** (2016) 164–171, https://doi.org/10.1016/j.jnucmat.2016.06.011
[223] LIN, B., QIU, S.Z., SU, G.H., TIAN, W.X., ZHANG, Y.P., Development and verification of molten corium–concrete interaction code, Prog. Nucl. Energ. **85** (2015) 701–706, https://doi.org/10.1016/j.pnucene.2015.07.003

[224] KITAGAKI, T., YANO, K., OGINO, H., WASHIYA, T., Thermodynamic evaluation of the solidification phase of molten core–concrete under estimated Fukushima Daiichi nuclear power plant accident conditions, J. Nucl. Mater. **486** (2017) 206–215, https://doi.org/10.1016/j.jnucmat.2017.01.032
[225] INTERNATIONAL ATOMIC ENERGY AGENCY, Thermophysical Properties Database of Materials for Light Water Reactors and Heavy Water Reactors. Final Report of a Coordinated Research Project 1999–2005, IAEA–TECDOC–1496, IAEA, Vienna (2006).
[226] FINK, J.K., Thermophysical properties of uranium dioxide, J. Nucl. Mater. **279** 1 (2000) 1–18, https://doi.org/10.1016/S0022-3115(99)00273-1
[227] KIM, W.K., SHIM, J.H., KAVIANY, M., Thermophysical properties of liquid $UO_2$, $ZrO_2$ and corium by molecular dynamics and predictive models, Journal of Nucl. Mater. **491** (2017) 126–137, https://doi.org/10.1016/j.jnucmat.2017.04.030
[228] POPOV, S.G., CARBAJO, J.J., IVANOV, V.K., YODER, G.L., Thermophysical Properties of MOX and $UO_2$ Fuels Including the Effects of Irradiation, Rep. ORNL/TM-2000/351, ORNL, Oak Ridge (2000), https://doi.org/10.2172/777671
[229] INTERNATIONAL ATOMIC ENERGY AGENCY, Thermophysical Properties of Materials for Water Cooled Reactors, IAEA-TECDOC-949, IAEA, Vienna (1997).
[230] KOROBENKO, V.N., SAVVATIMSKII, A.I., Temperature Dependence of the Density and Electrical Resistivity of Liquid Zirconium up to 4100 K, High Temp. **39** 4 (2001) 525–531, https://doi.org/10.1023/A:1017932122529
[231] NAGIN, C.A., The Cleanup of Three Mile Island Unit 2: Technical History 1979 to 1990. Rep. EPRI NP-6931., EPRI, Palo Alto (1990).
[232] GENERAL PUBLIC UTILITY, Accident-Generated Water Disposal Completion Report, GPU Inc., Parsippany , NJ (1993).
[233] URLAND, C.S., TMI-2 postaccident data acquisition and analysis experience, Rep.EPRI-NP--7156, EPRI, Palo Alto (1992).
[234] GOLD, R., et al., Neutron Dosimetry with Solid State Track Recorders in the Three-Mile Island Unit-2 Reactor Cavity, Nucl. Tracks Radiat. Meas. **10** 3 (1985) 447–459, https://doi.org/10.1016/0735-245X(85)90172-3
[235] BELLER, L.S., BROWN, H.L., Design and operation of the core topography data acquisition system for TMI-2, Rep. GEND-INF-012, EG&G Inc., Idaho Falls, ID (1984), https://doi.org/10.2172/6837047
[236] UNITED STATES NUCLEAR REGULATORY COMMISSION, Three Mile Island Accident of 1979 Knowledge Management Digest – Recovery and Cleanup, Rep. NUREG/KM-0001, Supplement 1, US NRC, Washington (2016).
[237] CROUCHER, D.W., Three Mile Island Unit–2 Core Status Summary: A Basis for Tool Development for Reactor Disassembly and Defueling, Rep. GEND–007, EG&G Idaho Inc., ID (1981), https://doi.org/10.2172/6424968
[238] FALK, D.E., SWENSON, C.E., TMI-2 Defueling System Design Description, Rep. GEND-INF-065, EG&G Inc., Idaho Falls, ID (1985), https://doi.org/10.2172/5571102
[239] BECHTEL NORTH AMERICAN POWER CORPORATION, TMI-2 Defueling Tools Engineering Report, Rep.GEND-INF-073, EG&G Inc., Idaho Falls, ID (1986), https://doi.org/10.2172/5904574

[240] PINCOCK, L., HINTZE, W., Stability of Molten Core Materials, Rep. INL/EXT-12-27136 Rev. 1, INL, Idaho Falls, ID (2013), https://doi.org/10.2172/1073781
[241] KIRKLAND, H.W., NEMSER, M.A., LANEY, W.M., Drilling Operations to Remove the Lower Core Support Assembly at Three Mile Island Unit 2, Nucl. Technol. **87** 4 (1989) 932–945, https://doi.org/10.13182/NT89-A27687
[242] BENGEL, P.R., SMITH, M.D., ESTABROOK G.A., TMI-2 Reactor Vessel Head Removal, Rep. GEND-INF-062, EG&G Inc., Idaho Falls, ID (1984), https://doi.org/10.2172/6181271
[243] BELYAEV, S.T., BOROVOI, A.A., BUSULUKOV, Y.P., "Some Aspects of Post Accident Activity in Control Zone of Chernobyl NPP", International Symposium On Recovery Operation in the Event on Nuclear Accident or Radiological Emergency (Proc. Int. Symp. Vienna, 1989), IAEA, Vienna (1989).
[244] IVANOV, O.P., SUDARKIN, A.N., STEPANOV, V.E., URUTSKOEV, L.I., Portable Digital X-Ray and Gamma-Ray Imager with Coded Mask: Performance Characteristics and Methods of Image Reconstruction., Nucl. Instrum. Methods Phys. Res. A **422** (1999) 729–734, https://doi.org/10.1016/S0168-9002(98)01026-2
[245] IVANOV, O.P., et al., "New portable gamma camera for nuclear environment and its application at rehabilitation works", IEEE Nuclear Science 2004 (Proc. Int. Conf. Rome, 2004), IEEE, New York (2004) 1559–1562, https://doi.org/10.1109/NSSMIC.2004.1462537
[246] BOROVOI, A.A., Analytical Report: Post-Accident Management of Destroyed Fuel from Chernobyl, IAEA working material, IAEA, Vienna (1990).
[247] VASIL'EV, S.K., PETROV, B.F., PLESKACHEVSKII, L.A., Complex of works of the radiometry laboratory of the Radium Institute in Chernobyl: June-November 1986, Proceedings of V.G. Khlopin Radium Institute **XIV** (2009) 23–45.
[248] USATYJ, A.F., "Generalized results of determination of distributions of major gamma radiation sources in the central hall of the Sarcophagus, recorded by dosimetric cords using EPR sensors", Proc. Sarcophagus Safety'94. The State of Chernobyl Nuclear Power Plant Unit 4. Proceedings of an International Symposium, 14-18 March 1994 Zeleney Mys, Ukraine, 1994 (abstract).
[249] USATYI, A.F., VEREIN, N.V., EPR – based dosimetry of large dimensional radiation fields (Chernobyl experience and new approaches), Appl. Radiat. Isot. **47** 11/12 (1996) 1351–1356, https://doi.org/10.1016/S0969-8043(96)00146-7
[250] Proceedings of International Conference "Fiftieth Anniversary of Nuclear Fission", Vol.2, Leningrad, USSR, October 16-20, 1989. Saint-Petersburg, V.G. Khlopin Radium Institute, 1992, Proc. (abstract) (in Russian).
[251] A.A., R.-K., "Use of relative fission product release to estimate the fuel temperature after Chernobyl accident", Proc. Proceedings of the First International Workshop on Severe Accidents and their Consciences, Sochi, USSR, 30 October – 3 November 1989, 1989 (abstract).
[252] BOROVOY, A.A., VELIKHOV, E.P., Experience of Chernobyl (Vol.2). National Research Center (Kurchatov Institute), Moscow (2013) 162 pp (in Russian).
[253] BELAYEV, S., BOROVOI, A., "Radioactivity Releases from the Chernobyl NPP Accident", International Conference Comparison of Consequences of Three Accidents: Kyshtim, Chernobyl, Windscale, Proc. Luxembourg, October 1–5, (1990).

[254] BOROVOI, A., IVANOV, A., SICH, A., "Use of robotic technologies and remote systems for diagnostic and research within the Chernobyl Sarcophagus", Proc. Proceedings of ANS Fifth Topical Meeting on Robotics and Remote Systems, Knoxvill, Tennessee, April 25–30, 1993, 1993 (abstract).
[255] YANO, K., et al.,"Direction on characterization of fuel debris for defueling process in Fukushima Daiichi Nuclear Power Station", International Nuclear Fuel Cycle Conference (GLOBAL 2013) (Proc. Int. Conf. Salt Lake City, 2013), Curran Associated Inc., Red Hook (2014).
[256] TOKYO ELECTRIC POWER COMPANY, The 6th Progress Report on the Investigation and Examination of Unconfirmed and Unsolved Issues on the Development Mechanism of the Fukushima Daiichi Nuclear Accident, (2022), https://www.tepco.co.jp/en/hd/decommission/information/accident_unconfirmed/pdf/20221110-e.pdf
[257] ARAI, T., Robots Technology for decommissioning of Fukushima Daiichi Nuclear Power Stations, (2019), https://irid.or.jp/_pdf/20190526.pdf
[258] TOKYO ELECTRIC POWER COMPANY, Development of a technology to investigate inside the Reactor Primary Containment Vessel (PCV), (2015), https://www.tepco.co.jp/en/nu/fukushima-np/handouts/2015/images/handouts_150430_04-e.pdf
[259] TOKYO ELECTRIC POWER COMPANY, Fukushima Daiichi Nuclear Power Station Unit 2 Primary Containment Vessel Internal Investigation Results, (2019), https://www.tepco.co.jp/en/wp-content/uploads/handouts_190228_01-e.pdf
[260] INTERNATIONAL RESEARCH INSTITUE FOR NUCLEAR DECOMMISSIONING, Improvement of PCV Internal Survey Device (Scorpion-Type Robot) [developer: Toshiba] (February 18, 2016), (2016) (in Japanese), https://irid.or.jp/topics/pcv%e5%86%85%e9%83%a8%e8%aa%bf%e6%9f%bb%e8%a3%85%e7%bd%ae%ef%bc%88%e3%82%b5%e3%82%bd%e3%83%aa%e5%9e%8b%e3%83%ad%e3%83%9c%e3%83%83%e3%83%88%ef%bc%89%e3%81%ae%e6%94%b9%e8%89%af%e3%81%ab%e3%81%a4/
[261] TOKYO ELECTRIC POWER COMPANY, Investigation inside Unit 2 Primary Containment Vessel, (2017) (in Japanese), https://www.tepco.co.jp/decommission/common/images/progress/retrieval/unit2_meeting_20170330.pdf
[262] TOKYO ELECTRIC POWER COMPANY, Fukushima Daiichi Nuclear Power Station Unit 2 Primary Containment Vessel Internal Investigation Results, (2018), https://www.tepco.co.jp/en/nu/fukushima-np/handouts/2018/images/handouts_180201_01-e.pdf
[263] SUGIURA, T., SHIMIZU, C., SAKAMOTO, N., Investigation by making contact with deposits believed to be nuclear fuel debris at bottom of PCV of Fukushima Daiichi Nuclear Power Station Unit 2, Toshiba Rebyu **74** 6 (2019) 63–66 (in Japanese).
[264] TOSHIBA ENERGY SYSTEMS & SOLUTIONS CORPORATION, Fukushima Daiichi Nuclear Power Station Unit 2 Developed a Device to Investigate Sediment Inside the Reactor Containment Vessel, (2019) (in Japanese), https://www.global.toshiba/jp/news/energy/2019/01/news-20190128-01.html

[265] INTERNATIONAL RESEARCH INSTITUE FOR NUCLEAR DECOMMISSIONING, Investigation Inside Primary Containment Vessel (PCV): Development of Submersible Crawling Robot to Survey Inside PCV of Fukushima Daiichi Unit 3 [development by Toshiba] (June 15, 2017), (2017), https://irid.or.jp/en/topics/pcv%e5%86%85%e9%83%a8%e8%aa%bf%e6%9f%bb%ef%bc%8f3%e5%8f%b7%e6%a9%9f%e5%8e%9f%e5%ad%90%e7%82%89%e6%a0%bc%e7%b4%8d%e5%ae%b9%e5%99%a8%e5%86%85%e9%83%a8%e3%82%92%e9%81%8a%e6%b3%b3%e3%81%97%e8%aa%bf/

[266] ONO, A., 2022 IAEA General Conference, Side Event-Fukushima Daiichi Decommissioning Current Status and Challenges, (2022), https://www.meti.go.jp/english/earthquake/nuclear/decommissioning/pdf/20221006_001b.pdf

[267] INTERNATIONAL RESEARCH INSTITUE FOR NUCLEAR DECOMMISSIONING, Boat-Type Submersible Access Devices to Investigate Interiors of PCV at Fukushima Daiichi Nuclear Power Station [developed by Hitachi GE Nuclear Energy, LTD. in 2019], (2019), https://irid.or.jp/en/topics/%e7%a6%8f%e5%b3%b6%e7%ac%ac%e4%b8%80%e5%8e%9f%e5%ad%90%e5%8a%9b%e7%99%ba%e9%9b%bb%e6%89%80%ef%bc%91%e5%8f%b7%e6%a9%9f%e5%8e%9f%e5%ad%90%e7%82%89%e6%a0%bc%e7%b4%8d%e5%ae%b9%e5%99%a8%e5%86%85%e9%83%a8/

[268] INTERNATIONAL RESEARCH INSTITUE FOR NUCLEAR DECOMMISSIONING, Annual Research Report 2019, (2019), https://irid.or.jp/wp-content/uploads/2020/08/pamphleth31_eng.pdf

[269] AMERICAN SOCIETY FOR TESTING AND MATERIALS INTERNATIONAL, Standard Guide for Drying of Spent Nuclear Fuel, ASTM C–1553–21, ASTM International, West Conshohocken, PA (2021), https://dx.doi.org/10.1520/C1553-21

[270] GERBER, M.S., Spent fuel removal concludes at Hanford's K Basins - Helping to restore the Columbia River's Hanford reach, Radwaste Solutions **12** 1 (2005) 10–22.

[271] STANDRING, P., "Dry Storage of Spent Fuels in the UK", Nuclear Waste Technology Review Board Fall 2019 Board Meeting (Proc. Washington (2019), NWTRB, Washington (2019 ).

[272] AMERICAN SOCIETY OF MECHANICAL ENGINEERS, Boiler and Pressure Vessel Code: Section VIII -Rules for Construction of Pressure Vessels Division 1, ASME BPVC.VIII.1, ASME, NY (2023).

[273] SCHMITT, R.C., TYACKE, M.J., QUINN, G.J., Historical Summary of the Three Mile Island Unit 2 Core Debris Transportation Campaign, Rep. DOE/ID-10400, EG&G Inc. Idaho, Idaho Falls, ID (1993), https://doi.org/10.2172/10140313

[274] CHRISTIAN, J.D., Analysis of TMI-2 Canister Water - JDC-08-97, Rep. INL/MIS-19-52748-Rev000, INL, Idaho Falls, ID (1997), https://doi.org/10.2172/1497035

[275] UNITED STATES NUCLEAR REGULATORY COMMISSION, Standard Review Plan for Dry Cask Storage Systems, Rep. NUREG–1536, US NRC, Washington (1997).

[276] PALMER, A., ET AL, "Drying Tests Conducted on Three Mile Island Fuel Canisters Containing Simulated Debris", ANS (Proc. Int. Conf. Reno 1996), CONF-9606116-18, 1996, (1996).

[277] CHRISTENSEN, A.B., CUSTER, K., GARDNER, R., KAYLOR, J., STALNAKER, J., Receipt and Storage Issues at the TMI-2 Irradiated Fuel Storage Installation, Proc. 10th International Conference on Nuclear Engineering, 2002 (abstract), https://doi.org/10.1115/ICONE10-22649

[278] IDAHO NATIONAL LABORATORY, Three-Mile Island Unit 2 Debris Independent Spent Fuel Storage Installation (ISFSI) Safety Analysis Report, Rep. TMI-2 SAR-II-8.4 (Rev. 6), INL, Idaho Falls, ID (2018).
[279] ZIRKER, L.R., RANKIN, R.A., FERRELL, L.J., Processes, Techniques, and Successes in Welding the Dry Shielded Canisters of the TMI-2 Reactor Core Debris, Rep. INEEL/CON-02-00113, INEEL, Idaho Falls, ID (2002).
[280] BELLER, B., "Management of Aging Storage Facilities and Spent Nuclear Fuel", Nuclear Waste Technology Review Board - Board Meeting (Proc. Washington (2014), NWTRB, Washington (2014).
[281] BELLER, B., Technology Innovation and International Partnership Workshop, September 14, 2010, Idaho Nuclear Fuel Stabilization & Disposition. US DoE, (2010).
[282] CARROLL, C., BROWNE, M., AKERS, D., BOYER, B., "Nuclear Material Accountancy Lessons Learned from the Three Mile Island (TMI) and Chernobyl Nuclear Power Plant (ChNPP) Accidents with Potential Application for Nuclear Material Accountancy at Fukushima Daiichi Nuclear Power Station", INMM 55th Annual Meeting (Proc. Int. Conf. Atlanta, 2014), INMM, Mount Laurel, NJ (2014).
[283] MURRAY, M., PERSIN, J., HORTON, G., NAKAJIMA, S., KABUKI, T., OYAMA, K., "Responding to Evolving Safeguards Challenges at Fukushima Dai–ichi", INMM & ESARD Joint Meeting (Proc. Int. Conf. Virtual Meeting, 2021), INMM, Mount Laurel, NJ (2021).
[284] INTERNATIONAL ATOMIC ENERGY AGENCY, IAEA Report on Decommissioning and Remediation after a Nuclear Accident, Action Plan on Nuclear Safety Series, IAEA, Vienna (2013).

# ANNEX

## RESEARCH PROJECTS WITHIN THE CORIUM CRP

### A–1: Management of Severely Damaged Spent Fuel and Corium

**COUNTRY/INTERNATIONAL ORGANIZATION:** Egypt

**CHIEF SCIENTIFIC INVESTIGATOR:** Mohamed K. Shaat

**CONTRACT NUMBER:** 19015

**COMPANY:** Egyptian Atomic Energy Authority (EAEA)

**BACKGROUND:** Spent nuclear fuel (SNF) should be safely managed following its removal from the reactor core. SNF is transferred to a water-pool adjacent to the reactor to allow fuel to cool down and its decay heat along with the decrease of radiation levels. It is stored in these pools for time periods ranging from a few years to decades. After cooling, SNF might be transferred to massive air-cooled dry casks for storage on site or in a centralized facility. The design of handling, packaging, transfer, and storage systems must include margins of safety for the nuclear criticality parameters, that are commensurate with methods used in calculations and demonstrate safety conditions and in the nature of the immediate environment under accident conditions. In the case of an accident such as the one at Fukushima nuclear power plant, where it was automatically shut down due to an earthquake and resulting tsunami caused most AC power in Units 1 to 4 to be lost. Unit 1 irradiated fuel had melted down and fallen to the bottom of the reactor pressure vessel (RPV) and a significant amount of the fuel fell out into the primary containment vessel (PCV) by destroying the RPV. At the same time, molten fuel might have penetrating through the concrete at the bottom of the primary containment. A parametric study of time dependent behaviour of the source term will be conducted to find out the radionuclide's activities, inventory and the radiological releases of source term starting from 2011 till the cleanup plan time of about 60 years after, that will help with partitioning the melted corium into small parts to the next stage of handling.

**SCIENTIFIC SCOPE:** The project studies the damaged nuclear fuel characterization through simulating and modelling the Fukushima accident using neutronics and thermal hydraulics codes to calculate the safety related parameters after the accident along with its environmental impacts [A1—4]. The used codes were Monte Carlo code "MCNP" to calculate the safety related parameters, i.e., criticality, inventory, and activity; RELAP/SCDAPSIM to model and simulate the station blackout "SBO" that occurred during the accident; Hotspot code to model radiological consequences and the environment pathways releases.

**RESEARCH APPROACH:** i) Characterization of the failed/damaged nuclear fuel; ii) Modelling and simulation for all nuclear, physical and chemical phenomena from retrieval through disposal; iii) Calculation of the source term releases and its radiation level, inventory of fission products and actinides during interim storage, handling, transfer to next stage and disposal; iv) Transfer knowledge to the future NPP in Egypt.

**A–2: Characterization of Ex-vessel Corium Melt**

**COUNTRY/INTERNATIONAL ORGANIZATION:** European Union

**CHIEF SCIENTIFIC INVESTIGATOR**: Philipp Pöml

**AGREEMENT NUMBER:** 18858

**COMPANY:** European Commission, Joint Research Centre (JRC) – Karlsruhe

**BACKGROUND:** While there have been considerable studies on corium melts, until now limited interpretation of data on the Chornobyl melt is available. Knowledge gaps affect the understanding of the physical and chemical conditions of fuel degradation and behaviour during the accident. Hence more detailed studies of melt samples are planned. The knowledge gathered at JRC-Karlsruhe during these studies will be reported and a review of current data from investigations and other relevant experiments and their integration to improve the overall understanding. The understanding of Chornobyl melt could provide useful information to contribute to defining effective site decommissioning strategies for severe accidents (Fukushima and Chornobyl), data for the modelling of ex-vessel corium behaviour and severe nuclear accidents.

**SCIENTIFIC SCOPE:** Analysis of three different types of samples: A melt inclusion (Zircon crystal); A hot particle; Bulk pieces of the Chornobyl melt [A5—6]. The main experimental techniques to be used are gamma spectroscopy, micro-analysis, microscopy, elastic and mechanical testing and high temperature thermo-physical measurements.

**RESEARCH APPROACH:** The key objective is to characterize element and phase distributions, and to measure relevant properties of the corium melt. This will contribute to an understanding of the conditions under which the compounds formed and the main properties relevant in assessing the stability of the damage fuel with a view to its removal and conditioning.

A review and synthesis of available knowledge collected in experimental studies carried out in JRC-Karlsruhe on corium melt from severe nuclear accidents. Analysis of samples from Chornobyl as outlined in the scope.

**A-3: Investigation of Current State of Bulk and Dispersed Samples of Lava-like Fuel Containing Materials from Chornobyl Accident**

**COUNTRY/INTERNATIONAL ORGANIZATION:** Russian Federation

**CHIEF SCIENTIFIC INVESTIGATOR:** Andrei Shiryaev

**CONTRACT NUMBER:** 20546

**COMPANY:** A. N. Frumkin Institute of Physical Chemistry & Electrochemistry – Russian Academy of Sciences

**BACKGROUND:** The accident of Chornobyl Nuclear Power Plant (ChNPP) 4th unit on 26 April 1986 lead to destruction of reactor core and release of a significant amount of solid and gaseous radioactive products to the environment due to explosion and subsequent fire. The fuel reacted with Zircaloy and construction materials (sand, concrete, serpentinite, stee), leading to formation of lava-like fuel- containing materials (LFCM) called Chornobyl lava. Several days after the accident considerable fraction of the initial lava pool spread into other rooms of the reactor building forming vertical and horizontal flows which solidified into a highly oxide dendrites, grains, and particles of Zr-U-O phases. On lower levels of the reactor building, the flow of brown lava entered water in the bubbler basin forming pumice-like material. The LFCM contain at least 80% of total amount of fuel ChNPP; the rest is believed to remain in inaccessible premises of the reactor. In the framework of this research, we will investigate deeper into structure of the bulk and dispersed samples of LFCM both collected in 1990 and stored at laboratory conditions and samples stored in "Shelter" in 2011-2013. The study will be complemented with the availability of modern analytical equipment to help with detailed investigation and understanding of the structural peculiarities of LFCM. The findings will contribute to identifying future behaviour of LFCM inside the former ChNPP and provide a solid basis for extrapolation to large scale data obtained in laboratory experiments on interaction of molten corium with sacrificial materials.

**SCIENTIFIC SCOPE:** The project covers the following [A7–10]:

(i) The structure of the glass matrix and compositionally similar nuclear glasses and (U and Cs) behaviour;
(ii) Interaction of the glassy matrix and solid inclusion in LFCM and the formation and growth of U-rich zircon "Chornobylite";
(iii) Studies of dispersed LFCM.

**RESEARCH APPROACH:** Present data about structure of LFCM samples obtained by reliable analytical methods. Gain deeper understanding of the behaviour of important inclusions in LFCM such as U-rich zircon and Zr-U-O phase as addressing their microstructure on atomic level and stability against interaction with water. This information is vital for strategies of handling the fuel-containing materials in the former ChNPP and of experiments on interaction of molten corium and concrete.

**A-4: Material Study of Corium and Other Highly Radioactive Materials Formed as a Result of Chornobyl Accident**

**COUNTRY/INTERNATIONAL ORGANIZATION:** Russian Federation

**CHIEF SCIENTIFIC INVESTIGATOR:** Boris Burakov

**AGREEMENT NUMBER:** 18781

**COMPANY:** V.G. Khlopin Radium Institute (KRI)

**BACKGROUND:** The accident at Chornobyl NPP 4th unit on 26 April 1986 was accompanied by the destruction and partial melting of a reactor core and release of solid and gaseous radioactive products. Various types of Chornobyl highly radioactive fuel containing materials named "lava" and "hot" particles that formed during first days of accident were collected by scientists of V.G. Khlopin Radium Institute (KRI). Part of this collection was studied by methods of optical and electron microscopy, microprobe, and X ray diffraction. The behaviour of nuclear fuel in first days of accident was considered as a three-stage process. the first occurred before the moment of the explosion and was exceptionally short-lasting, less than a few seconds. It was characterized by reaching a high temperature, more than 2873 K, in the epicentre of accident and formation of a Zr-U-O melt in a local part of the core, which is estimated to be not more than 30% of whole core volume. The second stage lasted for about 6 days after the explosion during which there was interaction between uranium products of the destroyed reactor: $UO_x$; $UO_x$ with Zr; Zr-U-O, with the environment and silicate structural materials of the 4th unit. The third stage after 6 days involved the process of final formation of the radioactive silicate melt or Chornobyl "lava" at one of the sections of the destroyed 4th unit. The formation of uranium minerals is continuing in Chornobyl. The following secondary uranium minerals were identified: $UO_4x4H_2O$ Studite; $UO_3x2H_2O$ Epianthinite; $UO_2xCO_3$ Rutherfordine and $Na_4(UO_2)(CO_3)_3$. These minerals formed due to the chemical interaction between "lava", water, and air. At the same time mechanical self-destruction of "lava" matrices was observed inside "shelter" as well as under laboratory conditions (for some samples after 11 Yrs. of storage). The results expected will allow understanding not only material science aspects of severe nuclear accidents but also a future behaviour of newly formed highly radioactive materials interacting with environment. These results will be used for modelling properties of high temperature melt in the system "Zircaloy cladding fuel" at different types of nuclear reactors and they will help to optimize future material study research of Fukushima's corium.

**SCIENTIFIC SCOPE:** Chornobyl samples results provide key-information to create computer codes of high temperature interaction between Zircaloy cladding and fuel under sever accident. In addition to that, to understand better the chemical alteration of corium and other highly radioactive materials. The samples were analysed by X ray diffraction analysis (XRD), scanning electron microscope (SEM), electron micro probe analyser (EMPA), and optical microscopy to identify U-Zr-bearing crystalline phases [A5–6, A11—14].

**RESEARCH APPROACH:** i) Summary of physico-chemical properties of Chornobyl highly radioactive samples; ii) Complete identification of U–Zr bearing crystalline phases formed as a result of high-temperature melting in the system "Zircaloy cladding fuel"; interaction of core and silicate melt and further chemical alteration by environment.

**A-5: Robots Technologies Applied to the Fukushima Daiichi Nuclear Power Station**

**COUNTRY/INTERNATIONAL ORGANIZATION:** Japan

**CHIEF SCIENTIFIC INVESTIGATOR:** Tetsuo Kotoku

**AGREEMENT NUMBER:** 21001

**COMPANY:** International Research Institute for Nuclear Decommissioning (IRID)

**BACKGROUND:** The research project provides practical and user–friendly robots to Fukushima Daiichi power station for accelerating the decommissioning work. Track records of the robots used since the outbreak of the accident in 2011 up to 2022.

**SCIENTIFIC SCOPE:** The project covers the technology development history through trial and error and addressing the needs at the site and the needs of the academia and industrial fields.

**RESEARCH APPROACH:** The results of R&D and application of the Robots technologies aimed at the use at Fukushima Daiichi power station under severely damaged internal conditions will be reported.

**A-6: Fuel Debris Characterization**

**COUNTRY/INTERNATIONAL ORGANIZATION:** Japan

**CHIEF SCIENTIFIC INVESTIGATOR:** Tadahiro Washiya

**AGREEMENT NUMBER:** 20712

**COMPANY:** Japanese Atomic Energy Agency (JAEA)

**BACKGROUND:** The Collaborative Laboratory for Advanced Decommissioning Science (CLADS) was set-up after the 1F event to undertake fundamental research in support of 1F decommissioning. The fuel debris handling and analysis division will analyse the debris when it is recovered from the reactors. To date the division has been gathering information on previous severe accident fuel debris analysis and preparing simulants for analysis based upon known materials. The results will be used to develop tools/techniques for future 1F debris retrieval, storage, conditioning, and disposal.

International collaboration will be encouraged as it will aid both knowledge management and developing expertise in fuel debris analysis techniques/result interpretation.

**SCIENTIFIC SCOPE:** Characterization of 1F fuel debris/MCCI simulants and 1F debris mechanical, thermal, physical, and chemical properties [A15—19]. The effects of alteration by sea water, B4C, Gd and Pu will also be investigated using simulants [A20—24].

**RESEARCH APPROACH:** Review and synthesis of available knowledge on severe accident fuel debris characterization/analysis (Chornobyl/TMI-2). The preparation of simulants to enable initial characterization and development of techniques for handling and analysing fuel debris. Collaboration with international researchers working in accident management/post-accident debris analysis. Analysis of 1F fuel debris samples when they become available.

**A-7: Management of Severely Damaged Spent Fuel on the Chornobyl NPP**

**COUNTRY/INTERNATIONAL ORGANIZATION:** Ukraine

**CHIEF SCIENTIFIC INVESTIGATOR:** Vladyslav Soloviov

**AGREEMENT NUMBER:** 20973

**COMPANY:** State Specialized Enterprise "Chornobyl Nuclear Power Plant" (SSE "Chornobyl NPP")

**BACKGROUND:** In April 2016, Chornobyl NPP (ChNPP) transferred all severely damaged spent fuel from Unit 1 and 2 to the intermediate spent fuel storage #1 (ISF-1) which is a temporary wet spent fuel. In 2017 a dry spent fuel storage #2 (ISF-2) was commissioned and ChNPP started transferring spent fuel from ISF-1 to ISF-2 for long term storage (100 years). At the same time, ISF-2 project did not implement the procedure for handling severely damaged spent fuel from Unit 1 and 2 stored in ISF-1. In this research project we are going to consider the possibility of long term storing severely damaged spent fuel from Unit 1 and 2.

**SCIENTIFIC SCOPE:** The project covers the possibility of storing and handling severely damaged spent fuel from Unit 1 and 2 using Gamma ray spectrometer (NaI detector), spent fuel measurement system contain fission chamber.

**RESEARCH APPROACH:** i) To assess tools and techniques for conditioning severely damaged spent fuel from Unit 1 and 2 for long term storage in dry spent fuel storage #2 (ISF-2); ii) To develop methodology for transferring and storing severely damaged spent fuel to ISF-2.

**A-8: Retrieval, Processing and Disposal of Severely Damaged Spent Fuel and Corium**

**COUNTRY/INTERNATIONAL ORGANIZATION:** United Kingdom

**CHIEF SCIENTIFIC INVESTIGATOR:** Neil Hyatt

**AGREEMENT NUMBER:** 22265

**COMPANY:** The University of Sheffield

**BACKGROUND:** A critical step in decommissioning of the damaged Chornobyl and Fukushima nuclear power plants concerns retrieval, management, and disposal of severely damaged nuclear fuels, including fuel debris, corium and melted concrete interaction (MCCI) products.

The hazard and expense of working with severely damaged nuclear fuels (SDNFs), generally requires shielded facilities with remote handling capability, limiting the scope of experimental investigations and accessible characterization techniques. Consequently, there is a need to develop low activity simulants of SDNFs, incorporating uranium and stable isotope fission products, which can be exploited for parametric experimental studies and characterization utilizing advanced techniques such as synchrotron X ray spectroscopy.

Representative low activity SDNF simulants will be designed with reference to available literature data and CRP expertise, to represent Chornobyl and/or Fukushima corium materials and/or UK fuel debris. Laboratory scale samples of simulant corium materials will be produced by high temperature reactions and characterized to determine the phase assemblage, microstructure, and density. The feasibility of reprocessing SDNFs will be assessed by investigating nitric acid dissolution of low activity simulants and first stage PUREX separation. Conceptual waste forms will be designed and prototyped at laboratory scale targeting glass and/or ceramic waste forms, by vitrification and/or hot isostatic pressing, respectively. The dissolution kinetics of the optimized simulant SDNFs and waste forms composition will be determined to evaluate their relative merit as for ultimate disposal if resources permit.

The study has relevance to inform and guide the management of fuel debris and damaged nuclear fuels, including wastes from post irradiation examination in the UK context. The University of Sheffield has previous experience in performing studies on the synthesis of Chornobyl lava-like fuel containing materials.

**SCIENTIFIC SCOPE:** Identification of potential options for managing severely damaged nuclear fuels (SDNFs), considering: i) reprocessing SDNFs to recover fissile materials and concentrate fission products; ii) direct conditioning of SDNFs, and immobilization of wastes from reprocessing to produce a passively safe waste form; iii) direct disposal of SDNFs, or disposal of passively safe waste forms derived from SDNFs.

**RESEARCH APPROACH:** The project will develop low activity simulants of corium materials arising from the Chornobyl and/or Fukushima accidents. These low activity simulants will enable investigation of reprocessing and thermal treatment of SDNFs and the disposability of SDNF materials or derived waste forms.

**A-9: Behaviour and Evolution of Stored Uranium and Oxide Fuels and Implications for Subsequent Storage**

**COUNTRY/INTERNATIONAL ORGANIZATION:** United Kingdom

**CHIEF SCIENTIFIC INVESTIGATOR:** David Hambley

**AGREEMENT NUMBER:** 18953

**COMPANY:** National Nuclear Laboratory (NNL)

**BACKGROUND:** Irradiated oxide fuel that has been in pond for many years will be recovered and examined to determine the evolution of the fuel and cladding. The spent fuel to be unrecovered includes intact fuel, PIE residues and damaged fuel which have been stored in a number of different configurations. It is anticipated that much of the fuel will have been exposed to pond water for some decades. Once exposed to water, irradiated uranium fuel oxides readily. The large volume expansion of resulting corrosion generally leads to progressive failure of the cladding and release of corrosion products. Assessments will be undertaken of the evolution of some uranium metal fuels that have been stored in open pond conditions and in nominally sealed containers with a view to understanding the implications of fuel evolution for transition to dry storage.

**SCIENTIFIC SCOPE:** The project covers the examination of the oxidation states of materials following long term exposure to pond conditions, characterization of corrosion products resulting in pond water and its composition evolution [A25]. In addition, the potential of self-heating during recovery and reprocessing operations and risks arising from different storage options [A26—27].

**RESEARCH APPROACH:** i) Understand the evolution of the irradiated oxide fuel matrix when exposed to pond water for many decades; ii) Establish models of the fuel-pond water systems that explain the observed behaviours; iii) Provide evidence of the range of behaviours that uranic fuels could exhibit depending on the conditions under which they are stored; iv) Develop understanding of the potential hazards during fuel recovery and transition to dry storage; v) Provide description of the range of behaviours that could be happened during recovery and storage of such fuels.

## BIBLIOGRAPHY TO THE ANNEX


[A1] BADAWI, A.A., ELSAHAT, A.E., ABOU ALO, M.R.F., SHAAT, M.K., An Investigation of Corium in Fukushima Daiichi Unit-1 Accident, Appl. Radiat. Isot. **186** (2022) 110264, https://doi.org/10.1016/j.apradiso.2022.110264

[A2] MAHMOUD, R.F., ABDU, M.M., SHAAT, M.K., Isotopic Inventory and Activity calculations for Fukushima Daiichi Unit-1 Accident, Arab J. Nucl. Sci. Appl. **54** 3 (2021) 26—33, https://doi.org/10.21608/ajnsa.2021.40762.1397

[A3] SHAAT, M.K., ABDELHADY, A., MAHMOUD, R.F., Radiological Impact due to Atmospheric Releases of the Source Term for F-D, Unit 1, Using HOTSPOT Code, Ann. Ecol. Environ. Sci. **3** 1 (2019) 33–39, https://doi.org/10.22259/2637-5338.0301005

[A4] MAHMOUD, R.F., ABDU, M.M., SHAAT, M.K., "Core modelling and source term calculations using MCNPX code for Fukushima Daiichi unit-1 nuclear power plant accident", International Conference on the Management of Spent Fuel from Nuclear Power Reactors: Learning from the Past, Enabling the Future (Proc. Int. Conf. Vienna, 2019), IAEA, Vienna (2020).

[A5] PÖML, P., BURAKOV, B., Study of a "hot" particle with a matrix of U-bearing metallic Zr: Clue to supercriticality during the Chernobyl nuclear accident, J. Nucl. Mater. **488** (2017) 314–318, https://doi.org/10.1016/j.jnucmat.2017.01.041

[A6] PÖML, P., BURAKOV, B., Study of the redistribution of U, Zr, Nb, Tc, Mo, Ru, Fe, Cr, and Ni between oxide and metallic phases in the matrix of a multiphase Chernobyl hot-particle extracted from a soil sample of the Western Plume, Radiochim. Acta **106** 12 (2018) 985–990, https://doi.org/10.1515/ract-2018-2957

[A7] SHIRYAEV, A.A., et al., Physico-chemical properties of Chernobyl lava and their destruction products, Prog. Nucl. Energy **92** (2016) 104–118, https://doi.org/10.1016/j.pnucene.2016.07.001

[A8] SHIRYAEV, A.A., et al., Study of mineral grains extracted from the Chernobyl "lava", Mineral Petrol. **114** 6 (2020) 489–499, https://doi.org/10.1007/s00710-020-00718-8

[A9] SHIRYAEV, A.A., et al., Forensic study of early stages of the Chernobyl accident: Story of three hot particles, J. Nucl. Mater. **511** (2018) 83–90, https://doi.org/10.1016/j.jnucmat.2018.09.003

[A10] SHIRYAEV, A.A., et al., Products of molten corium-metal interaction in chernobyl accident: Composition and leaching of radionuclides, Prog. Nucl. Energy **152** (2022) 104373, https://doi.org/10.1016/j.pnucene.2022.104373

[A11] BURAKOV, B.E., "Lava-like materials formed and solidified during Chernobyl accident", Comprehensive Nuclear Materials, 2nd ed., Elsevier, Netherlands (2020), https://doi.org/10.1016/B978-0-12-803581-8.11686-8

[A12] ZUBEKHINA, B.Y., BURAKOV, B.E., Leaching of actinides and other radionuclides from matrices of Chernobyl lava as analogues of vitrified HLW, J. Chem. Thermodyn. **114** (2017) 25–29, https://doi.org/10.1016/j.jct.2016.08.029

[A13] ZUBEKHINA, B.Y., BURAKOV, B.E., BOGDANOVA, O.G., PETROV, Y.Y., Leaching of $^{137}Cs$ from Chernobyl fuel debris: corium and lava, Radiochim. Acta **107** 12 (2019) 1155–1160, https://doi.org/10.1515/ract-2019-0009

[A14] ZUBEKHINA, B., et al., Long-term aging of Chernobyl fuel debris: Corium and lava, Sustainability **13** 3 (2021) 1073, https://doi.org/10.3390/su13031073

[A15] WASHIYA, T., YANO, K., KAJI, N., YAMADA, S., KAMIYA, M., "Study of treatment scenarios for fuel debris removed from Fukushima Daiichi NPS", ICONE-23 (Proc. Int. Conf. Chiba, Japan, May 17-21, 2015, JSME, Tokyo (2015), https://doi.org/10.1299/jsmeicone.2015.23._ICONE23-1_447

[A16] JAPAN ATOMIC ENERGY AGENCY, T.I., Analysis of debris samples of Tokyo Electric Power Company Holdings Fukushima Daiichi Nuclear Power Station (Translated document), JAEA-Review-2020-055, JAEA, Tokai-Mura (2020), https://doi.org/10.11484/jaea-review-2020-055

[A17] NAKAYOSHI, A., MITSUGI, T., SASAKI, S., MAEDA, K., Analysis of Deposits inside the Reactor at Fukushima Daiichi Nuclear Power Station in JFY 2017-2018 -The Subsidy Programs “Project of Decommissioning and Contaminated Water Management in the FY2016 Supplementary Budget, (Development of Technologies for Grasping and Analyzing Properties of Fuel Debris)”, Rep. 2022-011, J.-D.C., Japan (2022), https://doi.org/10.11484/jaea-data-code-2021-011

[A18] BARRACHIN, M., NAKAYOSHI, A., KURATA, M., MORREALE, A., ONDER, N., "Preliminary investigation of samples taken from the PCV inside of Fukushima-Daiichi Nuclear Power Plant and implications on severe accident analysis", NURETH19 (Proc. Int. Conf. Brussels, 2022) SCK CEN, Brussels (2022).

[A19] TAKANO, M., NISHI, T., High temperature reaction between sea salt deposit and $(U,Zr)O_2$ simulated corium debris, J. Nucl. Mater. **433** (2013) 32–39, https://doi.org/10.1016/j.jnucmat.2013.06.039

[A20] TAKANO, M., NISHI, T., SHIRASU, N., Characterization of solidified melt among materials of $UO_2$ fuel and $B_4C$ control blade, J. Nucl. Sci. Technol. **51** (2014) 859–875, https://doi.org/10.1080/00223131.2014.912567

[A21] PSHENICHNIKOV, A., YAMAZAKI, S., BOTTOMLEY, D., NAGAE, Y., KURATA, M., Features of a control blade degradation observed in situ during severe accident conditions in boiling water reactors, J. Nucl. Sci. Technol. **56** 5 (2019) 440–453, https://doi.org/10.1080/00223131.2019.1592724

[A22] BOUYER, V., JOURNEAU, C., HAQUET, J.F., ET, A., “Large Scale VULCANO Molten Core Concrete Interaction Test Considering Fukushima Daiichi Condition”, ERMSAR2019 (Proc. Int. Conf. Prague, 2019), Nuclear Research Czech Republic, Prague (2019).

[A23] IKUECHI, H., “Product Phase and Hardness Due to Molten Core Concrete Interaction (MCCI): Insights from Large Scale Test”, Annual Meeting of JAEA Sector of Fukushima Research and Development (Proc. Conf. Fukushima, 2018, JAEA, Tokai-Mura (2018) (in Japanese).

[A24] BRISSONNEAU, L., et al., Material characterization of the VULCANO corium concrete interaction test with concrete representative of Fukushima Daiichi Nuclear Plants, J. Nucl. Mater. **528** (2020) 151860, https://doi.org/10.1016/j.jnucmat.2019.151860

[A25] O'NEILL, R., GOODE, J., HAMBLEY, D., Failed fuel report: Characterisation and secondary alteration products, EU HORIZON 2020 - DISCO - Deliverable 2.2 - NNL 14742 (EU Ares(2019)3542316), NNL, Warrington (2019).

[A26] ORR, R., et al., Formation and physical properties of uranium hydride under conditions relevant to metallic fuel and nuclear waste storage, J. Nucl. Mater. **477** (2016) 236–245, https://doi.org/10.1016/j.jnucmat.2016.04.057
[A27] ORR, R., et al., Kinetics of the reaction between water and uranium hydride prepared under conditions relevant to uranium storage, J. Alloys Compd. **695** (2017) 3727–3735, https://doi.org/10.1016/j.jallcom.2016.11.314

## LIST OF ABBREVIATIONS

| | |
|---|---|
| 1F | Fukushima Daiichi nuclear power station |
| AC | alternating current |
| ACES | automatic cutting equipment system |
| AFHB | auxiliary fuel handling bridge |
| AFT | auxiliary fuel tubes |
| AGR | advanced gas cooled reactor |
| ALARA | as low as reasonably achievable |
| ANRE | Agency for Natural Resources and Energy (Japan) |
| ANS | American Nuclear Society |
| ASG | anti-stacking grooves |
| ASME | American Society of Mechanical Engineers |
| ASTM | American Society for Testing and Materials |
| AR | at-reactor |
| BET | Brunauer, Emmett and Teller analysis |
| BSAF | benchmark study of the accident at Fukushima Daiichi nuclear power plant |
| BSE | back scattered electron |
| BST | buffer storage tank |
| BWR | boiling water reactor |
| CAGR | commercial advanced gas cooled reactor |
| CEA | French Alternative Energies and Atomic Energy Commission |
| CEM | concrete element rich matrix |
| ChNPP | Chornobyl nuclear power plant |
| CLADS | Collaborative Laboratories for Advanced Decommissioning Science |
| CRD | control rod drive |
| CRDM | control rod drive mechanism |
| CRN | corium element rich nodules |
| CRP | coordinated research project |
| CSM | concrete storage modules |

| | |
|---|---|
| DFT | damaged fuel table |
| DOE | Department of Energy (USA) |
| DSC | dry shielded canister |
| DWC | double wall canister |
| EAEA | Egyptian Atomic Energy Authority |
| ECCS | emergency core cooling systems |
| ECMWF | The European Centre for Medium Range Weather Forecasts |
| ECP | electro-technical casting porcelain |
| EDS | energy dispersive spectroscopy |
| EDX | energy dispersive X ray spectroscopy |
| EPMA | electron probe micro analysis |
| EPRI | Electric Power Research Institute (USA) |
| EU | European Union |
| FA | fuel assembly |
| FDM | fuel debris material |
| FFAT | fresh fuel attribute test |
| FGDS | forced gas drying system |
| FGR | fission gas release |
| FP | fission product |
| FPFM | feed pond fuel monitor |
| FY | fiscal year |
| GDAS | global data assimilation system |
| GDF | geological disposal facility |
| GE | General Electric |
| GEND | General Public Utilities (GPU), Electric Power Research Institute (EPRI), the Nuclear Regulatory Commission (NRC), and the Department of Energy (DOE) |
| GPU | General Public Utilities (USA) |
| HAXPES | hard X ray photoelectron spectroscopy |
| HEPA | high efficiency particulate air |
| HF | hydrofluoric acid |

| | |
|---|---|
| HPCS | high pressure core spray system |
| HSM | horizontal storage modules |
| HV | Vickers hardness |
| HVDS | heated vacuum drying system |
| IAEA | International Atomic Energy Agency |
| IC | isolation condenser |
| ICP-MS | inductively coupled plasma mass spectrometry |
| ICP-OES | inductively coupled optical emission spectroscopy |
| ICRP | International Commission on Radiological Protection |
| INEL | Idaho National Engineering Laboratory (USA) |
| INL | Idaho National Laboratory (USA) |
| INPO | Institute of Nuclear Power Operations (USA) |
| INTEC | Idaho Nuclear Technology and Engineering Center (USA) |
| IRAT | irradiated fuel attribute tester |
| IRID | International Research Institute for Nuclear Decommissioning (Japan) |
| IRSN | Institute for Radiological Protection and Nuclear Safety (France) |
| ISF-1 | intermediate spent fuel storage no.1 |
| ISF-2 | intermediate spent fuel storage no.2 |
| ISFSI | independent spent fuel storage installation |
| ITU | Institute for Transuranium Elements (EC/JRC) |
| JAEA | Japan Atomic Energy Agency |
| JNES | Japan Nuclear Energy Safety Organization |
| JRC | Joint Research Centre (EC) |
| JST | Japan standard time |
| KRI | Khlopin Radium Institute (Russian Federation) |
| LCSA | lower core-support assembly |
| LED | light emitting diode |
| LEISAN | large scale equipment for investigation of severe accidents in nuclear reactors |
| LFCM | lava-like fuel containing masses |
| LIBS | laser induced breakdown spectroscopy |

| | |
|---|---|
| LICON | lightweight concrete |
| LOCA | loss of cooling accident |
| LPCS | low-pressure core spray system |
| LRTP | liquid radioactive waste treatment plant |
| LSC | liquid scintillation counting |
| LWR | light water cooled reactors |
| LV | Laguna Verde |
| MAAP-HP | modular accident analysis program-high pressure |
| MAAP-LP | modular accident analysis program–low pressure |
| MANFRED | multi-axis dual arm system |
| MCCI | molten corium–concrete interaction |
| MCNP | Monte Carlo N-Particle code |
| MCNPX | Monte Carlo N-Particle eXtended code |
| MEB | multi-element bottles |
| MELCOR | methods for estimation of leakages and consequences of releases |
| METI | Japanese Ministry of Economy, Trade, and Industry |
| MEXT | Japanese Ministry of Education, Culture, Sports, Science and Technology |
| NDA | Nuclear Decommissioning Authority (UK) |
| NDF | Nuclear Damage Compensation and Decommissioning Facilitation Corporation (Japan) |
| NEA | Nuclear Energy Agency of the OECD |
| NISA | Nuclear and Industrial Safety Agency (Japan) |
| NNL | National Nuclear Laboratory (UK) |
| NOAA | National Oceanic and Atmospheric Administration (USA) |
| NPP | nuclear power plant |
| NPS | nuclear power station |
| NR | normalized leach rate |
| NRC | Nuclear Regulatory Commission (USA) |
| NUHOMS | NUTECH horizontal modular storage system |
| NuPac | Nuclear Pacific (Australia) |
| NWS | Nuclear Waste Services (UK) |

| | |
|---|---|
| OASM | open air spent fuel monitor |
| OD | outside diameter |
| OECD | Organization Economic Co-operation and Development |
| OP | Onahama Peil |
| PCV | primary containment vessel |
| PHWR | pressurised heavy water reactor |
| PIE | post irradiation examination |
| PORV | pilot operated relief valve |
| PPI | pellet–pellet interface |
| PWR | pressurized water reactor |
| RAS | Russian Academy of Sciences |
| RBMK | high power channel–type reactor (reaktor bol'shoi moshchnosti kanal'nii, Russian Federation) |
| RCS | reactor coolant system |
| RELAP | reactor excursion and leak analysis program |
| RIA | reactivity-induced accident |
| RIAR | Research Institute of Atomic Reactors (Russian Federation) |
| ROSA | remotely operated service arm |
| RPV | reactor pressure vessel |
| SAR | safety analysis report |
| SBO | station blackout |
| SCB | special cask basket |
| SCDAP | severe core damage analysis package |
| SCDAPSIM | SCDAP simulation |
| SDSF | severely damaged spent fuel |
| SEM | scanning electron microscope |
| SFA | spent fuel assembly |
| SFPF | spent fuel processing facility |
| SGHWR | steam generating heavy water reactor |
| SNF | spent nuclear fuel |
| SNM | special nuclear material |

| | |
|---|---|
| SR-XA | synchrotron radiation X ray analysis |
| SRV | safety relief valve |
| SSE | State Specialized Enterprise (Ukraine) |
| STM | shielding technological module |
| STXM | scanning transmission X ray microscope |
| TAF | top of active fuel |
| TAN | Test Area North (USA) |
| TEM | transmission electron microscopy |
| TEPCO | Tokyo Electric Power Co. (Japan) |
| TGA | thermogravimetric analysis |
| THORP | thermal oxide reprocessing plant |
| TLD | thermoluminescent dosimetry |
| TMI | Three Mile Island |
| TNT | trinitrotoluene |
| TOC | total organic carbon |
| TV | television |
| UFK | combined filtering unit |
| UK | United Kingdom |
| USA | United States of America |
| USC | universal special casks |
| USSR | Union of Soviet Socialist Republics |
| UV | ultraviolet |
| VCS | visual control system |
| VDC | vacuum drying system |
| VVER | water–water power reactor (voda–vodyanoi energetichesky reaktor, Russian Federation) |
| WAGR | windscale advanced gas cooled reactor |
| WDX | wavelength-dispersive X ray spectroscopy |
| XAFS | X ray absorption fine structure |
| XCVD | next generation Cherenkov viewing device |
| XRD | X ray diffraction |

| | |
|---|---|
| XRF | X ray fluorescence |

## UNITS

| | |
|---|---|
| B | barn |
| Ci | curie |
| GWd/tHM | gigawatt-day per tonne of heavy metal ($10^9$ Wd/tHM) |
| GWd/tU | gigawatt-day per tonne of uranium ($10^9$ Wd/tU) |
| MWd/tU | megawatt-day per tonne of uranium ($10^6$ Wd/tU) |
| MWd/kgU | megawatt-day per kilogram of uranium ($10^6$ Wd/kgU) |
| K | kelvin |
| MBq/g | megabecquerel per gram ($10^6$ Bq/g) |
| wt% | percentage by weight |
| MJ | megajoule ($10^6$ J) |
| MPa | megapascal ($10^6$ Pa) |
| MW | megawatt ($10^6$ W) |
| MW(e) | megawatt (electrical) |
| MW(th) | megawatt (thermal) |
| PBq | petabecquerel ($10^{15}$ Bq) |
| t | tonne |

## CONTRIBUTORS TO DRAFTING AND REVIEW

| | |
|---|---|
| Abou Alo, R.F.M. | Egyptian Atomic Energy Authority, Egypt |
| Adachi, H. | International Research Institute for Nuclear Decommissioning, Japan |
| Ashworth, G. | James Fisher Nuclear, UK |
| Budu, M. | SOSNY Research and Development Company, Russian Federation |
| Burakov, B.E. | Ioffe Institute, Russian Federation |
| Callaghan, A. | Sellafield Ltd, UK |
| Constantin, A. | International Atomic Energy Agency |
| Corkhill, C. | The University of Sheffield, UK |
| Ding, H. | The University of Sheffield, UK |
| Farjallah, N. | International Atomic Energy Agency |
| González-Espartero, A. | International Atomic Energy Agency |
| Hambley, D. | National Nuclear Laboratory, UK |
| Harnett, L. | The University of Sheffield, UK |
| Hyatt N. | The University of Sheffield, UK |
| Ipatov, V. | ROSATOM, Russian Federation |
| Kotoku T. | International Research Institute for Nuclear Decommissioning, Japan |
| Koyama, S. | Japan Atomic Energy Agency, Japan |
| Kuzmin, I. | SOSNY Research and Development Company, Russian Federation |
| Li, S. | International Atomic Energy Agency |
| Lönartz, M.I. | University of Bonn, Germany |
| McManniman, L. | International Atomic Energy Agency |
| Mitsugi, T. | Japan Atomic Energy Agency, Japan |
| Nakayoshi, A. | Japan Atomic Energy Agency, Japan |
| Novikov, A. | Chornobyl Nuclear Power Plant, Ukraine |
| Paterson, H.C. | Sellafield Ltd, UK |
| Pöml, P. | European Commission Joint Research Centre |
| Robinson, A. | Idaho National Laboratory, USA |
| Šandalová, S. | International Atomic Energy Agency |
| Shaat, M.K. | Egyptian Atomic Energy Authority, Egypt |
| Shiryaev, A.A. | A.N. Frumkin Institute of Physical Chemistry and Electrochemistry, Russian Federation |

| | |
|---|---|
| Soloviov V. | State Specialized Enterprise Chornobyl Nuclear Power Plant, Ukraine |
| Standring, P. | International Atomic Energy Agency |
| Szőke, L. | Paks Nuclear Plant, Hungary |
| Vlasova I. | Lomonosov Moscow State University, Russian Federation |
| Washiya, T. | Japan Atomic Energy Agency, Japan |
| Winston, P. | Idaho National Laboratory, USA |
| Yano, K. | Japan Atomic Energy Agency, Japan |
| Zubekhina, B.Y. | Japan Atomic Energy Agency, Japan |

**Research Coordination Meetings**

Vienna, Austria: 13–16 February 2017
Tomioka, Japan: 5–9 November 2018
Vienna, Austria: 29 August–2 September 2022

**Consultants Meetings**

Vienna, Austria: 7–9 December 2015
Vienna, Austria: 13–16 February 2017
Tomioka, Japan: 5–9 November 2018
Virtual Meeting: 5–9 October 2020
Vienna, Austria: 29 August–2 September 2022

IAEA
International Atomic Energy Agency

# CONTACT IAEA PUBLISHING

Feedback on IAEA publications may be given via the on-line form available at:
www.iaea.org/publications/feedback

This form may also be used to report safety issues or environmental queries concerning IAEA publications.

Alternatively, contact IAEA Publishing:

Publishing Section
International Atomic Energy Agency
Vienna International Centre, PO Box 100, 1400 Vienna, Austria
Telephone: +43 1 2600 22529 or 22530
Email: sales.publications@iaea.org
www.iaea.org/publications

Priced and unpriced IAEA publications may be ordered directly from the IAEA.

## ORDERING LOCALLY

Priced IAEA publications may be purchased from regional distributors and from major local booksellers.